REPORT DOCUMENTATION PAGE

AFRL-SR-BL-TR-01-

0112

1. AGENCY USE ONLY (Leave blank)	2. REPORT DATE	3. REPORT TYPE AN
	Jan. 15, 2001	Final Technical Report: Jul 31, 1997 to Sep 30, 2000

4. TITLE AND SUBTITLE
"AASERT: Student Training Program in Rayleigh Imaging of Mach 8 Boundary Layer Flow Around An Elliptic Cone Body"

5. FUNDING NUMBERS
AASERT #F49620-97-1-0484

6. AUTHOR(S)
Prof. Richard B. Miles

7. PERFORMING ORGANIZATION NAME(S) AND ADDRESS(ES)
Princeton University
Dept. Mechanical & Aerospace Engrg.
Olden St.
Princeton, NJ 08544

8. PERFORMING ORGANIZATION REPORT NUMBER

9. SPONSORING / MONITORING AGENCY NAME(S) AND ADDRESS(ES)
AFOSR/NA
801 NorthRandolph St.
Room 732
Arlington, VA 22203-1977

10. SPONSORING / MONITORING AGENCY REPORT NUMBER

11. SUPPLEMENTARY NOTES

12a. DISTRIBUTION / AVAILABILITY STATEMENT
Approved for public release; distribution is unlimited

AIR FORCE OFFICE OF SCIENTIFIC RESEARCH (AFOSR)
NOTICE OF TRANSMITTAL DTIC. THIS TECHNICAL REPORT
HAS BEEN REVIEWED AND IS APPROVED FOR PUBLIC RELEASE
LAW AFR 190-12. DISTRIBUTION IS UNLIMITED.

12b. DISTRIBUTION CODE

13. ABSTRACT *(Maximum 200 Words)*

Since the original parent grant expired two years ago, the work has been done in close association with our on-going program on "Microwave-Driven Air Plasma Studies for Drag Reduction and Power Extraction in Supersonic Air (AFOSR Grant #F49620-00-1-0034)," as well as research aspects associated with the "Radiatively-Driven, Hypersonic Wind Tunnel" effort. The MHz-rate imaging on an elliptic cone body at Mach 8 reached completion this year with the graduation of Mark Huntley, a student supported by the AASERT program, and Pingfan Wu, a student associated with that effort but supported with other funds because of his non-citizenship. Brendan McAndrew and Robert Murray developed a microwave-coupled Mach 3 wind tunnel under AASERT program support, and they are using that facility to study air plasmas in high-speed flow. Vincent Chiravalle is expanding the plasma concept to examine potential for building compact, high specific, impulse thrusters as part of the plasma effort. Robert Anderson, who finished his Ph.D. this past summer, developed modeling for the Radiatively-Driven, Hypersonic Wind Tunnel effort, and Kumar Raman, who recently completed his Masters' Degree, made measurements of boundary layer growth and heat transfer in high Reynolds' number, real-gas, supersonic flow.

14. SUBJECT TERMS
Hypersonic flow, Rayleigh Imaging, Transition

15. NUMBER OF PAGES
5 plus 4 Appendices

16. PRICE CODE

17. SECURITY CLASSIFICATION OF REPORT	18. SECURITY CLASSIFICATION OF THIS PAGE	19. SECURITY CLASSIFICATION OF ABSTRACT	20. LIMITATION OF ABSTRACT
Unclassified	Unclassified	Unclassified	UL

FINAL TECHNICAL REPORT

AFOSR AASERT GRANT #F49620-97-1-0484

"STUDENT TRAINING PROGRAM IN RAYLEIGH IMAGING OF MACH 8 BOUNDARY LAYER FLOW AROUND AN ELLIPTIC CONE BODY"

Richard B. Miles
Department of Mechanical & Aerospace Engineering
Princeton University
Princeton, NJ 08544

January 15, 2001

ABSTRACT

Since the original parent grant expired two years ago, the work has been done in close association with our on-going program on "Microwave-Driven Air Plasma Studies for Drag Reduction and Power Extraction in Supersonic Air (AFOSR Grant #F49620-00-1-0034)," as well as research aspects associated with the "Radiatively-Driven, Hypersonic Wind Tunnel" effort. The MHz-rate imaging on an elliptic cone body at Mach 8 reached completion this year with the graduation of Mark Huntley, a student supported by the AASERT program, and Pingfan Wu, a student associated with that effort but supported with other funds because of his non-citizenship. Brendan McAndrew and Robert Murray developed a microwave-coupled Mach 3 wind tunnel under AASERT program support, and they are using that facility to study air plasmas in high-speed flow. Vincent Chiravalle is expanding the plasma concept to examine potential for building compact, high specific, impulse thrusters as part of the plasma effort. Robert Anderson, who finished his Ph.D. this past summer, developed modeling for the Radiatively-Driven, Hypersonic Wind Tunnel effort, and Kumar Raman, who recently completed his Masters' Degree, made measurements of boundary layer growth and heat transfer in high Reynolds' number, real-gas, supersonic flow.

A. DISCUSSION

The major contributions of the students associated with the AASERT program are reflected in the publications and theses which have been submitted to date. Appendix I includes publications associated with the original parent grant for this program, which was imaging transitional flow around elliptic cone bodies in a Mach 8 flow. This work used the recently developed pulse-burst laser system to capture transitional structures at a variety of Reynolds numbers. Images were taken at 500,000 frames per second, and provided, for the first time, a clear indication of the transition mechanism on these bodies. Papers included in Appendix I are:

APPENDIX I: Mach 8 Flow Fields

1. M.L. Baumgartner, P.J. Erbland, M.R. Etz, A. Yalin, B.K. Muzas, A.J. Smits, W.R. Lempert, and R.B. Miles, *"Structure of a Mach 8 Turbulent Boundary Layer,"* Paper #AIAA-97-0765, AIAA 35th Aerospace Sciences Meeting & Exhibit, Reno, NV., Jan. 6-10, 1997.

2. W.R. Lempert, P.F. Wu, and R.B. Miles, "Filtered Rayleigh Scattering Measurements Using a MHz-Rate, Pulse-Burst Laser System," Paper #AIAA-97-0500, AIAA 35th Aerospace Sciences Meeting & Exhibit, Reno, NV., Jan. 6-10, 1997.

3. P.J. Erbland, M.L. Baumgartner, A.P. Yalin, M.R. Etz, B. Muzas, W.R. Lempert, A.J. Smits, and R.B. Miles, *"Development of Planar Diagnostics for Imaging Mach Flow Fields Using Carbon Dioxide and Sodium Seeding,"* Paper #AIAA-97-0154, 35th Aerospace Sciences Meeting & Exhibit, Reno, NV, Jan. 6-10, 1997.

4. P.J. Erbland, **R. Murray**, M.R. Etz, **M. Huntley**, and R.B. Miles, *"Imaging the Evolution of Turbulent Structures in a Hypersonic Boundary Layer,"* Paper #AIAA-99-0769, 37th AIAA Aerospace Sciences Meeting & Exhibit, Reno, NV, Jan. 11-14, 1999.

5. P. Wu and R.B. Miles, *"MHz-Rate Visualization of Separation Shock Wave Structure,"* Paper #AIAA-2000-0647, AIAA 38th Aerospace Sciences Meeting & Exhibit, Reno, NV., Jan. 10-13, 2000.

6. **M.B. Huntley**, P. Wu, R.B. Miles, and A.J. Smits, *"MHz Rate Imaging of Boundary Layer Transition on Elliptic Cones at Mach 8,"* Paper #AIAA-00-0379, AIAA 38th Aerospace Sciences Meeting & Exhibit, Reno, NV, Jan. 10-13, 2000.

7. P. Wu, W.R. Lempert, and R.B. Miles, *"Megahertz Pulse-Burst Laser and Visualization of Shock Wave/Boundary Layer Interaction,"* AIAA J, Vol. 38, No. 4, April 200, pp. 672-679.

8. **M. Huntley** and A. Smits, *"Transition Studies on an Elliptic Cone in Mach 8 Flow Using Filtered Rayleigh Scattering,"* Eur. J. Mech. B-Fluids, Vol. 19, (2000), pp. 695-706.

9. P.J. Erbland, D.P. Rizzetta, and R.B. Miles, "Numerical and Experimental Investigation of CO_2 Condensate Behavior in Hypersonic Flow," Paper #AIAA-2000-2379, 21st AIAA Aerodynamic Measurement Technology and Ground Testing Conference, Denver, CO, June 19-22, 2000.

10. B. Auvity, M. Etz, **M. Huntley**, P. Wu, and A.J. Smits, *"Control of Hypersonic Boundary Layers by Helium Injection,"* Paper #AIAA-2000-2322, AIAA Fluids 2000 Conference, Denver, CO, June 19-22, 2000.

11. R.B. Miles, A.J. Smits, M.B. Huntley, P. Wu, and R. Tolboom, "Three-Dimensional Imaging of Hypersonic Flow at MHz-Rate," Paper #AIAA-2001-0846, 39th AIAA Aerospace Sciences Meeting & Exhibit, Reno, NV., Jan. 8-11, 2001.

B. MICROWAVE-DRIVEN AIR PLASMA STUDIES

Appendix II incorporates papers associated with the Microwave-Driven Air Plasma program. The major focus of this work has been the development of the new microwave-coupled, Mach 3 wind tunnel facility which is now being used to study plasma effects in supersonic flow. This facility is coupled to a microwave supply that can operate in the pulsed mode at 50 kW, or in a continuous mode at 7 KW. Microwaves are coupled into the flow along the centerline through dielectric nozzle blocks and resonant to produce a high microwave field in the test region. This work reflects the contributions of Brendan McAndrew and Robert Murray and is an on-going research project.

APPENDIX II: Microwave-Driven Air Plasma

1. **B. McAndrew**, P. Barker, and R.B. Miles, *"Development of a Supersonic Plasma Wind Tunnel,"* Paper #AIAA-2000-0533, AIAA 38th Aerospace Sciences Meeting & Exhibit, Reno, NV, Jan. 10-13, 2000.

2. S.O. Macheret, Yu. Z. Ionikh N.V. Chernysheva, A.P. Yalin, L. Martinelli, **B. McAndrew**, P.F. Barker, M.N. Shneider, and R.B. Miles, 2nd Workshop on Magneto and Plama Aerodynamics for Aerospace Application*"Shock Propagation in Weakly Ionized Gases and Plasma Control of High-Speed Flows,"*, Russian Academy of Sciences, Moscow, Russia, April 5-7, 2000.

C. HIGH IMPUSE PLASMA THRUSTERS

The potential for using microwave energy addition into supersonic flow is currently being explored as an approach to augment conventionally-driven microwave propulsion concepts. This work is being conducted by Vince Chiravalle under the joint oversight of Prof. Edgar Choueiri. To-date, the major contributions have been the development of microwave-coupled fluid flow models that allow the prediction of the dynamics of the microwave-driven discharge and its impact on the thrust. Papers associated with this work are included in Appendix III, and, again, represent an on-going research effort.

APPENDIX III: Microwave Energy Addition

1. **V.P. Chiravalle**, R.B. Miles, and E.Y. Choueiri, *"Laser Propulsion Using a Molecular Absorber,"* Paper #AIAA-98-3932, 34th AIAA/ASME/SAE/ASEE Joint Propulsion Conference & Exhibit, Cleveland, OH, July 13-15, 1998.

2. **V.P. Chiravalle,** R.B. Miles, and E.Y. Choueiri, "Numerical Simulation of Microwave-Sustained Supersonic Plasmas for Application to Space Propulsion," Paper #AIAA-01-0962, 39th AIAA Aerospace Sciences Meeting & Exhibit, Reno, NV, Jan. 8-11, 2001.

D. RADIATIVELY-DRIVEN, HYPERSONIC WIND TUNNEL PROGRAM

The Radiatively-Driven, Hypersonic Wind Tunnel (RDHWT) Program is a large-scale effort supported under the Arnold Engineering Development Center and seeks to develop a new concept for hypersonic ground test facilities based on the addition of energy into the supersonic portion of the flow. The impact of this is to permit the temperature in the plenum to be reduced, extending run times from milliseconds to seconds, and reducing the chemical decomposition of air. Both Robert Anderson and Kumar Raman have been jointly supported on this research effort by Prof. Garry Brown, and partially supported through the AASERT. In particular, Robert Anderson has developed a sophisticated series of models based on the Navier-Stokes flow solver, coupled to a real-gas equation-of-state, and incorporating ray tracing. These models have allowed the RDHWT program to predict the performance of various energy deposition configurations and compare experimental measurements with those predictions. Kumar Raman has been involved in studying transport behavior associated with high pressure, real-gas supersonic flow. In the RDHWT, an exceptionally high pressure is required in the plenum (>20,000 atm), so real-gas phenomena play an important role in fluid and transport physics. Of particular concern is the development of the boundary layer and the rate of heat transfer to the wall. Kumar Raman conducted a series of experiments to measure boundary layer growth and heat transfer at Reynolds numbers approaching the Reynolds numbers associated with the full-scale facility. These were achieved by using pressures on the order of 2000 atm, at or close to room temperature, in a blow-down facility located at Princeton's School of Engineering. That work, again, represents an on-going effort and papers associated with it are included in Appendix IV.

APPENDIX IV: Radiatiely-Driven, Hypersonic Wind Tunnel

1. P. Barker, J. Grinstead, A. Morgan, **R. Anderson**, P. Howard, G. Brown, R. Miles, R. Lipinski, K. Reed, G. Pena, L. Schneider, *"Radiatively-Driven Wind Tunnel Experiment with a 30 kW Electron Beam,"* Paper #AIAA-99-0688, 37th AIAA Aerospace Sciences Meeting and Exhibit, Reno, NV. Jan. 11-14, 1999.

2. **R.W. Anderson**, G.L. Brown, and R.B. Miles, *"Performance Characterization of a Radiativley Driven Hypersonic Wind Tunnel,"* Paper #AIAA-99-0822 37th AIAA Aerospace Sciences Meeting & Exhibit, Reno, NV, Jan. 11-14, 1999.

3. P. Barker, J. Grinstead, P. Howard, **R. Anderson,** G. Brown, R. Miles, R. Lipinski, G. Pena, L. Schneider, R. Howard, *"A 150 kW Electron Beam Heated, Radiatively-Driven Wind Tunnel Experiment,"* Paper #AIAA-2000-0159, 38th Aerospace Sciences Meeting & Exhibit, Jan. 10-13, 2000, Reno, NV.

4. **K. Raman, R.W. Anderson,** G.L. Brown, R.B. Miles, and M. Costantino, *"An Ultra-High Pressure, Ultra-High Reynolds Number, Blow-Down Wind Tunnel: Design and Preliminary Experiments,"* Paper #AIAA-2000-0534, 38th AIAA Aerospace Sciences Meeting and Exhibit, Reno, NV, Jan. 10-13, 2000.

5. P. Barker, P. Howard, **R. Anderson**, R. Miles, G. Brown, R. Lipinski, G. Pena, J. Grinstead, and R. Howard, "Proof-of-Principle Energy Addition Experiments for the REDHWT/MARIAL II Hypersonic Wind Tunnel," Paper #AIAA-2000-2276, 21st AIAA Advanced Measurement Technology and Ground Testing, 31st AIAA Plasmadynamics and Lasers, 34th AIAA Thermophysics, Fluids 2000 Conferences, Denver, CO, June 19-22, 2000.

6. **R.W. Anderson**, G.L. Brown, and R.B. Miles, *"Performance Models and Predictions for the RDHWT/MARIAH II Hypersonic Wind Tunnel,"* Paper #AIAA-2000-2274, 21st AIAA Aerodynamic Measurement Technology and Ground Testing Conference, Denver, CO, June 19-22, 2000.

APPENDIX I: Mach 8 Flow Fields

1. M.L. Baumgartner, P.J. Erbland, M.R. Etz, A. Yalin, B.K. Muzas, A.J. Smits, W.R. Lempert, and R.B. Miles, *"Structure of a Mach 8 Turbulent Boundary Layer,"* Paper #AIAA-97-0765, AIAA 35th Aerospace Sciences Meeting & Exhibit, Reno, NV., Jan. 6-10, 1997.

2. W.R. Lempert, P.F. Wu, and R.B. Miles, "Filtered Rayleigh Scattering Measurements Using a MHz-Rate, Pulse-Burst Laser System," Paper #AIAA-97-0500, AIAA 35th Aerospace Sciences Meeting & Exhibit, Reno, NV., Jan. 6-10, 1997.

3. P.J. Erbland, M.L. Baumgartner, A.P. Yalin, M.R. Etz, B. Muzas, W.R. Lempert, A.J. Smits, and R.B. Miles, *"Development of Planar Diagnostics for Imaging Mach Flow Fields Using Carbon Dioxide and Sodium Seeding,"* Paper #AIAA-97-0154, 35th Aerospace Sciences Meeting & Exhibit, Reno, NV, Jan. 6-10, 1997.

4. P.J. Erbland, **R. Murray**, M.R. Etz, **M. Huntley**, and R.B. Miles, *"Imaging the Evolution of Turbulent Structures in a Hypersonic Boundary Layer,"* Paper #AIAA-99-0769, 37th AIAA Aerospace Sciences Meeting & Exhibit, Reno, NV, Jan. 11-14, 1999.

5. P. Wu and R.B. Miles, *"MHz-Rate Visualization of Separation Shock Wave Structure,"* Paper #AIAA-2000-0647, AIAA 38th Aerospace Sciences Meeting & Exhibit, Reno, NV., Jan. 10-13, 2000.

6. **M.B. Huntley**, P. Wu, R.B. Miles, and A.J. Smits, *"MHz Rate Imaging of Boundary Layer Transition on Elliptic Cones at Mach 8,"* Paper #AIAA-00-0379, AIAA 38th Aerospace Sciences Meeting & Exhibit, Reno, NV, Jan. 10-13, 2000.

7. P. Wu, W.R. Lempert, and R.B. Miles, *"Megahertz Pulse-Burst Laser and Visualization of Shock Wave/Boundary Layer Interaction,"* AIAA J, Vol. 38, No. 4, April 200, pp. 672-679.

8. **M. Huntley** and A. Smits, *"Transition Studies on an Elliptic Cone in Mach 8 Flow Using Filtered Rayleigh Scattering,"* Eur. J. Mech. B-Fluids, Vol. 19, (2000), pp. 695-706.

9. P.J. Erbland, D.P. Rizzetta, and R.B. Miles, "Numerical and Experimental Investigation of CO_2 Condensate Behavior in Hypersonic Flow," Paper #AIAA-2000-2379, 21st AIAA Aerodynamic Measurement Technology and Ground Testing Conference, Denver, CO, June 19-22, 2000.

10. B. Auvity, M. Etz, **M. Huntley**, P. Wu, and A.J. Smits, *"Control of Hypersonic Boundary Layers by Helium Injection,"* Paper #AIAA-2000-2322, AIAA Fluids 2000 Conference, Denver, CO, June 19-22, 2000.

11. R.B. Miles, A.J. Smits, M.B. Huntley, P. Wu, and R. Tolboom, "Three-Dimensional Imaging of Hypersonic Flow at MHz-Rate," Paper #AIAA-2001-0846, 39th AIAA Aerospace Sciences Meeting & Exhibit, Reno, NV., Jan. 8-11, 2001.

AIAA 97-0765
Structure of a Mach 8 Turbulent Boundary Layer

M.L. Baumgartner, P.J. Erbland*,
M.R. Etz, A. Yalin, B.K. Muzas,
A.J. Smits, W.R. Lempert, and R.B. Miles
Princeton University
Department of Mechanical and Aerospace Engineering
Princeton, New Jersey 08544

*Wright Laboratory
Aeromechanics Division (WL/FIMA)
WPAFB, OH 45433

35th Aerospace Sciences Meeting & Exhibit
January 6-10, 1997 / Reno, NV

Structure of a Mach 8 Turbulent Boundary Layer

Mark L. Baumgartner*, Peter J. Erbland†, Michael R. Etz‡
Azer Yalin, Brian K. Muzas§
Alexander J. Smits,¶ Walter R. Lempert‖ and Richard B. Miles**

Department of Mechanical and Aerospace Engineering
Princeton University, Princeton, New Jersey 08544-0710

Abstract

Preliminary measurements of the effects of increasing Mach number on the structure of turbulent boundary layers are presented. The data were obtained using a Mach 2.5 pilot tunnel facility and a new Mach 8 boundary layer facility. The principal diagnostic technique was planar Rayleigh scattering. The results shed some light on the effects of Mach and Reynolds number on outer layer intermittency.

1 Introduction

It is clear that any comparisons between subsonic and supersonic boundary layers must take into account gradients in Mach number, as well as variations in fluid properties, which may be strong enough to lead to unexpected physical phenomena. Intuitively, we expect to see significant dynamical differences between subsonic and supersonic boundary layers, but it appears that many of these differences can be explained by simply accounting for the fluid-property variations that accompany the temperature variation, as would be the case in a heated incompressible boundary layer.

> "The dominating factor in the compressible turbulent-boundary layer problem is apparently then the effect of high temperature on the velocity profile near the wall and therefore on the shear stress. This latter observation was first advanced by von Kármán in 1935 but has been somewhat neglected in favor of interpolation formulae or of elaborate generalizations of the mixing length hypothesis." (Part I of [1]).

This suggests a rather passive role for the density differences in these flows, most clearly expressed by Morkovin's Hypothesis [2], in that the dynamics of a compressible boundary layer follow the incompressible pattern closely, as long as the Mach number associated with the fluctuations remains small. We can interpret that conclusion to mean that the fluctuating Mach number, M', remains small, where M' is the *rms* perturbation of the instantaneous Mach number from its mean value, taking into account the fact that both the velocity and the sound speed vary with time. If the fluctuating Mach number approaches unity at any point, we expect "true" compressibility effects such as shocklets, acoustic radiation, and the enhanced redistribution of energy by pressure fluctuations to become important. If we take $M' = 0.3$ as a threshold, we find that for zero-pressure-gradient adiabatic boundary layers at moderately high Reynolds numbers the freestream Mach number where compressibility effects become important for the turbulence behavior is about 4 or 5 (see Figure 1).

However, recent measurements in moderately supersonic flows ($M_e < 5$) have also indicated some interesting differences between turbulence in subsonic and supersonic boundary layers that do not seem to scale according to fluid-property variations. Differences in turbulence length and velocity scales, the intermittency of the outer layer, and the structure of the large-scale, shear-stress-containing motions have been observed, which may indicate that the turbulence dynamics are affected at a lower fluctuating Mach number than previously believed.

"True" compressibility effects, beyond the effects determined by fluid property variations, are usually described in terms of a Mach number representa-

*Student Member, AIAA
†Member, AIAA
‡Student Member, AIAA
§Student Member, AIAA
¶Associate Fellow, AIAA
‖Member, AIAA
**Member, AIAA

tive of the fluctuations. It is also possible that some of these apparent changes in the turbulence structure are due to Reynolds number effects, rather than Mach number effects. The characteristic Reynolds numbers encountered in high-speed flow cover a very large range, extending well beyond values of the Reynolds number typically found in the laboratory. Furthermore, the temperature gradients which are found in the boundary layer in supersonic flow lead to variations in Reynolds number across the layer in addition to the usual variation in the streamwise direction.

We will need to consider both incompressible and compressible flow scaling, to try to distinguish between Reynolds number dependencies and Mach number dependencies. In general, we will assume that Reynolds number variations carry over unchanged from incompressible to compressible flows. This assumption is not entirely justified, since changes in Mach and Reynolds numbers are closely coupled (for example, temperature gradients affect both parameters directly), and care must be taken in interpreting the data.

We present preliminary measurements of the effects of Mach and Reynolds number variations on the structure of turbulent boundary layers. The data were obtained at Princeton in a Mach 2.5 pilot tunnel facility and a new Mach 8 boundary layer facility using primarily non-intrusive diagnostic techniques, Planar Rayleigh Scattering imaging and Sodium Fluorescence. These techniques are described in detail by [3]. Only Rayleigh scattering images are presented here.

2 Mach 8 Facility

The tunnel is shown schematically in Figure 2. Briefly, the high pressure air supply is connected to the inlet of the heater assembly by a valve which expands the air from $3000psi$ ($20MPa$) to $1500psi$ (maximum) through $250psi$ (minimum) depending on the Reynolds number desired. After being heated, the air passes into the flow conditioning section and is then expanded through the nozzle to the design Mach number of 8. At the diffuser inlet, the flow accelerates briefly before being recompressed and then cooled to approximately ambient temperature in the heat exchanger. It then passes through the ejector system before exiting via a silencer outside. The inlet flow conditions are limited by the maximum pressure and temperature specified in the design of the heater assembly. The capacity of the air storage facility limits possible run times due to the large mass flow demands of the ejectors.

The components are described in somewhat more detail below. Additional details are given by [4].

The heater assembly was fabricated of $280ft$ ($83m$) of $2.5in$ NPS schedule 160 316L stainless steel pipe wound into a coil approximately $60in$ ($1.5m$) in diameter. In operation, the pipe is preheated electrically to the desired stagnation temperature at atmospheric pressure before the flow is turned on. The maximum air velocity in the heater piping is always less than $40m/s$. The coil takes approximately $24hr$ to heat to $1000F$ ($800K$) from room temperature. Two three-phase transformers in series (a $70kVA$ transformer and a custom-built $35kVA$ transformer) provide the voltage step-down ($480V$ primary, $25V$ secondary) to a rectifying circuit that in turn provides DC to the heater. The temperature is regulated using an Omega Model CN76163 temperature controller. After a typical run, $12h$ is needed to reheat the pipe. To minimize conductive heat transfer to the surroundings, the coil is supported by two insulated steel cradles; in addition, the coil and supports are housed in an insulating enclosure lined with firebrick and a $5in$ thick ceramic blanket. The enclosure is made of $1/8in$ thick steel and rests on a $3/8in$ thick plate which is supported $6in$ ($15cm$) above the floor.

The settling chamber has a circular cross-section. A 6° half-angle diffuser connects the heater outlet to the inlet of the settling chamber. The maximum velocity in the settling chamber is approximately $5m/s$. The chamber itself is constructed of $6in$ NPS schedule 160 stainless steel piping, and has an overall length of $18in$. The inside diameter of the settling chamber is matched smoothly with the diameter at the nozzle inlet.

The subsonic contraction upstream of the throat was designed to minimize the effects of adverse pressure gradients. Following the analysis of [5], two cubic functions were chosen for the contour of the contraction. The total length of the contraction was chosen to be $8.0in$ ($20cm$), giving a length-to-diameter ratio of 1.54. The length of the contraction is almost twice the minimum length recommended by [5] for the given inlet diameter. The length of the final design is approximately $55in$ ($1.4m$). The nozzle was constructed of three separate segments which were machined on a CNC lathe using 316L stainless steel. Each segment is approximately $18in$ long.

The nozzle downstream of the throat is based on an axisymmetric design in use at the Aircraft Division of Israeli Aircraft Industries (IAI) [6]. After expansion through the nozzle, the flow enters the test section. The nozzle gives a highly uniform Mach number distribution in the potential core region of the nozzle exit: the Mach number over the central $6in$ of the working section (diameter of $9in$) was measured to be 7.97 ± 0.15.

The test section is composed of two $9in$ ($23cm$)

inside diameter tubes, each $3.0ft$ ($91cm$) long. Four viewing ports in one of the sections enable flow diagnosis in two mutually orthogonal directions. The test section may be disassembled and rearranged to allow viewing of the flat plate along its entire length. The window extends over the midpoint of the viewing section, so that there is some overlap when the section is reversed. The small angle at which disturbances propagate at Mach 8 ($\approx 7°$) helps to minimize flow interference by the window cavities.

At the outlet of the test section, a 10° half angle axisymmetric diffuser acts to recompress and decelerate the flow. The flow first expands (as the cross-sectional area of the diffuser increases) before decelerating and being compressed through a complicated series of shocks. Subsonic deceleration then continues along the remaining length of the diffuser to the heat exchanger. The heat exchanger is designed to cool the air from approximately $1000F$ ($800K$) to $100F$ ($300K$) and uses a water-injection system, employing a series of eight nozzles placed about the circumference of the inlet.

The twin ejector system discharges to atmospheric pressure inside a concrete silencer located outside the building. The minimum design Reynolds number corresponds to a stagnation pressure of $400psia$ and at this operating condition a back pressure of about $0.8psi$ is needed to keep the tunnel started. The ejectors make use of the same high-pressure storage tanks that supply the tunnel. The mass flow used by the ejectors is about ten times the process mass flow; thus, the rate of air required to run the ejectors is the limiting factor in setting tunnel run times— 2 to 3 minute durations are typical. Because the ejectors mix the process flow with the ejector supply flow, they also serve as the last stage of the heat exchanger, bringing the flow temperature nearly back to ambient.

3 Rayleigh Scattering

The rapid development of laser-based diagnostics has made it possible to obtain instantaneous quantitative flow-field data, rather than point-wise data as obtained using hot-wire anemometry or LDV. One technique that has made considerable impact is Planar Rayleigh Scattering, first developed by [7]. Cross-sectional images of the air density can be obtained by direct Rayleigh scattering, and since the illumination is provided by a pulsed laser, the images are frozen in time. An example is given in Figure 3. The disadvantage of the method is that the presence of water in the air can have a strong effect on the interpretation of the image, even when the water concentration is extremely low (parts per million). Upstream of the nozzle, the water is in vapor form and its Rayleigh cross-section is smaller than air. However, as the flow expands through the nozzle, the water molecules can agglomerate into very small ice clusters, of the order of $30nm$ in diameter [8]. When the clusters are present in sufficient numbers, they can dominate the Rayleigh signal. Under these conditions, the images obtained in air give the density of the ice clusters, rather than the density of the air. The cluster density is a function of temperature, and it appears that there is a threshold temperature below which the cluster concentration is approximately constant, and above which the clusters rapidly disappear [9]. In the outer part of the layer shown in Figure 3, the particle density is still a measure of the air density, but as the wall is approached and the temperature increases the particles return to the vapor phase and the signal level drops significantly. There are two main consequences: resolution is lost near the wall (the level depends on the Mach number, the total temperature and the wall temperature), and strong shocks become visible as lines separating bright zones (low temperature) from dark zones (high temperature). If the Rayleigh signal was a true measure of the air density, then the signal levels should rise, not fall through the shock. These complications can be avoided by operating with pure gases such as nitrogen, or by operating at very low stagnation temperatures [10].

It still seems possible to obtain interesting results, even in the regime where ice clusters are a problem. As a flow visualization tool, Rayleigh scattering has given very useful insights into the outer layer structure of turbulent jets and boundary layers, and the structure of two- and three-dimensional shock wave boundary layer interactions. It might also be expected that spatial correlation measurements obtained using Rayleigh scattering should be less sensitive to the variable particle density, and the results obtained by [11] and [12] give results which compare very well with comparable hot-wire data.

A useful improvement in Planar Rayleigh Scattering is called Filtered Rayleigh Scattering (FRS). In FRS, a molecular filter is used to interrogate the Rayleigh signal, and by sweeping the laser over a range of frequencies it is possible to obtain, in a given plane, the flow velocity, density and temperature [14]. For flow visualization it has the attractive feature of allowing background suppression by using the molecular filter to eliminate the signal from the stationary wall which has zero Doppler-shift [15]. This is particularly useful for studying boundary layer flows, especially in low density flows such as those found in our Mach 8 facility.

4 Experiments

The boundary layer examined in this paper is classified as a hypersonic ($M = 8$), zero-pressure-gradient, cold wall ($T_w/T_{aw} = 0.7$), flat-plate boundary layer. The model used to generate the boundary layer had a $6in$ span and was $18.5in$ long. The surface finish of the model was $\approx 125\ \mu in$, considerably smaller than the viscous length scale characteristic of the flow ($\approx 0.003\ in$). The region of experimental interest extended in the streamwise direction from $x = 14.25in$ to $x = 17in$ (measured from the leading edge of the plate) and $1in$ to either side of the centerline in the spanwise direction.

Preliminary experimental surveys of the mean flow behavior indicated the presence of a transitional boundary layer in the region of interest. To trigger instabilities and to fix the point of transition near the leading edge, a two-dimensional (cylindrical) trip was mounted at $x = 2.3in$. The dimensions of the trip were chosen to be small enough to provide minimal flow intrusion, yet large enough to fully trip the layer. The trip diameter was $0.095in$, or about 30 times the viscous length scale at that location. The calculations used to determine the trip height can be found in [13].

Mean pitot pressure and temperature surveys were taken simultaneously in the boundary layer at a location $14.25in$ downstream of the leading edge. The surveys show a well-defined turbulent profile with small logarithmic and wake regions characteristic of a low Reynolds number turbulent boundary layer ($Re_\theta \approx 3500$). Figure 5 shows three profiles obtained in different runs, demonstrating both the character of the boundary layer and the repeatability of the experiment. The curves were scaled using the Clauser method.

The section on Rayleigh scattering described experiments in which scattering from water clusters was used to visualize the boundary layer structure in supersonic flows. In the Mach 8 facility, however, the extremely low freestream densities associated with hypersonic flows precluded the use of this technique. A new technique based on the scattering ability of CO_2 clusters was instead used. The static pressures and temperatures in the freestream are conducive to formation of clusters of CO_2 (provided there is a sufficient quantity of CO_2 in the supply stream), which can then be used to scatter laser light in the same manner as the water clusters in earlier experiments.

This visualization technique is discussed in detail in [3]; a brief overview is presented here. Liquid CO_2 is injected into the tunnel air supply just downstream of the control valve (and upstream of the heater coil). The CO_2 flow rate can be varied with a metering valve— for the data presented here, the volumetric flow rate of CO_2 was 0.5 gpm (corresponding to a CO_2 mass flow of $0.03kg/s$, or approximately 1% of the mass flow of air). The CO_2 stream and the air stream have ample time to mix as they flow through the heater coil (the coil has an L/D ratio of 1500).

As the flow expands in the nozzle the CO_2 condenses and precipitates as [what is assumed to be] sub-micron-sized particulates uniformly distributed throughout the freestream. These clusters of frozen CO_2 provide a very strong scattering signal when interrogated with a laser. As in the case of water clusters, the CO_2 clusters vaporize in the high-temperature regions of the boundary layer near the wall, but they provide a strong signal in the outer part of the layer and can be used to study the turbulent/non-turbulent interface.

The laser used to interrogate the flow was a Continuum high-power, Q-switched, injection-seeded, freqency-doubled Nd:YAG pulsed laser with pulse energies in the 300 mJ range [14]. The laser could be tuned to frequencies in the range from 520 nm to 550 nm, enabling the use of an iodine filter to eliminate the non-doppler-shifted signal scattered from the wall.

A survey of the boundary layer with 0.5 gpm CO_2 injection showed that the introduction of CO_2 into the supply stream has no discernable effect on the mean velocity profile (see Figure 5).

5 Results

An example of a cross-sectional Planar Rayleigh Scattering image of a Mach 2.5 flow was obtained by [7] and is given in Figure 4, which shows a horizontal slice at $y/\delta = 0.72$. The field of view is about 3δ across the flow and 2δ in the flow direction. The image has been processed so that the light regions represent low density turbulent fluid, interspersed with dark regions of higher density freestream fluid. The intermittency of the turbulent/non-turbulent interface is readily apparent.

Despite the success of Morkovin's Hypothesis, certain characteristics of high-speed turbulent flows cannot be explained by a simple density scaling. For example, there are suggestions that the intermittency profile is fuller than the corresponding subsonic profile. To study this question directly, [16] and [17] estimated the fractal dimension of the density interface. The results indicated a decrease with Mach number, where a representative value at Mach 2.9 was 1.2, compared with a typical value for a subsonic boundary layer of 1.35. This observation may be interpreted as a decrease in mixing across the turbulent/non-turbulent interface, and seems to support the observation that the level of intermit-

tency decreases with increasing Mach number.

A similar image for the Mach 8 boundary layer is shown in Figure 6. Here, the CO_2 technique described in the *Experiments* section was seeded into the flow upstream of the tunnel heater. The image shown in Figure 6 is a horizontal slice located at approximately $y/\delta = 0.74$. The field of view is about 2.3δ across the flow and 4δ in the flow direction; a $1\delta \times 1\delta$ square is shown for visual reference. Again, regions of high density freestream fluid appear as dark regions, and the regions of turbulent low-density fluid appear bright.

Interpreting the figure requires some care. The Mach number is considerably higher than in Figure 4, but the Reynolds number is lower. In fact, the Reynolds number based on freestream properties and momentum thickness is only about 3500. So the smooth appearance turbulent/non-turbulent interface may be attributed to low Reynolds number effects (a smaller range of scales), rather than the decrease in intermittency (and fractal dimension) anticipated for increasing Mach number. Comparisons with images obtained by [18] in a water channel using fluorescent dyes at $Re_\theta \approx 700$ show remarkable qualitative similarities (see Figure 7), suggesting again the role of Reynolds number rather than Mach number.

Further flow visualizations obtained in the Mach 8 facility are shown in Figures 8, 9, and 10. Figure 8 was obtained by passing the laser sheet vertically through the top window of the test section. Because the sheet actually impacts the plate, the laser power had to be decreased considerably resulting in a loss of contrast in the original images. Subsequent image processing was used to achieve the image quality shown in Figure 8. As in previous figures, a $1\delta \times 1\delta$ square is shown for visual reference.

Figure 9 is a montage showing images taken at various heights throughout the boundary layer. The images span almost the entire boundary layer, beginning from a y/δ of 0.132 ($y^+ \approx 25$) and extending away from the wall to a y/δ of 1.347 ($y^+ \approx 225$). Deep incursions of freestream fluid can be seen in the near-wall image and turbulent bulges are seen to extend well beyond the mean boundary layer edge in the images taken in the outer layer.

Figure 10 is a collection of nine images representative of the kinds of visualizations possible with the FRS technique. The images have been filtered and their contrast enhanced. The scale of each image is identical to the image in Figure 8.

Qualitatively, it is impossible to distinguish these compressible boundary layers from their incompressible counterparts. In order to make a quantitative comparison, the intermittency function was examined. Approximately 50 images identical to the ones shown in Figure 10 were processed line by line to find the fraction of turbulent fluid present at several heights in the boundary layer. A simple thresholding routine was used to determine whether or not a given pixel represented turbulent or non-turbulent fluid.

A threshold pixel value of 100 was chosen by visual comparison as the value best representing the cut-off point between turbulent and non-turbulent fluid. The threshold value was increased to 110 and decreased to 90 to ascertain the sensitivity of the images to threshold value. Threshold values beyond these limits were visually determined to misrepresent the turbulent/non-turbulent interfaces. In most of the images, however, the edge of the turbulent/non-turbulent interface is well-defined and so the intermittency is fairly insensitive to changes in image thresholding as seen in Figure 11.

The results from these preliminary calculations are shown in Figure 11 along with an incompressible curvefit from [25]. The Mach 8 data is fit extraordinarily well by the incompressible curvefit. Thus, there is preliminary quantitative evidence that the intermittency function may not decrease with an increase in Mach number as previously conjectured in [17] and [23].

6 Summary

Measurements of the effects of increasing Mach on the structure of turbulent boundary layers were presented using Rayleigh scattering visualization of density slices in the planes parallel and perpendicular to the wall. Differences due to Mach and Reynolds number were discussed, and indications are that the Reynolds number, not the Mach number, may play a strong role in the intermittency and fractal structure of the turbulent/non-turbulent interface.

The image data obtained from the Rayleigh scattering experiments is currently being correlated to determine average structure angle and length scales. Further details may be found in [13].

Acknowledgments

The support of AFOSR under Grants F49620-93-1-0427, F49620-93-1-0476 and F49620-93-1-0478 is gratefully acknowledged.

References

[1] D. Coles. Measurements in the boundary layer on a smooth flat plate in supersonic flow. *J.P.L. CalTech. Reports 20-69, 20-70, 20-71*, 1953.

[2] M.V. Morkovin. Effects of compressibility on turbulent flows. In A.J. Favre, editor, *Mécanique de la Turbulence*, pages 367–380. CNRS, 1962.

[3] P.J. Erbland, M.L. Baumgartner, A. Yalin, M.R. Etz, M.K. Muzas, R.B. Miles, W.R. Lempert, and A.J. Smits. Development of planar diagnostics for imaging Mach 8 flowfields using CO_2 and Na seeding. *35th AIAA Aerospace Sciences Meeting, Reno, NV*, 1997. To be presented.

[4] M.L. Baumgartner, A.J. Smits, T.A. Nau, and C.W. Rowley. A new hypersonic boundary layer facility. *AIAA Paper 95-0787*, 1995.

[5] J.H. Watmuff. Wind tunnel contraction design. In *Proceedings of the Ninth Australasian Fluid Mechanics Conference*, University of Auckland, NZ, 1986.

[6] M. Zilberman, J. Hefez, and M. Livne, 1990. Private communication.

[7] M.W. Smith, A.J. Smits, and R.B. Miles. Compressible boundary-layer density cross sections by UV Rayleigh scattering. *Optics Letters*, 14:916–918, 1989.

[8] P.P. Wegener and G.D. Stein. Light-scattering experiments and theory of homogeneous nucleation in condensing supersonic flow. *12th International Symposium on Combustion*, pages 1183–1191, 1968.

[9] T.A. Nau. Rayleigh scattering as a quantitative tool in compressible turbulent boundary layers. MSE Thesis, Princeton University, 1995.

[10] D.R. Smith, J. Poggie, W. Konrad, and A.J. Smits. Visualization of the structure of shock wave turbulent boundary layer interactions using Rayleigh scattering. *AIAA Paper 91-0651*, 1991.

[11] M.W. Smith. *Flow visualization in supersonic turbulent boundary layers.* Ph.D. Thesis, Princeton University, 1989.

[12] J. Poggie. *On the control of a compressible, reattaching shear layer.* Ph.D. Thesis, Princeton University, 1995.

[13] M.L. Baumgartner. Turbulence Structure in a Hypersonic Boundary Layer. Ph.D. Thesis, Princeton University, 1997.

[14] R.B. Miles, J.N. Forkey, and W.R. Lempert. Filtered Rayleigh scattering measurements in supersonic/hypersonic facilities. *AIAA Paper 92-3894*, 1992.

[15] J.N. Forkey, W.R. Lempert, S.M. Bogdonoff, and R.B. Miles. Volumetric imaging of supersonic boundary layers using filtered Rayleigh scattering background suppression. *AIAA Paper 94-0491*, 1994.

[16] K.R. Sreenivasan and A.W. Johnson, 1989. Private communication.

[17] J. Poggie. Quantitative flow visualization applied to the study of compressible turbulent flow. MSE Thesis, Princeton University, 1991.

[18] C. Delo and A.J. Smits. Visualization of the three-dimensional, time-evolving scalar concentration field in a low Reynolds number turbulent boundary layer. In R.M.C. So, C.G. Speziale, and B.E. Launder, editors, *Near-Wall Turbulent Flows.* Elsevier Science Publishers B. V., 1993.

[19] M. Eléna and J.P. Lacharme. Experimental study of a supersonic turbulent boundary layer using a laser Doppler anemometer. *Journal Mécanique Théorique et Appliquée*, 7:175–190, 1988.

[20] E.F. Spina and A.J. Smits. Organized structures in a compressible turbulent boundary layer. *Journal of Fluid Mechanics*, 182:85–109, 1987.

[21] F.K. Owen and C.C. Horstman. On the structure of hypersonic turbulent boundary layers. *Journal of Fluid Mechanics*, 53:611–636, 1972.

[22] A.J. Laderman and A. Demetriades. Mean and fluctuating flow measurements in the hypersonic boundary layer over a cooled wall. *Journal of Fluid Mechanics*, 63:121–144, 1974.

[23] E.F. Spina, A.J. Smits, and S.K. Robinson. The physics of supersonic turbulent boundary layers. *Annual Review of Fluid Mechanics*, 26:287–319, 1994.

[24] M.W. Smith and A.J. Smits. Visualization of the structure of supersonic turbulent boundary layers. *Experiments in Fluids*, 18:288–302, 1995.

[25] P.S. Klebanoff. Characteristics of turbulence in a boundary layer with zero pressure gradient. *NACA Rept. No. 1247*, 1955.

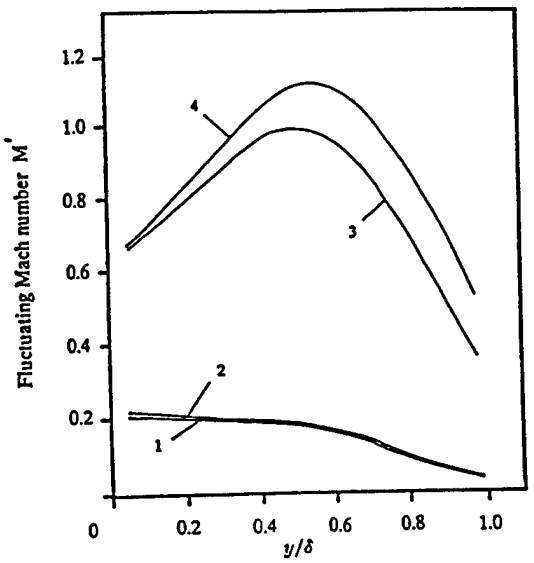

Figure 1: Fluctuating Mach number distributions (estimated). Flow 1: $M_e = 2.32$, $Re_\theta = 4,700$, adiabatic wall [19]; Flow 2: $M_e = 2.87$, $Re_\theta = 80,000$, adiabatic wall [20]; Flow 3: $M_e = 7.2$, $Re_\theta = 7,100$, $T_w/T_r = 0.2$ [21]; Flow 4: $M_e = 9.4$, $Re_\theta = 40,000$, $T_w/T_r = 0.4$ [22]. Figure from [23].

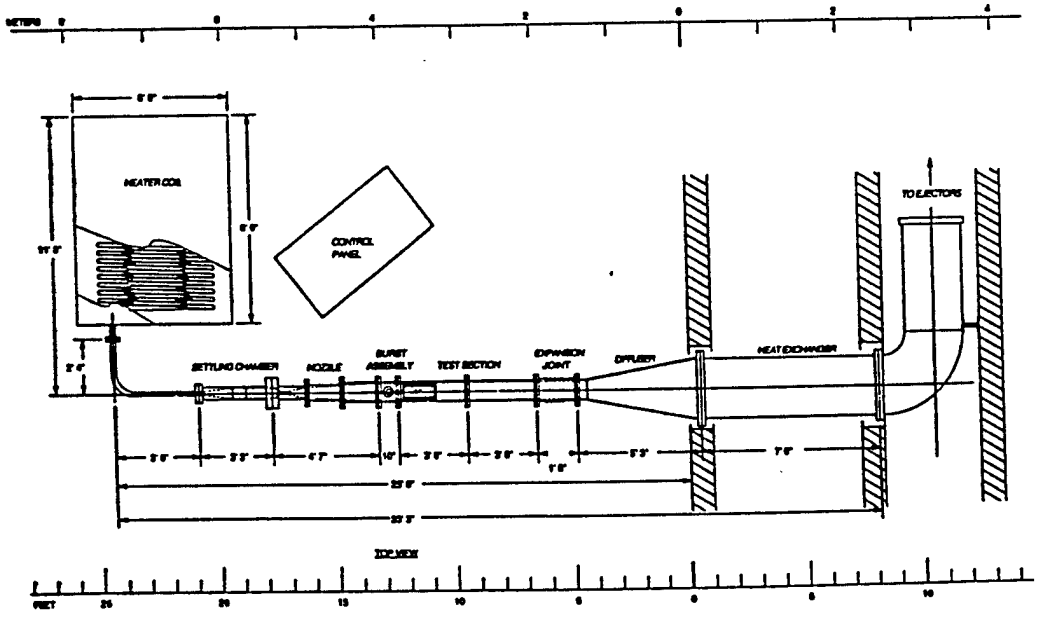

Figure 2: Schematic of the Hypersonic Boundary Layer Facility. The control valve is not shown in the drawing. The flow travels from left to right.

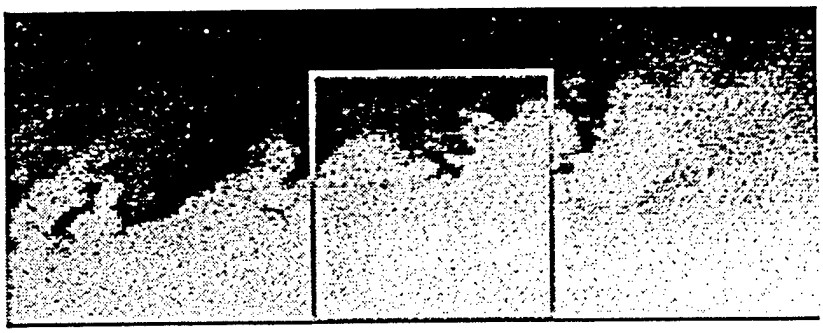

Figure 3: Flow visualization of supersonic turbulent boundary layer using Rayleigh scattering. Flow is from left to right. The freestream Mach number is 2.5, and Re_θ is about 25,000. Turbulent regions are light-colored; freestream regions are dark. Figure adapted from [24].

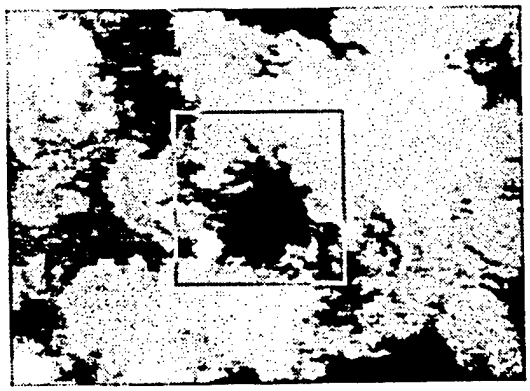

Figure 4: Rayleigh scattering image in a plane parallel to the wall at $y/\delta = 0.72$. The flow is from top to bottom. The field of view is about 3δ across the flow and 2δ in the flow direction. The Mach number is 2.5, and $Re_\theta = 25,000$. The figure has been modified to match the color scheme used in this paper. Original figure from [11].

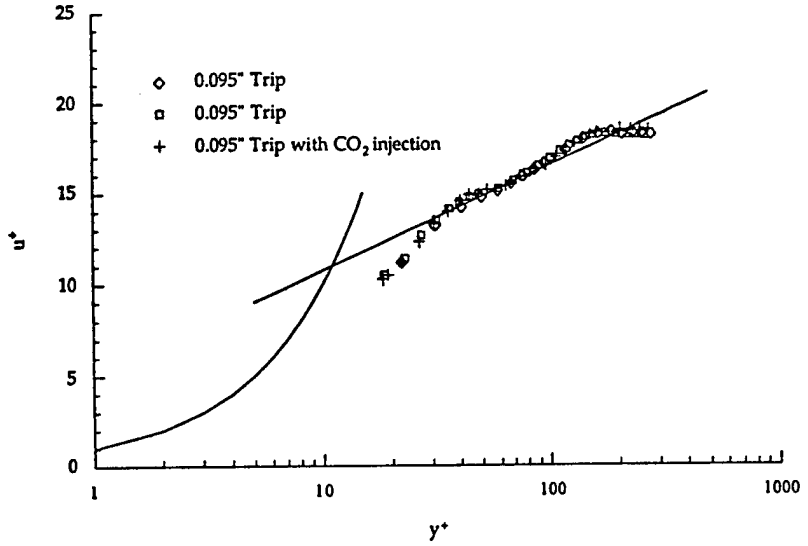

Figure 5: Non-dimensional velocity profiles for the studied boundary layer. The profiles were obtained both with and without CO_2 injection, demonstrating the character and repeatability of the boundary layer, as well as the negligible effect of adding CO_2 to the flow.

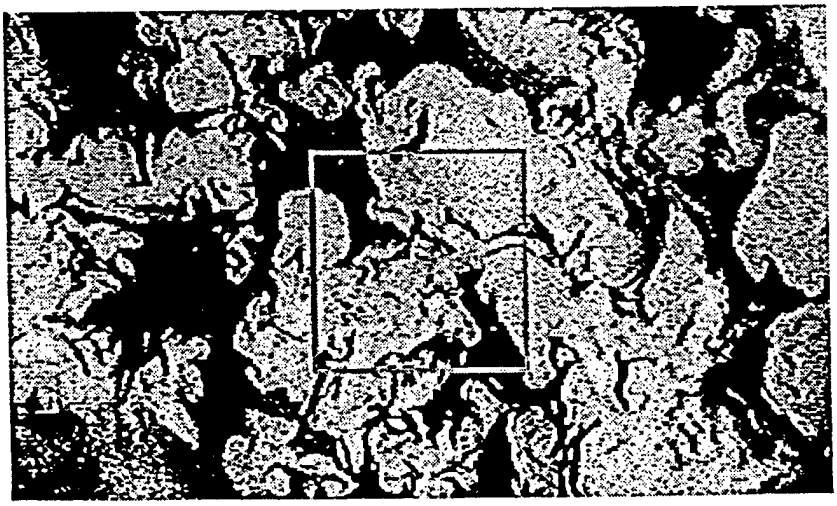

Figure 6: Flow visualization of a hypersonic turbulent boundary layer using Filtered Rayleigh Scattering in a plane parallel to the wall at $y/\delta = 0.72$. Flow is from left to right. The field of view is about 2.3δ across the flow and 4.0δ in the flow direction. The freestream Mach number is 8.0, and Re_θ is about 3500.

Figure 7: Flow visualization of a subsonic turbulent boundary layer using fluorescent dye in a water channel in a plane parallel to the wall at $y/\delta = 0.74$. Flow is from top to bottom. The field of view is about 3.2δ across the flow and 3.3δ in the flow direction. The freestream Mach number is 0, and Re_θ is about 700. Figure from [18].

Figure 8: Flow visualization of hypersonic turbulent boundary layer using Filtered Rayleigh Scattering in a plane perpendicular to the wall. Flow is from left to right and the wall is at the bottom of the image. The field of view is about 1.3δ up from the wall and 2.6δ in the flow direction. The freestream Mach number is 8.0, and Re_θ is about 3500.

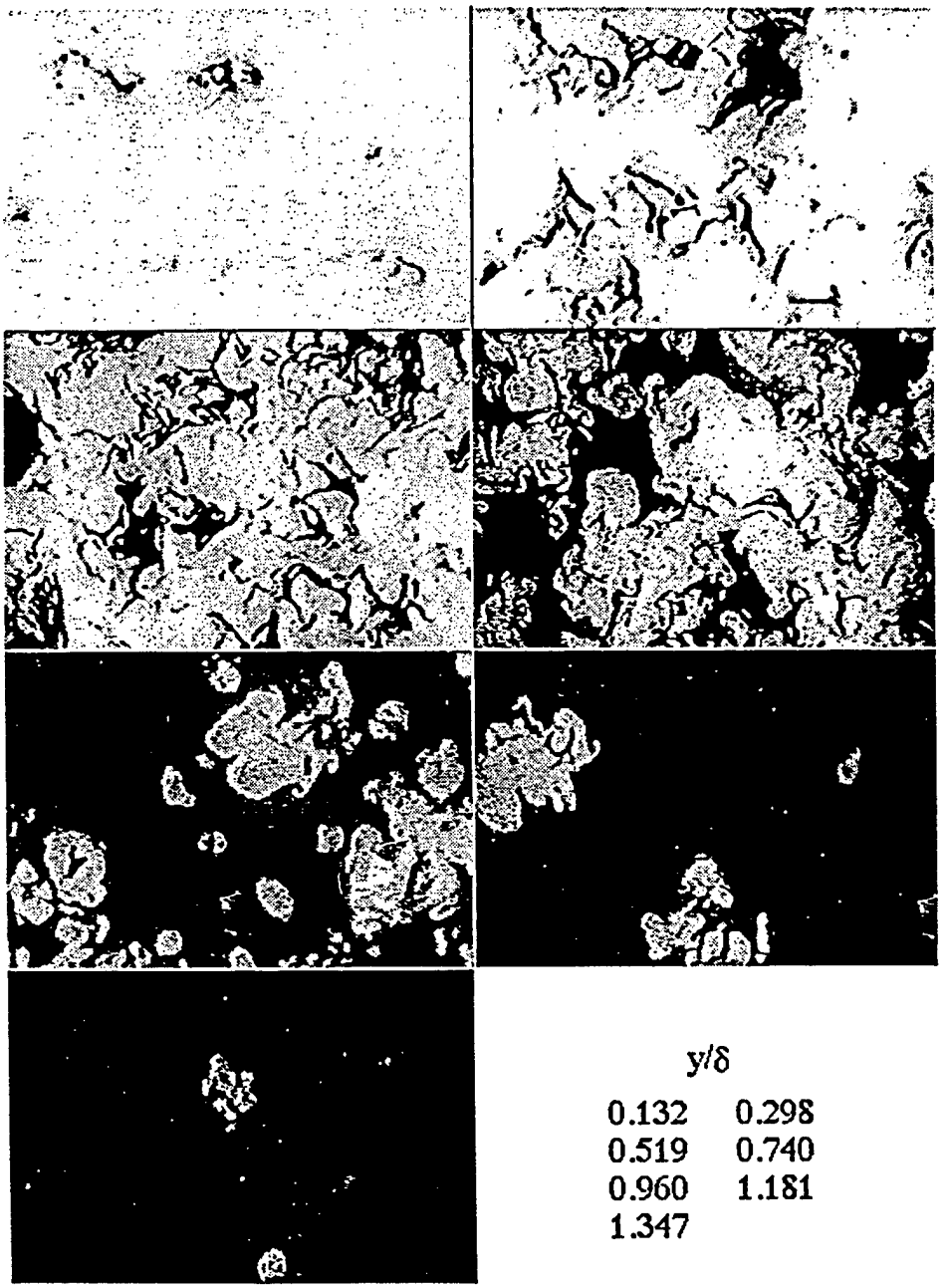

Figure 9: Flow visualizations of a hypersonic turbulent boundary layer using Filtered Rayleigh Scattering in planes parallel to the wall. The field of view in each image is about 2.3δ across the flow and 4.0δ in the flow direction. The freestream Mach number is 8.0, and Re_θ is about 3500.

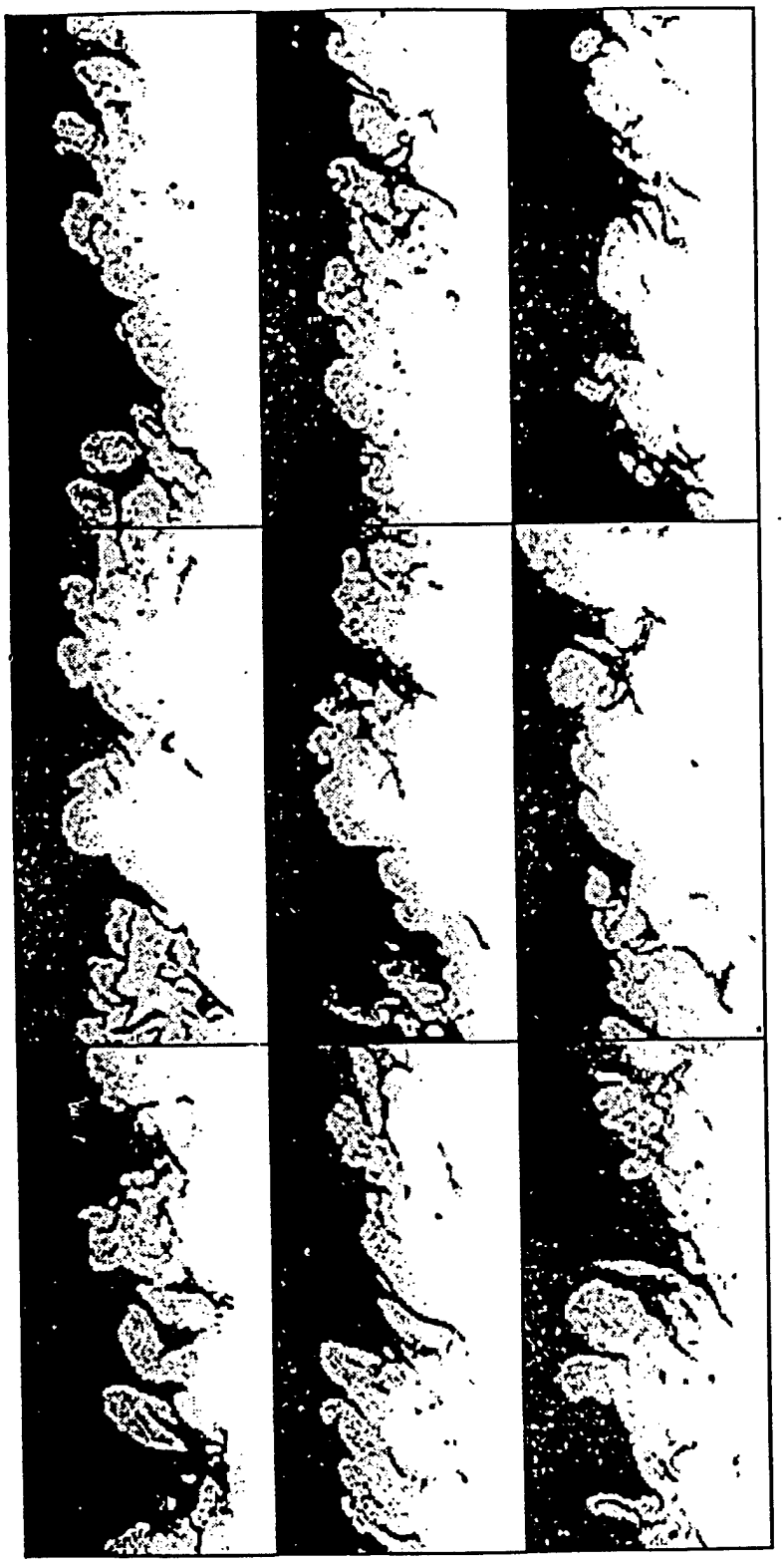

Figure 10: Flow visualizations of a hypersonic turbulent boundary layer using Filtered Rayleigh Scattering in a plane perpendicular to the wall. Flow is from left to right (image is shown in landscape) and the wall is at the bottom of each image. The field of view is about 1.3δ up from the wall and 2.6δ in the flow direction. The freestream Mach number is 8.0, and Re_θ is about 3500.

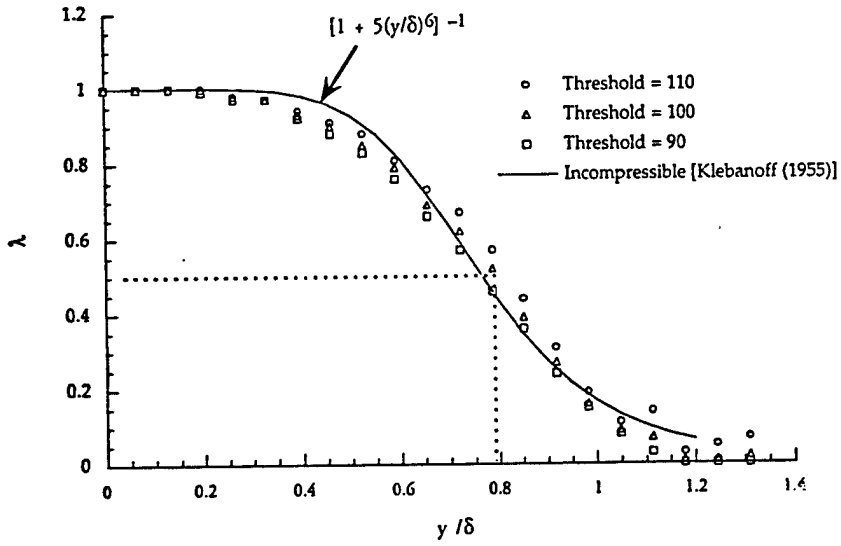

Figure 11: Intermittency function taken from approximately 50 images of the boundary layer similar to those in Figure 10. The composite length of the surveyed data set is over 100 δ. The dotted line indicates the location where $\lambda = 0.5$.

AIAA 97-0500

FILTERED RAYLEIGH SCATTERING MEASUREMENTS USING A MHz RATE PULSE-BURST LASER SYSTEM

W.R. Lempert, P-F. Wu, and R.B. Miles

PRINCETON UNIVERSITY
Dept. of Mechanical & Aerospace Engineering
Princeton, New Jersey 08544 U.S.A.

35th Aerospace Sciences Meeting & Exhibit
January 6-10, 1997 / Reno, NV

"FILTERED RAYLEIGH SCATTERING MEASUREMENTS USING A MHz RATE PULSE-BURST LASER SYSTEM"

W.R. Lempert,* P-F. Wu,† and R.B. Miles§

Department of Mechanical & Aerospace Engineering
PRINCETON UNIVERSITY
Princeton, New Jersey 08544 U.S.A.
609/258-2875

ABSTRACT

We present measurements of the spectral characteristics of a MHz rate, Nd:YAG pulse-burst laser system, with particular emphasis on data relevant to spectrally filtered scattering diagnostics which employ molecular iodine vapor filters. The time-averaged laser spectral profile is found to correspond quite well to that predicted from the Fourier transform of the observed temporal profile. The measured maximum extinction value of 5×10^{-5} for the second harmonic output is in good agreement with modeling predictions, based on a 10 cm path length iodine cell under typical operating conditions. Filtered images of time sequences of supersonic flow over a 14° wedge are also presented. The images clearly illustrate the unsteadiness of the oblique shock wave and the correlation of its dynamic behavior with large-scale turbulent boundary layer structure.

*Senior Research Scientist, Mechanical & Aerospace Engineering, Member AIAA.

†Graduate Student, Mechanical & Aerospace Engineering.

§Professor, Mechanical & Aerospace Engineering, Associate Fellow, AIAA.

1. INTRODUCTION

The ability to visualize time-evolving high speed flow is severely limited by the modest (order 10's-100's Hz) repetition rates, typical of high power laser systems. We have previously reported[1] a new high-speed imaging system capable of capturing a time sequence of up to 30 images at a maximum rate as high as 1 MHz. The system consists of a "pulse-burst" Nd:YAG laser and a framing CCD camera with integrated, on-chip storage. While it was not stressed in Ref. (1), the laser system has the additional feature that the spectral linewidth is exceedingly narrow, which presents the opportunity to perform spectrally resolved imaging using filtered scattering diagnostic techniques. Filtered scattering[2,3] refers to a class of diagnostic in which an atomic or molecular vapor filter is used to spectrally resolve flow field scattering which is Doppler shifted and/or thermally broadened. The technique has been applied to a wide variety of environments including supersonic jets[4,5] and inlet models,[6] mixing layers,[7] large-scale wind tunnels,[8] flow around automobiles,[9] and sooting flames.[10] Similar approaches have also been reported in the remote sensing community,[11,12] and have been proposed for supersonic inlet mass flux measurement.[13] A detailed discussion of the accuracy limits imposed by constraints of available imaging technology has been presented by McKenzie,[14] and the extension of the technique into the ultraviolet region of the spectrum has recently been presented by Finkelstein.[15]

Forkey[16] has recently presented a detailed measurement of the spectral characteristics of a typical injection-seeded Nd:YAG laser, in which it was shown that the central lasing frequency varies by as much as

+/- 50 MHz across the radial profile of the output beam, greatly affecting the apparent velocity field. In this paper, we present new results which characterize the spectral characteristics of the pulse-burst laser. In particular, measurements of the spectral profile are shown to compare well with the Fourier Transform of the temporal profile. Experimental attenuation of the pulsed second harmonic output in molecular iodine vapor was also measured and agreed well with predictions based on a recently presented iodine absorption model.[17] Finally, images are presented of a supersonic shockwave/boundary layer interaction in which the dynamics of shock unsteadiness and temporal correlation of its motion with large-scale turbulent boundary layer structure are clearly evident.

2. LASER SYSTEM OVERVIEW

A detailed description of the pulse-burst laser system has been given previously.[1] As illustrated in Fig. 1, it consists of the following six elements:

1. Monolithic, single-frequency, diode-pumped, cw Nd:YAG laser.
2. Four -Pass preamplifier #1.
3. Pulse slicer.
4. Two-pass preamplifier #2
5. Three-stage power amplifier chain.
6. Second harmonic crystal.

The single-frequency Nd:YAG laser is a Lightwave Electronics model 120-03, with cw power of approximately 20 mWatts. The output of this laser is polarization-coupled into preamplifier #1, which is a four-pass, 10 Hz repetition rate, flashlamp-pumped, 7 mm diameter by 110 mm long Nd:YAG rod. The net small signal, four-pass gain has been measured to be approximately 1500x, so that the output of preamplifier #1 is a single, approximately 60 microsecond duration, 30 Watt peak power pulse, repeated at a repetition rate of 10 Hz. This 60 microsecond pulse is formed into a "train" using a pulse slicer, custom built by Medox, Inc., Ann Arbor, Michigan. The pulse slicer consists of a pair of fast electro-optic Pockel cells, and is capable of creating a train of between 1 and 99 pulses, with minimum individual pulse duration of 10 nsec, and minimum inter-pulse period of 1 microsecond. The output of the pulse slicer is spatially filtered and double-passed through preamplifier #2. The net, double-pass gain is 20x, so that the output peak power is 600 Watts, corresponding to 12 microjoules for an individual, 20 nsec duration pulse. The power amplifier chain consists of three additional Nd:YAG rods, taken from a commercial laser system. The rods are 6.5, 8, and 9.5 mm diameter, respectively, and there is an optical isolator placed between power amplifiers #2 and #3. The peak gain of the individual stages has been measured to be 10, 10, and 8, respectively, resulting in an overall peak system gain of approximately 2.4×10^7. The corresponding energy is approximately 10 mJ for a single, 20 nsec duration pulse. The temporal evolution of the gain of the amplifier chain is illustrated in Fig. 2, which shows an oscilloscopic trace of a typical burst sequence consisting of 30, 20 nsec duration pulses, separated by 2 microseconds.

The final element of the laser system is the second harmonic generator. To date, we have obtained a maximum conversion efficiency of 10%, corresponding to a single pulse energy of approximately 1.0 mJ at the second harmonic wavelength of 0.532 microns. Preliminary measurements have suggested, however, that the conversion efficiency falls off at the trailing portion of the burst sequence. Figure 3 shows an oscilloscope trace of the fundamental (upper trace) and second harmonic (lower trace) outputs from a single, 30-pulse-burst sequence. This phenomenon has not yet been studied in detail, and its origin is unclear.

3. LASER SPECTRAL CHARACTERISTICS

a. Pulse Temporal Profile

An important feature of the pulse-burst system is that the spectral linewidth is exceedingly narrow. Since the cw, Nd:YAG master oscillator has a time-averaged linewidth of order 1 MHz, the individual pulses are predicted to have a time-average linewidth of order 50 MHz, based on the Fourier transform of a 20 nsec, rectangular temporal profile. ($\Delta\nu\Delta t = 0.88$ for a sinc^2/rectangle Fourier transform pair.)[18] Figure 4 shows a typical oscilloscope trace of a single fundamental pulse (upper trace), obtained with a fast (1 nsec rise time) silicon PIN photodiode. The pulse is approximately rectangular, with a full-width-at-half-maximum of approximately 16 nsec. (The apparent structure in the trailing edge of the pulse is due to "ringing" in the measurement and is not believed to be real.) While it is not obvious from Fig. 4, there is a small (order 1%) dc component to the output pulse due to the finite modulation depth of the pulse slicer. The lower trace in Fig. 4 shows the corresponding temporal profile at the second harmonic frequency. It can be seen that the pulse is also approximately rectangular, with a full-width-at-half-maximum of 14 nsec or approximately 10% less than that of the fundamental. It is worthwhile to point out that, in contrast to a Gaussian pulse, the temporal profile of the second harmonic of a perfectly rectangular pulse, assuming a simple intensity squared law for conversion efficiency, should be identical to that of the fundamental.

b. Pulse Spectral Profile

A 2 GHz, free spectral range, confocal Fabry-Perot spectrum analyzer (Burleigh model RC-46) was used to directly determine the spectral profile of the

fundamental output of the pulse-burst laser. For these measurements, the laser was operated at full gain, with a single pulse per burst, and the output attenuated with a combination of neutral density filters and front surface reflections from uncoated optical quartz flats. As illustrated in Fig. 5, the internal photodiode/mount assembly was removed from the etalon, and replaced with the same fast response time photodiode used to obtain the temporal traces of Fig. 4. The photodiode output was digitized with a commercial boxcar averager (Stanford Research Systems model SR 250) and the output recorded with a laboratory computer. For the data presented below, the boxcar was typically used to average the photodiode voltage over 30 laser shots. The wavelength of the cw master oscillator was slowly scanned (order 2 MHz/sec) by applying a computer generated voltage "staircase" to the input of the laser temperature controller, while holding the voltage to the etalon mirrors constant. (The laser, rather than the etalon, was tuned, because the etalon could not be scanned slowly enough to smoothly capture the profile of the pulsed laser). The tuning rate of the laser was calibrated by observing multiple Fabry-Perot orders as the laser was scanned. The observed scanning rate was 1.6 GHz/volt, and was assumed to be constant over the duration of the scan. The "effective" finesse of the etalon was obtained by identical spectral scans of the laser with the pulse slicer maintained in the "on" position. This produced a nominally 60 microsecond pulse, with corresponding Fourier Transform limited linewidth of 0.02 MHz, which is much less than the manufacturers specification of 1 MHz for the time mean linewidth of the cw master oscillator. The "effective" finesse is lower than the inherent (i.e., that due to reflectivity, etc.) finesse of the etalon due to slow, thermally induced drift in the central transmission wavelength, which occurs over the time scale of the spectral profile measurement. (order 1 minute). The "effective" finesse was measured to be approximately 100, corresponding to a spectral resolution of 2 MHz.

Figure 6 (dotted line) shows the time-averaged spectral profile of the fundamental output of the laser, corresponding to the same, nominally 16 nsec duration, pulse illustrated in Fig. 4. The relatively sharp spectral feature at line center is due to the dc temporal component, as discussed above. The central "lobe" of the pulsed component has a Full-Width-at-Half-Maximum (FWHM) linewidth of approximately 50 MHz, and weak side bands, characteristic of a sinc squared function, can just be discerned. [Note that $\text{sinc}^2(\upsilon)$ is a result of $I(t) = E(t)\,E^*(t)$.] Also shown in Fig. 6 is the discrete Fourier transform of the instantaneous temporal profile of Fig. 4a, convolved with the instrument function measured as described above. While the agreement is not perfect, note particularly the discrepancy in the relative magnitude of the side lobes, it is clear that the spectral profile is "approximately" Fourier transform limited. The discrepancy in the side lobe intensity has not been investigated in detail. Since the second harmonic conversion process is inherently non-linear, the side bands are expected to minimally impact iodine vapor-based filtered scattering diagnostics.

c. Iodine Cell Attenuation

Molecular iodine vapor extinction measurements have been performed in a manner similar to that described by Forkey.[17] The measurement is essentially a simple laser absorption experiment, except that a series of calibrated neutral density filters are used to attenuate the beam prior to spectral tuning into the resonance feature of the vapor. As the laser is tuned into the absorption band, the filters are sequentially removed, boosting the light level reaching the detector. In this way the dynamic range of the attenuation measurement can be increased beyond the limitations imposed by the A/D converter and the linear operating range of the photodiode. The actual experimental apparatus is similar to that shown in Fig. 5, except that the Fabry-Perot etalon is replaced by an iodine vapor cell. The vapor cell, described in detail previously,[17] was 10 cm in length, and operated with a side arm temperature of 313K, which was maintained to within +/- 0.1 K with a temperature controlled water bath. The corresponding iodine vapor pressure is approximately 1 torr.[19] Figure 7 shows a modeled absorption spectrum for the iodine cell over the full tuning range of the laser system. Extinction measurements were made using the strong feature, marked with an arrow, in the vicinity of 18788.5 cm^{-1} and previously referred to as iodine transition "A".[20] Figure 8 shows a typical result, where the laser has been slowly tuned over a range of approximately 2.5 GHz. The detected signal has been arbitrarily normalized in such a way as to set the apparent "transmission" equal to approximately 1 at the endpoints of the scan. At the approximate 1600 MHz point of the laser scan, a 200x neutral density filter was removed from the beam path, resulting in a large increase in signal reaching the detector. This signal decreases as the laser is further tuned into resonance, and a second, 20x filter is removed at the approximate 1800 MHz point. The process is reversed as the laser is tuned out of the iodine resonance. Figure 9 is a blow-up of the central 400 MHz of the experimental data (dotted line) from Fig. 8, overlaid with a modeling prediction (solid line) obtained using the computer code described in Ref. (17). In this case, the experimental data has been converted to absolute transmission by accounting for the attenuation of the neutral density filters. It can be seen that the experimental line center extinction is 5×10^{-5}, as compared to the modeled value of approximately 1.5×10^{-5}. It is important to note, however, that since the absorption is in the highly optically thick regime, it is only weakly dependent on

the actual absorption coefficient. This is most easily seen by noting that the extinction is given by:

$$I/I_0 = \exp\{-\sigma N l\} \quad (1)$$

where σ is the absorption cross-section, N the iodine number density, and l the cell path length. For a cell length of 10 cm, a discrepancy of approximately 10% in the product of σN is sufficient to account for the discrepancy between the measured and the predicted extinction. This is well within the combined uncertainty bounds.[17]

The agreement between the experimental and predicted maximum extinction is in contrast to results presented previously which employed a typical commercial injection-seeded laser system.[20,21] In that work, the maximum extinction measured was of the order of 500, as compared to modeling calculations which predicted as high as 10^{-6}. While the reason for the discrepancy was not known for certain, it was suggested that a laser linewidth significantly greater than the Fourier transform limit could be responsible. Although this has not been explored in detail, it is qualitatively consistent with recent work[16] in which an order 100 MHz variation in laser central frequency was observed across the profile of the second harmonic output beam. The difference between the two measurements appears to confirm the expected improvement in spectral performance inherent to pulsed amplification.

4. IMAGES OF SHOCK WAVE/BOUNDARY LAYER DYNAMICS

In order to demonstrate the ability to capture the dynamics of time-evolving, high speed flow phenomena, time sequences of planar images have been obtained of turbulent Mach 2.5 boundary flow over a 14° wedge. As illustrated in Fig. 10, the second harmonic output of the pulse-burst laser system was formed into an approximately 2 cm high by 100 micron thick sheet, which was incident to a laboratory scale, two-dimensional wind tunnel, at an angle of approximately 45° with respect to the free stream direction. A 14° wedge was attached to a wall of the tunnel at a location where the boundary layer thickness is approximately one third the total span. Images were obtained with the sheet oriented both perpendicular (streamwise view) and parallel (plan view) to the wedge. For the streamwise orientation, (illustrated in Fig. 10) the sheet was brought into the tunnel through a small slot, cut into the wedge at the flow centerline. In order to enhance the scattering signal, gaseous carbon dioxide was seeded into the plenum, which condensed downstream into a finely dispersed "fog" of order 100 nm diameter particles. The enhanced scattering resulting from the condensation more than compensates for the relatively low (order 1 mJ) available second harmonic pulse energy. In the warmer thermal boundary layer, the condensed carbon dioxide sublimes, resulting in very high image contrast. The scattering was captured at 90° to the sheet using a CCD framing camera described in Ref. (1). The CCD camera has a 30-image storage buffer built into the image sensor chip itself, and can frame at rates up to 1 MHz.

Figure 11 shows a typical sequence of nine streamwise view images. The images have been rotated with respect to the geometry of Fig. 10, so that the principal flow direction is from right-to-left. The time between images is 2 microseconds and the correlation of the "kink" in the oblique shock, which is formed in image 3, with the passage of a large-scale boundary layer structure, is clearly evident. Figure 12 shows a representative sequence of images obtained with the sheet incident parallel to the wedge, at a location near the upper edge of the boundary layer. The flow, also from right-to-left, is turned upward as it passes through the oblique shock formed by the wedge. Since the sheet is oriented parallel to the wedge, there appear to be large discontinuities in turbulent structure in the vicinity of the shock location. This is due to structures being turned into the sheet at the shock location. Again, the correlation of the dynamics of the shock with the motion of large-scale structure is readily apparent. (Note, in particular, images 5 - 9.)

The image sequences illustrated in Figs. 11 and 12 were obtained without the use of the molecular vapor filter, which is possible because of the inherently high contrast obtained from the carbon dioxide condensation. In order to demonstrate the potential of high frame rate filtered scattering, we have obtained image sequences, similar to those in Figs. 11 and 12, with the laser tuned to preferentially transmit regions of high/low velocity (i.e., large/small Doppler shift). The iodine filter was as described above (10 cm length, 40° cold tip temperature), and the laser was, again, tuned to the vicinity of the iodine "A" transition. Figure 13 shows three sets of six images each, obtained with a 2 microsecond interframe period. The images in the left column were obtained with the laser tuned far enough from resonance that the images are, effectively, unfiltered. Note that the scattering intensity immediately downstream of the shock, but above the boundary layer, is of the same magnitude as that of the free stream. The images in the center column were obtained with the laser tuned to preferentially transmit the high speed, free stream flow. In this case, the scattering immediately downstream of the shock is attenuated due to the lower flow velocity. Finally, in the images on the right, the laser has been tuned to preferentially transmit the lower velocity fluid, downstream of the shock.

5. CONCLUSIONS

The spectral characteristics of a MHz rate, Nd:YAG pulse-burst laser system have been examined, with particular emphasis on implications for filtered scattering imaging diagnostics. The time-averaged

spectral profile for 16 nsec, near rectangular, pulses was found to agree reasonably well with predictions based on the discrete Fourier transform of the temporal profile. Experimental extinction in molecular iodine was measured to be 5×10^{-5}, which is approximately two orders of magnitude greater than that previously reported[21] using a commercial injection-seeded Nd:YAG system. The difference is possibly attributable to the more ideal spectral characteristics resulting from pulsed amplification of the cw master oscillator. The laser system, and a companion CCD framing camera, were used to obtain image sequences clearly illustrating the temporal correlation between the large-scale structure of a Mach 2.5 turbulent boundary layer, and the curvature and unsteadiness of the oblique shock produced by a 14° wedge.

6. ACKNOWLEDGMENTS

The authors wish to acknowledge John L. Lowrance and Vince Mastrocola of Princeton Scientific Instruments, Inc., for providing the CCD framing camera and for assisting in its operation. The authors also wish to acknowledge Jay H. Grinstead for assistance in the imaging measurements, and Philip Howard for providing technical support.

The pulse-burst laser system has been developed with support from two grants from the United States Air Force Office of Scientific Research, Julian Tishkoff (University Research Initiative) and Leonidas Sakell (External Aerodynamics), technical monitors. Seed money was also provided by AT&T Bell Laboratories, John Bjorkholm, technical monitor, and the Princeton University Center for Photonics and Opto-Electronic Materials. The CCD framing camera has been developed under Small Business Innovative Research (SBIR) grants from the United States Office of Naval Research, Edwin Rood, technical monitor; and the United States Air Force, Wright Laboratory, Charles Tyler, technical monitor.

REFERENCES

1. W.R. Lempert, P-F Wu, B. Zhang, R.B. Miles, J.L. Lowrance, V. Mastrocola, and W.F. Kosonocky, "Pulse-Burst Laser System for High-Speed Flow Diagnostics," Paper #AIAA-96-0179, AIAA 34th Aerospace Sciences Mtg., Reno, NV, Jan. 15-18, 1996.

2. R. Miles and W. Lempert, "Two-Dimensional Measurement of Density, Velocity, and Temperature of Turbulent Air Flows from UV Rayleigh Scattering," Applied Physics B B51., p. 1 (July 1990).

3. H. Komine, S.J. Brosnan, A.B. Litton, and E.A. Stappaerts, "Real-Time Doppler Global Velocimetry, Paper #AIAA091-0337, (1991).

4. J.N. Forkey, W.R. Lempert, and R.B. Miles, "Accuracy Limits for Planar Measurements of Flow Field Velocity, Temperature, and Pressure Using Filtered Rayleigh Scattering," Experiments in Fluids (Submitted December 1996).

5. M.W. Smith and G.B. Northam, "Application of Absorption Filter-Planar Doppler Velocimetry to Sonic and Supersonic Jets," AIAA Paper #95-0299, Jan. 1995.

6. J.N. Forkey, W.R. Lempert, S.M. Bogdonoff, R.B. Miles, and G. Russell, "Volumetric Imaging of Supersonic Boundary Layers Using Filtered Rayleigh Scattering Background Suppression," Paper #AIAA-94-0491, AIAA 32nd Aerospace Sciences Mtg. & Exhibit, Jan. 10-13, 1994, Reno, NV.

7. G.S. Elliott, M. Samimy, and S.A. Arnette, "A Molecular Filter-Based Velocimetry Technique for High-Speed Flows," Experiments in Fluids 18, pp. 107-118 (1994).

8. J. Meyers, "Evolution of Doppler Global Velocimetry Data Processing," Eighth International Symposium on Applications of Laser Techniques to fluid Mechanics, Vol. 1, Lisbon, Portugal, July 8-11, 1996.

9. I. Röehle and R. Schodl, "Doppler Velocimetry in the Flow of a Swirler," Eighth International Symposium on Applications of Laser Techniques to fluid Mechanics, Vol. 1, Lisbon, Portugal, July 8-11, 1996.

10. D. Hoffman, K.-U Münch, and A. Leipertz, "Two-Dimensional Temperature Determination in Sooting Flames by Filtered Rayleigh Scattering," Optics Letters 21, p. 525 (1996).

11. H. Shimizu, S.A. Lee, and C.Y. She, "High Spectral Resolution LIDAR System with Atomic Blocking Filters for Measuring Atmospheric Parameters," Applied Optics 22, pp. 1373-1381 (1983).

12. P. Piironen and E.W. Eloranta, "Demonstration of a High-Spectral-Resolution LIDAR Based on an Iodine Absorption Filter," Optics Letters 19, p. 234 (1994).

13. J.A. Shirley and M. Winter, "Air Mass Flux Measurement System Using Doppler-Shifted Filtered Rayleigh Scattering, "AIAA Paper 93-0513, Jan. 1993.

14. R.L. McKenzie, "Measurement Capabilities of Planar Doppler Velocimetry Using Pulsed Lasers," AIAA Paper 95-0297, Jan. 1995.

15. N.D. Finkelstein, W.R. Lempert, R.B. Miles, A. Finch, and G.A. Rines, "Cavity-Locked, Injection-Seeded, Ti:Sapphire Laser and Application to Ultraviolet Flow Diagnostics," Paper #AIAA-96-0177, AIAA 34th Aerospace Sciences Mtg. & Exhibit, Reno, NV, Jan. 15-18, 1996.

16. J.N. Forkey, W.R. Lempert, and R.B. Miles, "Observation of a 100 MHz Frequency Variation Across the Output of a Frequency-Doubled, Injection-Seeded, Unstable Resonator, Q-Switched Nd:YAG Laser," Optics Letters (Accepted, November 1996).

17. J.N. Forkey, W.R. Lempert, and R.B. Miles, "Corrected and Calibrated I_2 Absorption Model at Frequency Doubled Nd:YAG Laser Wavelengths," Applied Optics (Submitted, November 1996).

18. R. Bracewell, "*The Fourier Transform and Its Applications,*" McGraw-Hill Electrical and Electronic Engineering Series, New York, 1965.

19. *Thermodynamics Research Center (TRC) thermodynamics tables--non-hydrocarbons*, Texas A&M University, p. ka--190 (1975).

20. R.B. Miles, J.N. Forkey, and W.R. Lempert, "Filtered Rayleigh Scattering Measurements in Supersonic/Hypersonic Facilities," Paper #AIAA-92-3894, AIAA 17th Aerospace Ground Testing Conference, Nashville, TN, July 6-8, 1992.

21. J.N. Forkey, "Development and Demonstration of Filtered Rayleigh Scattering--A Laser-based Flow Diagnostic for Planar Measurement of Velocity, Temperature, and Pressure," Ph.D. Thesis, Dept. of Mechanical & Aerospace Engineering, Princeton University, Princeton, New Jersey (June 1996).

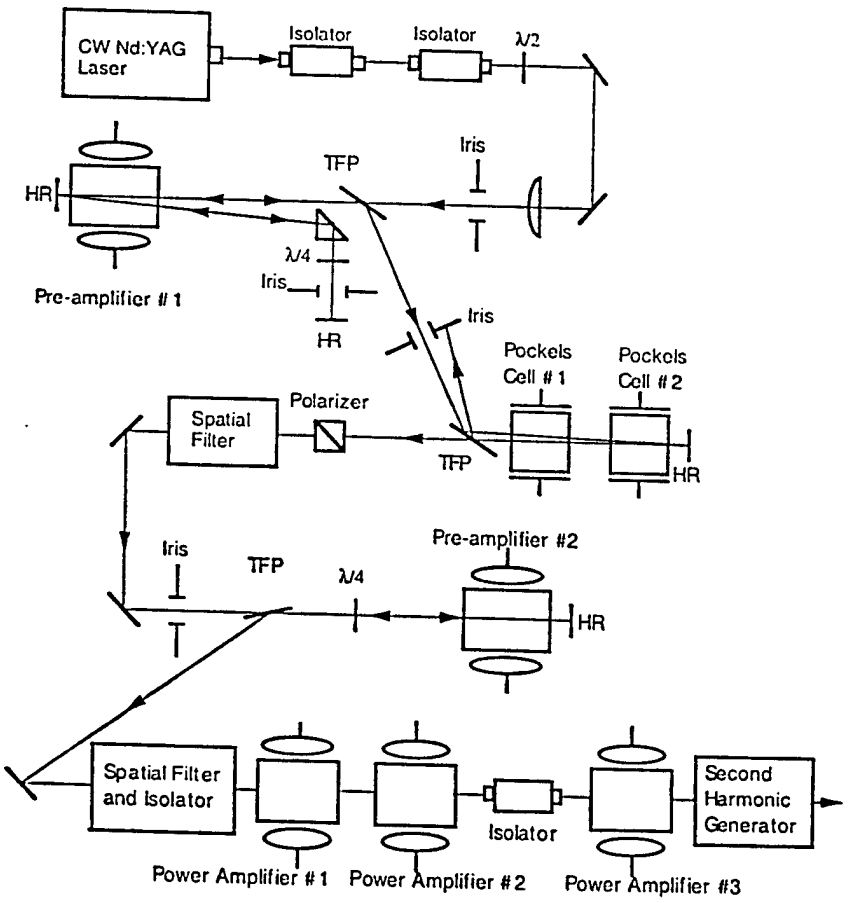

Fig. 1. Schematic diagram of the pulse-burst laser system.

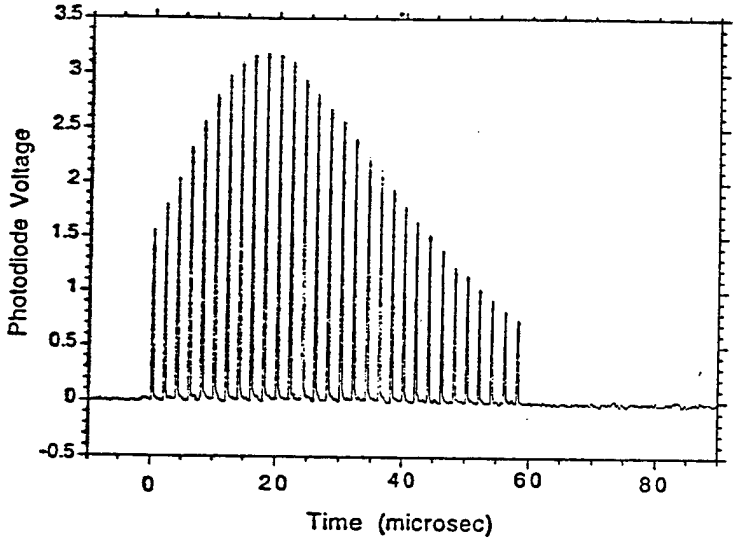

Fig. 2. Oscilloscope trace of typical pulse burst consisting of 30, 20 nsec duration pulses.

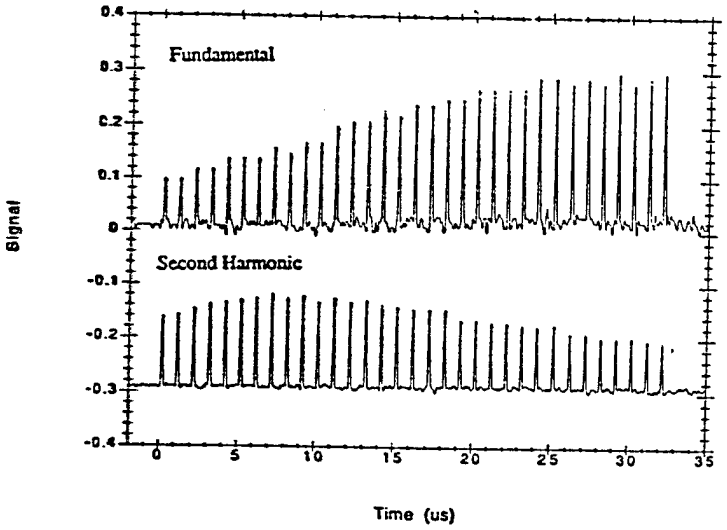

Fig. 3. Comparison of fundamental (upper trace) and second harmonic (lower trace) burst sequences.

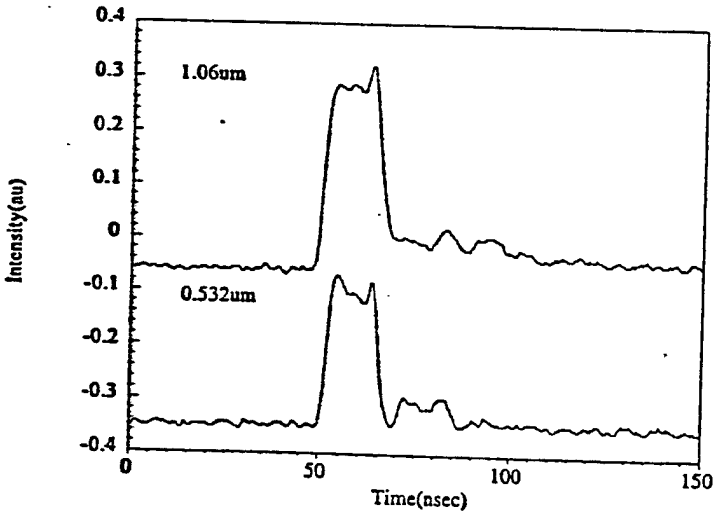

Fig. 4. Temporal profile of typical fundamental (upper trace) and corresponding second harmonic (lower trace) pulses. Fundamental/second harmonic pulse widths are 16/14 nsec, respectively.

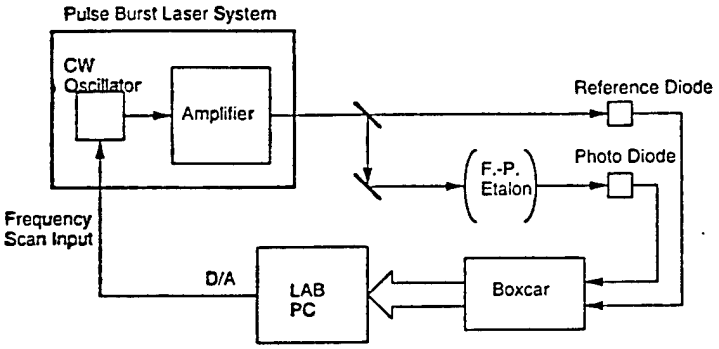

Fig. 5. Schematic diagram of spectral measurement.

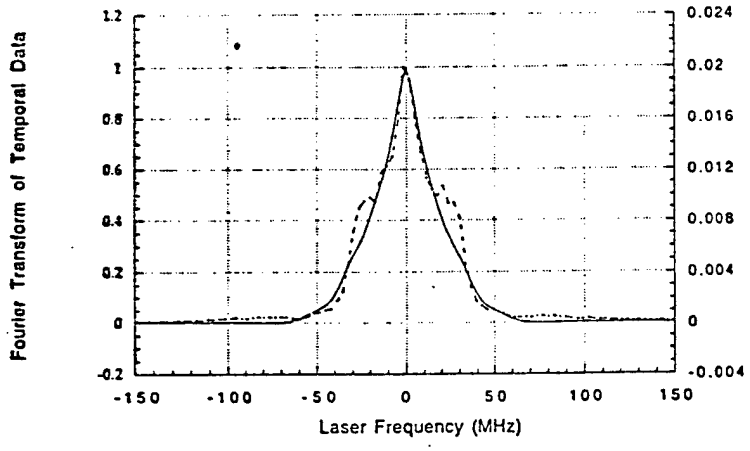

Fig. 6. Time-averaged spectral profile (dotted) of fundamental output of pulse-burst laser overlaid with Fourier transform (solid) of temporal profile from Fig 4.

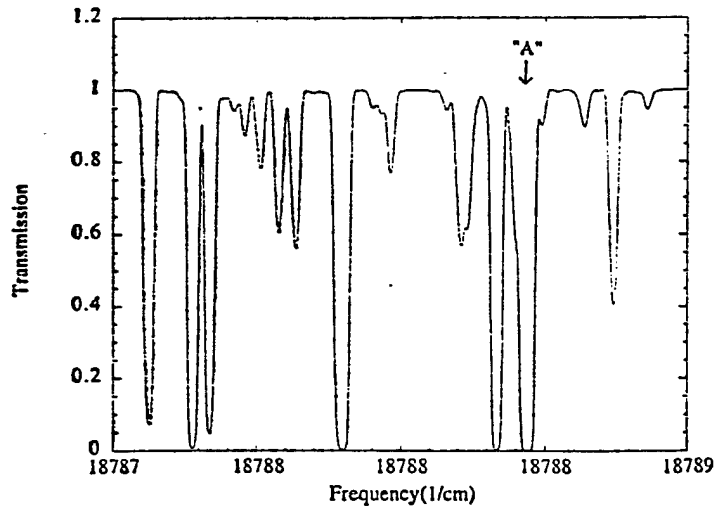

Fig. 7. Modeled iodine absorption over tuning range of Nd:YAG laser. Feature marked with arrow was used for extinction measurements.

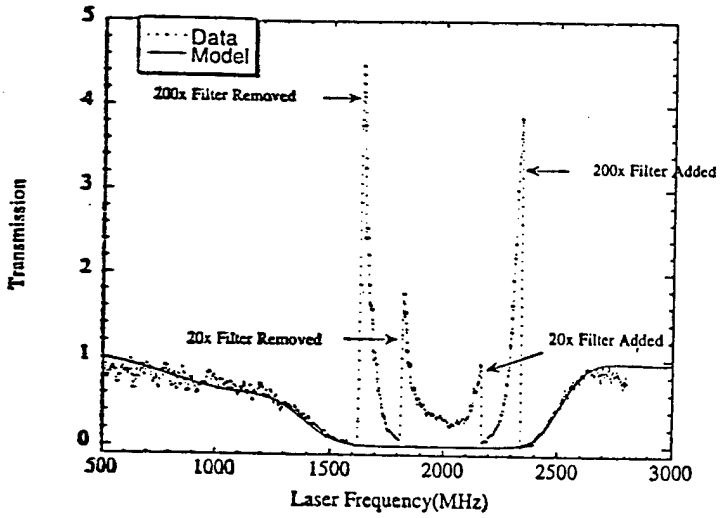

Fig. 8. Experimental (dotted) and modeled (solid) extinction for iodine transition "A". Cell cold tip temperature is 353 K. Cell length is 10 cm.

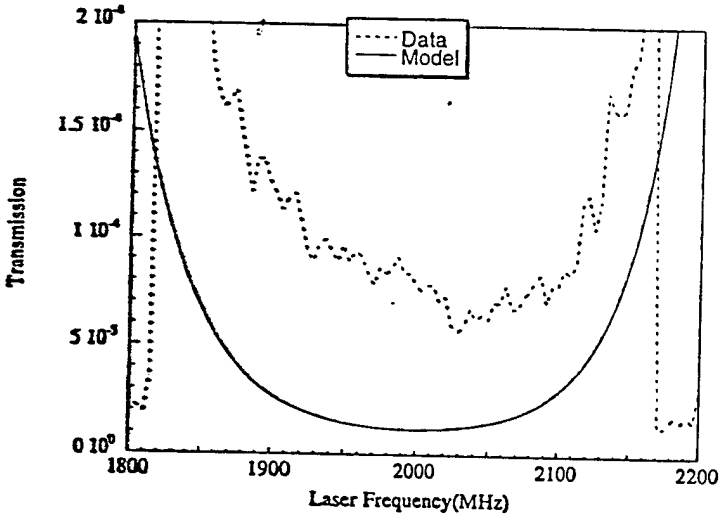

Fig. 9. Blow-Up of central portion of Fig. 8 illustrating absolute extinction near line center of transition "A".

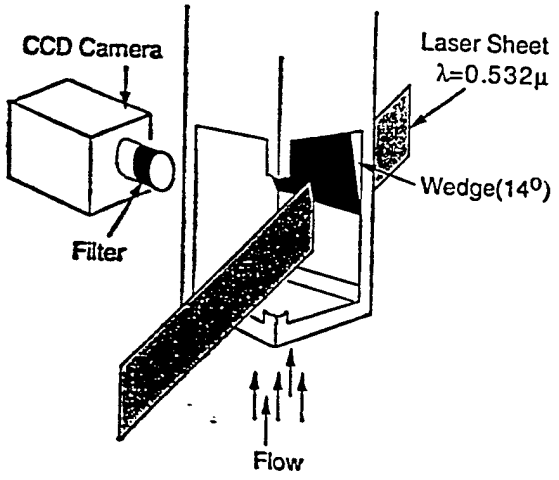

Fig. 10. Schematic diagram illustrating imaging geometry employed for MHz rate visualization of Mach 2.5 flow over 14° wedge.

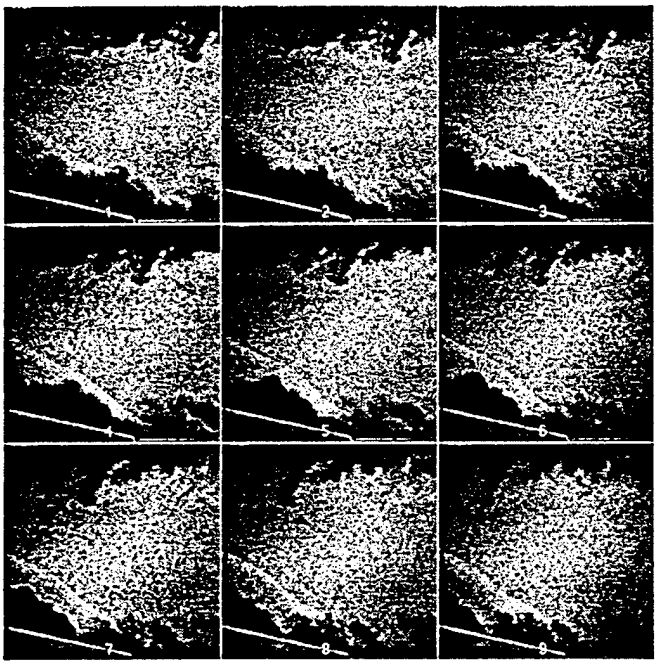

Figure 11
Sequence of 9 streamwise view images of Mach 2.5 flow over
14° wedge. Flow is from right to left. 2 microseconds between images.

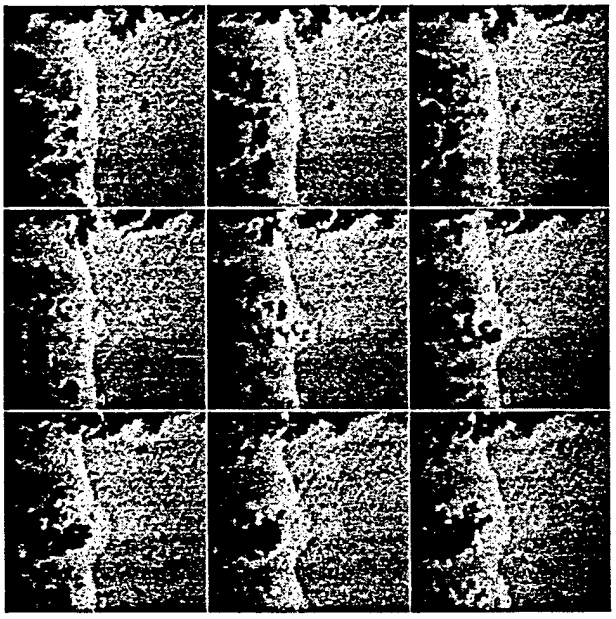

Figure 12
Sequence of 9 parallel view images of Mach 2.5 flow over
14° wedge. Flow is from right to left. 2 microseconds between images.

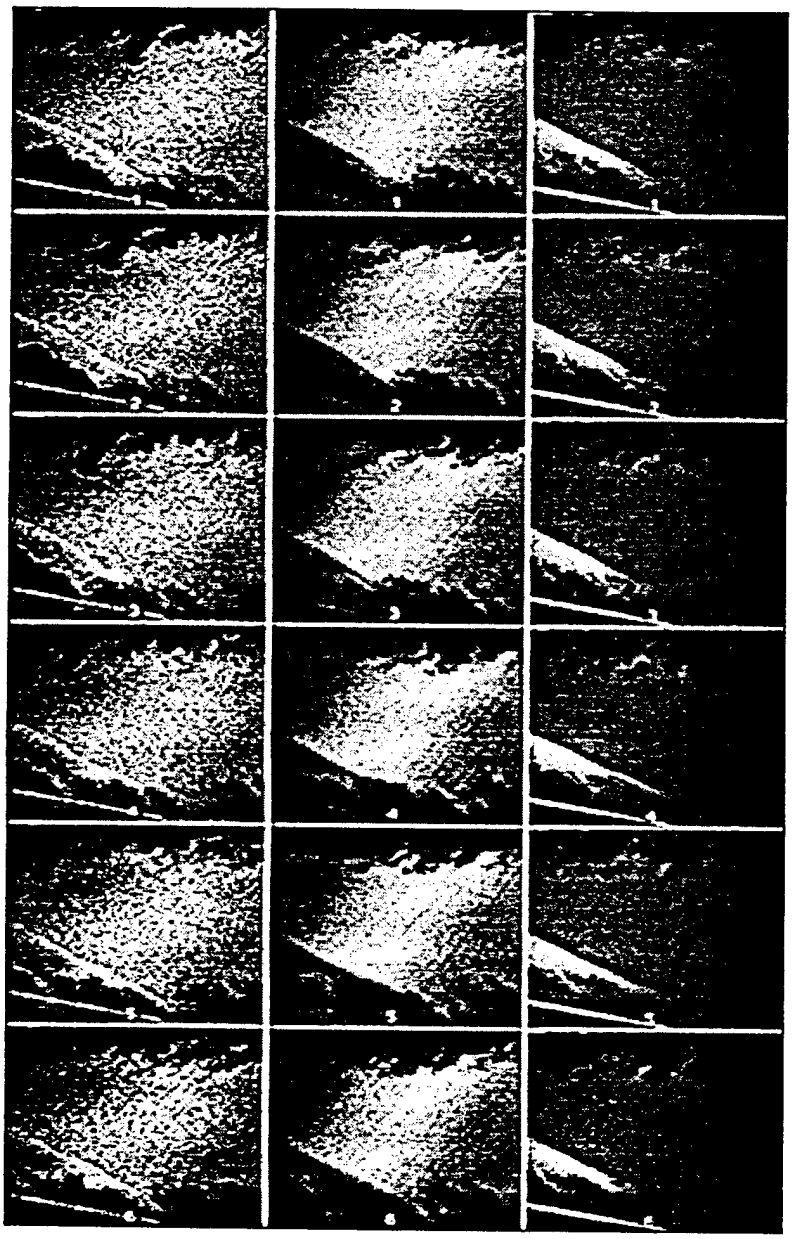

Figure 13
Comparison of filtered and unfiltered streamwise view images.
Flow from right to left. 2 μs interval between images.
left column: unfiltered images.
middle column: filtered to highlight high speed flow.
right column: filtered to highlight low speed flow.

AIAA 97-0154

Development of Planar Diagnostics for Imaging Mach 8 Flowfields Using Carbon Dioxide and Sodium Seeding

P.J. Erbland
Wright Laboratory
Aeromechanics Division (WL/FIMA)
WPAFB, OH 45433

M.L. Baumgartner, A.P. Yalin, M.R. Etz, B. Muzas
W.R. Lempert , A.J. Smits, and R.B. Miles
Princeton University
Dept. of Mechanical & Aerospace Engineering
Princeton, NJ 08544

35th Aerospace Sciences Meeting & Exhibit
January 6-10, 1997 / Reno, NV

Development of Planar Diagnostics for Imaging Mach 8 Flowfields Using Carbon Dioxide and Sodium Seeding

P.J. Erbland*
Wright Laboratory
Aeromechanics Division (WL/FIMA)
WPAFB, OH 45433

M.L. Baumgartner†, A.P. Yalin‡, M.R. Etz§, B. Muzas,¶
W.R. Lempert#, A.J. Smits, and R.B. Miles****
Dept. of Mechanical & Aerospace Engineering
Princeton University
Princeton, New Jersey 08544

ABSTRACT

In order to investigate the structure of Mach 8 flowfields and the mixing of wall injected fuels, two different diagnostic imaging techniques have been developed. The first uses carbon dioxide enhanced Filtered Rayleigh Scattering (FRS) for imaging the freestream flow and the boundary layer. The second technique uses laser induced fluorescence of sodium seeded into helium as a fuel simulant to provide information on injection and mixing in hypersonic flows. This paper will discuss the development of these diagnostics and their transition into the Mach 8 test facility at the Princeton Gas Dynamics Laboratory. Data are presented from an investigation of a Mach 8 zero pressure gradient boundary layer using the carbon dioxide enhanced FRS technique and from a study of the injection and mixing of sodium seeded helium into the boundary layer to illustrate the importance of these diagnostics to the understanding of the relevant fluid mechanics. An analysis of the boundary layer flow is provided along with an assessment of the implications of perturbing the flowfield using these seeding techniques.

* Graduate Student, Mechanical & Aerospace Engrg., Senior Member, AIAA
† Graduate Student, Mechanical & Aerospace Engrg., Member, AIAA
‡ Graduate Student, Mechanical & Aerospace Engrg.
§ Graduate Student, Mechanical & Aerospace Engrg., Student Member, AIAA
¶ Graduate Student, Mechanical & Aerospace Engrg. Dept., California Institute of Technology, Student Member, AIAA
# Senior Research Scientist, Mechanical & Aerospace Engrg., Member, AIAA
** Professor, Mechanical & Aerospace Engrg., Associate Fellow, AIAA

CO2 ENHANCED FILTERED RAYLEIGH SCATTERING (FRS)

Condensate Enhanced Scattering from Flows

In recent years, Rayleigh scattering and Filtered Rayleigh Scattering have seen significant application for the characterization of high speed flows. This includes both the imaging and analysis of flow structures[1-3] as well as the quantitative determination of velocity and the thermodynamic state[4-6]. Quantitative measurements have generally been limited to lower supersonic Mach numbers or facilities with very pure gases to insure that the data was not biased by the presence of condensed media. Work at higher Mach numbers has generally utilized scattering from small condensate particles, presumably ice crystals, produced in the flow during the expansion process. Condensate particles are found in virtually all high Mach number, air-supplied, blow-down aerodynamic test facilities despite use of water separators and chemical dryers in the production of the high pressure compressed air. Aerodynamic test facilities are typically heated sufficiently to prevent liquefaction of air but not the supercooling and the consequent condensation of any remaining water vapor. Often the presence of condensed media is not fully appreciated until quantitative Rayleigh density measurements are attempted, and then investigators are confronted with unreasonably high signals. The impact of this condensed media on the aerodynamic quality of the test flow is generally small due to the very low

concentrations of condensable vapor and the minor changes to gas properties produced by the heat released in the condensation process.

In using Rayleigh scattering to investigate flow structures such as shock interactions, the structures are revealed by the changes in the density dependent scattering intensity as the flow passes through compressions or expansions. In the applications investigating boundary layer phenomena, the boundary layer features are revealed by the interface between the cold core flow and the hot boundary layer fluid. As the gas in the boundary layer is heated, the temperature rises above the sublimation value for the condensed media and the condensate disappears. Therefore interfaces between regions with condensate and those without represent thermal sublimation contours. The successes demonstrated in previous applications have led to the present investigation of condensate enhanced Filtered Rayleigh Scattering (FRS) in the Mach 8 Hypersonic Boundary Layer Facility at the Princeton University Gas Dynamics Laboratory.

Prior to intentional condensate enhancement, Filtered Rayleigh Scattering measurements were attempted on the ambient flow in the Mach 8 tunnel. These measurements revealed no usable signal from the flow given the available experimental hardware. A subsequent test with gaseous carbon dioxide seeded into the air supply provided strong scattering signals and motivated the development of a metering system to allow accurate control of the flowrate and thermodynamic state of the CO_2 seed.

Carbon Dioxide Seeding System

The successful demonstration of carbon dioxide enhanced scattering led to an evaluation of several options for increasing the concentration of condensable media in the flow. These included increasing the water vapor content of the compressed air supply and adding either water or CO_2 downstream of the tunnel pressure control valve. Concerns regarding long term water vapor contamination of the air storage facility precluded the first option. The criteria used for selecting between the remaining options included minimizing the changes to the flow properties and creating the smallest particle sizes possible. Properties of the two candidate materials are listed in table 1[7]. The desire to minimize the heat released to the flow in the condensation process favored use of CO_2 which has a heat of vaporization of less than one seventh that of water at the conditions listed. Molecular weight considerations were secondary since for the same concentration, either vapor would change the molecular weight of air by roughly the same percentage, though in opposite directions. The saturation properties however are markedly different for the two molecules and the lower condensation temperature of CO_2 at a given pressure would delay onset of condensation in the nozzle and potentially produce smaller particles. Smaller particles are more likely to be in the Rayleigh rather than Mie scattering range ($r<<\lambda$), and they will exhibit a smaller lag in following flow velocity and temperature changes (faster vaporization). The combination of smaller particles and lower sublimation temperature of CO_2 would provide a more sensitive indication of the interface between the cold core flow and the hot boundary layer flow since the smaller particles would sublime more quickly and at a lower temperature than ice particles. These considerations prompted the selection of carbon dioxide rather than water as the material to be seeded into the flow.

Properties of Carbon Dioxide

Carbon dioxide is shipped in high pressure cylinders as a liquid under its own vapor pressure of 5.82 MPa (845 psia) at 294 K. The equilibrium solid/vapor and liquid/vapor (saturation) curves are plotted in figure 1, with notations for the triple and critical points[8-9]. Since the Mach 8 tunnel operates with stagnation pressures in the range of 1.7-8.3 MPa (250-1200 psia), seeding with CO_2 will involve operating in the saturation region, both above the critical point in the heating process and below the triple point in the test section. Recall that the critical temperature is the temperature above which a substance cannot exist in the liquid state. This is marked by the disappearance of the meniscus marking the liquid-vapor interface. At this temperature, the surface tension becomes zero and the densities of the liquid and saturated vapor are equal. Note that below the triple point temperature, solid carbon dioxide will sublime directly to a gas. The sublimation temperature has a much weaker pressure dependence than the vaporization temperature. This low pressure sensitivity is desirable for minimizing changes in the sublimation isotherm as the Reynolds number of the flow is changed. Figure 2 is a plot of the density of liquid CO_2 as a function of pressure and temperature and is included to illustrate the strong compressibility effects in the liquid-vapor saturation region[7-8]. The liquid compressibility had important consequences for the design of the CO_2 metering system.

Seeding System Design

The first tests of carbon dioxide enhanced FRS in the Mach 8 facility demonstrated that gaseous CO_2 could be used to enable Rayleigh scattering visualization. However, strong variations in the strength of the scattering signal were observed as the tests progressed. It was discovered that removal of significant amounts of gas phase CO_2 from the cylinder caused cooling of the liquid phase, a rapid decrease in the vapor pressure, and as a consequence, a decrease in

flowrate with time. Thus, a liquid CO_2 metering system was developed for the Mach 8 tunnel.

A schematic of the liquid carbon dioxide metering system is shown in figure 3. High pressure helium is used to force the CO_2 from the supply cylinders. These cylinders were modified to allow pressurization of the liquid phase through one port in the cylinder valve and simultaneous liquid extraction through a dip tube connected to the second port. The measurements of liquid pressure and temperature are essential for density determination due to the liquid compressibility mentioned earlier. An Omega liquid flow meter is used to measure the volume flow rate of CO_2 and a metering valve is used to set flow rates. Once the liquid passes through the metering valve it is flash vaporized or atomized by the crossing stream of tunnel supply air just downstream of the pressure control valve.

Condensation Effects on the Flowfield

The primary mechanism by which a condensing media will affect a supersonic flow is through the heat released in the condensation process. The release of heat produces a change in the static temperature, static pressure, and local Mach number. The transition from a supersaturated state to an equilibrium state can occur abruptly or over a considerable distance depending on the density and velocity of the flow. These phenomena and the process by which condensation occurs are discussed at length in many references. One of the better reviews is by Hill[10]. An important question is whether the condensation process occurs through heterogeneous condensation, that is clustering of molecules about a condensation site (dust, ice crystal) or by homogeneous nucleation; the formation of condensate drops by collision and grouping of condensable molecules. Hill concluded that in supersonic nozzles, the most likely condensation mechanism would be homogeneous nucleation, even in the presence of dust in the flow. Heterogeneous condensation might contribute if condensed particles of another vapor were available to serve as condensation sites. The presence of residual water vapor in the Mach 8 flow, albeit at a level of 10-50 ppm, presents the possibility that heterogeneous rather than homogeneous nucleation is active. Hill also observed that the condensate formed in nozzles is normally less than 100 nm in size, and this observation is supported by experimental work of Wegener and Stein[11]. Clearly these assessments imply that the condensate particles would fall in the Rayleigh range.

Experimental Configuration

Facility & Model

A schematic drawing of the Princeton University Mach 8 wind tunnel is show in figure 4. This is a blow-down facility which uses air as the test gas[12]. Stagnation pressures can be varied from 1.7-8.3 MPa (250-1200 psia). After passing through the pressure control valve, the supply air flows through a resistance heated helical coil where it is heated to the desired stagnation temperature (870 K maximum). The axisymmetric nozzle has a 23 cm (9") exit diameter and the test section is composed of two interchangeable sections, one of which has optical access from four sides via offset window cavities. At the exit of the test section, the flow enters an ejector pumped diffuser which is used to keep the test section at the desired operating pressure. Models are mounted rigidly to one of the tunnel walls, so the facility must be started with the model in place.

The model used for tests described in this paper is a 47.6 cm (18.75") long sharp flat plate, figure 5. The model has a 25 mm by 1 mm transverse (spanwise oriented) slot located on the centerline, 7 cm aft of the leading edge. This slot served as the injection site for the sodium laser induced fluorescence work discussed later in this paper. Initial CO_2 imaging and boundary layer surveys revealed that the boundary layer was transitional at the desired test conditions, so a 2.4 mm (0.095") diameter trip was added 5.7 cm (2.25") downstream of the leading edge.

Optical Configuration

A narrow linewidth, injection locked, frequency doubled Nd:YAG laser is used as the scattering source for the Rayleigh imaging. This laser has a 10 Hz repetition rate, an output of ~ 285 mJ per pulse at 532 nm, and a 10 ns pulse width. The pulse has spectral linewidth of about 150 MHz. The laser output was tuned to overlap a strong spectral absorption line in iodine vapor. A molecular iodine filter was placed in front of the camera so that stray scattering from the walls, windows, and the model surface was absorbed. The scattering from the flow was doppler shifted outside the absorption band of the filter due to velocity and could be observed by the camera

Images of flow structures with both streamwise and plan view perspectives were obtained. For each orientation, the laser beam was expanded into a focused sheet using a positive and negative cylindrical lens pair. The beam was then directed into the test section, passing from downstream to upstream at an angle of roughly 45° relative to the tunnel axis, as illustrated in figure 6. The sheet was estimated to be 100 μm thick at the focus, and the long focal length of the positive cylindrical lens was sufficient to keep the sheet thin across the full field of view of the camera. For the plan view the sheet was parallel to the plate surface and could be translated vertically to sweep through the boundary layer. For the stream view the sheet was introduced through the top window and was positioned along the centerline. The selected beam geometry

provided a doppler shift of ~1.7 GHz for scatterers traveling with the free stream. The iodine vapor cell used to filter the scattered light provided an absorption linewidth of ~1 GHz and an attenuation of 10^{-3}.

Imaging was accomplished using a double intensified CID camera with a 210 mm focal length lens at f/4.5 and a magnification of 2. A 10 cm long, 50 mm diameter iodine vapor cell was placed in front of the camera lens. The optical axis of the camera/filter system was orthogonal to the plane of the laser sheet. This resulted in a linear field of view of approximately 4 cm x 3 cm. Images were passed to a digital grab/hold unit and then to videotape for subsequent analysis. An unfiltered interline transfer CCD camera was mounted on centerline above the test section to view the entire aft end of the plate. This camera was mounted with its optical axis at about 30 degrees relative to vertical so that there is stretching in the spatial scale across the camera field of view. The function of this camera was to provide information on the uniformity of the seeding across the flow and allow evaluation of flow features beyond the field of view of the intensified camera.

Experimental Results

Operating Conditions

For the CO_2 enhanced FRS tests, the tunnel was operated over a range of stagnation conditions to demonstrate the viability of the technique, establish the performance of the seeding hardware, and gather data on the turbulent boundary layer over a range of Reynolds numbers. The stagnation, static, and model conditions are listed in table 2. The model was preheated by flowing air through the tunnel without starting the ejectors. When the model was at the desired temperature, the ejectors were activated to reduce the back pressure and start the tunnel. Facility run times are limited by the air supply demands of the ejectors. A typical test would last 90 to 150 seconds.

FRS and Seeding System Performance

Un-enhanced Rayleigh scattering from the low density freestream flow was so weak that no signal was observable on the imaging system. This is despite the likely presence of ice crystals as a result of condensation of residual water vapor in the air supply. Thus, gaseous CO_2 was added to investigate the feasibility of Rayleigh signal enhancement. These tests demonstrated substantial enhancement from the condensed CO_2, but exhibited problems with seeding uniformity and stability that prompted the development of the liquid CO_2 seeding system.

In testing conducted to date, the liquid CO_2 injection and metering system has provided stable and reliable control of the seeding process. The only shortcoming thus far has been the limited flow capacity of the helium regulator used to pressurize the CO_2 tanks. The limited flow capacity of this regulator has caused a variation in CO_2 drive pressure with flow setting. However, since the pressure and temperature of the liquid CO_2 are measured, this has not proven to be a problem. Conservatively high estimates of volume flow rate from the gaseous CO_2 injection tests led to the belief that up to 11 lpm (3 gpm) of liquid CO_2 would be required for seeding. Current testing has demonstrated that 0.76 lpm (0.2 gpm) provides a strong Rayleigh signal. This corresponds to a mass flow rate of 0.01 kg/s and a carbon dioxide to air flow mass fraction of 0.6%. Given the moderate laser power and camera gain (1000X out of potential of 50,000X) used at this time, we expect that an additional reduction in CO_2 flowrate of a factor of 5 to 10 is possible.

Boundary Layer Imaging

Planar images of the flow over the aft end of the flat plate were obtained to investigate the turbulent boundary layer structure. The camera field of view was 3 cm x 4 cm and was centered 3.1 cm (1.25") ahead of the plate trailing edge. For the plan view, the horizontal laser sheet was initially positioned outside of the boundary layer (17.5 mm) and then translated down into the layer (δ = 11.5 mm). As the sheet was moved toward the plate, dark structures appeared. Figure 7 is a montage of images taken at the same position in the boundary layer (11 mm above the plate) to illustrate the variation in frequency and size of structures with time. The brighter portion of each image is Rayleigh scattering from the condensate in the flow. The dark structures are regions of flow where the condensate has evaporated. These regions indicate ejections of hot fluid from the inner layer to the outer portion of the boundary layer and are referred to as outer layer bursts. Multi-pulse, multi-camera imaging using this perspective will allow quantitative determination of the convection velocity in the turbulent boundary layer. Note that interpretation of these data must be done with care since the boundaries of these structures represent thermal sublimation contours for the condensed CO_2. Thus, temperature rather than velocity information is being recorded. Detailed analysis of these data are contained in the paper by Baumgartner et.al.[13].

This diagnostic has also provided important qualitative insights regarding the flowfield and the tunnel operation. During the early tests of the liquid CO_2 injection system, the vertically mounted CCD camera recorded the data presented in figure 8. This is a montage of images taken with the horizontal laser sheet at different vertical positions within the boundary layer. In this figure, the flow is from bottom to top of the page. Several features are worthy of note. Structures (bursts) are visible along the right side of each image. This is the thickened turbulent boundary layer at the edge of the model. Analysis of these

images revealed that weak shocks were generated around these outer layer bursts.

The second feature worth noting is the pair of bright lines that seem to intersect on the model centerline near the end of the plate in the first image of the montage. These lines are believed to be the disturbance waves emanating from the corners of the leading edge at the front of the plate. This gives an excellent indication of the sensitivity of this diagnostic for imaging flow structures. The final feature of interest is the change in size and frequency of the outer layer bursts as the sheet is lowered into the boundary layer. The early appearance of structures on centerline implies early transition relative to the region of the plate between the centerline and the edges. After these images were taken, it was determined that the high temperature ceramic material used to seal the injection slot at the front of the plate was being gradually eroded during the course of a run, and that this disturbance was inducing early transition along the centerline. These data, in conjunction with boundary layer survey results, also indicated that the boundary layer was transitional at these Reynolds numbers and led to the addition of a trip at the front of the model.

Figure 9 presents information recorded with the laser sheet in the streamwise orientation. These images illustrate the interface between the hot boundary layer fluid and the cold free stream flow. The ejections of fluid from the inner layer to the outer region of the boundary layer are clearly evident. These data are useful for determining the intermittency in the boundary layer. Two dimensional spatial correlations of these images will provide data on the size and orientation of the turbulent structures for comparison to previous boundary layer investigations at lower Mach number[1].

Flow Perturbations

The experiments accomplished to date have demonstrated that a CO_2 seeding mass fraction of less than 0.6% (0.01 kg/s) of the primary tunnel flow is adequate to generate strong Rayleigh signals. The analytical evaluation of the effects of this amount of seed on the flow thermodynamics and fluid mechanics is just beginning. Additional work is planned to analytically predict and experimentally measure the flow perturbations produced by the seeding. This includes evaluating the size of the CO_2 particulates in order to verify that they are in the Rayleigh range.

SODIUM PLANAR LASER INDUCED FLUORESCENCE

Diagnostic Summary

A second diagnostic technique that is under development in the Princeton University Mach 8 tunnel is planar sodium Laser Induced Fluorescence (LIF). The goal of this development activity is to provide a means for studying and quantifying fuel/air mixing at the molecular scale in hypersonic flowfields. More specifically, this research seeks to develop a method for seeding atomic sodium vapor into helium (as a fuel simulant) and then injecting that helium into a hypersonic boundary layer to quantify mixing due to turbulence and large scale vortical structures. The initial development of the sodium seeding apparatus and discussion of the spectroscopic issues including quenching, saturation, and chemical reaction was previously presented by Yalin, et. al.[14]. This section of the paper will briefly summarize this technique and the hardware and then update the progress on the development program.

Experiment Summary

Seeding Apparatus

A seeding system has been developed that introduces pre-heated helium into a heated cell containing sodium liquid and vapor, and then delivers the mixture through heated lines to a model in the Mach 8 test facility. The amount of sodium delivered is a function of the sodium vapor pressure (controlled by the cell temperature) and the dynamics of the evaporation process as the helium is passed through the cell. The cell has been operated at 530 K and at this temperature the equilibrium vapor pressure for the sodium is ~ 10 Pa (~ 0.08 torr). The seeded helium is delivered to the model so that the helium temperature is reasonably close to the wall temperature. Recent modifications to the cell now allow measurements of both the sodium liquid and vapor phase temperatures. This will allow a more thorough understanding of the dynamics of the seeding process and consequently a better estimate of the sodium seeding rate. In addition, the temperature of the seeded helium delivered to the test article can now be monitored to determine the wall to injectant temperature ratio.

Spectroscopy

A doubled Nd:YAG laser delivering 285 mJ/pulse (532 nm) at 10 Hz with a 10 ns pulse width, is used to pump a Quantel TDL-50 dye laser. The dye laser is tuned to excite the sodium D2 line at 589.0 nm. The linewidth of the dye laser is ~ 3 GHz which is large compared to the hyperfine splitting in sodium (1.7 GHz for the ground state). This causes the atomic sodium to behave as a two level atom with strong re-radiation at the same wavelength as the excitation. The sodium has a radiative lifetime of 16 ns. Since the saturation intensity of the sodium transition is very low, very moderate pulse energies will insure saturation and consequently a fluorescence signal which is directly related to the sodium number density. Quenching is

primarily by nitrogen with a predicted rate of order 1.5 x 10^7 s^{-1} near the wall (in the boundary layer) which is of the same order as the spontaneous decay rate. This implies that after the laser pulse, the decay rate of the fluorescence signal can be expected to vary by about a factor of two for sodium that is well mixed with the nitrogen compared to sodium which is unmixed. The fluorescence signal during the laser pulse is indicative of the macromixing or distribution of seeded helium in the flow. The fluorescence signal after the laser pulse reflects the decay in the excited state population due to both spontaneous emission and quenching. By examining the fluorescence signal both during and after the laser pulse, and properly evaluating the ratio of these signals, the fraction of moleculary mixed atoms can be determined.

Model

The test article used in these experiments was the same sharp flat plate model described earlier in this paper, figure 5. It should be noted that the underside of the model had provisions for attaching a heated feed tube for delivery of the seeded helium. The seed gas entered through a circular hole in the bottom of the plate which led to an internal cavity intended to diffuse the jet of helium. The forward end of the cavity was connected to the slot in the upper surface of the plate.

Optical Configuration

The experiments to be described here employed dye laser energies of 0.1 mJ/pulse. The beam was formed into a 8 cm wide sheet using a positive and negative cylindrical lens pair, and was introduced through the top of the test section to provide a streamwise view of the flow, figure 10. The sheet was approximately 400 μm thick and was positioned along the centerline of the model. The fluorescence signal was imaged using a frame transfer CCD camera with a 75 mm focal length, f/1.8 camera lens. This provided a field of view of 8 cm x 6 cm. The CCD camera provided improved sensitivity at the wavelength of interest compared to the photocathode of the intensified camera used in the prior tests. The current camera has a quantum efficiency of 50% at 589 nm. Images were recorded on videotape for subsequent analysis.

Experimental Results

Operating Conditions

The data presented here were obtained with a stagnation pressure of 4.5 MPa (650 psia) and a stagnation temperature of 683 K (1230 R). The predicted static pressure and temperature for these conditions are 455 Pa (3.5 torr) and 49 K (88.2 R) respectively. The measured wall temperature was 612 K (1101 R). The boundary layer thickness at the injection point is predicted to be less than 5 mm.

At these conditions, the sodium absorption line shape is dominated by thermal broadening with a linewidth of 0.45 GHz in the free stream and 1.6 GHz near the wall. Recall that the laser linewidth is approximately 3 GHz. With the laser sheet dimensions given above the intensity was estimated to be 25 kW/cm^2, far above the 6 W/cm^2 saturation intensity of this transition, but sufficiently low to minimize scattering from the model. The injected helium mass flow rate was of the order of 0.1 g/s compared to the tunnel flow rate of 1.5 kg/sec.

During early experiments the laser was tuned to resonance with the sodium during the preheating of the model (before the ejectors were started). In many tests it was found that resonance would be lost once the ejectors were started and the static pressure and temperature in the test section decreased. This was attributed to thermal broadening of the lineshape during the preheat which made precise identification of the absorption line center difficult. Once the tunnel was started, thermal narrowing of the lineshape resulted in poor overlap of the laser and absorption profiles and loss of resonance. A low pressure sodium reference cell was fabricated to address this problem. This is an evacuated aluminosilicate glass cylinder with flat end walls for optical viewing and a side tube which holds a small quantity of sodium. The cell and side tube are electrically heated to vaporize a small amount of sodium and the dye laser is introduced through a beam port located opposite the sodium side tube. The light is scattered throughout the cell and resonance is observed as the appearance of a cloud of sodium vapor within the cell. Use of this cell for pre-tuning the laser corrected the problems with loss of resonance

Experimental Progress

Planar images were acquired of the injection of sodium seeded helium through the transverse slot of the flat plate model discussed earlier. Figure 11 illustrates the type of data acquired for the maximum helium flowrate of 0.1 g/sec. The field of view of these images is 8 cm by 2 cm. Note that the macromixing is clearly visible in the flow and that fluorescible sodium persists to the edge of the camera field of view. This supports earlier contentions that reaction of sodium with residual water vapor in the air supply and oxidation affects in dry air should not create a major sink for sodium within the characteristic times and lengths of interest. Note also the variation in thickness of the sheet and the lifting of the seeded flow from the surface in the bottom panels. These images motivated a more detailed examination of the flowfield with the plate configured for sodium injection. That study demonstrated that the additional blockage introduced by the seeding hardware produced instability in the tunnel

operation and periodic movement of a shock onto the aft end of the plate. The resulting boundary layer separation and separation-induced shock produced the lifting of the sodium observed in this image. The blockage problem has now been corrected and the next test entry will employ the sodium laser induced fluorescence to investigate penetration and mixing in the Mach 8 boundary layer for various carrier gases and momentum ratios.

CONCLUSIONS

Two planar imaging diagnostics have been developed for low density hypersonic flows. These techniques provide valuable insight into the structure of the flowfield and boundary layer. A seeding system for carbon dioxide enhanced Filtered Rayleigh Scattering has been developed and seeding mass fractions less than 0.6 % of the tunnel flow have been demonstrated to be sufficient for strong Rayleigh signals. Images of a turbulent flat plate boundary layer have yielded valuable data from which the size, and orientation of outer layer structures can be deduced. Future work will concentrate on evaluating the affects of the carbon dioxide condensation on the flow properties and behavior.

Sodium planar Laser Induced Fluorescence images have been obtained for seeded helium injection through a transverse linear slot in a flat plate. These data indicate successful seeding and delivery and good persistence of the fluorescible sodium within the flow. Future measurements will use this technique to study injection and mixing in the Mach 8 boundary layer for various carrier gases and momentum ratios, and to obtain quantitative images of scalar mixing in hypersonic flow.

ACKNOWLEDGMENTS

The authors wish to thank Robert Bogart and Philip Howard for technical assistance. This work was sponsored by the U.S. Air Force Wright Laboratories, Dr. George Seibert (Radiatively Driven Hypersonic Wind Tunnel Program), and the U.S. Air Force Office of Scientific Research, Dr. Julian Tishkoff (University Research Initiative) and Dr. Leonidas Sakell (External Aerodynamics), technical monitors.

REFERENCES

1. Smith, M.W., and Smits, A.J., "Visualization of the Structure of Supersonic Turbulent Boundary Layers," Experiments in Fluids, No. 18, 1995, pp. 288-302.
2. Forkey, J. Cogne, S., Smits, A. Bogdonoff, S. Lempert, W.R., and Miles, R.B., "Time-Sequenced and Spectrally Filtered Rayleigh Imaging of Shock Wave and Boundary Layer Structure for Inlet Characterization," AIAA-93-2300, 29th Joint Propulsion Conference, June 1993, Monterey, CA.
3. Alvi, F.S., and Settles, G.S., "Physical Model of the Swept Shock-Wave/Boundary Layer Interaction Flowfield," AIAA Journal 30, Sept. 1992, p. 2252.
4. Forkey, J.N. Finkelstein, N.D. Lempert, W.R., and Miles, R.B. "Demonstration and Characterization of Filtered Rayleigh Scattering for Planar Velocity Measurements," AIAA Journal, Vol. 34, No. 3, 1995, pp. 442-448.
5. Shirinzadeh, B., "Rayleigh Scattering Measurements in Supersonic Facilities," AIAA-96-2187, 19th AIAA Advanced Measurement and Ground Testing Technology Conference, 17-20 June, 1996, New Orleans, LA.
6. Shirinzadeh, B., Hillard, M., Blair, A., and Exton, R., "Study of Cluster Formation and Its Effects on Rayleigh and Raman Scattering Measurements in a Mach 6 Wind Tunnel," AIAA-91-1496, AIAA 22nd Fluid Dynamic, Plasma Physics, and Lasers Conference, 24-27 June, 1991, Honolulu, Hawaii.
7. Vargaftik, N.B., Handbook of Physical Properties of Liquids and Gases: Pure Substances and Mixtures, pp. 43-44, 167-178, Hemisphere Publishing Corp., 1975.
8. Din, F. Thermodynamic Functions of Gases, Vol. I, pp. 123, 133, Butterworth & Co., London, 1962.
9. Quinn, E.L., Jones, C.L. Carbon Dioxide, Chapter III, Reinhold Publishing Corp. New York, NY, 1936.
10. Hill, P.G., "Condensation of Water Vapor During Supersonic Expansion in Nozzles," Journal of Fluid Mechanics, Vol. 25, Pt. 3, 1966, pp. 593-620.
11. Wegener, P.P. and Stein D.S. "Light-Scattering Experiments and Theory of Homogeneous Nucleation in Condensing Supersonic Flow," Supersonic Combustion, 1968.
12. Baumgartner, M.L., Smits, A.J., Nau, T.A., and Rowley, C.W., "A New Hypersonic Boundary Layer Facility," AIAA-95-0787, 1995.
13. Baumgartner, M.L., Erbland, P.J., Etz, M.R., Yalin, A.P., Muzas, B.K. Smits, A.J. Lempert, W.R., Miles, R.B., "Structure of a Mach 8 Boundary Layer," to be presented at the 35th AIAA Aerospace Sciences Meeting, January 1997, Reno, NV.
14. Yalin, A.P., Lempert, W.R., Etz, M.R., Erbland, P.J., Smits, A.J., and Miles, R.B., "Planar Imaging in a Mach 8 Flow Using Sodium Laser-Induced Fluorescence," 19th AIAA Advanced Measurement and Ground Testing Conference, 17-20 June, 1996, New Orleans LA.

Table 1		
Property	CO_2	H_2O
Molecular Weight	44.01	18.016
Melting Temp @ 1 atm	194.58 K	273.15 K
Critical Temp	304.19 K	647.27 K
Heat of Vaporization (TP)	347.3 kJ/kg (@ 216.55K)	2501 kJ/kg (@ 273.15 K)
Vapor Pressure @ 300 K	67.1 bar	0.035 bar

Table 1. Properties of carbon dioxide and water relevant to selection of seeding material.

Table 2		
	Low Reynolds Number	High Reynolds Number
P_o	3.53 MPa	6.73 MPa
T_o	776 K	782 K
ρ_o	15.9 kg/m^3	30 kg/m^3
mdot	0.91 kg/s	1.73 kg/s
Re_{inf}	8.5 x 10^6 m^{-1}	1.7 x 10^7 m^{-1}
Re_θ	2100	3500
P_{st}	344 Pa	689 Pa
T_{st}	56 K	57 K
ρ_{st}	0.021 kg/m^3	0.042 kg/m^3
P_{plate}	689 Pa	841 Pa
T_{plate}	483 K	528 K

Table 2. Test conditions for CO_2 enhanced FRS imaging of a Mach 8, zero pressure gradient, turbulent boundary layer at low and high Reynolds numbers.

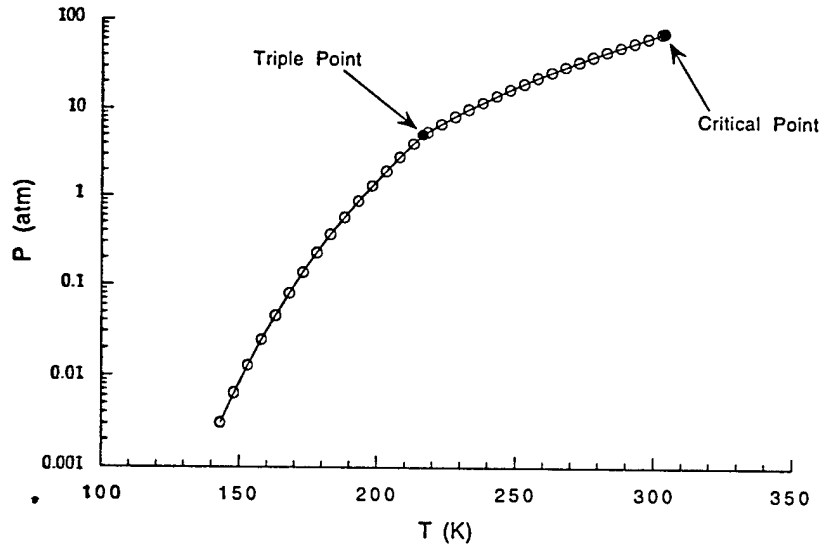

Figure 1. Solid/vapor and liquid vapor saturation curve for carbon dioxide.

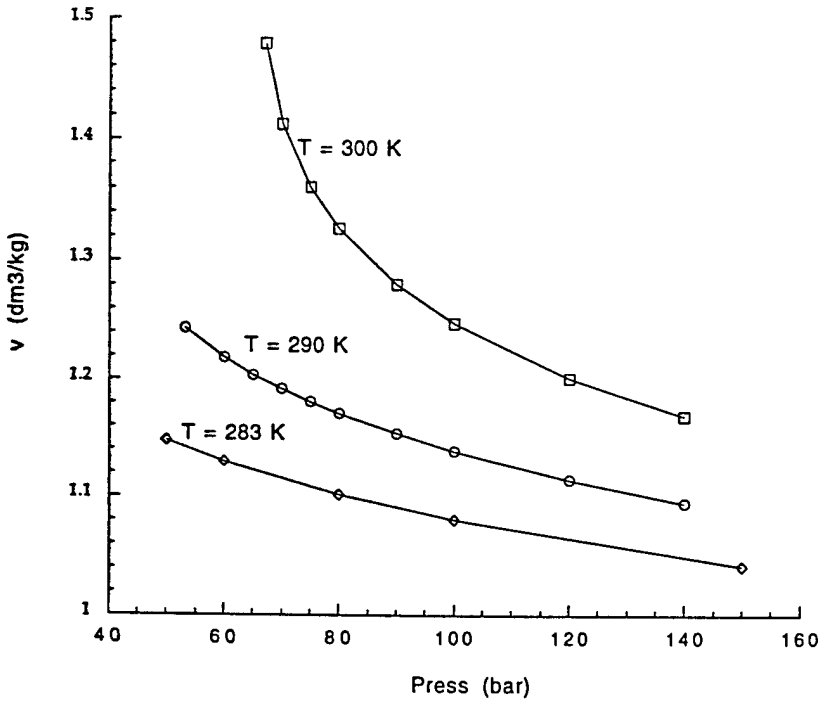

Figure 2. Carbon dioxide liquid compressibility data.

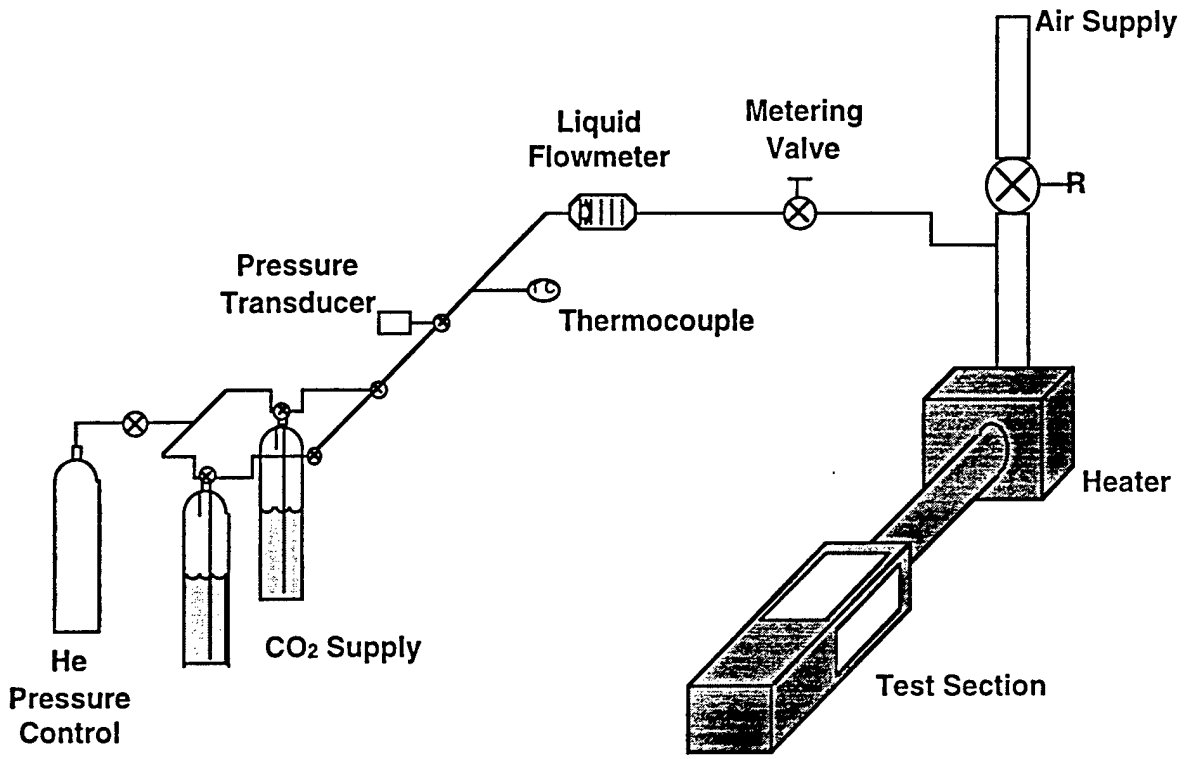

Figure 3. Liquid carbon dioxide metering and injection system.

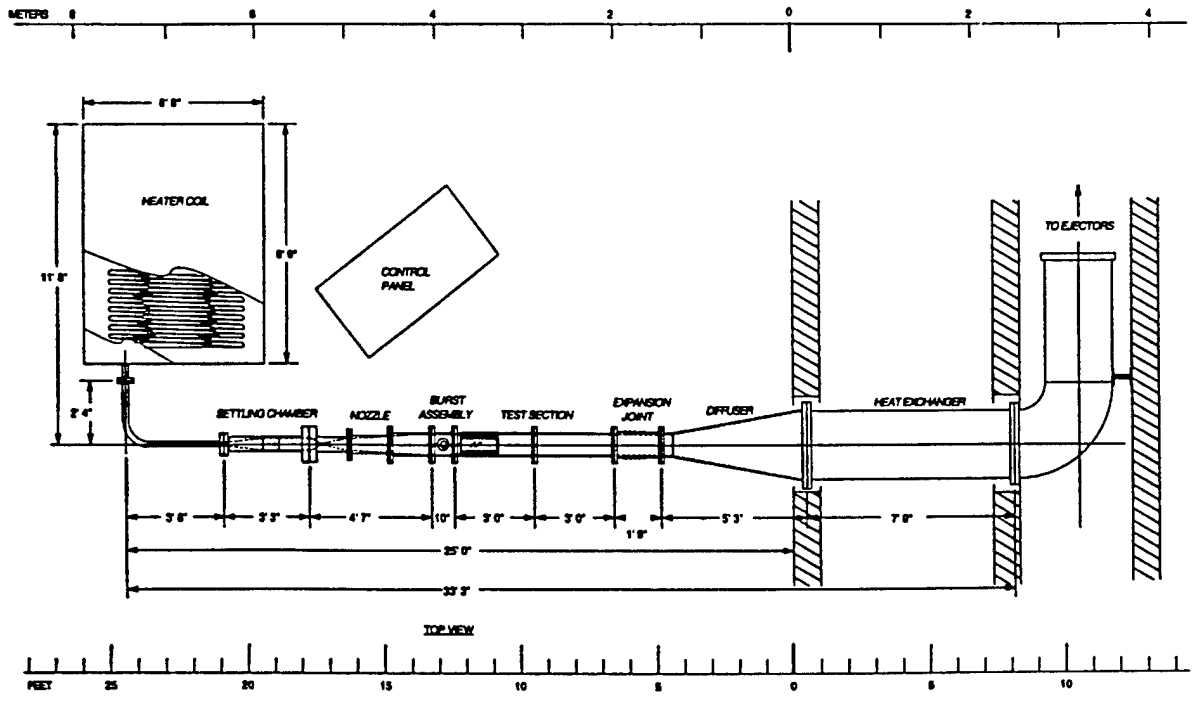

Figure 4. Schematic diagram of hypersonic test facility.

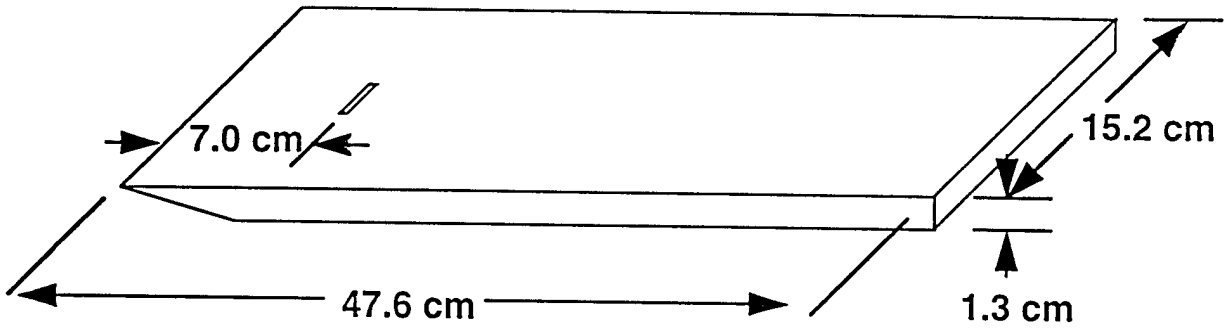

Figure 5. Schematic diagram of flat plate test article with transverse linear slot injector.

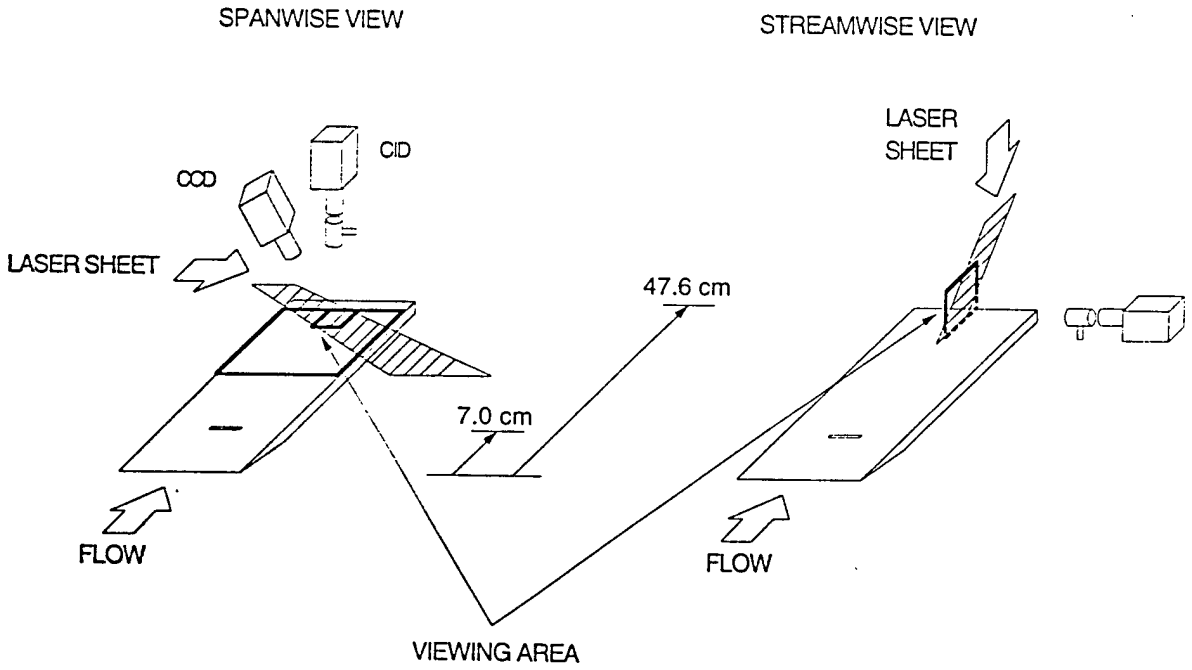

Figure 6. Schematic diagram of sheet orientations with viewing areas indicated. In both cases the viewing area is approximately 4 cm x 3 cm with the long dimension in the streamwise direction.

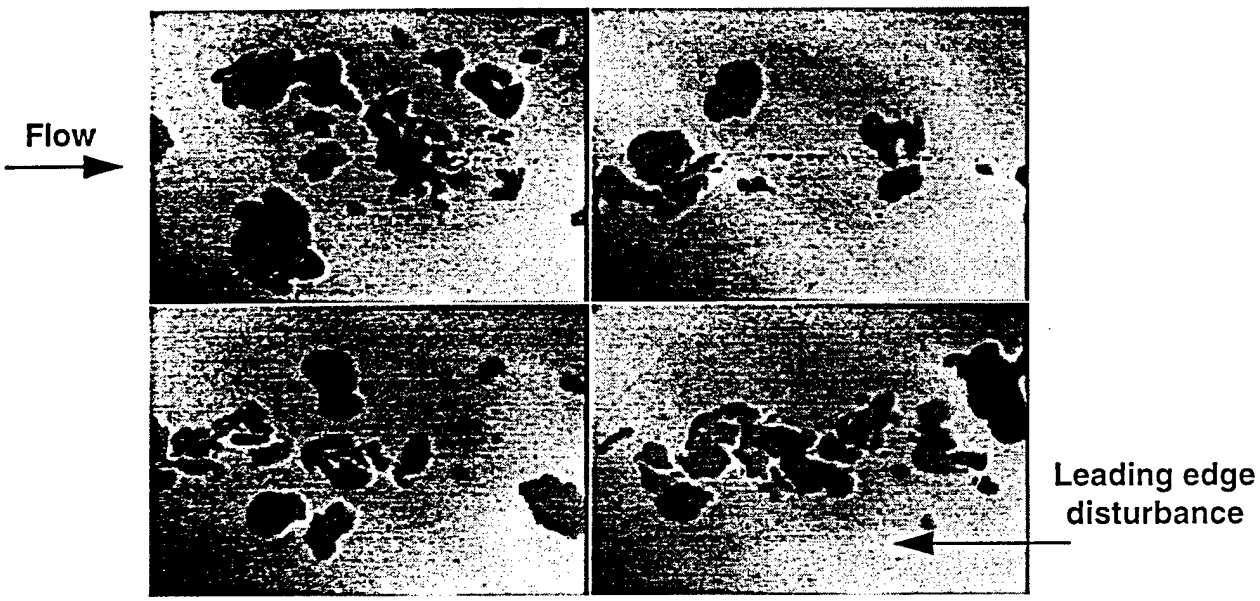

Figure 7. CO_2 enhanced Filtered Rayleigh Scattering of a Mach 8 turbulent flat plate boundary layer. Spanwise view. Laser sheet is 11 mm above the surface of the plate.

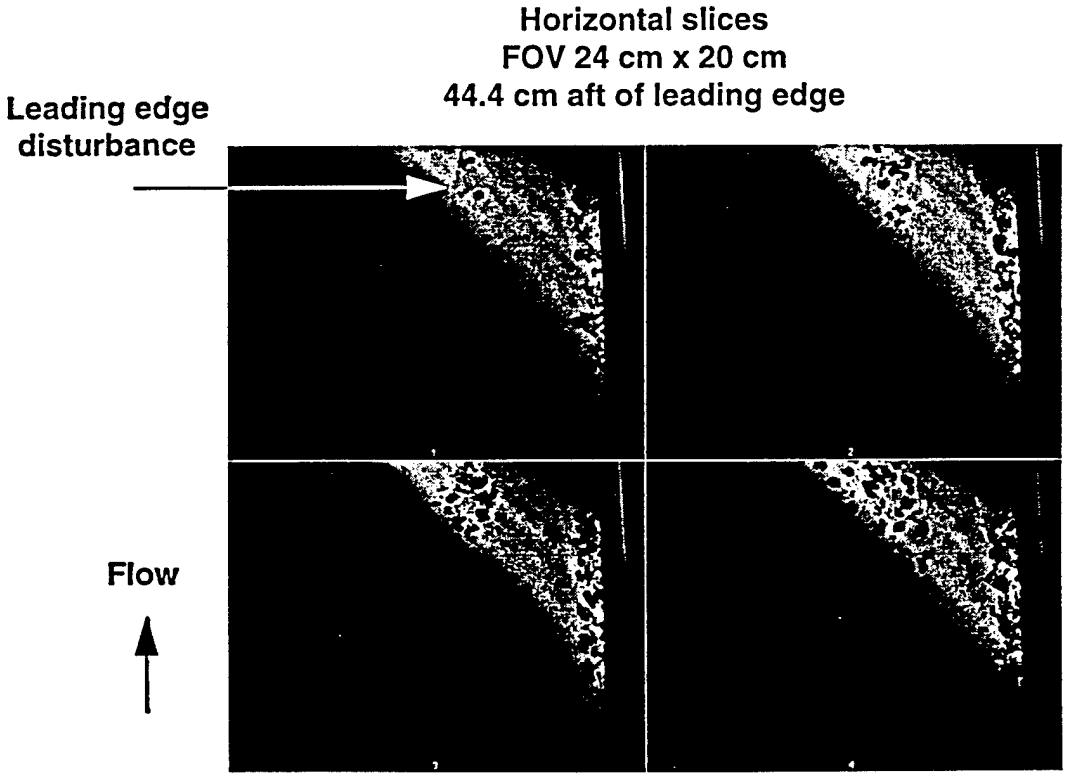

Figure 8. CO_2 enhanced Filtered Rayleigh Scattering of a Mach 8 turbulent flat plate boundary layer. Spanwise view. Progression of frames is from top left to bottom right. Laser sheet is lowered toward surface of the plate in frames 1-4.

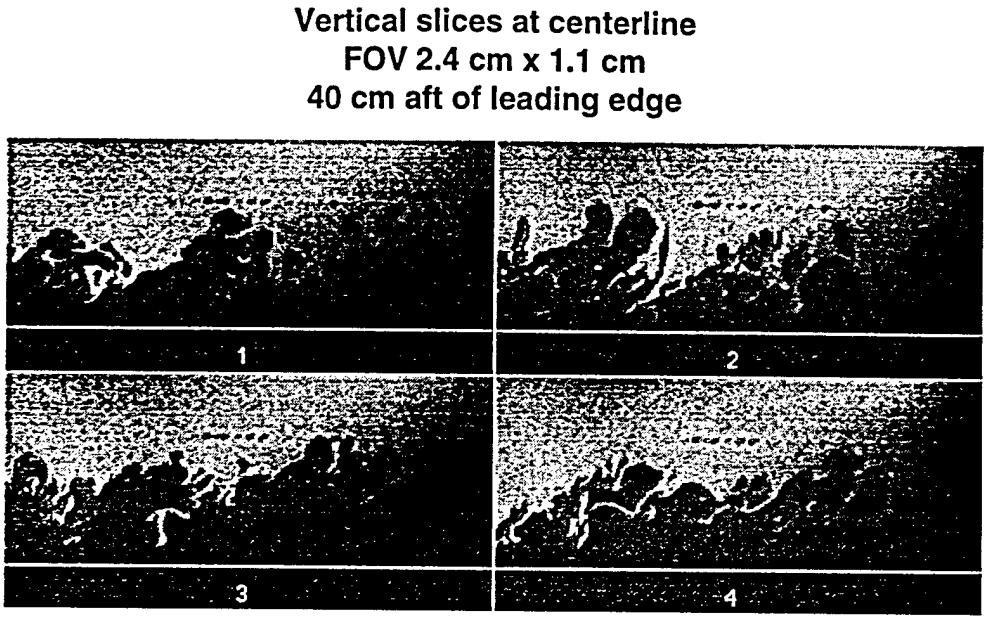

Figure 9. CO_2 enhanced Filtered Rayleigh Scattering of a Mach 8 turbulent flat plate boundary layer. Streamwise view. High Reynolds number test condition. Horizontal white line marks plate surface.

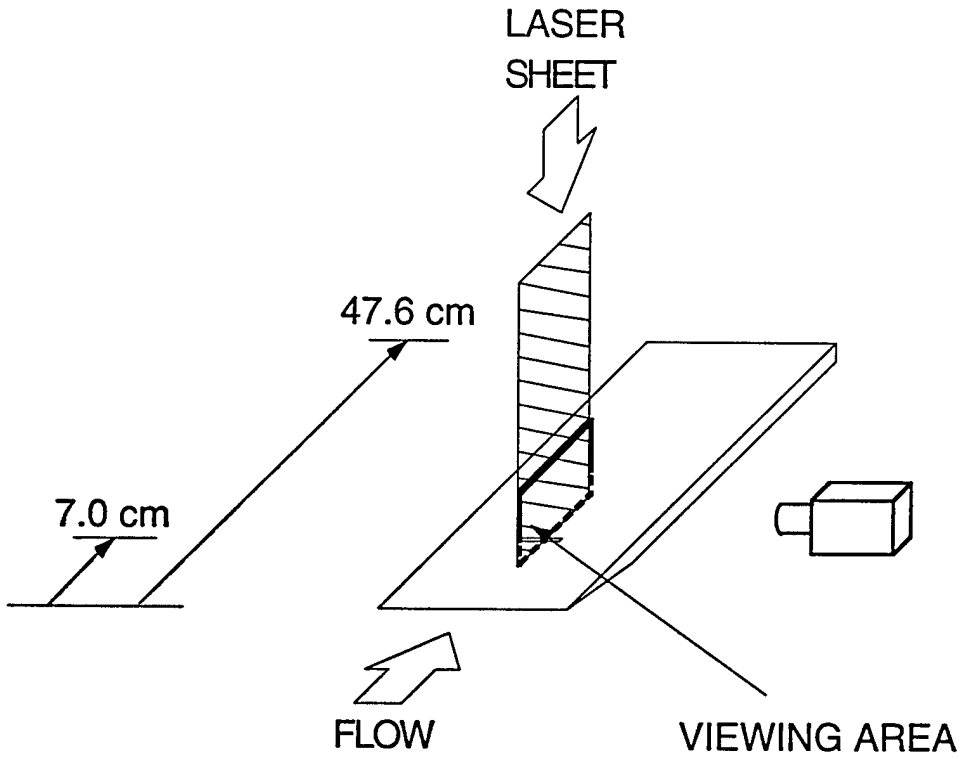

Figure 10. Schematic diagram of sodium PLIF sheet orientations with viewing area indicated. The viewing area is 8 cm x 6 cm with the long dimension in the streamwise direction.

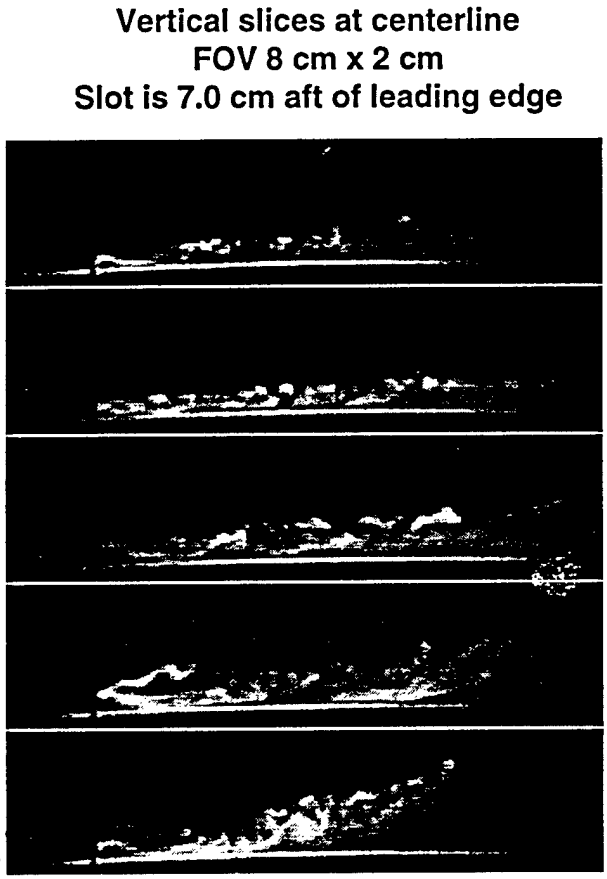

Figure 11. Planar Laser Induced Fluorescence of sodium seeded helium injected through the transverse slot in the flat plate. Streamwise view. Flow is from left to right. Note the flow separation in the lower panels.

AIAA 99-0769

Imaging the Evolution of Turbulent Structures in a Hypersonic Boundary Layer

P.J. Erbland
Air Force Research Laboratory
Computational Sciences Branch (AFRL/VAAC)
WPAFB, OH 45433

R. Murray
Rutgers University
Dept. of Mechanical & Aerospace Engineering
Piscataway, New Jersey 08854

M.R. Etz, M. Huntley, and R.B. Miles
Princeton University
Dept. of Mechanical & Aerospace Engineering
Princeton, NJ 08544

37th AIAA Aerospace Sciences Meeting and Exhibit
January 11-14, 1999 / Reno, NV

AIAA-99-0769

IMAGING THE EVOLUTION OF TURBULENT STRUCTURES IN A HYPERSONIC BOUNDARY LAYER

P.J. Erbland*
Air Force Research Laboratory
AFRL/VAAC
WPAFB, OH 45433

R. Murray†,
Dept. of Mechanical & Aerospace Engineering
Rutgers University
Piscataway, New Jersey 08854

M.R. Etz‡, M. Huntley†, and R.B. Miles§
Dept. of Mechanical & Aerospace Engineering
Princeton University
Princeton, New Jersey 08544

ABSTRACT

The convection and temporal evolution of flow structures in a Mach 8, zero pressure gradient turbulent boundary layer have been examined using carbon dioxide enhanced, double-pulsed Filtered Rayleigh Scattering (FRS). Image data were acquired for several elevations outside of and within the boundary layer at a free stream unit Reynolds number of 1.3×10^7 m^{-1}. Structure evolution was observed over distances of several centimeters to evaluate the rate at which the outer layer bursts grow. Preliminary analysis reveals that the structures extending outside the boundary layer (1.3δ) move with the free stream while further into the boundary layer, the average velocity decreases to $0.95U_\infty$ - $0.98U_\infty$. These data clearly show the motion and growth of the discrete turbulent structures and demonstrate the value of enhanced FRS diagnostics for studying the evolution of a turbulent boundary layer. The possibility of successfully correlating turbulent structure image data with conventional hot wire/film data in a hypersonic flow is now at hand.

INTRODUCTION

The behavior of compressible turbulent boundary layers and mixing layers has been the subject of intensive study and modeling for decades. Many different techniques have been used to characterize these flows including a range of intrusive probes (hot wires, hot films) and optical methods such as schlieren, interferometry, Rayleigh scattering, and laser induced fluorescence. Efforts to visualize the turbulent motion in boundary layers have often used injection and entrainment of tracer materials at the wall to allow tracking of near wall fluid as it mixes with the free stream. Rayleigh and Mie scattering have been used at supersonic Mach numbers (M=2.5-3) to investigate mixing layers, shock/boundary layer interactions, and turbulent boundary layer structures. Many of these studies employed scattering from condensable water vapor in the air supply to mark the interface between the cold free stream and the warm gas in the boundary layer. The utility of this technique in supersonic flows has led to the development of carbon dioxide enhanced Filtered Rayleigh Scattering (FRS) for the investigation of hypersonic flows. This diagnostic is particularly suited to interrogating the behavior, evolution, and convection of large-scale structures in the middle and outer region of the boundary layer.

A number of the techniques mentioned above have been applied to the study of the convection velocity of structures within high speed boundary layers. As discussed by Spina[1], efforts to characterize the convection velocity span a wide range of Mach and Reynolds numbers. High frequency wall pressure

---

* Aerospace Engineer, Senior Member, AIAA

† Graduate Student, Mechanical & Aerospace Eng., Member, AIAA

‡ Engineer, now at Lockheed-Martin Corp., CA, Member, AIAA

§ Professor, Mechanical & Aerospace Eng., Associate Fellow, AIAA

measurements have been used to infer convection velocity in supersonic and hypersonic flows[2-3]. The velocity is determined by correlation of signals from multiple, spatially separated transducers. These data generally show convection velocities in the range of 0.65-0.9U_∞. Several of the studies revealed dependence of the inferred velocity on the transducer spacing[3], and this has been attributed to frequency contributions from structures of different scale. However, this technique cannot directly indicate the scale nor the position of the disturbances within the boundary layer that contribute to the inferred velocity.

Many researchers have employed intrusive probes to determine the structure convection velocity as a function of position within the turbulent boundary layer. Streamwise separated hot wires have been used in supersonic and hypersonic flows to determine both the instantaneous and broadband convection velocities. Again the velocity is inferred from space-time correlations of the fluctuating signals from the sensors. The data span a broad Mach number range and Re_θ varies from 5000-80,000. Spina[1] used hot wires with streamwise separations of 0.11-0.18δ to determine the convection velocity of large-scale organized motions in a Mach 3 boundary layer. The correlations indicated that the broadband convection velocity was 0.9U_∞ across the entire outer region of the boundary layer. This is illustrated in figure 1 from Spina[4], which presents the broadband convection velocity distribution in the boundary layer superimposed on the mean velocity profile. The data points (ξ/δ) correspond to different hot wire separations. Conditional sampling and pattern recognition analysis revealed that the majority of the large-scale structures convected at nearly the same velocity. Owen and Horstman[5] used hot wires with streamwise separations of δ to 12δ to infer the convection velocity as a function of position in a M_∞ = 7.2 flow. Their results indicated a broadband velocity of nominally 0.8U_∞ over most of the outer region of the boundary layer.

Optical techniques have also been utilized to study boundary layer evolution and structure convection in high-speed flows. Smith and Smits[6] used high-speed schlieren in a M_∞ = 2.9 flow to detect organized motions associated with the distinct density gradients present in compressible boundary layers. It is interesting that they obtained a distribution of velocities which ranged from 0.82-0.98U_∞ and a mean convection velocity of 0.9U_∞ using this technique. Cogne and Forkey[7-8] used double-pulsed Rayleigh scattering in the same facility to image the streamwise evolution of large-scale structures. They determined the convection velocity by measuring displacement of individual points on those structures between the two frames. They observed that evolution of different parts of a given structure varied widely and that adjacent structures gave significantly different convection velocities implying strong interaction between structures. Their results revealed a distribution of convection velocities at all elevations as shown in figure 2, with the outer region (y/δ = 0.5-1.2) having values ranging from 0.87-0.98U_∞. Cogne's results also indicated some instances of very high convection velocities (0.82-0.92U_∞) deep in the boundary layer (y/δ = 0.1-0.2). It should be noted that since these structures grow in size as they convect, the use of features at the boundary of a structure can lead to biased values of the velocity. Therefore, selection of points must be accomplished with care. Based on a comparison of these results to the conditionally sampled data of Spina, Cogne concluded that Rayleigh image data present a more accurate picture of the instantaneous convection velocity distribution in the flow than hot-wire derived data.

Collectively, these studies have led to several interesting observations regarding the convection of large-scale structures in high-speed boundary layers. Both Spina[1] and Owen and Horstman[4] (hot wire results) observed that convection velocity of large-scale structures varied little across the outer region of the boundary layer. However for wire separations of 3.5 to 12δ, Owen and Horstman (M_∞ = 7.2) observed a broadband convection velocity approximately 10% lower than Spina. This disparity was postulated to be due to the relatively low frequency response of the hot wires used. The data of Smith and Smits[6], and Cogne[7], based on optical measurements, and Spina's pattern matched hot wire data, consistently indicate a distribution of structure velocities within the boundary layer, and these data all fall within the uncertainty of Spina's broadband results. This is a rich foundation on which to build. Based on these data, one might expect to see a distribution of convection velocities in a hypersonic boundary layer similar to that observed in the supersonic results discussed here.

The primary motivation for the current work was to demonstrate the ability to make Rayleigh scattering based optical convection velocity measurements in a hypersonic boundary layer. A secondary objective was to demonstrate the high quality of the resulting data relative to other potential techniques. For example, the use of wall pressure and intrusive probe techniques require that the fluctuation data be correlated to determine the convection velocities. The results are then only as good as the quality of the signal correlations, and that can have significant consequences. Chung[3] noted that a 1μsec error in their space-time correlation results produced a 10% error in their estimated convection velocity data. The determination of individual structure velocities requires use of conditional sampling and pattern matching with the attendant limitations on the range of structure scales that can be clearly discerned. By comparison, optical techniques allow direct imaging of the boundary layer and the determination of convection velocity of individual structures by time sequenced illumination. Moreover, broadband convection velocities

can be recovered by using correlation techniques on the images and ensemble averaging of large data sets. The accuracy of the derived velocities is limited by the spatial resolution of the camera systems, the timing accuracy of the laser pulses, and accuracy to which displacement of individual structures can be determined.

Finally, since density and streamwise velocity fluctuations are strongly correlated (Morkovin[9]) then providing that the CO_2 enhanced FRS indicates strong density changes, the structures detected by this technique can be interpreted as the same motions that dominate the mass flux space-time correlations from hot wire testing. Since this diagnostic is actually marking regions where CO_2 clusters have sublimated, it is more indicative of a strong change in temperature. However, if the assumption of constant pressure is allowed, which is reasonable for a zero pressure gradient boundary layer, then this reflects a density change in the flow as well. Thus, the structures observed with FRS should be directly comparable to the fluctuations measured with hot wires or films. This contention is supported by the work of Nau[10] who studied this very issue in a Mach 3 boundary layer. She compared the fluctuations measured by hot wires and condensate enhanced double-pulsed Rayleigh scattering and observed strong correspondence between the amplitude of the fluctuating Rayleigh scattering signal and the amplitude of the hot wire signal. She concluded that the high correlation between the two techniques indicates that the Rayleigh scattering does indeed represent density fluctuations of the flow for the wall distances studied ($y/\delta = 0.51$-0.68). Presumably this would hold out to the edge of the boundary layer as well.

It is with this perspective in mind, and a future desire to reconcile hot wire and optically based measurement approaches, that the current testing was conducted. These tests were intended to; (1) demonstrate the feasibility of double-pulsed FRS for imaging a hypersonic boundary layer, (2) provide new insight into the convection velocity of large-scale structures in that flow, (3) provide data to exercise the correlation techniques needed to infer structure velocities, and (4) establish baseline performance data for future simultaneous double-pulse FRS and hot film measurements.

EXPERIMENT DESCRIPTION

The CO_2 enhanced Filtered Rayleigh Scattering (FRS) diagnostic provides instantaneous planar images of boundary layer structures. The technique requires mixing a small amount of gaseous CO_2 into the tunnel air supply. The CO_2 condenses during the nozzle expansion forming small nanoscale clusters in the free stream which have a larger scattering cross section than the surrounding gas. Using Filtered Rayleigh Scattering, regions of cold flow where condensed CO_2 clusters are present appear bright, and regions of hot boundary layer gas where the CO_2 clusters have evaporated appear dark. An injection locked, frequency doubled Nd:YAG laser (532 nm) is used to illuminate the flow. The beam is expanded into a sheet and passed through the test section at an angle of 45 degrees relative to the flow axis to provide a Doppler shift in the CO_2 scattering. A narrow band molecular iodine absorption filter is employed to block background scattering from the tunnel walls and windows. The scattering from the flow is Doppler shifted outside the absorption band of the filter and is recorded by an intensified camera. Details of this diagnostic have been described previously by Erbland[11].

For the tests discussed here, the laser beam was formed into a horizontal sheet using a positive and negative cylindrical lens pair. The sheet was introduced through the side window passing from downstream to upstream at an angle of ~ 45° relative to the tunnel axis as illustrated in figure 3. The sheet was oriented parallel to the surface of the plate to take horizontal cross sections of the boundary layer. The final turning mirror and the sheet forming optics were mounted on a common platform and translated vertically to image the flow at different elevations above the plate. The sheet was estimated to be 100 μm thick at the focus, and the long focal length of the positive cylindrical lens was sufficient to keep the sheet thin across the full field of view of the camera.

A horizontal sheet orientation (planform illumination) was chosen in order to simplify the analysis and interpretation of the structure motion. Prior double-pulse investigations of supersonic flows using a vertical sheet (streamwise illumination – Cogne[7], Murray[12]) left a challenging problem for post-test analysis. The determination of convection velocity using the motion of discrete points at the structure interface risked biasing of the results due to structure growth and evolution. Techniques to correlate the motion of entire structures compromised the ability to discern velocity at different elevations in the boundary layer. The current approach allowed analysis of convection velocity at specific elevations, and both discrete point methods and correlation techniques could be evaluated to select the most appropriate and effective method for data reduction.

Two identical intensified CCD imaging systems, having matched fields of view, were used to capture the two laser pulses. Each system consisted of a Stanford Computer Optics 4Quick05 intensified CCD camera with a 210 mm focal length lens at f/4.5 and a magnification of ~ 0.26. A 10 cm long, 50 mm diameter iodine vapor cell was placed in front of each camera lens. The optical axis of the camera/filter system was orthogonal to the plane of the laser sheet. This resulted in a linear field of view of approximately 7.7 cm streamwise x 5.8 cm spanwise, centered 4.8 cm upstream of the trailing edge of the plate. The cameras were positioned on opposite sides of the tunnel and viewed the plate through a 40/60 beam splitter. The magnification of the cameras was identical although there was a small rotational offset and

lateral displacement between the two images that was discovered and dealt with during data analysis. Figure 3 illustrates the laser/camera orientations for this experiment. The camera video was passed to digital grab/hold units and then written to videotape for subsequent analysis.

The iodine filter design used in this work was developed and characterized by Forkey[7]. The nominal bandwidth of the iodine absorption line employed in this experiment was 1 GHz and the cell provided an attenuation of three orders of magnitude. The beam/flow geometry provided a Doppler shift of 1.7 GHz for scattering centers traveling with the free stream.

Laser illumination was provided by a Continuum double pulsed Nd:YAG laser with 290 mJ of energy available in the single pulse mode. This device can be Q-switched twice during a single flashlamp decay to provide two short duration laser pulses. Pulse durations were ~10ns, which effectively freezes the motion of the large-scale structures in the images. The interpulse separation was variable from 15-200 μsec, though if injection seeding was used this was limited in practice to between 30 and 200 μsec. Shorter separations were not possible because the first pulse disturbed the seeder, which takes about 30 μs to recover. Separations as long as 200 μs were unrealistic for these tests. Moreover, they are impractical since temporal jitter of the second pulse increases due to decreased pump energy. In the multiple Q-switched mode, the energies of the initial and delayed pulses were controlled by their relative placement in the laser gain curve. Achieving equal pulse energies for a given interpulse delay required monitoring the individual pulse energies while adjusting the initial Q-switch delay.

It was discovered that short interpulse delays resulted in a substantial reduction in the energy of each pulse compared to the single pulse energy. In fact, although the laser was capable of delivering single pulse energies of 290 mJ, the maximum combined energy of the two pulses for a 35 μsec delay was only 105 mJ. Therefore, success in imaging the flow required that either the seeding level or the camera intensifier gain be increased to compensate for the reduced laser intensity. We elected to use higher camera gains with the attendant noise penalties in order to minimize the CO_2 seeding of the flow.

Experiments were conducted in the Princeton Gas Dynamics Laboratory Mach 8 tunnel, on a zero pressure gradient, tripped turbulent boundary layer. The model was a 47 cm long, 15.2 cm wide, sharp flat plate with a 2.4 mm diameter spanwise running trip located 5.7 cm downstream of the leading edge. Tests were conducted at a mean free stream Reynolds number of 1.3×10^7 m^{-1}. Boundary layer properties were estimated based on a review of flow survey data taken in prior studies of this model at similar test conditions. The boundary layer thickness (δ) at the imaging location was ≈12 mm, and $Re_\theta \approx 4100$. Seeding rates of 0.56 lpm (0.2 gpm) were used during these tests. This corresponds to a CO_2 mass flow rate of 0.011 kg/s compared to the tunnel flow of 1.6 kg/s or a CO_2 to air mass fraction of 0.67%. The laser interpulse delay was 35±0.1μs, which resulted in structure convection of 44 mm (3.7δ) between images for features traveling at the free stream velocity.

RESULTS AND DISCUSSION

General Observations

Figures 4 and 5 illustrate typical raw image pairs acquired using CO_2 enhanced FRS with the laser sheet positioned at different elevations above and within the boundary layer. For each image pair the flow is from left to right, the top image is the initial image, and the bottom (delayed) image was acquired after a 35 μs delay. The elevation of the laser sheet over the plate is noted above each image pair. The bright regions are scattering from the CO_2 condensate in the flow. The dark patches are "outer layer bursts"; ejections of hot boundary layer gas from the near wall region. Each image pair has certain features boxed to aid in identifying common structures. Note that the evolution of the structures varies greatly, some features evolve very little while others show growth that is quite dramatic.

Examination of many images led to several observations. First, the structures generally retained their position relative to other structures regardless of size. That is, their relative motion was much less than their absolute motion as one might expect. Second, the dominant type of shape change seemed to be structure growth or expansion, although many instances of apparent stretching were also noted. In some cases, structures that appeared to be monolithic in the first image were cut or divided by lines of cold free stream fluid in the delayed image. Instances of structures growing toward and deforming other structures were also observed. There appeared to be no preferred direction of growth for structures i.e. upstream, downstream, or lateral. Rotation of structures was not readily apparent although there were a few instances where distinct features or even entire structures seemed to rotate between frames. Finally, at the lowest elevations in the boundary layer, discrimination of individual structures became quite difficult and it was the entrained pockets of cold free stream flow that were most easily discernable between images.

The double-pulse FRS technique worked very well despite the low pulse energies. As the laser sheet was lowered in the boundary layer, scattering from the model increased. This was due to secondary reflections off of the planar surfaces of the cylindrical lenses which scattered light onto the plate. The images from the camera viewing the flow using the 40% reflecting mirror surface exhibited lower signal to noise and this is readily evident in the initial image of each pair.

The majority of the image pairs taken at a given height in the boundary layer were useful for analysis. Occasionally one of the two laser pulses would not lock properly. This was detectable because the broadened laser scattering from the model would pass through the iodine filter and the plate features would be visible. These image pairs were discarded before analysis.

Data Analysis

Two techniques were used to analyze these data, structure-center analysis and two-dimensional image correlation. At the upper elevations in the boundary layer, manual analysis was accomplished by identifying structure centers in the initial and delayed images and then calculating the displacement of the center. This technique could not be used deeper in the boundary layer because the structures changed so dramatically that identification of a center was not feasible. The second method was applied at all elevations. This used two-dimensional image correlation to identify the motion of groups of structures between the two images. The resulting position data from both approaches were corrected to account for slight misalignments between the two imaging systems. Pre and post run alignment data allowed development of transformations which mapped the image coordinates onto the model-centered reference grid. The reference grid coordinates were then used for calculating all structure velocities.

Structure-center Analysis

This manual analysis approach was intended to provide a sanity check on the correlation results and was only applied at the upper two elevations in the boundary layer. At these elevations the structures were discrete enough to allow reasonably accurate visual identification and approximate designation of centers. Structures were selected that retained shape between two frames. In a few cases where the use of a structure center was not possible due to the gross changes in all structures in the frame, a distinct and unchanging feature on one of the structures was selected to mark the structure motion. Use of structure boundaries was avoided in order to prevent bias to the convection measurements due to growth. These analyses provided useful data to compare to the correlation results and also provided insight into the convection velocity of individual structures. These data also provided information on the distribution of structure convection velocities near the edge of the boundary layer.

The results shown here represent the preliminary analysis of a subset of the available data in order to gain insight into the viability of this approach. Figure 6 illustrates the distribution of structure convection velocities determined using this approach for the outer two measurement locations which both happen to correspond to $y/\delta > 1$. The measurements have been normalized by the calculated free stream velocity. Note that the free stream velocity changes during the course of the run due to the limited thermal capacity of the facility heater. The normalization accounts for the varying total temperature of the flow at different times during the run. Without this additional step, the convection velocity of the second measurement location, closer to the plate was higher than the first. The mean and standard deviation of the velocities at each position are also presented in this figure. An uncertainty analysis is required before these data can be used to draw definitive conclusions about the flow but one can observe that the structures extending to $y/\delta > 1$ seem to move with the free stream velocity.

Correlation Analysis

Correlation techniques have proven very useful for characterizing the evolution of large-scale turbulent structures and determining their convection velocity. The correlation routines used in this analysis were developed by Robert Murray[12-13] of Rutgers University and are based on a Linear Correlation Coefficient as developed in Numerical Recipes in C[14].

In general, the correlation between two images is determined as follows. An initial correlation window is selected in the initial image. This window is then correlated with corresponding window locations in the second image (delayed correlation window) for all possible horizontal and vertical offsets. This generates a correlation map or surface; the correlation coefficient as a function of the horizontal and vertical shift of the window. The peak of this surface corresponds to the (x,z) shift that gives the maximum correlation. We take this shift to be the distance that the structures within the selected window in the initial image traveled during the time delay between the images.

The image correlation approach developed by Murray differs in several important ways from common practice. First, spatial averages of the initial and delayed image correlation windows were subtracted from the fluctuating pixel values during the correlation. This was necessary since for some of the image pairs, the turbulent structure sizes were of the order of the correlation window size. Consequently the average values of the fluctuating pixel fields in the correlation windows may not go to zero as they would for large window sizes containing many structures. This modification served to reduce correlation of the background due to a net positive or negative pixel value in the correlation window, and allowed more accurate correlation of the structure form. The second significant modification was the variable normalization employed in the correlation. For window sizes on the order of turbulent structure sizes, the normal assumption of a statistical distribution of pixel values, independent of window location, does not hold. Therefore the normalization term does not remain constant over the entire correlation surface and must be adjusted according to the region of the image being correlated. Murray implemented an algorithm to recalculate the normalization and insure that the

correlation procedure correctly normalizes each point on the correlation surface.

In these analyses, the initial correlation window in the initial image was only correlated against that portion of the delayed image where the structures were likely to be found. This was done in order to reduce the computational burden of the correlations and increase the effective scale of the correlation maps for presentation purposes. A "target" window was selected within the delayed image and correlations were performed for each position of the initial window within this target window. Selection of the target window size and location was accomplished by first examining the image pairs to identify the nominal displacement of the structures. The target window was centered at that location. The target window size was determined by taking the initial correlation window size and allowing for ± 50 pixel shifts in the horizontal and ± 32 pixel shifts in the vertical directions. The validity of this approach was demonstrated in prior studies by correlating the initial window against the entire delayed image and then correlating against progressively smaller target windows.

Two issues that are central to the fidelity of the correlations are the preprocessing of the image files and the selection of the initial and target window sizes and locations. The brightness in each image is due to the instantaneous laser pulse energy, the sheet energy distribution, the instantaneous seeding concentration, and the imaging system characteristics including the sensitivity and spatial uniformity of the intensifier and CCD combination. Although the image processing could have addressed the individual contributions, we found that normalizing by the average image did a sufficient job of accounting for the integrated contributions of these factors. The effectiveness of this normalization was evident in the flatness or uniformity of the processed images. Thus, preprocessing involved averaging the images from a given camera, normalizing each image by the average, averaging the resulting normalized images, and subtracting this average from each image to obtain the fluctuating pixel values required for the correlation. Images from each elevation in the boundary layer were processed separately. An example of the raw and final processed images are shown in figure 7. This figure also illustrates the initial and target window sizes and locations for the correlations.

The initial correlation window size and location were held constant for all of the convection velocity calculations. To insure that the correlation results did not depend on these parameters, several different initial window sizes and positions were evaluated. These trials changed the x value of the average correlation surface by only 1.2 pixels. This study resulted in defining the initial window from $x = 0$ to $x = 180$ and $z = 40$ to $z = 300$ (180 pixels by 260 pixels). For each image set, the target window was located from $x = 275$ to $x = 555$ and $z = 0$ to $z = 325$ (280 pixels by 325 pixels).

Since the correlation was evaluated for each position of the initial window mapped onto the target window, the dimension of the correlation surface was equal to the difference in dimensions between the initial and target windows. Thus the correlation surfaces have a dimension of 100 X 65. Figure 8 shows correlation contours for individual image pairs taken at $y/\delta = 0.87$. Note that each image pair provided a distinct peak with a significant gradient away from the peak. This is an indication of good individual correlations and implies that each image pair can be used as a measure of velocity rather than having to average large numbers of images to get acceptable statistical values. This is further illustrated by figure 9 which shows contour plots of the average correlation surfaces for analysis of 20 and 100 image pairs at $y/\delta = 0.66$. This figure also shows cross plots (sections) of these profiles at the dz symmetry point ($dz = -5.5$). Use of more than 20 frames changed the magnitude of the correlation value but had almost no effect on the location of the peak correlation. The excellent agreement between the average correlation surfaces for these two sample sizes indicates that a 20 image set is sufficient for accurate determination of the convection velocity from these data. Figure 10 shows contour plots of the average correlation surfaces for each of the elevations in the boundary layer.

Several general comments are in order here. First, the individual correlation levels appear to be low but in fact the correlations are quite good. This is demonstrated by the fact that the individual image pairs correlated well. That is, they gave distinct individual peaks for most image pairs. The primary reason for the low correlation levels is thought to be the evolution of the structures. As the structures evolve, the quality of the correlation should decrease but the position of the correlation maximum should remain approximately the same (providing the convection velocity is constant). Another factor contributing to low correlation values may be the presence of significant noise in the images, especially those from camera 1. Noise will not pull the correlation one way or another. Rather random noise averages out but lowers the values of the correlation coefficients. It was also observed that the number of "good" individual correlations at the upper elevations displayed some sensitivity to the size of the target window in the delayed image. However, the peak in the average correlation surface changed by less than two pixels, so the affect on the average structure convection velocity was not significant. Finally note that each average correlation surface displays a negative dz offset. This is primarily a result of correlating the images before applying the correction for imaging system misalignment. Since the primary correction was a simple dx,dz translation of one camera frame relative to the other, the correlations could be performed on the raw images and then the corrections applied to the correlation results. However, even after this correction a small negative dz value (3 pixels)

remained in all of the results implying a small (10 m/s) crossflow velocity component away from the centerline.

Results

Figure 11 is a plot of the convection velocity as determined by the average correlation surfaces. This is obtained by simply dividing the peak correlation value (pixel shift) by the time delay between the images and applying the scale factors from the camera grid alignment. The average convection velocity as determined by the structure-center analysis is also presented for the outer two elevations in the boundary layer. All data are normalized by the free stream velocity computed from plenum conditions. The agreement between the average convection velocities determined by the two methods is acceptable. Note that the convection velocity is roughly the free stream value in the outer measurement locations and drops progressively to a value of $0.95U_\infty$ at $y/\delta = 0.45$. The fact that the normalized velocity at the upper two locations is slightly larger than unity (0.1% or 1.2m/s) indicates that uncertainties need to be carefully evaluated in both these measurements and the supporting tunnel measurement system before final conclusions can be drawn.

These data compare very well with convection velocity data derived from experiments at lower Mach numbers. The average convection velocities show a trend of decreasing velocity as the wall is approached, very similar to the mild trend in Spina's broadband hot wire data in figure 1. However, note that Cogne and Forkey (figure 2) found that convection velocities for structures extending outside the Mach 3 boundary layer still moved at less than the free stream value whereas these results indicate motion with the free stream. With respect to the structure-center derived velocity distribution data shown in figure 4, it is interesting that the distribution of convection values in the outer region is much tighter than that seen by either Cogne or Smith and Smits.

CONCLUSIONS

CO_2 enhanced, double-pulsed Filtered Rayleigh Scattering was used to measure the convection velocity of large-scale structures in a Mach 8, zero pressure gradient turbulent boundary layer. Two techniques were used to analyze the data, structure-center analysis and two-dimensional image correlation. The two techniques provided consistent results. The 2-D image correlations provided an effective and accurate way to deduce the image shifts even deep in the boundary layer where discrimination of individual structures was difficult. The resulting velocity data agreed well with data acquired at lower Mach numbers, lending credence to Spina's contention that a "universal" convection velocity profile may exist for all turbulent boundary layers.

These preliminary results demonstrate that this technique offers significant promise for future study of turbulent boundary layers. In particular, the simultaneous implementation of double-pulsed FRS and hot wire or hot film measurements in a hypersonic turbulent boundary layer is now possible. Additional work is required on the sensitivity of the correlation analysis to correlation parameters and additional attention needs to be paid to improving image signal to noise and assessing experimental uncertainties.

ACKNOWLEDGEMENTS

The authors wish to thank Robert Bogart and Philip Howard for technical assistance. We are also indebted to Professor Alexander Smits for allowing us the use of the Mach 8 Tunnel at the Princeton Gas Dynamics Laboratory. This work was sponsored by the U.S. Air Force Research Laboratory, Dr. George Seibert, and the U.S. Air Force Office of Scientific Research, Dr. Steve Walker, technical monitors.

REFERENCES

1. Spina, E.F., Donovan, J.F., Smits, A.J., "Convection Velocity in Supersonic Turbulent Boundary Layers," Phys. Fluids A 3 (12), pp 3124-3126, Dec 1991.

2. Speaker, W.V. and Ailman, C.M., "Spectra and Space-Time Correlations of the Fluctuating Pressures at a Wall Beneath a Supersonic Turbulent Boundary Layer Perturbed by Steps and Shock Waves," NASA CR-486, 1966.

3. Chung, K.M., Lu, F.K., "An Experimental Study of a Cold-Wall Hypersonic Boundary Layer," AIAA-92-0312, 30th Aerospace Sciences Meeting, 6-9 January, 1992.

4. Spina, E.F., "Organized Structures in a Supersonic Turbulent Boundary Layer," PhD Thesis, Department of Mechanical and Aerospace Engineering, Princeton University, Oct 1988.

5. Owen, F.K., Horstman, C.C., "On the Structure of Hypersonic Turbulent Boundary Layers," J. Fluid Mech. 53, 611, (1972).

6. Smith, M.W., Smits, A.J. "Cinematic Visualization of Coherent Density Structures in a Supersonic Turbulent Boundary Layer," AIAA-88-0500, 26th Aerospace Sciences Meeting, January, 1988.

7. Cogne, S., Forkey, J., Lempert, W.R., Miles, R.B., and Smits, A.J., "The Evolution of Large-Scale Structures in a Supersonic Turbulent Boundary Layer," FED-Vol. 151, ASME fluids Engineering Conference on Transitional and Turbulent Compressible Flows, Washington, D.C., June 20-24, 1993.

8. Forkey, J., Cogne, S., Smits, A.J., Bogdonoff, S., Lempert, W.R., Miles, R.B., "Time-Sequenced and Spectrally Filtered Rayleigh Imaging of Shock Wave and Boundary Layer Structure for Inlet Characterization," AIAA-93-2300, AIAA/SAE/ASME/ASEE 29th Joint Propulsion Conference and Exhibit, 28-30 June, 1993.

9. Morkovin, M.V., "Effects of Compressibility on Turbulent Flows," in The Mechanics of Turbulence, Proceedings of the Intl Symposium on the Mechanics of Turbulence, CNRS, Paris, 1962, Gordon and Breach, 1964.

10. Nau, T.A., "Rayleigh Scattering as a Quantitative Tool in Compressible Turbulent Boundary Layers," MS Thesis 2026T, Department of Mechanical and Aerospace Engineering, Princeton University, Princeton NJ, 1995.

11. Erbland, P.J., et. al., "Development of Planar Diagnostics for Imaging Mach 8 Flowfields Using Carbon Dioxide and Sodium Seeding," AIAA-97-0154, 35th Aerospace Sciences Meeting, 6-10 January, 1997.

12. Murray, R.C., Elliott, G.S., "The Compressible Shear Layer Over a Two-Dimensional Cavity," AIAA-98-0430, 36th Aerospace Sciences Meeting, 12-15 January, 1998.

13. Murray, R.C., "Compressible Shear Layer Over a Two-Dimensional Cavity," MS Thesis, Mechanical and Aerospace Engineering Department, Rutgers University, New Brunswick NJ, 1999.

14. Press, Teukolsky, Vetterling, and Flannery, 1992, Numerical Recipes in C, (Oakleigh, Victoria, Australia; Cambridge University Press).

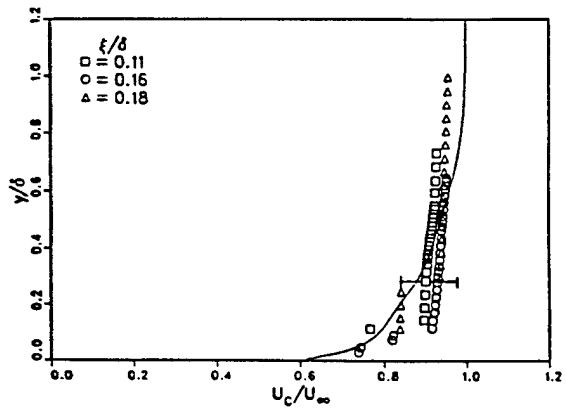

Figure 1. Broadband convection velocity for a Mach 2.9 turbulent boundary layer determined using space-time correlations of data from streamwise separated hot wires. ξ/δ indicates dimensionless wire spacings. Data are superimposed on the mean velocity profile. From Spina[4].

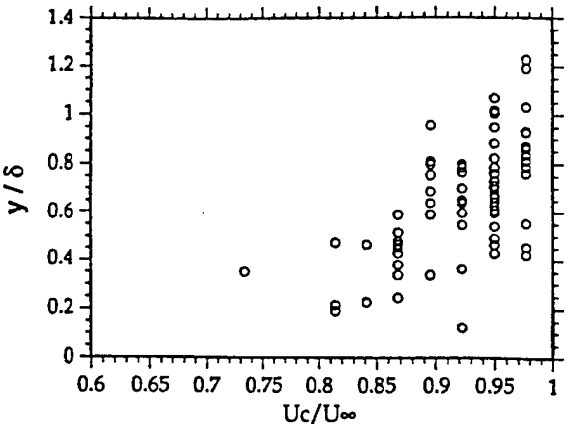

Figure 2. Individual convection velocities for a Mach 2.9 turbulent boundary layer from double-pulsed Rayleigh scattering with vertical (streamwise) illumination. From Cogne[7].

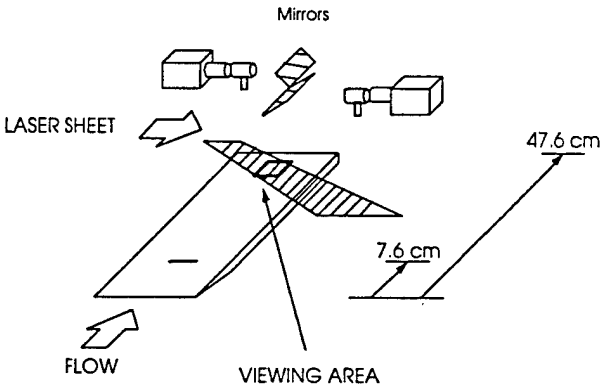

Figure 3. Laser sheet and camera orientation for double-pulsed Filtered Rayleigh Scattering experiments.

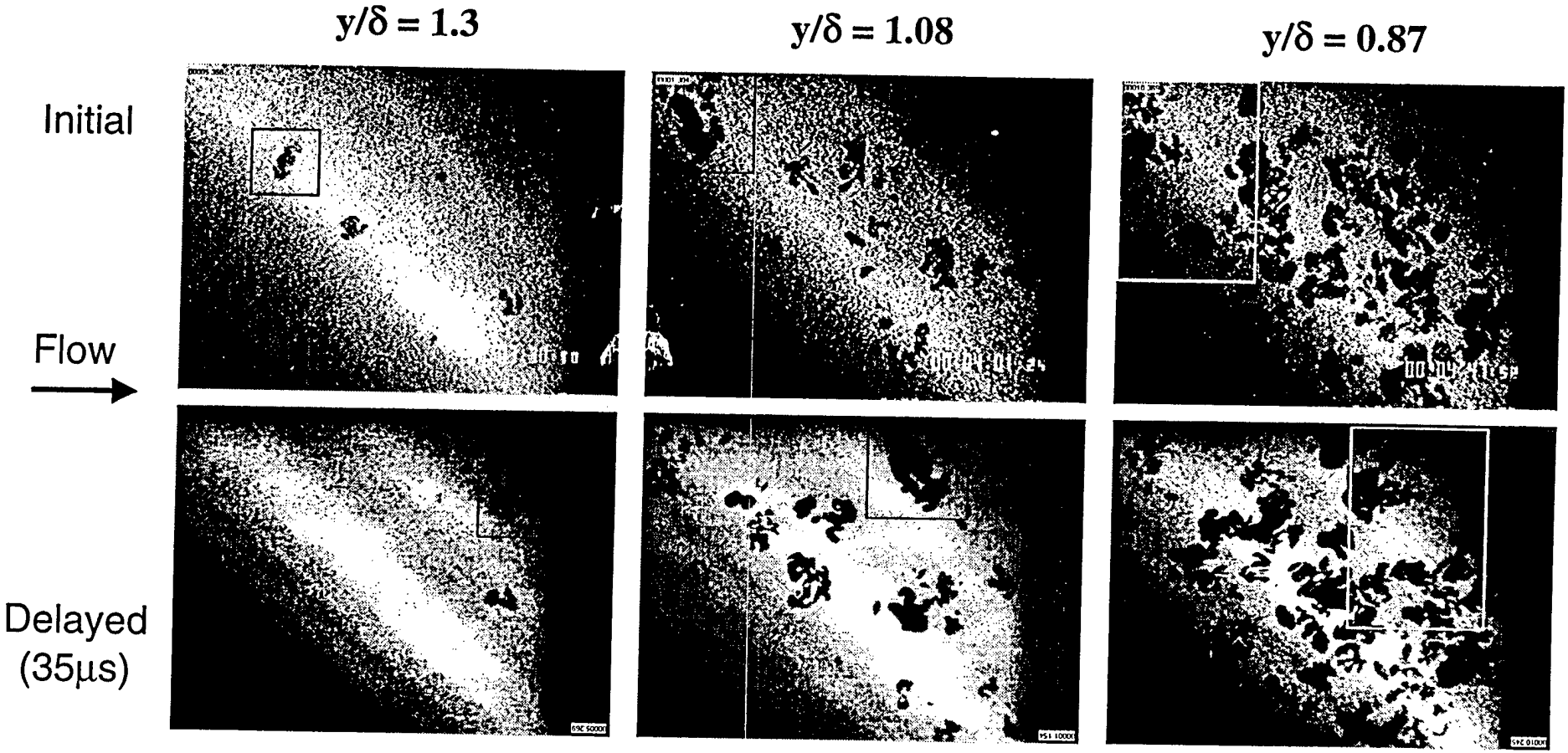

Figure 4. Typical image pairs showing convection and evolution of turbulent structure cross sections at three elevations in the boundary layer. Flow is from left to right. The top images were acquired first. Boxes indicate features of interest.

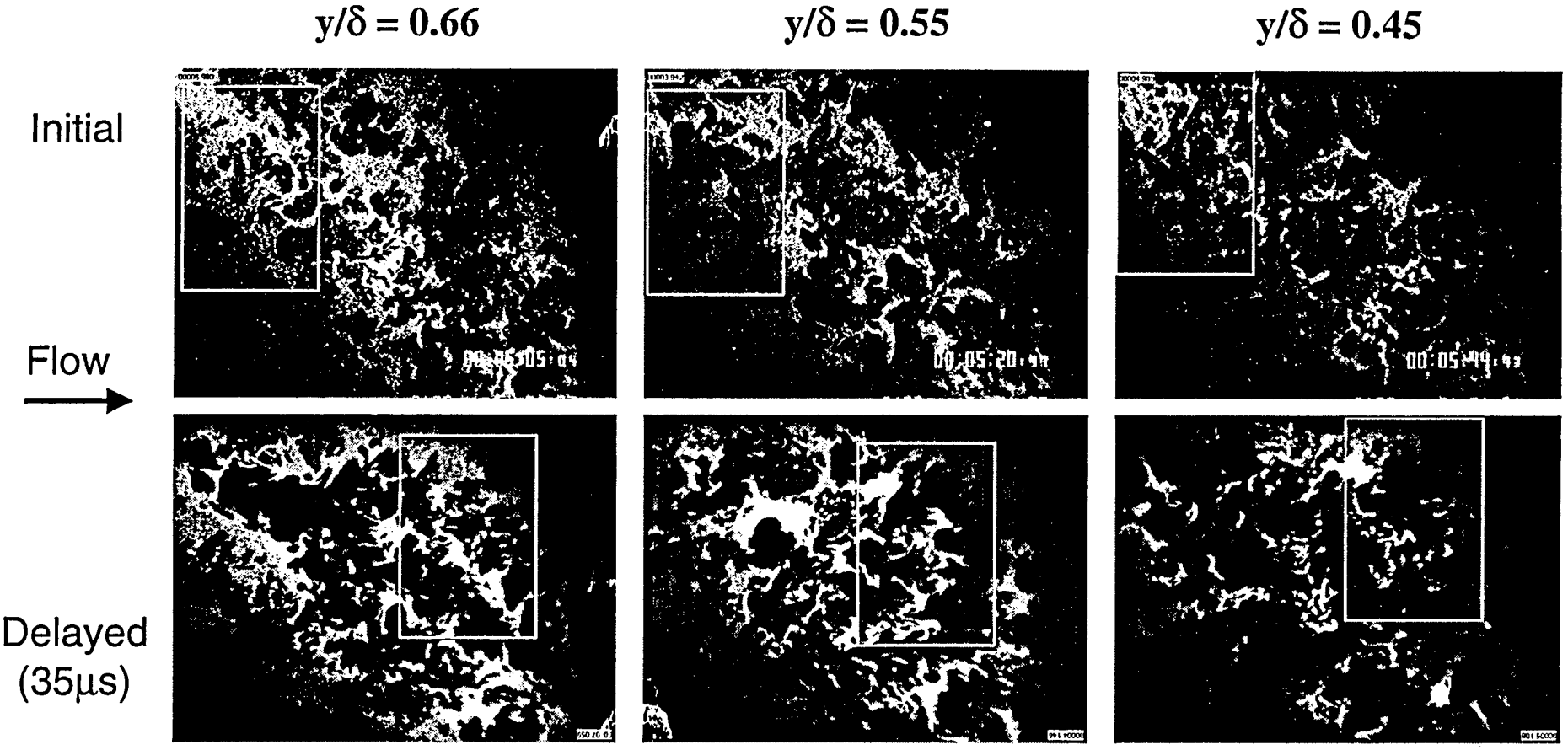

Figure 5. Typical image pairs showing convection and evolution of turbulent structure cross sections at three elevations in the boundary layer. Flow is from left to right. The top images were acquired first. Boxes indicate features of interest.

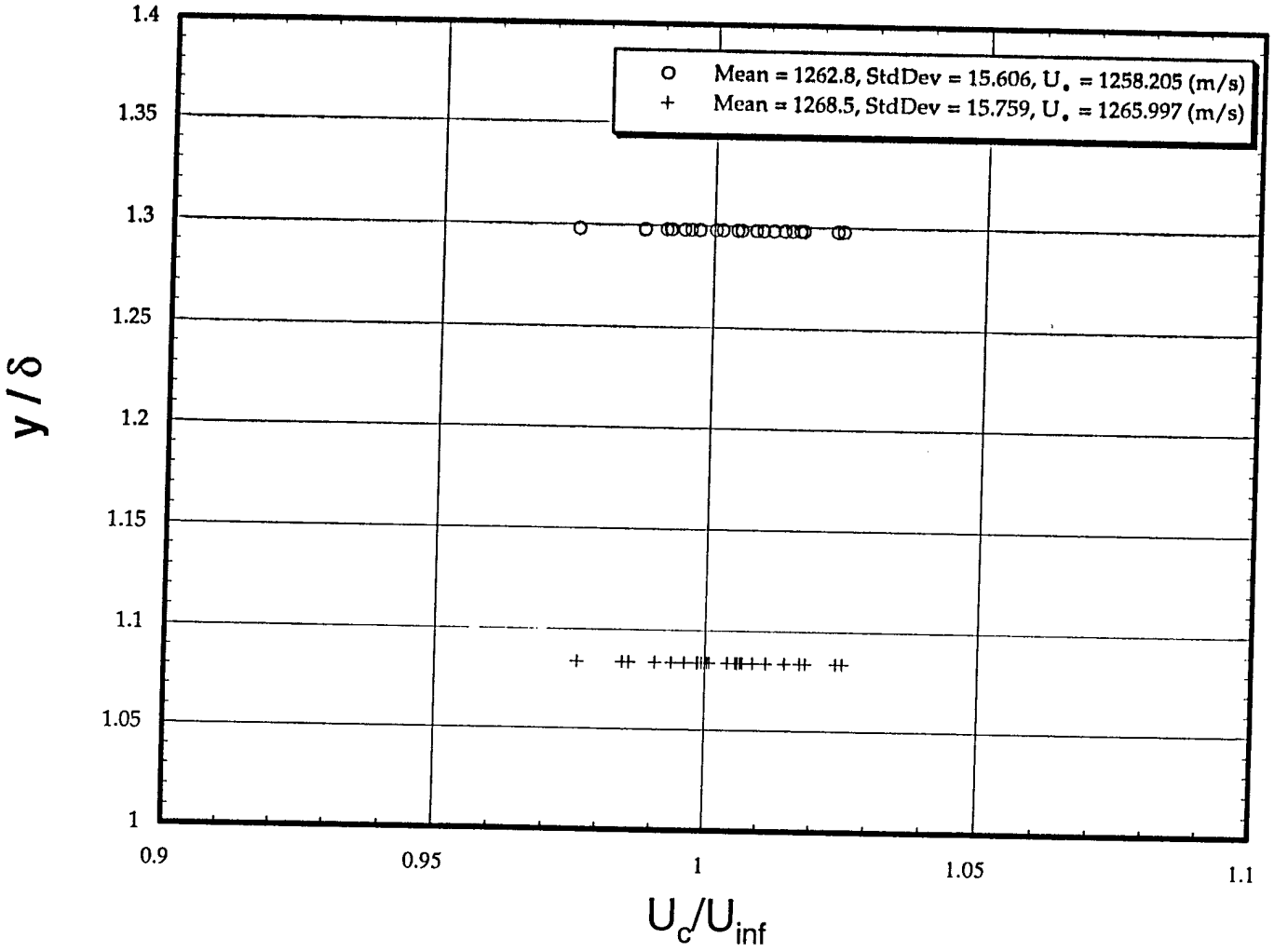

Figure 6. Distribution of structure convection velocity at the outer edge of a Mach 8 turbulent boundary layer. Results derived from structure-center analysis of double-pulsed FRS data. Legend lists velocity statistics.

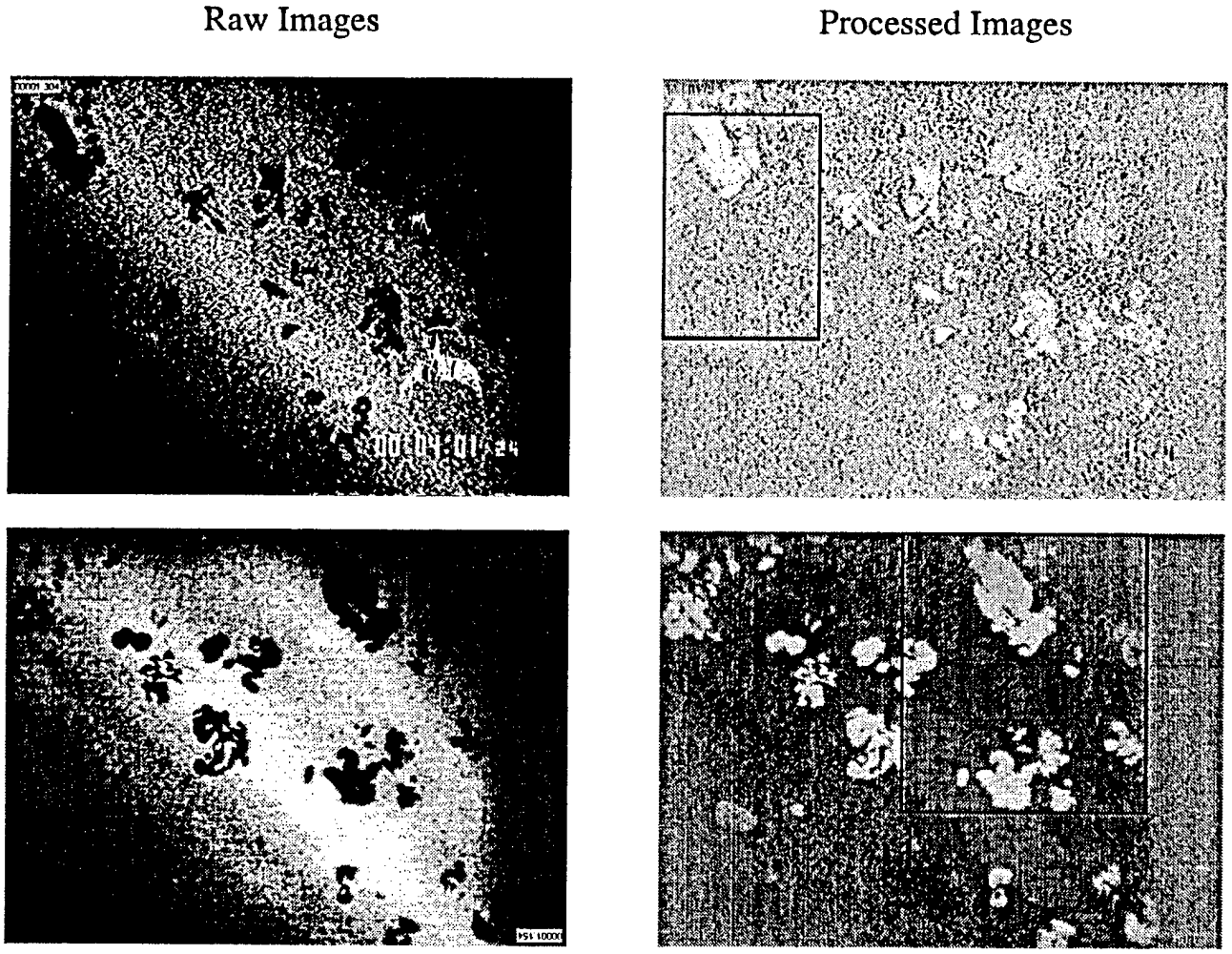

Figure 7. Typical raw (left) and processed versions of an image pair at $y/\delta = 1.08$. Flow is from left to right. The top figure is the initial and the bottom the delayed image. The boxes in the processed images mark the initial and target correlation windows.

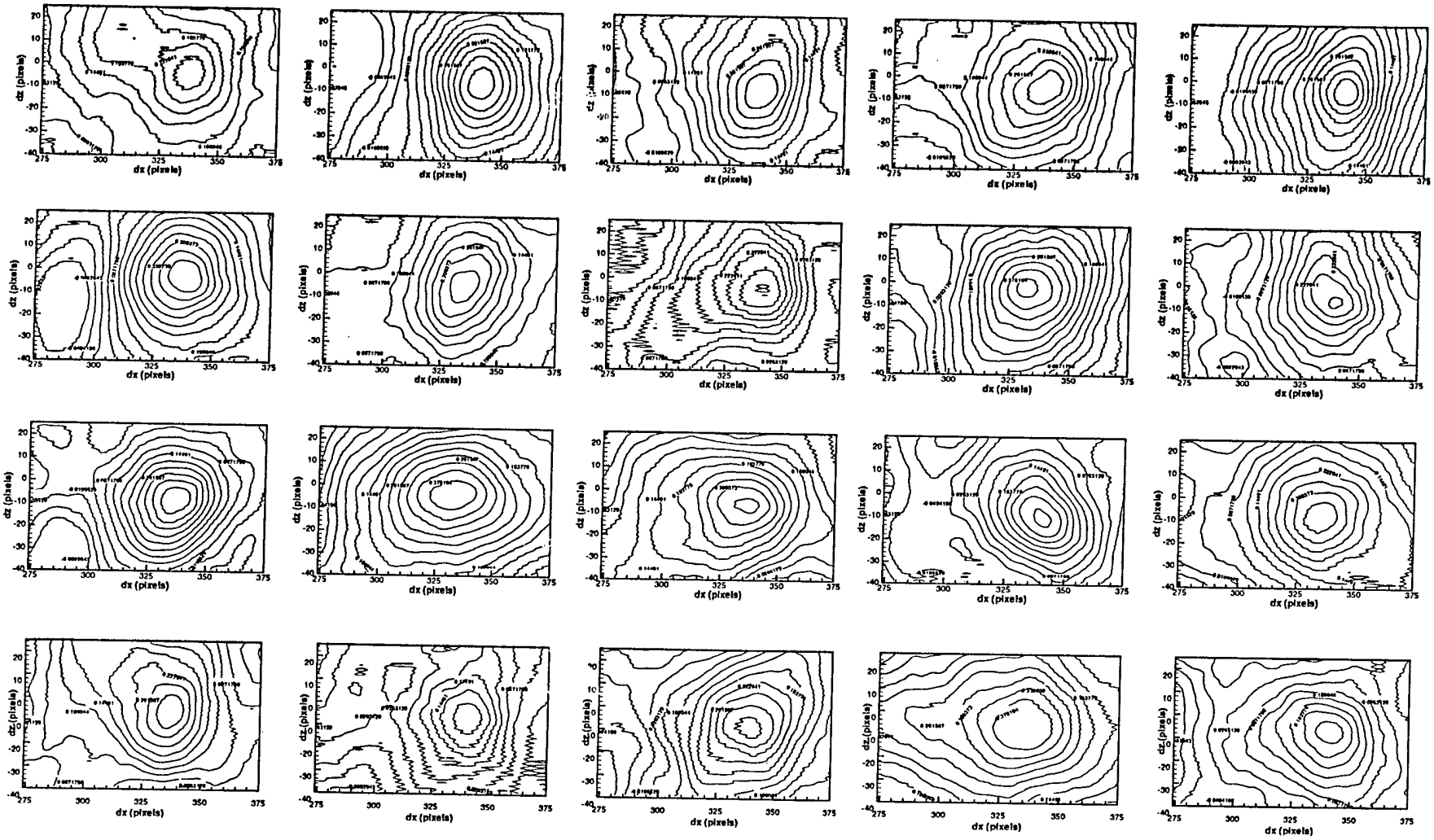

Figure 8. Contour plots of the correlation surfaces for 20 image pairs recorded at $y/\delta = 0.87$ in a Mach 8, zero pressure gradient turbulent boundary layer. Correlations reflect structure motions as dx and dz pixel shifts.

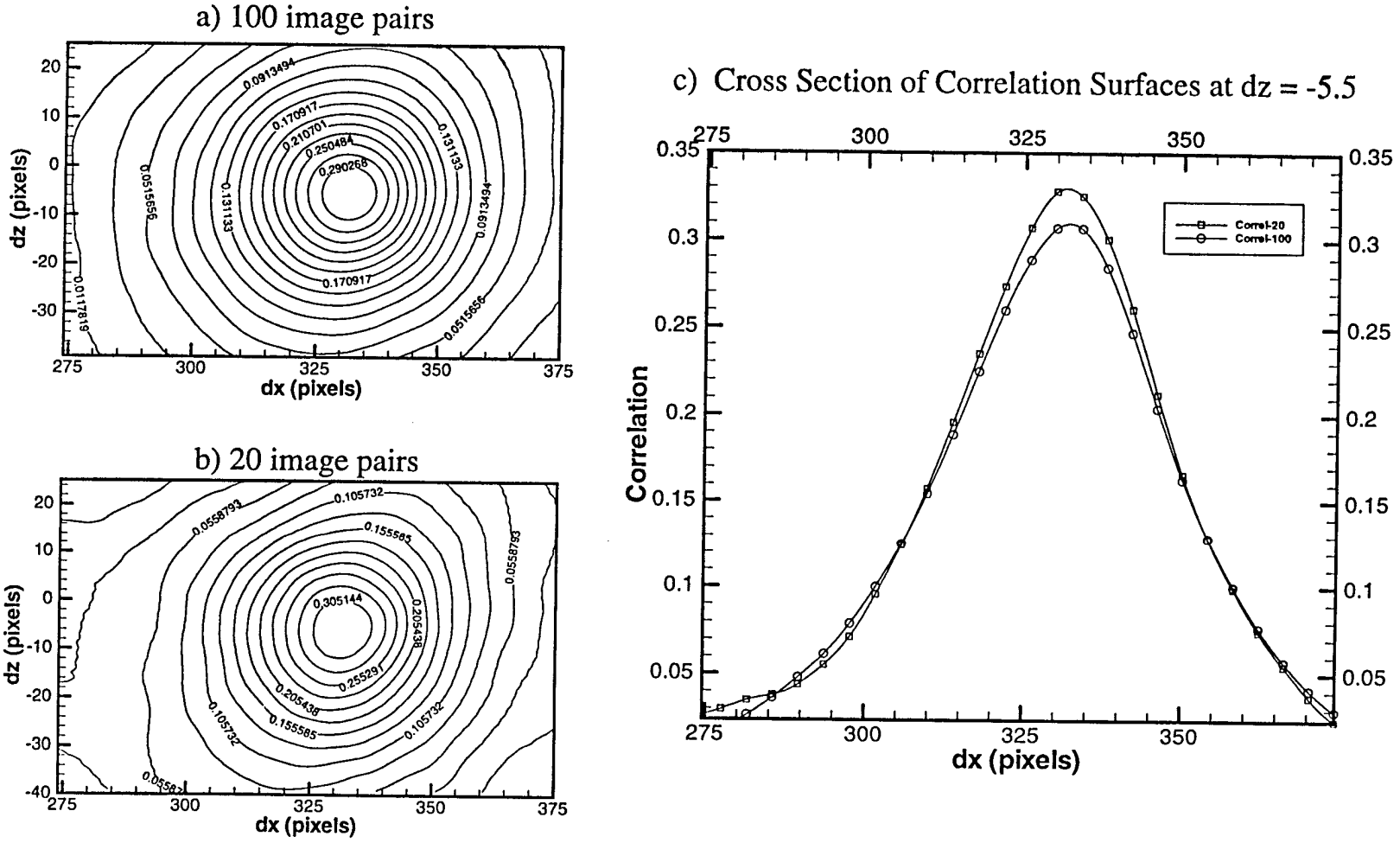

Figure 9. Panels a and b are contour plots of the averaged correlation surfaces for 100 and 20 image pairs recorded at $y/\delta = 0.66$ in a Mach 8, zero pressure gradient turbulent boundary layer. Panel c presents cross sections of these surfaces taken at dz = -5.5 (peak location). Symbols are only used to identify the curves.

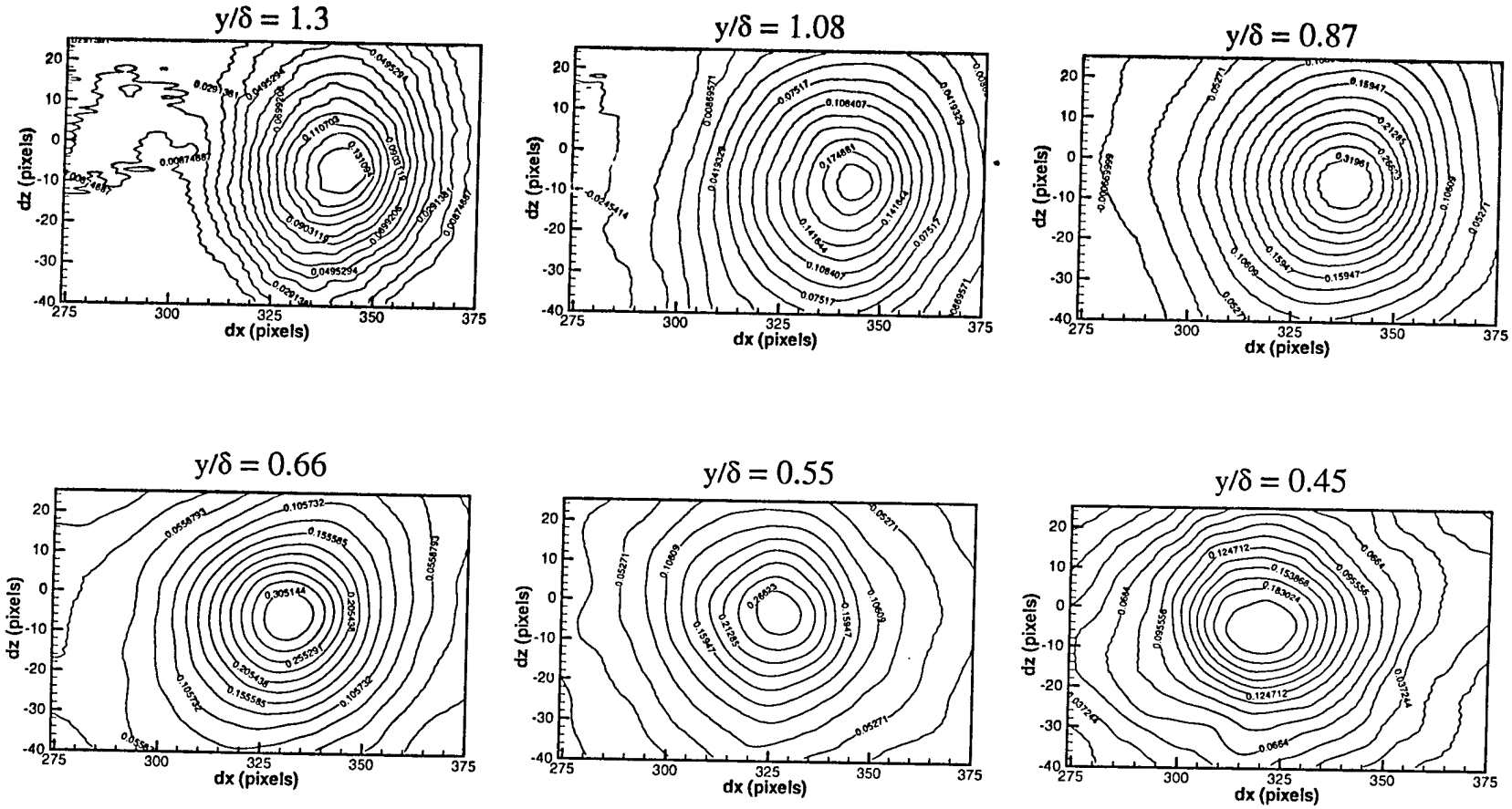

Figure 10. Contour plots of the averaged correlation surfaces at six elevations in a Mach 8, zero pressure gradient turbulent boundary layer. Correlations reflect structure motions as dx and dz pixel shifts. The position of the laser sheet for each data set is noted above the figure.

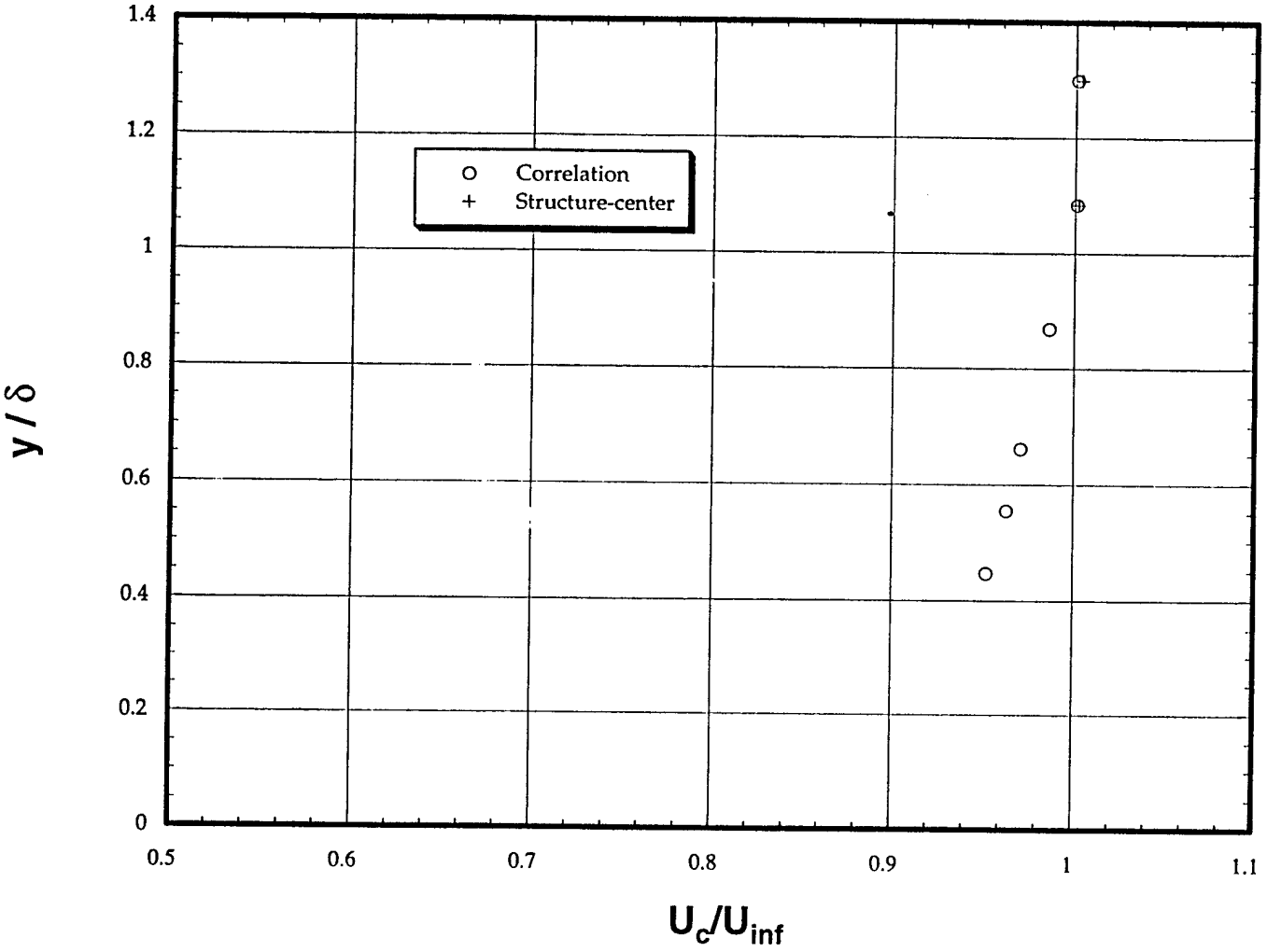

Figure 11. Average convection velocity at various positions within a Mach 8, zero pressure gradient turbulent boundary layer. From 2-D image correlation analysis and structure-center analysis of double-pulsed FRS data.

AIAA-2000-0647

MHz Rate Visualization of Separation Shock Wave Structure

P. Wu, and R.B. Miles
Princeton University
Dept. of Mechanical & Aerospace Engineering
Princeton, NJ 08544

38th Aerospace Sciences Meeting & Exhibit
10-13 January 2000 / Reno, NV

"MHz Visualization of Separation Shock Structure"

Pingfan Wu*, and Richard B. Miles§
Department of Mechanical and Aerospace Engineering
Princeton University, Princeton, NJ 08544

Abstract

The interactions between shock-waves and turbulent boundary-layers in a Mach 2.5 wind tunnel have been visualized by a MHz-rate imaging system. The shock waves were produced by two-dimensional compression corners having angles of 14° and 24°, and the flows were, respectively, attached and separated. At the compression corner, the sequential images clearly indicate the correlation between the shock motion and incoming turbulent boundary layer. Some large eddies in the boundary layer cause the shock to move in the streamwise direction for distances as large as the boundary layer thickness at a frequency as high as 100 kHz. Other eddies do not seem to effect the shock wave. The images also show the influence of the shock waves on the boundary layer structures.

* Graduate Student, Mechanical & Aerospace Engineering, Student Member AIAA.
§ Professor, Mechanical & Aerospace Engineering, Associate Fellow AIAA.

1. Introduction:

The shock-wave/boundary-layer interaction (SWBLI) is a very important supersonic flow phenomenon which can cause changes in heat transfer, flow separation, amplification of turbulence, generation of strong secondary flows, and unsteadiness.[1] Figure 1 shows the separation shock structure of two typical two-dimensional interactions in the laminar flow: a compression-corner interaction and an incident shock interaction. While the SWBLI in the laminar flow has been studied in detail and is now fairly well understood,[2] the more complex interactions between shock waves and turbulent boundary layers continue to be of great interest. Because of the high Reynolds numbers encountered in most practical applications, Direct Numerical Simulation (DNS) cannot be used to calculate the dynamics of turbulent flow interactions with correct or projected computer platforms. Experiment is still the only approach to the study of this process.

Experiments have shown that the shock is unsteady in the presence of a turbulent boundary layer. Through the works in the past 25 years, it has been recognized that the incoming turbulent boundary drives the shock motion.[3-5] But the characteristics of the boundary layer and shock wave coupling are still not clear, particularly:

1) What is the scale of the shock motion? Is it just small-scale jitter, or large-scale fluctuation?
2) What features of the boundary layer structure drive the shock motion?
3) How does the shock wave influence the boundary layer?

The major limitation on the experiments is the instrumentation. Most of the work aimed at investigating unsteadiness in the shock wave has relied on measurements by pressure transducers

along the wall. In the spatial domain, the pressure transducers only yield a point-measurement at the wall. They give no information about the flowfield. In the frequency domain, the fastest frequency response among these transducers is only 50 kHz.[3] Beresh and Dolling[6,7] have used the double-pulse planar laser imaging (PLI) and particle imaging velocimetry (PIV) to interpret the separation shock and flow motion. Their planar images give enough resolution to visualize the large eddy structure, but two sequential images are not enough to show the shock evolution.

People have long suspected that the large eddies in the boundary layer interact directly with the shock.[4,5] In Cantwell's review paper,[8] the data show that the physical dimensions of the large eddies are on the order of the boundary layer thickness, δ. The data also show that the convection velocity U_c of the large eddies is on the same order of the free stream flow velocity U_e (more specifically, is 0.6 ~~ 0.9 U_e). The large eddy frequency (U_e/δ) of the supersonic flow is usually above 100 kHz. So it can be assumed that important phenomena associated with the shock-wave/boundary-layer interaction may occur at or above 100 kHz.

In this paper, the unsteady shock structure was visualized by a MHz-rate imaging system. The MHz-rate imaging system[9] can capture 30 sequential images at framing rates as short as 1 image per microsecond. These image sequences show the dynamics of the shock-wave/boundary-layer interaction process. The interactions in a Mach 2.5 wind tunnel were produced by two-dimensional compression corners having angles of 14° and 24°, and the flows were respectively attached and separated from the tip of the wedge.

2. Facilities:

The MHz-rate imaging system consists of a pulse-burst laser and a CCD framing camera. The MHz repetition rate pulse-burst laser system can generate more than 30 pulses at each burst. The individual pulses can repeat as fast as 1 MHz and the burst repeats at 9 Hz. The time duration of each pulse is variable, and for this work was set to about 10 ns. The average pulse energy is 100 mJ at 1.06 μm and 25 mJ at 0.532 μm. The linewidth of the laser pulse (~90 MHz) is close to the Fourier transform limit, so it is suitable to be used in techniques that require narrow linewidth, such as filtered Rayleigh scattering (FRS).

The MHz framing rate CCD camera is built by Princeton Scientific Instruments, Inc. It uses on-chip storage technique and can store 30 frames. More details about the MHz-rate laser and camera technology can be found in reference 9.

The Mach 2.5 wind tunnel has a test section of 13 cm × 26 cm. The test section is 16 inches downstream of the throat, so the incoming boundary layer undergoes natural transition well upstream of the test section. All the four sides of the test section are made of glass windows to provide optical access. The stagnation temperate T_0 is 258 K and stagnation pressure P_0 is 120 psig. The Reynolds number based on the momentum thickness is approximately 14,000. The boundary layer thickness δ is approximately 3.3 mm.

In order to enhance the Rayleigh scattering signal, gaseous CO_2 was seeded into the flow well upstream of the plenum at a level less than 1% (weight). In the cold free stream, the CO_2 condensed to fine clusters whose dimensional scale is around 10 nm. In the hot boundary layer, the CO_2 cluster vaporized (sublimed). Smith[10] has compared the signal measured by the probe and scattering from the condensed clusters. He found that the scattering from the condensed clusters represents very well the outer boundary layer density profile.

The model to generate shock waves in the tunnel is a brass wedge. It is 2 inches long by 1 inch wide by 0.085 inches thick and fasten to one side of the wind tunnel. In order to get streamwise view, a 0.031-inch wide slit was cut in the center of the wedge to let the laser sheet pass through. The size of the slit is hundreds of times larger than the viscous length ν/U_τ, and might be expected to introduce errors at the small scales. However, since we are primarily interested in the unsteadiness of the shock system associated with the large-scale motion, whose characteristic length, δ, is more than three times larger than the slit size, the influence of the slit on the overall dynamics process is not too severe.

3. Experiment:

Figure 2 illustrates the experimental setup that was used to obtain the streamwise view of the shock structure. The direction of the flow is from left to right. The second harmonic output of the pulse-burst laser was formed into an approximately 1.5 cm high by 100 μm thick sheet and directed into the flow at 60° with respect to the free stream motion. The angle 60° was chosen to generate enough of Doppler frequency shift for filtered Rayleigh scattering, which was used to suppress background scattering and to highlight velocity discontinuities. Only 1-mJ per pulse of laser energy is needed to generate enough scattered signal. The MHz framing rate CCD camera had its optical axis perpendicular to the plane of laser sheet. In front of the camera, there is an iodine cell to filter the scattered light.

The frequency of the pulse-burst laser was tuned by a PC. A small amount of the laser output was transmitted by the high power reflection mirror. The transmitted light was split by a 50/50 mirror. One part of the signal was collected by a photodiode (PD2) to monitor the fluctuation of laser output. The other part of the signal passed through an iodine filter and then was collected by another photodiode (PD1) to determine the light attenuation through iodine cell and laser frequency. This signal was used to set the laser frequency for the filtered Rayleigh scattering experiments.

4. Experimental Results:

4.1 14° wedge:

Figure 3 shows a typical sequence of 6 streamwise view images of the boundary layer over the 14° wedge and the shock wave generated by the wedge. The images size is 0.5 inch × 0.5 inch, and the time interval between frames is 2 μs. The bright straight line at the right bottom corner is the wedge. The foot of the shock is attached to the tip of the wedge. The shock wave fluctuates in response to certain incoming turbulent boundary layer structures.

The shock-wave/boundary-layer interaction is usually three dimensional, so the experiment was also setup to obtain planform view images. The layout was similar to that illustrated in the figure 2, except the laser sheet was parallel to the wall of the wind tunnel and grazed the surface of the wedge. The distance between the laser sheet and the wall was about 3 mm. Figure 4 shows sequential planform images, each separated by 2 μs. The shock wave now turns into a wavy line and the boundary layer structure is seen as dark region in the flow. A discontinuity in the boundary layer can also be seen as it crosses the shock. This is because the oblique shock changes the direction of the flow, forcing it out toward laser sheet plane. From these images, it is particularly apparent that the oscillation of the shock is correlated with the incoming boundary layer structure. The displacement of the shock wave, which is most apparent in image 4, is about one boundary layer thickness. The time lapse from frame #1 to #6 is only 10 μs, so this feature develops at a rate greater than 100 kHz.

4.2 24° wedge:

Figure 5 shows a typical sequence of 30 streamwise view images of boundary layer over the 24° wedge with images size of 0.5 inch × 0.5 inch. The framing rate is again 500 kHz. Because the shock is much stronger than the case of the 14° wedge, flow is separated and there is a stand-off distance between the foot of the shock and the tip of the wedge. The shock position and shape is still very sensitive to the incoming boundary layer structure. The foot of the shock is difficult to see with this technique, but from frame #12 to #15, we can see the shock wave in the center portion of the boundary layer moving along the direction parallel to the wall a distance on the order of δ.

As the flow crosses the shock, its speed decreases and the scattered light has a small Doppler frequency shift. As the frequency of the pulse-burst laser is tuned, the Doppler shifted scattered signal from different velocity regions can be differentially attenuated by the iodine cell. With the laser frequency tuned near the center of the iodine absorption, scattering from lower speed flow and non moving elements such as the surface of the wedge is selectively attenuated, as illustrated in the figure 6(a). Alternatively, as shown in the figure 6(b), the scattering from the high speed flow can be suppressed. Where the flow speed changes

discontinuously when it crosses the shock, there is a sharp contrast line seen in the figure 6(a). But for some frames, the intensity of the scattering across the shock changes gradually. So not only the position of the shock has moved, but it appears that the structure of the shock has fluctuated from a single shock to an array of compression fans or a group of shocklets.

5. Discussion:

After analyzing hundreds of sequences of shock-wave/boundary-layer interactions, both from 14° and 24° wedges, some common features of the sequences can be found.

After it passes the shock, the overall boundary layer structure still keeps its identity, except that the shape of the structure is compressed in the direction normal to the streamwise direction. The interaction of the shock wave on the outer boundary layer is a rapid distortion process (reference 1, Chapter 4.4), which means that the interaction time is much shorter than the turbulent structure energy-containing motions time scale T_t ($T_t=k/\varepsilon$, where k is the mean turbulent kinetic energy $q'^2/2$ and ε is its mean dissipation rate per unit mass). Thus, the eddies still keep their "identity" after the shock. Figure 7 is a particularly good example of this. After the boundary layer structure passes the shock, its length in the streamwise direction scales in the same ratio as the speed of the outer layer across the shock. Because the air density increases after the shock, from the continuity equation, the turbulent vortices are compressed normal to the streamwise direction.

The shock fluctuation in the outer boundary layer is correlated with the incoming boundary layer structure, no matter whether the flow is separated by the shock (24°) or not (14°). Some incoming boundary layer structure forces the shock to move in the streamwise direction at a frequency as high as 100 kHz. In these cases, not only the position of the shock changes, but also the structure of the shock wave changes (see figure 5 frame #9 to #17 and figure 6(a)).

The fluctuation of the shock wave also depends on the structure of the incoming boundary layer. The boundary layer structures with a square end (also labeled as "hatchback" structures) seem to have the largest influence on the shock motion (see figure 5 frame #8 to #15, figure 6, and figure 8(b)). But the shock system seem not to be influenced by the "finger" shape structures which inclined about 45° in the streamwise direction (see figure 5 frame #17 to #21, figure 8(a)).

6. Conclusion:

The interaction between the shock wave and turbulent boundary layer in a Mach 2.5 wind tunnel has been visualized at MHz rate. The shock waves were produced by two-dimensional compression corners having angles of 14° and 24°, and the flows were respectively attached and separated from the tip of the wedge.

From the sequential images, we can see that:

1) The shock motion is strongly correlated with the incoming boundary layer structure. The shock was forced to fluctuate at large-scale (boundary layer thickness) in the streamwise direction and high frequency (100 kHz). Not only the position of the shock, but the shape of the shock also fluctuates from a single shock to compression fans or groups of shocklets.
2) Different features of the boundary layer structure have different influence on the shock. The "finger" structures which are parallel to the shock have less influence on the shock than the "hatchback" structure.
3) Because it is an interaction process, the shock wave also influences the boundary layer structure. The process of boundary layer passing shock wave can be described by the rapid distortion approximation.

Acknowledgements:

This work is supported by Air Force Office of Scientific Research (Grant #: F49620-97-0373).

Reference:

1. Smits, A.J, and Dussauge, J.-P., *Turbulent Shear Layers in Supersonic Flow*, AIP Press (1996).

2. Adamson, T.C., and Messiter, A.F., "Analysis of Two-Dimensional Interactions Between Shock Waves and Boundary Layers," *Annual Review of Fluid Mechanics*, Vol. 12, 103-138 (1980).

3. Erergil, M.E., and D.S. Dolling, "Correlation of Separation Shock Motion with Pressure Fluctuations in the Incoming Boundary Layer, " *AIAA Journal*, Vol. 29, No. 11, 1868-1877 (1991).

4. Hunt, D. and Nixon. D, "A Very Large Eddy Simulation of an Unsteady Shock Wave Turbulent Boundary Layer Interaction, " AIAA paper 95-2212, *26th AIAA Fluid Dynamics Conference, June 19-22, San Diego, CA* (1995).

5. Smith, D.R., Poggie, J., Konrad, W., and Smits, A.J., "Visualziation of the Structure of Shock Wave Turbulent Boundary Layer Interactions using Rayleigh Scattering," AIAA paper 91-0651, *29th Aerospace Science Meeting, January 7-10, Reno, NV* (1991).

6. Beresh, S.J., Clemens, N.T., Dolling, D.S., and Comninos, M., "Investigation of the Causes of Large-Scale Unsteadiness of Shock-Induced Separated Flow Using Planar Laser Imaging," AIAA paper 97-0064, *35th Aerospace Sciences Meeting & Exhibit, January 6-10, Reno, NV* (1997).

7. Beresh, S.J., Clemens, N.T., and Dolling, D.S., "The Relationship Between Upstream Turbulent Boundary Layer Velocity Fluctuations and Separation Shock Unsteadiness," AIAA paper 99-0295, *37th AIAA Aerospace Sciences Meeting and Exhibit, January 11-14, Reno, NV* (1999).

8. Cantwell, B.J., "Organized Motion in Turbulent Flow, " *Annual Review of Fluid Mechanics*, Vol. 13, 457-515 (1981).

9. Wu, P., Lempert, W.L., and Miles, R.B., " MHz-rate Pulse-Burst Laser and Visualization of Shock-Wave/Boundary-Layer Interaction," *AIAA Journal*, 38(1) (2000).

10. Smith, M.W., and Smits, A.J., "Visualization of the Structure of Supersonic Turbulent Boundary Layers,"*Experiments in Fluids*, Vol. 18, No.4, 288-302 (1995).

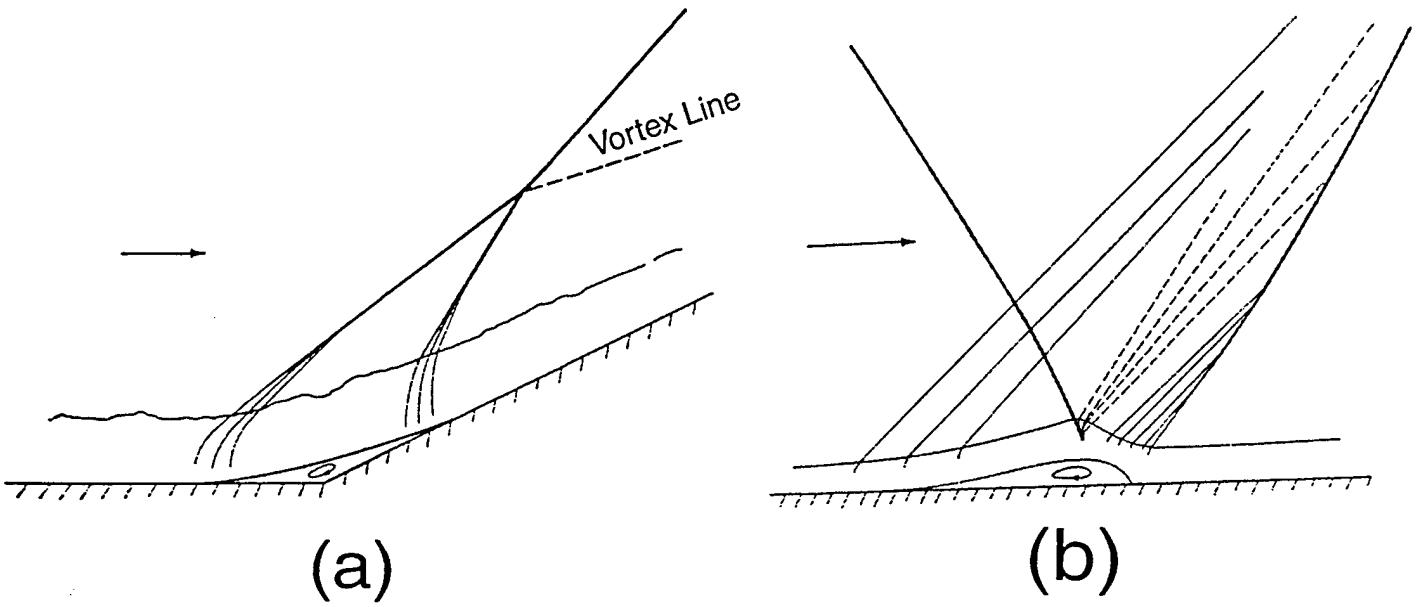

Figure 1: Typical two-dimensional interactions between shock waves and laminar boundary layers: (a) compression-corner interaction; (b) incident shock oblique shock interaction. Reproduced from Smits & Dussauge (reference 1).

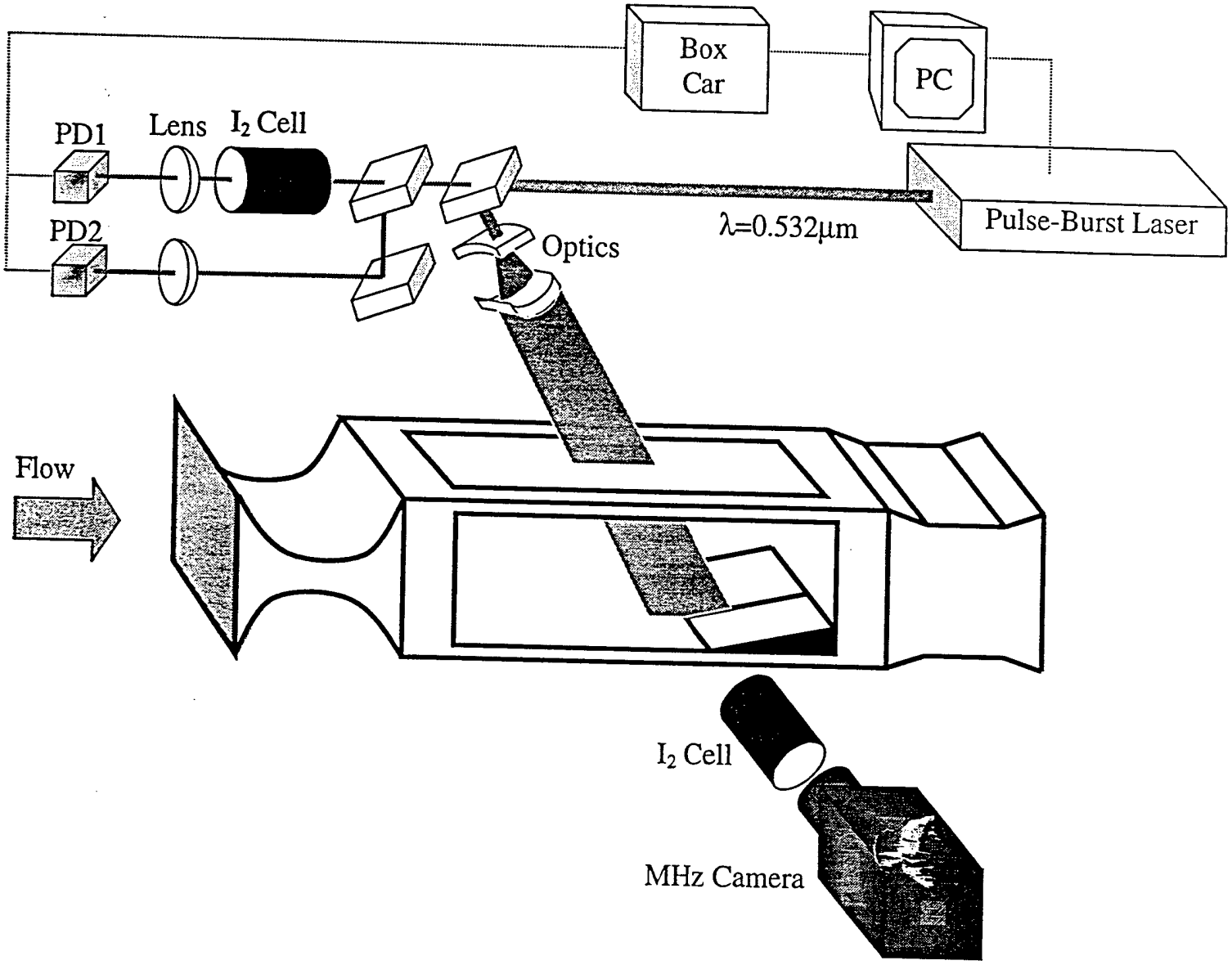

Figure 2:Experimental setup of shock-wave/boundary-layer interaction in Mach 2.5 wind tunnel.

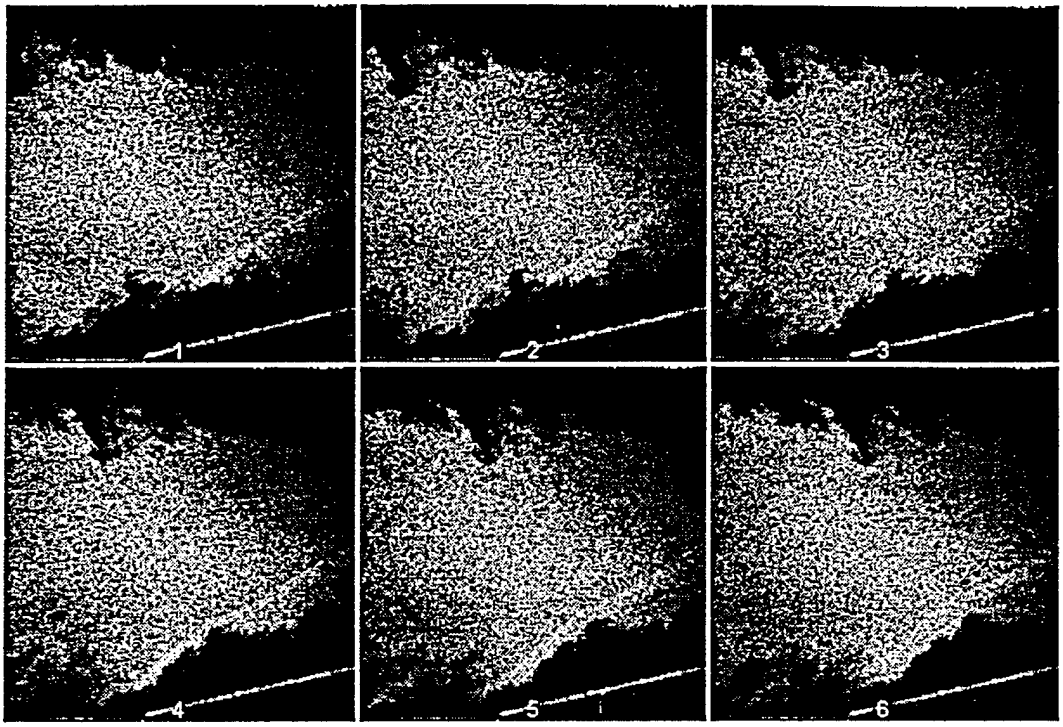

Figure 3: Sequential streamwise images of Mach 2.5 flow over 14° wedge. Flow is from left to right. The frame size is 0.5 inches and frame rate is 500 kHz.

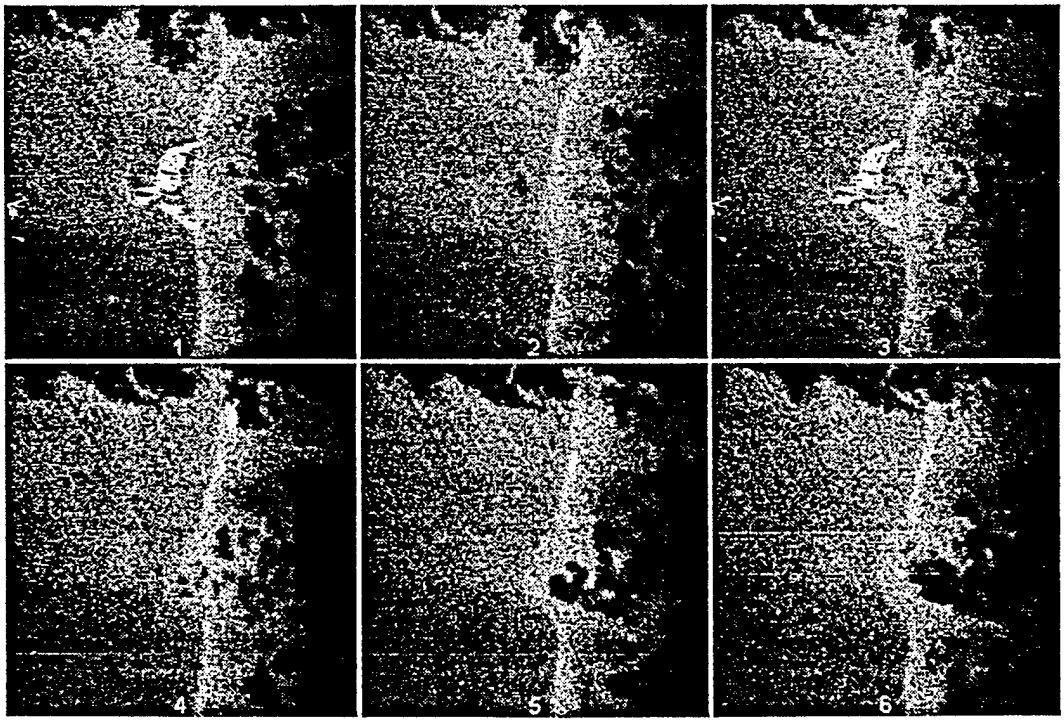

Figure 4: Sequential planform images of Mach 2.5 flow over 14° wedge. The frame size is 0.5 inches and frame rate is 500 kHz.

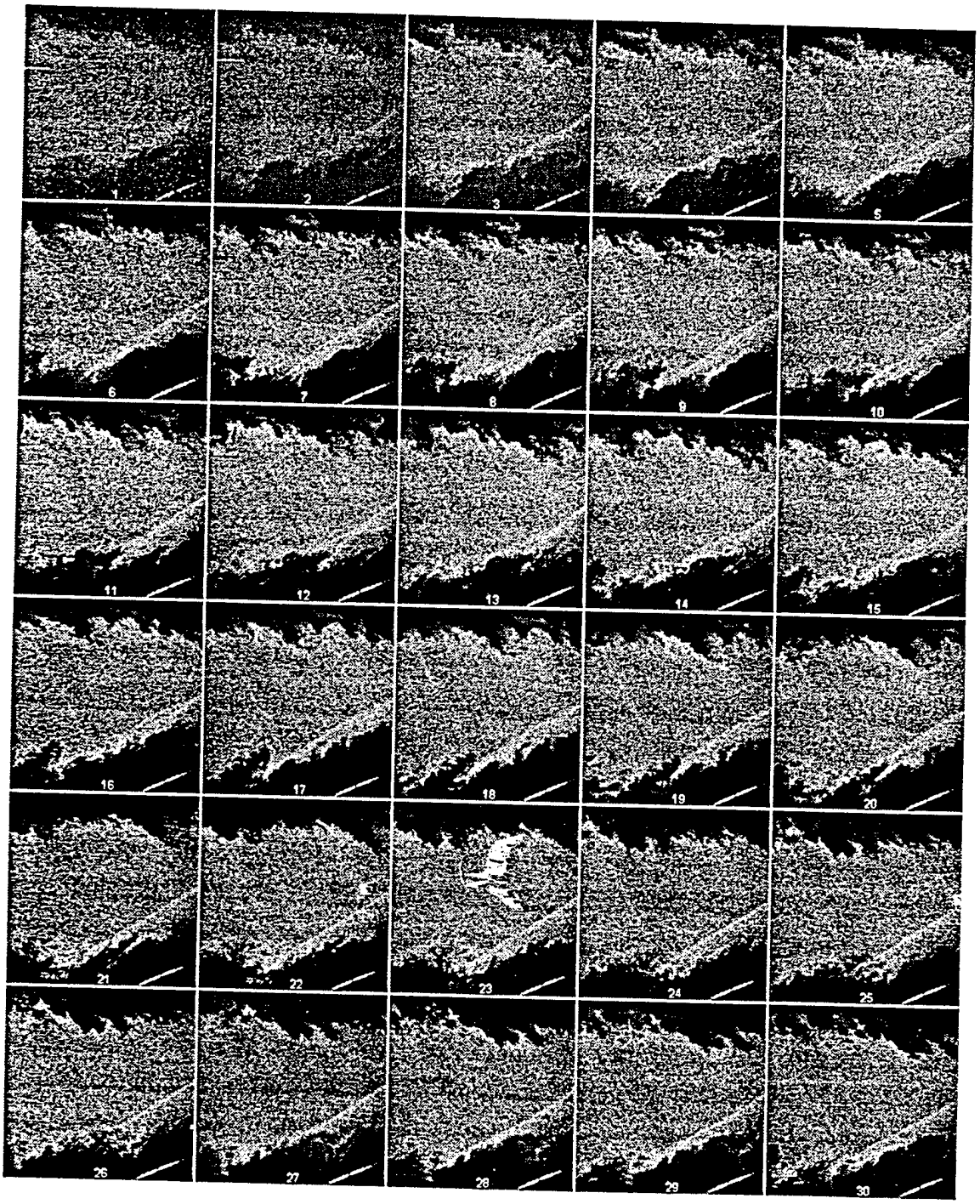

Figure 5: Sequential streamwise images of Mach 2.5 flow over 24° wedge. Frame size is 0.5 inches and frame rate is 500 kHz.

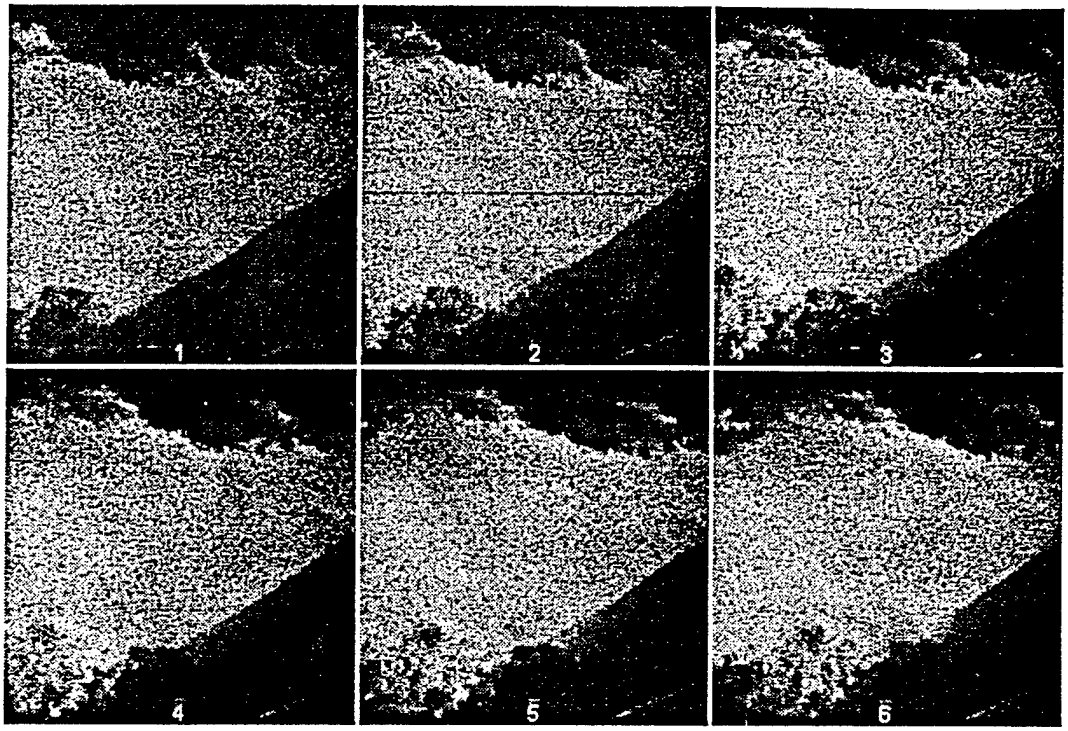

(a)

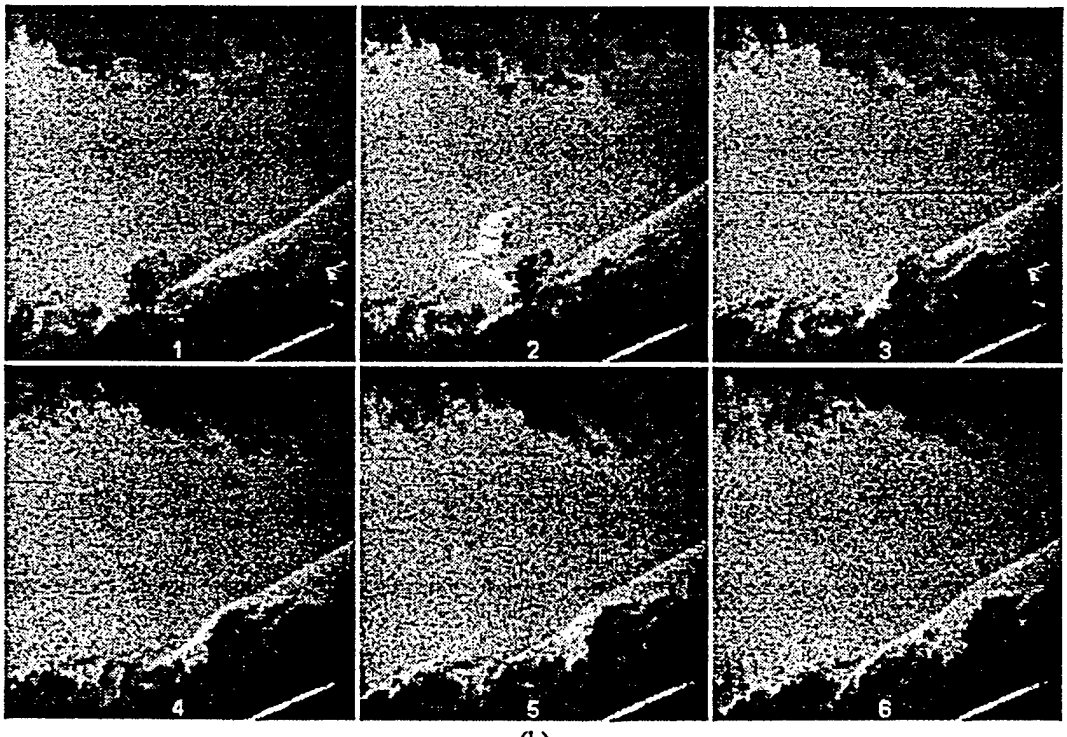

(b)

Figure 6: Filtered has been used to highlight different speeds of the flow. (a) Laser frequency was tuned so that the filter absorbed low speed part of the flow; (b) Laser is tuned so that the filter absorbed high speed part of the flow.

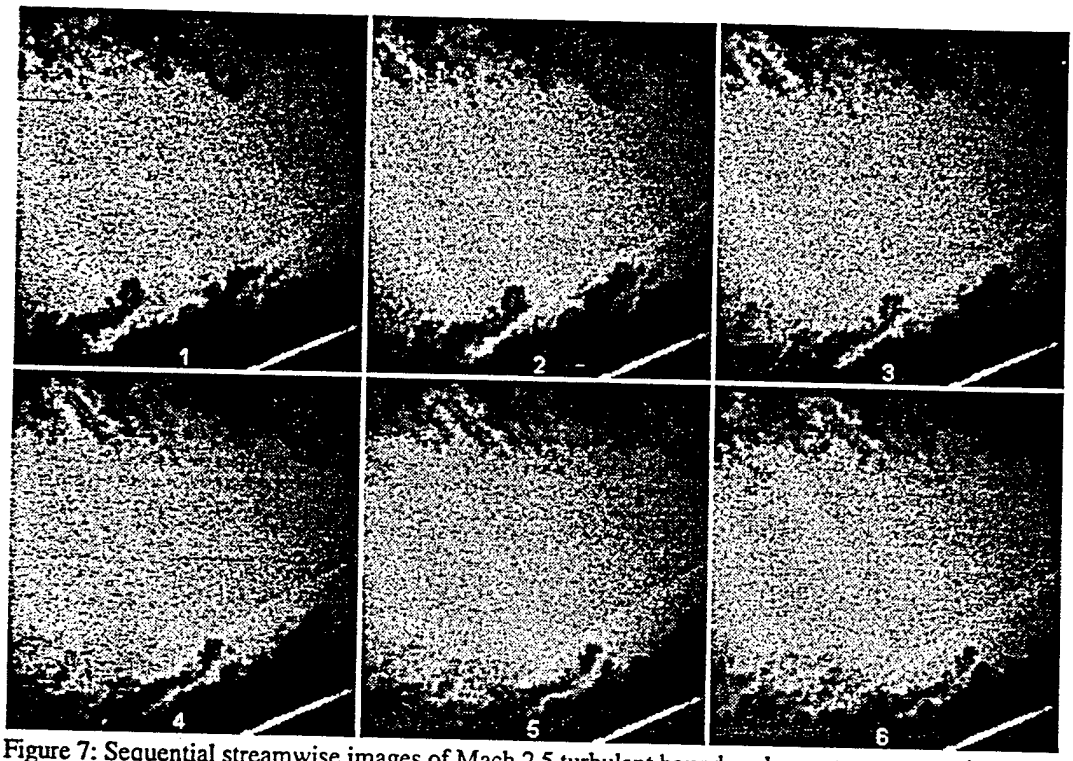

Figure 7: Sequential streamwise images of Mach 2.5 turbulent boundary layer structure passing shock wave. The frame size is 0.5 inches and frame rate is 500 kHz.

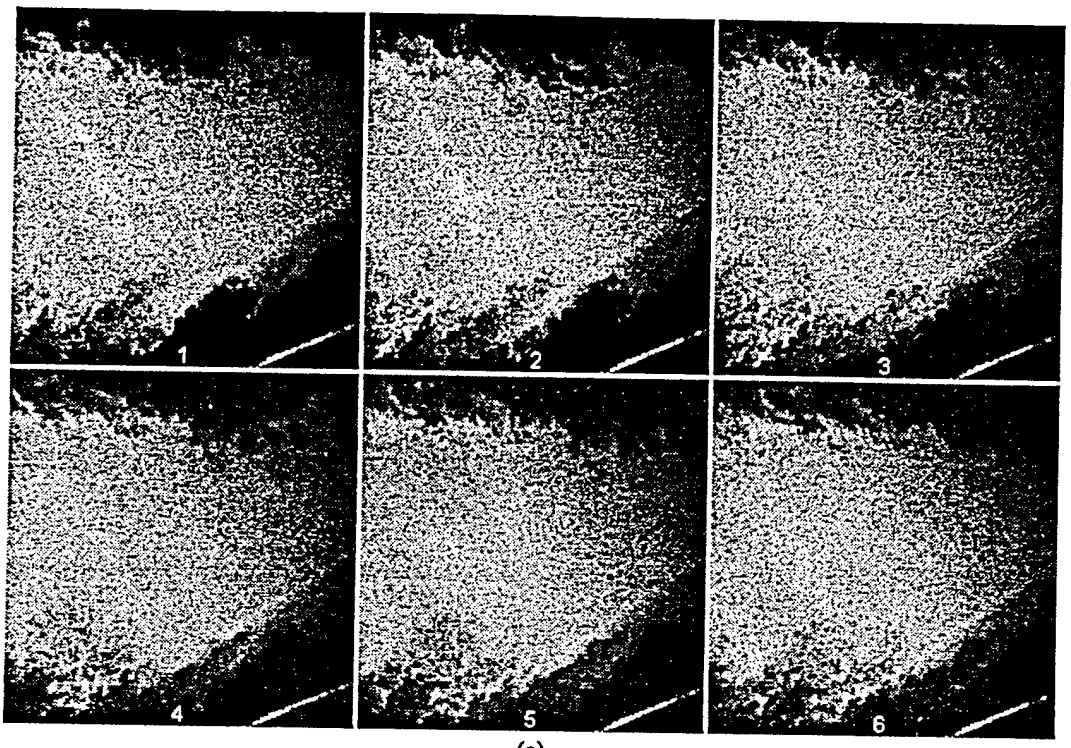

(a)

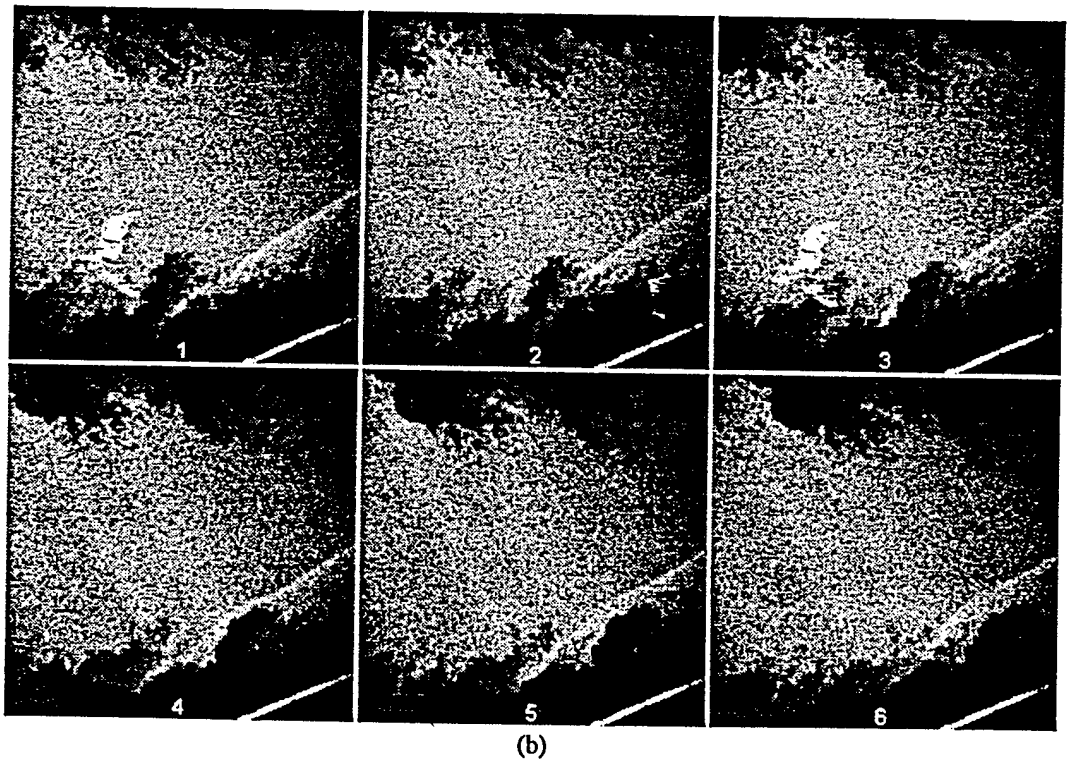

(b)

Figure 8: Comparing the influence on the shock waves by the "finger" (a) and "hatch back" boundary layer structure. The frame size is 0.5 inches and frame rate is 500 kHz.

AIAA 00-0379

MHz Rate Imaging of Boundary Layer Transition on Elliptic Cones at Mach 8

M.B. Huntley, P. Wu, R.B. Miles, and A.J. Smits
Department of Mechanical and Aerospace Engineering
Princeton University
Princeton NJ 08544

38th Aerospace Sciences Meeting & Exhibit
10-13 January 2000
Reno, NV

AIAA 2000-0379

MHZ RATE IMAGING OF BOUNDARY LAYER TRANSITION ON ELLIPTIC CONES AT MACH 8

M.B. Huntley*, P. Wu*, R.B. Miles†, and A.J. Smits‡
Dept. Of Mechanical & Aerospace Engineering
Princeton University
Princeton, New Jersey 08544

ABSTRACT

A series of flow visualizations has been performed on both 4:1 and 2:1 sharp-nosed elliptic cones at Mach 8. A new high-speed imaging system consisting of a pulse-burst Nd:YAG laser and a 1 MHz rate CCD framing camera was used to produce 30-frame motion pictures and volumetric images of the flow. Boundary layers ranging from fully laminar to late-transitional in character were imaged using Filtered Rayleigh Scattering with streamwise, spanwise, and planform laser sheet orientations. The pressure gradient and associated crossflow from the major axis to the minor axis of the cone cause increased growth and subsequent early transition of the centerline boundary layer. Volumetric image sets of the centerline region reveal hairpin structures characteristic of the early stages of subsonic turbulent spot formation. At low Reynolds number, the unstable region on the cone is confined to the bulge of the centerline boundary layer and the lateral evolution of these hairpin structures is minimal. Images of the off-axis regions reveal the presence of elongated streaks, which are believed to be the footprints of stable traveling crossflow vortices. At higher Reynolds numbers the breakdown of these streaks involve the formation of a series of chain-like structures. The behavior appears qualitatively similar to visualizations of the breakdown of crossflow vortices at subsonic speeds.

INTRODUCTION

Many aspects of the transition process from laminar to turbulent flow are poorly understood. This is especially true in the hypersonic regime, where the experimental database is limited and restricted almost entirely to two-dimensional and axisymmetric flow fields. Realistic hypersonic lifting bodies, however, possess regions of three-dimensional flow, which can drastically alter the transition behavior of the boundary layer[1]. For high Mach number flight, transition is a critical parameter since the aerodynamic heating effects greatly influence the overall vehicle design. Investigations of these complicated flow fields present a challenge for traditional point measurement techniques such as hot wires or hot films due to the generation of velocity components perpendicular to the flow axis. Application of modern laser-based flow visualization techniques has been limited due to the inability to produce the repetition rates needed to capture boundary layer evolution in high Mach number flows. Recent developments in both laser[2] and camera[3] technology have now made possible the ability to investigate the detailed flow field of three-dimensional bodies at high Mach number.

The current concept for the forebody of a hypersonic lifting vehicle can be modeled as a sharp cone with elliptic cross sections. The elliptic cone geometry is therefore a relevant shape which possesses a fully three-dimensional flow field at zero angle of attack. Advances in visualization capabilities have provided the opportunity to investigate the behavior of the boundary layer with the goal of determining the influence of three-dimensionality on the transition characteristics.

---

* Graduate Student, Dept. of Mechanical & Aerospace Eng., Member, AIAA

† Professor, Dept. of Mechanical & Aerospace Eng., Fellow, AIAA

‡ Chairman, Dept. of Mechanical & Aerospace Eng., Associate Fellow, AIAA

Boundary Layer Transition

The instability mechanisms for two-dimensional compressible flows have been identified[4] and verified experimentally[5,6]. At low supersonic Mach number, a viscous instability develops which is the compressible counterpart to Tollmien-Schlichting waves. Unlike incompressible flows, the most unstable "first-mode" waves develop at oblique angles to the flow. At higher Mach number ($M > 4$), an inviscid instability becomes important which is associated with a generalized inflection point in the boundary layer. These high frequency "second mode" disturbances are acoustic in nature, and have no counterpart in incompressible flows. The most unstable wave is two-dimensional and previous stability experiments have shown that these disturbances dominate the transition process at high Mach number.

In a three-dimensional flow field there are additional modes of instability. On a complex geometry, spanwise pressure gradients are formed when streamlines are deflected at varying angles. The low momentum fluid in the boundary layer is most affected by these gradients, inducing components of velocity (crossflow) perpendicular to the boundary layer edge velocity vector. The crossflow velocity is zero at the wall and the edge of the boundary layer, and therefore possesses a maximum in the interior of the boundary layer. The resulting inflection point near the edge of the boundary layer is the mechanism for crossflow instability.

The crossflow instability has been studied extensively in subsonic flows over swept wings[7], rotating disks[8], and rotating cones[9,10]. Co-rotating or counter-rotating crossflow vortices are formed with their axes aligned approximately parallel to the boundary layer edge velocity vector. Spanwise wavelengths are typically on the order of the boundary layer thickness. Experiments have often shown the presence of stationary crossflow vortices, while calculations have determined that the most amplified disturbance tends to be a traveling wave. The discrepancy is thought to be due to roughness effects on the surface of the model.[11] The breakdown process on three-dimensional geometries involves a secondary instability process. Visualizations[12,9] have revealed chain-like horseshoe patterns which form along the axes of the crossflow vortices. Kohama provides a schematic of this process in Figure 1.

Studies of three-dimensional flows at hypersonic Mach numbers have been limited mainly to axisymmetric cones at angle of attack[13,14,15]. In these flows, a pressure gradient induces crossflow from the windward to the leeward ray. All of the investigations reported that small angle of attack greatly decreases the transition Reynolds number along the leeward ray. The crossflow velocity in this region should be nearly zero, since it is an axis of symmetry, but the boundary layer thickness increases significantly. Therefore, while the three-dimensional shape influences the transition behavior, the largest effect occurs in a region where the induced crossflow is zero.

Similar behavior has been observed in the studies of elliptic cones[16,17,18]. The elliptic cone geometry at zero angle of attack produces a spanwise pressure gradient between the leading edge (major axis) and the centerline (minor axis) due to varying shock strength. The pressure gradients and induced crossflow velocities are strongest in the off-axis regions close to the "shoulder" of the model, but experiments have found that transition occurs first on the centerline where the crossflow velocities are zero. Kimmel et al. have made the most complete investigation of the transition behavior of an elliptic cone. For a 2:1 geometry, hot-film probes and surface measurements found a large increase in the thickness of the centerline boundary layer due to the accumulation of crossflow mass flux. This flux of low momentum fluid resulted in an inflectional velocity profile and subsequent early transition. Using surface heat-transfer measurements with cold wall conditions, the top centerline transition started at $Re_x = 0.5 \times 10^6$ and the boundary layer was considered fully turbulent at approximately 1.5×10^6.

Computations of elliptic cone flow fields have also shown the existence of a bulge in the centerline boundary layer[19,20,21]. The only complete transition prediction on an elliptic cone was completed by Huang et al. on a 4:1 geometry at Mach 4[19]. The Parabolized Stability Equations analysis predicted that the crossflow instability would be responsible for transition well before the inflected centerline boundary layer. In fact, the computed growth rates were used with an e^N correlation and predicted that boundary layer transition would occur at Reynolds numbers as low as 130,000. Subsequent experiments by Schneider[22] found that the boundary layer remained laminar at length Reynolds numbers up to 400,000.

Flow Visualization

In most subsonic flow problems, the initial step in understanding complex phenomena is to invoke some method of flow visualization. Even a qualitative image can give the researcher valuable insights into some of the general flow features. Unfortunately, for many years, oil flow or single-shot schlieren and shadowgraphy were the only options available for hypersonic flow visualization.

More recently, laser-based diagnostics have been developed. Filtered Rayleigh scattering has been used for the characterization of turbulent structures[23,24,25] as well as quantitative measurements of velocity and thermodynamic state[26,27]. Visualizations have utilized the scattering from low levels of freestream condensate particles. Imaging of the boundary layer is made possible due to the aerodynamic heating effects at high Mach number. The near-wall particles are sublimated, thereby enabling the imaging of the interface between condensed (high signal levels) and sublimated (low signal levels) particles. Molecular filters are used to extract quantitative information by taking advantage of Doppler shifts in the scattering signal (velocity) and thermal broadening (temperature). Rayleigh scattering has also been used with lasers capable of double-pulse operation. With sequential images, correlation procedures have been used to extract convection velocities and limited information regarding the structure evolution[28,29].

Although high Mach number imaging techniques have made significant advances in the last decade, the ability to make time-resolved measurements is necessary to investigate unsteady flow phenomena such as boundary layer transition. For hypersonic flows, sampling frequencies of 500 kHz or greater are needed to capture large-scale boundary layer structure evolution. Commercially available Nd:YAG laser systems are limited to ~10Hz because of the maximum average power thermal loading that the solid-state lasing elements can tolerate. In order to achieve continuous operation at the desired repetition rates, pulse energies would be limited to microjoules (1000 times too small for Rayleigh scattering measurements).

Recently, a pulse "burst" concept has been demonstrated[30] which achieves the desired repetition rates while reducing the duty cycle to achieve high energies in each individual pulse. Wu et al. have demonstrated the pulse-burst laser system by making Filtered Rayleigh scattering measurements of a shock-boundary layer interaction at Mach 2.5. The burst repetition rate is limited to 9Hz. The "burst" itself consists of 30 high energy (~10-20mJ) pulses with separations as low as 1 microsecond (1 MHz). With this system, 30-frame motion pictures of the unsteady phenomena can be recorded at sampling rates as high as 1 MHz.

The goal of the present investigation is to utilize the most recent advances in laser diagnostics to capture unsteady flow phenomena in hypersonic flow. Time-resolved data sets of elliptic cone models provide insight into the three-dimensional nature of the instabilities as well as the subsequent breakdown of the most unstable modes. These images represent the current state of the art for high speed flow diagnostics.

EXPERIMENTAL METHOD

Apparatus and Models

Experiments were conducted in the Princeton Gas Dynamics Laboratory Mach 8 Facility which is a blowdown tunnel with 0.23-meter axisymmetric test section. The Mach number is 8.0 ± 0.15 over a range of freestream unit Reynolds numbers from 2.0×10^6 to 21×10^6. Stagnation pressure can be varied from 1.0 to 10.3 MPa with stagnation temperatures up to 870 K. The test section has rectangular offset window cavities giving optical access from four sides. Models are mounted rigidly to the tunnel wall through one of the window cavities which requires the tunnel to be started with the model in place. A detailed description of this facility was given by Baumgartner[31].

In order to extend the experimental database to three-dimensional configurations, two elliptic cone models are studied. The first model is a sharp-nosed ($d < 0.2$mm) 4:1 elliptic cone that measures 0.242 m with 17.5 degree half-angle on the major axis. The geometry was manufactured to match the transition computations of Huang et al[19]. The second model tested was a 2:1 cone with 13.8 degree half-angle in the major axis. The length of this model was 0.1524 m, and it was actually a spare nose section for the 1.016 m cone used by Kimmel et al. in their experiments conducted in Tunnel B at AEDC. Computations[21] as well as surface heat flux and hot-film experiments[17] have been completed on this 2:1 configuration.

Imaging Technique

The experiment used carbon dioxide enhanced Filtered Rayleigh Scattering (FRS) for imaging the freestream flow and the boundary layer. Carbon dioxide is injected upstream of the stagnation chamber in quantities ranging from 0.8% to 2.8% of the total tunnel mass flux. According to our current understanding of the technique, the structure of the boundary layer is imaged by the interface between the cold freestream and the hot boundary layer fluid. As the fluid containing condensed CO_2 becomes entrained in the boundary layer, aerodynamic heating effects cause the temperature to rise above the sublimation value and the condensate disappears. The boundary layer is therefore imaged as a region of low intensity Rayleigh signal, bounded by bright freestream regions. In order to increase the signal-to-noise ratio for the images, the laser output was tuned to overlap a strong

spectral absorption line in iodine vapor. A molecular iodine filter was placed in front of the camera so that stray scattering from the model surface was absorbed. The Rayleigh scattering signal from the moving flow was then Doppler shifted outside the absorption band of the filter so that it could be observed by the camera.

MHz-Rate Imaging System

Motion pictures of the boundary layer were created using a "pulse-burst" laser system in conjunction with a high-speed CCD camera.

Complete details of the laser system are given by Wu et al.[2] Briefly, the Nd:YAG-based laser has the capability of producing a "train" of 30-40 high energy pulses with pulse separation times as short as one microsecond. The pulse-burst concept is illustrated schematically in Figure 2. A pulse sequence is generated using a low power (order milliwatt) continuous-wave master oscillator in combination with a high-speed pulse slicer. The low power sequence is then amplified in a series of flashlamp-pumped amplifiers which have "gain" for a total period of approximately 100 microseconds. By sending the pulse sequence to the rising edge of the gain curve, a "burst" of uniform high-energy (10-20 mJ at 532 nm) pulses is generated. The burst repetition rate is 9 Hz, to limit the thermal loading on the solid state lasing elements.

The laser is paired with a novel CCD framing camera recently developed by Princeton Scientific Instruments, Inc. The CCD camera has a 30-image storage buffer built into the image sensor chip itself, and can frame at rates up to 1 MHz. Details of the camera system are given by Kosonocky et al.[3]

In summary, the imaging system used for these experiments is capable of creating 30-image motion picture sets of the flow with 180 × 180 pixel resolution at framing rates as high as 1 MHz. Since there is a limitation on the number of frames that can be imaged (and therefore the total sampling time), all of the experiments in this investigation used sampling rates of 500kHz. The lower repetition rate results in higher laser pulse energy and also maximizes the sampling window so that individual structures could be tracked across a larger field of view.

EXPERIMENTAL DETAILS

Tunnel Conditions

A schematic of the test facility is shown in Figure 3. Approximately 63 m^3 of air for the blowdown facility is pumped to 16 MPa and stored in four large tanks. The high pressure air is connected to the heater assembly by a valve which expands the air to the desired stagnation pressure. The heater assembly consists if 83 m of pipe wound into a coil which is preheated electrically to the desired stagnation temperature before the flow is turned on. Typical uninterupted run times are 2-3 minutes, limited by the air supply as well as the total amount of heat stored in the coil assembly. The surface temperature of the model is typically "preheated" for a short time before the start of the run in order to generate more uniform temperature distribution over the length of the run.

Unfortunately, continuous operation of the facility for the full run time proved to be inefficient for experiments using the MHz imaging system. The high-speed CCD camera has a 30-image storage buffer built into the image sensor chip itself. Upon receipt of a master trigger, the camera operates continuously until a stop trigger is issued. At this point, nearly 45 seconds are required for the last 30 images to be read-out to a standard personal computer. If the tunnel were operated continuously, valuable air and heat would be lost during this transfer process and only 2 or 3 30-image "sets" could be generated during one run. More efficient use of the air supply was achieved simply by operating the tunnel for multiple short runs (typically 20-30 seconds). Once the tunnel conditions had reached equilibrium values, one 30-image set was captured and stored in the buffer and the tunnel was then shut off during the image transfer process. Using this technique, 4 to 6 image sets could be generated in one typical series of runs. Although freestream tunnel conditions were fairly repeatable for each of the short runs, the surface temperature of the cone would increase for each successive run. Typical temperature ratios for the first image set were $T_w/T_{aw} = 0.59$. Surface temperature ratios for the final image set varied with unit Reynolds number, and were sometimes as high as $T_w/T_{aw} = 0.74$.

Freestream unit Reynolds numbers were varied by changing the stagnation pressure of the air stream. Unit Reynolds numbers were constant to within 2% over the course of each run. Stagnation pressures were varied from 1.0 MPa up to 8.3 MPa. Stagnation temperatures varied slightly from run to run (±50 C), since heat transfer to the flow from the heater coil was more efficient at higher stagnation pressures. Temperatures typically varied less than 2% during the run, ranging from 763 K up to 815 K. Overall, each of the cones was tested at unit Reynolds numbers from 2.8 to 14.2 × 10^6 per meter. At these Reynolds numbers, the boundary layer thickness on the centerline of the cones ranged from approximately three to six millimeters. The broadband rms mass flux on the centerline of the tunnel was measured at 3.4% ± 0.5% for freestream

unit Reynolds number of 7.0×10^6/m. The energy in the freestream disturbance spectrum is concentrated at frequencies much lower than the instabilities observed in these experiments.

The seeding rate of carbon dioxide was constant to within ±5% for all runs. Details of the CO_2 seeding system are given by Erbland et al[32]. High pressure (~1400 psi) liquid CO_2 is injected upstream of the tunnel heater coil. Once the liquid passes through the metering valve, it is flash vaporized and mixed with the crossing stream of tunnel supply air. The mass flow rate of injected CO_2 was 0.050 ± 0.0025 for all runs, and the mass fraction of CO_2 varied from 0.8% up to 2.8% over the range of freestream unit Reynolds numbers.

Optical Configurations

Planar images of the boundary layer were taken using spanwise and planform laser sheet orientations. A schematic of the laser and camera orientations for the 4:1 elliptic cone is shown in Figure 4. For each orientation, the laser beam was expanded into a focused sheet by using a positive and negative cylindrical lens pair. The sheet was typically expanded 4-7 cm and was estimated to be 100 μm thick at the focus. The long focal length of the positive cylindrical lens was sufficient to keep the sheet at approximately the same thickness across the full field of view of the camera.

The spanwise sheet was oriented perpendicular to the freestream flow. The orientation of the spanwise camera was from "behind" the model but outside the tunnel, at a viewing angle of approximately 30° with respect to the flow direction. The spanwise field of view was typically 3 × 3 cm.

The planform laser sheet was oriented parallel to the model surface and could be translated vertically to sweep through different heights of the boundary layer. The planform camera was positioned perpendicular to the laser sheet with a typical viewing area of 6 × 6 cm.

30-image motion pictures of the flow at 500 kHz were produced for both the planform and spanwise orientations over a range of Reynolds numbers. In each case, a simultaneous single-shot imaging system was also set up such that one "snap-shot" of the flow was produced at the same instant as the fifteenth image in the sequential series. For example, with the pulse-burst laser recording a 30-image spanwise sequence of the boundary layer evolution, a single-shot of the planform field of view was also taken which was synchronized with the fifteenth frame of the spanwise motion picture. The polarization of each laser sheet was optimized such that the Rayleigh signal from the secondary orientation was minimized. Therefore the camera set up to view in the *spanwise* orientation would image very little scatter from the *planform* sheet and vice versa.

The ability to simultaneously image both fields of view will be used as a parameter for determining the accuracy of the three-dimensional image reconstructed from the spanwise image sequence.

RESULTS AND DISCUSSION

The following images were produced using Rayleigh scattering from condensed carbon dioxide clusters. In each of the frames, the interface between the dark (sublimated CO_2) and bright (condensed CO_2) regions is illuminated. Preliminary surveys on a laminar boundary layer have shown that this interface actually occurs at approximately 0.8δ. For supersonic turbulent boundary layers, it has been shown that the technique accurately represents the instantaneous large-scale motions in the middle and outer regions of the boundary layer.[33] The following images therefore illustrate the evolution of structures that are formed near the edge of the boundary layer in the early stages of the nonlinear transition process.

Planform images

The elliptic cone shape creates a pressure gradient between the major axis and the minor axis, which in turn induces velocity components perpendicular to the flow axis. The resultant crossflow mass flux collects on the top centerline of the cone, causing a thickening of the centerline boundary layer.

Figure 5 represents sequential images at 500 kHz taken through the bulge in the centerline boundary layer on the 4:1 cone in the early stages of transition at $Re_x = 1.68 \times 10^6$. The planform sheet is positioned parallel to the surface at a height of 4.75 mm. The field of view spans 3.8 cm ($\sim 8\delta_{cl}$) and the flow is left to right. The structure which starts on the left side of image 5.1 is characteristic of the early stages of the breakdown process. In fact, a similar structure has convected into the field of view of frame 5.7. A third structure is present in image 5.14, and frame 5.21 shows yet another occurrence of this large-scale boundary layer structure. These structures are easily identified by the two symmetric small-scale "arms" which appear to wrap themselves around a circular "head" which has formed downstream. The resulting C-shape represents the entrainment of freestream fluid by the boundary layer structure. Many image sets taken in this range of Reynolds numbers capture isolated structures, while others reveal a train of structures similar to those shown in Figure 5.

The 14-image sequence in Figure 6 was taken 2.75 mm from the surface of the 2:1 elliptic cone at $Re_x = 1.27 \times 10^6$. Again, frames 6.7 to 6.14 show the convection of a large-scale disturbance strikingly similar to that observed on the 4:1 cone. Here the structures form at slightly lower Reynolds numbers, which is unexpected, since the three-dimensional effects are not as strong on the 2:1 geometry.

Since the images actually represent the scattering from condensed CO_2 particles, it is possible to make inferences about the velocity components perpendicular to the wall. The spanwise images which follow support the contention that the bright regions on the interior of the structure of Figure 5.5 represent downward motions and entrainment of carbon dioxide. The dark regions have already been close enough to the wall to sublimate the CO_2 and therefore must be moving away from the wall.

It is also interesting to note that the individual structures do not appear to change shape significantly in the time scales in which they are observed (~30 μs). While there may be some detectable evolution, the movement is mainly streamwise convection across the field of view. This observation is critical for the construction of volumetric images, which will be presented below.

The breakdown of the centerline bulge was illuminated in Figures 5 and 6 by passing the laser sheet close to the edge of the boundary layer and observing wrinkles in the sublimation interface induced by the flow structures. By positioning the sheet closer to the surface, Figure 7 (taken at $Re_x = 2.4 \times 10^6$) reveals some of the characteristic flow structures that emerge in the off-axis regions. For this image set on the 4:1 cone the planform sheet is at 2.0 mm, so that the edge of the off-axis boundary layer is illuminated. The flow is from left to right and the field of view is 3.8 cm. The striking feature of this image set is the series of elongated streaks that form in the outboard regions and convect downstream.

Again, the bright regions represent entrained CO_2 clusters, and therefore velocity components oriented towards the wall. These observations suggest the presence of regions of concentrated vorticity. Since these streaks occur off-axis in regions with higher crossflow velocity, the visualizations may reveal the footprints of stable traveling crossflow vortices. Subsonic smoke visualizations of rotating axisymmetric cones have also observed the formation of stable crossflow vortices,[9,11] where the streak pattern in the smoke marks the core of the crossflow vortex. In these Rayleigh scattering images, we expect the vortex core to be aligned with the edge of the light/dark interface such that the induced downward velocity entrains freestream CO_2 clusters on one side, and lifts up regions of sublimated CO_2 on the opposite side.

Further evidence of crossflow vortices is found in visualizations of breakdown in the off-axis boundary layer. Figures 8a and 8b are single-shot planform images illustrating the characteristic chain-like structure that is observed during the onset of transition. The small white box encloses what appears to be the formation of secondary instabilities, which form along the axis of the crossflow vortices. Kohama has observed similar behavior on rotating cones and attributed the secondary structures to the formation of horseshoe vortices (see Figure 1).

Spanwise images

Centerline Structure

In the spanwise images of Figure 9, the flow direction is out of the image plane. The centerline of the cone is aligned approximately with the center of the bulge in the boundary layer and $Re_x = 1.53 \times 10^6$. The spanwise field of view is only 3.2 cm, and the bright regions in the bottom-right corner of each image represent laser scatter from the surface of the model that was not completely absorbed by the iodine filter. In this orientation the apparent frame-to-frame evolution seems to be much greater than in Figure 5 (see frames 9.17 to 9.24). Most of the "evolution" in the spanwise orientation is a result of cutting through different planes of the C-shaped structures seen in Figure 5 as they convect through the fixed X-position for spanwise interrogation.

By illuminating Y-Z planes with convection in the X-direction, it is possible to reconstruct a quasi-three-dimensional image of the boundary layer by making a "frozen flow" assumption. For structures near the edge of the boundary layer, the convection speed is approximately 1200 m/s. Therefore, for an imaging system with pulse separations of only 2 μs, the boundary layer is partitioned into slices capable of resolving all structures with streamwise separations greater than 2.4 mm. Since the centerline boundary layer is typically close to 5 mm, the images have effectively partitioned the flow at scales smaller than half the boundary layer thickness.

Figure 10 is a volumetric representation of the 29-image montage of Figure 9. The individual images have been stacked in temporal order with Frame 9.1 on the right (downstream) and Frame 9.29 on the left side of the image. The spacing in the "streamwise" direction (X') was set using an average convection velocity found from planform motion pictures taken near the edge of the boundary layer at the same

Reynolds number. Once the frames were stacked in order, the "gaps" were filled in by linear interpolation of the grayscales between sequential frames. The surface illuminated in Figure 10 is actually the interface between the condensed and sublimated carbon dioxide. The interface is made visible by making all of the freestream grayscales (bright regions) transparent. Finally, the direction of light illumination can be adjusted to create the shadow effect and accentuate the three-dimensional nature of the transitional structures.

The volumetric images give a more in-depth look at the structures first seen in Figure 5. From Frame 9.20 (X' ≈ 4.5 cm in Figure 10), it is apparent that the "arms" in the structure actually represent small-scale vortical motions which emerge upstream of a large bulge in the boundary layer. Figure 11, also taken on the 4:1 cone, exhibits similar behavior. The image set has captured three characteristic structures, each consisting of a lift-up of boundary layer fluid followed by two vortical structures. The pairs of small-scale "arms" appear to wrap around the hemispherical bulges that have formed downstream.

At first glance these structures appear to be somewhat unusual and unique features of hypersonic transition. It is necessary to interpret the flow visualization technique correctly before such a claim can be made. Although the visualization technique has no counterpart in subsonic flows, it most closely resembles a form of distributed dye injection at the surface of the model. Any of the fluid that has come in close contact with the wall has been "tagged" by being free of the condensed carbon dioxide. Therefore, the "lift-ups" in Figure 11 must be caused by a flow structure that induces an ejection of fluid from the wall. Such behavior is characteristic of a hairpin vortex structure, where fluid between the "legs" is lifted up into the freestream flow. The train of characteristic structures in Figures 5 and 11 may simply represent the footprints of a series of hairpin loops that have formed in the low momentum centerline bulge.

The formation of hairpin loops is characteristic of subcritical transition in subsonic flows. For example, Acarlar and Smith[34] observed the formation of hairpin vortices when low momentum fluid was injected in a laminar boundary layer through a streamwise slot (Figure 12). The low-speed 'synthetic streak' developed a three-dimensional, shear-layer instability, which generated hairpin structures. Secondary streamwise vortical structures were also observed which formed outboard of the counter-rotating legs of the hairpin vortices.

The subcritical transition caused by fluid injection is analogous to the behavior of the centerline boundary layer on the elliptic cone. Low-momentum fluid is "injected" into the centerline boundary layer from either side as a result of the crossflow mass flux. The shear-layer instability then appears to create hairpin vortices, which lift up the boundary layer fluid as well as form secondary vortical structures.

Off-axis Structure

In the pulse-burst image sequence of Figure 7, elongated streaks were observed in the off-axis region. Volumetric image sets on both cones also capture this phenomenon, but caution must be used in interpreting the angles observed. Since individual frames are being imaged at different times, any outboard movement of the structure will appear as a larger structure angle in the reconstructed image.

The spanwise field of view is only 3.2 cm (24% of the total span) in Figure 11, but close inspection of the regions outside of the centerline structures reveals the same coherent streaks seen in Figure 7. These streaks were observed in nearly all of the image sets, even those taken at low Reynolds number. In order to image more of the off-axis behavior, Re_x values were decreases by moving forward on the model. Figure 13 represents a volumetric reconstruction of the boundary layer at $Re_x = 0.87 \times 10^6$ which captures 33% of the total spanwise length. The centerline of the cone appears laminar, but the off-axis regions still show evidence of the traveling wave structures.

The elongated streaks were also observed on the 2:1 model. Figure 14 (46% of the total span) reveals a series of six coherent elongated structures in the regions outside of the centerline ($Re_x = 1.49 \times 10^6$). The relatively small boundary layer of the 2:1 model makes it difficult to resolve individual structures on the centerline at 500 kHz. Therefore, the centerline of the 2:1 cone in Figure 14 does not show the coherent hairpin footprints that were observed on the 4:1 cone due to the inability to resolve the smaller scales at 500 kHz.

The individual frames show that many of the characteristics of the 2:1 and 4:1 cones are the same. Figure 15 shows four of the individual frames which were used to construct Figure 14. The individual behavior of frames 15.4, 15.17, 15.25, and 15.30 appears strikingly similar to frames 9.5, 9.7, 9.20, and 9.27 which were taken on the 4:1 cone. In order to fully resolve this issue, further imaging at higher frame rates (at least 1 MHz) is necessary.

Frozen Flow Assumption

For each of the volumetric image sets constructed from the spanwise field of view, a correpsonding

single-shot image was taken in the planform orientation with a separate camera and laser. In order to obtain some information on the evolution of the structures, a comparison was made between the single-shot image and the equivalent cut through the volumetric reconstruction (Figures 16a and 16b, $Re_x = 1.53 \times 10^6$). The single-shot planform image (4.0 mm from the surface) was taken simultaneously with frame 9 of the pulse-burst image set shown in Figure 11. Therefore, the right edge of the volumetric reconstruction was taken 18 μs *before* the single-shot image, and the left edge was taken 38 μs *after* the single-shot. From direct comparison of the two images, it is clear that all of the main structures have retained their character over the time scales required for construction of the three-dimensional image.

For higher Reynolds number flows, the development of high-energy small-scale structures presents a challenge for this visualization procedure. Figure 17 is an attempt to construct a 3-dimensional image of the centerline boundary layer on the 4:1 cone in the late stages of transition ($Re_x = 2.46 \times 10^6$). From this image, it is clear that the 500 kHz repetition rate is not sufficient to resolve small-scale individual flow structures. Unfortunately, as the scales become smaller, the characteristic "eddy turnover time" associated with their motions also decreases. Therefore, the evolution of these structures would be more pronounced in the time associated with convection through the spanwise interrogation plane.

CONCLUSIONS

A new high-speed imaging system was used to produce 500 kHz motion pictures of the boundary layer over 4:1 and 2:1 elliptic cones at Mach 8. Planar image sets were produced in both the planform (X-Z) and spanwise (Y-Z) orientations using CO_2-enhanced Filtered Rayleigh Scattering. Volumetric images of the transitional boundary layer were constructed from spanwise motion pictures.

Planform image sets taken near the edge of the centerline boundary layer revealed a series of large-scale transitional structures. Subsequent volumetric images showed that these structures were characterized by a lift-up of low momentum boundary layer fluid and small-scale streamwise-oriented vortical structures. Comparisons with subsonic visualizations revealed that these structures may be footprints of hairpin loops which have formed due to the inflectional centerline velocity profile.

Elongated streaks were observed in images of the off-axis regions of both models. Although transition occurs first in the centerline region of the cone ($Re_x \approx 1.5 \times 10^6$), evidence of the off-axis wave pattern was observed at Reynolds numbers below 0.8 million. These streaks appear to be the footprints of stable traveling crossflow vortices. Subsequent breakdown of these streaks is qualitatively similar to the formation of secondary structures aligned with the crossflow vortex core, which has been observed in subsonic crossflow-dominated flows.

ACKNOWLEDGEMENTS

The support of AFOSR Grants F49620-97-1-0181 and F49620-97-1-0484 is gratefully acknowledged.

REFERENCES

[1] J.D. Anderson. *Hypersonic and High Temperature Gas Dynamics*, McGraw-Hill, New York, 1989.

[2] P. Wu, W.R. Lempert, R.B. Miles, and L. Bromley. Tunable pulse-burst laser system for high-speed imaging diagnostics. *AIAA Paper 98-0310*, 1998.

[3] W.F. Kosonocky, G. Yang, C. Ye, R.K. Kabra, J.L. Lowrance, V. Mastrocola, F.V. Shallcross, and V. Patel. 360 x 360 element, very high frame rate, burst image sensor. *1996 IEEE International Solid-State Circuits Conference, San Francisco, CA*, Feb. 8-10, 1996.

[4] L.M. Mack. Boundary-layer linear stability theory. *Special Course on Stability and Transition of Laminar Flow*, edited by R. Michel. *AGARD* R-709: 3-1-3-81, 1984.

[5] G.B. Schubauer and H.K. Skramstad. Laminar boundary layer oscillations and transition on a flat plate. *Journal of Aeronautical Sciences*, 14:69-76, 1947.

[6] J.M. Kendall. Wind tunnel experiments relating to supersonic and hypersonic boundary layer transition. *AIAA Journal*, 13:290-99, 1975.

[7] W.S. Saric and L.G. Yeates. Experiments on the stability of crossflow vortices in swept-wing flows. *AIAA Paper 85-0493*, 1985.

[8] N. Gregory, J.T. Stuart, and W.S. Walker. On the stability of three-dimensional boundary layers with applications to the flow due to a rotating disk. *Philos. Trans. R. Soc. London Ser. A*, 248:155-99, 1955.

[9] Y. Kohama. Turbulent transition process of the spiral vortices appearing in the laminar boundary layer of a rotating cone. *Phys-Chem. Hydrodyn.*, 6(5):659-670.

[10] Y. Kohama. Flow structures formed by axisymmetric spinning bodies. *AIAA Journal*, 23:1445-54, 1985.

[11] H.L. Reed and W.S. Saric. Stability of three-dimensional boundary layers. *Ann. Rev. Fluid Mech.*, 21:235-84, 1989.

[12] J.T. Kegelman, R.C. Nelson, and T.J. Mueller. The boundary layer on an axisymmetric body with and without spin. *AIAA Journal*, 21:1485-91, 1983.
[13] G.P. Doggett, N. Chokani, and S.P. Wilkinson. Effect of angle of attack on hypersonic boundary layer stability. *AIAA Journal*, 35(3):464-470, 1997.
[14] M. Holden, D. Bower, and K. Chadwick. Measurements of boundary layer transition on cones at angle of attack for mach numbers from 11 to 13. *AIAA Paper 95-2294*, 1995.
[15] K.F. Stetson, E.R. Thompson, J.C. Donaldson, and L.G. Siler. Laminar boundary layer stability experiments on a cone at Mach 8, part 3: sharp cone at angle of attack. *AIAA Paper 85-0492*, 1985.
[16] V. Zakkay, and M. Visich, Jr. Experimental pressure distribution on conical elliptic bodies at M=3.09 and 6.0. *Polytechnic Institute of Brooklyn, PIBAL Report No. 467*, March 1959.
[17] R.L. Kimmel, J. Poggie, and S.N. Schwoerke. Laminar-turbulent transition in a Mach 8 elliptic cone flow. *AIAA Journal*, 37(9):1080-1087, 1999.
[18] J.D. Schmisseur, S.P. Schneider, and S.H. Collicott. Receptivity of the Mach 4 boundary-layer on an elliptic cone to laser-generated localized freestream perturbations. *AIAA Paper 98-0532*, 1998.
[19] S.L. Huang, G.K. Stuckert, and T. Herbert. Crossflow instability of the supersonic flow over a 4:1 elliptic cone. *AFOSR Technical Report 95-0077TR*, 1995.
[20] I.J. Lyttle and H.S. Reed. Use of transition correlations for three-dimensional boundary layers within hypersonic viscous flows. *Transitional and Turbulent Compressible Flows, ASME FED*, 224:87-94, 1995.
[21] R.L. Kimmel, M.A. Klein, and S.N. Schwoerke. Three-dimensional hypersonic laminar boundary layer computations for transition experiment design. *Journal of Spacecraft and Rockets*, 34(4):409-415, 1997.
[22] S.P. Schneider, S.H. Collicott, J.D. Schmnisseur, D. Ladoon, L.A. Randall, S.E. Munro, and T.R. Salyer. Laminar-turbulent transition research in the Purdue Mach-4 quiet-flow Ludwieg tube. *AIAA Paper 96-2191*, 1996.
[23] M.W. Smith and A.J. Smits. Visualization of the structure of supersonic turbulent boundary layers. *Exp. In Fluids*, 18:288-302, 1995.
[24] S. Cogne, J. Forkey, W.R. Lempert, R.B. Miles, and A.J. Smits. The evolution of large-scale structures in a supersonic turbulent boundary layer. *Fluids Engineering Conference on Transitional and Turbulent Compressible Flows, Washington, D.C., ASME FED*, 151, June 20-24, 1993.
[25] M.L. Baumgarter, P.J. Erbland, M.R. Etz, A.P. Yalin, B.K. Muzas, A.J. Smits, W.R. Lempert, and R.B. Miles. Structure of a Mach 8 boundary layer. *AIAA Paper 97-0765*, 1997.
[26] J.N. Forkey, N.D. Finkelstein, W.R. Lempert, and R.B. Miles. Demonstration and characterization of filtered Rayleigh scattering for planar velocity measurements. *AIAA Journal*, 34(3):442-448, 1995.
[27] B. Shirinzadeh. Rayleigh scattering measurements in supersonic facilities. *AIAA Paper 96-2187*, 1996.
[28] R.C. Murray and G.S. Elliot. The compressible shear layer over a two-dimensional cavity. *AIAA Paper 98-0430*, 1998.
[29] P.J. Erbland, R. Murray, M.R. Etz, M.B. Huntley, and R.B. Miles. Imaging the evolution of turbulent structures in a hypersonic boundary layer. *AIAA Paper 99-0769*, 1999.
[30] W.R. Lempert, P. Wu, B. Zhang, R.B. Miles, J.L. Lowrance, V. Mastrocola, and W.F. Kosonocky. Pulse-burst laser system for high-speed flow diagnostics. *AIAA Paper 96-0179*, 1996.
[31] M.L. Baumgarter. Turbulence structure in a hypersonic boundary layer. *Ph.D. Thesis, Princeton University*, 1997.
[32] P.J. Erbland, M.L. Baumgarter, A.P. Yalin, M.R. Etz, B.K. Muzas, W.R. Lempert, A.J. Smits, and R.B. Miles. Development of planar diagnostics for imaging Mach 8 flowfields using carbon dioxide and sodium seeding. *AIAA Paper 97-0154*, 1997.
[33] T.A. Nau Rayleigh scattering as a quantitative tool in compressible turbulent boundary layers. *MS Thesis, Princeton University*, 2026T, 1995.
[34] M.S. Acarlar and C.S. Smith. A study of hairpin vortices in a laminar boundary layer. Part 2. Hairpin vortices generated by fluid injection. *Journal of Fluid Mech.*, 175:43-83, 1987.

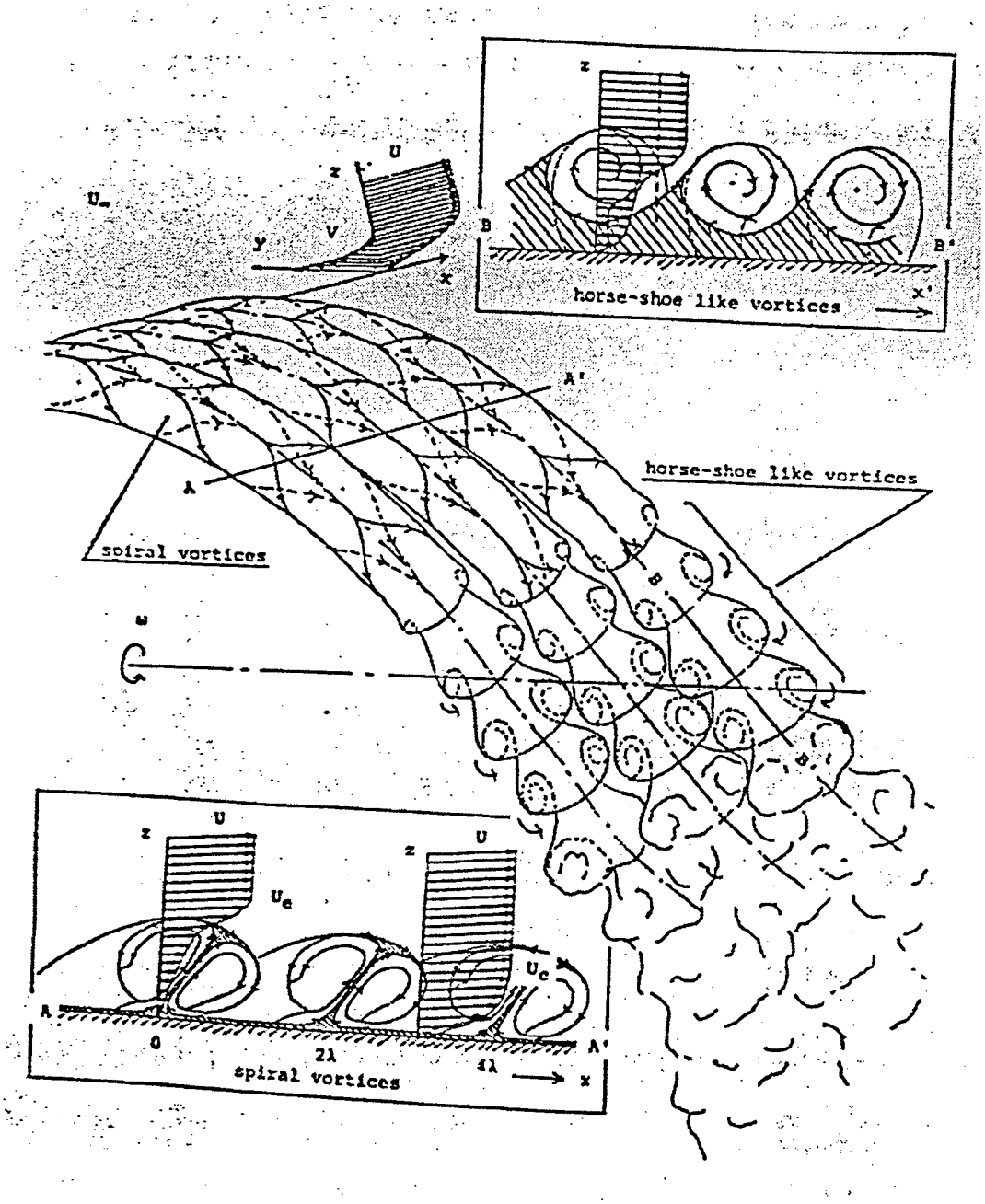

Figure 1. Schematic of breakdown process of crossflow vortices on a spinning axisymmetric cone. (Kohama[9])

(a) CW laser is sliced into pulse-burst, repeated every 0.1s

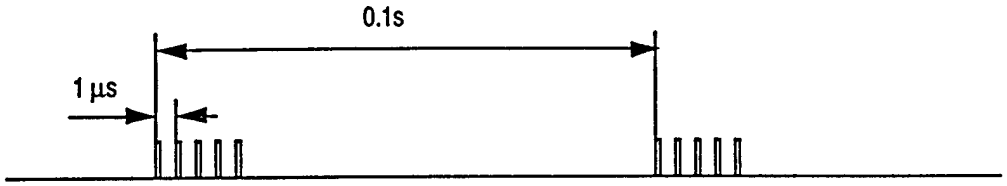

(b) Nd:YAG gain curve

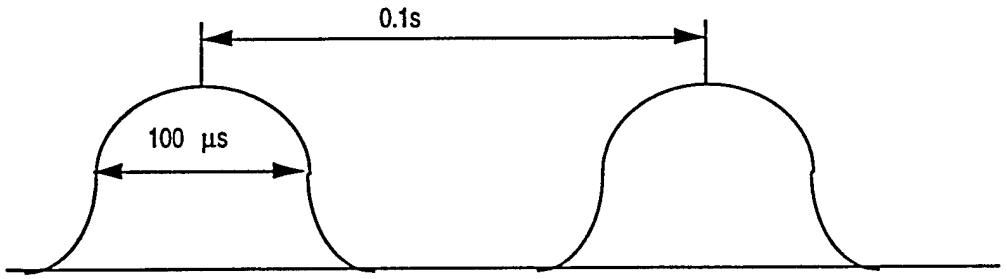

(c) Result is high power "burst" of 1~~99 pulses

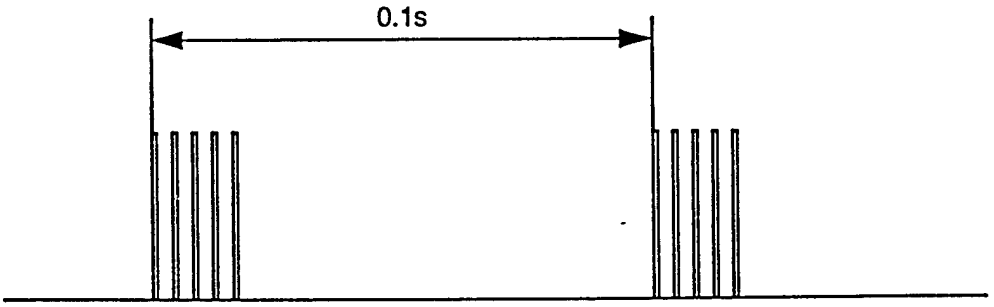

Figure 2. Pulse burst concept. (Lempert et al.[30])

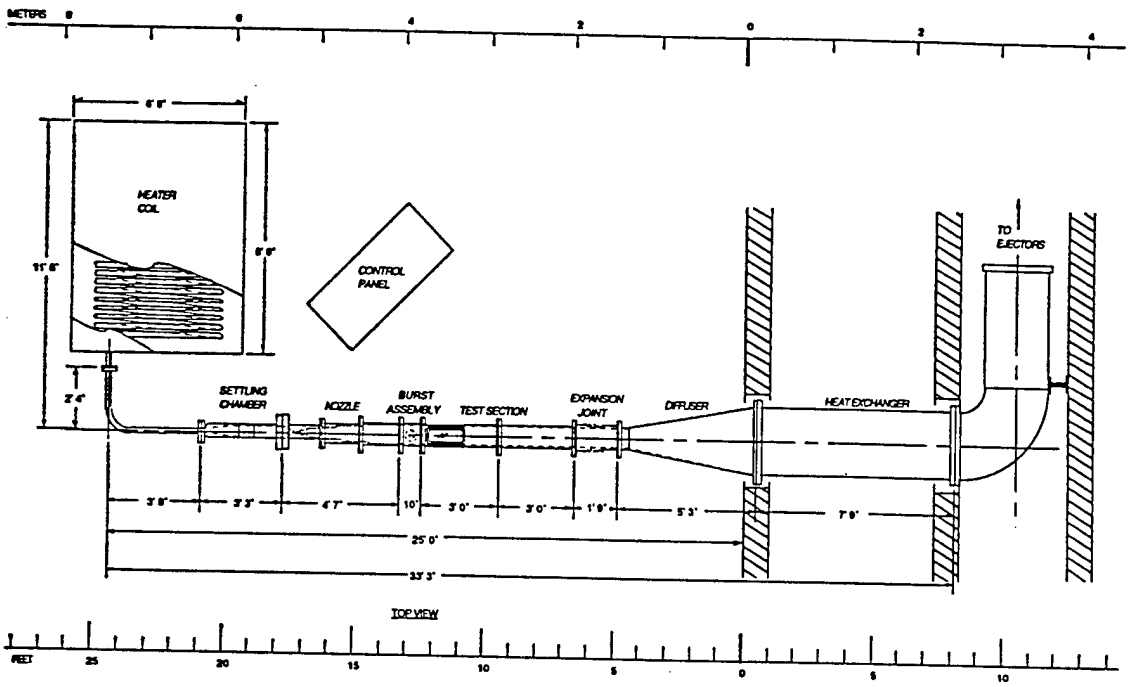

Figure 3. Schematic of Princeton Mach 8 Facility.

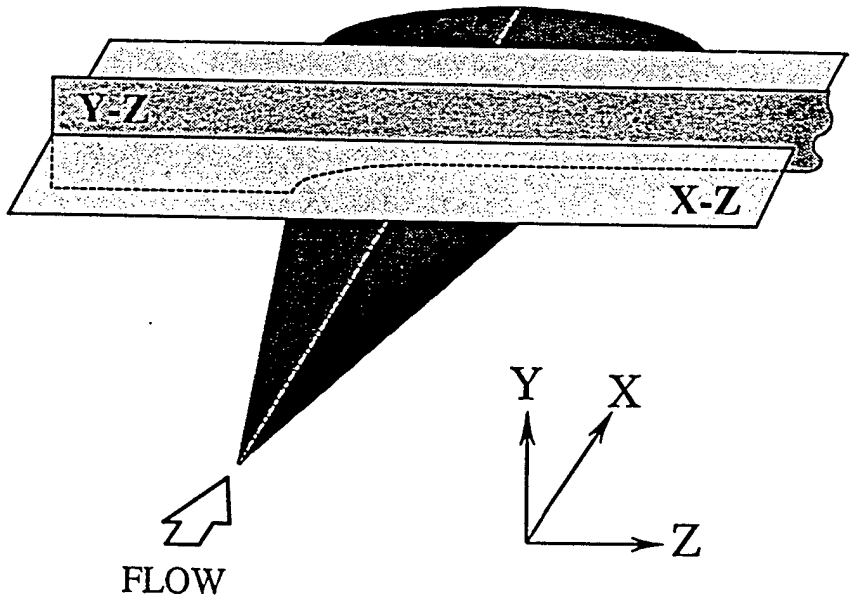

Figure 4. Laser sheet orientations for spanwise (Y-Z) and planform (X-Z) imaging.

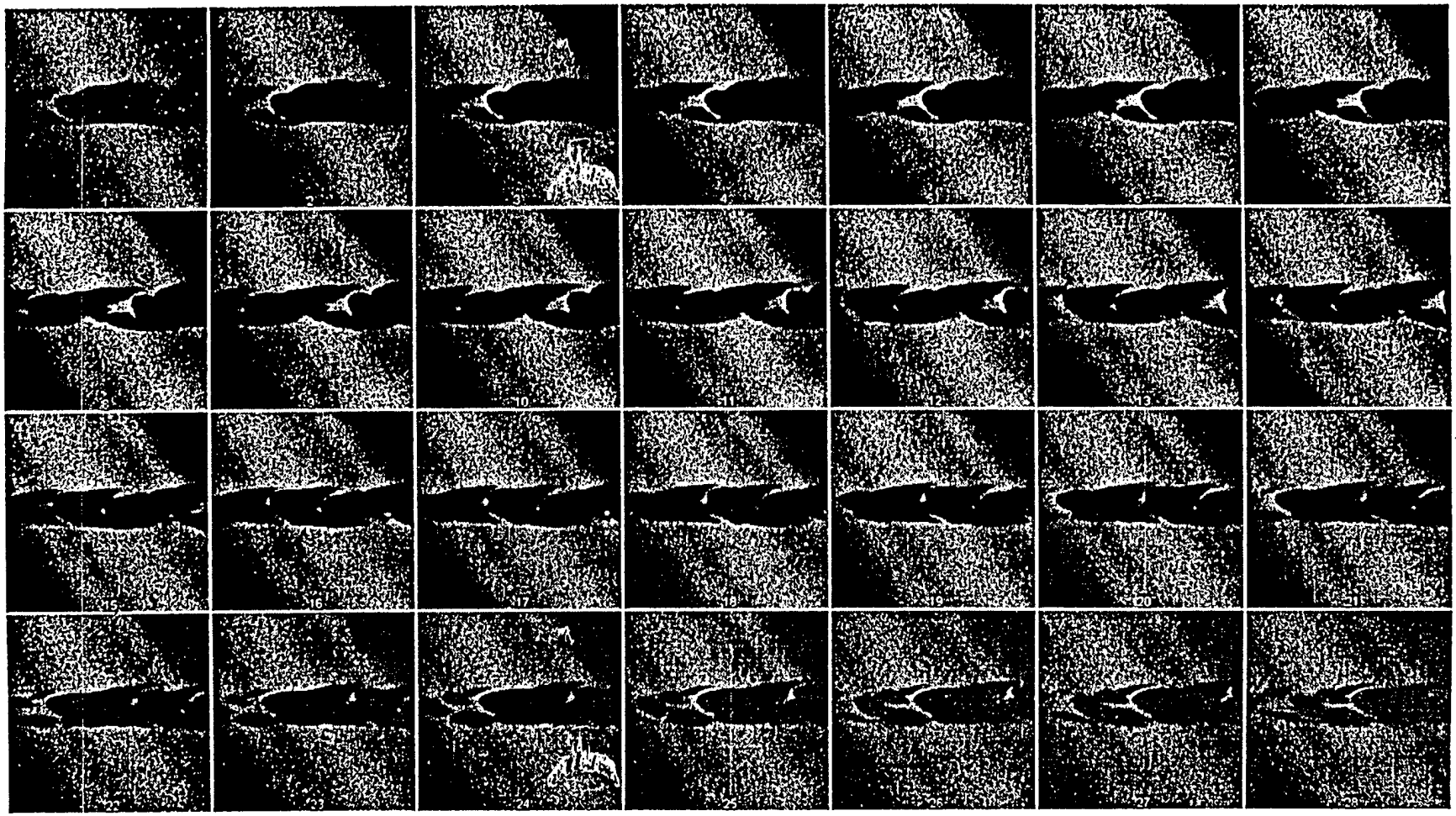

Figure 5. Planform motion picture at 500 kHz of centerline region on 4:1 elliptic cone. Field of view is 3.8 cm and flow is from left to right. Planform sheet is 4.75 mm from the surface. (Re_x=1.68×10^6)

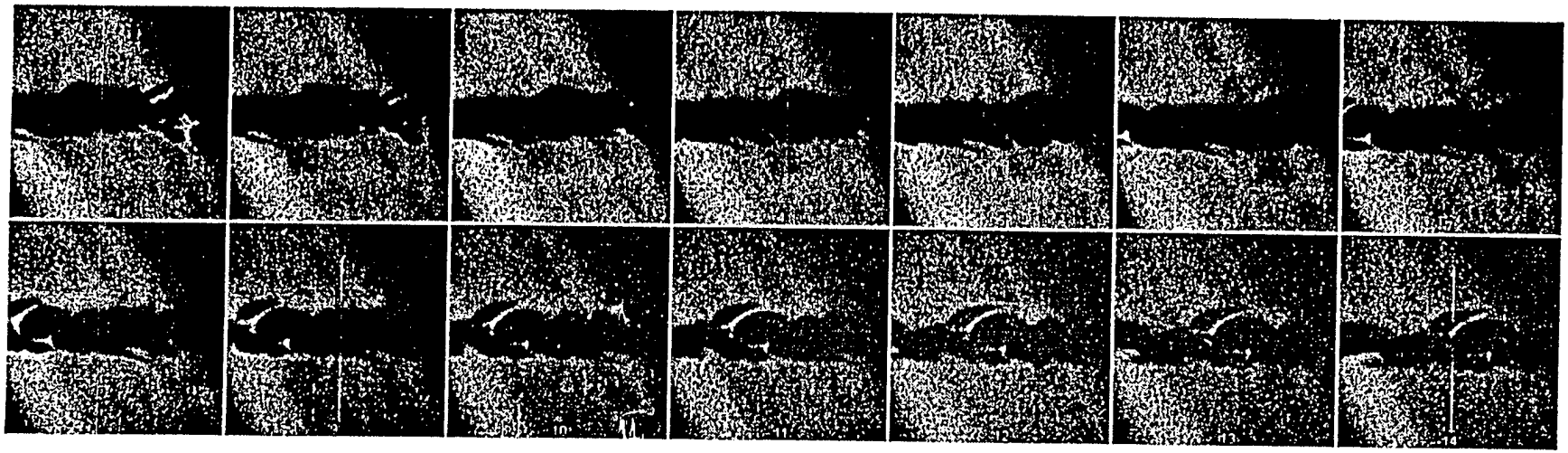

Figure 6. Planform motion picture at 500 kHz of centerline region on 2:1 elliptic cone. Field of view is 3.3 cm and flow is from left to right. Planform sheet is 2.75 mm from the surface. (Re_x=1.27×10^6)

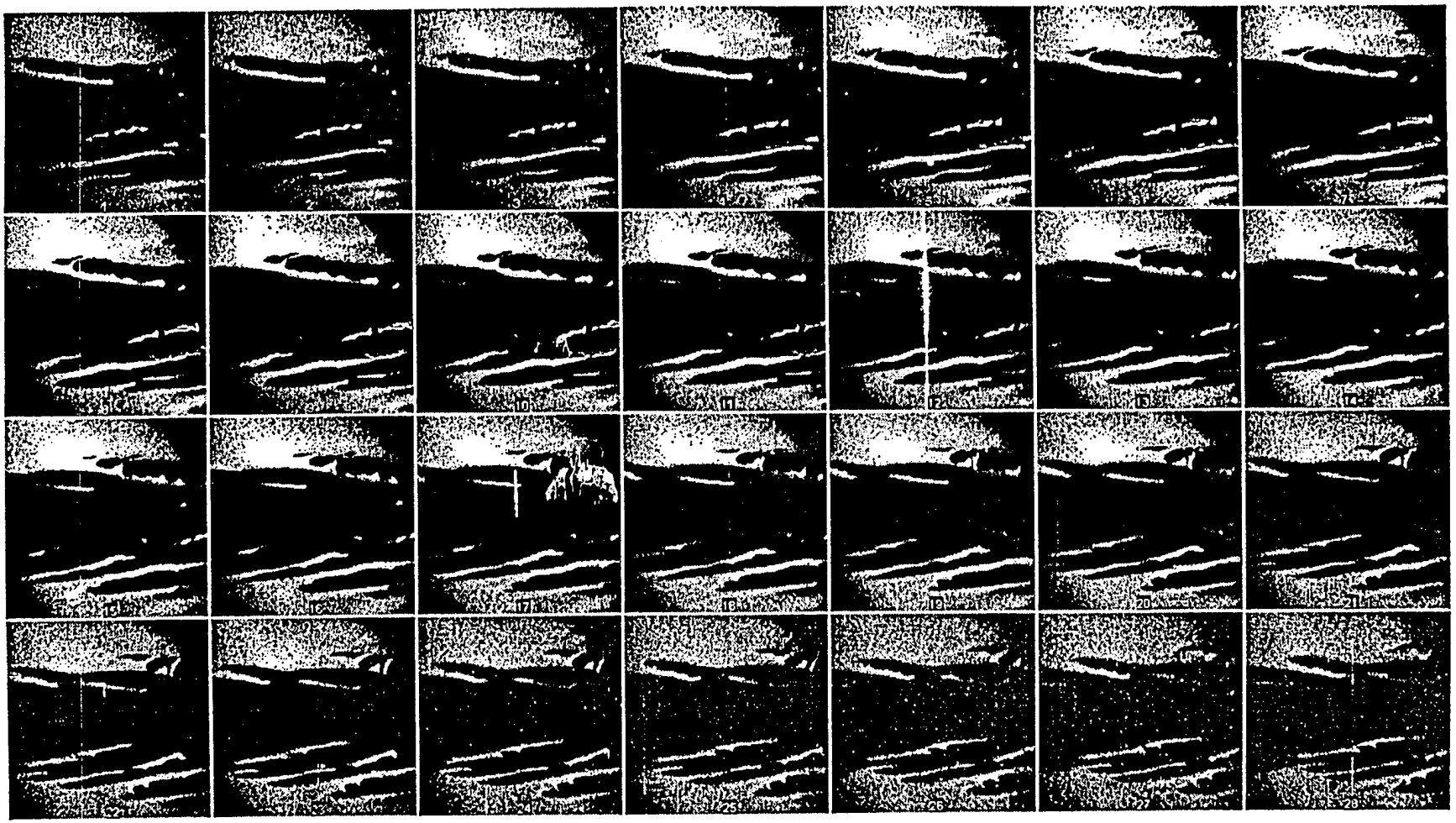

Figure 7. Planform motion picture at 500 kHz of centerline region on 4:1 elliptic cone. Field of view is 3.8 cm and flow is from left to right. Planform sheet is 2.0 mm from the surface. ($Re_x=2.44\times10^6$)

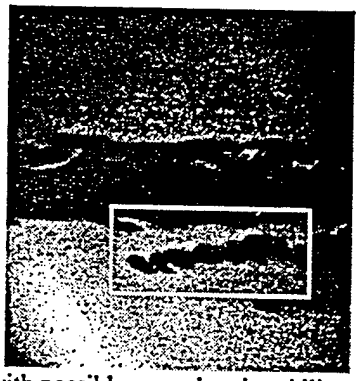

Figure 8a. Planform single-shot image with possible secondary instability shown inside white box. ($Re_x=2.44\times10^6$)

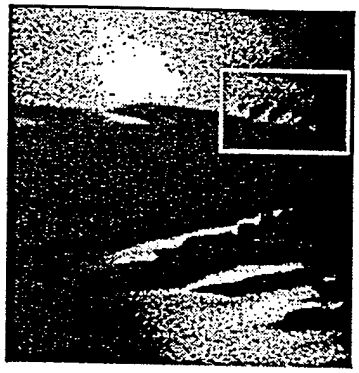

Figure 8b Planform single-shot image with possible secondary instability shown inside white box. ($Re_x=2.18\times10^6$)

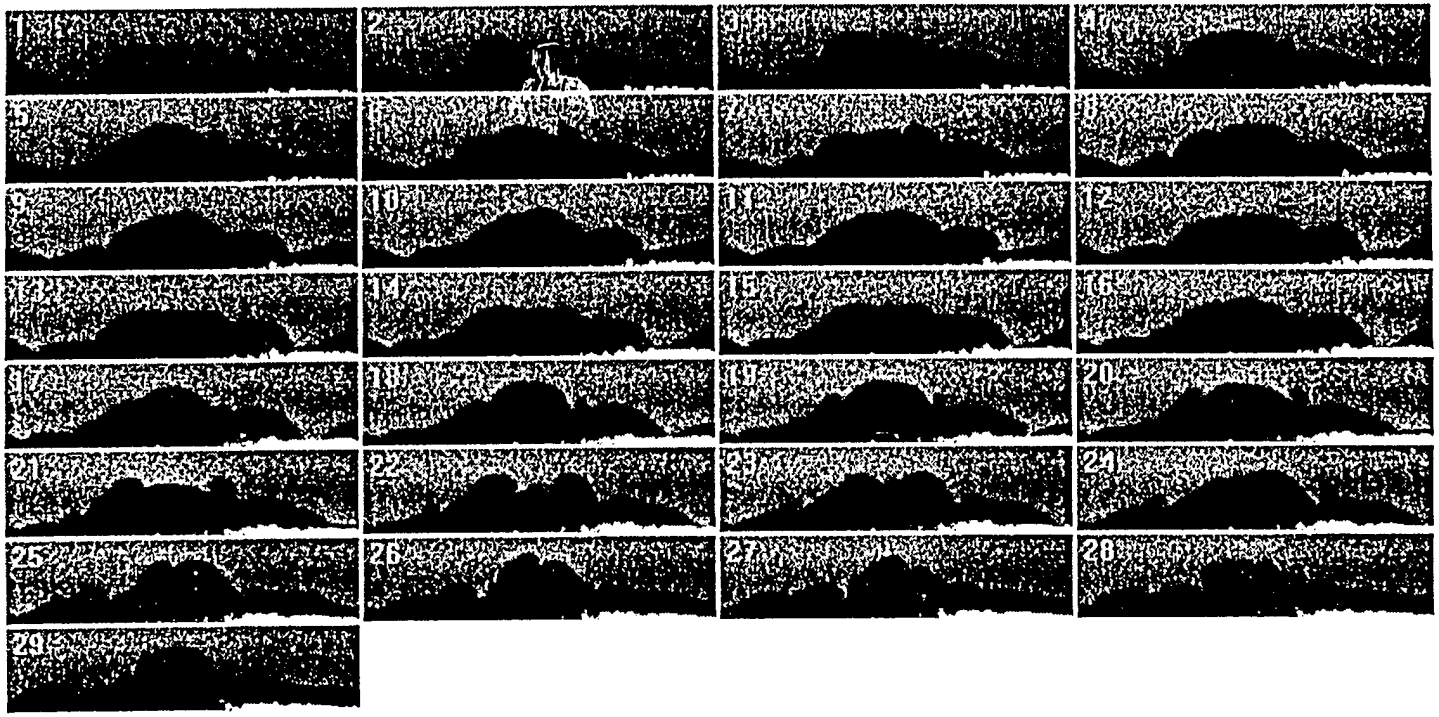

Figure 9. Spanwise motion picture at 500 kHz of centerline region on 4:1 elliptic cone. Field of view is 0.8×3.2 cm and flow is out of the image plane. (Re_x=1.53×10^6)

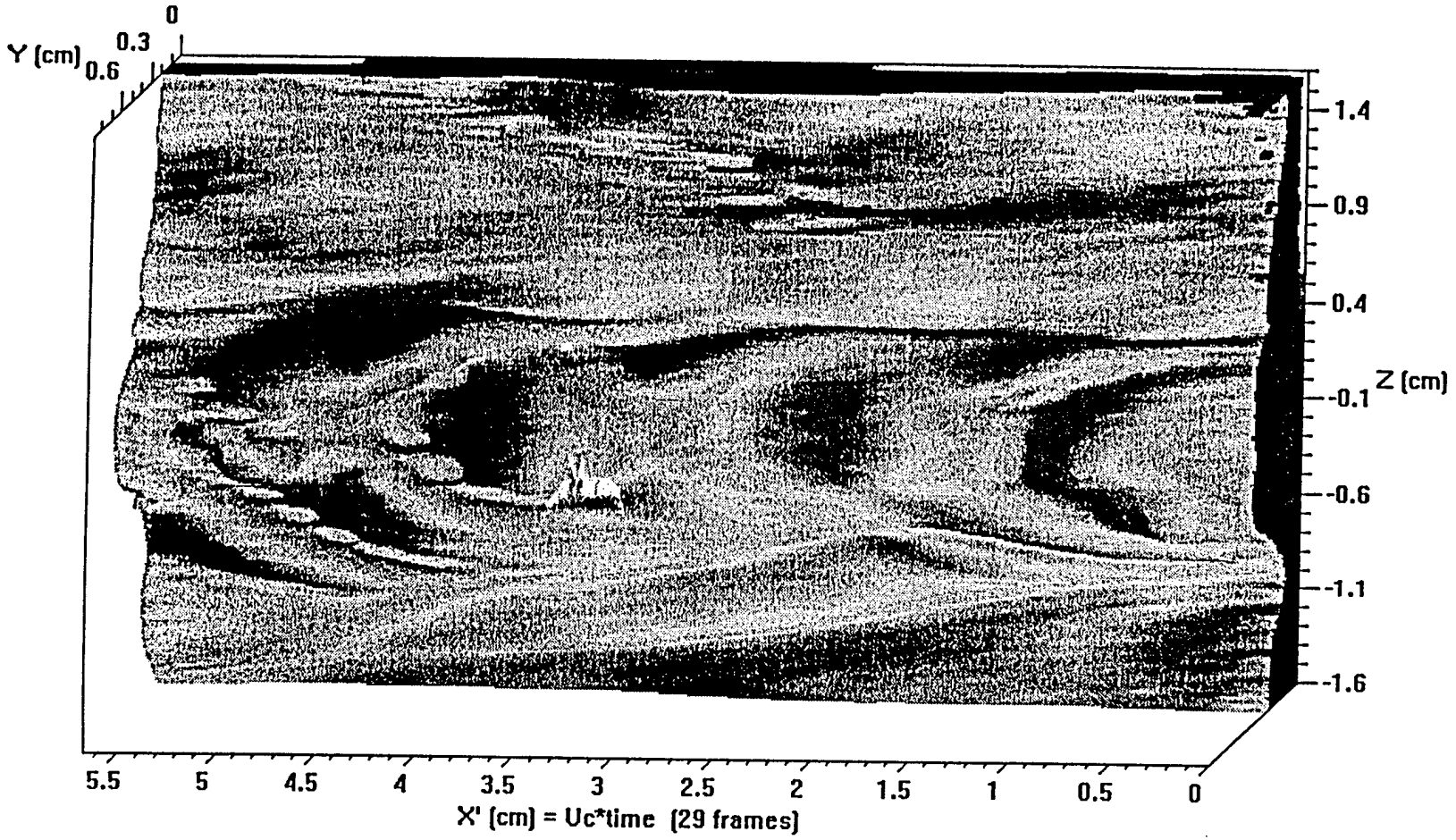

Figure 10. Volumetric reconstruction of centerline region on 4:1 cone using 29-frame motion picture from Fig. 11. X' axis is scaled using a convection velocity determined from planform image sets. Linear interpolation of grayscales between frames. Freestream grayscales values are transparent so that image represents sublimation interface of carbon dioxide. (Re_x=1.53×10^6)

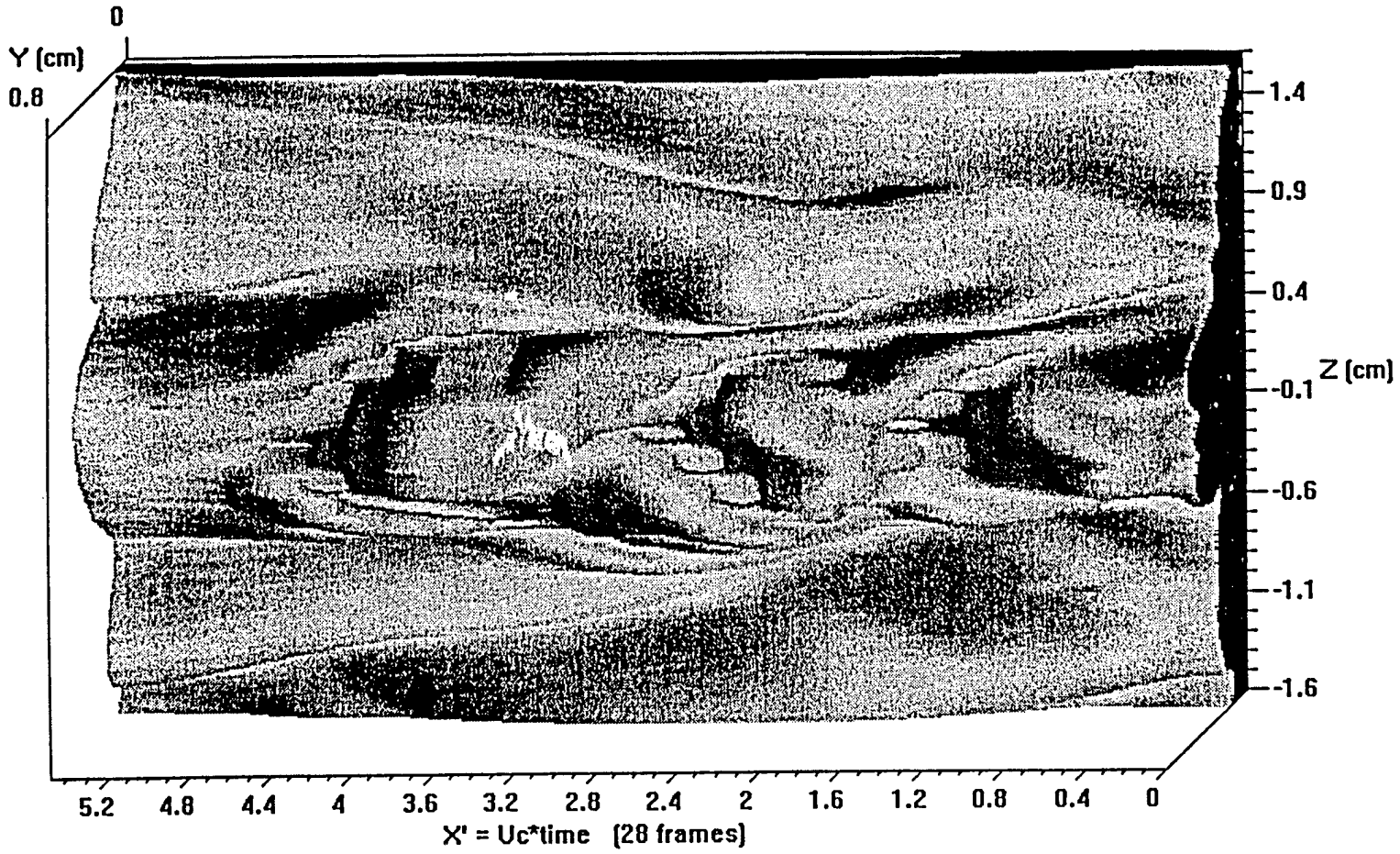

Figure 11. Volumetric reconstruction of centerline region on 4:1 cone using a 28-frame 500 kHz spanwise motion picture. X' axis is scaled using a convection velocity determined from planform image sets. Linear interpolation of grayscales between frames. Freestream grayscales values are transparent so that image represents sublimation interface of carbon dioxide. (Re_x=1.57×10^6)

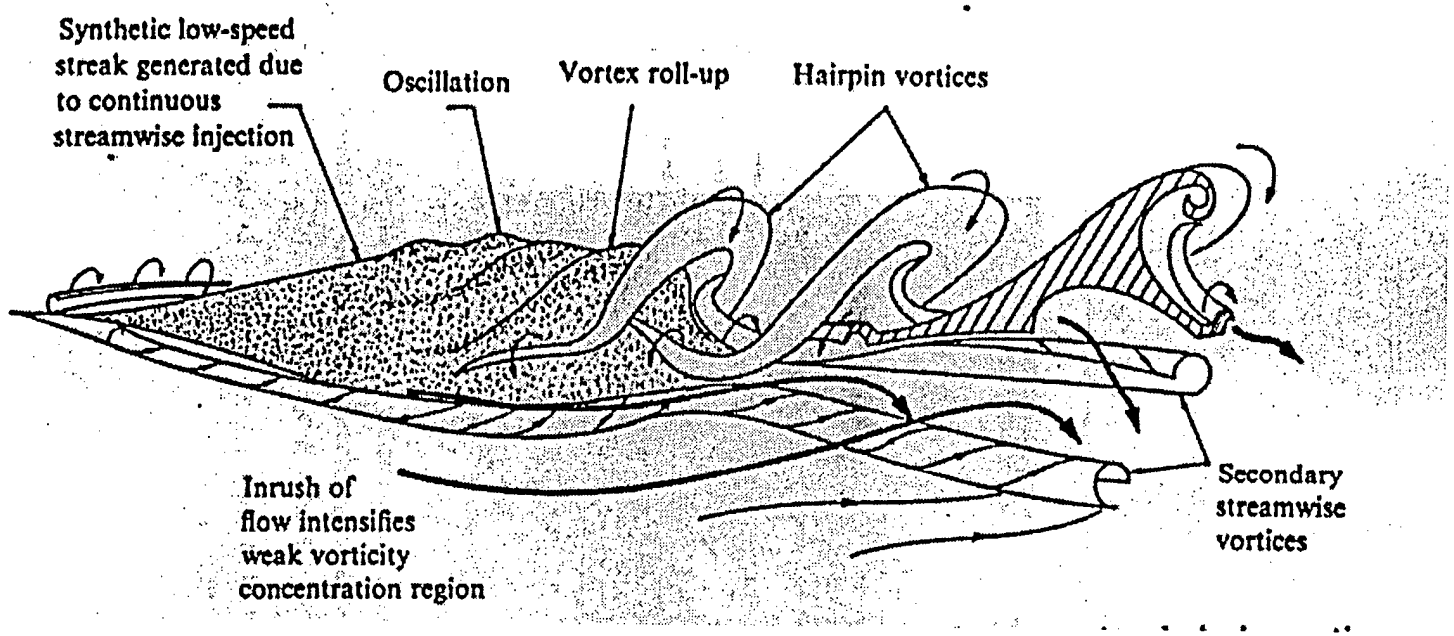

Figure 12. Schematic of hairpin vortex formation. (Acarlar and Smith[34])

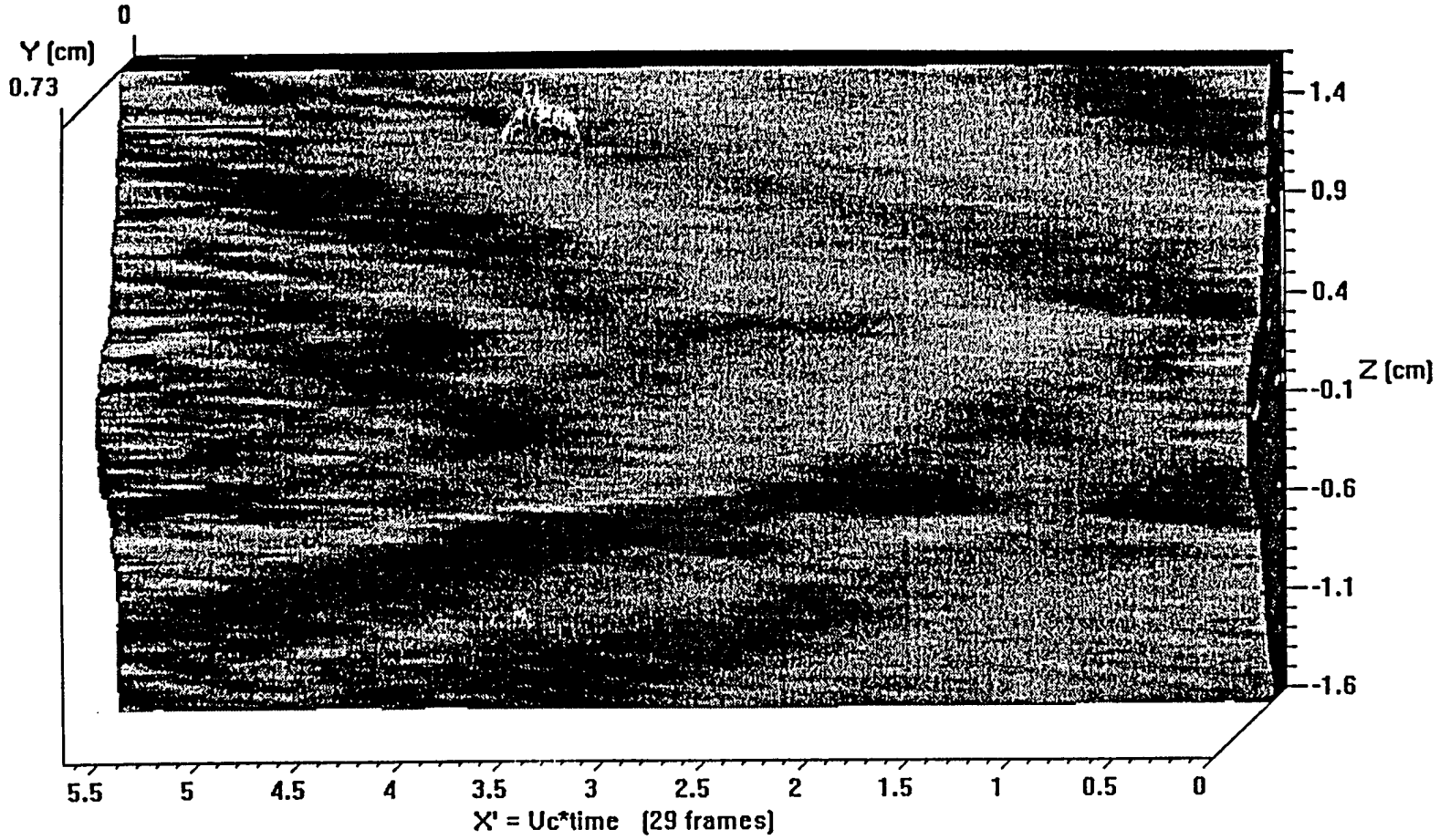

Figure 13. Volumetric reconstruction of centerline region on 4:1 cone using a 28-frame 500 kHz spanwise motion picture. Light illumination from the right side enhances off-axis waves. (Re_x=0.87×10^6)

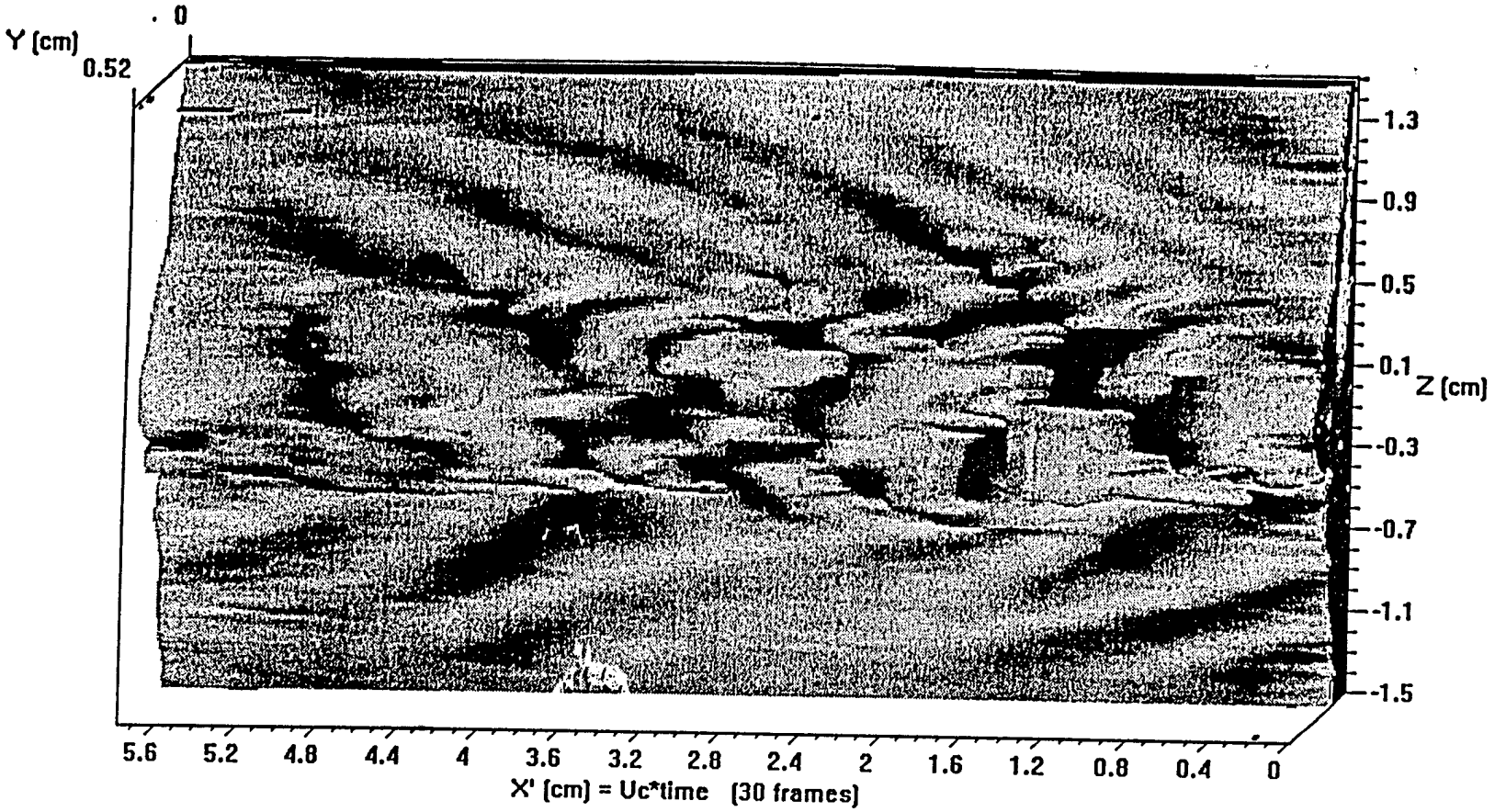

Figure 14. Volumetric reconstruction of centerline boundary layer on 2:1 cone. (Re_x=1.49×10^6)

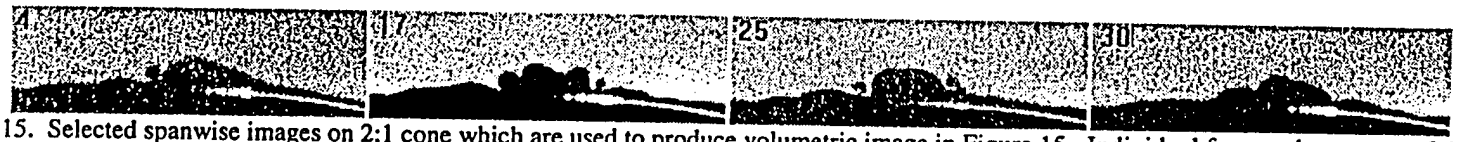

Figure 15. Selected spanwise images on 2:1 cone which are used to produce volumetric image in Figure 15. Individual frames show many of the same characteristics which were observed in the images taken on the 4:1 cone.

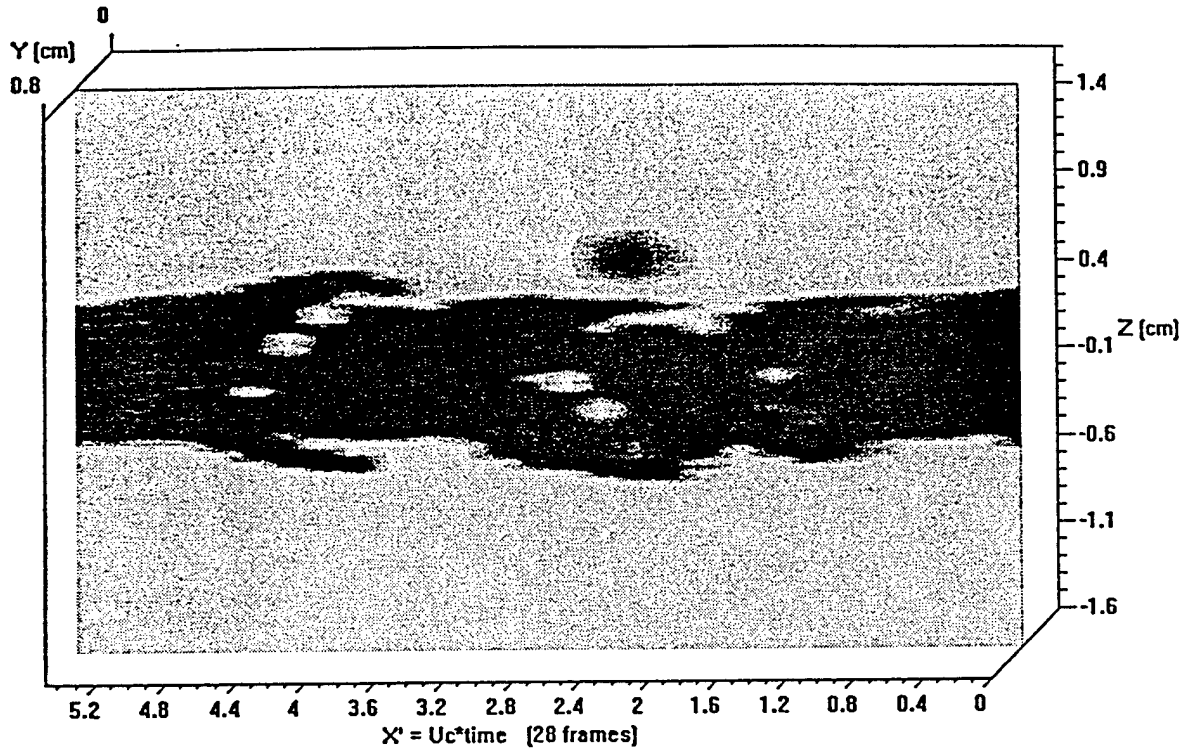

Figure 16a. Cut through X'-Z plane in volumetric reconstruction of Figure 13 at Y=4.0 mm.

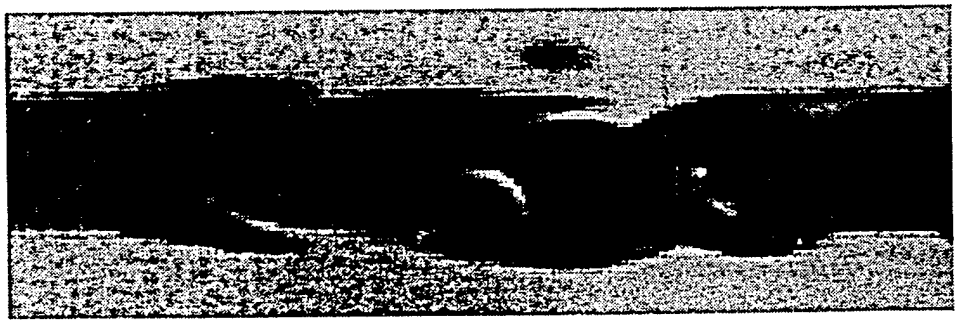

Figure 16b. Single-shot planform image taken simultaneously with frame #9 in the motion picture. Planform sheet is 4.0 mm from the surface. Flow is from left to right and field of view is 1.75×5.5 cm.

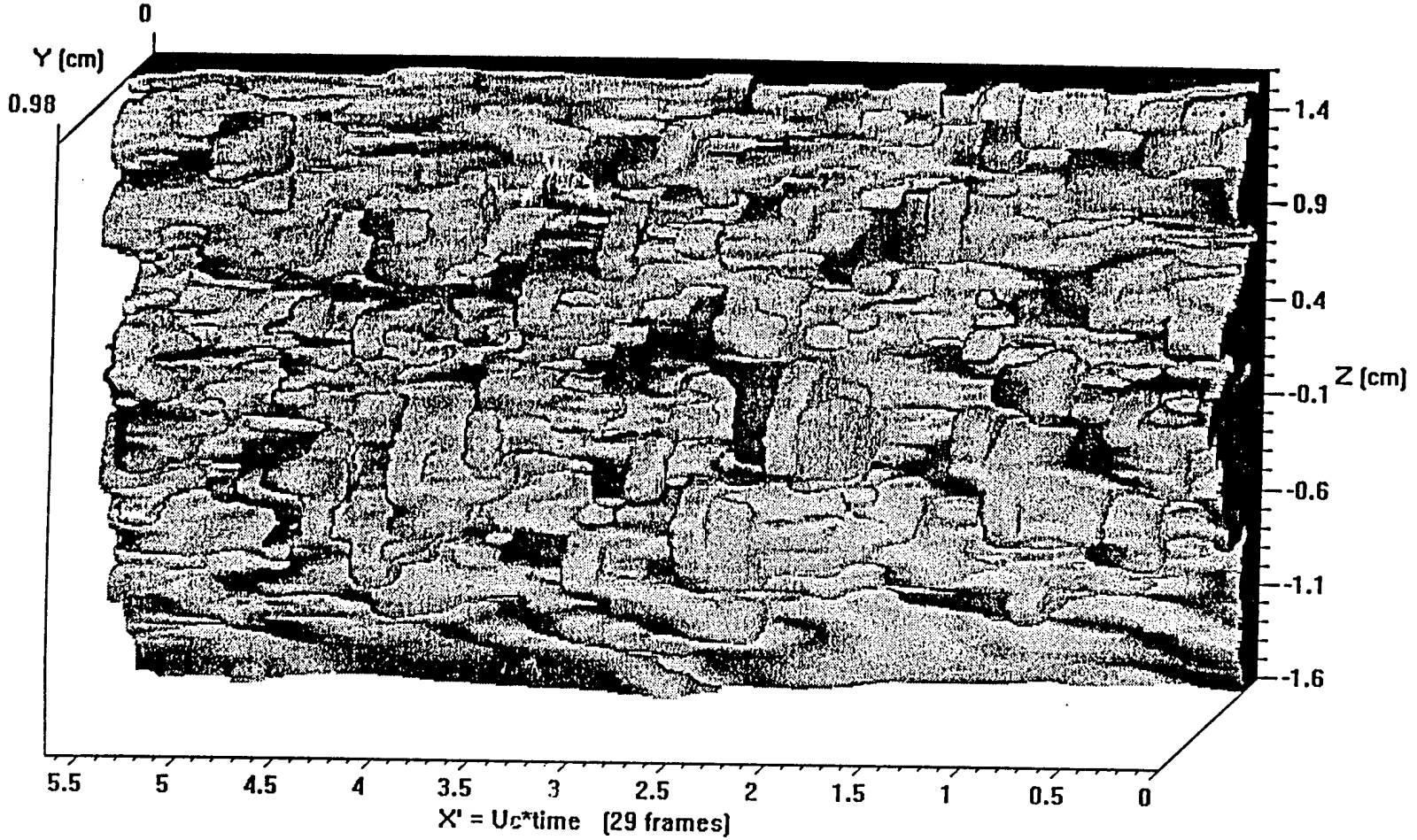

Figure 17. Volumetric reconstruction of centerline boundary layer on 4:1 cone. (Re_x=2.46×10^6)

Megahertz Pulse-Burst Laser and Visualization of Shock-Wave/Boundary-Layer Interaction

P. Wu, W. R. Lempert, R. B. Miles

Reprinted from

AIAA Journal

Volume 38, Number 4, Pages 672–679

AIAA

A publication of the
American Institute of Aeronautics and Astronautics, Inc.
1801 Alexander Bell Drive, Suite 500
Reston, VA 20191–4344

AIAA JOURNAL
Vol. 38, No. 4, April 2000

Megahertz Pulse-Burst Laser and Visualization of Shock-Wave/Boundary-Layer Interaction

Pingfan Wu,* Walter R. Lempert,† and Richard B. Miles‡
Princeton University, Princeton, New Jersey 08544

The development and application of a Nd:YAG pulse-burst laser system, which is capable of operating at up to 1-MHz pulse repetition rate with high pulse energy and narrow spectral linewidth, is presented. The laser system can generate a burst of from 1 to 99 pulses over a maximum time interval of 100 μs. The average single pulse energy at 1.064μ is 10 mJ. This laser is paired with a new megahertz-rate charge-coupled device framing camera to obtain images of a Mach 2.5 flow over a 14-deg angle wedge at a 500-kHz repetition rate. The sequential images clearly show the dynamic interaction between the incoming turbulent boundary layer and the unsteady oblique shock wave.

I. Introduction

In recent years there has been enormous progress in the development and application of diagnostic imaging techniques, such as planar laser-induced fluorescence (PLIF),[1] Rayleigh scattering,[2] and Raman scattering.[3] However, the ability to capture time-evolving information has been severely constrained by the limitations of laser technology. For example, the pulse repetition rates of commercially available high-energy solid-state lasers are limited up to 30 Hz. Nd:YAG lasers combining continuous pumping with repetitive Q switching at up to 50 kHz have been built.[4] However, the pulse energy at these rates is only about 100 μJ. Also available are 20-kHz repetition-rate metal vapor lasers,[5] with single pulse energy a few millijoules. Newly developed, repetitively Q-switched ruby lasers have pushed the repetition rate up to 500 kHz.[6,7] After amplification the individual pulse energy can get hundreds of millijoules.[7] However, when the repetition rate extends to 1 MHz, repetitive Q-switched operation becomes very unreliable.[6]

Our objective has been to develop a laser imaging system to capture high-speed and unsteady flow phenomena, such as turbulent structure and shock-wave/boundary-layer interactions. The dynamics of the highly unsteady shock-wave/boundary-layer interaction is very important in the stability and control of supersonic vehicle. Because the particular characteristics of the turbulence are still unknown, the dynamic visualization of shock wave and boundary-layer structure becomes very important. The characteristic small-scale eddy turnover time is on the order of microseconds, and so a megahertz repetition-rate laser source and imaging system become critical for this application.

The pulse burst concept is chosen for megahertz rate imaging diagnostics systems because the product of repetition rate and energy per pulse is constrained by the thermal loading that the solid-state lasing elements can tolerate. The current maximum power for a commercially available pulsed Nd:YAG system is approximately 15 W at 1.06 μm (1.5 J/pulse at 10 Hz). This means that, for example, if the megahertz pulse laser were to be run as a continuous duty cycle system, thermal considerations alone would limit the output energy to approximately 150 μJ per pulse. This is approximately 100 times too low to be generally useful for flow imaging experiments. The key to the burst concept is the reduction of the duty cycle in order to achieve high energies in each individual pulse. A typical pulse-burst can be seen in Fig. 1a: every 0.1 s a burst of about 30 pulses is generated (in this figure only 5 pulses are shown).

In this paper we present the design of a Nd:YAG-based, high-power, narrow-linewidth, pulse-burst laser source that can generate a burst of from 1 to 99 laser pulses with an interpulse period as short as 1 μs and a pulsewidth from 10 to 100 ns. The spectral width of these pulses is comparable to the Fourier transform of their temporal profiles, which makes this pulse-burst laser an ideal source for narrow-linewidth, long coherence length applications such as holographic interferometry and filtered Rayleigh scattering (FRS).[8,9] In particular, the FRS is useful for the imaging of high-speed flows because it can be used to suppress background scattering from windows and walls as well as to highlight particular velocity components.

This pulse-burst laser system has been paired with a Princeton Scientific Instruments' fast-framing charge-coupled-device (CCD) camera that can capture up to 30 images at a rate of up to 1 μs a frame. The laser and the camera were set up to visualize the Mach 2.5 flow over a 14-deg wedge from streamwise view and planform view at a 0.5-MHz rate. The optically thick iodine vapor filter was placed in front of the camera and used to highlight different velocity components of the flow by selectively passing different Doppler-shifted frequencies. The images that were acquired clearly illustrate the unsteadiness of the oblique shock wave and show that the unsteady shock motion is closely coupled to the incoming boundary-layer structure.

II. General Description of the Laser

The challenge is to create a controllable pulse-burst system, which produces a uniform set of high-energy pulses with very low background. The background is primarily caused by amplified spontaneous emission that occurs naturally through the amplifier chain. Incidental feedback must also be carefully controlled so that the system does not develop parasitic lasing. In addition, the gain seen by each pulse in the pulse burst is slightly different because of the gain saturation from the previous pulse. In the design of this system, it was decided not to use a regenerative amplifier configuration because of the limited versatility of such a system and concerns regarding gain depletion and Q-switch leakage. The design of the pulse-burst laser system is, therefore, based on a master oscillator power amplifier (MOPA) configuration, as shown in Fig. 2. The laser system consists of six principle parts: 1) monolithic, single-frequency, diode-pumped, CW Nd:YAG laser; 2) four-pass preamplifier 1; 3) pulse slicer (a pair of Pockels cells); 4) two-pass preamplifier 2; 5) three-stage high-energy amplifier chain; and 6) second harmonic crystal.

A continuous wave (CW) Nd:YAG ring laser serves as the master oscillator. The laser can be frequency tuned and has a single mode output. Because this laser is amplified through the amplifier chain,

Received 1 April 1999; revision received 16 August 1999; accepted for publication 18 August 1999.

*Graduate Student, Department of Mechanical and Aerospace Engineering. Student Member AIAA.

†Senior Research Scientist, Department of Mechanical and Aerospace Engineering; currently Associate Professor, Department of Mechanical Engineering, Ohio State University, Columbus, OH 43210.

‡Professor, Department of Mechanical and Aerospace Engineering. Associate Fellow AIAA.

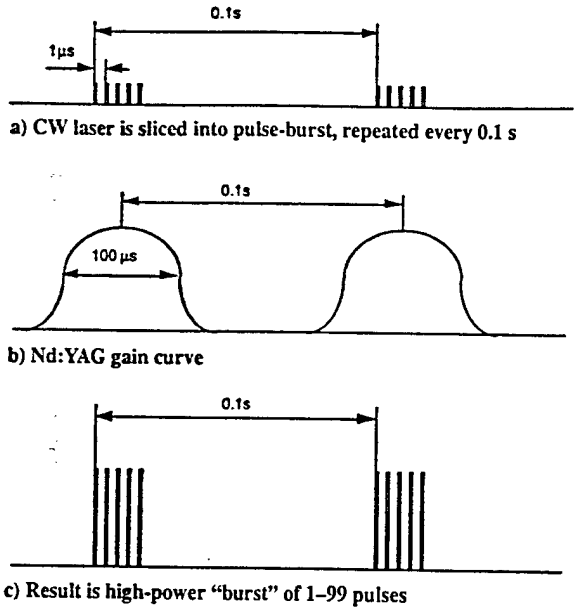

Fig. 1 Concept of pulse-burst laser system.

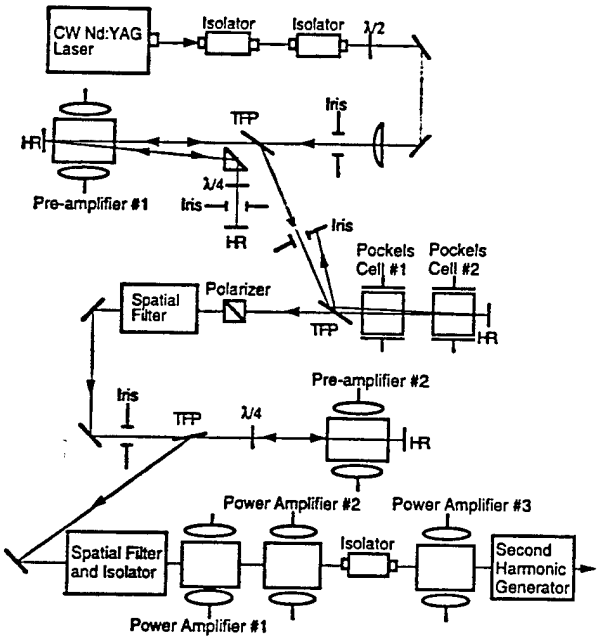

Fig. 2 Schematic diagram of pulse-burst laser system.

its frequency determines the output frequency of the pulse-burst laser system. To minimize amplified spontaneous emission (ASE), the four-pass preamplifier 1 amplifies this CW laser light over the 100-μs-or-so gain window of the flashlamp-pumped Nd:YAG laser rods. The power remains below saturation, and so there is no loss in gain associated with amplifying a CW laser as compared to a pulsed laser in this stage. This CW preamplification suppresses the ASE that would otherwise be present between pulses had the pulse slicing been done before preamplifier 1. ASE occurs continuously during the flashlamp pumping time so that if the light were chopped with a $\frac{1}{100}$ duty cycle the ASE generated in preamplifier 1 would be stronger than the amplified laser signal. This is avoided by putting the pulse slicer after preamplifier 1. The slicer not only chops the pulse but also blocks the cross-talk between preamplifier 1 and preamplifier 2 and, therefore, serves as an isolation stage in the amplifier chain.

III. System Performance

A. Master Oscillator

The master oscillator is a commercially available monolithic Nd:YAG ring laser with output power about 20 mW (Lightwave 120-03A). The frequency of this laser can be voltage-tuned over a range of approximately 1 cm^{-1} at 1.06 μm. The CW laser beam has a very good spectral and spatial profile. The linewidth is about 5 kHz (in 1 ms), and the frequency drift is about 50 MHz/h.

B. Preamplifier 1

Preamplifier 1 is a four-pass, 10-Hz repetition-rate, flashlamp-pumped, 6.5 mm diam × 110 mm long Nd:YAG rod. A long-focal-length (1-m) lens reduces the beam diameter to approximately 2 mm to accommodate the multiple passes. The overall gain of the four-pass system, taking optical losses into account, is approximately 2500 times. Preamplifier 1 is currently operated at much lower level than its maximum gain in order to prevent spontaneous lasing.

C. Pulse Slicer

The pulse slicer, custom built by Medox, Inc. (Ann Arbor, Michigan), consists of a pair of electro-optic Pockels cells, similar to those used as Q switches for standard solid-state laser systems. By applying a suitable voltage, a $\lambda/4$ polarization retardation is imposed upon the laser beam by each Pockels cell for each pass. Consequently, when either one of the cells is on, the resulting polarization is rotated 90 deg (from vertical to horizontal) and is, therefore, transmitted through the thin-film polarizer (TFP). When both (or neither) of the Pockels cells are on, the polarization of the beam is unchanged, and it is reflected by the TFP and blocked by an iris diaphragm.

Figure 3 shows a timing diagram for the pair of Pockels cells. Each individual Pockels cell has a minimum rise time of approximately 4 ns and an on time duration ($t2$) of approximately 150 ns. The delay between the rising edges $t1$ is variable from 5 to 100 ns. The slicer is on, during the interval $t1$ when Pockels cell 1 is high and Pockels cell 2 is low. From the diagram it is apparent that the falling edge is much slower than the rising edge, which is the reason two Pockels cells are used instead of one. For this system the timing of the laser pulses solely depends on the rising edge of the high voltage, which is applied to the Pockels cells. The high-voltage timing is determined by a 500-MHz precision clock that controls the Pockels cells' power supply unit, resulting the timing jitter for the laser pulses that is less than 2 ns. The timing of pulses here is much more precise than the repetitively Q-switched laser,[7] in which even the Q-switched pulse buildup time will cause time uncertainty 10 ns.

D. Preamplifier 2

After the pulse slicer the output pulse train is spatially filtered and then double-passed through preamplifier 2. The spatial filter has two functions: 1) decrease the ASE and 2) clean the spatial profile of the laser.

Preamplifier 2 is an 8 mm diam × 110 mm long Nd:YAG rod. The peak double-pass gain of preamplifier 2 is approximately 13 times. The output peak pulse power is about 650 W, corresponding to an average 13 μJ for a single, 20-ns-duration pulse. Again to prevent

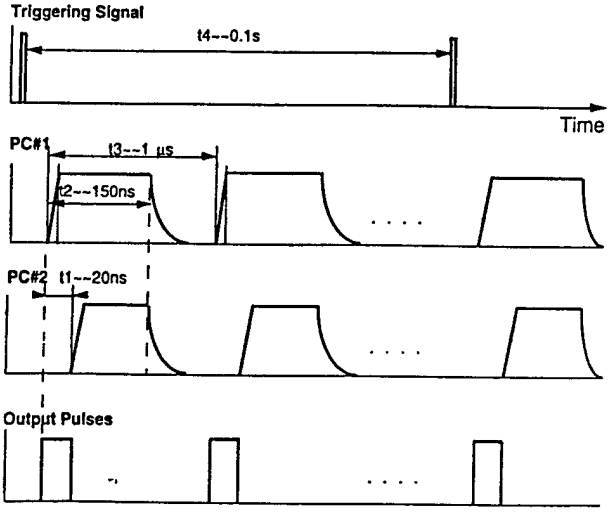

Fig. 3 Timing diagram for the work of the pair of Pockels cells.

spontaneous lasing, preamplifier 2 is operated at a gain level lower than maximum power.

E. Power Amplifier Chain and Second Harmonic Generation

The power amplifier chain consists of three additional Nd:YAG rods, taken from a commercial (Continuum Model YG-592) laser system. The rods are 6.5, 6.5, and 9.5 mm diam, respectively. Between power amplifiers 2 and 3, there are a telescope beam expansion system (not shown in the figure) and a 10-mm-diam optical isolator (Electro-optics Technology, Inc., Traverse City, Michigan). The peak gain of the individual stage has been measured to be 10, 10, and 8 times, respectively, resulting in an overall peak system gain of approximately 2.5×10^7 (including preamplifiers). The corresponding energy is approximately 10 mJ for a single 20-ns duration pulse at 30 pulses per burst.

An important aspect of the system is the saturation of the final power amplifier. For the amplification of a single pulse, Frantz and Nodvik[10] and Lowdermilk and Murry[11] have given the relation

$$E_{\text{out}} = I_{\text{sat}} \times A \times \ell n \left\{ 1 + \left[\exp\left(\frac{E_{\text{in}}}{I_{\text{sat}} \times A} \right) - 1 \right] \times G_0 \right\} \quad (1)$$

where E_{in} and E_{out} are, respectively, the input and output energy of the pulse through the amplifier. I_{sat} is called the saturation flux of the amplifier, which is 440 mJ/cm^2 for a Nd:YAG amplifier. A is the area of the cross section of the amplifier. G_0 is the small signal gain of the amplifier, which is defined as

$$G_0 = \exp(g_0 L) = \exp(n\sigma L) \quad (2)$$

where n is the inverted population density and σ is the cross section of the stimulated radiation. L is the length of the rod. We can relate the small signal gain G_0 to the stored energy E_{store}:

$$E_{\text{store}} = nh\nu LA = A \times (h\nu/\sigma) \times \ell n G_0 \quad (3)$$

where h is the Planck constant and ν is the frequency of the laser. For a specific laser amplifier the cross section A and $h\nu/\sigma$ are constant. The small signal gain G_0 is exponentially related to the stored energy E_{store}. In the pulse-burst laser system, as a pulse is being amplified, it depletes the stored energy from the amplifier, and G_0 decreases. From Eq. (1) the pulse amplification ratios decrease from pulse to pulse in the same burst. We have found the overall stored energy in the power amplifiers is about 800 mJ. For a pulse burst with 30 pulses, the first 29 pulses and other losses will take more than 300 mJ from the rods. The gain of the 30th pulse is only about $\frac{1}{8}$ of the gain of the first pulse in the burst. To compensate for this depletion, the preamplifiers are run on the rising edge of the temporal gain curve. This gives an increasing energy per pulse after preamplifier 2 (Fig. 4a), which leads to a more uniform pulse burst after the final amplifier (Fig. 4b). The oscilloscope (Tektronix Model TDS 360) trace was detected by photodiode with 1-ns response time (Thorlabs Model DET210).

Because of gain depletion, the pulse-to-pulse energy is still far from constant. Especially after doubling, the lowest pulse energy is only about one-third of the highest pulse energy in the same burst. For this reason the dynamic range of the imaging system will decrease by a factor of three, which is still tolerable in our system. With further engineering the nonuniform pulse energy problem can be overcome by using a diode laser to replace the CW Nd:YAG laser as the master oscillator. The diode laser power is easily controlled through the driving current. In that case the input energy of each pulse can be tailored to get a uniform output after the final amplifier.

The final part of the laser system is the second harmonic generator. A telescope system (not shown in the picture) reduces the laser beam diameter to 4 mm before it passes through the doubling crystal. The peak intensity of fundamental light into the doubling crystal is about 4.5 MW/cm^2. The variation in pulse energy is accentuated by the second harmonic process as shown in Fig. 4c. The shape of a single pulse of second harmonic light closely follows that of the fundamental because both are rectangular in time. In contrast to a Gaussian pulse, the temporal profile of the second harmonic of a perfectly rectangular pulse, assuming a simple intensity squared law for conversion efficiency, is identical to that of the fundamental. The full width at half-maximum (FWHM) of the second harmonic is about 14 ns as compared to 16 ns primarily because of the rise time of fundamental pulse. With this system we only get average 0.4 mJ per pulse of second harmonic 0.532 μm. The reason for the low conversion ratio is the low 1.06-μm input intensity. Follow-on work indicates that pulse energy on the order of 25 mJ per pulse at 0.532 μm are achievable with greater amplitude of 1.06-μm light.

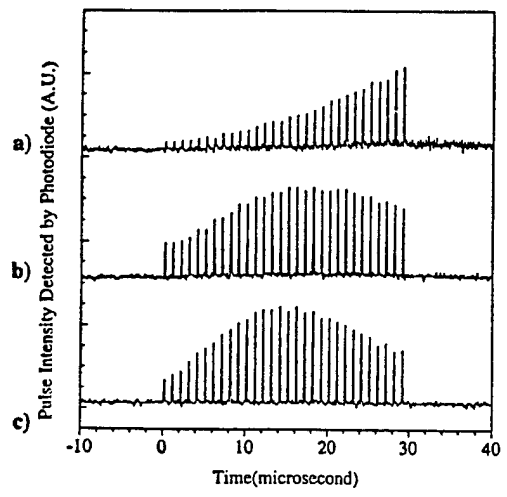

Fig. 4 Single-pulse burst a) before and b) after the final three stages of amplifier train; c) is the second harmonic of the pulse burst. There are 30 pulses per burst, with interpulse separation of 1 μs and single-pulse duration of about 20 ns.

IV. Laser Spectral Profile

For many diagnostics applications, narrow spectral linewidth and frequency tunability over a limited range are important. Because the narrow-linewidth CW laser serves as a master oscillator and there is no resonator cavity in the amplification stage, the configuration of the pulse-burst laser system gives a very good spectral profile.

Each individual second harmonic pulse is predicted to have a time-average linewidth on the order of 63 MHz, based on the Fourier transform of a 14-ns rectangular temporal profile ($\delta\upsilon \times \delta t = 0.88$ for a sinc^2/rectangular Fourier transform pair).

As shown in Fig. 5, a 2-GHz free spectral range, confocal Fabry–Perot spectrum analyzer (Burleigh Model RC-46) was used to directly measure the spectral profile of the second harmonic output of the pulse-burst laser. For these measurements the laser was operated at full gain, and the output was attenuated by reflection from an uncoated quartz flat (not shown in Fig. 5). The internal photodiode/mount assembly was removed from the etalon and replaced with a fast response photodiode. The pulsed output from the photodetector was integrated by a boxcar averager (Stanford Research Systems Model SRS 250) and sent to a PC computer. For the data presented next, the boxcar averaged the photodiode voltage over 30 laser shots. Simultaneously, the wavelength of the CW master oscillator was slowly scanned (on the order 1 MHz/s) by applying a computer generated voltage "staircase" (2.5 mV a step) to the input of the laser voltage controller, while holding the voltage to the etalon mirrors constant. The laser, rather than the etalon, was tuned

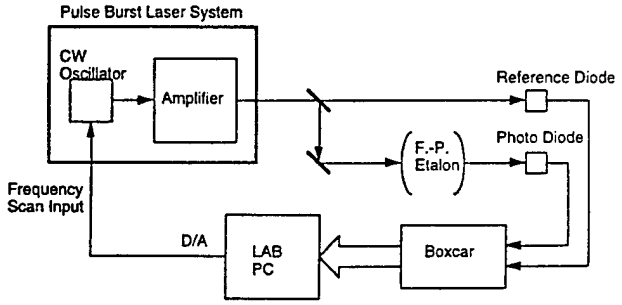

Fig. 5 Schematic diagram for measuring the spectral profile of the pulse-burst laser.

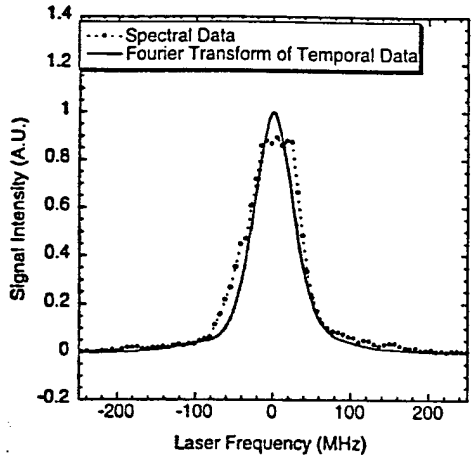

Fig. 6 Time-averaged spectral profile (····) of second harmonic output of pulse-burst laser and the convolution (——) between the etalon equipment function and Fourier transform of the temporal single-pulse profile.

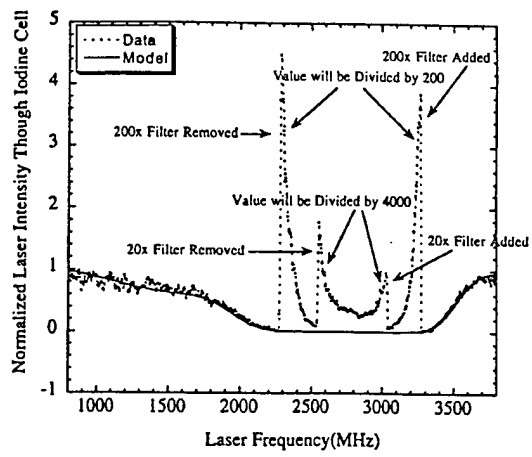

Fig. 7 Experimental attenuation of pulse-burst laser intensity through the iodine cell (····). Convolution of modeled transmission and laser spectral profile from Fig. 6 (——).

because the etalon could not be scanned slowly enough to capture the profile of the pulsed laser smoothly. The frequency tuning rate of the laser was calibrated with the Fabry–Perot free spectral range. The observed scanning rate was 3 GHz/V and was assumed to be constant over the duration of the scan. The effective finesse of the etalon is measured by passing the CW laser (very narrow linewidth) through the etalon with exactly the same beam path. The measured finesse is about 70, corresponding to spectral resolution of 28 MHz.

Figure 6 (dotted line) shows the measured time-averaged spectral profile of the second harmonic output of the laser, operating nominally with 14-ns duration pulses. Also shown is the convolution between the instrumental function of the etalon and the Fourier transform of a real 14-ns FWHM pulse. It is clear that the spectral profile is approximately the Fourier transform limit of the laser pulse. The Fourier transform of the pulse burst with 30 pulses would be modulated by a high-frequency comb function, but because of the finesse of the etalon, this high frequency cannot be detected.

V. Attenuation of Transmission Through Molecular Iodine Vapor Cell

FRS[8] has the abilities of extracting a weak signal by suppressing background scattering, as well as obtaining quantitative measurements of velocity, temperature, and density of flow simultaneously. The key component of FRS is an optically thick, well-characterized molecular iodine vapor filter that has a very sharp absorption line. The iodine filter, which has been described in detail previously,[9] is 9.98 cm long with cell temperature of 80°C and side-arm temperature at 40°C. The side-arm temperature is maintained to within ±0.1 K with a circulating hot-water bath. In the Rayleigh-scattering experiment, if the frequency of laser source is tuned to the center of the absorption line, the background scattering will be absorbed by the iodine cell while the flowfield signal will pass through the cell because of the Doppler frequency shift. If we tune the laser frequency through the absorption line when measuring the scattered intensity through iodine cell, we can get the spectral shift and the spectral profile of the scattered flow signal and obtain the velocity and temperature of the flow.[8]

Before doing a FRS experiment, it is important to characterize the attenuation of transmission through the iodine cell and the laser spectral purity by scanning the frequency of the laser source through the absorption band. The actual experimental apparatus is similar to Fig. 5, except the Fabry–Perot etalon is replaced by an iodine cell. The second harmonic (0.532-μm) output of the pulse-burst laser hit an aluminum post, and scattered light was collected and passed through the iodine cell. The signal was observed by a photodetector and transferred to the boxcar integrator, as described earlier. At the same time the frequency of the laser was tuned through the absorption lines of iodine. A reference detector was used to monitor the laser output intensity fluctuations as the frequency was tuned. A series of calibrated neutral density filters was used to attenuate the beam prior to tuning into the resonance feature of the iodine

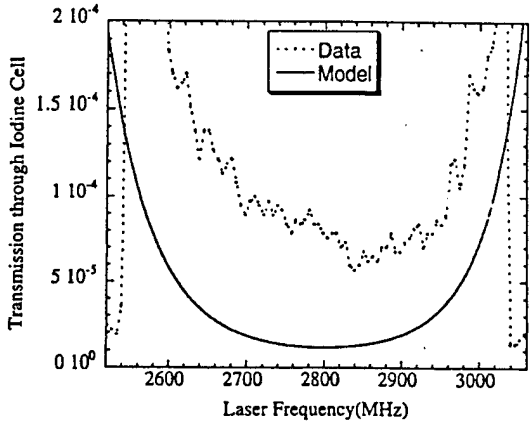

Fig. 8 Blowup of central portion of Fig. 7, illustrating absolute transmission near center iodine absorption line.

vapor. As the laser was tuned into the absorption band, the filters were sequentially removed, boosting the light level reaching the detector. Thus the dynamic range of the attenuation measurement was increased beyond the limitations imposed by the linear operating range of the photodiode.

The dotted line in Fig. 7 shows the experimental result as the frequency was slowly tuned across the absorption line A (around frequency 18788.5 cm^{-1})[9] of the iodine cell. The detected signal has been normalized in such a way as to set the apparent transmission equal to approximately 1 at the endpoints of the scan. When the laser scan passed approximately the 2200-MHz point, a 200-times neutral density filter (Schott Glass Technology, Inc., NG10) was removed from the beam path, resulting in a large increase in signal reaching the detector. Then a second 20-times neutral density filter (Schott NG9) was removed. The neutral density filters were put back as the laser frequency was tuned out of the resonance of iodine. The solid line in Fig. 7 is the convolution between the pulse-burst laser linewidth and the theoretically predicted transmission across the absorption line A. Figure 8 is a blowup of the central 500 MHz of the experimental data (dotted line) and the theoretically predicted transmission (solid line). In this case the experimental data have been converted to absolute transmission by accounting for the attenuation of the neutral density filters. The experimental line center transmission is 5×10^{-5}, as compared to the modeled value of approximately 1.5×10^{-5}. The experimental curve fits well to the theoretical model with a correction for residual transmission. This residual transmission is presumed to arise from the nonideal wings of the laser spectrum and residual ASE. The experiment results not only mean that the pulse-burst laser has very good attenuation when passing through the resonance of the iodine, but the spectral profile of the laser is very good. The laser clearly operates with single mode. These results should be compared to a commercial injection seeded Nd:YAG laser

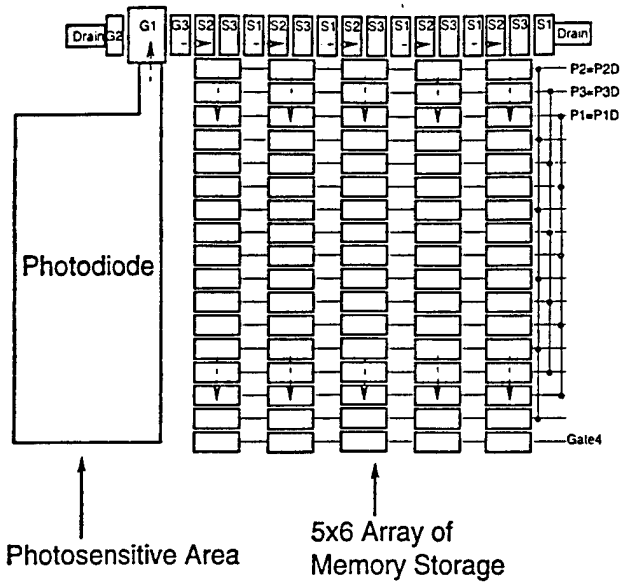

Fig. 9 Architecture of one pixel of megahertz-rate CCD camera. The CCD chip is developed by John Lowrance from Princeton Scientific Instruments, Inc., and Walter Kosonochy from the New Jersey Institute of Technology.

for which the attenuation through iodine resonance only reaches a factor of the order of 300 (Ref. 12), and locking is intermittent.

VI. Fast-Framing Megahertz CCD Camera

A new fast-framing CCD camera[13] developed by Princeton Scientific Instruments, Inc., is used to collect images formed by the pulse-burst laser. The CCD camera chip (U.S. Patent 5355165) has a 30-image storage buffer built into each pixel of the image sensor chip itself and can frame at a rate up to 1 MHz. The pixel format is 360 × 360, divided into four quadrants of 180 × 180 each. A simplified diagram of the architecture of 1 pixel is shown in Fig. 9. Each pixel consists of a photoactive region and a 5 × 6 array of memory elements. The charge is sequentially shifted across the top row of five storage elements at an interval as fast as 1 μs. Subsequently, the charge in each row of memory elements is shifted down in parallel. Upon receipt of a master trigger, the camera operates continuously until a stop trigger is issued. At this point the last 30 images are read out to a standard PC computer.

By coupling the megahertz CCD camera with the pulse-burst laser, a megahertz high-speed flow diagnostic system has been built. This system can capture up to 30 sequential images of rapidly fluctuating phenomena. In the case of high-speed flow, 30 images are usually sufficient to follow the evolution of a structure all the way through the field of view.

VII. Visualization of Shock-Wave/Boundary-Layer Interaction in Mach 2.5 Wind Tunnel

To capture the dynamics of shock-wave/boundary-layer interaction, the pulse-burst laser system has been used to get 0.5-MHz repetition-rate sequential planar images of a turbulent Mach 2.5 boundary flow over a 14-deg wedge.

Figure 10 illustrates the experimental setup to obtain the streamwise view of the dynamics of the turbulent boundary-layer flow. The Mach 2.5 wind tunnel has a cross section of 1 × 0.5 in. The observation region is 16 in. downstream of the throat so that the boundary layer grows to a thickness of about 2 mm. The direction of the flow in the figure is from right to left. To get the streamwise view, a 0.8-mm-wide slit was cut in the centerline of the wedge to let the laser sheet pass through. The size of the slit is small enough to have almost no influence on the overall dynamic process. The second harmonic output of the pulse-burst laser was formed into an approximately 1.5 cm high × 100 μm thick sheet and directed into the flow at an angle of 45 deg with respect to the freestream motion. The angle of 45 deg was chosen to generate enough of a Doppler frequency shift for FRS background suppression. The camera had

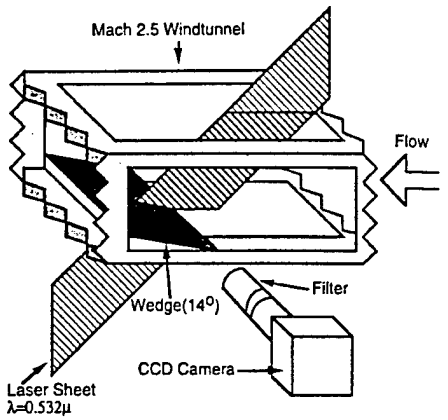

Fig. 10 Experimental setup of side-view visualization of shock-wave/boundary-layer interaction by shooting Mach 2.5 turbulent flow over a 14-deg wedge.

its optical axis perpendicular to the plane of the laser sheet. The flow was run with a stagnation pressure of 120 psig and a stagnation temperature of 258 K. As the Mach 2.5 flow passes by the wedge, an oblique shock forms.

To enhance the scattering signal, gaseous CO_2 was seeded into the flow at a level less than 1% (wt). After the nozzle, because of the temperature decrease of the flow, CO_2 condensed into a finely dispersed fog. We have measured the scattered signal while changing the polarization of incoming laser light. We found the scattering is in the Rayleigh-scattering region so that the condensed CO_2 cluster size is much smaller than the laser wavelength (532 nm). The CO_2 was seeded far upstream in the plenum and was chosen for its ease of handling and because it mixed homogeneously with the air. CO_2 causes less disturbance to the flow than using water vapor as seeder.[14] In the warmer thermal boundary layer the CO_2 is in vapor form, resulting in very high image contrast. The boundary layer is visualized owing to the combined effects of density changes within the boundary layer and CO_2 cluster evaporation. These two effects are related because both result from temperature recovery within the boundary layer. Smith and Smits[15] found the condensed cluster scattering intensity profile in the outer part of a supersonic boundary layer showed good agreement with those obtained using a probe survey.

Figure 11 shows a typical sequence of 25 streamwise view images with an image size of 0.5 × 0.5 in. The time interval between images is 2 μs. The bright straight line at the left bottom corner is the wedge. In particular, comparing images 9 to 15, we can see the curvature of the shock wave has been changed. The unsteady shock-wave motion is coupled with the incoming boundary-layer structure shown in the upstream of shock wave in image 9. The images are conveniently formed into a loop movie to give a dynamic view of the interaction.[§]

The shock-wave/boundary-layer interaction is usually three-dimensional, and so the experiment was also set up to obtain planform view images of the shock-wave/boundary-layer interaction. The layout was similar to that illustrated in Fig. 10 except the laser sheet was parallel to the wall of wind tunnel and grazed the surface of wedge. Figure 12 shows six sequential planform view images each separated by 2 μs. The shock wave now turns into a wavy line, and the boundary-layer structure is seen as the dark region in the flow. From these images it is particularly apparent how the shape of the shock wave changes as the boundary-layer structure passes. A discontinuity in the boundary layer can also be seen as it crosses the shock because the oblique shock changes the direction of the flow, forcing it out toward laser sheet plane.

As the flow crosses the shock, its speed decreases, and the scattered light has a smaller Doppler frequency shift. To highlight the different parts of the flow, we put the molecular iodine vapor cell in front of the camera and tuned the frequency of the laser. With the laser frequency tuned near the center of the iodine absorption, scattering from lower-speed flow and nonmoving elements such as

[§]This movie can be seen on the Web at http://www.princeton.edu/~milesgrp/Movie/PBL1.html.

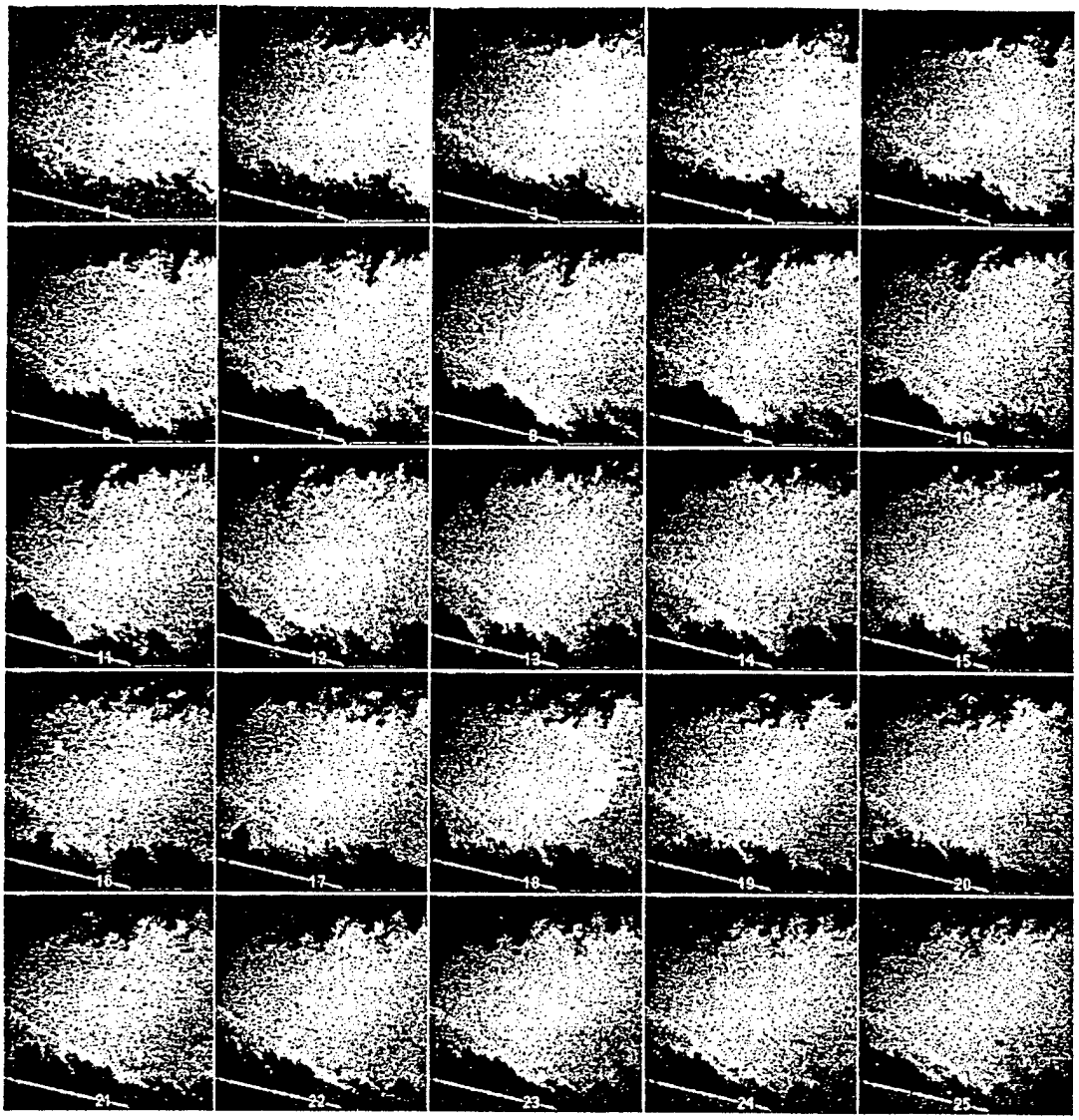

Fig. 11 Sequence of 25 streamwise view images of Mach 2.5 flow over 14-deg wedge. Flow is from right to left with 2 μs between images.

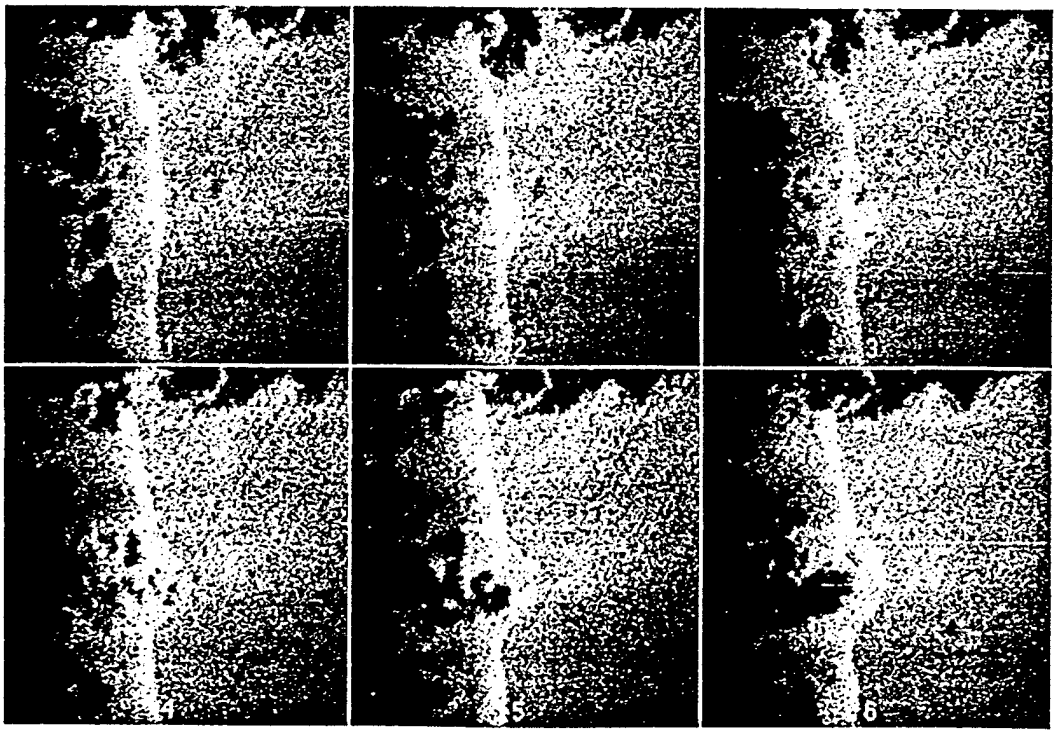

Fig. 12 Sequence of six planform view images of Mach 2.5 flow over 14-deg wedge. Flow is from right to left with 2 μs between images.

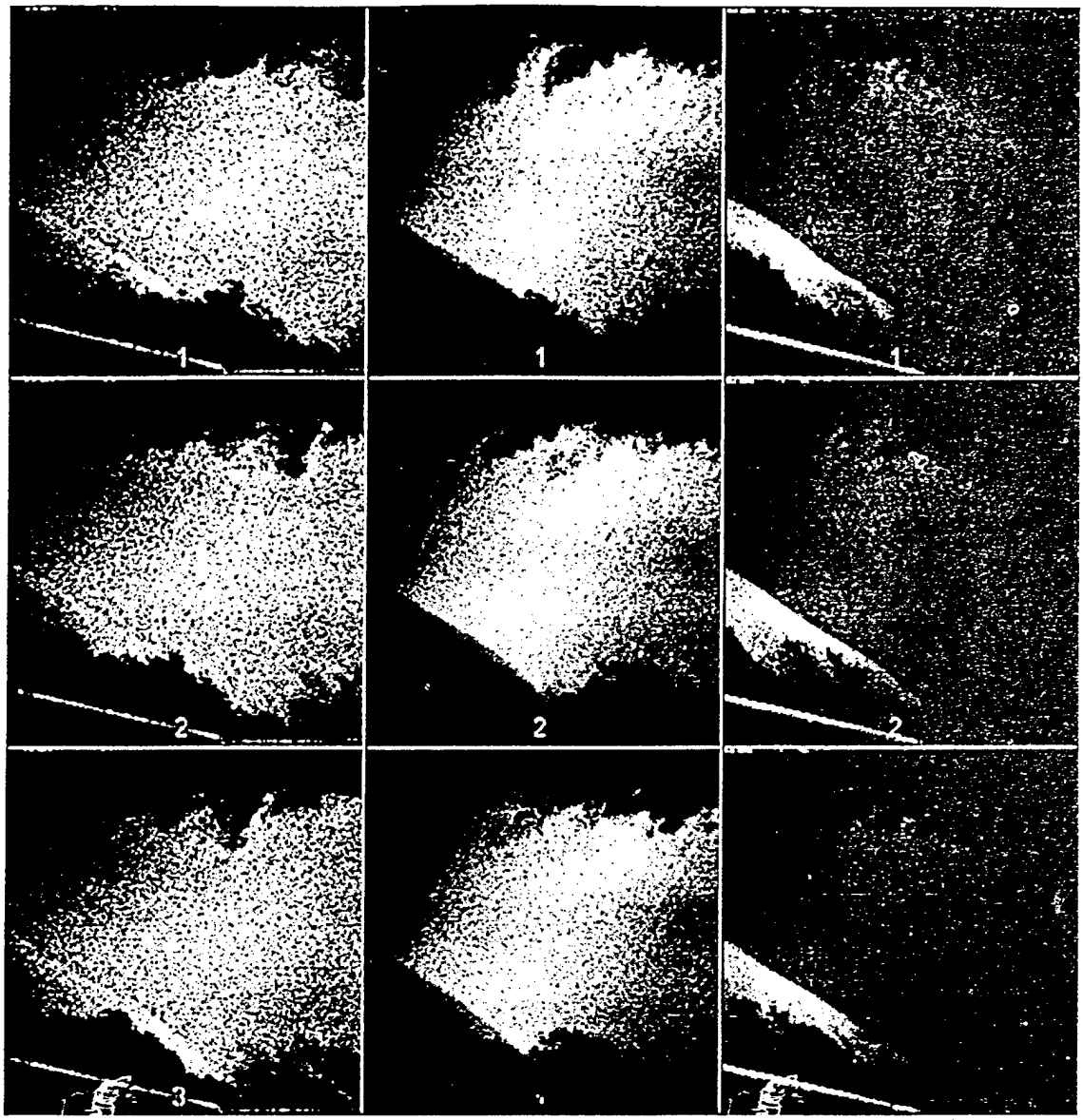

Fig. 13 Comparison of filtered and unfiltered side-view images. Flow from right to left with 4-μs time interval between images: left column, unfiltered images; middle column, filtered to highlight high-speed flow; and right column, filtered to highlight low-speed flow.

the surface of the wedge is selectively attenuated, as illustrated in the middle column of Fig. 13. Alternatively, as shown in right column of Fig. 13, the scattering from the high-speed flow can also be suppressed by tuning the laser so that the Doppler-shifted-scattering coincides with the absorption line of iodine. The sequence of images in the right column also shows another weak oblique shock at the upper right corner. Without the filter the signal from the mean stream flow is so strong that it completely masks that shock-wave structure.

VIII. Conclusion and Future Work

A megahertz pulse-burst laser system has been developed and has been used for the visualization of shock-wave/boundary-layer interactions in a Mach 2.5 wind tunnel at a 0.5-MHz repetition rate.

The pulse-burst laser is capable of producing a programmable burst of from 1 to 99 pulses, with individual pulse duration from 10 to 100 ns and interpulse separation from 1 to 10 μs. A fundamental output energy (at 1.06 μm) of approximately 10 mJ has been achieved in each of 30 individual, 20-ns duration pulses. The second harmonic output was about 400 μJ per individual pulse.

Experimental results have shown that the laser has a narrow linewidth. The range of frequency tunability is about 1 cm^{-1} at 1.06 μm. The transmission through a 9.98-cm-long molecular iodine vapor filter (40°C side band, 80°C cell temperature) was measured to be 5×10^{-5}, which conforms well with model prediction. Consequently, the system can be used for FRS and other frequency or long coherence-length-related laser diagnostics, such as holography.

As an application of the megahertz pulse-burst laser system, the visualization of a Mach 2.5 flow over a 14-deg wedge shows the unsteadiness of a shock wave and its coupling to the structure of the incoming boundary layer.

We are now building a second-generation high-power pulse-burst laser system. Average single-pulse fundamental and second harmonic energy on the order of 100 and 25 mJ have been achieved, respectively. The new pulse-burst imaging system will be used for imaging in the plasma propulsion facility in the Electric Propulsion and Plasma Diagnostics Laboratory.

Acknowledgments

The authors wish to acknowledge Jay H. Grinstead and Philip Howard for their assistance in the Mach 2.5 imaging measurement. We would also like to thank A. J. Smits for the helpful discussion in the shock-wave/boundary-layer interaction and Princeton Scientific Instruments, Inc., for providing the megahertz-framing-rate CCD camera. The pulse-burst laser system has been developed with support from two grants from the U.S. Air Force Office of Scientific Research, Julian Tishkoff (University Research Initiative)

and Leonidas Sakell (External Aerodynamics), Technical Monitors. Money was also provided by NASA Phase I Project Grant NASA-97090 and the state-sponsored New Jersey Center for Opto-Electronics. The second-generation pulse-burst laser is supported by the Air Force Office of Scientific Research (Grant F49620-97-1-0373) as part of a joint Department of Defense University Research Initiative Program with the Princeton Electric Propulsion group. The CCD framing camera has been developed by Princeton Scientific Instruments, Inc., under Small Business Innovative Research grants from U.S. Office of Naval Research with Edwin Rood as Technical Monitor and the U.S. Air Force, Wright Laboratories, with Charles Tyler as Technical Monitor.

References

[1]Kyachoff, G., Seitzman, J., and Hanson, R. K., "Instantaneous Temperature Field Measurements Using Planar Laser-Induced Fluorescence," *Optics Letters*, Vol. 10, No. 9, 1985, pp. 439–441.

[2]Miles, R. B., and Lempert, W. R., "Two-Dimensional Measurement of Density, Velocity, and Temperature in Turbulent High-Speed Air Flows by UV Rayleigh Scattering," *Applied Physics*, Vol. B51, No. 1, 1990, pp. 1–7.

[3]Cheng, T. S., Wehrmeyer, J. A., and Pitz, R. W., "Simultaneous Temperature and Multispecies Measurement in a Lifted Hydrogen Diffusion Flame," *Combustion and Flame*, Vol. 91, No. 3/4, 1992, pp. 323–345.

[4]Wagner, J. W., Deaton, J. B., and Spicer, J. B., "Generation of Ultrasound by Repetitively Q-Switching a Pulsed Nd:YAG Laser," *Applied Optics*, Vol. 27, No. 22, 1988, pp. 4696–4700.

[5]Ruff, G. A., Bernal, L. P., and Faeth, G. M., "High Speed In-Line Holocinematography for Dispersed-Phase Dynamics," *Applied Optics*, Vol. 29, No. 31, 1990, pp. 4544–4546.

[6]Huntley, J. M., "High-Speed Laser Speckle Photography. Part 1: Repetitively Q-Switched Ruby Laser Light Source," *Optical Engineering*, Vol. 33, No. 5, 1994, pp. 1692–1699.

[7]Grace, J. M., Nebolsine, P. E., and Goldey, C. L., "Repetitively Pulsed Ruby Lasers as Light Sources for High-Speed Photography," *Optical Engineering*, Vol. 37, No. 8, 1998, pp. 2205–2212.

[8]Forkey, J. N., Finkelstein, N. D., Lempert, W. R., and Miles, R. B., "Demonstration and Characterization of Filtered Rayleigh Scattering for Planar Velocity Measurements," *AIAA Journal*, Vol. 34, No. 3, 1996, pp. 442–448.

[9]Forkey, J. N., Lempert, W. R., and Miles, R. B., "Corrected and Calibrated I_2 Absorption Model at Frequency Doubled Nd:YAG Laser Wavelengths," *Applied Optics*, Vol. 36, No. 27, 1997, pp. 6729–6738.

[10]Frantz, L. M., and Nodvik, J. S., "Theory of Pulse Propagation in a Laser Amplifier," *Journal of Applied Physics*, Vol. 34, No. 8, 1963, pp. 2346–2349.

[11]Lowdermilk, W. H., and Murry, J. E., "The Multipass Amplifier: Theory and Numerical Analysis," *Journal of Applied Physics*, Vol. 51, No. 5, 1980, pp. 2436–2444.

[12]Forkey, J. N., Lempert, W. R., and Miles, R. B., "Observation of a 100-MHz Frequency Variation Across the Output of a Frequency-Doubled Injection-Seeded Unstable-Resonator Q-Switched Nd:YAG Lasers," *Optics Letters*, Vol. 22, No. 4, 1997, pp. 230–232.

[13]Kosonocky, W. F., Yang, G., Ye, C., Kabra, R. K., Lowrance, J. L., Mastrocola, V., Shallcross, F. V., and Patel, V., "360*360 Element, Very High Framing Rate, Burst Image Sensor," 1996 IEEE International Solid-State Circuits Conf., San Francisco, Feb. 1996.

[14]Erbland, P. J., Baumgartner, M. L., Etz, M. R., Yalin, A., and Miles, R. B., "Development of Planar Diagnostics for Imaging Mach 8 Flowfields Using Carbon Dioxide and Sodium Seeding," AIAA Paper 97-0154, 1997.

[15]Smith, M. W., and Smits, A. J., "Visualization of the Structure of Supersonic Turbulent Boundary Layers," *Experiments in Fluids*, Vol. 18, No. 4, 1995, pp. 288–302.

R. P. Lucht
Associate Editor

Eur. J. Mech. B - Fluids 19 (2000) 695–706

S0997-7546(00)00130-8/FLA

Transition studies on an elliptic cone in Mach 8 flow using Filtered Rayleigh Scattering

Mark Huntley *, Alexander Smits

Gas Dynamics Laboratory, Princeton University, Princeton, NJ 08544, USA

(Received 7 April 1999; revised 3 April 2000; accepted 4 April 2000)

Abstract – Boundary layer transition on a sharp-nosed elliptic cone in a Mach 8 flow was experimentally investigated using CO_2-enhanced Filtered Rayleigh Scattering. The 4:1 elliptic cone was tested at Reynolds numbers ranging from 0.44×10^6 to 3.5×10^6, based on free stream conditions and streamwise distance measured from the cone tip. Boundary layers ranging from fully laminar to late-transitional in character were imaged using single-shot streamwise, spanwise and planform laser orientations. Images taken of the early stages of transition reveal for the first time that transition begins with the emergence of small-scale structures near the centerline axis of the cone (minor axis), rather than in the outboard cross-flow region. The three-dimensional character of these structures is further explored by simultaneously imaging the planform and spanwise planes. © 2000 Éditions scientifiques et médicales Elsevier SAS

experimental / hypersonic / transition / cone / Rayleigh scattering

1. Introduction

Many aspects of the transition process from laminar to turbulent flow are poorly understood. This is especially true in the hypersonic regime where the experimental database is very small and restricted almost entirely to two-dimensional and axisymmetric flow fields. For these flows computational [1] and experimental [2] results have shown that two-dimensional Mack modes dominate the transition process above Mach 4. Realistic hypersonic lifting bodies, however, possess regions of three-dimensional flow which can drastically alter the transition behavior of the boundary layer. Any three-dimensionality inevitably produces spanwise pressure gradients. These gradients induce crossflow, where the flow direction of the interior of the boundary layer is no longer co-planar with the edge velocity vector. The low-momentum boundary layer fluid near the surface is deflected more than the fluid near the edge of the boundary layer. Crossflow vortices may be established which under some circumstances may dominate the transition process. PSE stability analysis on a 4:1 elliptic cone by Huang et al. [3] predicted that transition would occur due to an unstable stationary crossflow vortex at Re_x values as low as 1.3×10^5. Stetson et al. [4] used hot-wire probes to show that crossflow on axisymmetric cones at angle of attack significantly affected transition, but only investigated the leeward and windward rays where the spanwise pressure gradients and associated crossflow were zero. More recent experiments by Poggie and Kimmel [5], also using hot-wires, examined the stability characteristics on a 2:1 elliptic cone, but could not conclusively determine the existence of crossflow vortices.

The hot-wire studies provide very limited information on the spatial character of the transition process. Flow visualization can add a great deal of insight into these complex geometries, but for flows above Mach 3, techniques have been restricted primarily to schlieren, shadowgraph and oil flow. The recent efforts of the Gas Dynamics Lab and the Applied Physics Group at Princeton University have led to the application of new laser

* Correspondence and reprints; e-mail: huntley@princeton.edu

diagnostics to hypersonic flow, and the visualization results have provided new insights into the behavior of high-speed flows, as reported here.

2. Experiment

Tests were carried out in the Princeton Mach 8 Facility which is a blowdown tunnel with 0.23 meter axisymmetric test section. The Mach number is 8.0 ± 0.15 over a range of freestream unit Reynolds numbers from 2.0×10^6 to 21×10^6. Stagnation pressure can be varied from 1.0 to 10.3 MPa with stagnation temperatures up to 870 K. The test section has rectangular offset window cavities giving optical access from four sides. Models are mounted rigidly to the tunnel wall through the window cavities which requires the tunnel to be started with the model in place. A detailed description of this facility was given by Baumgartner [6].

In order to extend the experimental data base to three-dimensional configurations, an elliptic cone with 4 : 1 cross section is studied. The model measures 0.242 m with 17.5 degree half-angle on the major axis and was manufactured to match the computations of Huang et al. [3].

Experiments were conducted at a Mach number of 8.0 ± 0.15 with average stagnation temperatures of 783 ± 25 K. Run times were typically about two minutes. The heat energy was stored in 85 m of stainless steel piping which is coiled into 19 turns. The coil was electrically heated to the desired stagnation temperature before the run. For these experiments, the tunnel and model were started moderately cold (~400 K surface temperature) which resulted in roughly a ± 25 K deviation in stagnation temperature during the run and less than 30 K increase in the surface temperature of the model. Therefore, the cold wall condition produced ratios of T_w/T_0 ranging from 0.50 to 0.56 throughout the course of a typical two-minute run. For these experiments, the freestream unit Reynolds number ranged from 2.0×10^6 to 15.9×10^6 by varying stagnation pressures from 0.93 ± 0.02 to 8.17 ± 0.07 MPa.

The experiment used carbon dioxide enhanced Filtered Rayleigh Scattering (FRS) for imaging the freestream flow and the boundary layer [7]. Carbon dioxide is injected upstream of the heater coil assembly in quantities ranging from 1–4% of the total tunnel mass flux. According to our current understanding of the technique, the structure of the boundary layer is imaged by the interface between the cold freestream and the hot boundary layer fluid. As the fluid containing condensed CO_2 becomes turbulent by entrainment into the boundary layer, the temperature rises above the sublimation value and the condensate disappears. The boundary layer is therefore imaged as a region of low intensity Rayleigh signal, bounded by bright freestream regions [7]. Comparisons have been made between the imaged interface and pitot surveys of the laminar centerline boundary layer on the cone. The results show that the height of the interface is within 10% of the measured boundary layer thickness. For supersonic turbulent boundary layers, it has been shown that the technique accurately represents the instantaneous large-scale motions in the middle and outer regions of the boundary layer [8].

A narrow linewidth, injection locked, frequency-doubled Nd:YAG laser is used as the scattering source for the Rayleigh imaging. The laser has a 10 Hz repetition rate with a pulse width of 10 ns. Energy output to the test section was ~35 mJ per pulse at 532 nm. The beam was shaped using a positive and negative cylindrical lens pair which produced a uniform focused sheet approximately 50 mm × 100 μm. The laser output was tuned to overlap a strong spectral absorption line in iodine vapor. A molecular iodine filter was placed in front of the camera so that stray scattering from the model surface was absorbed. The Rayleigh scattering signal from the moving flow was then Doppler shifted outside the absorption band of the filter so that it could be observed by the camera.

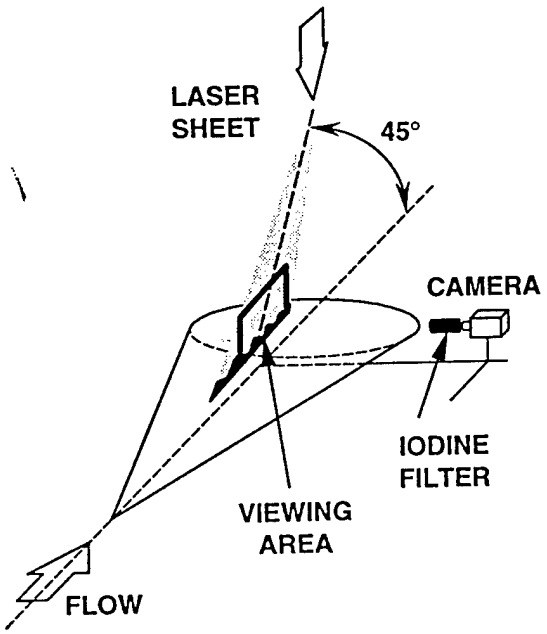

Figure 1. Sheet orientation for streamwise imaging along 4 : 1 model. Laser sheet aligned with centerline of the cone. Field of view was 7 cm in length, centered about the position 20 cm from the nose.

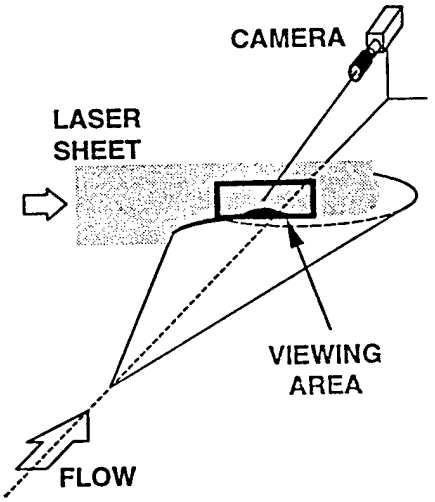

Figure 2. Sheet orientation for spanwise imaging along 4 : 1 model. Laser sheet aligned perpendicular to the flow axis, 21 cm from the nose of the model.

Images of the boundary layer along the model were obtained with streamwise (*figure 1*) and spanwise (*figure 2*) laser sheet orientations. Imaging was accomplished using a double-intensified CID camera with a 100 mm long and 50 mm diameter iodine vapor cell placed in front of the camera lens. For the streamwise view, the camera/filter system was placed orthogonal to the laser sheet with field of view of ~50 mm along the centerline of the cone. For the spanwise field of view, the camera line of sight was placed at approximately a 30 degree angle with respect to the axis of the tunnel. The camera itself was about 0.75 m downstream of the model looking forward in order to image the plane perpendicular to the flow axis.

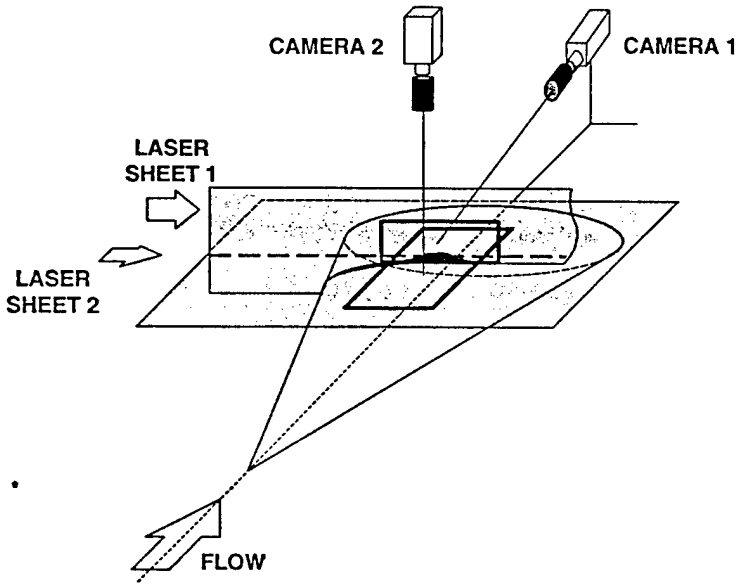

Figure 3. Sheet orientation for simultaneous imaging of spanwise and planform planes. Dashed line represents the intersection of the two image planes.

By splitting a high energy (~80 mJ) laser pulse into two sheets, simultaneous imaging of the spanwise and planform planes was possible (*figure 3*). The planform plane is defined as the slice across the top centerline (minor axis) of the cone. The laser sheet was expanded in a plane parallel to the centerline ray of the model so that the distance from the sheet to the model surface along the centerline was constant.

The two laser sheets were positioned to overlap at a line approximately 21 cm from the nose of the model. The height of the planform sheet above the model centerline could be adjusted from zero to 6 mm above the surface. Since the imaging planes were nearly perpendicular and Rayleigh scattering is an elastic collision process, the light polarization was rotated to minimize the unwanted signal from the secondary plane, while maximizing the scattering signal to illuminate the desired cross-section of the boundary layer. In this way, the scatter from the planform sheet in the spanwise images is nearly eliminated and vice versa. For the simultaneous image pairs which follow, a white dashed line is used to show the intersection of the two sheets.

Efforts at simultaneously imaging the streamwise and spanwise image planes were much less successful. Since the streamwise sheet must contact the model, simply rotating the polarization of the incoming laser light is no longer effective. The efficiency of the iodine filter was not high enough to absorb all of the stray scatter from the model, and therefore signal to noise ratios remained too low to produce useful image data.

3. Results

Single-shot FRS images of the centerline boundary layer taken with both streamwise and spanwise laser sheet orientations are presented. The individual frames illustrate the structures present as the boundary layer undergoes transition. Stability analysis [3] has predicted that transition would occur in the regions off-axis where the crossflow velocities are highest. Instead, recent experiments [5] have found that the first evidence of transition occurs in the centerline region, where the symmetry requires that the crossflow velocity is zero. The spanwise images reveal the mechanism by which the centerline boundary layer breaks down. This process is shown here for the first time.

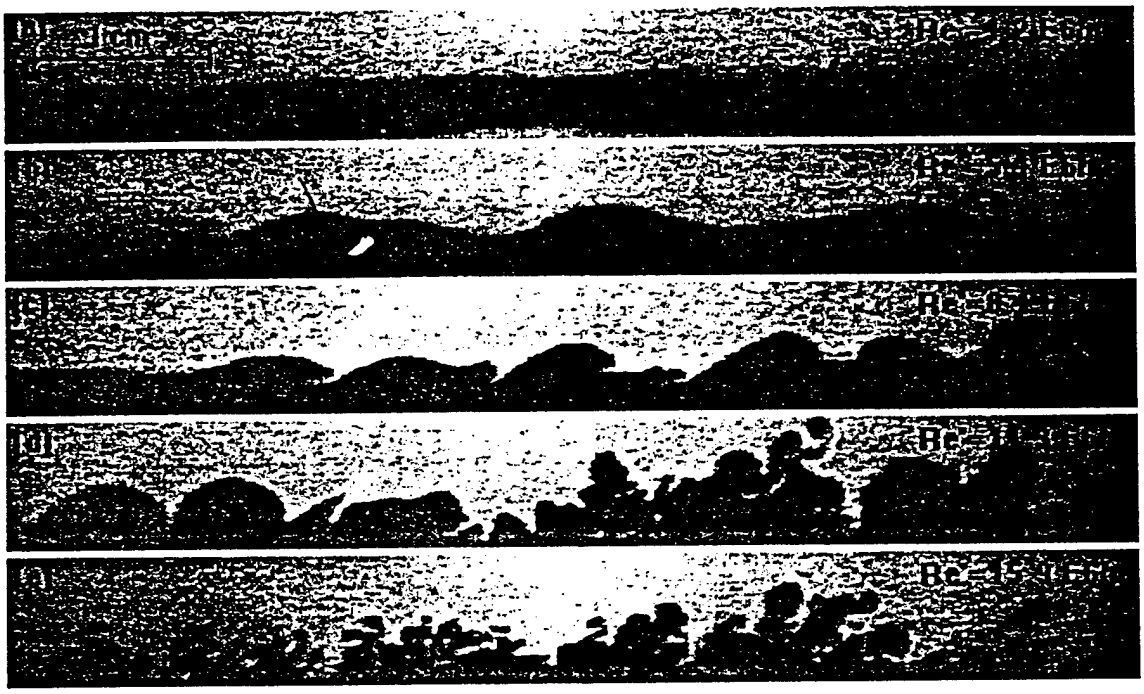

Figure 4. Streamwise Filtered Rayleigh Scattering on 4 : 1 Elliptic Cone. Flow is left to right. The center of each frame is approximately 21 cm from the nose of the model. The model surface coincides with the bottom line of each frame.

Simultaneous images of planform and spanwise slices through the boundary layer are also presented. Images taken at various heights throughout the boundary layer show the spanwise extent and shape of the structures which appear in the early stages of transition.

3.1. Streamwise images

Figure 4 is a montage of images taken at the same streamwise position along the 4 : 1 cone for five different unit Reynolds numbers. Each image is meant to be a representative sample of the boundary layer behavior at that particular value of Re_x. The character ranges from what appears to be fully laminar in frame *4(a)* to late-transitional in frames *4(d)* and *4(e)*. All of the images were taken with a moderate cold wall condition ($Tw/To = 0.53 \pm 0.03$) with a streamwise field of view ranging from 19 to 25 cm from the nose of the model. Pitot surveys of the centerline boundary layer have shown that the visualized interface between condensed (light) and sublimated (dark) CO_2 occurs at approximately 0.9δ. Frame *4(b)*, taken at $Re' = 5.4 \times 10^6/m$, contains a traveling wave with a wavelength between four and five times the boundary layer thickness. Higher frequency traveling waves appear in frame *4(c)*. At this higher Reynolds number, the wavelength decreases to delta approximately twice the boundary layer thickness. Since the visualization technique is sensitive to temperature, the observed waves represents density fluctuations. Using hot-wire anemometry on a 7 degree axisymmetric cone at Mach 8, Stetson et al. [9] determined that high Mach number instabilities produce large density fluctuations and relatively small fluctuations in velocity. The second mode instabilites were highly 'tuned' to the boundary layer thickness, and possessed a wavelength of two times the boundary layer thickness. It was also estimated that another peak frequency (believed to be the first harmonic of the second mode) would correspond to a wavelength approximately equal to the boundary layer thickness.

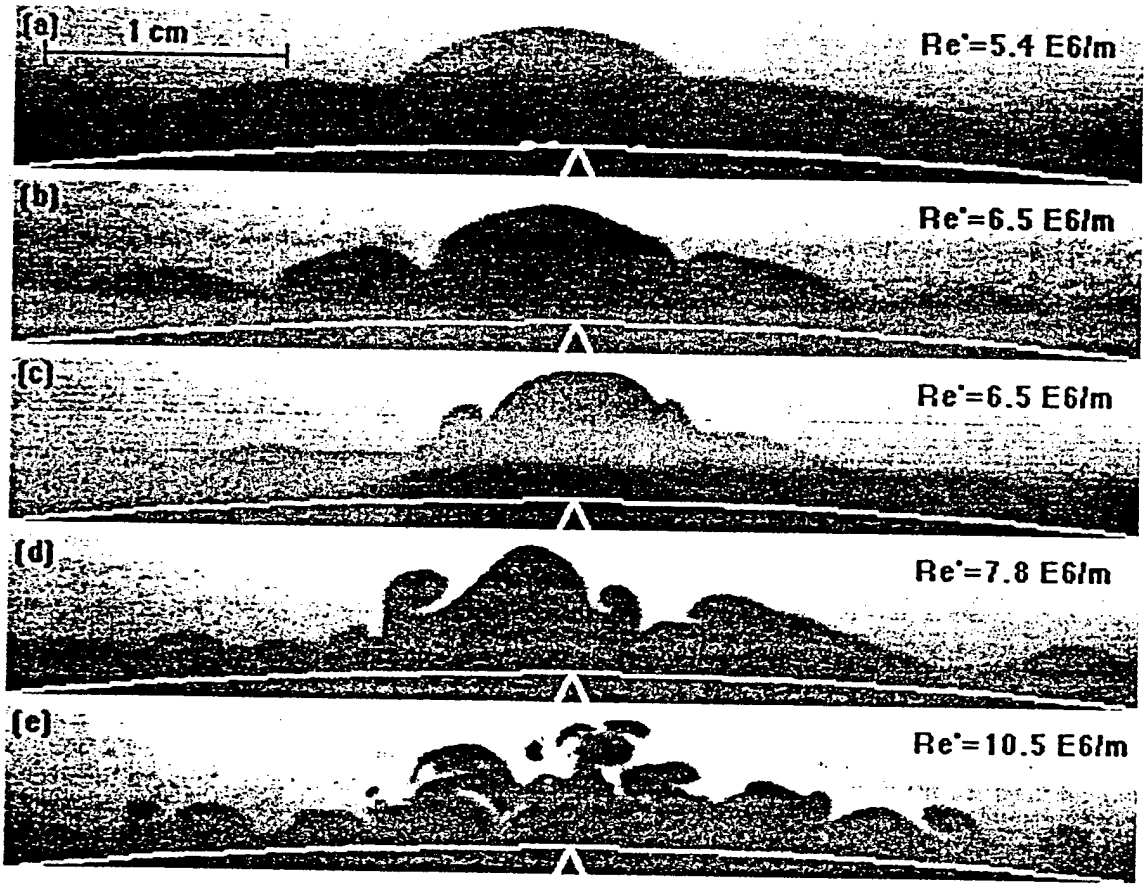

Figure 5. Spanwise Filtered Rayleigh Scattering on 4 : 1 Elliptic Cone. Flow is out of the plane of the paper. Laser sheet is positioned 21 cm from the nose of model. The cone centerline is marked by the arrow in the bottom of the image.

Frame *4(c)* still possesses some traveling wave character, but the interface is becoming highly distorted. As the unit Reynolds number is increased further, frame *4(d)* shows the emergence of small-scale bulges forming on the edges of the larger scales. The final frame, taken at $Re' = 15.9 \times 10^6$, shows almost no evidence of the previous traveling wave structures, and clearly exhibits the small scale characteristic of a turbulent boundary layer.

Overall, from streamwise images taken on centerline, the 4 : 1 model appears to exhibit transition behavior which is characteristic of two-dimensional or axisymmetric configurations.

3.2. *Spanwise images*

Figure 5 is a montage of single-shot FRS images which were all taken at the same position (21.0 cm from the nose) along the cone while varying the unit Reynolds number. Each frame is meant to show representative behavior of the boundary layer at that particular Reynolds number. In these images the flow is moving out of the page, and the white arrow at the bottom of each image represents the position of the centerline (minor axis) of the cone. Over the range of Re_x from 1.1×10^6 to 2.2×10^6, these images present a much more complex picture of the dynamics of boundary layer transition than that which was observed in the streamwise images.

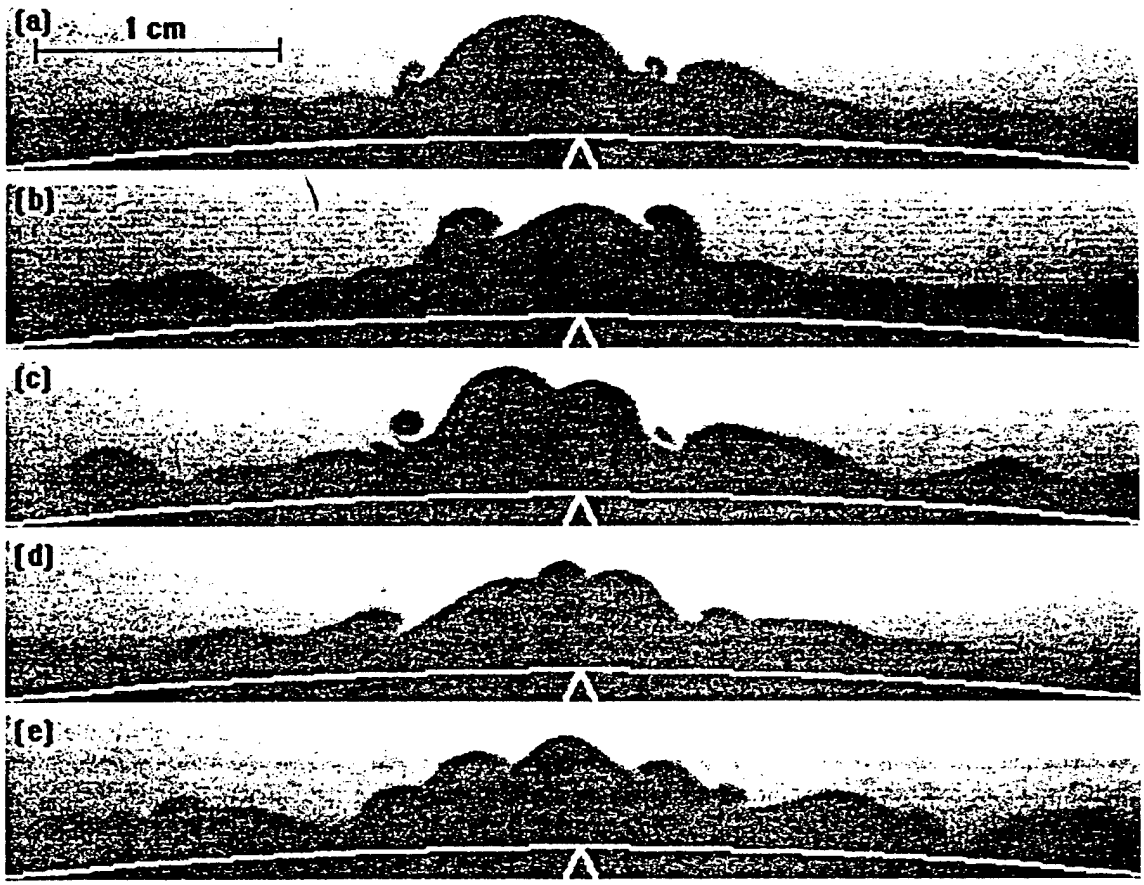

Figure 6. Single-shot spanwise images on 4:1 cone showing the emergence of small-scale vortices. Laser sheet is positioned 21 cm from nose. All images are taken at $Re' = 7.8 \times 10^6$.

The bulge in the boundary layer near the centerline in *figure 5(a)* is a result of the influx of low-momentum fluid from the high-pressure leading edge to the low-pressure centerline of the model. Computations of the laminar flowfield on elliptic cones have also shown the existence of this centerline bulge [3,10,11].

Frames *5(b)* and *5(c)* were taken at $Re_x = 1.4 \times 10^6$. The equivalent streamwise images (frame *4(b)*) show the beginnings of large traveling waves aligned with the flow. *Figure 5(b)* shows wave-like structures which have developed on either side of centerline in the spanwise plane perpendicular to the flow. In spanwise images *5(c)* and *5(d)* there is also evidence of much smaller scale structures which develop in the regions slightly off the cone centerline. At higher Reynolds numbers, the off-centerline structures can become larger, seemingly wrapping up and growing at the expense of the low-momentum fluid which makes up the centerline bulge.

From these single-shot images, it is clear that the observed small-scale structures possess a vortical character. From the entrainment of condensed CO_2 from the freestream in *figure 5(d)*, it is possible to conclude that the direction of rotation of these spanwise vortices. With the flow direction out of the page, the small-scale vortical structure to the right of centerline is 'rolling up' with streamwise vorticity oriented downstream. Conversely, the structures to the left of centerline possess vorticity oriented upstream.

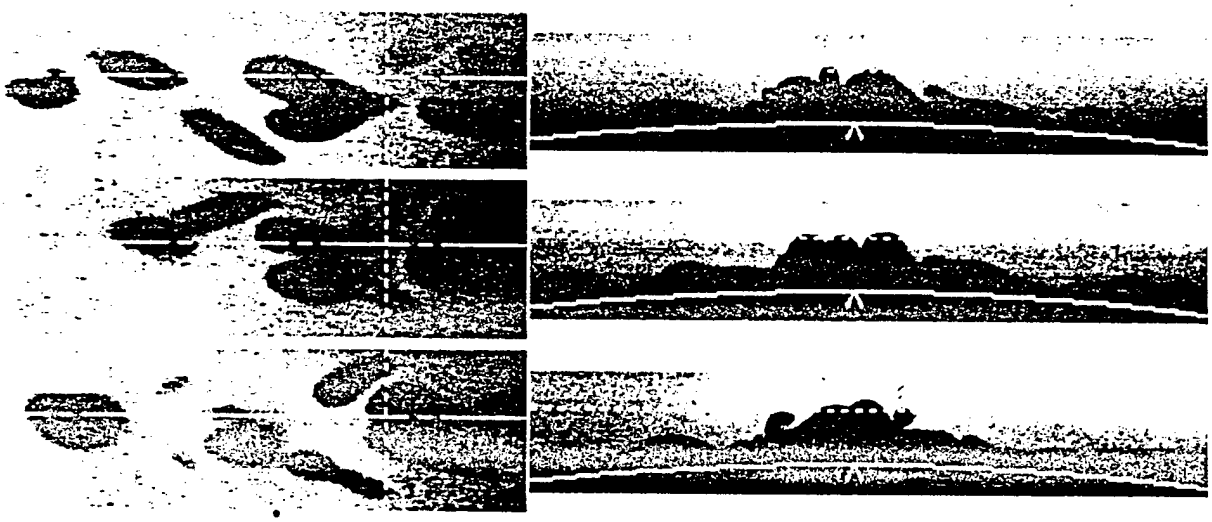

Figure 7. Simultaneous images of planform (left) and spanwise (right) planes. Dashed line represents the intersection of the two planes. Flow is from left to right in planform image and out of the paper plane for the spanwise image. Planform sheet is positioned 4.0 mm from the model surface.

Figure 6 is a montage of single shot images taken at the same Reynolds number. The images illustrate the great variety of distortions that the centerline bulge undergoes as it breaks down. What was once a single bulge, seemingly bifurcates into two (*6(c)*) or even three (*6(d)*) smaller bulges. The significance of this behavior will become more evident when the planform images are considered. All of the images show evidence of small-scale structures which possess streamwise vorticity. Even though the size of the structure varies, the inferred vorticity is always directed downstream for the structures which develop to the right of centerline.

Unlike some other visualization techniques which suffer from path integration limitations (e.g. schlieren and shadowgraph), the Filtered Rayleigh Scattering technique allowed us to illuminate a thin cross-section of the boundary layer over the elliptic cone. The images appear to capture a purely three-dimensional transition mechanism. The bulge in the boundary layer (which results from mass flux to the centerline induced by spanwise pressure gradients) starts to break down by first developing small-scale vortical structures on either or both sides. The structures evolve and eventually lead to further non-linear processes. In *figure 5(e)*, the centerline bulge has broken down into smaller scales typical of a late-transitional boundary layer while the regions farther off centerline still appear to be in the early stages of transition. Although on a much smaller scale, the same process seems to be occurring on the spanwise bulges which have developed at a distance 1.5 cm from the centerline on both sides. Near the left and right edges of *figure 5(e)*, there are small-scale vortical structures which are 'attached' to smaller spanwise bulges and appear to possess the same direction of streamwise vorticity seen in the lower Reynolds number images.

3.3. Simultaneous imaging

Figure 7 is a montage of three pairs of simultaneous images taken of the boundary layer in the early stages of transition. The dashed line in the planform images represents the position of the spanwise sheet, while the dashed line in the spanwise image represents the position of the planform sheet. For this series, the planform sheet is placed at a distance 4 mm from the centerline surface of the model. The most striking feature in frames *7(a)* and *7(b)* is the appearance of a heart-shaped structure in the planform images. In looking at the corresponding spanwise images, it is clear that the middle bulge is actually the tail end of the heart-shaped

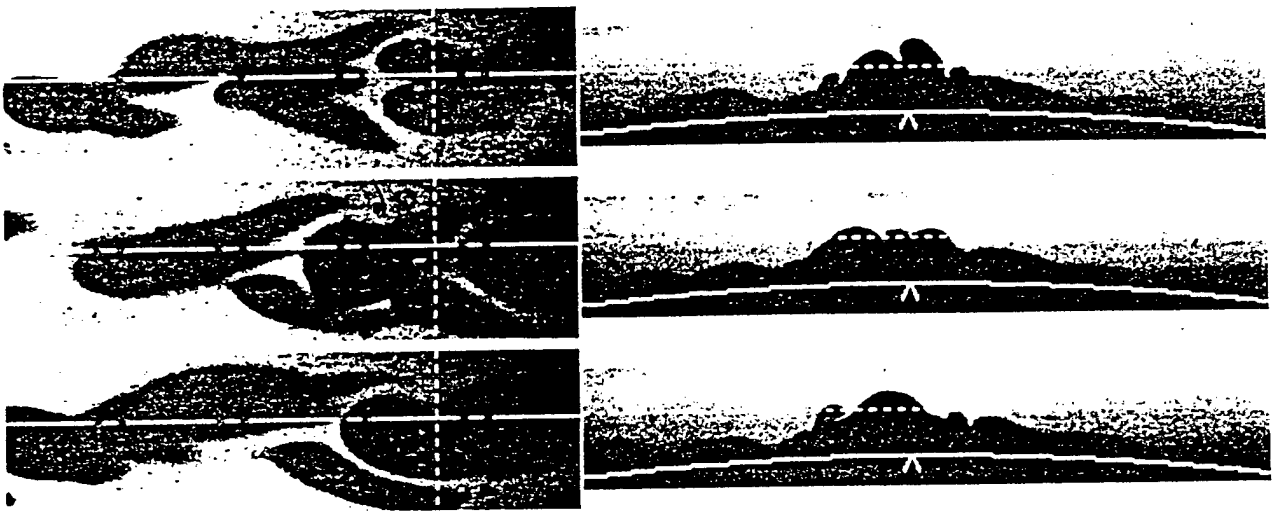

Figure 8. Simultaneous images of planform (left) and spanwise (right) planes. Dashed line represents the intersection of the two planes. Flow is from left to right in planform image and out of the paper plane for the spanwise image. Planform sheet is positioned 3.5 mm from the model surface.

structure. The two 'side bulges' show up in the planform view as long thin structures which are aligned at almost 45 degrees from the flow axis.

In frame 7(*c*), the spanwise sheet cuts through the front end of the distorted heart-shaped structure. The spanwise image shows that the centerline bulge seems to have broken into two large bulges. The small scale vortical structures which are attached to this 'double-bulge' in the spanwise image again show up as elongated structures in the planform image which are aligned roughly 45 degrees to the flow axis.

These images help to illuminate the behavior observed in the spanwise images shown in *figure 6*. From the planform images, it appears that the centerline bulge is actually highly three-dimensional. When sliced through the upstream edge, images similar to *figure 6*(*c*) are produced. When the spanwise sheet cuts through the middle of the heart, images similar to 6(*a*) or 6(*b*) are produced where a single bulge is present with smaller scales developing off-axis. Finally, when images are taken of the downstream edge of the planform heart, the smaller scales have grown to sizes which are equivalent to the original centerline bulge, and it appears as though three bulges exist (*figures* 6(*d*), 7(*a*), 7(*b*)).

The images in *figures 8* and *9* are taken with the planform sheet positioned 3.5 and 3.0 mm from the surface, respectively. Again, image pairs have been chosen which capture the different stages of the planform heart-shaped structures. For the planform images taken towards the interior of the boundary layer, the extent of the small vortical structures is shown. From *figure 9*(*a*), it is apparent that the small-scale structures imaged in the spanwise view actually extend far upstream. In fact, what appeared to be two separate structures may be one continuous loop which wraps around the upstream edge of the heart-shaped structure.

The planform images are of importance in determining the physical mechanism behind these structures which appear in the early stages of transition. Since our use of the Filtered Rayleigh Scattering technique depends on condensed CO_2 to enhance the signal, it is possible to make assumptions about the flow direction in the planform images. The bright regions of condensed CO_2 are assumed to possess downward velocity, since this would represent freestream fluid which is being entrained in the boundary layer but which has not yet been close enough to the wall to sublimate the CO_2. Conversely, the dark regions represent fluid that has already come in close contact with the wall, and is now moving away from the surface.

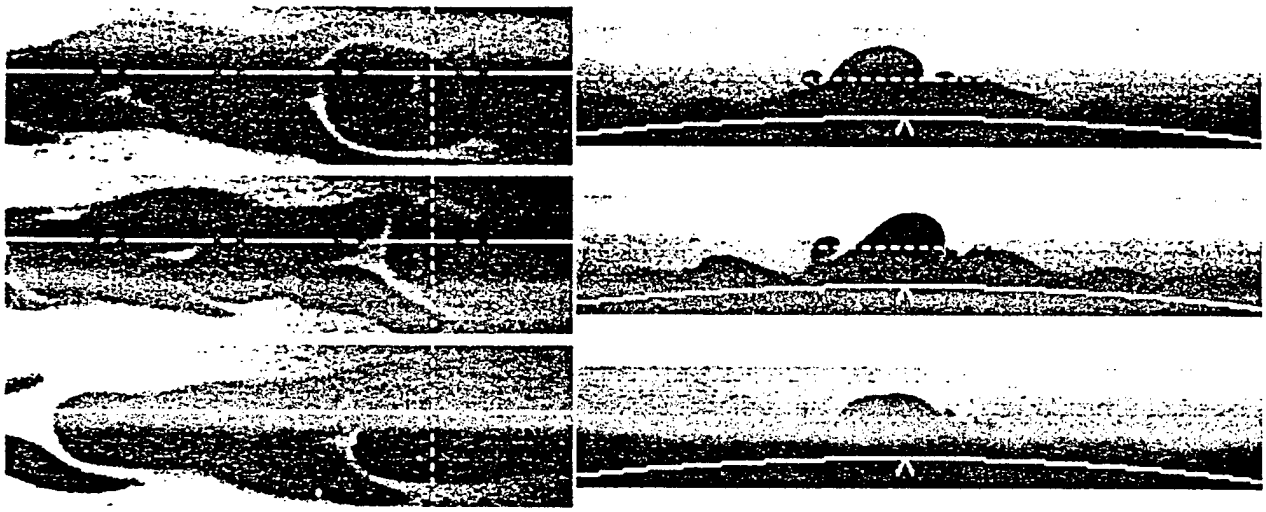

Figure 9. Simultaneous images of planform (left) and spanwise (right) planes. Dashed line represents the intersection of the two planes. Flow is from left to right in planform image and out of the paper plane for the spanwise image. Planform sheet is positioned 3.0 mm from the model surface.

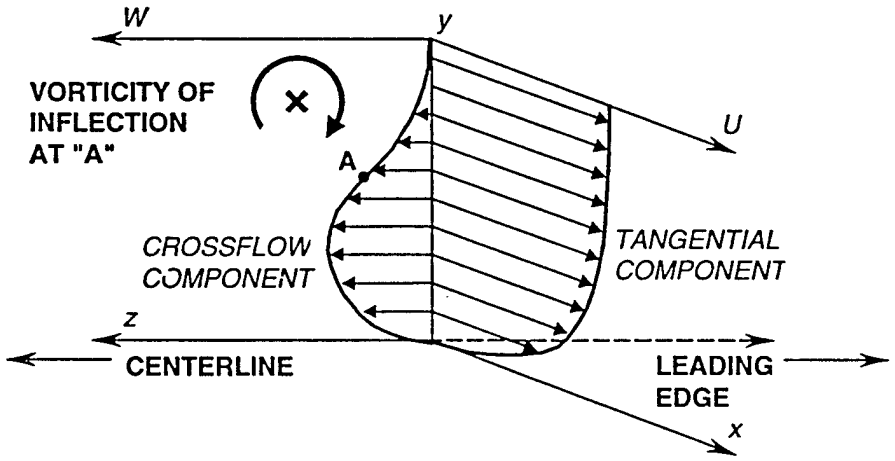

Figure 10. Diagram of inflectional crossflow velocity profile in the off-axis region to the right of centerline. Associated vorticity is oriented upstream.

4. Conclusions

Streamwise visualizations have shown the existence of traveling wave instabilities on the centerline of the elliptic cone. Wavelengths indicate that the disturbances may be associated with the second mode instabilities characteristic of two-dimensional and axisymmetric configurations.

Spanwise visualization of the boundary layer showed small-scale structures which were not apparent in the streamwise direction. Previous computational research (Huang et al. [3]) has indicated that the inflectional crossflow velocity profile could lead to an inviscid instability and early transition on elliptic cone geometries. In our spanwise views, this proposed inviscid instability should appear far off centerline in the region of maximum crossflow. The inflectional instability should grow as a Kelvin–Helmholtz-type roll-up with a component of vorticity oriented upstream for flow on the starboard side of the cone. *Figure 10* illustrates this concept.

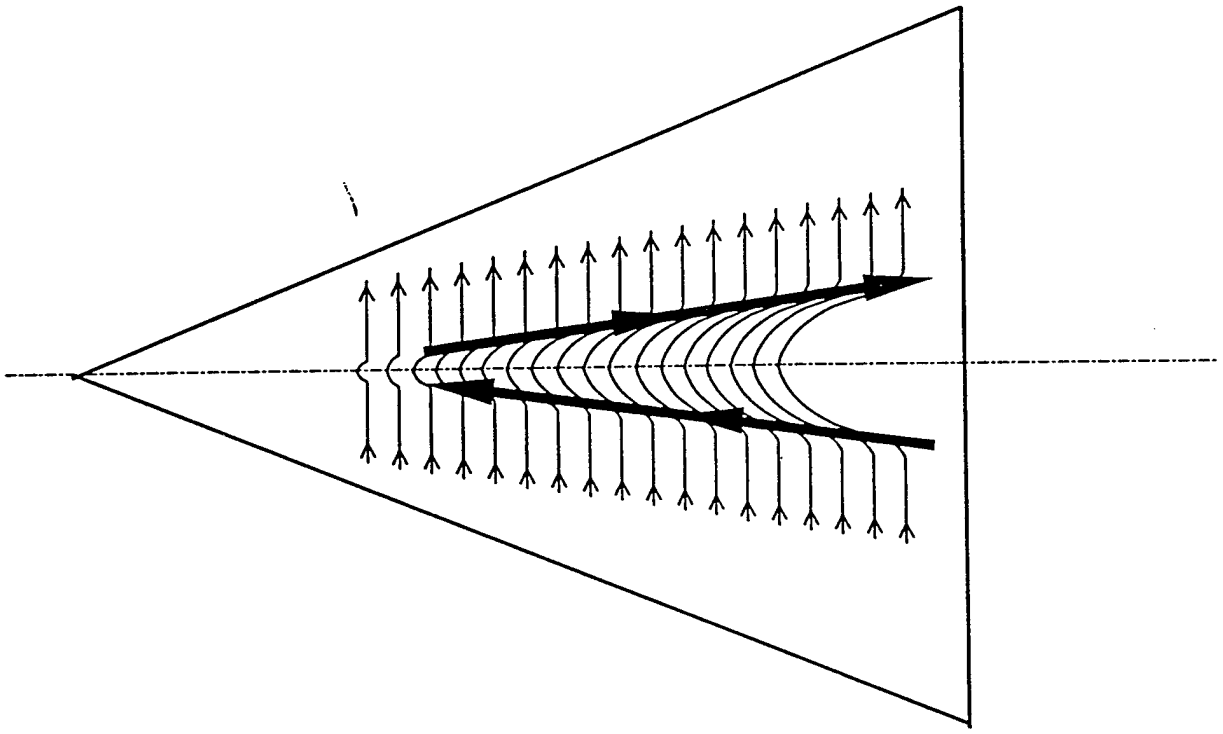

Figure 11. Diagram showing distortion of boundary layer vortex sheet due to presence of centerline bulge. The bold lines represents the resulting components of streamwise vorticity which match the direction observed in the spanwise visualizations.

From the flow visualizations presented in this paper, evidence of transition begins close to the centerline and not in the regions of maximum crossflow. The process begins with the emergence of streamwise vortices on either side of the centerline bulge. The orientation of the vorticity vector is downstream for the structure appearing to the right of centerline. This suggests a mechanism which would require a crossflow profile with an inflection of the opposite sense to that shown in *figure 10*. Certainly, the instability mechanism is not directly associated with the predicted crossflow instability. In light of this finding, the linearized assumption made in the numerical results may not accurately predict transition in flow fields with a high degree of three-dimensionality.

The mechanism by which streamwise vorticity is produced involves the stretching and tilting of vortex lines which originate in the boundary layer. *Figure 11* illustrates how the streamwise components of vorticity could be strengthened by the distortion of the vortex lines due to the low-momentum bulge which forms on the centerline. In the presence of the growing bulge, the vortex lines on the centerline may lag behind the sections which are farther off-axis. Tilting of the line to accommodate the slower-moving centerline sections could occur, and the streamwise component of vorticity will then increase. The final result is a flow field over the top of the cone which includes large concentrations of streamwise vorticity positioned on either side of the centerline axis. The vortex tube to the right of centerline is oriented downstream, while the adjacent tube possesses vorticity oriented upstream.

The vorticity associated with the crossflow velocity profile is not responsible for the structures observed in the spanwise visualizations. The main role of the crossflow appears to be a mechanism which causes a spanwise mass flux component, directed to the centerline. This mass flux gathers along the axis of symmetry and causes a bulge in the centerline velocity profile which distorts the spanwise vorticity in the boundary layer. The resulting streamwise components of vorticity match the position and direction of the vortical structures observed in the

spanwise visualizations. The final breakdown of the boundary layer observed in the streamwise visualizations still appears qualitatively similar to that which occurs on axisymmetric configurations [9].

Questions still remain as to the role of the traveling waves seen in the streamwise visualizations and how they effect the behavior of the spanwise mechanisms. Future work on this model will include the imaging of consecutive frames to analyze the development of structures seen in these single-shot images.

Acknowledgments

The support from AFOSR grant F49620-97-1-0181 is gratefully acknowledged.

References

[1] Mack L.M., Boundary-layer stability theory, Special course on stability and transition of laminar flow, AGARD Report 709, 1984.
[2] Stetson K.F., Kimmel R.L., On hypersonic boundary-layer stability, AIAA Paper 92-0737, 1992.
[3] Huang S.L., Stuckert G.K., Herbert T., Crossflow instability of the supersonic flow over a 4:1 elliptic cone, AFOSR Report F49620-94-C-0053, 1995.
[4] Stetson K.F., Thompson E.R., Donaldson J.C., Siler L.G., Laminar boundary-layer stability experiments on a cone at Mach 8, part 3: sharp cone at angle of attack, AIAA Paper 85-0492, 1985.
[5] Poggie J., Kimmel R.L., Traveling instabilities in elliptic cone boundary-layer transition at Mach 8, AIAA Paper 98-0435, 1998.
[6] Baumgartner M.L., Turbulence structure in a hypersonic boundary layer, Ph.D. Thesis, Princeton University, 1997.
[7] Erbland P.J., Baumgartner M.L., Yalin A.P., Etz M.R., Muzas B., Lempert W.R., Smits A.J., Miles R.B., Development of planar diagnostics for imaging Mach 8 flowfields using carbon dioxide and sodium seeding, AIAA Paper 97-0154, 1997.
[8] Poggie J., Smits A.J., Quantitative visualization of supersonic flow using Rayleigh scattering, AIAA Paper 96-0436, 1996.
[9] Stetson K.F., Thompson E.R., Donaldson J.C., Siler L.G., Laminar boundary layer stability experiments on a cone at Mach 8, part 1: sharp cone, AIAA Paper 83-1761, 1983.
[10] Kimmel R.L., Schwoerke S.N., Klein M.A., Three-dimensional hypersonic laminar boundary layer computations for transition experiment design, AIAA Paper 96-2080, 1996.
[11] Lyttle I.J., Reed H.S., Use of transition correlations for three-dimensional boundary layers within hypersonic flows, AIAA Paper 95-2293, 1995.

AIAA 2000-2379

Numerical and Experimental Investigation of CO_2 Condensate Behavior in Hypersonic Flow

P. J. Erbland and **D. P. Rizzetta**
Air Vehicles Directorate
Air Force Research Laboratory
Wright-Patterson AFB, OH

R. B. Miles
Department of Mechanical and Aerospace Engineering
Princeton University
Princeton, NJ

21st AIAA Aerodynamic Measurement Technology and Ground Testing Conference
19-22 June 2000 / Denver, CO

AIAA-2000-2379

NUMERICAL AND EXPERIMENTAL INVESTIGATION OF CO_2 CONDENSATE BEHAVIOR IN HYPERSONIC FLOW

P.J. Erbland*, D. P. Rizzetta†
Air Force Research Laboratory
AFRL/VAAC
WPAFB, OH 45433

R.B. Miles‡
Dept. of Mechanical & Aerospace Engineering
Princeton University
Princeton, New Jersey 08544

ABSTRACT

Experimental and numerical investigations have been conducted to quantify the effects of carbon dioxide condensation on the fluid mechanics of an air/carbon dioxide mixture in a hypersonic nozzle expansion. Nozzle wall pressures and nozzle exit pitot surveys were used to evaluate the change in flow properties as a function of CO_2 seeding level. As expected, the wall static pressures increased with seeding level due to heat released in the condensation process, and the pitot surveys were relatively insensitive to seeding. A non-condensing axisymmetric Navier-Stokes solution was developed for comparison to wall pressure and nozzle-exit flow survey measurements. The numerical results demonstrated good agreement with the non-condensing experimental data. Boundary-layer displacement thickness estimates and detailed wall pressure distribution data derived from this solution were used to define several effective one-dimensional area distributions for the nozzle. A quasi-one-dimensional (Q1D) non-equilibrium condensing flow model was then used to predict the behavior of the condensing carbon-dioxide vapor. This tool employed a homogeneous nucleation model which included effects of CO_2 cluster translational and rotational free energy. Using reasonable scaling of cluster surface tension values, the Q1D analyses accurately predicted the location and, to a lesser degree, the magnitude of the perturbation to the wall pressure distribution. The study demonstrates that the Lothe-Pound nucleation model, rather than the classical model used in prior studies of pure carbon dioxide[1], is appropriate for this carrier gas/vapor system.

INTRODUCTION

This research was conducted to support development of an optical diagnostic technique known as condensate-enhanced Filtered Rayleigh Scattering (FRS). This technique provides instantaneous planar imaging of high-speed low-density flows and is currently being employed to study the structure of compressible turbulent boundary layers. The technique requires mixing a small amount of gaseous carbon dioxide into the tunnel air supply. The CO_2 condenses during the nozzle expansion forming small nano-scale clusters in the free stream which have a larger optical scattering cross section than the surrounding gas. Using FRS, regions of cold flow where condensed CO_2 clusters are present appear bright, and regions of hot boundary layer gas where the CO_2 clusters have evaporated appear dark. This allows the visualization of large-scale turbulent motions in the outer portion of the boundary layer over models. A schematic of a typical application of this approach is shown in Figure 1. Details of this diagnostic have been described previously by Erbland[2].

The development of this technique for imaging hypersonic low-density flows represents an extension of previous successful applications of Rayleigh scattering for the study of turbulent boundary layers and shock/boundary-layer interactions in supersonic wind tunnels[3-7]. In those applications, the flow scattering was found to be caused principally by clusters of residual

* Aerospace Engineer, Senior Member, AIAA
† Aerospace Engineer, Associate Fellow, AIAA
‡ Professor, Mechanical & Aerospace Eng., Fellow, AIAA

water vapor and carbon dioxide which were present despite drying of the supply gas.

Initial experiments to image the unseeded hypersonic flow of interest for this study revealed that the scattering was grossly insufficient for instantaneous planar imaging. This led to the decision to increase the quantity of condensable vapor in the flow. The considerations that went into the selection of carbon dioxide as the desired vapor, and the design of the resulting seeding system are discussed by Erbland[2].

It was recognized at the outset that the addition of condensable vapor would perturb the kinematic and thermodynamic state of the flow due to heat release, and that this perturbation would need to be evaluated. Fortunately significant work to understand the phenomena associated with condensation induced heat release in rapidly expanding supersonic flows has already been accomplished[8-14].

The problem of vapor condensation in nozzle flows has received significant attention dating back to the advent of supersonic wind tunnels in the 1930s[8]. Initial work sought to understand the presence of shock-like structures in the near-throat region of supersonic nozzles. Investigations concluded that these structures were caused by heat release due to condensation of ambient water vapor present in the tunnel supply gas. This discovery and subsequent work in condensation of air components for hypersonic nozzles led to standard procedures for drying and heating tunnel supply gas to minimize condensation effects.

Interest in this problem was also spurred by the steam-cycle power generation industry, the material processing community and most recently researchers studying molecular-level reaction tailoring. Research efforts over the past three decades have investigated a number of gases and gas mixtures including pure steam, pure carbon dioxide, sulfur hexaflouride, water/air mixtures (moist air), and alcohol/air mixtures. Several excellent overviews and monographs on the subject are available including those by Wegener[8], Hill[9], Abraham[10], and Ryzhov[11].

The majority of the experimental studies to characterize supersonic nozzle flow condensation have been conducted in small-scale, two-dimensional (quasi-one-dimensional) test facilities[8,11-14]. Data consist of wall static pressure measurements, pitot pressure measurements, and light scattering (Schlieren, interferometry, Rayleigh scattering). The objectives of these measurements have been primarily to characterize the location and magnitude of flow perturbations produced by the heat release and secondly to determine the size and number density of the resulting clusters.

Analytical studies of condensation effects have primarily employed quasi-one-dimensional non-equilibrium flow models[8-14] which used some variant of classical nucleation theory to predict the formation and growth rates of molecular clusters. Those models have consistently shown good agreement with experimental observations for a wide range of gas/vapor mixtures provided adequate thermophysical property data were available for the condensed vapor. More recently, several investigators have employed Method-of-Characteristics based techniques[11] and Navier-Stokes codes[15-16] to address this problem. Although these techniques offer more insight into the physical behavior of the flow, their numerical complexity and computational cost are not always justified by the additional information gained relative to 1D solutions. Ryzhov[11] notes that calculations of nonequilibrium condensation reveal that neither the location of streamlines in 2D nozzle flows, nor the mass flow rate are affected by condensation. Thus two-dimensional nozzle flows with nonequilibrium condensation may be adequately studied using the theory of one-dimensional flows. This is accomplished by computing the two-dimensional non-condensing flow and then computing the nonequilibrium condensation using the one-dimensional approximation following individual streamtubes. Based on the historical success and relative simplicity of the Q1D modeling[12-14], this approach was selected to assess the condensing flow response.

The objectives of the current effort were to; (1) characterize the flow perturbations produced by differing levels of carbon dioxide flow seeding, (2) evaluate the ability to predict those perturbations using a low-order model, and (3) evaluate the resulting condensate characteristics, in particular the cluster size. This was accomplished by making appropriate facility and flow measurements and then comparing the results to axisymmetric non-condensing flow solutions and to Q1D non-equilibrium predictions of the flow with condensation.

CONDENSATION IN HIGH SPEED NOZZLE EXPANSIONS

The condensation of a given component of a gas mixture in a supersonic/hypersonic nozzle expansion can occur once the thermodynamic state of the gas crosses the saturation curve for the vapor. This is a result of the steeper slope of the saturation curve for the vapor compared to that of the nozzle expansion isentrope. Depending on the expansion rate in the nozzle (dT/dx) some amount of supercooling (equivalently supersaturation) of the vapor will occur. That is, the flow will expand to a temperature below the saturation temperature before detectable condensation begins. Figure 2 shows the flow isentropes for typical seeding rates employed in this study as well as the saturation

curve for carbon dioxide. Table 1 lists the seeding mass and mole fractions corresponding to the seeding parameter (Vdot) values listed in this figure when the test facility is operated at reference test conditions of Po = 6.89 Mpa (1000 psia) and To = 825 K. The point at which the isentrope crosses the saturation curve defines the Mach number of equilibrium condensation M_i. This is the location at which condensation would occur if an equilibrium process were to take place. For long, large-scale nozzles, lower levels of supercooling are to be expected and a more nearly equilibrium process will result. Short high expansion rate nozzles produce larger supercoolings and greater nonequilibrium. The process discussed here is illustrated in Figure 3 which shows the transition from subsaturated ($S<1$) to supersaturated ($S>1$) flow in the nozzle and the corresponding change in the flow static pressure due to the condensation heat release. Here the saturation ratio is $S = p_v / p_s$, where p_v is the partial pressure of the vapor and p_s is the vapor saturation pressure at the temperature of the system.

For a vapor system that has reached its saturation state, condensation occurs through one of two mechanisms. The more common *is heterogeneous nucleation* which occurs when foreign bodies such as ions, hygroscopic condensation nuclei, or wall surfaces are available to assist the vapor system to get over its activation free-energy barrier. The second mechanism is *homogeneous nucleation* wherein individual molecules of the vapor come together to form clusters of the condensed phase, unaided by condensation sites. This mechanism is dominant in systems of very high purity vapor where foreign bodies and walls are not present and in very rapid expansions where high levels of supersaturation are attained despite the possible presence of foreign bodies and walls. This homogeneous nucleation process has been shown to be the active mechanism controlling vapor condensation in supersonic (hypersonic) nozzles, even in the presence of large numbers of condensation nuclei. Thus the supercooling observed in rapid nozzle expansions is a consequence of the condensation mechanism active in the flow.

In a vapor system subjected to homogeneous nucleation, vapor-liquid or vapor-solid phase transitions are blocked by an activation free energy barrier, ΔF [see Abraham[10]]. This arises from surface free energy increases resulting from the appearance of embryos of the more condensed phase. Such a thermodynamic system can be analyzed to determine the free enthalpy (free energy) of the vapor-droplet system and the change in this value as a result of formation of a given sized cluster. This leads to an expression for the free energy change of the form

$$\Delta F = 4\pi r^2\sigma - \frac{4}{3}\pi r^3 \rho_c RT \ln S . \qquad (1)$$

Here the first term corresponds to the free energy of formation of the embryo of radius r where σ is the surface free energy of the cluster. The second term is the contribution due to the bulk free energy change in going from a vapor at (p_v,T) to a condensed phase inside the embryo, where ρ_c is the density of the condensed phase.

In a sub-saturated or just-saturated vapor, the saturation ratio is $S \le 1$. In such a system, there exists a statistically steady population of embryos or clusters characterized by a Boltzmann-like distribution function of the form

$$n_q = n_1 e^{-\Delta F / kT} \qquad (2)$$

where n_q is the number density of clusters containing q molecules, n_1 is the number density of vapor molecules in the system, k is the Boltzmann constant, T the absolute temperature, and ΔF is the free energy change (increase) of the system due to the formation of a small spherical cluster containing q molecules at constant temperature and constant pressure. These clusters exist due to random collisions of the vapor molecules. Although the population is steady, the actual clusters of any given size are continuously forming and dissolving by the action of different molecules.

When the system becomes supersaturated $S > 1$, the free energy term exhibits a maximum which is dependent on the radius of the embryo. The critical radius (r^*) is the size that a cluster must achieve to reach the peak in the free energy barrier and can be expressed as

$$r^* = 2\sigma / \rho_c RT \ln S . \qquad (3)$$

If a cluster were to exceed this size then it would experience growth at the expense of the supersaturated vapor. A cluster smaller than this size has a tendency to evaporate since it contributes to a system free energy which is higher than the minimum value for a supersaturated vapor with no condensed phase present.

The free-energy activation barrier can then be expressed as

$$\Delta F^* = \frac{16\pi\sigma^3}{3(\rho_c RT \ln S)^2} = \frac{4}{3}\pi r^{*2}\sigma \qquad (4)$$

where σ is the surface free energy of the cluster which for liquid droplets, according to the capillarity approximation[12], is assumed equal to the flat-plane surface tension of the liquid. Modern molecular dynamics calculations of the free energy of clusters have provided support for the use of this macrosocopic property, even for critical sized clusters containing only 10s of molecules[13].

These equations show that both the surface free energy barrier and the critical radius decrease as the saturation ratio increases. Consequently increasing supersaturation (S) enhances the possibility that the combined molecular and macroscopic fluctuation processes will send some embryo or cluster over the top of the activation barrier in a given time. This explains the large supersaturation ratios and the rapid and complete collapse of that state over a short distance in a nozzle. It also explains the nearly monodisperse nature of the resulting condensate.

The formation of survivable nuclei works to reduce the supersaturation by depleting the vapor phase (decreasing the partial pressure of the condensable vapor). This pushes the system toward equilibrium. At the same time the continued expansion process in the nozzle works to retain the supersaturated state by decreasing the static temperature and thereby reducing the saturation vapor pressure. Consequently the majority of the nuclei are formed at nearly the same level of supersaturation and thus these critical nuclei have a very narrow size distribution. Subsequent growth affects the nuclei in the same manner assuming particle collisions are rare, a fair assumption since the particles are of the same size and travelling with the mean flow. This has been demonstrated to be the case in both analytical and experimental studies of a number of carrier-gas/vapor mixtures including water vapor condensation in rapid nozzle expansions[12,17].

Once condensation begins, the formation and growth of critical nuclei can be computed using formation rate equations derived from the foregoing analysis and growth equations derived from kinetic theory. The condensation process occurs over a relatively short distance and releases heat to the flow. For a constant area section (Rayleigh flow process) this heat release produces a decrease in flow Mach number and total pressure, and an increase in the total temperature, static temperature and static pressure. The actual bulk flow response will depend on the rate at which heat is released relative to the rate of change of the nozzle area. Regardless of the local process details, the net effect on the parameters of interest will be as identified above. Thus the presence of condensation will cause a reduction in test section Mach number. The magnitude of this perturbation will depend on the quantity of heat released, which in turn depends on the type and amount of vapor condensed. Thus small seeding levels using vapors with low sublimation enthalpy are desirable to minimize the flow disturbance.

AIR/CO_2 CONDENSATION EXPERIMENTS

Experiments were conducted in the Princeton Gas Dynamics Laboratory Mach 8 blow down wind tunnel, Figure 4, at nominal test conditions listed in Table 2. The supply air is heated to the desired stagnation temperature by passing it through an 83 m long helical coil. This results in a time dependent total temperature behavior as illustrated in Figure 5. The maximum temperature variation during a run is nominally ± 20°C (2.5%). The nozzle was instrumented with 7 pressure taps located at positions to provide optimal insight into the expected CO_2 condensation behavior.

Carbon dioxide is introduced using the metering and injection system illustrated in Figure 6. In brief, helium is introduced into the gas "head" of a dual port carbon dioxide cylinder to provide a constant pressure CO_2 supply. The liquid phase is removed through a dip tube and the pressure, temperature and flow rate of the liquid CO_2 are measured prior to injection into the process stream just downstream of the pressure control valve. The mixture of air and CO_2 passes through the heater coil where the gases are mixed and heated to the desired stagnation temperature. The flow then enters the stagnation chamber where flow total temperature and pressure are measured. This gas mixture expands through a converging-diverging nozzle where the carbon dioxide vapor condenses, and into the test section. The CO_2 metering and injection system is described in detail by Erbland[2].

Two types of measurements were accomplished to characterize the flow behavior. Nozzle static pressure measurements provided a baseline, non-condensing pressure distribution and indicated changes in the flow static pressure due to condensation heat release. Surveys of the pitot pressure and total temperature at the nozzle exit were also accomplished to establish the non-condensing Mach number distribution and boundary-layer thickness, and to identify any changes in the boundary layer due to carbon dioxide seeding and condensation.

Nozzle static pressures were measured using MKS Baratron pressure transducers and a scannivalve system for sampling the various ports. The total uncertainty in these static pressure measurements was less than 1%. For the flow surveys the probe tip was positioned 3.8 mm ahead of the nozzle exit plane and was traversed from the wall toward the flow centerline. Multiple runs were required to survey the region of interest so repeat runs were conducted to insure that reliable data were obtained.

These nozzle exit surveys indicated a non-condensing Mach number of nominally 8.1 with an estimated uncertainty of ±0.12 and a distribution shown in Figure 7.

Surveys were also conducted to examine the effects of flow seeding on the nozzle wall boundary layer. The higher seeding rates were employed to provide the greatest likelihood of detecting any changes. It was known at the outset that pitot pressure is relatively insensitive to condensation effects[18-19]. However, little condensed phase is expected in the thick nozzle-exit boundary layer. Consequently the pitot probe should provide an accurate indication of any significant mean changes in the boundary layer structure.

Pitot pressure surveys were conducted for CO_2 seeding mass fractions (initial humidity ω_0) of 0.0, 0.016 and 0.035, at total conditions of nominally P_o = 1000 psia and T_o= 825 K. Figure 8 illustrates the pitot/total pressure ratio for these three cases. Mach number cannot be shown since the condensation-induced total pressure losses preclude the use of normal shock relations to infer Mach number from the pitot/total pressure ratio. In the wall region the pitot pressure shows little variation with seeding rate. In the core flow a small change in pitot pressure (5-6%) is observed. A change of this magnitude in a non-condensing Mach 8 flow would correspond to a variation of ~0.1Mach. These results are consistent with previous research indicating that condensation has little influence on the boundary-layer thickness[8].

A typical comparison of nozzle wall pressures for ω_0 = 0.0, 0.007, and 0.0157 is shown in Figure 9. The start of condensation is indicated by the rise in wall pressure above the noncondensing value due to the heat released in the condensation process. This figure shows that as the seeding mass fraction increases the start of nucleation moves upstream in the nozzle.

NUMERICAL INVESTIGATIONS

The numerical investigations for this study involved non-condensing axisymmetric Navier-Stokes (NS) solutions and Q1D non-equilibrium condensing flow computations. The Navier-Stokes solutions were used to examine the nozzle flowfield uniformity and to obtain an "effective" 1-D area distribution for use in the condensing solution. The Q1D solutions were used to investigate the details of the condensation process including nucleation and growth behavior, the cluster size, and the ability of this model to predict the experimentally measured condensing flow behavior (pressure rise).

Axisymmetric Navier-Stokes Analyses

The nozzle flowfield was simulated using the General Aerodynamic Simulation Program[20] (GASP) V.3.2 by AeroSoft Incorporated. This is a fully-conservative shock capturing code which has been used extensively by the aerospace community for analysis of supersonic and hypersonic nozzle flows, including flows with chemical reaction. The code uses a finite-volume, cell-centered discretization to solve the integral form of the time-dependent three-dimensional Reynolds-Averaged Navier-Stokes (RANS) equations. The code can also be employed in the Parabolized Navier-Stokes (PNS) or space-marching mode.

The strategy involved in solving this problem was to first run a PNS solution to establish the basic flowfield. This solution served as the initial condition for the time-marching RANS solution. Iterations were conducted with a CFL of unity to obtain converged results. A brief discussion of the relevant problem details is presented below.

Geometry/Grid

The geometry description of the Mach 8 nozzle was based on the design coordinates given by Baumgartner[21]. These data were checked at several reference stations and corrected in the throat region using measurements obtained during the installation of the nozzle static pressure ports. An axisymmetric structured-grid having 1025 axial by 257 radial grid points was generated using these wall coordinates. Radial grid points were highly clustered near the walls and moderately clustered at the centerline symmetry plane. The grid was also clustered in the axial direction from the throat through the completion of the rapid expansion. A grid convergence (refinement) study was conducted using the grid sequencing option in GASP. This revealed that a grid of 257 axial by 129 radial points provided grid-converged solutions. Based on the turbulent solutions, the distance of the first cell center from the wall was found to correspond to y^+ of less than 1 at the nozzle exit.

Boundary Conditions

The inflow boundary was specified to be a uniform sonic line (M=1.0001) with static density and pressure calculated from plenum total conditions using perfect-gas isentropic relations. This approach was selected based on the results of several previous studies which demonstrated that nozzle solutions based on uniform inflow were identical to those which employed a full model of the inlet contraction[22-23]. A simple supersonic outflow condition was employed at the exit with first-order extrapolation from the last cell to the boundary.

The remaining boundary conditions consisted of; flow tangency on the sides of the wedge, an axisymmetric

condition along the x-axis, and either an isothermal or adiabatic no-slip wall with a vanishing normal pressure gradient. The isothermal wall temperature was selected to be 400°K (720°R) based on several reference wall temperature measurements. These two conditions were selected to bracket the range of expected wall temperatures in the nozzle.

Solution Approaches

For the PNS solutions, the flow was marched in the streamwise direction employing a full-flux function, 2nd-order fully upwind reconstruction with catastrophic p and ρ limiting. The radial direction used Roe's flux-difference splitting, 3rd-order upwind biased reconstruction, and min-mod numerical limiting to obtain a well-behaved solution in flows having discontinuities. It was also necessary to specify an inviscid flux in the circumferential direction to account for the contribution to the momentum flux from the pressure acting on the faces associated with that direction. Since there were no interior cells in that direction, the spatial accuracy and limiting in that direction would not affect the solution. Integration was accomplished using an LU decomposition on a single radial computational line with relaxation in the circumferential sweep direction.

For the RANS solutions, Roe's scheme was used in all three directions. The streamwise and radial directions used 3rd-order upwind biased reconstruction at the cell faces, and min-mod numerical limiting. The circumferential direction was handled identically to the PNS case. A two-factor approximate factorization approach was used for the implicit time integration.

Two turbulence models were employed. the first was the zero-equation Baldwin-Lomax model. This model is valid for attached flows with mild pressure gradients and has been used extensively in computations. For a more sophisticated model the Wilcox K-ω model was selected. This model has advantages over the K-ε model in that it performs well for flows with positive and negative pressure gradients. In addition, it can be integrated through the viscous sublayer without the use of the damping functions which are required to control the singularity of terms present in the ε equation at a no slip surface.

Numerical Results - Comparison to Experiment

All numerical solutions treated air as a perfect gas and assumed the flow was turbulent from the initial upstream station. The space-marching PNS solutions were obtained by iterating at each plane until the L2 norm of the update residual was reduced by 5 orders of magnitude or the absolute value of the residual became smaller than 1e-11. Time marching was then used to refine the solutions until non-physical total temperature perturbations near the centerline had propagated out through the exit plane. Solutions were computed using the two turbulence models, Baldwin-Lomax (BL) and Wilcox' K-ω, two different wall conditions, adiabatic and isothermal (T_w=400°K) and two different total temperatures (815 and 845°K). These solutions were compared with one another and with the experimental measurements to determine which models provided reasonable agreement with experiment.

Figure 10 shows the exit pitot pressure distribution for the various solutions compared with experimental data. The BL solutions more closely match the experimental results. In the core flow region, the difference between the experimental and computational pitot pressure values corresponds to a difference in Mach number of about 0.1. This is certainly within the uncertainty of the experimentally derived Mach number (±0.12). Figure 11 shows that reasonable agreement is also achieved in comparing the computed nozzle wall static pressure to the experimental data. All of the solutions recover the gross behavior of the nozzle expansion. Figure 12 is an expanded scale of the downstream portion of the nozzle. This shows that the solutions lie slightly above the experimental wall pressure values in the middle of the nozzle but pass through the data near the exit. Based on these results, the BL adiabatic-wall results were used to develop "effective" 1D area distributions for use in the Q1D condensing flow analysis. Figure 13 shows the Mach number contours for this nozzle solution.

Effective 1D Area Distributions

Two approaches were employed to develop "effective" one-dimensional area distributions from the preceeding numerical solutions. The first was to compute a displacement thickness ($\delta^*(x)$) and use this to adjust the cross sectional area at each axial station. This was accomplished by mapping the numerical solution data to a wall-normal coordinate system and then integrating for the desired properties. This integration accounted for both strong transverse curvature effects and normal pressure gradients following the *linear-extension reference flow method* recommended by Fernholz and Finley[24]. The second approach was to use the numerically computed wall pressure distribution (p_w/p_0) to compute a corresponding area distribution by assuming isentropic 1D flow from the throat to the exit.

Q1D Nonequilibrium Condensation Analyses

In order to analyze the effects of condensation on the nozzle flow properties, a Q1D nonequilibrium condensing flow model was developed. This model draws on a significant base of prior research in this field[4-14].

Although a number of gas/vapor systems have been investigated in previous research, the air/carbon-dioxide system is not among them. Duff[25] studied condensation of rapidly expanding pure CO_2 flows. His goal was to determine whether existing nucleation theory was useful in predicting its behavior. He found that if the nuclei were taken to be spherical drops in the subcooled liquid state, even at temperatures well below the triple point, classical nucleation theory permitted a close absolute prediction of his experimental results. This is in spite of the fact that the local temperatures at which significant nucleation occurred were from 20-50°C below the triple point. Based on this he proposed that CO_2 nuclei are crystals only at temperatures far below the triple point.

In developing the theory for this study, the classical nucleation model was not assumed. Rather, all appropriate terms were included in the nucleation rate equation to be discussed below.

Q1D Gas Dynamic Equations

The gas dynamic formulation of this problem follows the model of Wegener and Mack[8]. Before writing the Q1D equations in the form used for this study, we first note that the total mass of the system can be expressed as the sum of the air (m_a), vapor (m_v) and condensed mass (m_c), $m = m_a + m_v + m_c$. Consequently, if we define an effective condensate density in terms of the local mass of condensate and local gas volume of the system ($\rho_c' = m_c/V$), then the density can be written as $\rho = \rho_a + \rho_v + \rho_c$.

The appropriate gas dynamic equations for this problem can then be written as:

Continuity

$$\frac{d\rho}{\rho} + \frac{du}{u} + \frac{dA}{A} = 0 \qquad (5)$$

Momentum

$$\frac{du}{u} + \frac{(1-g)}{\gamma M^2}\frac{dp}{p} = 0 \qquad (6)$$

Energy

$$\frac{c_p}{c_{p_0}}(\gamma-1)M^2\frac{du}{u} + \frac{dT}{T} - \frac{d(Lg)}{c_{p_0}T} = 0 \qquad (7)$$

and the state equation and Mach number take the form:

$$\frac{dp}{p} = \frac{d\rho}{\rho} + \frac{dT}{T} - \frac{\mu_m}{\mu_v}\frac{dg}{(1-g)} \qquad (8)$$

$$\frac{dM}{M} = \frac{du}{u} - \frac{dT}{2T} + \frac{dg}{2(1-g)}\left[\left(\frac{\mu_m}{\mu_v}\right) - 1\right] \qquad (9)$$

In the preceding expressions ρ is density, u velocity, A area, p pressure, T static temperature, M Mach number, g the condensed-phase mass fraction ($g = m_c/m$), μ_m the mixture molecular weight, μ_v the vapor molecular weight, c_p the mixture specific heat, c_{p_0} the initial mixture specific heat (g=0), γ the mixture specific heat ratio, and L the enthalpy of sublimation or vaporization as appropriate.

Required auxiliary equations include:

$$\frac{1}{\mu_m} = \frac{(1-\omega_0)}{(1-g)}\frac{1}{\mu_a} + \frac{(\omega_0 - g)}{(1-g)}\frac{1}{\mu_v} \qquad (10)$$

where $\omega_0 = m_v/m$ is the initial vapor mass fraction or specific humidity and μ_a is the molecular weight of air,

$$c_p = \frac{(1-\omega_0)}{(1-g)}c_{pa} + \frac{(\omega_0 - g)}{(1-g)}c_{pv}, \qquad (11)$$

where c_{pa} is the specific heat of air and c_{pv} the specific heat of the vapor, and

$$\gamma = \frac{c_p}{c_p - R_u/\mu_m}. \qquad (12)$$

The unknowns include ρ, A, u, p, T, g. However, the area (A) will be specified in the problem. Thus an additional equation is required for the condensate mass fraction. This quantity depends on both the nucleation rate and the rate of growth of the condensed phase.

Aside from the one-dimensional approximation, the most important assumptions in this model are that the cluster moves with the surrounding gas, is at the same temperature as the surrounding gas, and that the cluster is at a uniform temperature. All of these assumptions have been readily supported in prior studies of condensing gas/vapor mixtures in high speed nozzle flows[8,9,12,13,26].

Nucleation Rate Expression

Historical work on homogeneous nucleation processes have produced several different nucleation models[10]. These models provide expressions for the rate of formation of critical sized drops in a supersaturated vapor (clusters/cm³sec). Although different in detail they all share the general form $J = Ke^{-\Delta F^*/kT}$, where ΔF^* is the free energy change involved in the formation of one critical drop of size r^*. The dependence of the exponential term on the critical radius is essentially the same in all theories. This term dominates the behavior of the nucleation rate.

Depending on the free energy contributions considered in the embryo formation, the pre-exponential term (K) can vary by a factor of up to 10^{17} for the two major variants of this expression. The "classical" nucleation model, also referred to as the Becker-Doering[10] (B-D) model includes only the surface free energy of the cluster, expressed in terms of the surface tension. Later work by Frenkel[27] and subsequently Lothe and Pound[28] (L-P), based on statistical mechanical arguments, also included terms to account for free energies of translation and rotation, and conservation of degrees of freedom in small clusters. In essence they treated the cluster as a large gas molecule within a free molecule flow of surrounding vapor. It is the inclusion of these additional free enthalpy contributions that cause the nucleation rates computed using the L-P model to exceed that of the classical model by such a large factor.

Abraham[10] thoroughly reviewed the various studies and observed that certain gas/vapor systems followed the classical B-D model while others demonstrated better agreement with L-P. He compared the B-D and L-P free energies to those predicted using a Monte Carlo analysis of small (13-100 atom) Argon clusters as a standard and demonstrated that the L-P model provided significantly better predictions of the free energy than B-D. In fact the predictions are within 3-5kT of the Monte-Carlo solution for most of the cluster sizes. Based on this and other arguments, he concluded that the L-P model had the greatest validity and should be used. Consequently, the nucleation rate equation was taken to be[10]:

$$J = \left(\frac{p_v}{kT}\right)^2 \frac{m_c}{\rho_c}\left(\frac{2\sigma}{\pi m_c}\right)^{\frac{q_{tr}q_r}{q_{rep}}} \exp\left[-\frac{4\pi r^{*2}\sigma}{3kT}\right] \quad (13)$$

where r^* is evaluated using equation (3), p_v is the vapor pressure, k Boltzmann's constant, q_{tr} is the translational partition function, q_r the rotational partition function, and q_{rep} the replacement free energy contribution which is derived from proper accounting for the total number of internal modes of motion (degrees of freedom). These contributions are evaluated as

$$q_{tr} = \left(\frac{2\pi m^* m_c kT}{h^2}\right)^{3/2} \frac{(kT)}{p_v} \quad (14)$$

$$q_r = \left(\frac{8\pi^2 I^* kT}{h^2}\right)^{3/2} \pi^{1/2} \quad (15)$$

where n^* is the number of molecules in a critical cluster, $n^* = (4\rho_c \pi r^{*3}/3m_c)$ and I^* is the moment of inertia which may be approximated by that of a sphere of uniform density as

$$I^* = \frac{2}{5} n^* m_c r^{*2} = \frac{2}{5} n^{*5/3} m_c \left(\frac{3m_c}{4\pi\rho_c}\right) \quad (16)$$

The replacement free energy was evaluated by Abraham for both linear and cubic crystals. He concluded that the term should be between $-15kT \le f_{rep} \le -5kT$. For the value suggested by Lothe & Pound of $-5kT$, this leads to $q_{rep} = \exp(5)$.

Note that this equation has a cubic dependence on the surface tension of the cluster (Eqn. 3 and 13). This is one of the most important and least defined factors in the nucleation analysis.

Growth Equation

The clusters can grow by two mechanisms, attachment of vapor molecules impinging on the surface and by coalescence with other droplets. Contributions due to coalescence have been considered by a number of authors and generally found to be quite small Wegener[12]. Proper modeling of growth by impingement depends on the effective Knudsen number of the flow within which the clusters move. For this study, the Knudsen numbers are significantly greater than 10 so the clusters move in a free molecule flow. Hill[9] and Wegener[13] develop models for this case using kinetic theory relations to treat mass and energy conservation for the growing cluster. These models apply to molecular impingement on a body moving with the bulk motion of the gas.

For the current study, we assumed that the cluster temperature is equal to the surrounding flow temperature and that the temperature within the cluster is uniform. This assumption is valid when the condensing vapor is a small fraction of the gas/vapor mixture. In that case one can expect $10^2 - 10^3$ collisions between gas molecules and the cluster for every collision with a vapor molecule.

The resulting droplet growth rate, that is, the change in radius per unit time in a free molecular flow can be expressed as (see Wegener[13]),

$$\frac{dr}{dt} = \hat{\alpha}\frac{m_c}{\rho_c}\left[D(p_v,T)\right] \qquad (17)$$

where

$$D(p_v,T) = p_v/(2\pi\overline{m}_c kT)^{1/2} \qquad (18)$$

is the impingement rate of molecules on the stationary target, derived from kinetic theory, $\hat{\alpha}$ is a modified condensation coefficient

$$\hat{\alpha} = \alpha\left[1-\left(\frac{p_v}{p_s(T)}\right)^{\left(\frac{r^*}{r}-1\right)}\right] \qquad (19)$$

and α is the condensation or mass accommodation coefficient for the vapor. The modified coefficient $\hat{\alpha}$ accounts for the growth of the cluster due to impingement of vapor molecules at pressure p_v, and evaporation from the droplet whose internal pressure is p_s. Note that due to the surface tension, the internal droplet pressure can be higher than the surrounding vapor pressure. Thus the flow may be supersaturated with respect to a large cluster and sub-saturated with respect to a small cluster. The term $\overline{m}_c$ in equation 18 is the reduced mass of the cluster $\overline{m}_c = m_c M/(m_c + M)$ where M is the total cluster mass. For small droplets this allows that the Brownian motion of the cluster may be comparable to that of the molecules so that the collision rate would increase.

As shown in equation 19, the cluster growth rate depends on the current cluster radius r. To make the solution tractable, and in accordance with prior treatments of similar problems, a surface-averaged cluster radius was computed during the computational procedure[9]. This parameter provided a mean radius for use in the growth rate calculations.

Numerical Algorithm

Using the preceding growth rate expressions, a differential equation describing the rate of formation of condensed phase g along the nozzle can be derived[1]. This equation was combined with the foregoing gasdynamic expressions which were reformulated to give a set of 7 coupled ordinary differential equations describing the Q1D, non-equilibrium condensing flow of a gas/vapor mixture. These equations are presented in Appendix 1.

A fourth-order Runge-Kutta algorithm was written to solve these differential equations. The solver takes an arbitrary input area distribution and specified initial conditions at the inlet plane and solves for the gasdynamic state and condensate mass fraction at each step. Currently the gas/vapor mix is treated as a perfect gas mixture using constant specific heat values and a thermally perfect equation of state. The capability is provided for a fourth-order accurate interpolation of the input area distribution to obtain any desired grid spacing. This includes a routine to arbitrarily redistribute the grid as necessary to maintain a high point density in regions of strong gradients.

The gasdynamic portion of this algorithm was validated by comparison with solutions obtained using simple 1D isentropic flow equations. Grid refinement studies were conducted on condensing flow solutions to insure that adequate resolution of the high gradient nucleation regions was attained. These studies revealed that the baseline 257 point grid substantially underpredicted the peak nucleation rate. Solutions on 2001 and 4001 point grids were compared and no difference in nucleation rate was detected. All results presented here are on a 2001 point solution grid.

Thermodynamic Properties and Data

The importance of selecting appropriate property data for the analysis cannot be overstated. Since the flow state crosses the saturation curve well below the triple point of CO_2, we utilized solid property data to the maximum extent possible. Table 3 lists relevant data values along with curve fits developed for several of the parameters.

The most important property selection, as determined by its influence on the solution, is the surface free energy of the cluster, σ. This parameter enters the nucleation rate equation as a cubic term (see Eqn. 3 and 13). The principal concern is that the literature provides no data on the surface free energy of solid CO_2. Consequently three different models were evaluated for predicting the carbon dioxide surface tension. The first model ($\sigma_\infty(T)$) extrapolated the existing liquid data past the triple point as a function of temperature. The second model (σ_r) used the relationship developed by Tolman[29] for small cluster radii. This model suggests that the small-cluster surface tension lies below its bulk value. The expression is given by Wegener[26] as

$$\frac{\sigma_r}{\sigma_\infty(T)} = \frac{1}{1+2\delta/r} \qquad (20)$$

where σ_r is the cluster surface tension, σ_∞ is the extrapolated flat-plane surface tension at temperature T, r is the cluster radius, and δ is a constant for a given liquid which is about equal to the intermolecular spacing.

The value of 1 Å was selected in this work. The third model was based the enthalpy-density ratio method for scaling liquid to solid surface tension as suggested by Wu[14]. This model was found to produce significantly lower surface tension values than either of the other models and so was disregarded. Finally, parametric variations of the σ_∞ model were used to check the sensitivity of the computations to this parameter.

Numerical Results-Comparison to Experiment

Q1D solutions were computed using both of the effective 1D area distributions discussed above. These solutions were then compared with experimental wall pressure data. The non-condensing Q1D solutions using the displacement-thickness-corrected area distribution produced static pressure values that were substantially lower than both the axisymmetric NS solution and the experimental data. Consequently, the area distribution derived from the NS solution wall pressure data were used for subsequent calculations. Since this area distribution closely reproduces the static pressure values experienced by the flow streamtube near the nozzle wall, it should provide more accurate gasdynamic state data for the condensing flow calculations.

All solutions presented here were computed for the nominal tunnel operating conditions of Po=6.89 MPa and To=815 K. In order to show the sensitivity to surface tension, Figure 14 presents the non-condensing and Q1D condensing solutions for ω_0=.007 using three different surface tension models, $\sigma = \sigma_r$, $0.9\sigma_\infty$, and $0.95\sigma_\infty$. The abcissa is the distance along the nozzle and the ordinate is the static/total pressure ratio. The arrows indicate the departure of the condensing flow pressure from the isentropic value. Note that the lower surface tension values of the σ_r model causes the condensation induced disturbance to appear further upstream as noted by the departure of the pressure values from the isentropic (ω_0=0.0) case. In addition, the static pressure change at the nozzle exit is slightly lower than that observed with the $0.9\sigma_\infty$ case (higher surface tension value). In both of these cases over 99.9% of the CO_2 has condensed out. However, since the heat release occurred at a lower supersonic Mach number for the σ_r case, a smaller total pressure loss and static pressure perturbation resulted at the nozzle exit. This behavior is fully consistent with that observed in Rayleigh flow situations where the strength of the perturbation is proportional to both the quantity of heat released and the Mach number at which the heat release takes place. This is readily illustrated in treatments of the Rayleigh flow problem such as that given by Shapiro[30].

The reason for the difference in behavior between the first two cases is that the lower surface tension value allows nucleation to begin sooner and higher nucleation rates are attained. The third case is interesting in that it shows almost no change in pressure. In this case the higher surface tension suppresses the nucleation rate sufficiently that only 20% of the available vapor is able to condense before the end of the nozzle and this is not sufficient to produce a significant change in the static pressure.

Figure 15 presents non-condensing and condensing solutions computed with $0.9\sigma_\infty$ for two different seeding rates, ω_0=.007 and .0157. Note that the experimental wall pressure values were averaged over several runs since the number of data points in any single run at any single nozzle station were limited due to port sampling procedures. These results show that the condensation onset is well predicted. The pressure rise due to heat release is accurate for ω_0=.007 but is somewhat overpredicted for the higher seeding rate. The need to use a scaling of the extrapolated liquid surface tension values is reasonable given the lack of experimental data on that parameter. This agreement is actually quite remarkable given the assumptions involved in the development of the model and the uncertainty in thermodynamic properties. Yet this is typical of the efficacy of this Q1D approach.

Figure 16 presents the nucleation rate, cluster number density, condensate mass fraction, and Mach number versus position along the nozzle for the Q1D solution with ω_0=.007 and $0.9\sigma_\infty$. The behavior of the mass fraction curve indicates that much of the vapor condenses due to nucleation rather than growth processes. Also note that the nucleation begins at a flow Mach number of M_n=5.64 whereas the condensation effects are first observed due to a pressure rise at a condensation Mach number of M_c=6.6. The saturation Mach number for this seeding rate was given in Figure 2 as M_s=5.2. Figure 17 shows the radius and number of molecules in the critical sized clusters and the surface-averaged or "mean" radius through the nucleation zone. Most of the clusters have an initial radius of 4-5 Å and contain on the order of 10-15 molecules. Since the nucleation zone is relatively short and the clusters are nominally the same size, there should be little change in the size distribution due to growth. This implies that the condensate clusters are nearly monodisperse. This is consistent with the observations of Wegener[11], Lai[17] and Turner[31] for other gas/vapor systems.

Table 4 presents a comparison of the pressure and Mach number perturbation produced by CO_2 condensation for each of the seeding rates. This is presented as the %difference between the non-condensing and the condensing solution. The experimental wall pressure perturbation is also listed. This table indicates that the smallest disturbance occurs for ω_0=.007 and this seeding rate will reduce the test Mach number by roughly 3.6%. Thus at the lowest seeding level employed for this study, the perturbation produced by this seeding technique, while not inconsequential, is certainly small. More importantly, this study demonstrates that the Q1D model provides the ability to predict these perturbations with reasonable confidence, at least within the range of conditions studied thus far.

It is important to note that these predictions are fully consistent not only with the wall pressure measurements, but also with the Rayleigh scattering behavior observed in optical measurements of the flowfield. Qualitative polarization investigations revealed the scattering to be in the Rayleigh range. Quantitative measurements by Wu[32] indicated that the mean radius of the clusters was less than 10 nm. Those experiments were conducted at a substantially higher seeding rate than was employed here. Thus the mean radius value of 2-3 nm predicted with this model is consistent with those observations.

Based on these results, it is clear that the L-P nucleation model is the proper choice for the air/CO_2 vapor mixture. Use of the classical model would reduce the nucleation rate by ~10^{16}, producing little nucleation at all. These results are in contradiction to the results of Duff[25] wherein the classical model provided good agreement. It is the authors' contention that Duff's agreement with the classical model is a result of the carbon dioxide surface tension model he used. Figure 18 shows the surface tension curve fit used by Duff, the fit used in the current study, and the liquid surface tension data from Duff's reference[34]. Clearly Duff's linear fit underpredicts the data by a significant amount, ~ 25-30 % for the temperature range of his experiments. A surface tension increase by this amount would have caused the classical model to severely underpredict the nucleation rate in Duff's experiments. Thus, had Duff used a more credible fit to existing data, the L-P model would have provided a much better comparison.

CONCLUSIONS

Experimental and numerical investigations have been conducted to quantify the effects of carbon dioxide condensation on the fluid mechanics of an air/carbon dioxide mixture in an axisymmetric hypersonic nozzle expansion. Nozzle wall pressures and nozzle exit pitot surveys were used to evaluate the change in flow properties as a function of CO_2 seeding level. As expected, the wall static pressures increased with seeding level due to heat released in the condensation process, and the pitot surveys were relatively insensitive to seeding. Numerical studies demonstrated that the non-condensing flow behavior can be credibly predicted using an axisymmetric NS solution. Effective 1D area distributions were derived from these solutions. A Q1D noneqilibrium flow model was developed to predict the effects of condensation. Provided reasonable scaling of the extrapolated liquid surface tension values is allowed, this model predicts the onset location very accurately and provides a good estimate of the magnitude of the pressure perturbation due to condensation, especially at the lower seeding rate. In contrast to previous work using pure carbon dioxide, this study demonstrates the applicability of the Lothe-Pound nucleation model over the classical model for this carrier gas/vapor system. The resulting analyses indicate that condensed-phase formation is primarily due to nucleation rather than growth. These analyses also reveal that the condensate is composed of a narrow distribution of very small clusters having a mean radius of nominally 2.4 nm. This supports previous FRS observations that the scattering particles are in the Rayleigh size range.

REFERENCES

1. Duff, K.M., Hill, P.G., "Condensation of Carbon Dioxide in Supersonic Nozzles," in Proceedings of the 1966 Heat Transfer and Fluid Mechanics Institute, Edited by Saad, M.A., © 1966, Stanford University Press.

2. Erbland, P.J., et. al., "Development of Planar Diagnostics for Imaging Mach 8 Flowfields Using Carbon Dioxide and Sodium Seeding," AIAA-97-0154, 35th Aerospace Sciences Meeting, 6-10 January, 1997.

3. Smith, D.R., Poggie, J., Konrad, W., Smits, A.J., "Visualization of the Structure of Shock Wave Turbulent Boundary Layer Interactions Using Rayleigh Scattering," AIAA-91-0651, January 1991.

4. Alvi, F.S., Settles, G.S., "Physical Model of the Swept Shock Wave/Boundary-Layer Interaction Flowfield," AIAA J., Vol. 30, No. 9, Sept. 1992.

5. Elliott, G.S., Samimy, M., Arnette, S.A., "Study of Compressible Mixing Layers Using Filtered Rayleigh Scattering Based Visualizations," AIAA J., Vol. 30, No. 10, October 1992.

6. Cogne, S., Forkey, J., Lempert, W.R., Miles, R.B., and Smits, A.J., "The Evolution of Large-Scale Structures in a Supersonic Turbulent Boundary Layer," FED-Vol. 151, ASME Fluids Engineering Conference on Transitional and Turbulent Compressible Flows, Washington, D.C., June 20-24, 1993.

7. Poggie, J., Smits, A.J., "Quantitative Visualization of Supersonic Flow Using Rayleigh Scattering," AIAA-96-0436. Jan., 1996.

8. Wegener, P.P., Mack, L.M., "Condensation in Supersonic and Hypersonic Wind Tunnels," Advances in Applied Mechanics V, © 1958, Academic Press.

9. Hill, P.G., "Condensation of Water Vapour During Supersonic Expansion in Nozzles," J. Fluid Mech. Vol. 25 (3), pp. 593-620, 1966.

10. Abraham, F.F., *Homogeneous Nucleation Theory, The Pretransition Theory of Vapor Condensation*, Supplement 1, Advances in Theoretical Chemistry, © 1974, Academic Press, Inc.

11. Ryzhov, Y.A., Pirumov, U.G., Gorbunov, V.N., Nonequilibrium Condensation in High-Speed Gas Flows, © 1989 by OPA (Amsterdam) B.V.

12. Wegener, P., Stein, G.D., "Light Scattering Experiments and Theory of Homogeneous Nucleation in Condensing Supersonic Flow," 12th International Symposium on Combustion, © 1969, The Combustion Institute.

13. Wegener, P.P., Clumpner, J.A., Wu, B.J.C., "Homogeneous Nucleation and Growth of Ethanol Drops in Supersonic Flow," Phys. Fluids, Vol. 13 (11), Nov. 1972.

14. Wu, B.J.C., Wegener, P.P., Stein, G.D., "Condensation of Sulfur Hexaflouride in steady supersonic nozzle flow," J. Chem. Phys, 68(1), 1 Jan 1978.

15. Schnerr, G.H., "Two-Phase Flows with Phase Transition," VKI Lecture Series 1995-06, © 1995, the von Karman Institute.

16. Perrell, E.R., Erickson, W.D., Candler, G.V., "Numerical Simulation of Nonequilibrium Condensation in a Hypersonic Wind Tunnel," J. Thermophysics 10 (2), June 1996.

17. Lai, D.S., Kadambi, J.R., "Monodisperse Droplet Generation by Spontaneous Condensation of Steam Flow in Nozzles," Particlulate Science and Technology 8:55-75, 1990.

18. Pope, A., Goin, K.L., High-Speed Wind Tunnel Testing, John Wiley & Sons, New York, © 1965.

19. Matthews, R.K., "Hypersonic Flow Field Measurements - Intrusive," in Methodology of Hypersonic Testing, VKI Lecture Series 1993-03, February, 1993.

20. Aerosoft Inc., "*The General Aerodynamic Simulation Program Version 3 Users Manual*," Blacksburg Virginia, 1996.

21. Baumgartner, M.L., *Turbulence Structure in a Hypersonic Boundary Layer*, PhD Thesis, Department of Mechanical and Aerospace Engineering, Princeton University, June 1997.

22. Tilmann, C.P., Bowerson, R.D., Buter, T.A., "On the Design and Construction of an Academic Amch 5 Wind Tunnel," Paper AIAA-99-0800, 37th AIAA Aerospace Sciences Meeting, Jan 1999, Reno, NV.

23. Jentink, T., "CFD Validaton for Nozzle Flowfields," AIAA-91-2565, AIAA 27th Joint Propulsion Converence, June 1991, Sacramento, CA.

24. Fernholz, H.H., Finley, P.J., "A Critical Commentary on Mean Flow Data for Two-Dimensional Compressible Turbulent Boundary Layers," AGARD-AG-253, May 1980

25. Duff, K.M., *Non-Equilibrium Condensation of Carbon Dioxide in Supersonic Nozzles*, PhD Dissertation, MIT, Jan 1966.

26. Wegener, P.P., "Gasdynamics of Expansion Flows with Condensation, and Homogeneous Nucleation of Water Vapor," in *Non-Equilibrium Flows, Part I*, Wegener, P.P. editor, © 1969, Marcel Dekker, Inc.

27. Frenkel, J., *Kinetic Theory of Liquids*, © 1946, Oxford University Press

28. Lothe, J., Pound, G.M., "Reconsiderations of Nucleation Theory," J. Chem. Phy., Vol. 36 (8), April 1962

29. Tolman, R.C., J. Chem. Phys. Vol. 17 (33), 1949.

30. Shapiro, A.H. *The Dynamics and Thermodynamics of Compressible Fluid Flow*, © 1953, The Ronald Press Co.

31. Turner, J.R., Kodas, T.T., Sheldon, K.F., "Monodisperse Particle Production by Vapor Condensation in Nozzles," J.Chem.Phys. 88 (1), 1 Jan 1988.

32. Wu, P.F., MHz-Rate Pulse-Burst Laser Imaging System: Development and Application in the High-Speed Flow Diagnostics, PhD Thesis, Department of Mechanical and Aerospace Engineering, Princeton University, June 2000.

33. Kalafati-Ragozin, D.D."Analysis of the Thermodynamic Properties of Carbon Dioxide in the Region of Sublimation," Thermal Engineering, Vol. 41, No. 11, 1994.

34. Quinn, E.L.. Jones, C.L., Carbon Dioxide, © 1936, Reinhold Publishing Corp.

35. Din, F., Thermodynamic Functions of Gases, Volume 1, © 1962, Butterworth & Co. Ltd.

36. Bryson, C.E., Cazcarra, V. Levenson, L.L., "Sublimation Rates and Vapor Pressures of H20, CO2, N2O, and Xe," J. of Chemical and Eng. Data, Vol. 19, No. 2, 1974.

37. Weida, M.J., Sperhac, J.M., Nesbitt, D.J., "Sublimation Dynamics of CO_2 Thin Films: A High Resolution Diode Laser Study of Quantum State Resolved Sticking Coefficients," J. Chem. Phys., Vol. 105, No. 2, July 1996.

APPENDIX 1

This appendix presents the set of coupled ordinary differential equations used in the Q1D nonequilibrium model. Further information may be obtained from several of the references[1,8,9].

The integro-differential equation describing the rate of moisture (condensate) formation along the nozzle was derived by Hill[9]. This leads to the first four coupled ordinary differential equations, which take the form:

$$\frac{dY_1}{dx} = 8\pi JA$$

$$\frac{dY_2}{dx} = Y_1 \frac{1}{u}\frac{dr}{dt} + r_o dY_1$$

$$\frac{dY_3}{dx} = Y_2 \frac{1}{u}\frac{dr}{dt} + JA(4\pi r_o^{\,2})$$

$$\frac{dg}{dx} = \frac{\rho_c}{\rho A u}\left[Y_3 \frac{1}{u}\frac{dr}{dt} + JA(\frac{4}{3}\pi r_o^{\,3})\right].$$

The variables Y_1-Y_3 are dummy variables used in the solution of the condensate formation rate equation. Variable g is the condensate mass fraction and r_o is the initial size of new (critical) clusters at each step in the solution. The other variables are described in the text.

The remaining equations are derived from the gas dynamic relationships. The principle difference to be noted relative to Duff[8] and Hill[9] is the inclusion of terms which account for the properties of the gas-vapor mixture. These equations can be expressed as:

$$\frac{dP}{dx} = P\frac{\left[\left[\frac{L}{c_{po}T} - \frac{\mu_m}{\mu_v(1-g)}\right]\frac{dg}{dx} - \frac{1}{A}\frac{dA}{dx}\right]}{1-(1-g)\left[\frac{c_p}{c_{po}}\frac{(\gamma-1)}{\gamma} + \frac{1}{\gamma M^2}\right]}$$

$$\frac{dT}{dx} = T\left[\frac{L}{c_{po}T}\frac{dg}{dx} + \frac{c_p}{c_{po}}\frac{(\gamma-1)}{\gamma}(1-g)\frac{1}{P}\frac{dP}{dx}\right]$$

$$\frac{dM}{dx} = M\left[-\frac{(1-g)}{\gamma M^2}\frac{1}{P}\frac{dP}{dx} - \frac{1}{2T}\frac{dT}{dx} + \frac{[(\mu_m/\mu_v)-1]}{2(1-g)}\frac{dg}{dx}\right]$$

The numerical algorithm uses these 7 equations, the auxiliary relations for γ, μ_m, c_p, and u which are presented in the text, the specified area distribution, physical property data for the gas and condensate, and appropriate initial conditions to solve the one-dimensional condensing flow problem.

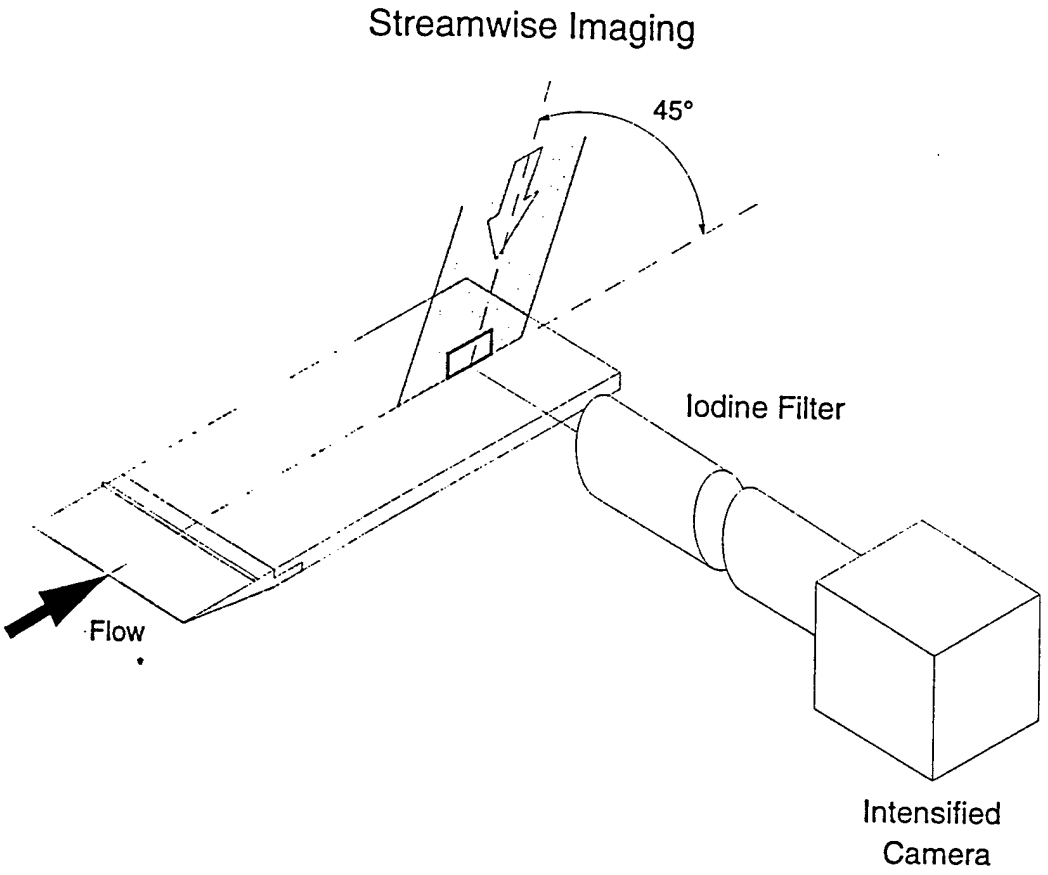

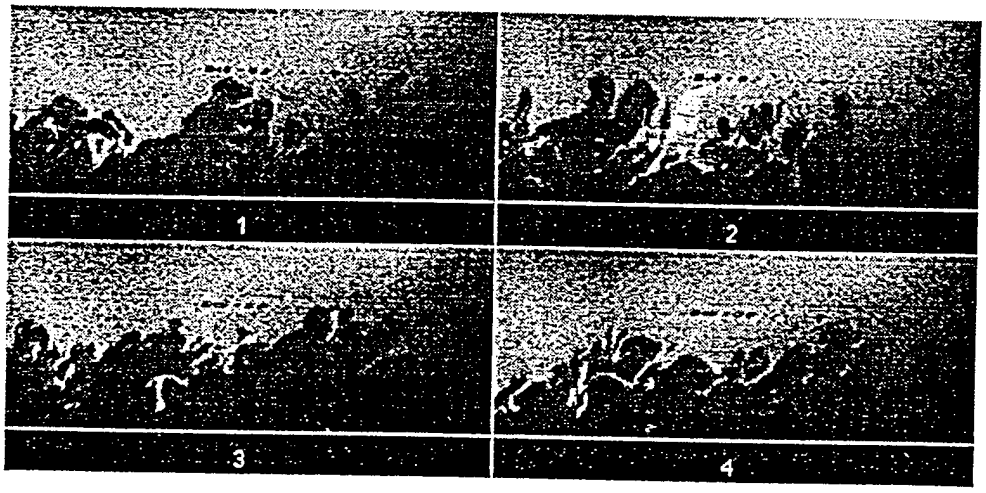

Figure 1. Schematic of turbulent boundary layer imaging using carbon dioxide enhanced Filtered Rayleigh Scattering (FRS). The upper panel shows the laser sheet and camera orientation for imaging a streamwise section of the boundary layer at the surface of a flat plate. The lower panel shows typical images of the boundary layer recorded along the centerline for Po=1000 psia and To=800° K. Flow is from left to right and the white line marks the surface of the model.

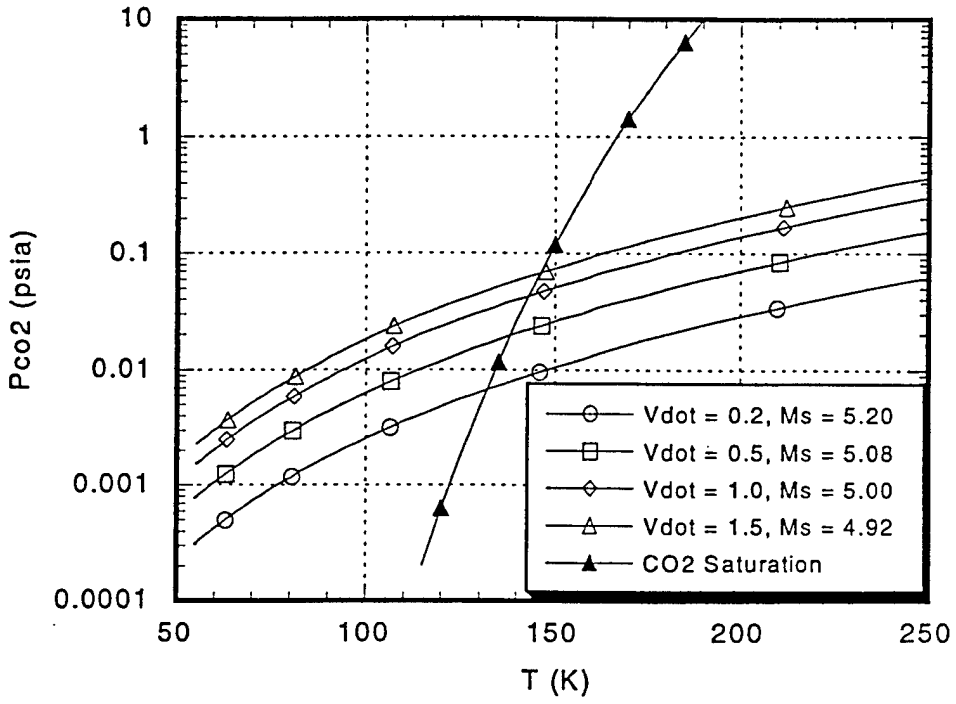

Figure 2. CO_2 solid/vapor saturation curve and flow isentropes for various CO_2 seeding levels. Ms is the saturation or equilibrium condensation Mach number. To the left side of the saturation curve CO_2 is solid and to the right it is a vapor.

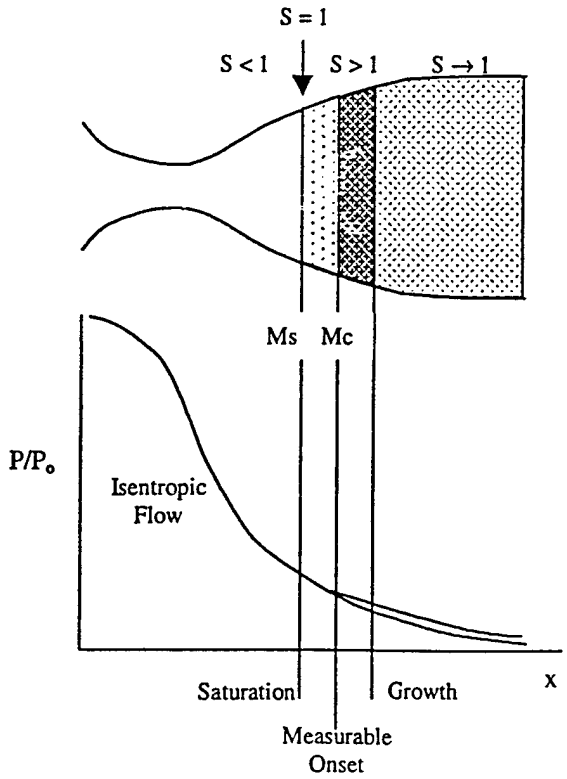

Figure 3. Schematic of the condensation process in a hypersonic nozzle.

Volume Flow Parameter	Mass Fraction	Mole Fraction
0.2	.0070	.0046
0.5	.0157	.0104
1.0	.0348	.0232

Table 1. CO_2 seeding levels at reference test conditions of Po = 6.89 Mpa and To = 825K.

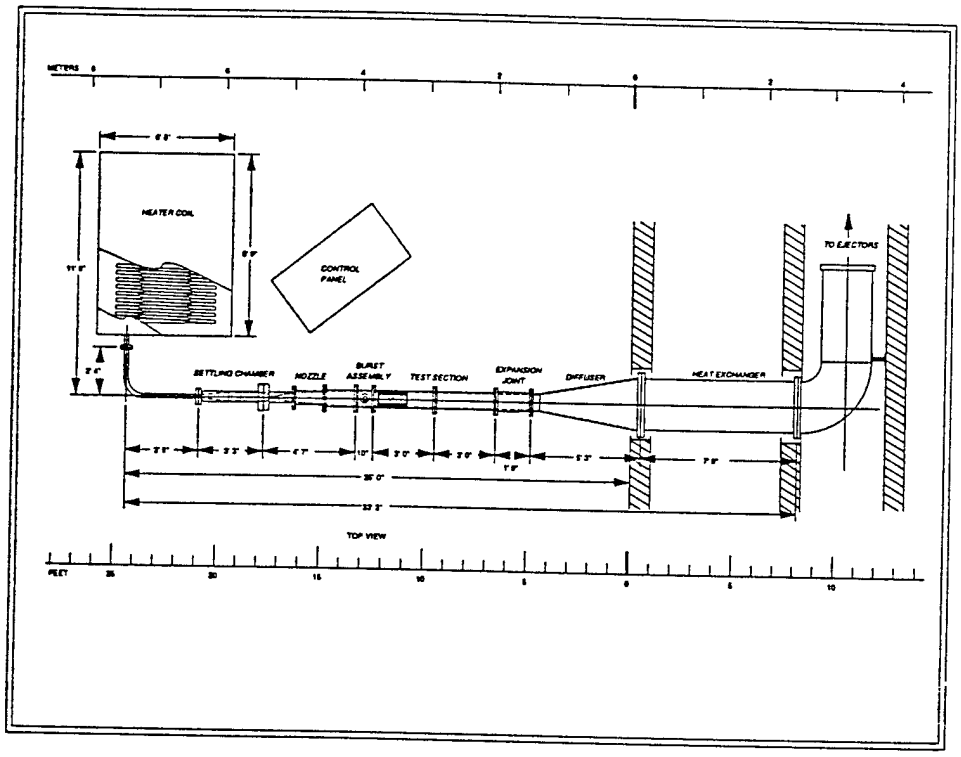

Figure 4. Schematic of the Mach 8 test facility.

P_0 (Pa)	T_0 (K)	M_∞	$\dot{m}$ (kg/s)	p_∞ (Pa)	T_∞ (K)	Re_∞ (1/m)
6.89e6	825	8.0	1.66	706.	60.	1.29e7

Table 2. Nominal "reference" test conditions for both non-condensing and condensing experiments. Free stream parameters will change due to condensation induced heat release.

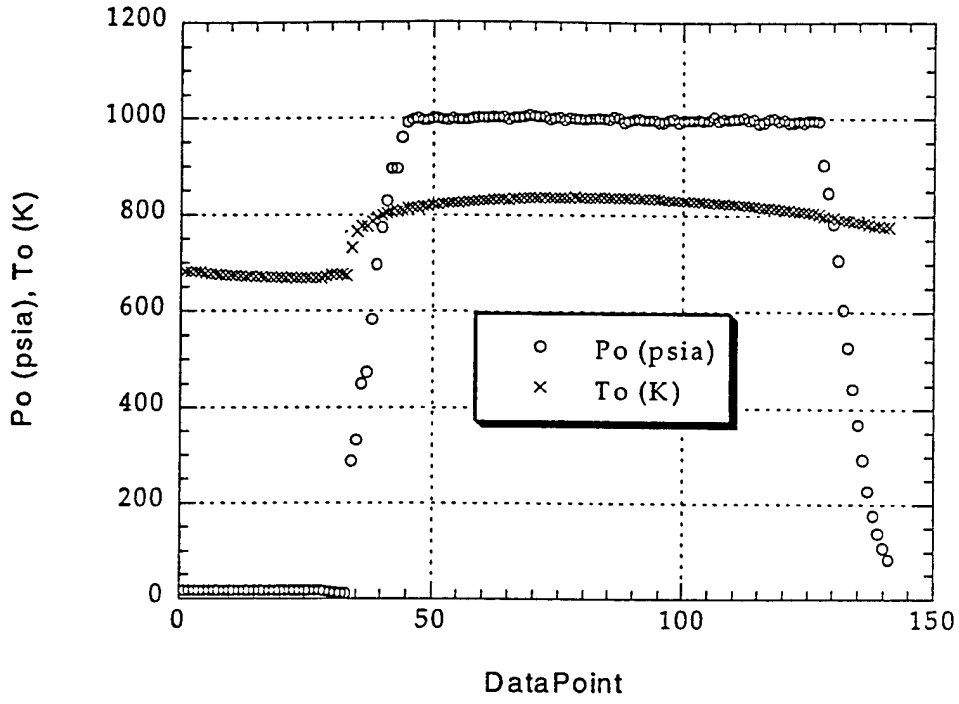

Figure 5. Variation in total temperature and pressure during a typical test.

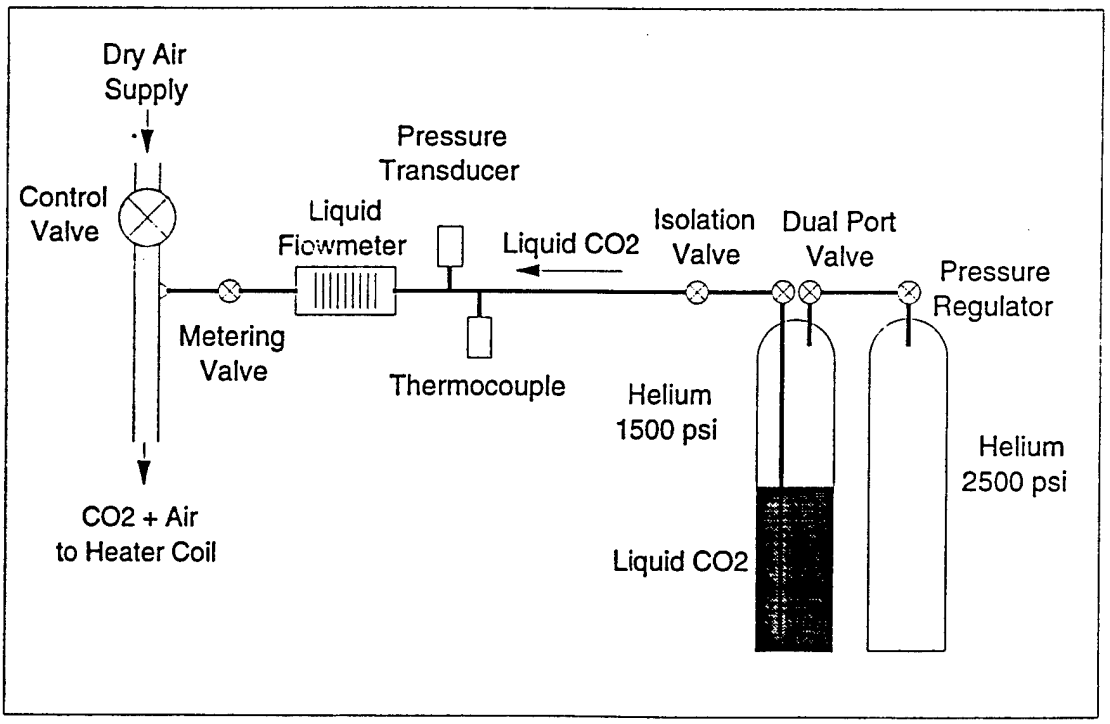

Figure 6. Schematic of the carbon dioxide flow seeding system.

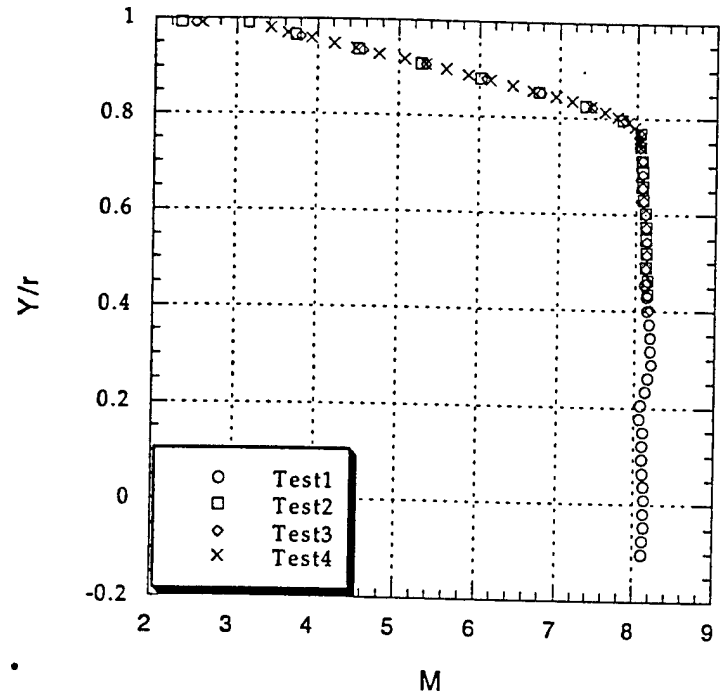

Figure 7. Non-condensing Mach number distribution for the upper half of the nozzle at the exit plane.

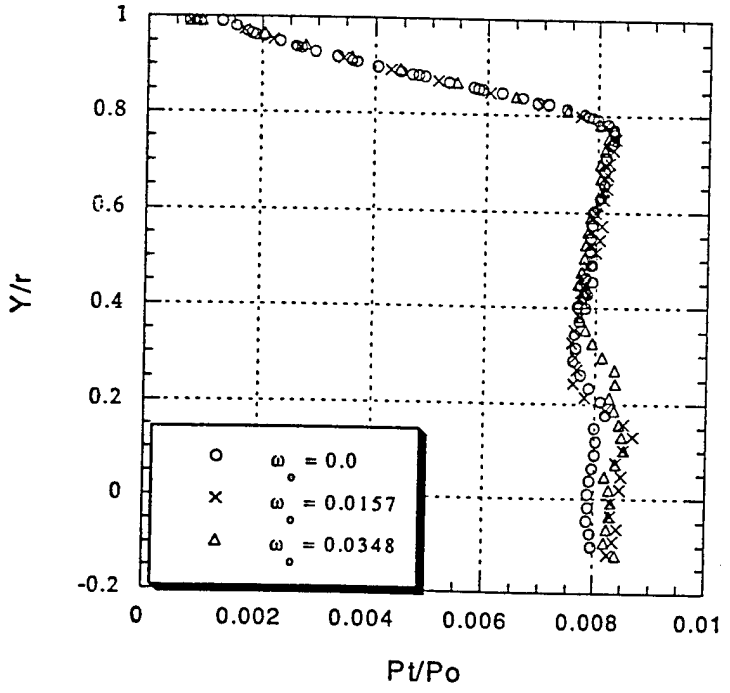

Figure 8. Pitot pressure ratio at the nozzle exit for unseeded and seeded flow. Seeding mass fraction is noted in the legend. Little change is apparent in the wall region though a 5-6% change was observed in the core. In an isentropic flow this would correspond to a decrease of ~0.1 Mach in this region.

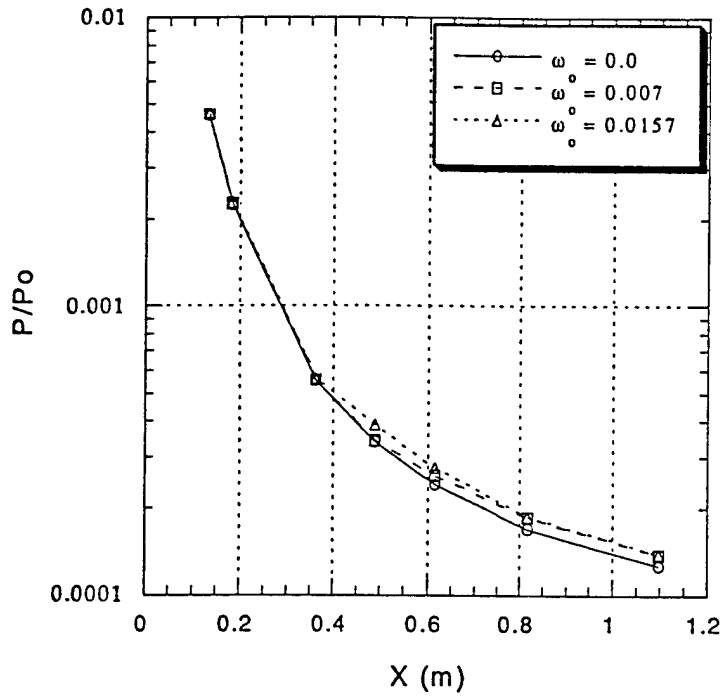

Figure 9. Nozzle wall pressure increase due to vapor condensation. Seeding rates are noted in the legend. Note that the start of condensation moves upstream as seed fraction is increased.

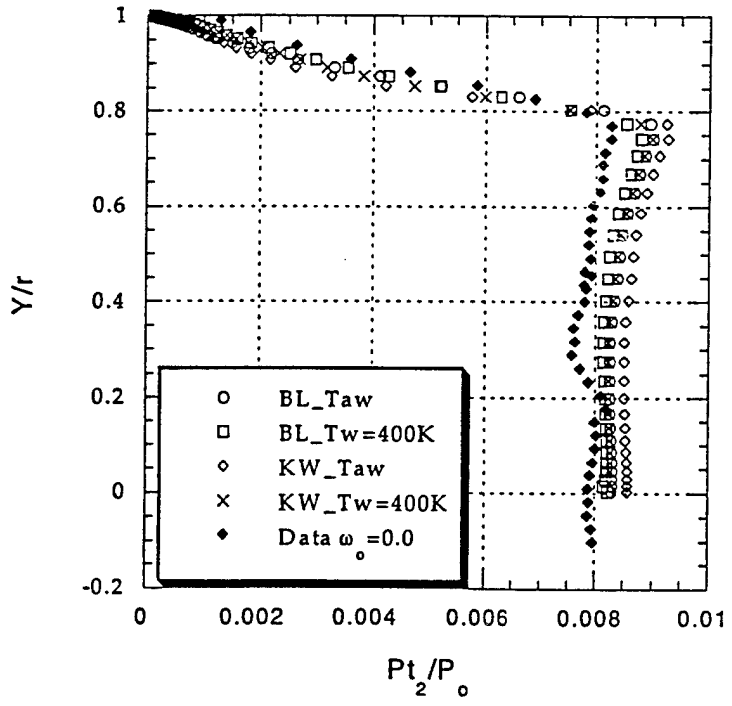

Figure 10. Comparison of NS solutions with experimental data at nozzle exit plane. BL and KW indicate that the Baldwin-Lomax and K-ω turbulence models were used in the respective solutions. Taw and Tw indicate adiabatic wall temperature and specified wall temperature boundary conditions.

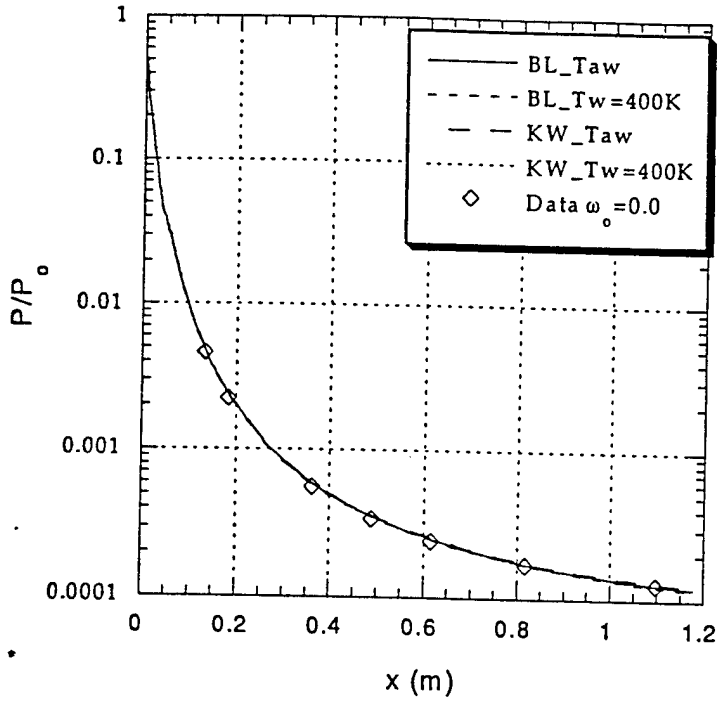

Figure 11. Comparison of computational and averaged experimental wall pressure data showing that all numerical solutions recover the gross behavior of the nozzle expansion. Legend abbreviations are described in figure 10.

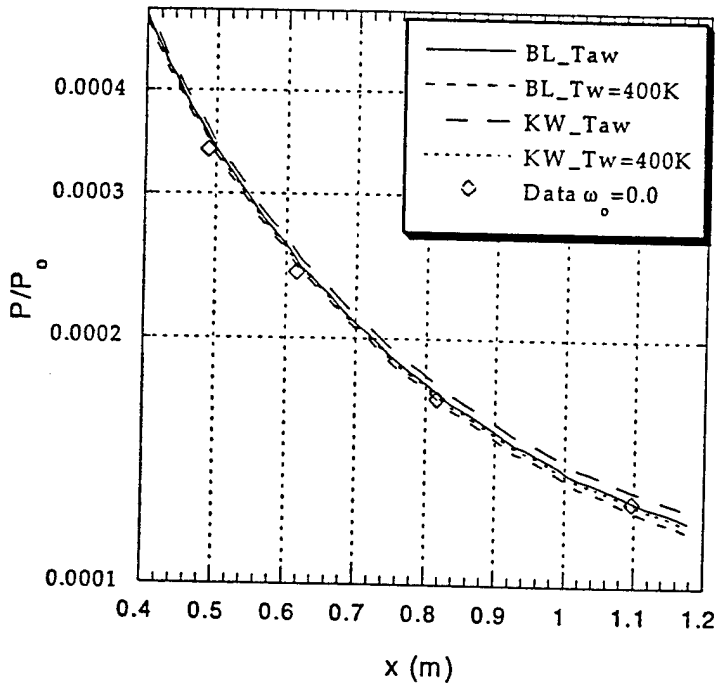

Figure 12. Comparison of computational and averaged experimental wall pressure data for the downstream portion of the nozzle. The Baldwin-Lomax adiabatic wall results were used for the condensing flow analysis. Legend abbreviations are described in figure 10.

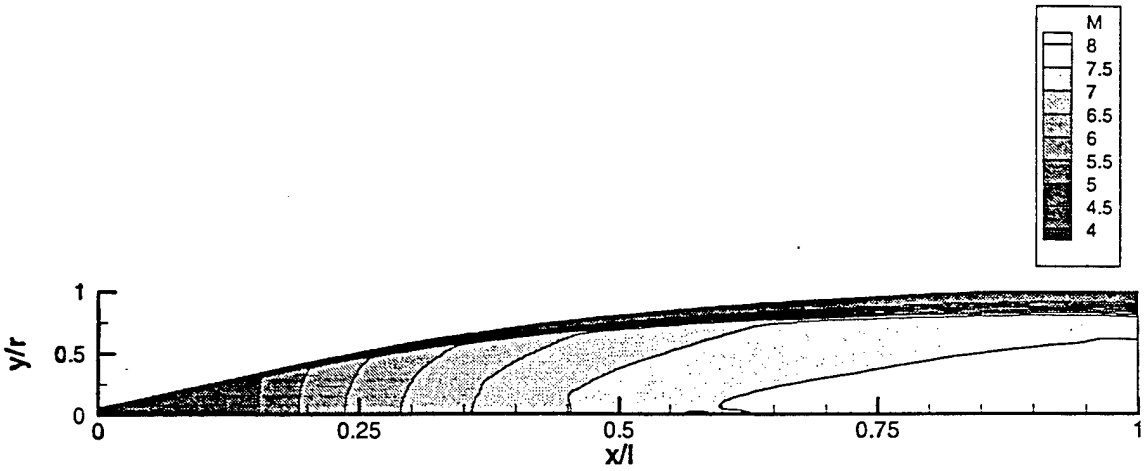

Figure 13. Nozzle Mach number contours for the NS solution using the Baldwin-Lomax turbulence model and an adiabatic wall.

Parameter	Value/Fit	Source
c_{pa} @ 273.15K	1.003 (kJ/kgK)	
c_{pv} @ 273.15K	0.827 (kJ/kgK)	
$L[T(K)]$ (solid)	587.08 + 1.2989*T - 1.7877e-2*T^2 + 9.4026e-5*T^3 - 1.9876e-7*T^4 (kJ/kg)	Kalafati-Ragozin[33]
$\sigma_{\infty}[T(C)]$ (liquid)	(4.648-0.17783*T + 8.876e-4*T^2 - 1.214e-6*T^3) *1e-3 (N/m)	Quinn[34]
ρ_c (solid)	1662.3 + 2.0495*T - 3.7767e-2*T^2 + 2.1973e-4*T^3 - 4.7933e-7*T^4 (kg/m^3)	Din[35]
$p_s[T(K)]$ (solid)	10exp(12.713 - 1443.1/T), $T \le 100K$ 10exp(12.156 - 1384.2/T), $100 < T \le 140K$ 10exp(12.015 - 1364.5/T), $140 < T \le 216K$	Bryson[36], Kalafati-Ragozin[33]
α	1.0	Bryson[36], Weida[37]

Table 3. Carbon Dioxide property data used for Q1D solutions.

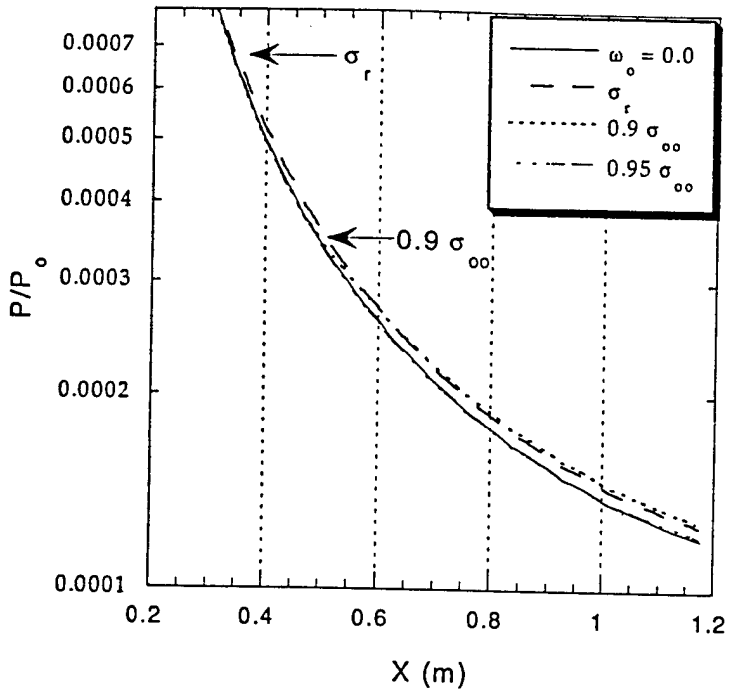

Figure 14. Comparison of Q1D predicted nucleation behavior for a seeding mass fraction of ω_o=.007 using different surface tension models. Lower σ produces higher nucleation rates and allows nucleation sooner in the nozzle.

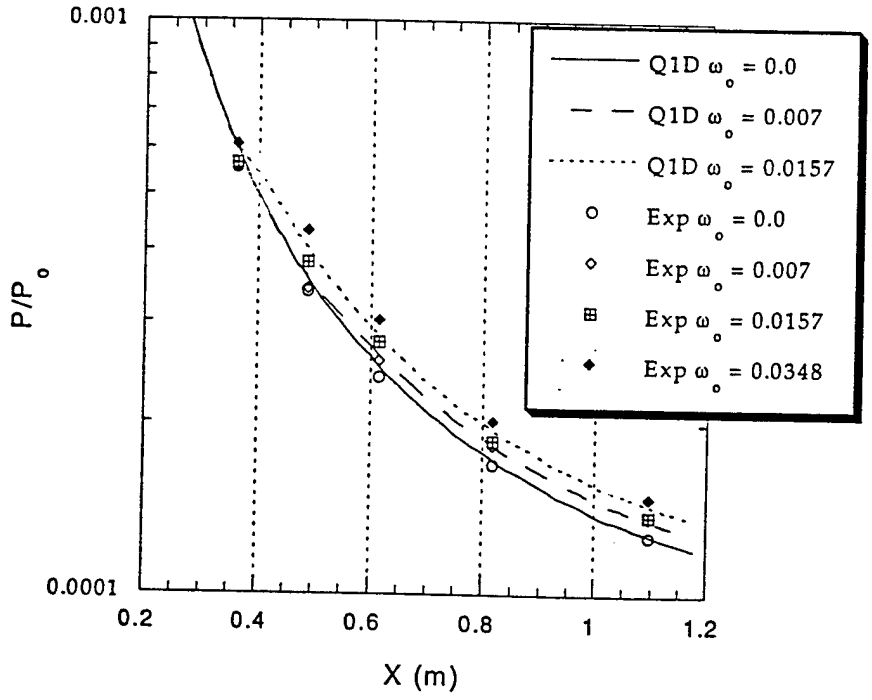

Figure 15. Comparison of experimental and Q1D pressure distributions for several flow seeding rates. Condensation onset is well predicted. Pressure rise due to heat release is accurate for ω_o=.007 but is overpredicted for the higher seeding rates.

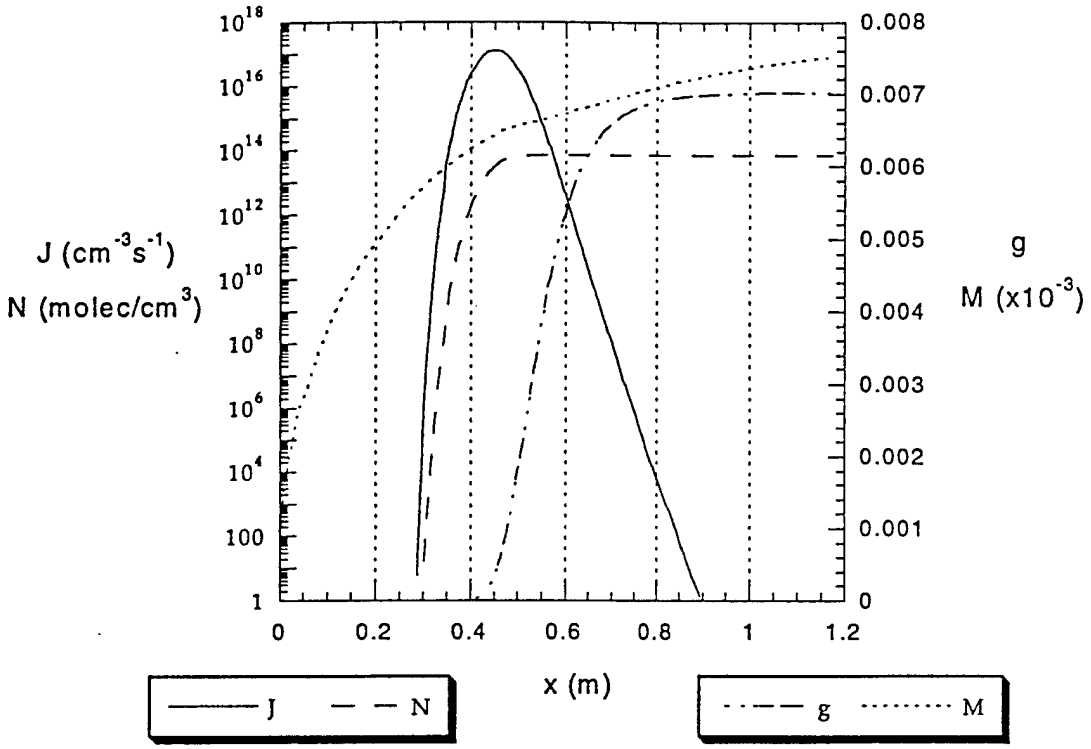

Figure 16. Nucleation rate (J), cluster number density (N), condensate mass fraction (g), and Mach number (M) for seeding mass fraction ω_s=.007.

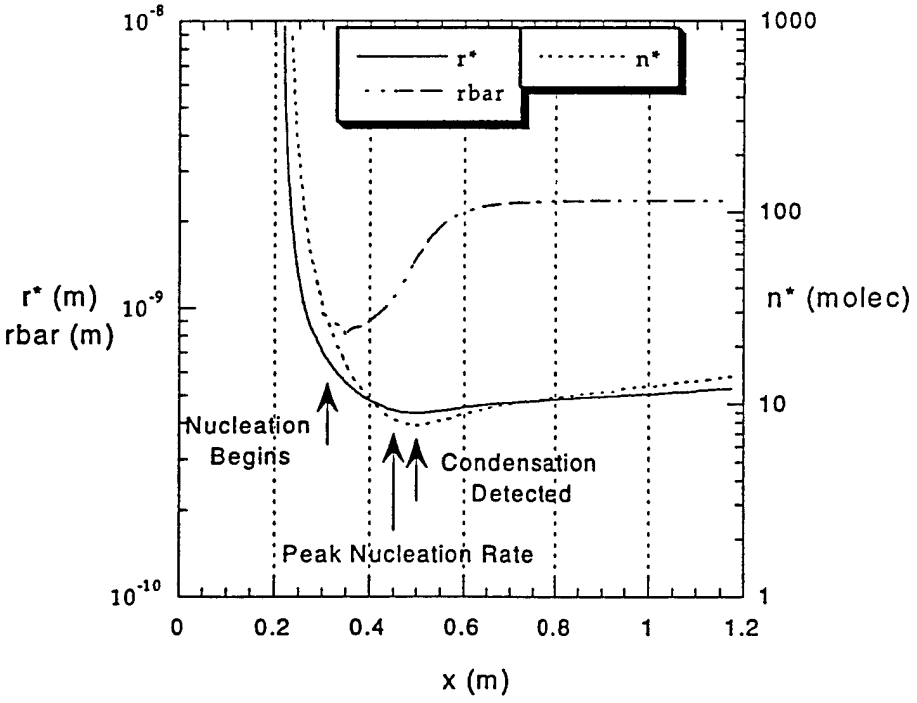

Figure 17. Radius and number of molecules in a critical cluster and surface-averaged (mean) cluster radius from the Q1D analysis for ω_s=.007.

ω_0	$\Delta p/p_{nc}$ (Q1D)	$\Delta p/p_{nc}$ (Exp)	$\Delta M/M_{nc}$ (Q1D)
0.007	6.6 %	7.79 %	3.61 % (decrease)
0.0157	12.74 %	8.54 %	6.9 % (decrease)
0.0384		16.71 %	

Table 4. Comparison of pressure and Mach number perturbation as predicted by Q1D analysis presented as % change in the parameter at the nozzle exit.

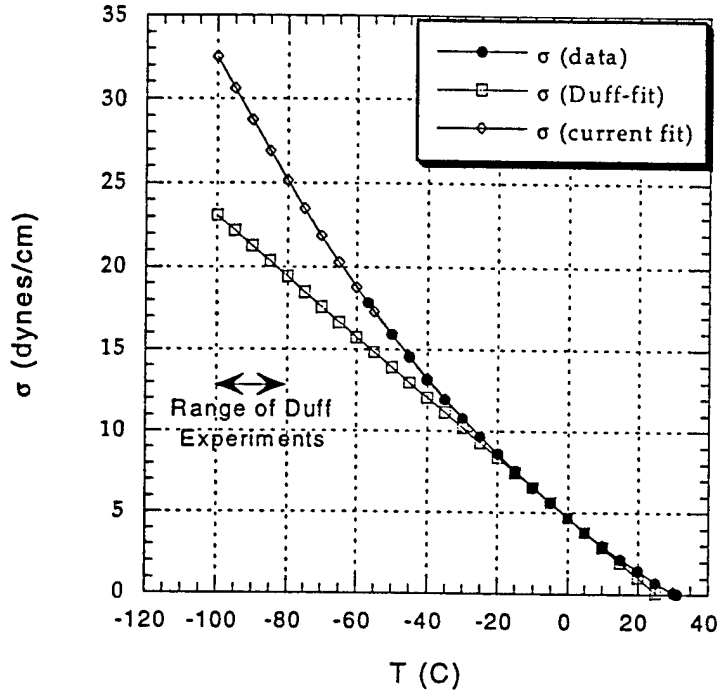

Figure 18. Surface tension data and curve fits used in the work by Duff and in the current effort.

AIAA 2000-2322

Control of Hypersonic Boundary Layers by Helium Injection

B. Auvity, M. Etz, M. Huntley, Pingfan Wu and A. J. Smits
Department of Mechanical and Aerospace Engineering,
Princeton University,
Princeton, NJ 08544

Fluids 2000
19-22 June 2000 / Denver, CO

Control of Hypersonic Boundary Layers by Helium Injection

*B. Auvity, M. Etz, M. Huntley, Pingfan P. Wu and A. J. Smits**

Department of Mechanical and Aerospace Engineering
Princeton University
Princeton, New Jersey 08544-0710

†

Abstract

Results are presented on the control of a zero-pressure gradient Mach 8 boundary layer using low-momentum helium gas injected through a transverse slot. Planar Filtered Rayleigh Scattering and Sodium Laser-Induced Fluorescence were used to study the flow. The boundary layer structure was visualized with and without helium injection in three orthogonal planes. Using a new MHz imaging system, short movies were obtained showing the evolution of the boundary layer downstream of the slot. These sequential images were used to construct volumetric representations of the instantaneous boundary layer behavior. The results indicate that low levels of helium injection can have a substantial effect on the boundary layer structure. Highly organized longitudinal structures develop downstream of the slot and persist for long distances downstream, remaining fixed in their spanwise position. They appear to be streamwise vortices, and it is speculated that they are formed near the injection slot due to local concave streamline curvature.

1 Introduction

Missiles and other high-speed vehicles frequently have on-board optical systems for tracking and imaging. The performance of these devices is seriously degraded by local flow field properties that lead to index-of-refraction variations. Primarily, these arise from density discontinuities across shock waves, and the presence of turbulent free shear layers and turbulent boundary layers. In addition, perturbations can arise from thruster jets, and, at very high velocities, from molecular dissociation, ionization, and excited state atomic and molecular electronic transitions. At supersonic speeds, the major source of optical distortion is from shock waves and boundary layer structure. For tracking applications a primary issue is the variation of "bore-sight" error with missile angle-of-attack. Bore-sight error is the difference between the apparent location of the target and its actual location relative to the missile reference frame. As the missile angle-of-attack varies, the apparent location of the target changes because the light rays are bent as they pass through shock waves and through the boundary layer before entering the window. In addition, density fluctuations in the boundary layer cause image break-up and rapidly varying motions, reducing both image and target resolution.

This paper addresses the possibility of reducing optical distortion by modifying high-speed boundary layer characteristics. In particular, we study slot injection of different gases into a boundary layer in a Mach 8 flow. The experiments use Filtered Rayleigh Scattering (FRS), in combination with a new MHz-rate imaging, pulse-burst laser system, to obtain rapidly sequenced, images of the instantaneous density field.

1.1 The turbulent refractive index field

In a turbulent compressible flow, the flow velocity, density and pressure all vary in space and time. Mean density gradients exist across the boundary layer, which increase in strength with the freestream Mach number. Equally important for the aero-optic problem is the unsteady variation of the density gradients due to turbulent fluctuations, since the refractive index gradients are proportional to the density gradients.

The density variations can be estimated from measurements of the velocity fluctuations using Morkovin's "Strong Reynolds Analogy" (SRA) [1]. This analogy states that, as long as the fluctuations in total temperature are small, the fluctuations in temperature are related to the fluctuations in veloc-

*Associate Fellow, AIAA

ity according to [2]:

$$\frac{T'}{\bar{T}} = (\gamma - 1)\, M^2\, \frac{u'}{\bar{U}}$$

From the ideal gas relationship, $p = \rho RT$, so that for small fluctuations:

$$\frac{p'}{\bar{p}} = \frac{\rho'}{\bar{\rho}} + \frac{T'}{\bar{T}},$$

and it follows that:

$$\frac{\rho'}{\bar{\rho}} = -(\gamma - 1)\, M^2\, \frac{u'}{\bar{U}}.$$

The small perturbation approximations are not too restrictive, and appear to hold true for turbulent boundary layers, even at Mach 8 [3].

It is clear that the level of the density variations depends strongly on Mach number. We see that for subsonic air flows, density fluctuations are very small, at least an order-of-magnitude smaller than the velocity fluctuations. At transonic speeds, however, the optical transmissibility of boundary layers and free shear layers begins to be affected by weak gradients in the mean and instantaneous density field.

At higher Mach numbers, the density gradients rapidly increase in strength. The SRA indicates that the density fluctuations will exceed the velocity fluctuations in magnitude for Mach numbers greater than about 2.2, and at a Mach number of 10 in a perfect gas, the density fluctuations are about 20 times greater in magnitude than the velocity fluctuations. Despite some uncertainties in the SRA [2], it is obvious that the fluctuations in density and its gradients become severe at high Mach numbers. The consequences for optical and other electro-magnetic communications with high-altitude interceptors (Mach numbers of 5 to 12) also become very important.

1.2 The aero-optic problem

Windows for high-speed missiles can be generally classed into two configurations: flush-mounted and domed. The flush-mounted configuration may include internal cooling and often requires external cooling through the injection of helium upstream of the window. The domed configuration protrudes out from the side of the missile and presents a more complicated cooling problem which may also involve the injection of an inert gas such as argon.

Here we study the control of the refractive-index field of a Mach 8 turbulent boundary layer using helium injection to help understand and possibly reduce the distortion of images and communication signals experienced in high-speed flight. To improve the optical transmissibility of high-speed turbulent shear layers, it is necessary to modify the characteristics of the turbulence, especially the large-scale motions since they represent coherent variations of density, and therefore refractive index. This may be done by either eliminating the presence of the large-scale structures altogether, or by modifying their behavior in some way so that their influence is reduced or so that it becomes predictable in a spatial and temporal sense.

1.3 Control by helium injection

Eliminating the large-scales seems a difficult task. If all production of turbulence ceased, the large scales would decay with a time constant given by the eddy's energy content divided by its rate of dissipation. Consequently, the large-scale motions have very long time scales, since dissipation mechanisms are only effective at the very smallest scales, and the energy cascade to small scales occurs very slowly compared to the lifetime of a typical large-scale motion.

However, we have recently demonstrated the strong stabilizing effects of low levels of helium injection into a Mach 8 transitional boundary layer [4], [5]. The experiments appeared to show that helium injection delays transition indefinitely. The dramatic effects due to the helium injection were clearly evident from single-shot images in a streamwise plane obtained using Filtered Rayleigh Scattering. Interestingly, injection of air at the same location with the same momentum flow rate had no significant effect. While the phenomenon was far from understood, it was speculated that the injection of helium effectively reduces the Reynolds number near the wall (the kinematic viscosity of helium is a factor of 8 higher than that of air at the same temperature). It appeared that transition was delayed, and turbulent mixing was inhibited. In support of this conjecture, sodium fluorescence images clearly showed the presence of a relatively thin, highly stable helium layer near the wall [4].

Here we present more detailed studies of this phenomenon. In particular, a MHz imaging system was used to study the three-dimensional character of the flow field affected by the helium. These new results allowed a more complete understanding of the effects of helium injection on hypersonic boundary layers, and its possible use in aero-optics.

2 Hypersonic Facility and Diagnostic Techniques

2.1 Hypersonic facility

The hypersonic wind tunnel facility used in the experiments consists of four major parts: the high pressure air supply, the heating system, the hypersonic wind tunnel itself, and the ejector system

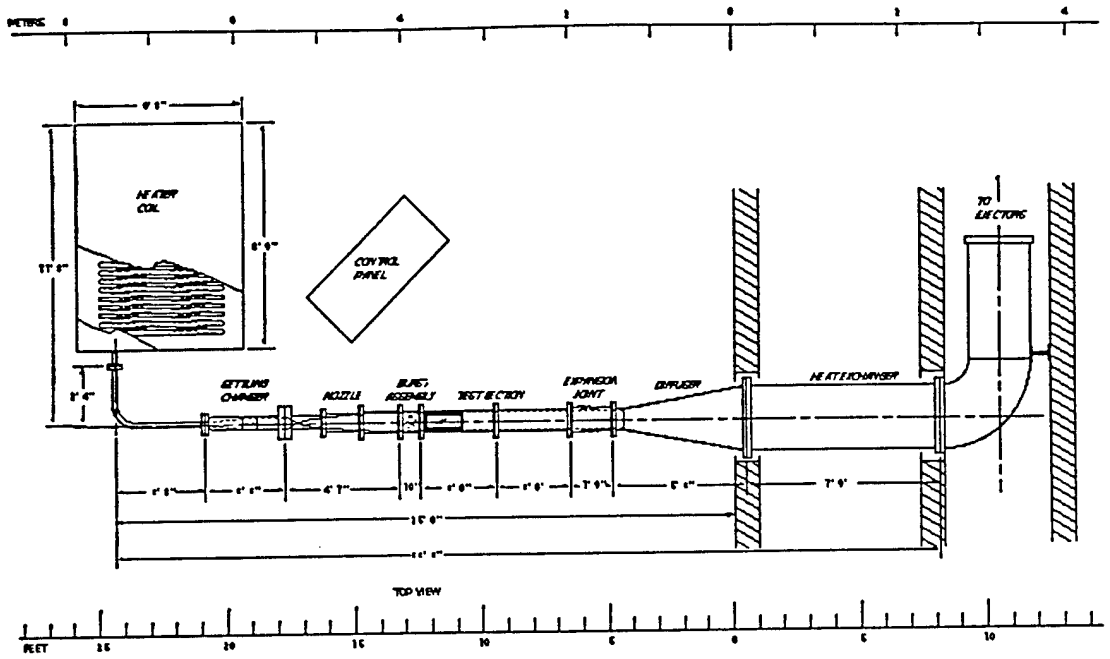

Figure 1: Schematic of the hypersonic facility.

which provides the low back pressures to start and maintain hypersonic flow in the test section. A schematic of the facility is shown in figure 1.

The high pressure air supply consists of four tanks that can store 63 m^3 of air at pressures up to 20 MPa. The air is filtered, cooled and dried to remove particles, oil, and water before it is stored in the tanks.

The axisymmetric test section has an inner diameter equal to 152 mm. The unit Reynolds number in the test section can be varied from 5×10^6 m^{-1} to 20×10^6 m^{-1} by adjusting the stagnation pressure in the settling chamber (between 1.7 MPa up to 10 Mpa) and the stagnation temperature (from 680K to 870K).

At the diffuser inlet, the flow accelerates briefly before being compressed through a complicated shock system (there is no second throat) and then cooled to approximately ambient temperature in the heat exchanger located upstream of the ejectors.

2.2 Injection conditions

The boundary layer developed on a flat plate, shown schematically in figure 2. The plate is 152 mm wide and 470 mm long. It is supported by a sting and placed in the center of the test section. The helium is injected through a slot 25.4 mm long and 1 mm wide, placed 70 mm downstream from the leading edge. A cavity machined inside the plate served as a settling chamber for the injected gas. The stagnation pressure and temperature of the injected gas were measured in this cavity. The flow through the slot was always choked. In the earlier work by Etz [4], a trip wire was placed 59 mm from the leading edge, but in the present study no trip was used.

Etz [4] visualized the helium injection using sodium Laser Induced Fluorescence (LIF), and found it necessary to pre-heat the helium up to $T_{He} \approx 660$K before injection. LIF was not used in the present study, and the helium was not preheated, although aerodynamic heating of the delivery tube that was exposed to the freestream hypersonic flow produced a stagnation temperature $T_{He} \approx 530$K. The maximum stagnation pressure of the injected gas was 40×10^3 Pa.

Studies on circular jets in crossflow have shown that a strong correlation exists between the penetration of the jet into the flow and the ratio of the freestream momentum to the jet momentum. This ratio J, called the injection rate, is defined as follows:

$$J = \frac{(\rho u^2)_{inj}}{(\rho u^2)_\infty} = \frac{(\gamma p M^2)_{inj}}{(\gamma p M^2)_\infty}.$$

Therefore J can also be interpreted as the ratio of the respective dynamic pressures.

Three operating conditions were used (see table 1). Condition 2 is identical to the condition used by Etz [4].

2.3 Diagnostic techniques

Filtered Rayleigh Scattering (FRS) was used to visualize the structure of the boundary layer. Rayleigh scattering is defined as the scattering of light from

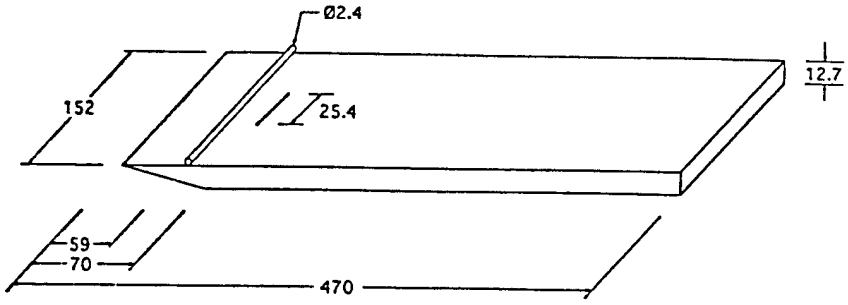

Figure 2: Schematic of the flat plate (dimensions in mm).

	P_0 (MPa)	T_0 (K)	Re#/m
Condition 1	5.81	750	11×10^6
Condition 2	6.92	750	14×10^6
Condition 3	8.30	750	16×10^6

Table 1: Summary of operating conditions.

particles that are of the order of (or less than) the wavelength of light. If the scatterers are individual molecules, then the velocity, temperature, pressure and the density can be determined from the shape and location of the intensity versus frequency curve of the scattered light. If the scatterers are not individual molecules, the static temperature and pressure information may be lost, but other useful information about the flow may still be obtained. Here, as in [4], the scatterers are condensed nanometer-scale particles of CO_2, which are used to enhance the Rayleigh scattering signal. The carbon dioxide was injected upstream of the stagnation chamber in quantities ranging from 0.8% to 2.8% of the tunnel mass flux. As the air-CO_2 mixture cools in the Mach 8 nozzle, the CO_2 condenses and forms nanometer-scale clusters. When the CO_2 clusters become entrained in the boundary layer, aerodynamic heating effects in the boundary layer causes the temperature to rise above the sublimation value and the condensate vaporizes. The boundary layer is therefore imaged as a region of low intensity Rayleigh signal, bounded by bright regions corresponding to freestream fluid. The interface between the hot boundary layer fluid and the cold freestream flow is well-represented by the intensity of the Rayleigh scattering signal since the time scale of the sublimation is small compared to typical time scales of the entrainment process [6]. Probe surveys performed in a laminar hypersonic boundary layer also show that the average position of the interface is located close to δ, where δ is the boundary layer thickness [7]. For supersonic turbulent boundary layers, Nau [8] showed that there is also a high correlation between the instantaneous large-scale motions in the middle and outer region of the boundary layer as revealed by hot-wire signals and Rayleigh scattering images.

The light source used by Etz [4] and in most of the present study is a Nd:YAG laser which pulses at 10 Hz. The duration of each pulse is 10 ns, and for single-image FRS the energy of each pulse is about 100 mJ at 532 nm. The laser sheet thickness was about 0.1 mm. The sheet was placed either perpendicular to the flat plate in the spanwise direction to obtain a spanwise view of the boundary layer, or parallel to the flat plate to obtain a planform view. The field of view was centered on a location 300 mm downstream of the injection slot (figure 3).

Figure 4 illustrates the principle of FRS. The scattering signal is Doppler-shifted by an amount proportional to the velocity of the flow. The magnitude of the shift also depends on the angles between the camera, the laser light direction vector and the predominant flow vector. The largest shift occurs when either the laser or the camera angle is parallel to the flow vector and the remaining component (either the camera angle or the laser direction) is perpendicular to the flow vector. The lineshape of the scattered profile gives information on the temperature and pressure of the flow, and the total intensity of the profile is proportional to the density. The magnitudes of the signals shown in figure 4 are not to scale. Typically, the intensity of the background scattering at the frequency of the laser outweighs the intensity of the scattered signal, and without frequency discrimination, the scattered profile can be overwhelmed by the intensity of the background scattering. In Filtered Rayleigh Scattering, a molecular filter is used to provide this spectral discrimination to screen out the background scattering (figure 4).

3 Earlier Results

Figure 5 shows stagnation pressure and stagnation temperature profiles obtained without injection, with air injection at $J = 0.12$, and with helium in-

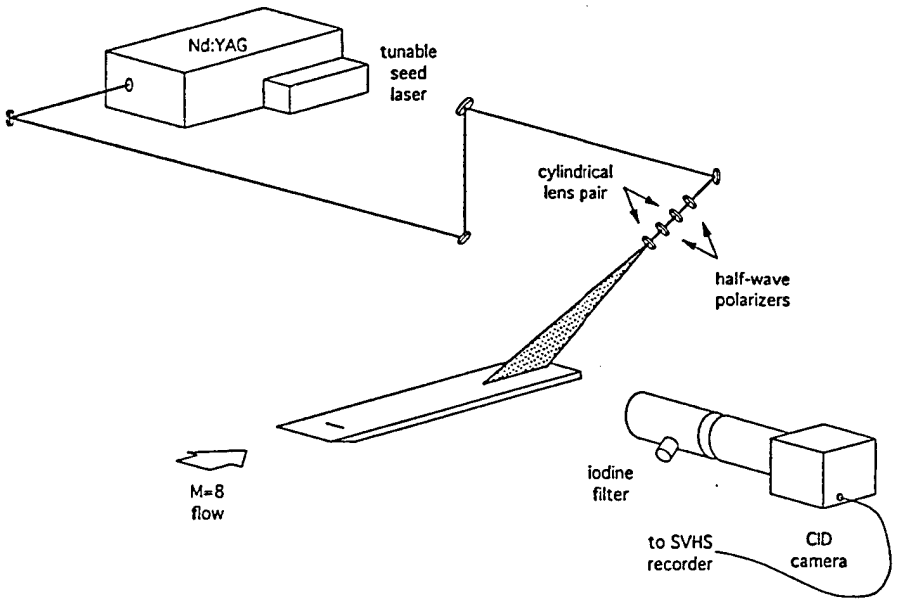

Figure 3: Optical arrangements for FRS visualizations.

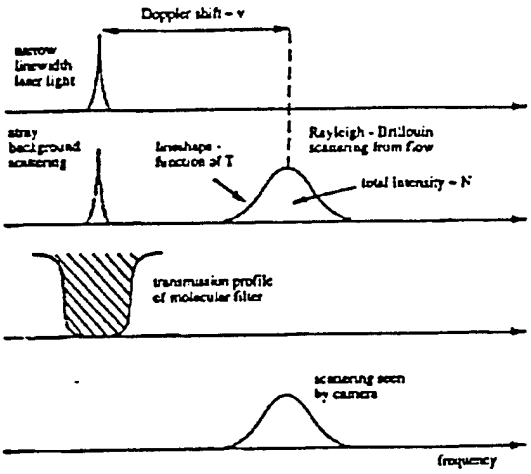

Figure 4: Filtered Rayleigh Scattering concept.

jection at the same rate, all at a location 300 mm downstream of the injection point. Injection of air does not significantly affect the profiles, but the helium injection has a strong effect. A layer of fluid with low, nearly constant momentum is present in the half lower part of the boundary layer. This layer consists of a low-density fluid with high temperature and it appears that the injected helium remains close to the wall.

Streamwise FRS visualizations at this location (figure 6) show that the boundary layers without injection and with air injection exhibit characteristics typical of turbulent boundary layers: a wide range of scales, deep entrainment and large-scale motions in the outer layer. With helium injection, however, the entrainment is reduced, no distinct structures are visible, and the boundary layer/freestream interface is not highly convoluted. The boundary layer appears similar to an early transitional or laminar flow.

Streamwise LIF images, where the helium was tagged with sodium, show that the helium remains confined to a relatively thin region near the wall (figure 7a). The flow has an intermittently laminar appearance. In contrast, when nitrogen is injected with the same injection rate (LIF visualizations with air injection were not possible to realize), the flow appears fully turbulent with a wide range of scales (figure 7b).

Etz [4] suggested that helium injection inhibited the mixing inside the boundary layer and delayed the boundary layer transition through a local decrease in Reynolds number (the kinematic viscosity of helium is eight times higher than that of air at the same temperature). The work presented here will show that this interpretation is partially incorrect and that the structure of the boundary layer with helium injection is more complicated than understood earlier.

4 Boundary layer structure without injection

Planform views of the boundary layer obtained at each of the three stagnation conditions (see section

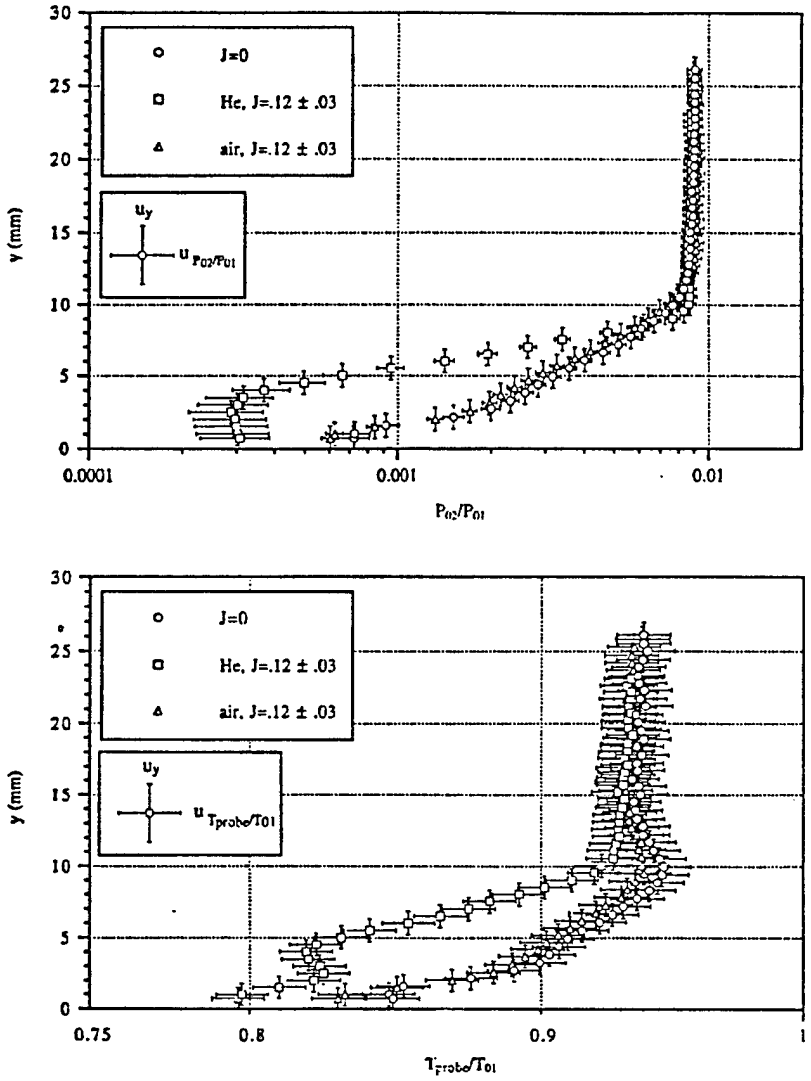

Figure 5: (a) Stagnation pressure, and (b) stagnation temperature profiles at a location 300 mm downstream of the injection point.

Figure 6: Streamwise FRS images of the boundary layer 300 mm downstream of the injection point (a) with helium injection $J = 0.12$; (b) without helium $J = 0$, and (c) with air injection $J = 0.12$. The flow is from the left to the right.

Figure 7: Streamwise LIF images 300 mm downstream of the injection point (a) with helium injection $J = 0.12$, and (b) with nitrogen injection $J = 0.13$. The flow is from the left to the right.

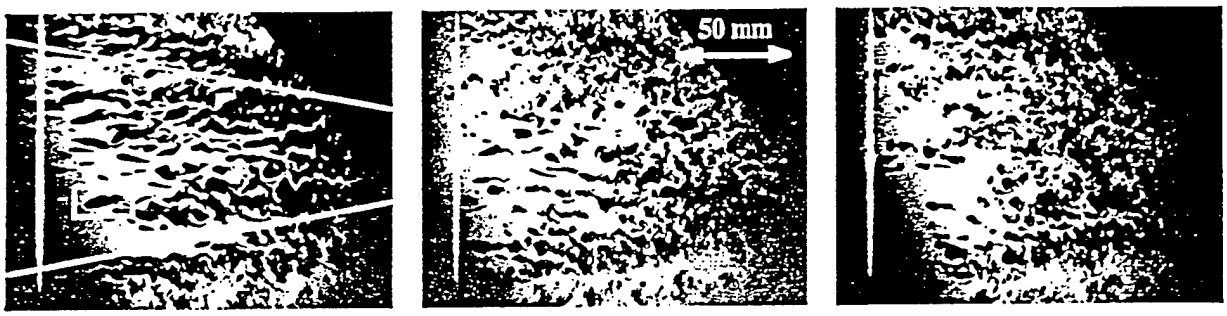

Figure 8: Planform views of the boundary layer for conditions 1, 2 and 3, from left to right. The flow is from left to right.

2.2) are shown in figure 8. The flow is from the left to the right. The field of view extends from 290 mm to 460 mm from the leading edge. The laser sheet is 4.5 mm away from the plate, and the boundary layer thickness is about 8 mm in the middle of the image, where $Re_\theta = 4000$. Figure 9 shows spanwise views for the same three stagnation conditions taken 320 mm from the leading edge (the location of the laser sheet used for the spanwise visualizations can be seen on the left of the planform views as a bright thin line). Note that the bright regions correspond to freestream fluid and the dark regions correspond to boundary layer fluid. Figure 8 provides a global view of the structure of the boundary layer on the plate. Compression waves coming from the edges of the leading edge can be seen (marked with inclined line in figure 8a). Each shock wave angle corresponds approximately to the Mach angle for Mach 8 flow, namely 7°, indicating that the shocks are weak. Downstream of the shocks, a darker region forms in which boundary layer structures similar to these observable in the middle of the flat plate can still be seen. The dark area is associated with an increase in the temperature of the flow downstream of the weak shock, and although there may be some thickening of the boundary layer, no significant changes in the boundary layer structure seem to occur. This apparent thickening of the boundary layer can be observed on the right and left sides of the planform views shown in figure 9. In figures 8a and 9a, the boundary layer exhibits several features of an early transitional boundary layer. The outer part of the boundary layer is marked by large, relatively smooth structures of elongated shape (as highlighted in figure 8a). In contrast, the structures shown in figures 8c and 9c are more similar to those seen in a turbulent boundary layer. A wide range of scales can be distinguished, and although some structures have a scale comparable to those seen in figure 8a, very small scale motions are also present. The convolution of the boundary layer edge is more extreme, as in figure 9c, with a relatively deep incursion of freestream fluid toward to the wall which is absent in figure 9a and much more frequent than in figure 9b. The trip used by Etz [4] resulted in a fully turbulent boundary layer 300 mm downstream of the injection slot regardless of the stagnation conditions (see also [9]. Without the tripping device, a transitional boundary layer exists 300 mm downstream of the injection slot for the lower stagnation conditions, whereas a marginally turbulent boundary layer forms at this location for the higher stagnation conditions. However, the images presented in figures 8 and 9 provide no information on the boundary layer structure at the location of the injection. However, the empirical formula given by Anderson [10] provides an estimate for the position where transition is expected to occur. For the present case, we find that the position of the transition is expected to occur between 250 and 300 mm, depending on the stagnation conditions. This value is consistent with our observations and supports the assumption that the injection takes place in a laminar or transitional boundary layer.

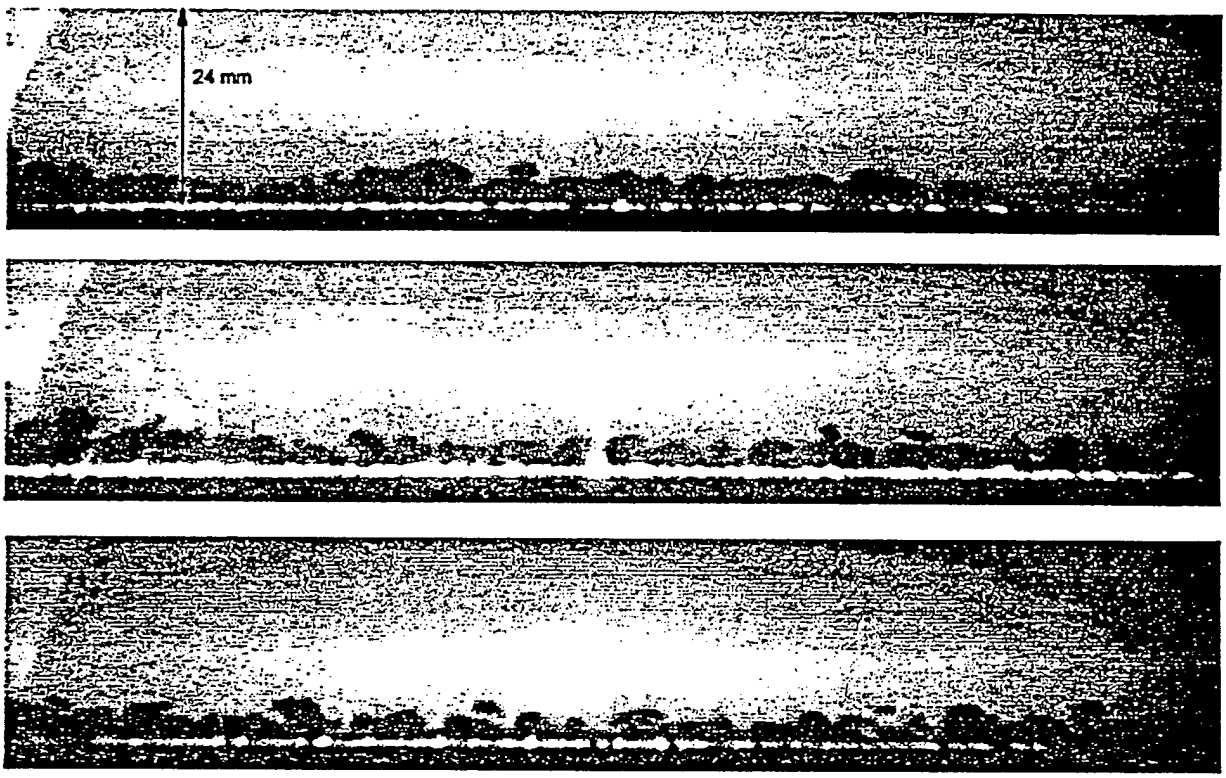

Figure 9: Spanwise views of the boundary layer for conditions 1, 2 and 3, from top to bottom. The flow is out of the page.

Figure 10: Planform views of the boundary layer with helium injection for different stagnation conditions. (a) Condition 1, $J = 0.16$; (b) Condition 2, $J = 0.12$; (c) Condition 3, $J = 0.16$. The flow is from the left to the right.

5 Boundary layer structure with helium injection

Figure 10 presents three planform views of the boundary layer for the three different stagnation conditions with helium injection. The field of view is the same as in figure 8 and the laser sheet is located 4.5 mm away from the surface. The helium injection greatly affects the structure of the boundary layer downstream of the injection location. A dark area of relatively constant width is clearly seen in the middle of every image in figure 10. The width of this region is slightly larger than the width of the injection slot, and it is about the same for the three images presented in figure 10. It appears that very little lateral diffusion of helium takes place and it remains confined to a region of constant width. Within the dark region, bright thin lines are present, and they are particularly pronounced in figure 10b. On each side, the dark area is bounded by uninterrupted bright regions.

Spanwise views give insight into the structure of the boundary layer downstream of the injection slot. In figure 11, three spanwise views obtained for the same stagnation conditions as in figure 10 are presented. The grey line show on each image represents the lateral location of the injection slot and is drawn on the plate surface.

Contrary to the suggestion made by Etz [4], the boundary layer with helium injection is not in a laminar state but instead demonstrates many aligned "crests" and "troughs." The troughs represent a decrease in the boundary layer thickness and appear as bright lines in figure 10 suggesting that the boundary layer structure seen on images in figure 11 is maintained in the streamwise direction. In order to confirm this, an average of about thirty images was formed for Condition 2 with different injection rates (figure 12).

The time-averaged images with helium injection show a distinct boundary layer structure, especially at the higher injection rates, whereas the boundary layer without injection presents no such structure. The troughs seen in figure 11 have a stable position on average for all the injection rates presented in figure 12. As the injection rate increases, the troughs become more pronounced, suggesting an increased entrainment toward to the wall, and the crests are higher, suggesting the motions outward from the wall are greater. In figure 12c, four distinct crests with similar dimensions can be seen in the region corresponding to the width of the injection slot (b1, b2, b3 and b4). As the injection rate increases, the dimension of the crest b2 increases while that of the crest b3 decreases. The crests b3 and b4 seem to merge for $J = 0.13$. With the increase in J, both the crests located on the sides of the set b1–b4 move away from the center.

Spanwise time-averaged images of the boundary layer similar to those shown in figure 12 were also obtained for Condition 1 with injection rates between 0.07 and 0.13. An identical structure of the boundary layer was observed with a similar crest evolution with injection rate.

Figure 13 shows time-averaged spanwise views of the boundary layer for injection rates higher than those in figure 12. As the injection rate increases, crests b3 and b4 merge and the boundary layer structure in the region corresponding to the width of the injection slot consists principally of three crests (see figure 13b). However, for injection rates higher than $J \approx 0.25$, the boundary layer structure is less discernible, suggesting a greater disorganization in the outer layer. Crests can always be seen in the individual images but without occupying fixed positions.

The structure of the boundary layer for $J < 0.20$ consists of successive spanwise crests and troughs and can be interpreted as a series of entrained fluid motions toward to the wall alternating with ejected fluid motions outward from the wall. Since the spanwise organization of the boundary layer seems to persist in the streamwise direction, this structure may be attributed to the existence of streamwise counter-rotating vortices in the boundary layer. The conjectured fluid motions which take place inside the boundary layer with helium injection is presented in figure 14. However, we do not have sufficient evidence to prove that such streamwise vortices are actually present. However, many images strongly suggest that counter-rotating motions are active in the boundary layer. For instance, in figure 11c, a mushroom-shape structure characteristic of streamwise counter-rotating vortices can be seen. Further experimental verification of this conjecture is necessary. For example, surface flow visualization may provide additional evidence.

If streamwise vortices occur in the boundary layer downstream of slot injection of helium, the appearance of a crest in the averaged spanwise images may correspond to the presence of one pair of counter-rotating vortices. Such streamwise vortices, also called Görtler vortices, have been observed in boundary layers submitted to concave surface curvature (see, for example, [11], even in cases where the concave curvature is very small (δ/R_c equal to about 1% where δ is the boundary layer thickness and R_c is the radius of curvature, as in [12], and for cases where the length of the curved region is short (length of the curvature equal to about ten times the boundary layer thickness, as in [13]. Consequently, the appearance of the streamwise vortices may be associated with concave streamline curvature in the region where the helium is injected.

The stable spanwise succession of crests and

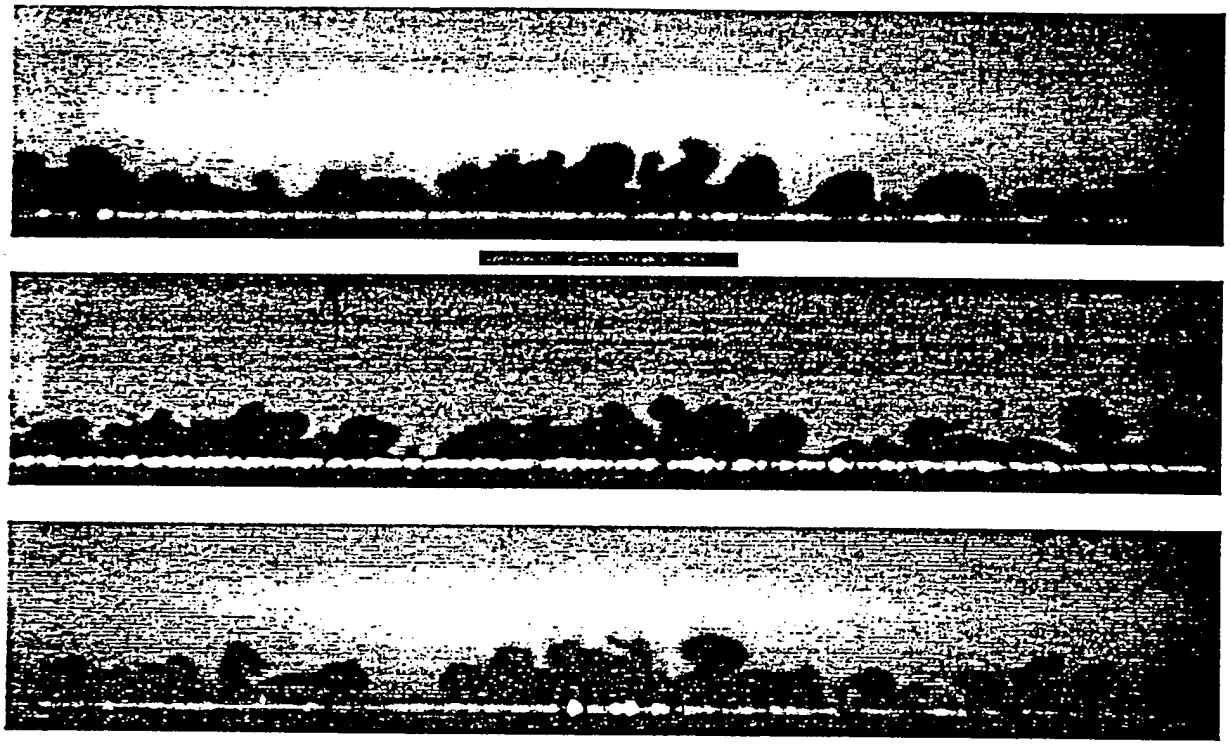

Figure 11: Spanwise view of the boundary layer with helium injection for different stagnation conditions. (a) Condition 1, $J = 0.16$; (b) Condition 2, $J = 0.12$; (c) Condition 3, $J = 0.16$. The flow is out of the page.

troughs is the most pronounced for injection rates ranging from 0.09 up to 0.13. With J greater than 0.13, the boundary layer thickness keeps growing, but the ejection and entrainment motions become more sporadic. For boundary layers experiencing the effects of concave curvature, [11] found that the longitudinal roll cells have a streamwise extent of only a few boundary layer thicknesses and they are unsteady. The helium injection induces a strong structuring effect on the boundary layer, and if this organization occurs because of the presence of streamwise vortices, the position of the streamwise vortices are found to be stable from $J = 0.09$ to $J = 0.13$ over the range of stagnation conditions explored here. The stable structure of the boundary layer explains why Etz [4], on the basis of streamwise visualizations such as those shown in figure 6a, suggested that the boundary layer was in a laminar state. As J increases above 0.13, the boundary layer structure is less pronounced, so that it appeared in a more turbulent state in the streamwise visualizations made by Etz.

For $J = 0.09$, the distance between successive crests, corresponding to the spanwise wavelength of the conjectured streamwise vortices, is about 7 or 8 mm. The boundary layer thickness is about 8 mm at the same location. As J increases, the size of the vortices increases (resulting in an increase in the spanwise wavelength) and the boundary layer thickness increases too. So, for J between 0.09 and 0.20, the spanwise wavelength of the streamwise vortices is approximately equal to the boundary layer thickness. For boundary layers growing on a concave surface, the spanwise wavelength of the streamwise vortices is typically one to two boundary layer thicknesses and depends somewhat on the conditions upstream of the region of concave curvature [12]. The spanwise wavelength of the crests is consistent with this experience. In the case of helium injection, the wavelength can also be expected to be influenced by the width of the injection slot since it limits the spanwise extent of the vortices.

Surveys using a dual Pitot-stagnation temperature probe were made by Etz [4]. The transverse distance between the Pitot probe and the thermocouple was 6.4 mm. The results show no significant change in the boundary layer thickness with helium injection. However, the spanwise visualizations show a considerable increase in the boundary layer thickness with injection rate (see, for example figure 9 without helium injection compared to figure 11 with helium injection). We attribute this difference to the large distance between the stagnation pressure and stagnation temperature probes, since it means they effectively spanned two structures.

For low injection rates ($J < 0.15$), the near-field helium penetration is of the order of the boundary-layer thickness, as seen in the LIF visualizations made by Etz [4]. The boundary layer is deflected away from the wall by the jet, experiencing concave curvature resulting in the generation of streamwise vortices. As J exceeds 0.13, the organization of the

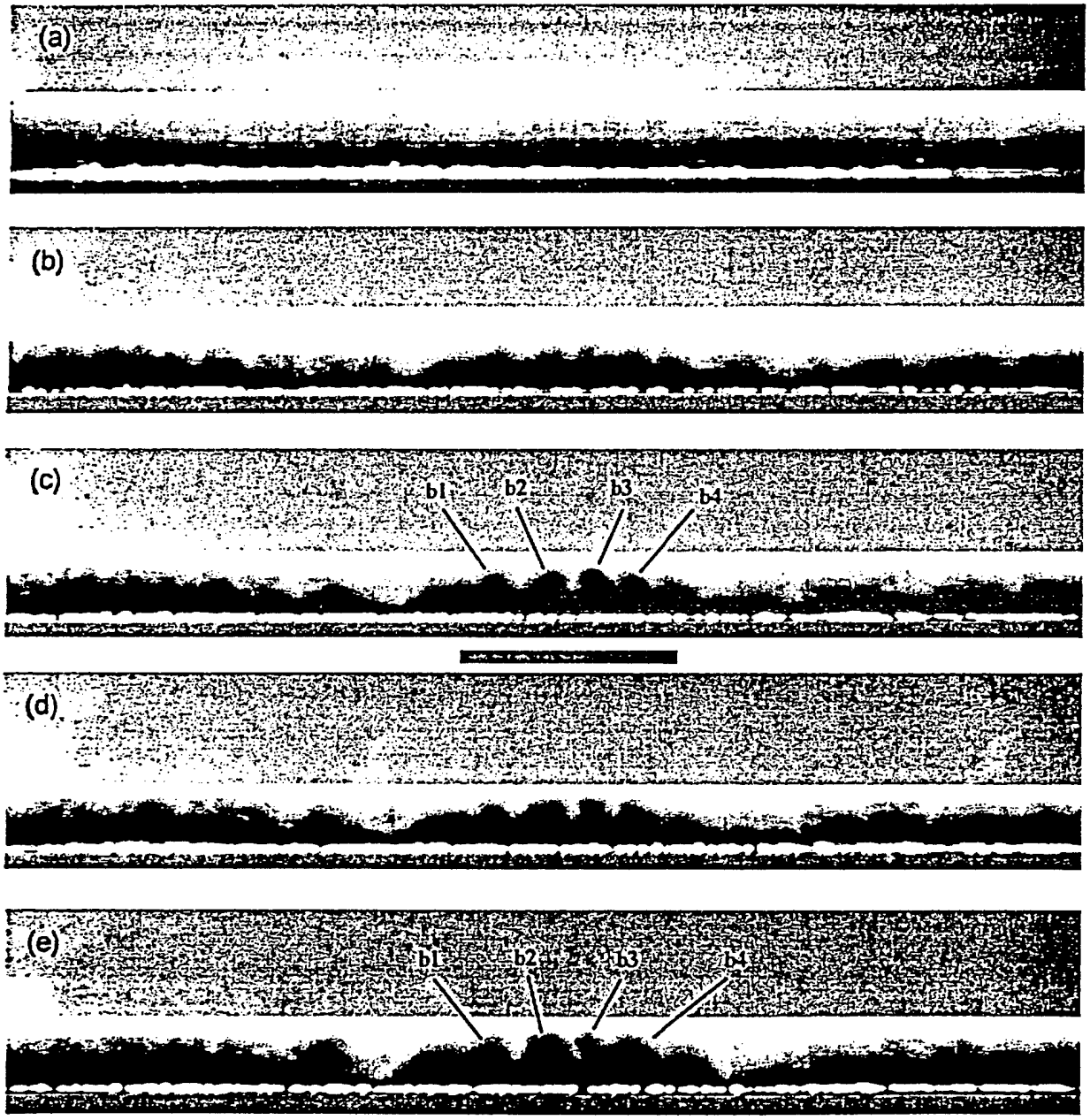

Figure 12: Time-averaged spanwise images of the boundary layer for different injection rates at Condition 2. (a) $J = 0$; (b) $J = 0.07$; (c) $J = 0.09$; (d) $J = 0.11$; (e) $J = 0.13$. The flow is out of the page.

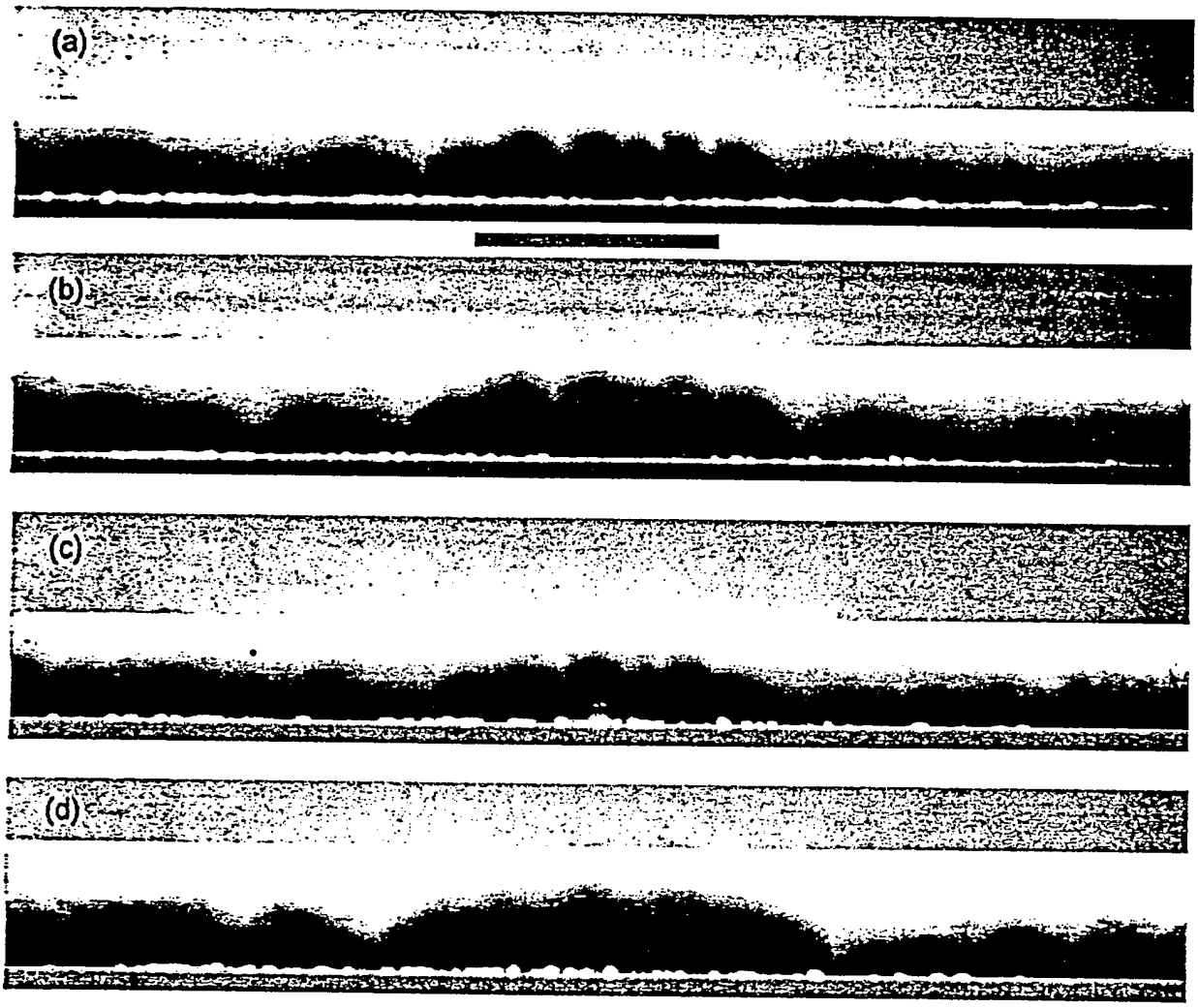

Figure 13: Time-averaged spanwise images of the boundary layer for conditions 1 and 3 and different injection rates. (a) Condition 1, $J = 0.16$; (b) Condition 1, $J = 0.24$; (c) Condition 3, $J = 0.16$; (d) Condition 3; $J = 0.31$. The flow is out of the page.

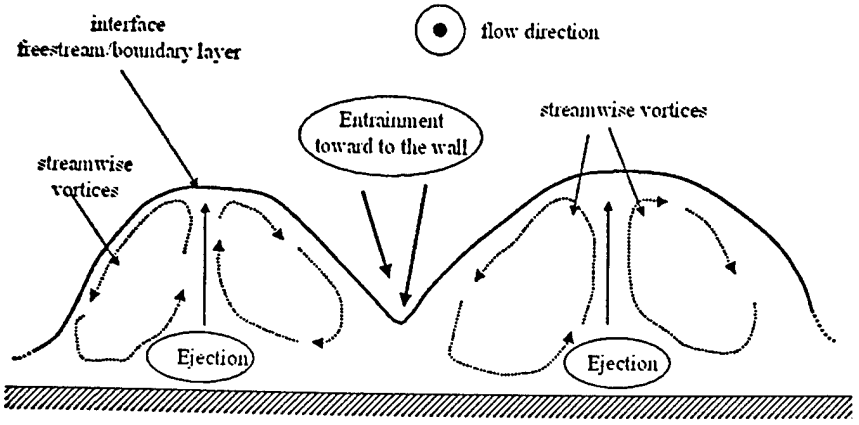

Figure 14: Conjecture on fluid motions inside the boundary layer with helium injection.

boundary layer becomes less pronounced. When J is higher, a more significant curvature effect is present but the penetration distance of the jet exceeds the boundary layer thickness, and the injection creates large disturbances in the boundary layer preventing the formation of organized streamwise motions.

Both of the crests located on the sides of the set b1-b4, in figure 12 reveal the presence of side vortices created at the edges of the injection slot. Figure 15 gives a schematic of fluid motions which may take place near the edges of the injection slot. Each side vortex induces a fluid entrainment toward to the wall which can be seen as the long and distinct bright regions skirting the region of helium injection in figure 10. An induced rotating motion forms away from that region, as drawn in figure 15. The induced rotating motions can be observed in the averaged spanwise visualizations given in figure 12. They are particularly well marked on the left of the images. As J increases, the sizes of the side vortices increase and their positions move away from the edges of the injection slot. This motion can be seen in figures 12c to 12e.

6 Boundary layer structure with injection of nitrogen

Spanwise visualizations of the boundary layer with nitrogen injection were made 300 mm downstream of the injection slot. Three images of the boundary layer with $J = 0.11$ with the stagnation Condition 2 are presented in figure 16. The wall is indicated by the uniform grey area. In these images, the boundary layer exhibits many features of a fully turbulent flow: the presence of a large range of scales, deep entrainment toward to the wall and a highly convoluted boundary layer edge. No distinct structures are observed in time-averaged images, in contrast to the case with helium injection. Furthermore, nitrogen injection appears to provoke transition of the boundary layer to the fully turbulent state. Note that, for Condition 2 without injection, the boundary layer is only in a marginal turbulent state (see figure 9c).

LIF streamwise visualizations at the injection point made by Etz [4] give insight into the jet behavior in the cases of helium and nitrogen injection (see figure 17).

While the jet momenta are almost equal, the jet structure is completely different in the helium and nitrogen cases. For helium injection (figure 17a), the jet can easily be seen in the LIF images. The jet penetrates inside the flow field up to the edge of the boundary layer where it is bent. Just downstream of the injection slot, the main part of the injected jet is entrained toward to the wall, although some helium can be observed in the external layer. For nitrogen injection (figure 17b), the jet can not be distinguished clearly in the LIF visualizations. The nitrogen jet mixes with the boundary layer fluid even in the near field of the jet. However, in both cases, the jet penetration is similar: just downstream of the injection slot, the injected gas can be observed all across the height of the boundary layer. The similarity in the near-field penetration distance is evidence that the penetration is controlled by the jet momentum. So, the difference in the jet structure can only be explained by the difference in the kinematic viscosity between helium and nitrogen. At 530K, the kinematic viscosity of helium is eight times the kinematic viscosity of nitrogen. For comparison, the jet Reynolds number for helium is very low ($Re_{jet} \approx 130$) and it is three times higher for nitrogen. At these low Reynolds numbers, the greater viscosity for helium inhibits the mixing between the injected gas and the boundary layer fluid. Nitrogen injection in the boundary layer increases the mixing and so, promotes transition to turbulence. In contrast, helium injection does not promote mixing and the helium stays distinct in the downstream flow. The slot injection of helium imposes concave curvature effects on the boundary layer. The curvature effects promote the formation of streamwise vortices, which are responsible for the entrainment of helium toward to the wall just downstream of the injection slot, as observed in figure 17a.

7 Three-dimensional reconstruction of the boundary layer

7.1 Mega-Hertz imaging system

The new imaging system available in the Gas Dynamics Laboratory uses a "pulse-burst" laser system in conjunction with a high-speed CCD camera. Complete details of the laser system are given in [14]. Briefly, the Nd:YAG laser has the capability of producing a "train" of 30–40 high energy pulses with pulse separation times as shorts as one microsecond. The pulse-burst concept is illustrated schematically in figure 18. A pulse sequence is generated using a low power CW master oscillator in combination with a high-speed pulse slicer. The low power sequence is then amplified in a series of flashlamp-pumped amplifiers which have "gain" for a total period of approximately 100 microseconds. By sending the pulse sequence to the rising edge of the gain curve, a burst of uniform high-energy (10–20 mJ at 532 nm) pulses is generated. The burst repetition rate is 9 Hz to limit the thermal loading on the solid state lasing elements.

The laser is paired with a novel CCD framing camera recently developed by Princeton Scientific

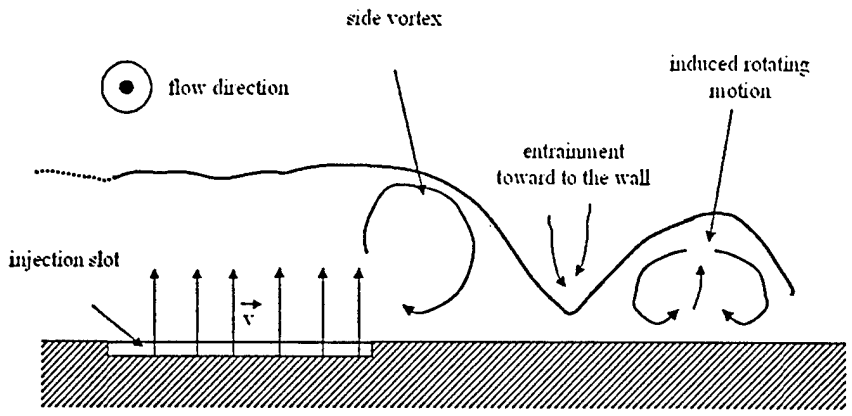

Figure 15: Schematic of the fluid motions near the edge of the injection slot.

Figure 16: Spanwise visualizations of the boundary layer with nitrogen injection, $J = 0.11$. Flow is out of the page.

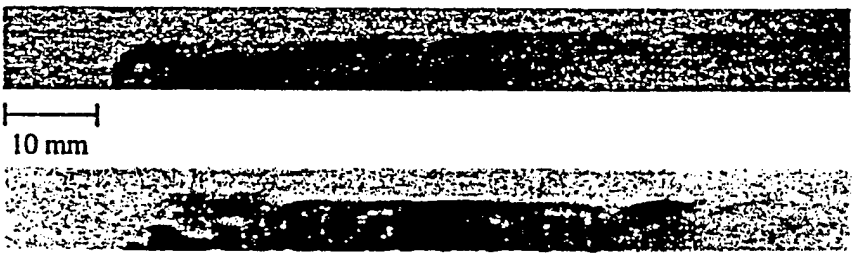

Figure 17: LIF streamwise visualizations of the boundary layer under Condition 2 near the injection slot. (a) With helium injection, $J = 0.13$; (b) with nitrogen injection, $J = 0.12$.

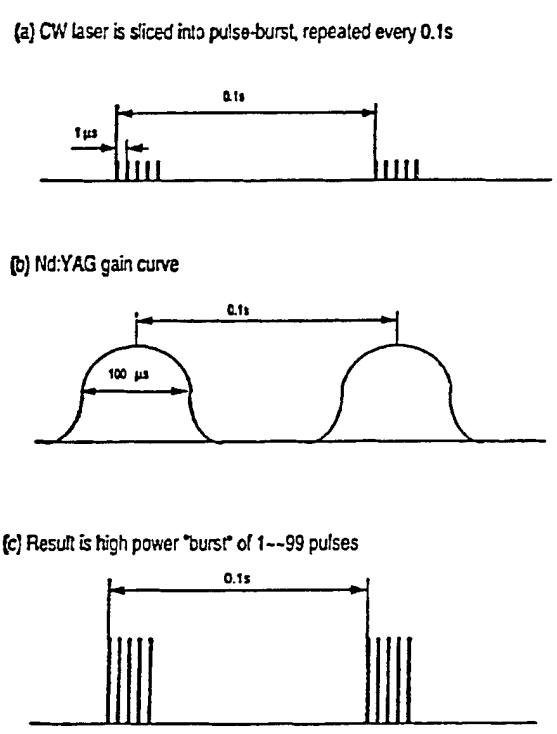

Figure 18: Pulse burst concept.

Instruments, Inc. The CCD camera has a 30-image storage buffer built into the image sensor chip itself, and can frame at rates up to 1 MHz. The camera resolution is 180 by 180 pixels. This imaging system can collect a time sequence of 20–30 images. The chosen repetition rate is 500 kHz in order to obtain high laser pulse energy and maximize the sampling window. If the laser sheet is oriented normal to the wall in the spanwise direction, the sequential images can be assembled into a quasi-three-dimensional volumetric image, as long as Taylor hypothesis can be invoked. This requires that the large-scale motions evolve over distances large compared to the boundary layer thickness.

7.2 3D reconstruction of the boundary layer with and without helium injection

Figure 19 shows eight successive spanwise frames of the boundary layer without injection, taken at a frequency of 500 kHz. The development of a large structure in the outer layer of the boundary layer can be observed near the middle of the field of view. Generally the boundary layer in Condition 2 can be described as late transitional, as described earlier in section 4.1.1.

A 30-frame sequence obtained without injection is presented as a volumetric image in figure 20. The individual images have been stacked in temporal order with the first frame on the right and the last frame on the left. The spacing in the streamwise direction was set using an average convection velocity, U_c. In figure 20, U_c was chosen to equal the freestream velocity (1140 m/s). The convection velocity of the large scale motions is probably slightly lower than that value. [15] estimates the convection velocity to lie between 90% and 100% of the freestream velocity in the case of transitional hypersonic boundary layers. [16] found a convection velocity for the large scale structures in the order of 90% of the freestream velocity in the case of turbulent supersonic boundary layers. The gap between the frames were filled in by linear interpolation of the greyscales. The surface illuminated in figure 20 is actually the interface between the condensed and sublimated carbon dioxide (nominally the instantaneous boundary layer edge). The interface is made visible by making all the freestream greyscales (the bright region) transparent. The direction of light illumination can be adjusted to create the shadow effect and accentuate the three dimensional nature of the boundary layer. The longish structure marked in figure 20 is similar to that marked in figure 8a.

Figure 21 represents a reconstruction of the boundary layer under Condition 2 with helium injection for $J = 0.09$. Figure 22 is a representation of the boundary layer in the same conditions as in figure 21 except that $J = 0.13$. In both cases the physical size of the 3D representation is similar to that shown in figure 20. The spanwise structure of the boundary layer shown in the time-averaged spanwise images can also be clearly in figures 21 and 22. Crests and troughs with a significant streamwise extent are present, in positions similar to that found in the time-averaged images. More smaller-scale disturbances can be observed in the crests for $J = 0.13$ than for $J = 0.09$, but the troughs are deeper for $J = 0.13$.

8 Conclusions

Low momentum sonic helium injection through a slot in a hypersonic boundary layer was studied using Filtered Rayleigh Scattering. A novel MHz imaging system was used to obtain a volumetric reconstruction of the boundary layer. Helium injection significantly affected the boundary layer structure downstream of the injection point, greatly increasing its streamwise organization. In the spanwise direction, the boundary layer structure consisted of a spanwise succession of crests, characteristic of increased boundary layer thickness, and troughs, characteristic of increased incursions of freestream fluid. The positions of the crests and troughs were found to be stable for injection rates ranging from $J = 0.09$ to $J = 0.15$, regardless of the freestream stagnation conditions (at least for the conditions examined

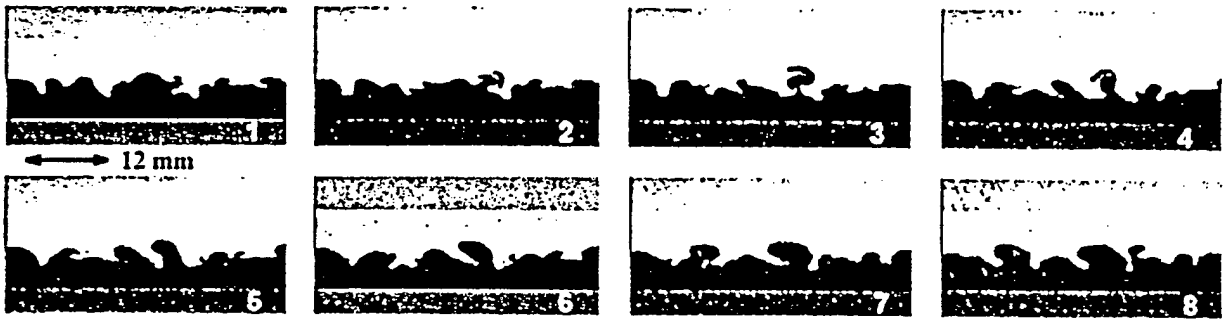

Figure 19: Spanwise images of the boundary layer without injection, Condition 2. The flow is out of the page. Time between successive images is 2 ms.

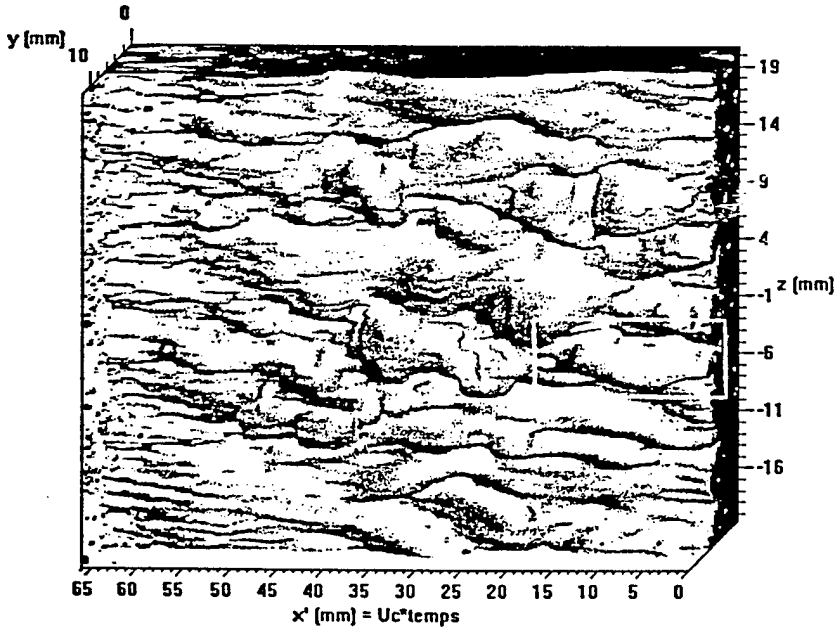

Figure 20: Volumetric reconstruction of the boundary layer without injection. The flow is from left to right. Stagnation Condition 2.

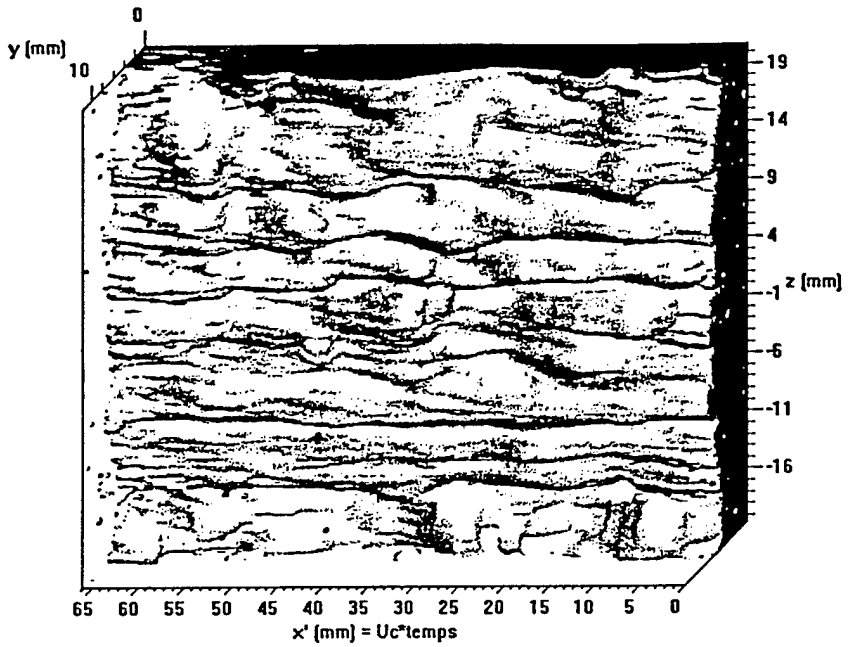

Figure 21: Volumetric representation of the boundary layer with helium injection, $J = 0.09$. The flow is from the left to the right. Stagnation Condition 2.

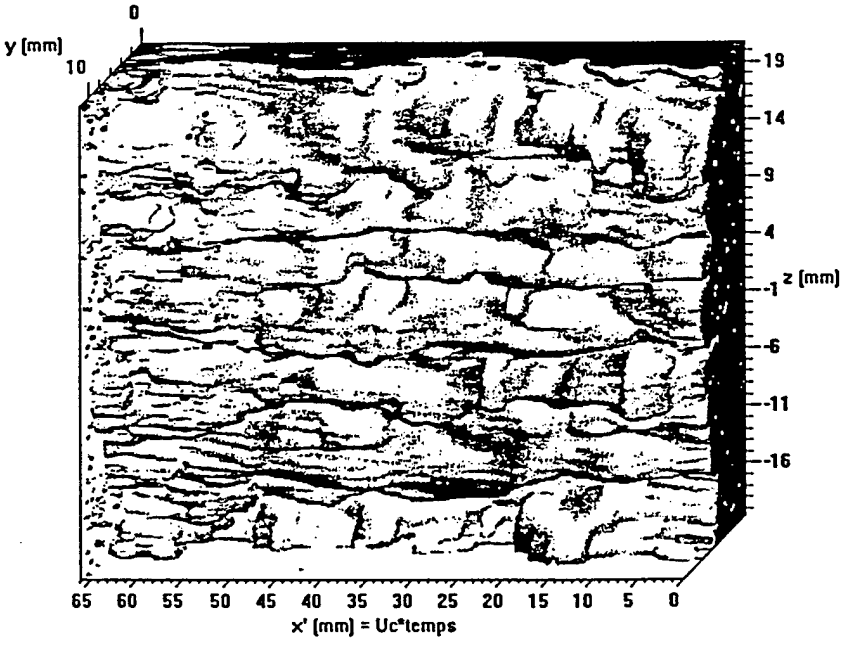

Figure 22: Volumetric representation of the boundary layer with helium injection, $J = 0.13$. The flow is from the left to the right. Stagnation Condition 2.

here). It was postulated that this structure was due to the existence of streamwise vortices in the boundary layer created at the injection point by concave streamline curvature. Another gas (nitrogen) was tested under the same flow and injection conditions and no such effect was revealed. The higher kinematic viscosity of helium compared to that of nitrogen seems to be the reason for the observed phenomena, since it reduces mixing of the jet fluid with the boundary layer fluid, and enhances the concave curvature without promoting significant large-scale disturbances to the boundary layer.

A key question is how long this stabilizing effect will persist downstream, and if helium injection into a fully turbulent flow will cause the appearance of similar stable streamwise vortices. The phenomenon obviously has important implications for aero-optic applications, flow control and heat transfer to the wall from the external flow. Further studies at higher Reynolds number and lower Mach number are in progress.

Acknowledgments

The research in high Reynolds number flows is supported by AFOSR through grant F-49620-00-1-0139, monitored by Dr. Tom Beutner.

References

[1] Morkovin, M.V. (1962) Effects of compressibility on turbulent flows. *Mécanique de la Turbulence*, CNRS", ed. A.J. Favre, 367–380.

[2] , Smits, A.J. and Dussauge, J.P. (1996) *Turbulent Shear Layers in Supersonic Flow.* AIP Press.

[3] Baumgartner M.L., Smits A.J., Nau T. and Rowley C.W. (1995) Design and testing of a new hypersonic wind tunnel. AIAA Paper 95-0787

[4] Etz M.R. (1998) The effects of transverse sonic gas injection on a hypersonic boundary layer. MSE Thesis, Princeton University.

[5] Erbland P.J., Baumgartner M.L., Yalin A.P. *et al.* (1997) Development of planar diagnostics for imaging Mach 8 flowfields using carbon dioxide and sodium seeding. AIAA Paper 97-0154.

[6] Erbland P.J. (2000) *Filtered Rayleigh Scattering and Homogeneous Nucleation of CO_2 in Supersonic Flows.* Ph.D. Thesis, Princeton University.

[7] Huntley M., Wu P., Miles R.B and Smits A.J. (2000) MHz rate imaging of boundary layer transition on elliptic cones at Mach 8. AIAA Paper 00-0379.

[8] Nau T.A. (1995) Rayleigh scattering as a quantitative tool in compressible turbulent boundary layers. MSE Thesis, Princeton University, 2026T.

[9] Baumgartner M.L. (1997) Turbulence structure in a hypersonic boundary layer. Ph.D. Thesis, Princeton University.

[10] Anderson J.D. (1989) *Hypersonic and high temperature gas dynamics.* McGraw-Hill, New-York.

[11] Barlow R.S and Johnston J.P. (1988) Structure of a turbulent boundary layer on a concave surface. Journal of Fluid Mechanics, vol. 191, pp. 137-176.

[12] Hoffmann P.H., Muck K.C. and Bradshaw P. (1985) The effect of concave surface curvature on turbulent boundary layers. Journal of Fluid Mechanics, vol. 161, pp. 371-403.

[13] Smits A.J., Young, S.Y.B. and Bradshaw, P. (1977) The response of turbulent boundary layers to sudden short regions of concave curvature. Journal of Fluid Mechanics, vol.117, pp.1-58.

[14] Wu P., Lempert W.R., Miles R.D. and Bromley L. (1998) Tunable pulse-burst laser system for high-speed imaging diagnostics. AIAA Paper 98-0310.

[15] Huntley M. (2000) Private communication.

[16] Smith M.W. and Smits A.J. (1995) Visualization of the structure of supersonic turbulent boundary layers. Exp. in Fluids, 18, pp. 288-302.

[17] Smits A.J. and Wood (1985) The response of turbulent boundary layers to sudden perturbations. Annual Review of Fluid Mechanics, vol.17, pp.321-358.

AIAA 2001-0846

THREE-DIMENSIONAL IMAGING OF HYPERSONIC FLOW AT MHz-RATE

Richard B. Miles, Alexander J. Smits
Princeton University, Dept. of Mechanical & Aerospace Engineering
Princeton, NJ
Mark B.Huntley, Whitehill Manufacturing Corp., Chester, PA
Pingfan Wu, ADC Telecommunications, Ewing, NJ
Rene Tolboom, University of Nijmegen, The Netherlands

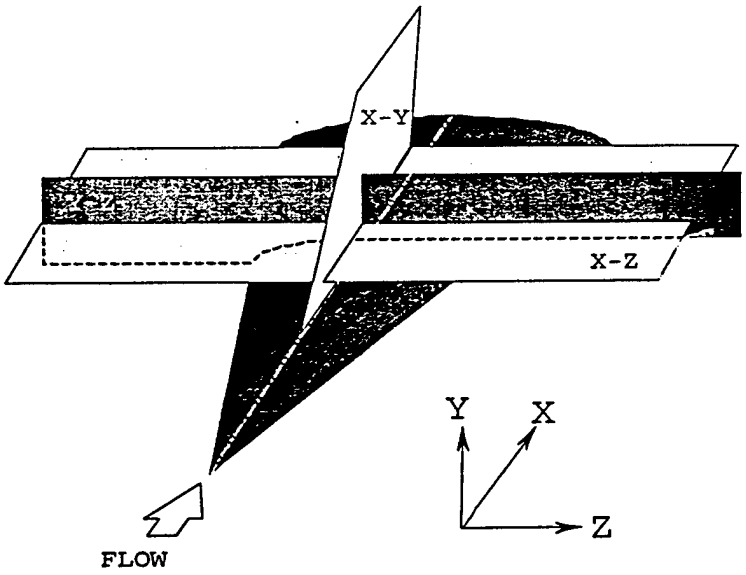

39th AIAA Aerospace Sciences Meeting & Exhibit
8-11 January 2001 / Reno, NV

THREE-DIMENSIONAL IMAGING OF HYPERSONIC FLOW AT MHz-RATE

Richard B. Miles, Alexander J. Smits[†]
Department of Mechanical and Aerospace Engineering
Princeton University, Princeton, NJ 08544

Mark B. Huntley
Whitehill Manufacturing Corporation
2540 Green St., Chester PA 19013

Pingfan Wu
ADC Telecommunications
250 Phillips Blvd., Suite 255, Ewing, NJ 08618

and

Rene Tolboom
University of Nijmegen, Faculty of Science, Applied Physics
Toernooiveld 1, NL-6500 GL Nijmegen, The Netherlands

Abstract

This paper reports the development of simultaneous MHz-rate multi-dimensional imaging and three-dimensional rendering of Mach 8 transitional flow using a pulse-burst laser and high-rate CCD framing camera system. Experiments are conducted on elliptic cone models and show the evolution of the boundary layer structure near the centerline of the model where the transition occurs. Images are taken using Rayleigh scattering from a CO_2 fog of particulates which condense in the cold core portions of the flow but not in the boundary layer. Planform and spanwise images are simultaneously recorded so the full three- dimensional evolution of the outer portion of the boundary layer can be monitored. The slow transitional structure evolution rate allows the "frozen flow" approximation to be used so the sequential spanwise images can be assembled into a full three-dimensional rendering of the outer boundary layer surface.

[*]Professor, Mechanical & Aerospace Engineering, Fellow AIAA
[†]Professor, Mechanical & Aerospace Engineering, Associate Fellow AIAA

Introduction

Our understanding of complex, high-speed flow is limited, in large part, because of the difficulty in acquiring data. In supersonic flows the fluctuation frequencies can be as high as 1 MHz, and the dimensions of structures on the order of millimeters or less. Our ability to predict the dynamics of such flows is well beyond the capability of current computational methods. Even for the application of approximate flow solvers, validation requires reliable flow field data. For example, the accurate prediction of transition on a hypersonic vehicle is not possible at the present time, and this lack of understanding has served as an aerodynamic roadblock in optimizing the control of hypersonic vehicles. The traditional techniques of single-point measurement with hotwire or pitot tube are not sufficient for the study of such complex three-dimensional phenomena. Typically, quantitative flow imaging has an order-of–magnitude higher level of spatial detail.

Various imaging concepts have recently been developed to produce single plane cross-sectional images, and these have already begun to yield significant new insight into boundary layer structures, shock wave/boundary layer interactions, and the transition from laminar-to-turbulent flow. These techniques are generally based on light scattering methods or on laser-induced fluorescence. The work

reported here is an extension of the light scattering approach to the multi-dimensional and time-sequenced imaging of high-speed flows.[1] The particular focus is on capturing the transitional structure in a Mach 8 boundary layer on a model which simulates a practical vehicle configuration. To develop an understanding of complex hypersonic flows, it is necessary to move beyond the study of canonical flat-plate zero pressure-gradient boundary layers. In particular, it is important to predict transition and the development of turbulent boundary layers on a lifting three-dimensional body at high Mach number. The initial boundary layer on this body will be laminar, followed by a region of transition. If the length Reynolds number is high enough, a turbulent boundary layer develops over the rest of the body. All aspects of this boundary layer development are of interest since the behavior of high Mach number boundary layers is not well understood. In particular, the role of cross flow on the transition to turbulence has been a topic of concern since the suppression of this mechanism may lead to a significant reduction in vehicle drag.[2]

A MHz-rate imaging system has been used to capture simultaneous orthogonal images of transitional boundary layer structure and render full three-dimensional constructions of boundary layer features. The flow studied is cold air at Mach 8, where the Mach number is high enough to be well within the hypersonic regime, but the temperature is low enough to avoid real gas effects. The three-dimensional body is an elliptic cone, which is representative of a generic hypersonic vehicle.[3]

Pulse-Burst Laser and Imaging System

The MHz repetition rate, pulse-burst imaging system[4] can capture 30 sequential images at framing rates as fast as 1 μs a frame. The system consists of the pulse-burst laser and a MHz-rate CCD framing camera. Figure 1 is a diagram showing the elements of the pulse-burst laser. The basic layout is a Master Oscillator–Power Amplifier configuration, with a diode-pumped, frequency-tunable, Nd:YAG laser oscillator. The cw output of the oscillator is first amplified by a four-pass, 10 Hertz, flashlamp-pumped Nd:YAG pre-amplifier. The gain is present for approximately 100 μsec, so the output of the pre-amplifier is a 10 Hertz, 100 μsec long pulse which is subsequently sliced into the desired pulse train with a pair of Pockels cells, and further amplified to an output of approximately 100 mJ per individual pulse. The four-pass pre-amplifier operates in the small signal gain regime, so the gain is not saturated, and there is no penalty for amplifying the entire cw output of the master oscillator before slicing. The advantage of pre-amplifying the cw output before slicing is that it suppresses the amplified spontaneous emission that would otherwise occur between individual pulses of the train, effectively increasing the power of the master oscillator by a factor of 5000. Sequential stages are isolated, and the beam profile is defined by a soft aperture that is re-imaged through the latter amplifier stages. The camera was built by Princeton Scientific Instruments and operates with a resolution of 180 X 180 pixels. Each pixel has associated with it 30 storage elements, so up to 30 frames can be recorded on the chip itself before readout. The framing rate is up to 1 MHz, so it matches well the capabilities of the pulse-burst laser.

This pulse-burst imaging system is used to capture images of boundary layer structure in supersonic and hypersonic flows through Rayleigh scattering from a CO_2 particulate fog. This fog is formed by seeding approximately 1% CO_2 gas into the air stream well upstream of the plenum. The air/CO_2 mixture cools to below the CO_2 condensation point in the core of the expansion, but not in the boundary layer where the temperature is higher. Studies in our laboratory have shown that the CO_2 particles are on the scale of 10 nm or smaller in diameter, follow the flow precisely, and sublime or condense in times that are fast enough to avoid significant lag.[1,5]

The camera is located behind a molecular vapor iodine filter which is used to suppress the scattering from the model.[6] The operation of this filter is shown in Fig. 2. The laser is tuned so that its output frequency overlaps a strong absorption transition in molecular iodine vapor. That causes light scattered from non-moving surfaces to be strongly absorbed before it reaches the camera. On the other hand, light scattered from the moving particles in the flow is shifted in frequency so that it passes through the filter and is captured by the camera. In this manner, the relatively weak scattering from the flow can be imaged, even in the presence of strong scattering from the surface of the model.[7]

Experimental Configuration

The experiments were conducted in a Mach 8 blow-down tunnel at the Princeton University Gas Dynamics Laboratory.[8] This facility has a 0.23 meter diameter axisymmetric test section and operates at a Reynolds number ranging from 2.0×10^6 to 21×10^6. The model used was a 4:1 elliptic cone which was chosen to simulate a generic hypersonic vehicle. Figure 3 shows how similar the X-33 space vehicle model and the elliptic cone are. Because of the shape, the shock wave generated along the major axis is stronger than that along the minor axis, and, as a consequence, a circumferential pressure gradient forms on the cone surface. A cross flow forms which drives the low momentum boundary layer toward the centerline. The velocity profile of the cross flow is inflectional and very unstable. Numerical simulation has predicted that the cross flow vortices may be the primary disturbance leading to transition.

Simultaneous Two-Plane Imaging

Since both the camera and the laser being used to capture the time-evolving images are one-of-a-kind devices, a system which was able to capture two simultaneous orthogonal plane images of the flow field had to be configured to illuminate the flow, beginning with only one laser beam and capture the orthogonal images onto a single camera. Figure 4 shows the three possible orientations of the laser sheet: streamwise, planform, and spanwise. In the experiments, the spanwise (Y-Z) and planform (X-Z) planes were imaged, since off-centerline interactions were of special interest.

Figure 5 shows the experimental setup. The second harmonic output of the pulse-burst laser delivered an average of 20 mJ per pulse. The laser beam was split by a 50/50 beam-splitter into two beams. One beam was shaped to a sheet along the spanwise orientation, while the other beam was shaped to a planform laser sheet. Both the spanwise and planform views were imaged to the single MHz framing rate CCD camera. The imaging system configuration is shown in Figure 6. The CCD camera image plane was split into two regions: the upper region which observed the spanwise image, and the lower region which observed the streamwise image. Placement of the mirrors that were used to form this double image is shown diagramatically in both Figures 5 and 6

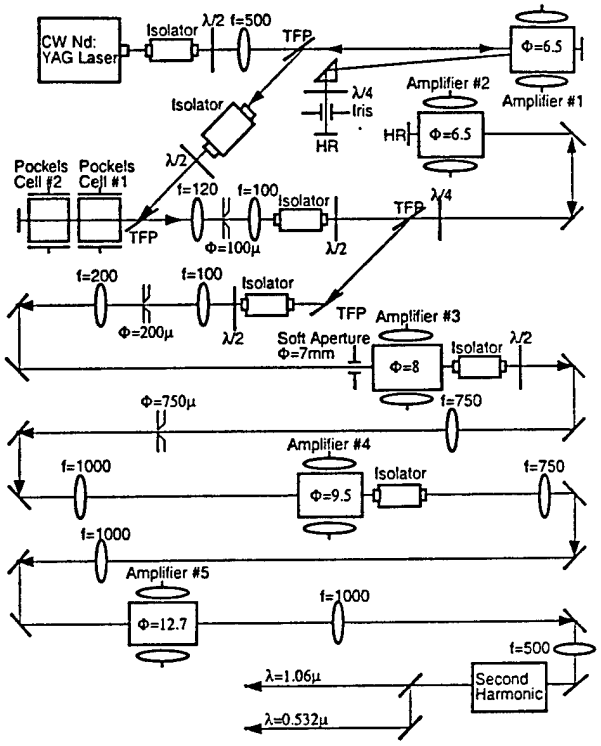

Figure 1. Diagram of the pulse-burst laser system.

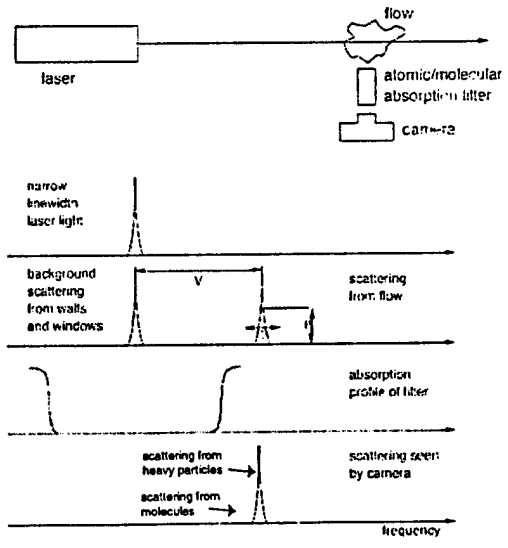

Figure 2. Suppression of background scattering by a molecular filter

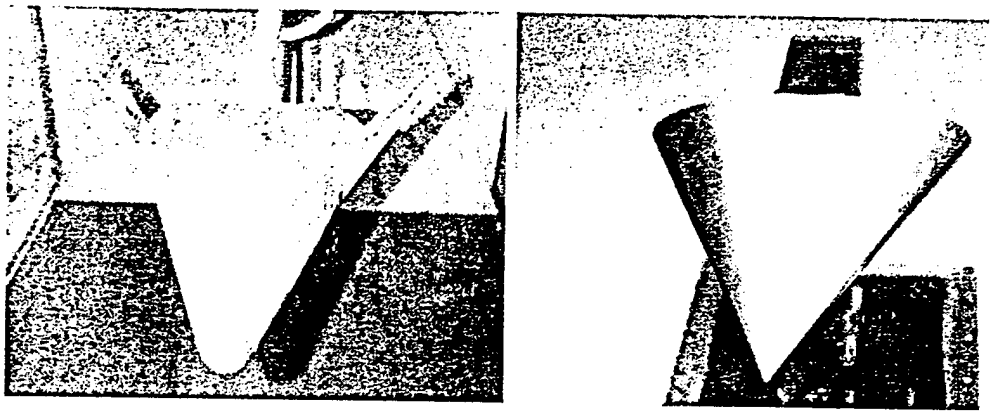

Figure 3. Comparison of the geometry of the X-33 vehicle with the 4:1 elliptic cone model used in these experiments.

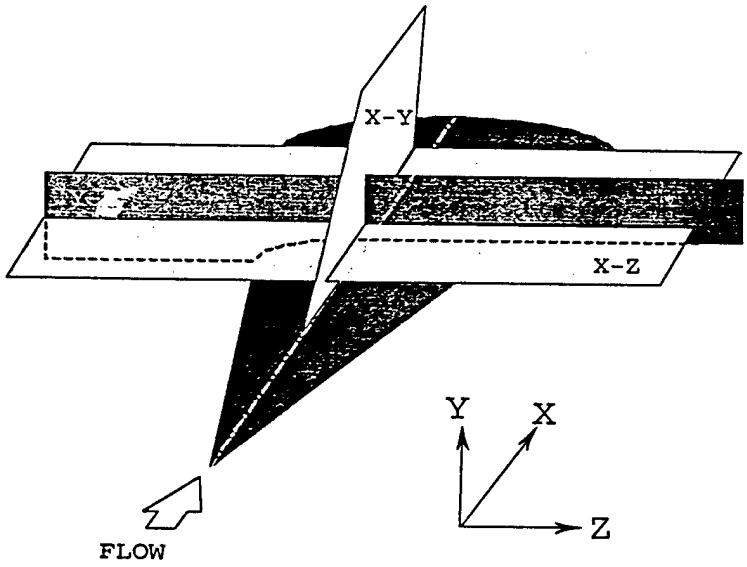

Figure 4. Orientations of the diagnostic planes on the elliptic model.

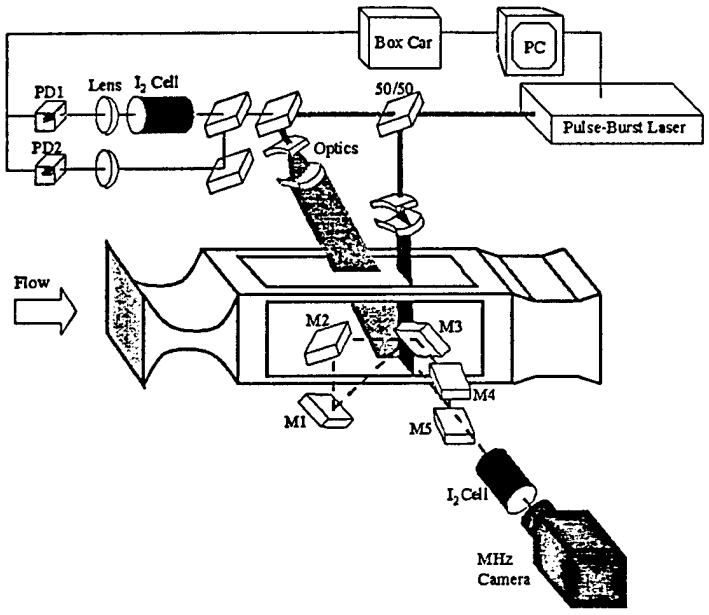

Figure 5. Diagram of the experimental set-up for simultaneous MHz-rate imaging of the spanwise and planform planes.

The planform image was collected in a normal manner with two lenses, but the lenses were separated far enough to allow the formation of an intermediate image plane. The planform image was masked in this intermediate plane so that it occupied only the lower two-thirds of the camera CCD. The spanwise image was rotated by reflection so that its aspect fit into the upper one-third of the image. The spanwise image was also imaged to an intermediate plane and masked so that it did not overlap with the planform image. In this manner, a composite image with the spanwise portion occupying the upper one-third, and the planform portion occupying the lower two-thirds, was formed.

Figure 7 shows a sequence of 25 composite images at a 0.5 MHz frame rate. CO_2 has been seeded into the flow to enhance the Rayleigh scattering. In the upper spanwise images, the flow is moving away from the observer. In the lower planform images, the flow is from left-to-right. In order to capture the spanwise images, the laser also had to impinge on the model. The laser illumination came predominantly from the left side of the spanwise images and, without the iodine filter, light scattered off the model completely obscured the image. With the filter, some residual light scattering from the surface made it through (the attenuation is approximately a factor of 10^5). This scattering is quite evident in the planform images and indicates the position of the spanwise laser sheet.

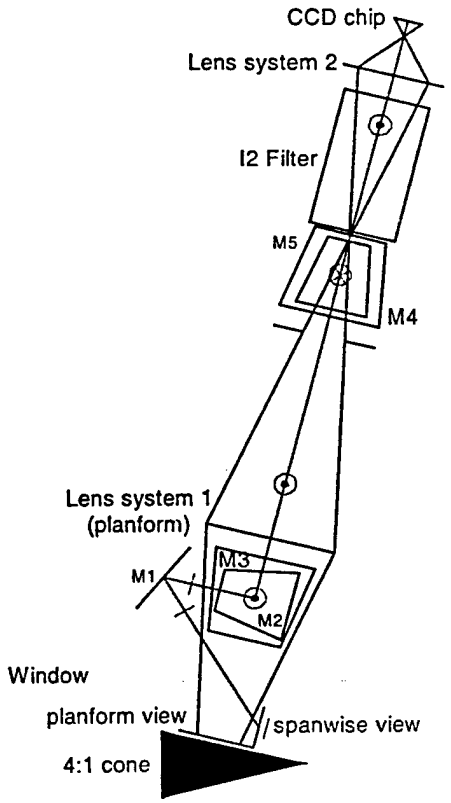

Figure 6. Focusing geometry for the generation of the two-field composite image.

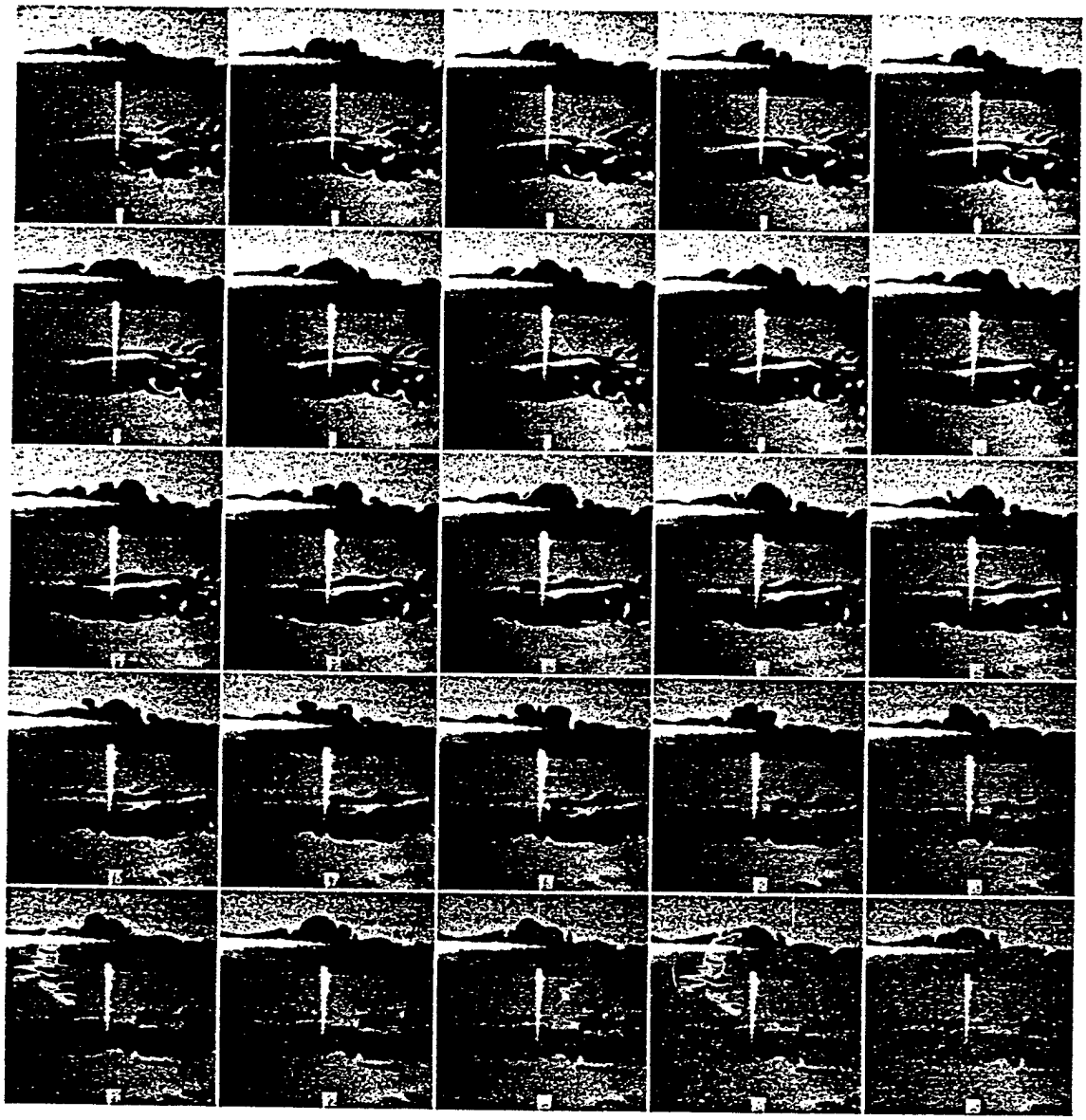

Figure 7. Sequential spanwise and planform images recorded by a single camera. The upper one-third is the spanwise image with a frame size (from left-to-right) of 1.25". The lower two- thirds is the planform view image with a frame size 2.5". The framing rate is 0.5 MHz.

The surface scattering can also be seen in the spanwise images and helps to define the location of the surface. The planform laser sheet was 2.5 mm away from the cone centerline, and the spanwise laser sheet was 8.5 inches from the tip of the cone. The boundary layer thickness, δ, is around 4 mm. The wind tunnel was running at $P_0 = 600$ psi, $Re = 8.57 \times 10^6$/m, $Re_x = 1.82 \times 10^6$.

The sequential images capture the structure and motion of the flow in three dimensions. We can locate the counterpart of the structures seen in the spanwise images in the planform images. Note, for example, that the streaks seen to the sides of the centerline in the planform images correspond to the rolled up vorticies seen in the spanwise images. The pressure gradient that drives the boundary layer toward the centerline causes it to thicken, as can be seen in the spanwise images. The associated cross flow is responsible for the boundary layer instability and for features typical of low-speed transition, including the formation on hairpin-like vortex structures. A hairpin vortex-like structure can be seen on the left side of the spanwise structure in images number 4 through 11. Even though the spanwise images show rapid flow fluctuations, the planform images indicate that there is little structure evolution, and the fluctuations in the spanwise images are almost entirely due to convection of the structure through the image plane.

Volume Rendering

The fact that the flow evolution is slow in comparison to the convection rate introduces the possibility of using the spanwise images to construct a quasi-instantansous volume image of the flow field. This is done using the "frozen flow" assumption, which simply means that the displacement of the structure through the location where the spanwise images are being recorded is equivalent to recording simultaneous stacks of spanwise images of the structure at one instant in time. The fact the planform images are being taken at each sampling instant gives a definitive measure of the validity of the "frozen flow" assumption. The recon-struction requires that the flow velocity be known and constant across the spanwise sampling plane. This, of course, cannot be the case for the inner portions of the flow, which are moving slower due to the presence of the wall of the ellipse. However, the CO_2 condensation technique only marks the outer portion of the boundary layer where the temperature discontinuity occurs. Thus, the velocity of the observed structure is very close to the free stream velocity. Figure 8 shows six sequential spanwise images, and the apparent displaced location of these image planes on the planform image taken simultaneously with the fifth (16μsec) spanwise image. Figure 9 shows a sequence of 28 planform images taken on the 4:1 ellipse at a Reynolds number of $Re_x = 1.57 \times 10^6$. These images were used to construct the three-dimensional rendering shown in Fig. 10. Planes were captured at spatial increments of 2.4 mm and smoothed to produce a continuous surface to facilitate viewing. Some residual stepwise variation remains in the regions where the structure of the features is finer than the scale of the sampling interval. This image represents the structure seen looking down on the surface with the flow moving from left-to-right. The position of a light source is indicated by the star, and the structural features are highlighted by shading. Figure 11 shows a planform section taken from the volume rendering compared to the true planform section taken by the laser. The shaded plane shows the location where the timing of the spanwise data coincides with the planform image. Around that location the frozen flow approximation is most valid. The flow farther from that point does not quite overlap the volume rendering because the flow structure evolved somewhat in the time it took to convect to the sample plane.

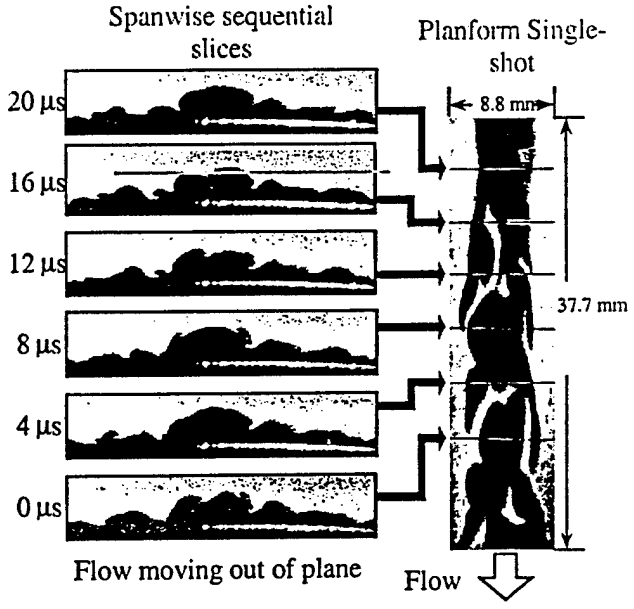

Figure 8. Images taken at a 500 kHz rate indicating the associated displacement of the structure through the spanwise imaging plane. The planform image was taken simultaneously with the second fifth image at the 16 μsec time step.

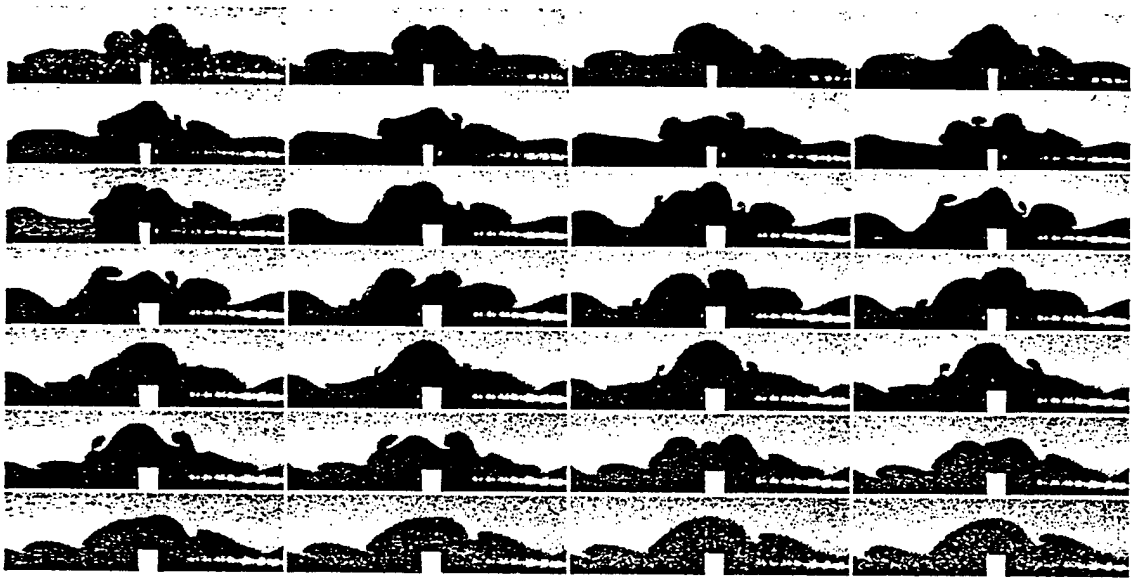

Figure 9. Sequential spanwise images of a Mach 8 flow over a 4:1 cone at medium Reynolds number (Re_x=1.57×10^6). The frame size from left-to-right is 1.25 inches, and the framing rate is 0.5 MHz.

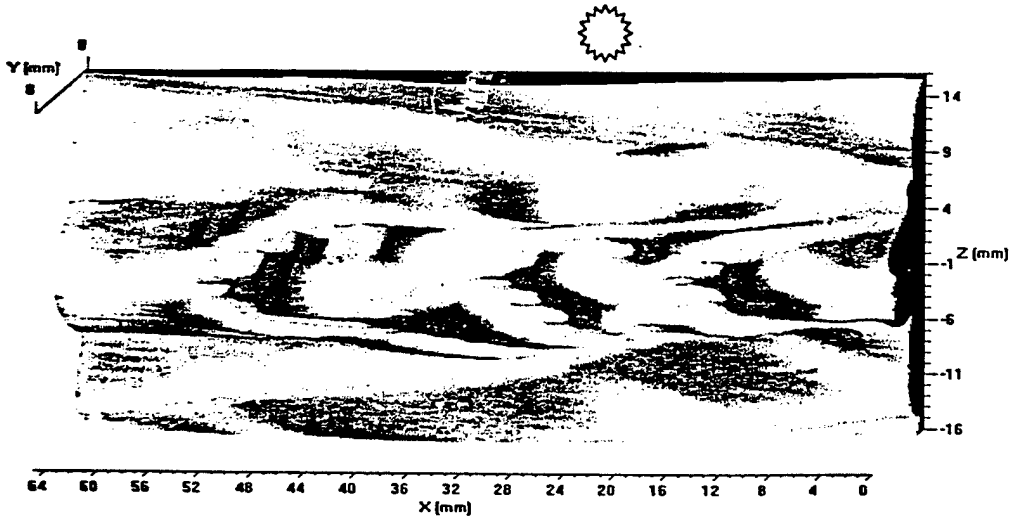

Figure 10. Volume rendering of boundary layer structure over a 4:1 elliptic cone at Re_x=1.57×10^6. The star indicates the location of the shading light source.

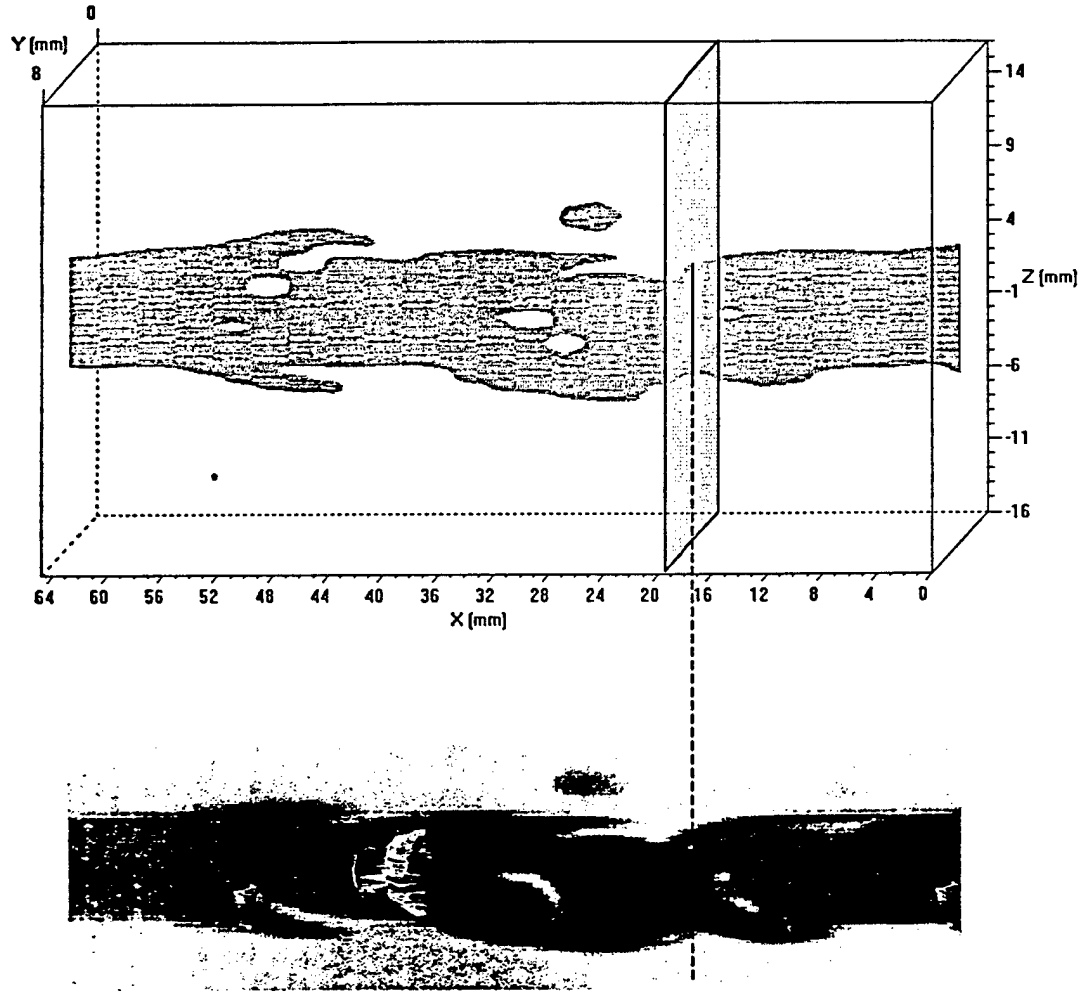

Figure 11. Comparison between (a) a slice cut through the volumetric reconstruction of Fig. 10 along the planform orientation at Y=4mm, and (b) a single-shot planform image (4 mm from the cone surface) taken simultaneously with frame #9 in Fig. 9. The shaded plane and line show the point where the planform image timing coincides with the spanwise plane. Flow is from left-to-right, and the timing sequence of the spanwise image proceeds at 2 μsec intervals corresponding to 2.4 mm steps from right-to-left.

In the volume rendering (Fig. 10), the cross flow wave structure is apparent. These waves lie close to the surface and only show up on the planform sections taken very close to the surface. They can, for example, be seen in near-surface images, such as those in Fig. 12 taken at 1.5 mm height at $Re_x=2.6\times10^6$. A feature of the frozen flow method for obtaining the volume rendering is that, if the wave structure is stationary, then the rendering would show what appears to be parallel wave features (zero wave angle) since all the images are taken at the same absolute location downstream of the tip of the elliptical model. On the other hand, if the wave structure is moving, then the apparent wave angle is not zero. In the rendering, the wave angle is not zero, so the waves are convecting with the flow and correspond to travelling wave disturbances that are characteristic of a high disturbance environment. The cross flow wave structure can also be observed in Fig. 12, where it is also apparent that the wave structure moves with the flow.

The cross-flow traveling waves are also apparent on a 2:1 elliptic cone. A rendering of this structure is shown in Fig. 13. In this image, the laser sheet is 5 inches from the tip of the cone, the stagnation pressure is P_0= 800 psi, the unit Reynolds number is Re= 1.09×10^7/m, and $Re_x = 1.3 \times 10^6$. This rendering seems to show the appearance of a transitional spot very reminiscent of transition on a flat plate at low Reynolds numbers.

Summary

In this paper, we have presented both a dual imaging system and a three-dimensional imaging technique for the study of boundary layer structure in high-speed environments. Images from a transitional boundary layer over elliptic cone models at Mach 8 were used to demonstrate the utility of these new approaches to flow field diagnostics. The flow was seeded with approximately 1% of CO_2 in gas phase upstream of the plenum, and the condensation of that vapor in the cold core region of the flow provided high scattering contrast for the observation of boundary layer structures. The imaging system used a pulse-burst laser capable of operating at up to 1 MHz pulse repetition rate and a high-speed CCD framing camera with on-pixel storage elements. An iodine molecular filter was placed in front of the camera to eliminate scattering from the surface of the models. The dual imaging system was used to capture both spanwise and planform planes of a turbulent boundary layer on 4:1 elliptic cone models at Mach 8. These images show the full three- dimensional nature of the boundary layer evolution and can be analyzed to develop an understanding of the dynamics of transitional structure for this complex geometry. The optical system was designed to produce a composite image on the CCD camera, so both projections were captured onto a single camera frame. Since the planform images indicated that the flow evolved slowly, compared to its passage through the observation region, the "frozen flow" approximation could be applied with good accuracy. This approximation meant that the spanwise images which were captured could be rendered into a volume image that very closely reproduces the three-dimensional structure of the boundary layer.

Acknowledgements

The work reported here was supported by the Air Force Office of Scientific Research. The authors would like to thank Princeton Scientific Instruments for the use of their CCD framing camera. Rene Tolboom participated in this work as a visiting student from the University of Nijmegen.

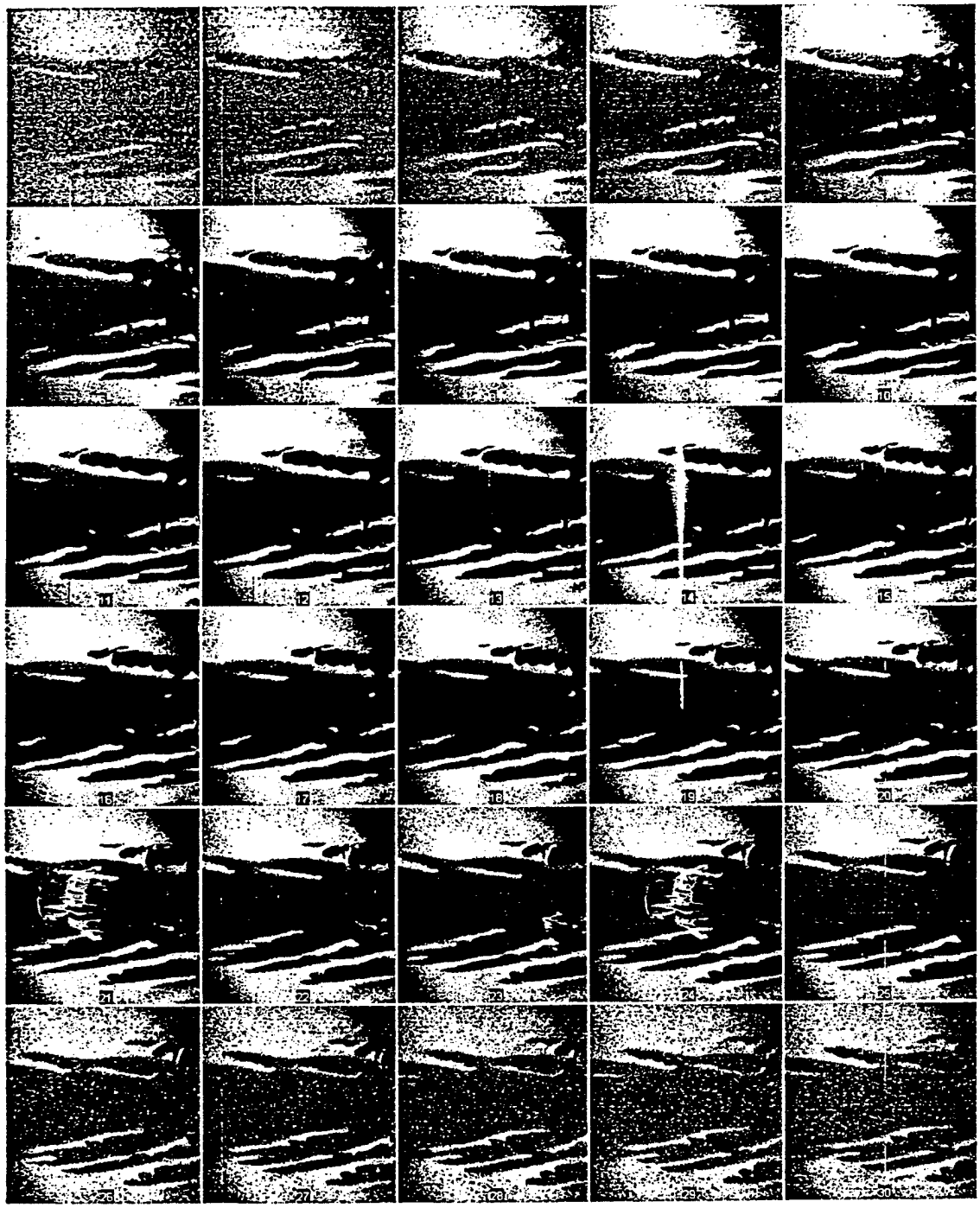

Figure 12. Sequential planform images of Mach 8 flow over a 4:1 cone. The laser sheet is 1.5 mm away from the cone surface, $Re_x = 2.6 \times 10^6$. Flow is from left-to-right.

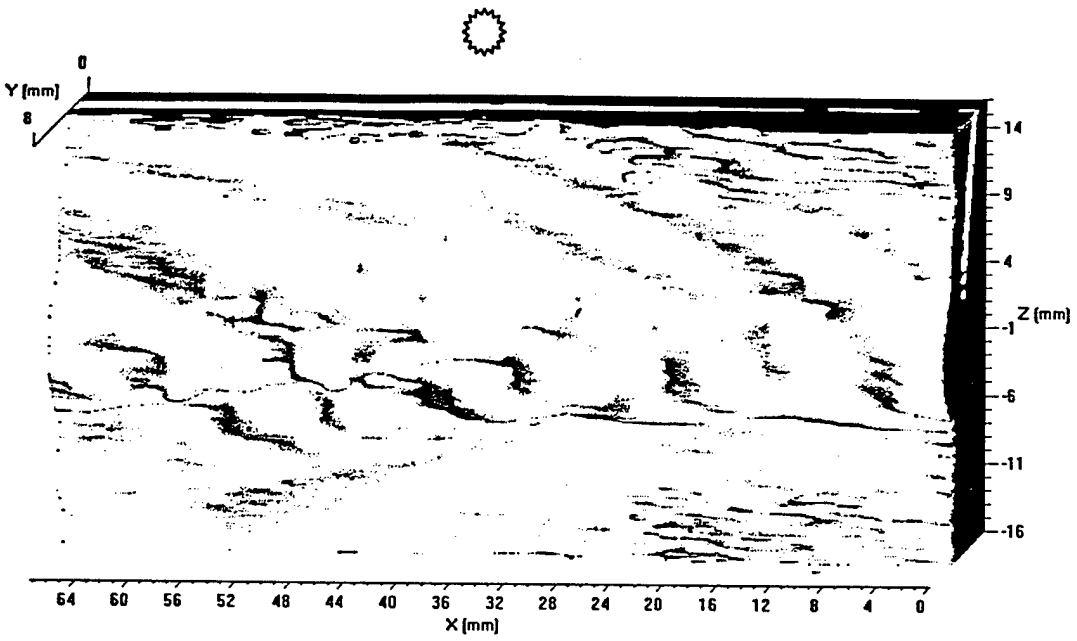

Figure 13. Volume rendering of boundary layer structure over a 2:1 elliptic cone model at $Re_x = 1.3 \times 10^6$. The star indicates the location of the shading light source.

References

1. Wu, P., "MHz-Rate, Pulse-Burst Laser Imaging System: Development and Application in High-Speed Flow Diagnostics," Ph.D. Thesis, Princeton University, June 2000.

2. W.S. Saric, B. Ruben, J.R. Carrillo, and M.S. Reibert, "Nonlinear Stability and Transition in 3-D Boundary Layers," Meccanica 33, (1998), pp. 469-487.

3. M.B. Huntley, P. Wu, R.B. Miles, and A.J. Smits, "MHz Rate Imaging of Boundary Layer Transition on Elliptic Cones at Mach 8," AIAA-00-0379, 38th Aerospace Sciences Meeting & Exhibit, Reno, NV, Jan. 10-13.

4. P.P. Wu and R.B. Miles, "High Energy, Pulse-Burst Laser System for Megahertz-Rate Flow Visualization," Optics Letters 22, (Nov. 15, 2000), p. 1639.

5. P.J. Erbland, D. Rizzetta, and R.B. Miles, "Numerical and Experimental Investigation of CO_2 Condensate Behavior in Hypersonic Flow," AIAA-00-2379, 21st AIAA Aerodynamic Measurement Technology and Ground Testing Conference, Denver, CO, June 19-22, 2000.

6. J.N. Forkey, W.R. Lempert, and R.B. Miles, "Corrected and Calibrated I_2 Absorption Model at Frequency-Doubled Nd:YAG Laser Wavelengths," Applied Optics 36 (1997), pp. 6729-6738.

7. P. Wu,, W.R. Lempert, and R.B. Miles, "MHz Pulse-Burst Laser and Visualization of Shockwave/Boundary Layer Interaction," AIAA Journal 38, (2000), pp. 672-679.

8. M.L. Baumgartner, "Turbulence Structure in a Hypersonic Boundary Layer," Ph.D. Thesis, Princeton University, Dept. Mechanical & Aerospace Engineering, June 1997.

APPENDIX II: Microwave-Driven Air Plasma

1. **B. McAndrew**, P. Barker, and R.B. Miles, *"Development of a Supersonic Plasma Wind Tunnel,"* Paper #AIAA-2000-0533, AIAA 38th Aerospace Sciences Meeting & Exhibit, Reno, NV, Jan. 10-13, 2000.

2. S.O. Macheret, Yu. Z. Ionikh **N.V. Chernysheva**, A.P. Yalin, L. Martinelli, **B. McAndrew**, P.F. Barker, M.N. Shneider, and R.B. Miles, 2nd Workshop on Magneto and Plama Aerodynamics for Aerospace Application*"Shock Propagation in Weakly Ionized Gases and Plasma Control of High-Speed Flows,"*, Russian Academy of Sciences, Moscow, Russia, April 5-7, 2000.

AIAA 2000-0533

DEVELOPMENT OF A SUPERSONIC PLASMA WIND TUNNEL

B.McAndrew, P.Barker, and R.B.Miles

Princeton University

38th Aerospace Sciences Meeting & Exhibit

10-13 January 2000 / Reno, NV

AIAA-2000-0533

DEVELOPMENT OF A SUPERSONIC PLASMA WIND TUNNEL

B. McAndrew*, P. Barker†, and R. Miles‡

ABSTRACT

The study of controlled plasma discharges in supersonic air has become an area of increasing interest. These discharges may be used for flow control, drag reduction, combustion initiation and stabilization, as well as for power extraction and plasma shielding applications. In order to study the formation of such discharges and their impact on the flow, proper testing facilities are required. This paper details the work done in the design, construction, and testing of a supersonic plasma wind tunnel.

INTRODUCTION

Over the past decade, research into the interaction of plasma with a gas flow has yielded some results which have not yet been fully explained[1-5]. For example, changes in shock wave strength and shock standoff distance caused by the presence of plasma have been observed experimentally, but cannot be fully explained with present theoretical models. A better understanding of these interactions, as well as the potential applications for the controlled modification of shock structure, motivates the present work.

WIND TUNNEL DESIGN

The basic configuration of the wind tunnel is controlled by the need to create a plasma in the region of supersonic flow. A schematic of the facility is shown in Figure 1 below.

A Plasma is created with a 50 kW, 1 ms pulse of microwave radiation at 2.45 GHz, which induces electric breakdown of the air in the region of supersonic flow. Microwaves are introduced into the plenum through an EM window mounted over a port on one wall. The direction of propagation is then turned 90° by an aluminum reflector, so the microwaves travel coaxially with the flow through the plenum chamber and nozzle section. The aluminum reflector is made with a dense array of ¼" holes in it to allow passage of air while simultaneously reflecting the microwaves. The breakdown location is controlled by two factors; a reduced static pressure in the high speed section, and an increased field intensity downstream of the throat.

Microwave discharges occur more easily at low pressure due to the reduced collision frequency. Thus, introducing microwaves through the plenum where the air is at high pressure avoids the risk of parasitic breakdown near the window housing and window surface.

As shown in Figure 1, the waveguide walls are tapered to create an enhancement of the electric field as the microwaves propagate downstream. The nozzle contours within the taper are made of dielectric material so as to transmit the microwave radiation. The taper continues down to and slightly beyond the cutoff dimensions for radiation at 2.45 GHz. This generates a reflection, reversing the propagation direction as the microwaves reach the cutoff point. This taper is used as one end of a microwave resonator. The other end of the resonator is formed by a triple stub tuner on the generator side of the entrance window. This arrangement allows for the build up of a standing wave in the wind tunnel. In order to provide a further field enhancement at the intended breakdown location, and to provide for spatial localization of the plasma, two 1 cm long metal pins are mounted opposite each other on the inside walls of the wind tunnel. The magnetron is protected from spurious reflections by a circulator and dummy load.

The flow of air proceeds from the plenum, through the nozzle, and into the 2"x2" test section. The air is then discharged into a vacuum tank. The nozzles are contoured to achieve Mach 3 flow in the test section. Flow conditions in the test section are 20 Torr static pressure, 110 K static temperature, and a Mach number of 3.

MICROWAVE FIELD DISTRIBUTION

The microwave field distribution was measured along the centerline of the wind tunnel from the reflector plate to the wind tunnel exit plane. For these measurements, the microwave field was generated

* Graduate Student
† Research Staff Member, Member AIAA
‡ Professor, Associate Fellow AIAA

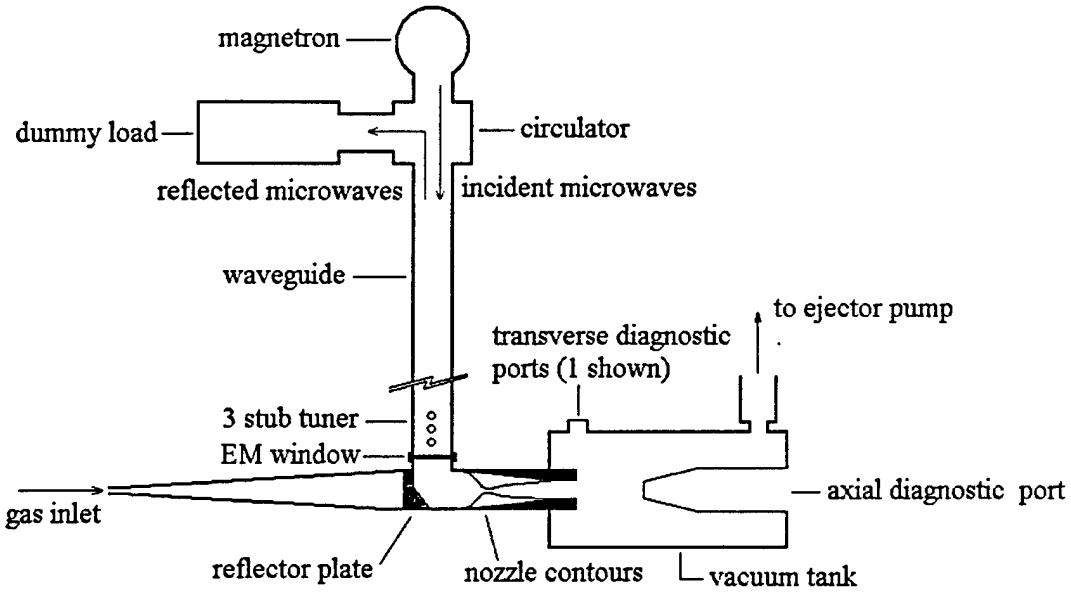

FIGURE 1: FACILITY SCHEMATIC

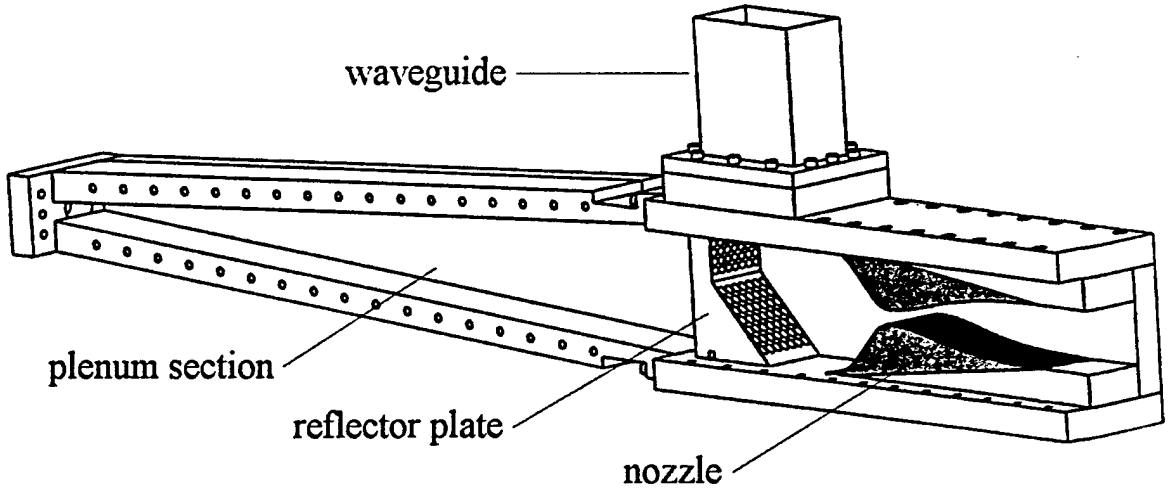

FIGURE 2: PLENUM AND NOZZLE CUTAWAY DRAWING

using a 100 mw source operating in a continuous mode at 2.45 GHz. This source was coupled into the wind tunnel with the same triple stub tuner and window arrangement used for the 50 kW, 1 ms pulse breakdown experiments. The measurements were made with a probe consisting of a 1 cm antenna protruding from a length of semi-rigid coaxial cable. This probe was introduced into the wind tunnel from the downstream end and traversed through the wind tunnel in increments. The 2.45 GHz signal obtained with the probe was attenuated and rectified with a crystal diode before being recorded on a digital oscilloscope. An average of several such traverse measurements is shown in Figure 3.

NUMERICAL SIMULATIONS

To complement the measurements described above, as well as to permit parametric studies of the effect of changes in the electrical properties of the wind tunnel, a commercial finite element code was used to simulate the electric field standing wave pattern.

The code used was the High Frequency Structure Simulator package from Hewlett Packard, which was run on a UNIX based workstation. The results of several case studies, including a comparison with the measurements described above, are presented in Figures 4 through 8.

In the above simulations, incident wave phase is chosen to show the standing wave pattern at its maximum intensity. For the cases shown in Figures 4 and 5 the region of highest field intensity remains localized at the same point throughout each cycle of the incident wave propagation. For the cases shown in Figures 6 and 7, due to the lossy dielectric, deviations from a perfect standing wave pattern occur. In particular, the region of highest field intensity changes dramatically as the incident wave goes through one cycle. The field can be seen to be strongly dependent on dielectric material properties, which has important implications for the generation of plasma inside the wind tunnel.

BREAKDOWN MEASUREMENTS

Using the G-10 nozzle breakdown can occur in either of two locations, depending upon conditions. Under static conditions below about 30 Torr, breakdown occurs upstream of the throat, slightly below the centerline of the wind tunnel. Above 30 Torr under static conditions breakdown occurs downstream of the throat at the intended location. These two positions correspond with the two peaks in field intensity in the simulation. Note that under flow conditions, with higher pressure upstream of the throat than downstream, the breakdown will also occur in the downstream location.

Breakdown in the wind tunnel was recorded with photodiodes and high speed photographic equipment. The pressure was chosen for the static case so as to match gas density with the flow conditions. Measurements of the plasma luminosity were made both with flow and under static conditions. In all cases the tests were performed in air with a microwave pulse duration of 1 ms. The results indicate the initiation of the plasma within 10 μs after the start of the microwave pulse without flow, and within 20 μs after the start of the pulse with flow. A brighter plasma was observed with flow than without flow, as shown in Figures 9 and 10.

The photographs shown in Figure 11 were made with a gated, intensified CCD camera. The view is through the axial diagnostic port shown in Figure 1, looking upstream into the wind tunnel. Images were taken of the plasma both with the wind tunnel running and under static conditions at 60 Torr and room temperature. The pressure was chosen for static conditions to match the density with the Mach 3 flow for comparison. In all cases the camera gate was maintained at 3 μs. The images show the plasma generated while the wind tunnel was running to be brighter and more contracted than the plasma generated under static conditions. The location of the plasma within the tunnel appears to be stable for the duration of the 1 ms pulse. Note that each image represents a separate instance of plasma generation.

CONCLUSIONS

A Mach 3 wind tunnel with integrated microwave plasma generating capability has been designed and tested. The importance of the electrical properties of the wind tunnel for microwave propagation and breakdown has been shown. Self induced plasma generation has been achieved with a microwave pulse length of 1 ms. A stable, well localized plasma has been maintained in the wind tunnel with flow. Measurements of the plasma indicate a brighter and more filamentary discharge with flow than without flow.

ACKNOWLEDGEMENTS

Funding for this work has been provided by an AFOSR grant.

REFERENCES

1. W. Beaulieu, V. Bytyrin, A. Klimov, S. Leonov, A. Pashina, and B. Timofeev, "Plasma Aerodynamic Wind Tunnel Tests with 1/6 Scale Model of Nose Part of F-15," 3rd Weakly Ionized Gases Workshop, Norfolk, VA, November 1-5, 1999.
2. A. Klimov, S. Leonov, A. Pashina, V. Skvortsov, T. Cain, and B. Timofeev, "Influence of a Corona Discharge on the Supersonic Drag of an Axisymmetric Body," 3rd Weakly Ionized Gases Workshop, Norfolk, VA, November 1-5, 1999.
3. S. Merriman, I. Adamovich, and J.W. Rich, "Studies of Oblique Shock Waves in Weakly Ionized Nonequilibrium Plasmas," 3rd Weakly Ionized Gases Workshop, Norfolk, VA, November 1-5, 1999.
4. R. Yano, V. Contini, E. Ploenjes, P. Palm, S. Merriman, I. Adamovich, W. Lempert, V. Subramaniam, and J.W. Rich, "Flow Visualization in a Supersonic Nonequilibrium Plasma Wind Tunnel," 30th Plasmadynamics and Lasers Conference, Norfolk, VA, June, 1999.
5. V. Soloviev, V. Krivstov, A. Konchakov, N.D. Malmuth, "Mechanisms of Shock Wave Dispersion and Attenuation in Weakly Ionized Cold Discharge Plasmas," IVTAN Perspectives of MHD and Plasma Technologies in Aerospace Applications Conference, Moscow, Russia, March 24-25, 1999.
6. S. Macheret, L. Martinelli, and R. Miles, "Shock Wave Propagation in Non-Uniform Gases and Plasmas," 37th AIAA Aerospace Sciences Meeting and Exhibit, Reno, NV, January 11-14, 1999.
7. A. Yalin, Y. Ionikh, R. Miles, "Temperature Measurements in Glow Discharges with Ultraviolet Filtered Rayleigh Scattering," 30th AIAA Plasmadynamics and Lasers Conference, Norfolk, VA, June 28-July 1, 1999.
8. P. Harsha and E. Gurjanov, "AJAX: New Directions in Hypersonic Technology," 8th Aerospace Planes and Hypersonic Technologies Meeting, Norfolk, VA, April, 1996.
9. A.D. MacDonald, *Microwave Breakdown in Gases*, Wiley, 1966.
10. R. Collin, *Foundations for Microwave Engineering*, McGraw-Hill, 1966.
11. G. Matthaei, L. Young, E. Jones, *Microwave Filters, Impedance Matching Networks, and Coupling Structures*, McGraw-Hill, 1964.

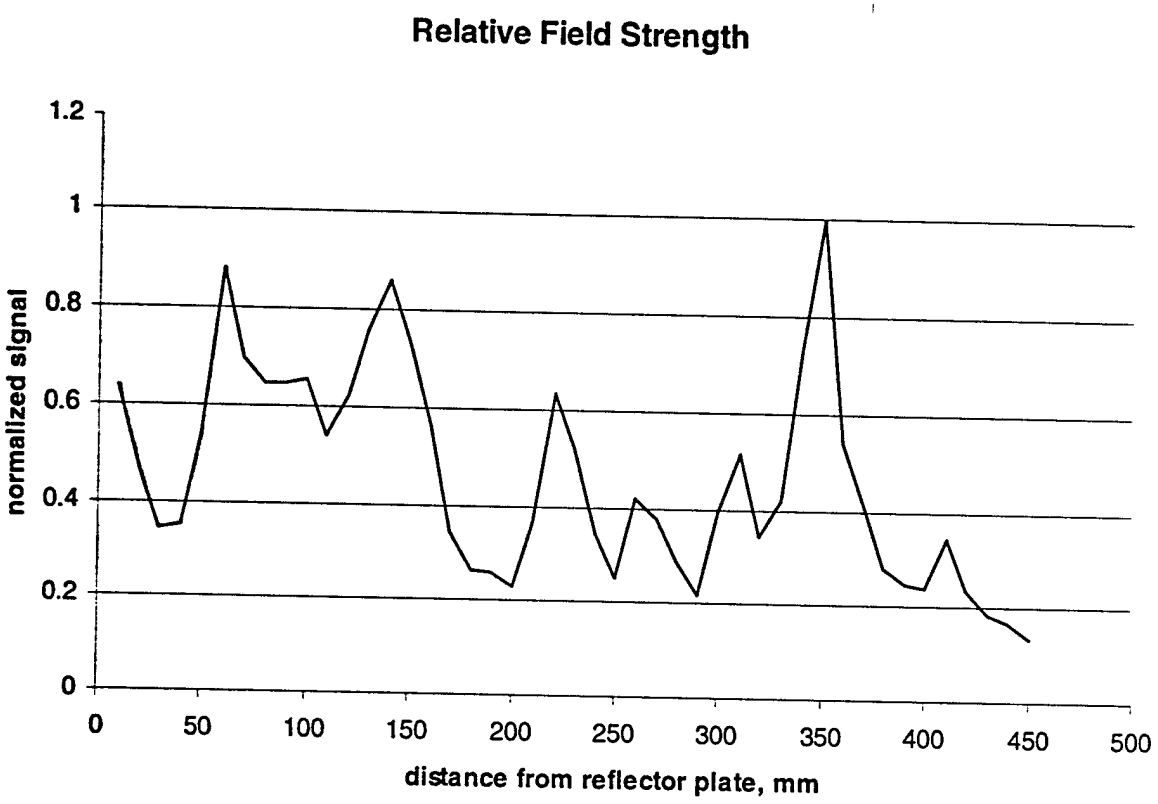

FIGURE 3: MEASURED ELECTRIC FIELD ALONG WIND TUNNEL CENTERLINE

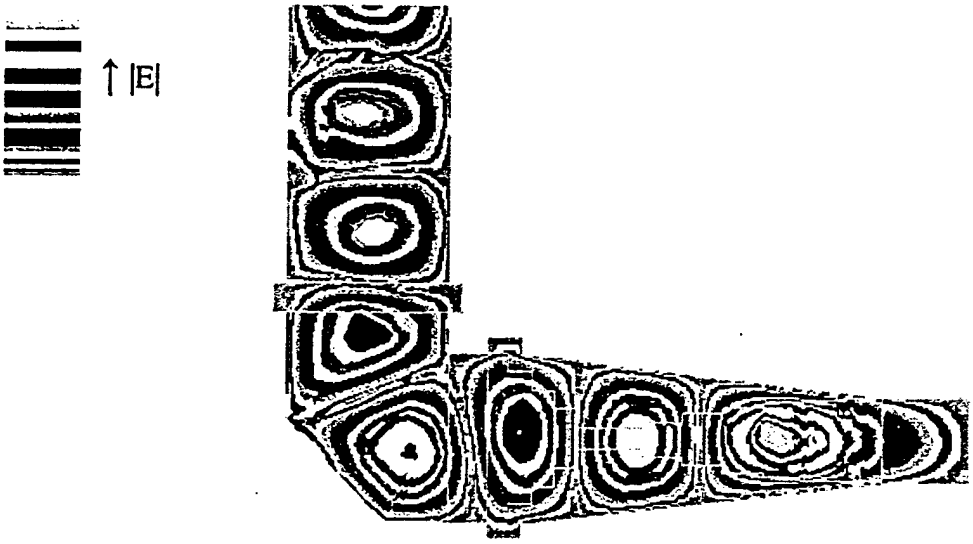

FIGURE 4: ELECTRIC FIELD MAGNITUDE WITH AIR FILLED WAVEGUIDE (NO DIELECTRIC)

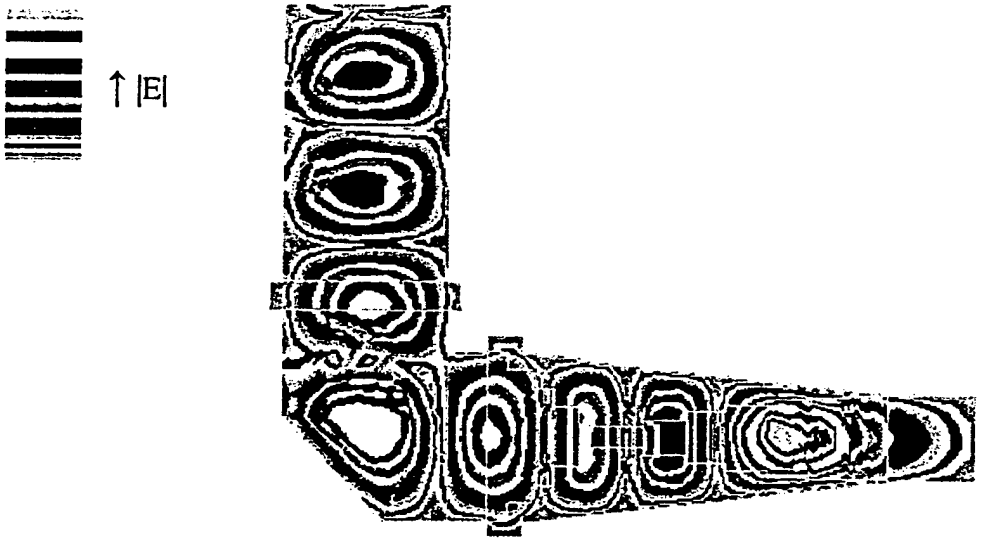

FIGURE 5: ELECTRIC FIELD MAGNITUDE WITH TEFLON NOZZLE
Relative permittivity = 2.08 Dielectric loss tangent = 0.00037

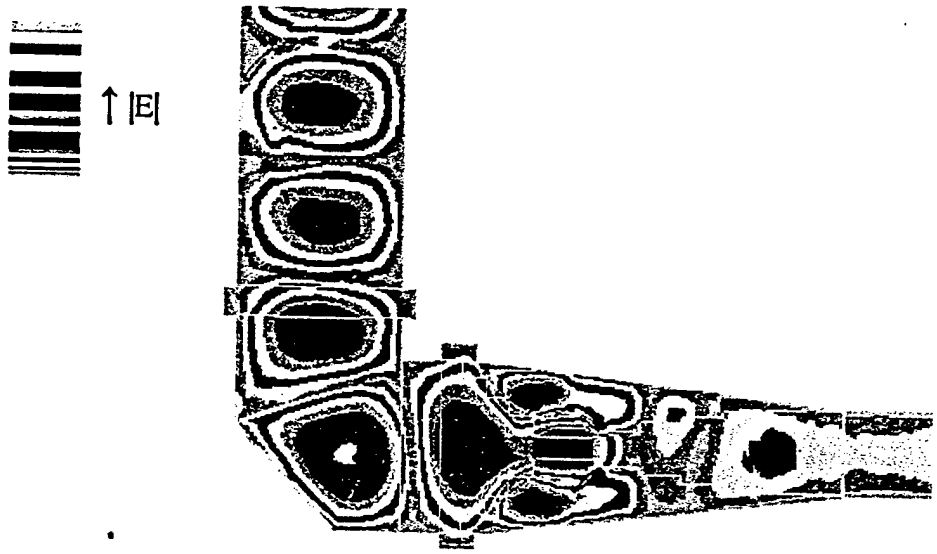

FIGURE 6: ELECTRIC FIELD MAGNITUDE WITH G-10 NOZZLES
Relative permittivity = 5.0 Dielectric loss tangent = 0.019
Incident wave phase = 157°

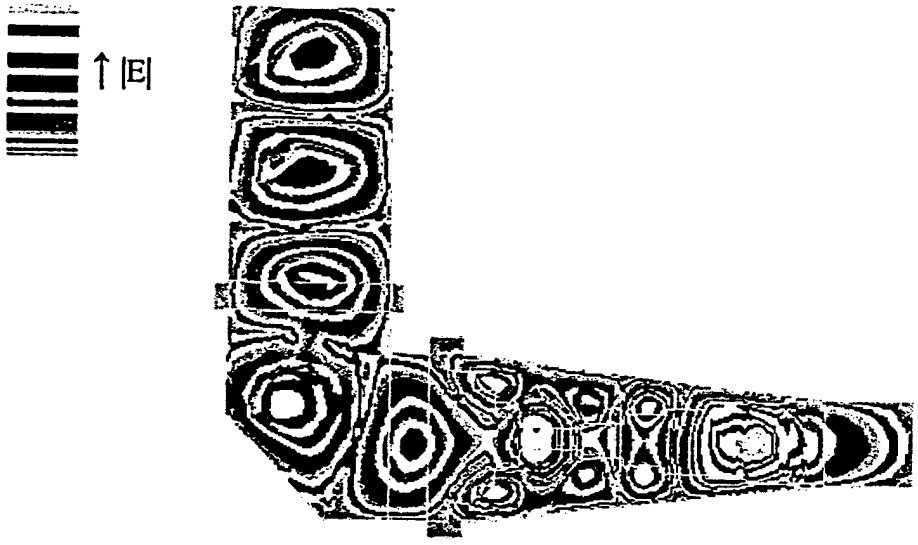

FIGURE 7: ELECTRIC FIELD MAGNITUDE WITH G-10 NOZZLES
Relative permittivity = 5.0 Dielectric loss tangent = 0.019
Incident wave phase = 70°

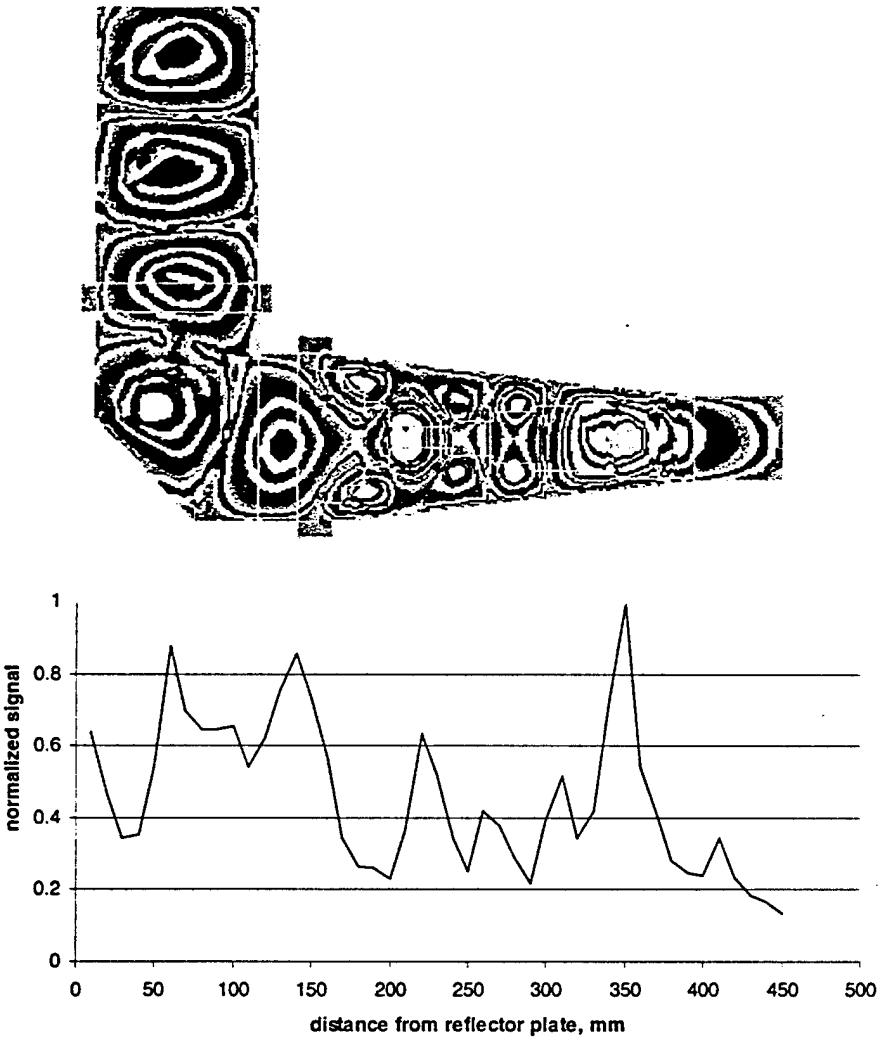

FIGURE 8: COMPARISON BETWEEN SIMULATION AND MEASUREMENT USING G-10 NOZZLES

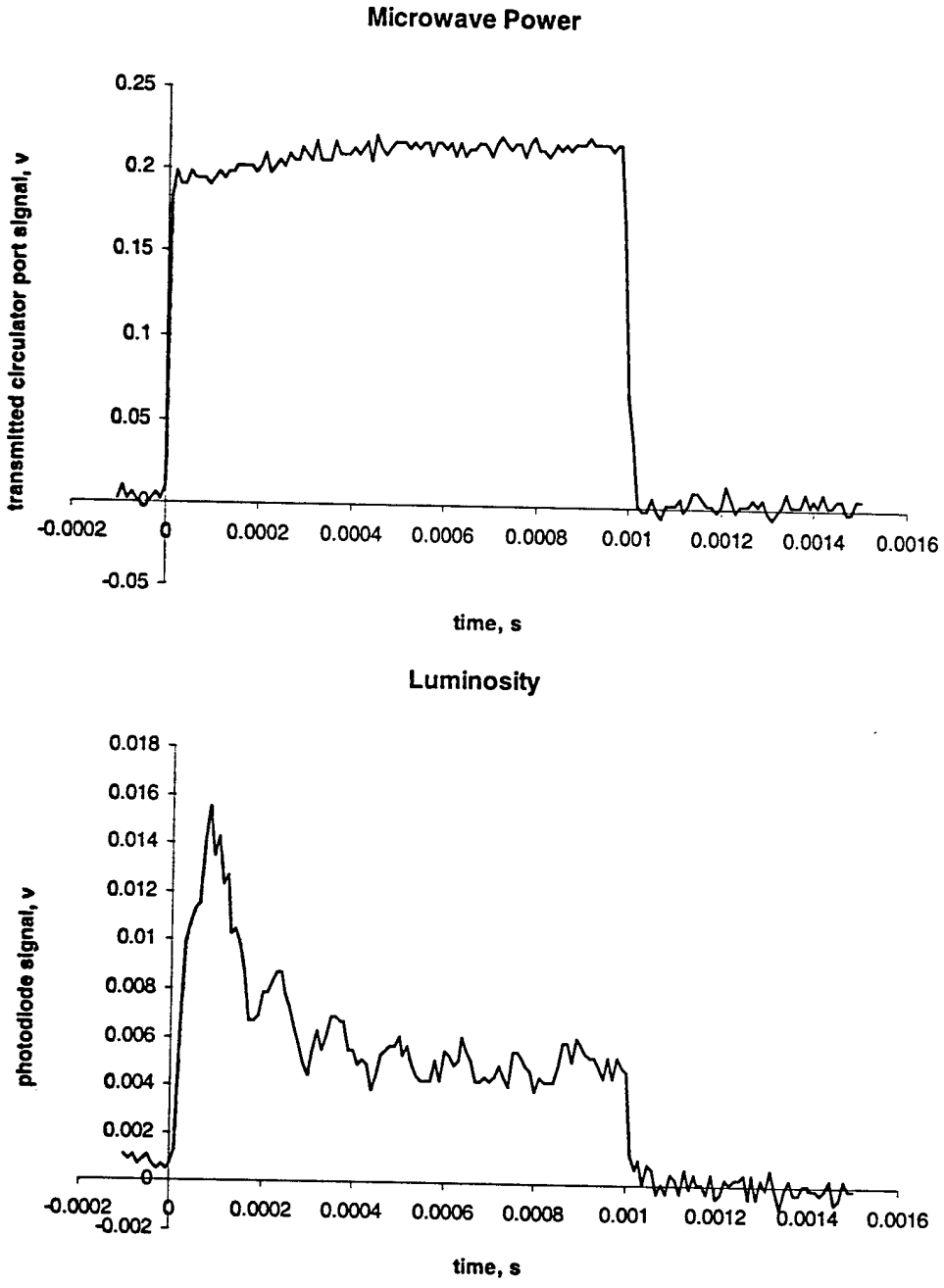

FIGURE 9: PLASMA LUMINOSITY WITHOUT FLOW (60 TORR, 300 K)

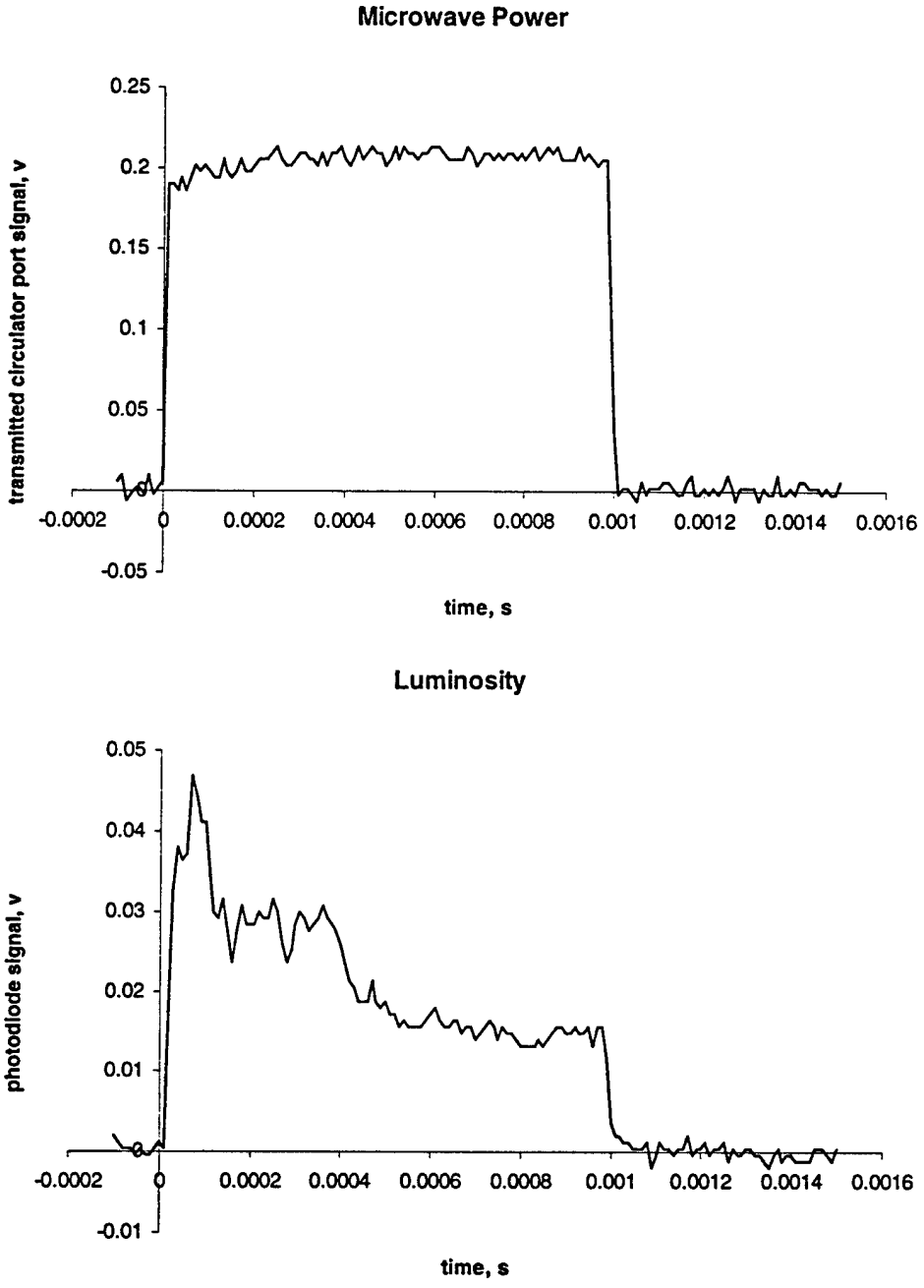

FIGURE 10: PLASMA LUMINOSITY WITH FLOW

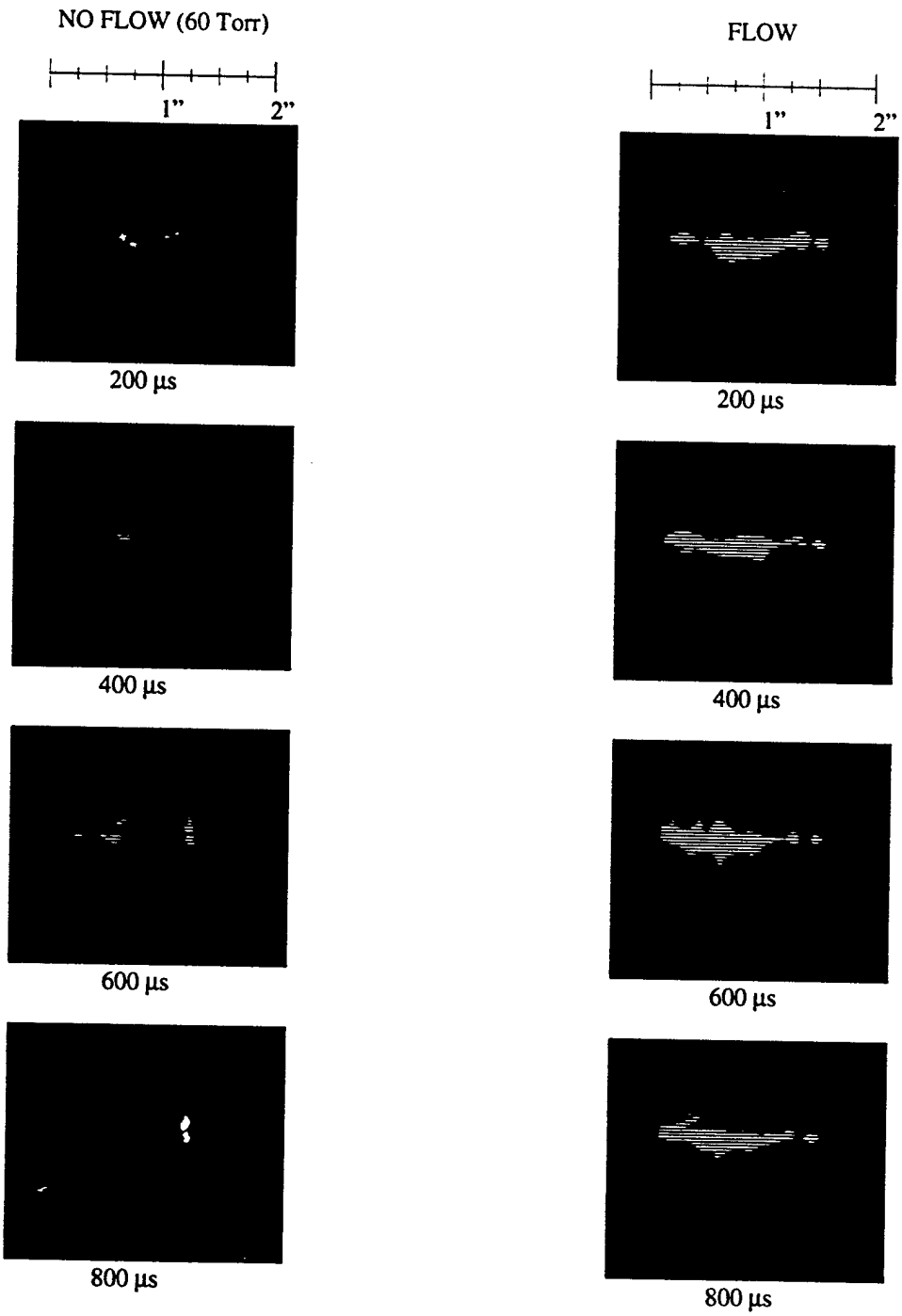

FIGURE 11: COMPARISON OF PLASMA WITH AND WITHOUT FLOW

2nd Workshop on Magento and Plasma Aerodynamics for Aerospace Applications
Russian Academy of Sciences, Mowcow, Russia (April 5-7, 2000)

SHOCK PROPAGATION IN WEAKLY IONIZED GASES AND PLASMA CONTROL OF HIGH-SPEED FLOWS

S.O.Macheret, Yu.Z.Ionikh, N.V.Chernysheva, A.P.Yalin, L.Martinelli, B.McAndrew, P.F.Barker, M.N.Shneider, and R.B.Miles

Princeton University
Department of Mechanical and Aerospace Engineering, D-414 Engineering Quadrangle
Princeton, NJ 08544, U.S.A.
E-mail: macheret@princeton.edu

Abstract

The paper describes experimental and theoretical studies of shock propagation in weakly ionized plasmas and of plasma effects on supersonic aerodynamics. Laser Schlieren measurements of shock profiles and velocities in continuous and pulsed glow discharges in conjunction with CFD modeling show that "anomalies" are explained by conventional gas dynamics, with critical role of non-one-dimensionality due to transverse temperature gradients. Experiments with pulsed discharges directly prove the thermal mechanism of shock dispersion. For aerodynamic applications, localized and controllable energy addition to the flow through plasma could provide a tool of controlling shocks and heat fluxes, and of steering. Filamentary microwave plasma initiated and guided by low-power lasers and electron beams could be such a flexible and efficient tool. Successful development and testing of a small-scale wind tunnel with microwave-driven plasma is reported.

1. Introduction

Weakly ionized gases (plasmas) could find several types of applications in high-speed aerodynamics, such as shock wave control, drag reduction, vehicle steering, sonic boom attenuation, ignition of combustion in engines, and MHD power extraction and enthalpy by-pass. There are at least two groups of fundamental issues that have to be resolved prior to any practical applications:

1. What is the mechanism, or mechanisms, of plasma effects on supersonic flow, especially on shock waves? Are the mechanisms thermal, due mostly to Joule heating, or there exists a plasma-specific phenomenon (electric double layer, ion-acoustic or other waves, etc.) that affects shock waves?
2. How efficiently one can generate, sustain, and control plasmas in high-speed airflow?

Several research projects at Princeton University address these and other plasma-related issues. In this paper, we review some of the ideas and results of these projects. First, we describe theoretical and experimental studies of "anomalous" effects in shock propagation through glow-discharge plasmas [1 – 4, 7, 8]. We show that the experimentally observed effects can be explained by conventional gas dynamics that takes into account non-one-dimensionality of the problem. Since microwave streamer discharges can propagate supersonically and could be useful in aerodynamics as concentrated energy sources, we discuss triggering and guiding those discharges by lasers [3, 5] and recent development of an experimental facility for studies of microwave plasmas in supersonic flow [6]. Electron beams are also discussed as an energy-efficient way of generating plasmas that can be sustained in high-speed flows [9].

2. Experiments on shock propagation in steady-state glow discharges [4, 1]

2.1. Experimental facility and procedures [2 – 4]

Experimental studies of shock waves in weakly ionized plasmas were performed in longitudinal continuos or pulsed glow discharges. The discharge tube, 3.8 cm i.d. and 120 cm full length, was made of quartz. Shock waves were generated by a spark discharge at the one end of the tube. The shock wave entered the discharge through a narrow (2 mm) ring electrode made of stainless steel foil mounted flush with the wall. The electrode nearest to the spark was always the anode, in order to prevent the incoming shock wave from passing by the hot cathode region.

Laser Schlieren method was used for detecting the shock front. A He-Ne laser beam crossed the discharge horizontally along the diameter and was then focused onto the plane of a knife by a lens (f=50 cm). The beam 1/e diameter was about 0.3 mm. A photodiode with a response time of 20 ns measured the light intensity after the knife edge. The signal was recorded by a digital oscilloscope with 1 kΩ resistor at the input, and a time resolution $\approx 0.1\,\mu s$.

After the laser beam crossed the discharge it was retro-reflected from a small 90° prism and passed through the discharge once more with the spatial offset and then focused onto the knife edge. This produced two closely separated Schlieren signals of opposite signs. Shock wave velocity was found by dividing the distance between the two beam passages (12 to 21 mm) by the time gap between

Schlieren signals. This method provided an accuracy of absolute velocity near 3% (≈10 m/s) and that of relative velocity about 0.5% (2 m/s).

Experiments were performed in an Ar-N_2 mixture (1% of N_2). Addition of nitrogen substantially improved the radial uniformity of the discharge. A pure argon discharge contracted at currents i>30 – 40 mA (for pressures p≥30 Torr). With nitrogen the discharge was not contracted at all conditions studied (p≤100 Torr, i≤100 mA). To prevent electrophoresis and accumulation of impurities, the gas mixture was pumped through the discharge with a rate of 300 sccm, which corresponded to 5 – 10 cm/s linear speed in the tube.

For p=30—50 Torr, i=30–100 mA the measured electric field was from 8 to14 V/cm. Assuming a Bessel radial profile for gas temperature, we calculated the reduced electric field E/N (N is gas number density) and electron number density n_e. Averaged over the tube cross section, these values are E/N=1.2–1.4 Td, $n_e=(1.2–4)\cdot10^{10}$ cm^{-3}.

We have used Ultraviolet Filtered Rayleigh Scattering (UV FRS) developed in our group [10 – 12] to measure temperature profiles of the discharges. For the range of experimental conditions studied, p=30 – 50 Torr, i=30 – 100 mA, the steady-state centerline temperature range was found to be from 440±30 K to 830±70 K. Fig. 1 shows the experimental temperature profile of an argon plasma at pressure 50 Torr and current 20 mA. Similar measurements were done in argon + 1% nitrogen mixture at 50 Torr and different values of electric current. The experimental points are in good agreement with computation. On the plot, the experimental points are fitted with a Gaussian curve.

2.2. Results of shock studies in steady-state discharges and comparison with CFD modeling [1, 4]

In our earlier work [1], we performed a 2D inviscid modeling of shock propagation through a discharge-heated gas and concluded that transverse gradient and non-one-dimensionality play a crucial role in shock propagation in glow discharges, and that multi-peak laser Schlieren signals are simply due to the shock curvature. For better comparison with experiments, the code was made from 2D into axisymmetric.

The plasma region between the infinitesimally thin electrodes was considered uniform along the tube axis (x), and to have a symmetric radial temperature profile described by the Gaussian fit to the experimentally measured profile. Both wall temperature and the gas temperature outside the discharge were put equal to room temperature. Mach number of the incident shock was selected so as to give the shock velocity in the uniform room-temperature gas at a given location close to that measured experimentally with the discharge off. For comparison with laser Schlieren measurements, the density gradient integrated in x direction across the "laser beam" and averaged in the radial direction across the tube was computed.

Fig.2 shows measured and computed Schlieren signals in pure argon. Similar comparison was done for Ar+1%N_2. Agreement between the computations and experiments, in both shock velocities and the two-peak signal shapes, is excellent. The two-peak structure of the laser Schlieren signals is due to the curvature of the shock front in a region with transverse temperature gradient. The first peak in the Schlieren signal comes from the portion of the shock that propagates through the hot centerline region. The high temperature and low density in this region result in both higher speed of the shock and lower intensity of the peak compared with those corresponding to colder near-wall regions. The portion of the shock moving through the cold near-wall region lags behind and produces a strong peak in the signal due to the high density near the wall.

For further quantitative comparison between computational and experimental results, Figures 3 and 4 show the width of Schlieren signals versus centerline temperature and the shock velocity versus average temperature in the discharge. Again, excellent agreement exists between computations and experimental data. This provides a strong evidence of conventional, thermal mechanism of shock propagation in weakly ionized plasmas.

3. Shock propagation in pulsed discharges [2 – 4]

To distinguish between thermal and plasma-specific mechanisms of shock propagation, it would be desirable to eliminate temperature effects while maintaining plasma with the same density of charged particles, electric field, etc. Fortunately, in pulsed discharges, a relatively long time interval exists when electron, ion, and excited molecule densities are quite high while the temperature is low.

In our studies, the pulsed mode of the discharge was produced by using a transistor switch in series with the discharge. The rise time for the current pulse was 20 μs, and the pulse duration was about 0.5 ms. It was found that this time was insufficient to get a uniform discharge. In fact, when the discharge was turned on, undesirable transitional processes (for example, discharges on the wall of the tube) were observed. Therefore a weak pilot discharge with 1 mA current was maintained between pulses, which resulted in a fairly uniform volume pulsed discharge. Fig.5 shows the discharge pulse shape and the time dependence of discharge integral emission (with no shock wave). Clearly, near the middle of the pulse the emission reaches its steady-state value, similar to that of the continuous discharge. The initial peak of intensity is a result of the higher electric field arising in the discharge immediately after the transistor switch is opened.

As shown in Fig. 6, for the pilot discharge a small acceleration, accompanied by some widening and weakening of the signal can be noticed, but the changes are very small compared to the higher-current continuous discharge. This is no surprise since the electron number density in the pilot discharge is $\approx 10^8$ cm^{-3} only and the measured axial gas temperature is less than 320 K. Much more important is that Schlieren signal obtained from the pulsed discharge, as seen in Fig. 6, closely matches both no-discharge and pilot-discharge curves, and is very unlike the signal from the continuous discharge. After the transistor switch is turned on, the discharge current reaches its new steady-state value in ≈ 20 μs. This value is almost the same as in continuous discharge. The electric field strength E in the pulse was found to be somewhat larger than in the continuous discharge, but the E/N values were almost identical. Thus, the electron number densities and mean electron energies should be very close to those in the continuos discharge. This is confirmed by the behavior of the discharge emission (Fig.5).

The increase in gas temperature during the pulse, calculated from the simple energy balance equation, is ΔT=0.4 K – 0.6 K. Thus, the pulsed discharge has electron component parameters (E/N, n_e, T_e) the same as in the continuous discharge, but the gas temperature is the same as in the pilot discharge, that is, close to room temperature. Comparing the three Schlieren curves of Fig.6 shows that changing the electron density by two orders of magnitude does not affect shock wave propagation, while changing gas temperature from $T_g \approx 320$ K to $T_g \approx 500$–600 K (from the pilot or pulsed discharge to the continuous discharge) affects the shock dramatically. This result is a strong evidence of thermal mechanism of shock wave – plasma interaction.

Further evidence of the thermal mechanism is provided by comparison of shock profiles in two different gases, Ar and Ar-N_2, in Fig.7. For a meaningful comparison, one has to take into account that addition of nitrogen changes the electron drift velocity and also can affect ionization and recombination processes. As a result, plasma parameters such as E/N, electron number density, and gas temperature are different for Ar and Ar-N_2 plasmas even if the gas pressure and discharge current are similar. Data presented in Fig.7 show that for the condition of equal gas temperatures similarity of the signals is the best. This supports unambiguously the thermal mechanism of shock dispersion.

4. Laser triggering and guiding of microwave discharges [3, 5]

Studies of microwave discharges in free air and other gases [13, 14, and references therein] have established that at pressures of hundreds of Torr, microwave plasmas sustained by traveling waves can exist in two principal forms. At low microwave intensity, the plasma is uniform and hot (several thousand degrees). When the microwave electric field is high enough, the plasma exist as a few dynamically evolving streamers, or filaments. On open-shutter photographs, the plasma looks like a "bird's nest", although only a few filaments exist at each moment of time. Each filament grows because of the polarizational amplification of electric field near its ends. In fact, due to the amplification effect, streamers can grow even in the so-called subcritical field, with the average electric field strength considerably below the critical breakdown threshold. This permits development of propagating filamentary microwave plasmas in subcritical fields by initiating the first streamer by a metallic pin or a sphere.

Microwave streamer plasmas are very interesting from both fundamental and practical standpoints. For aerodynamic applications, the ability of filamentary discharges to propagate supersonically in a quiescent gas, or to be stationary in a supersonic flow, is especially important. Microwave filaments can be successfully used for shock wave attenuation, because of concentrated energy addition. Sharply non-uniform temperature distribution in the "bird's nest" would disperse and attenuate shocks similar to, but stronger than, glow discharge plasma with non-uniform temperature. To prevent appearance of undesirable discharges in wrong places and in the wrong time, the microwave field strength should be kept below the critical breakdown field, so that the plasma could be started only with a remote initiator: a laser or an electron beam. Additionally, lasers can potentially guide plasma filaments and could even create a regular grid of plasma filaments instead of the "bird's nest". It is important that the plasma would be sustained by a microwave power, and only triggered and guided by the laser.

In our laboratory, ArF laser was successfully used to initiate and guide microwave streamers [3, 5]. The microwave source used in the experiments had 50 kW of power at a frequency of 2.45 GHz, pulse length of 1 ms, and pulse repetition rate of a few Hz (essentially, a single-pulse regime). The power level was not enough to study plasmas in free air, and streamers were initiated in a microwave waveguide-based resonant cavity filled with the room air. Without initiation, the electric field in the waveguide was below that needed for breakdown.

When ArF laser beam was directed through a narrow window and focused at a location inside the waveguide, a streamer would start. The streamer would continue to grow long after the 15-ns laser pulse, following the trace left by the laser beam, as shown in Fig.8. As seen in the figure, the streamer followed the trace of the laser beam rather than the electric field that was, of course, normal to the walls of the waveguide, even though the laser beam was directed at an angle to the electric field. In fact, in the experiments, streamers still developed when the pulsed laser beam was directed at almost 45^0 to the field.

As seen in Fig.8, during the growth of the streamer its ends are brighter than the middle section. This could be expected, since the electric field is stronger at both tips. A few microseconds after initiation, the streamer became bright throughout its length. At the end of its development, the streamer would reach the wall of the waveguide and would keep there until the end of the microwave pulse. The average electron number density in the streamer, estimated from the Stark profile of H_β line, was on the order of 10^{15} cm^{-3}.

The experimental results are encouraging, and further studies, including laser-initiated microwave streamers in deeply subcritical fields, initiation of more than one streamer at a time, and studies of laser initiation and guiding of microwave plasmas in both free air and resonant cavities could be very interesting.

5. Development of a supersonic plasma wind tunnel [6]

The basic configuration of the wind tunnel is determined by the need to create a plasma in the region of supersonic flow. A schematic of the facility is shown in Fig. 9, and Fig.10 shows the plenum and nozzle cutaway. A plasma is created with a 50 kW, 1 ms pulse of microwave source at 2.45 GHz, which induces electric breakdown of the air in the region of supersonic flow. Microwaves are introduced into the plenum through an EM window mounted over a port on one wall. The direction of propagation is then turned 90° by an aluminum reflector, so the microwaves travel coaxially with the flow through the plenum chamber and nozzle section. The aluminum reflector is made with a dense array of ¼ inch holes in it to allow passage of air while simultaneously reflecting the microwaves. The breakdown location is controlled by two factors: a reduced static pressure in the high-speed section and increased field intensity downstream of the throat. Microwave discharges occur more easily at low pressure due to the reduced collision frequency, and introducing microwaves through the plenum where the air is at high pressure avoids the risk of parasitic breakdown near the window housing and window surface.

As shown in Fig. 9, the waveguide walls are tapered to create an enhancement of the electric field as the microwaves propagate downstream. The nozzle contours within the taper are made of dielectric material so as to transmit the microwave radiation. The taper continues down to and slightly beyond the cutoff dimensions for 2.45 GHz. This generates a reflection, reversing the propagation direction as the microwaves reach the cutoff point. This taper is used as one end of a microwave resonator. The other end of the resonator is formed by a triple stub tuner on the generator side of the entrance window. This arrangement allows for the build-up of a standing wave in the wind tunnel. In order to provide a further field enhancement at the intended breakdown location, and to provide for spatial localization of the plasma, two 1 cm long metal pins are mounted opposite each other on the inside walls of the wind tunnel. In principle, plasma could be triggered and guided by a laser instead of pins (see the previous section), and the laser control will be explored in future work.

The flow of air proceeds from the plenum, through the nozzle, and into the 2"x2" test section. The air is then discharged into a vacuum tank. The nozzles are contoured to achieve Mach 3 flow in the test section. Flow conditions in the test section are 20 Torr static pressure, 110 K static temperature, and a Mach number of 3.

The microwave field distribution was measured along the centerline of the wind tunnel from the reflector plate to the wind tunnel exit plane. To complement the measurements described above, as well as to permit parametric studies of the effect of changes in the electrical properties of the wind tunnel, a commercial finite element code was used to simulate the electric field standing wave pattern.

Electric breakdown can occur in either of two locations, depending upon conditions. Under static conditions below about 30 Torr, breakdown occurs upstream of the throat, slightly below the centerline of the wind tunnel. Above 30 Torr under static conditions breakdown occurs downstream of the throat at the intended location. These two positions correspond to the two peaks in field intensity found in the simulation. Note that under flow conditions, with higher pressure upstream of the throat than downstream, the breakdown will also occur in the downstream location.

Breakdown in the wind tunnel was recorded with photodiodes and high-speed camera. Measurements of the plasma luminosity were made both with flow and under static conditions. In all cases the tests were performed in air with microwave pulse duration of 1 ms. The results indicate the initiation of the plasma within 10 μs after the start of the microwave pulse without flow, and within 20 μs after the start of the pulse with flow. Brighter plasma was observed with flow than without flow, as shown in Fig. 11.

The photographs shown in Fig. 11 were made with a gated, intensified CCD camera. The view is through the axial diagnostic port shown in Fig. 9, looking upstream into the wind tunnel. Images of the plasma were taken both with the wind tunnel running and under static conditions at 60 Torr and room temperature. The pressure was chosen for static conditions to match the density with the Mach 3 flow for comparison. In all cases the camera gate was maintained at 3 μs. The images show the plasma generated while the wind tunnel was brighter and more contracted than the plasma generated under static conditions. The location of the plasma within the tunnel appears to be stable for the duration of the 1 ms pulse. Note that each image represents a separate instance of plasma generation.

Thus, a Mach 3 wind tunnel with integrated microwave plasma generating capability has been designed and tested. Further work on plasma aerodynamics in this facility is currently under way.

6. Electron beam generated plasmas [9] and their application in plasma aerodynamics

Beams of high-energy electrons represent a very energy-efficient way of generating plasmas in both closed tubes and channels and open air. When the initial energy of beam electrons is high enough, the beam can penetrate the gas and generate plasma far from the injection point. E-beams can be guided by magnetic fields, minimizing lateral spread of the plasma. If ionization level or electrical conductivity has to be maximized, e-beams can create nonequilibrium ionization in cold gas with energy cost of only 35 eV per ion-electron pair, which is 2-3 orders of magnitude better than electric field-sustained discharges. Plasmas created by e-beams are stable and reasonably uniform, and can be sustained in supersonic flow.

As an example, Fig.12 shows computed parameters of the plasma generated by e-beam with current density of 10 mA/cm^2 in air at 1 atm, 2000 K. (The temperature is maintained at 2000 K by convectively cooling the gas). At steady state, the current of low-energy plasma electrons back to the injection plane balances the beam current. The number density of plasma electrons reaches 10^{13} cm^{-3}. The calculations were performed with the so-called "forward-back" approximation.

The efficient ionization of low-temperature air by e-beams makes them attractive as ionizers in hypersonic MHD channels such as those in the AJAX concept. Theoretical analysis of e-beam plasmas in MHD channels is reported in a separate paper at this conference and in other recent papers.

Acknowledgement

This work was supported by the U.S. Air Force Office of Scientific Research.

References

1. S.O.Macheret, L.Martinelli, and R.B.Miles, "Shock Propagation and Structure in Non-Uniform Gases and Plasmas," Paper AIAA-99-0598
2. Y.Z.Ionikh, N.V.Chernysheva, A.V.Meshchanov, A.P.Yalin, and R.B.Miles, "Direct Evidence for Thermal Mechanism of Plasma Influence on Shock Wave Propagation," *Phys. Lett. A*, Vol. 259, 1999, pp. 387 – 392.
3. S.O.Macheret, Y.Z.Ionikh, L.Martinelli, P.F.Barker, and R.B.Miles, "External Control of Plasmas for High-Speed Aerodynamics," paper AIAA-99-4853.
4. Y.Z.Ionikh, N.V.Chernysheva, A.P.Yalin, S.O.Macheret, L. Martinelli, and R.B.Miles, "Shock Wave Propagation Through Glow Discharge Plasmas: Evidence of Thermal Mechanism of Shock Dispersion", Paper AIAA-2000-0714.
5. S.O.Macheret, P.F.Barker, K.Waichman, R.B.Miles, E.Ploenjes, P.Palm, I.V.Adamovich, W.R.Lempert, and J.W.Rich, "Optically Pumped and Controlled Electric Discharges", Paper AIAA-99-3636.
6. B.McAndrew, P.Barker, and R.Miles, "Development of a Supersonic Plasma Wind Tunnel", Paper AIAA-2000-0533.
7. I.V.Adamovich, V.V.Subramaniam, J.W.Rich, and S.O.Macheret, Paper AIAA-97-2499.
8. I.V.Adamovich, V.V.Subramaniam, J.W.Rich, and S.O.Macheret, "Phenomenological Analysis of Shock-Wave Propagation in Weakly Ionized Plasmas," *AIAA Journal*, Vol. 36, No. 5, 1998, pp. 816-822.
9. S.O.Macheret, M.N.Shneider, and R.B.Miles, "New Types of Electron Beam Generated Electric Discharges in Dense Gases: a "Fountain" and a "Thunderstorm"," Paper AIAA-99-3635.
10. A.P.Yalin and R.B.Miles, *Optics Lett.*, Vol. 24, No. 9, 1999, pp. 590 – 592.
11. A.P.Yalin, Y.Ionikh, and R.B.Miles, Paper AIAA-99-3431.
12. N.D.Finkelstein, W.R.Lempert, and R.B.Miles, Paper AIAA-97-0157.
13. L.P.Grachev, I.I.Esakov, and K.V.Khodataev, *Tech. Phys.*, Vol.44, 1999, p.1276.
14. V.G.Brovkin and Yu.F.Kolesnichenko, *Tech. Phys. Lett.*, Vol. 17, 1991, p.41.

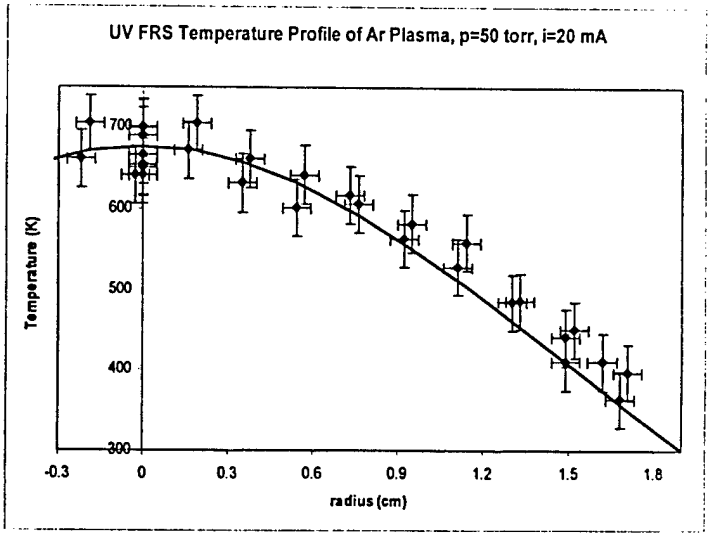

Fig.1. Radial temperature profile in Ar glow discharge tube measured by UV Filtered Rayleigh Scattering. Pressure and electric current are indicated on the plot. Fitting curve is Gaussian.

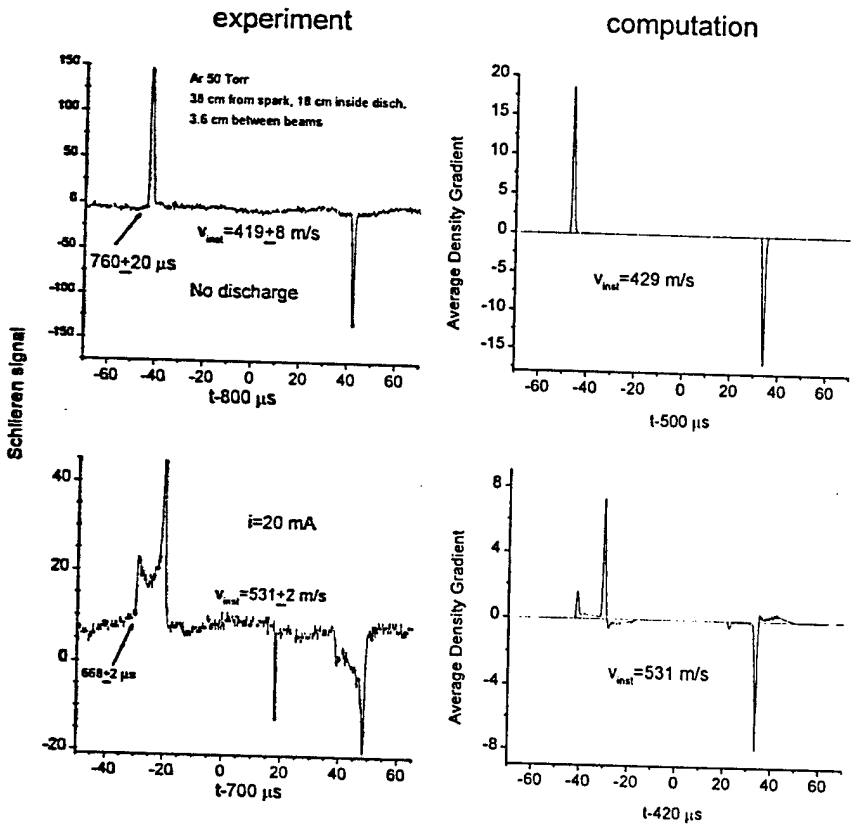

Fig.2. Experimentally measured and simulated laser Schlieren signals for shocks in glow discharge in Ar at 50 Torr. The discharge current is 20 mA. The first of the two laser beams is located 18 cm from the entrance to the discharge, and the spacing between the two beams is 3.6 cm. The measured and computed shock velocities are indicated on the figure.

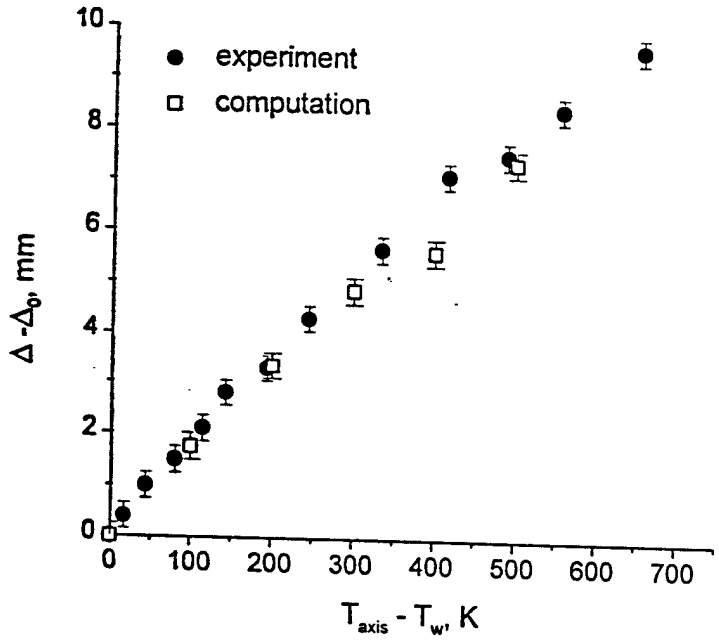

Fig.3. Width of the Schlieren signal in the discharge (Δ) minus the signal width with the dicharge off (Δ_0) versus temperature difference between the axis and the wall. Gas mixture Ar+0.16%N_2, pressure 50 Torr. First laser beam is 24.8 cm inside the discharge; spacing between the two beams is 2.9 cm.

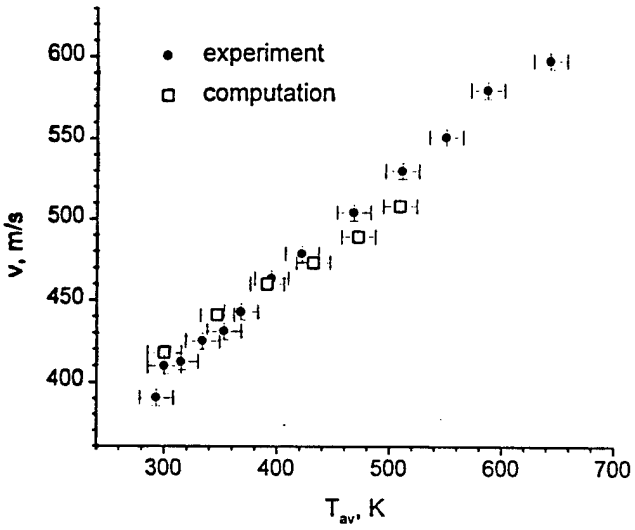

Fig.4. Shock wave velocity versus average temperature in the discharge. Conditions are the same as in Fig.3.

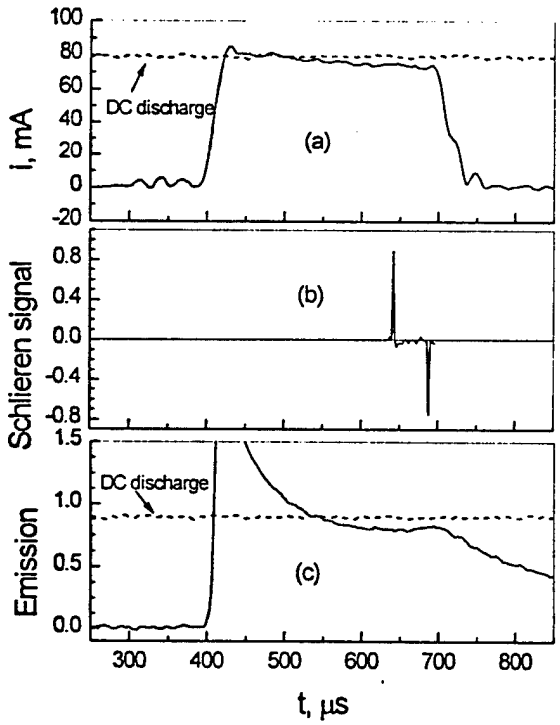

Fig.5. Time dependence of discharge current (a), Schlieren signal (b), and discharge emission intensity (c). Time t=0 corresponds to the spark shot.

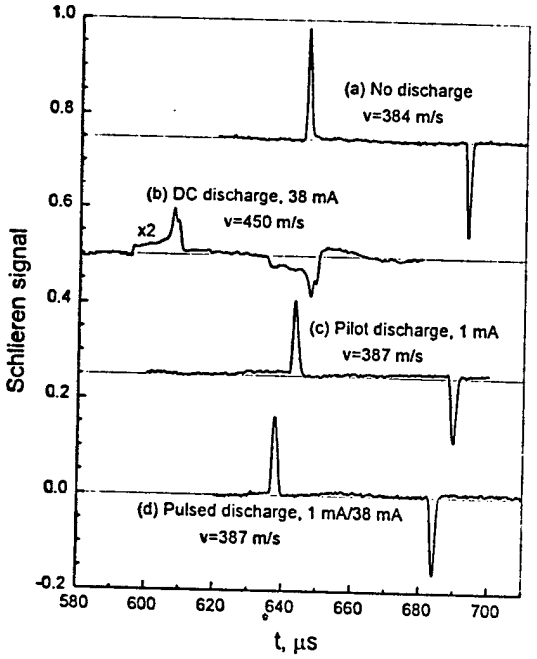

Fig.6. Schlieren signals for Ar-N_2 mixture (1% N_2). Pressure 50 Torr; 29 cm from the spark, 9 cm inside the discharge; 1.8 cm between the two laser beam passages.

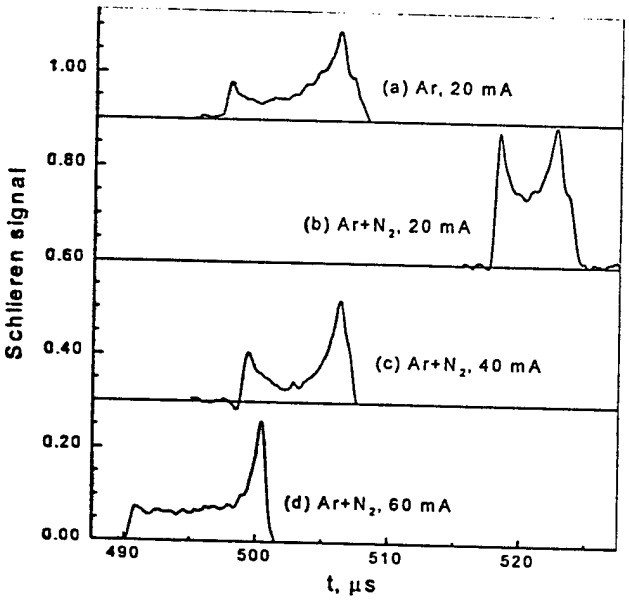

Fig.7. Comparison of shock Schlieren signals at a fixed location in Ar and Ar+N_2 discharges at 50 Torr and equal currents [(a), (b)], equal gas temperatures [(a), (c)], and equal electron densities [(a), (d)]

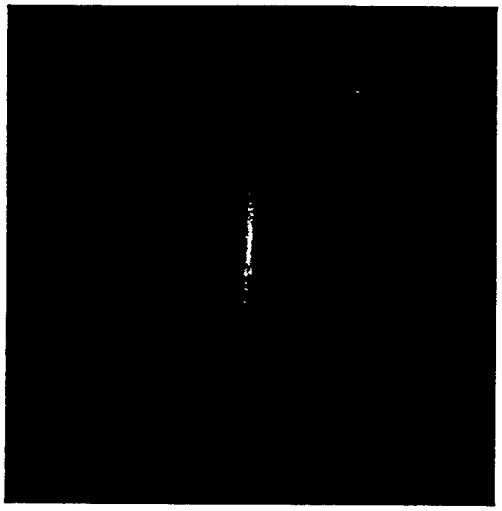

Rayleigh Scattering from ArF Laser
t = 0 ns

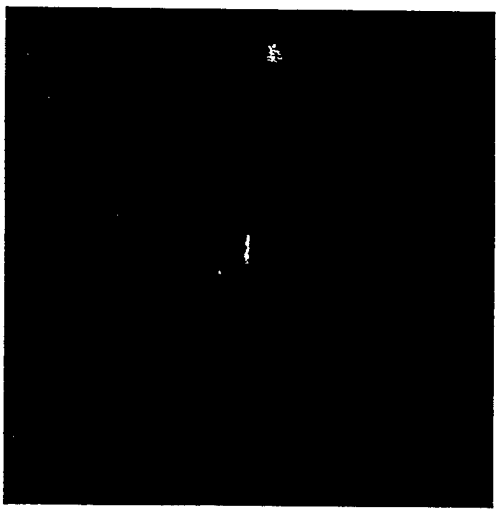

t = 40 ns

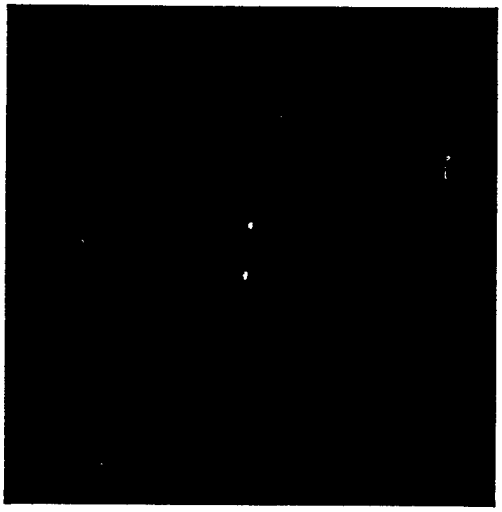

t = 240 ns

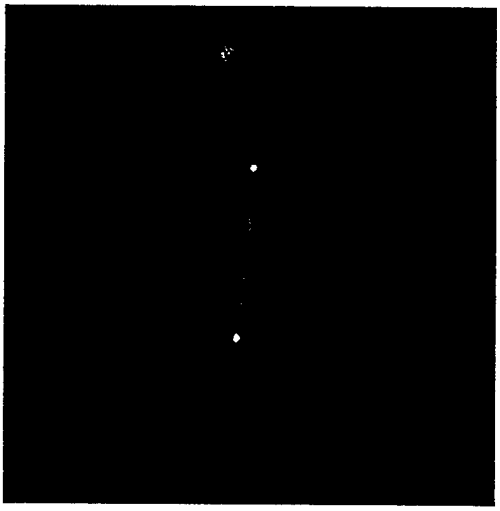

t = 1.94 μs

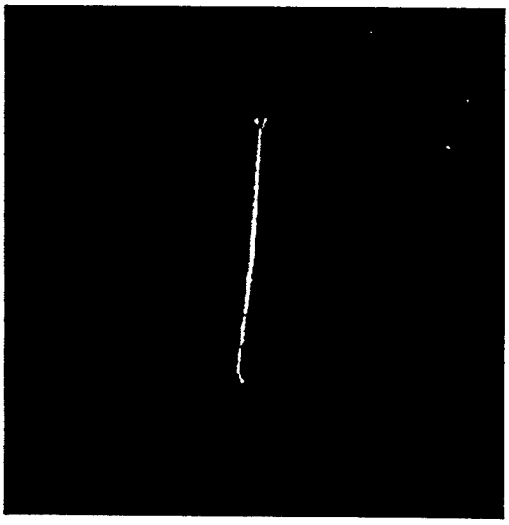

t = 12 μs

Fig.8. Development of the microwave streamer initiated in the waveguide by a laser pulse. Parameters of the microwave source: frequency – 2.45 GHz, pulse power – 50 kW, pulse length – 1 ms. Parameters of the ArF laser: wavelength – 193 nm, pulse energy – 50 mJ, pulse length – 15 ns.

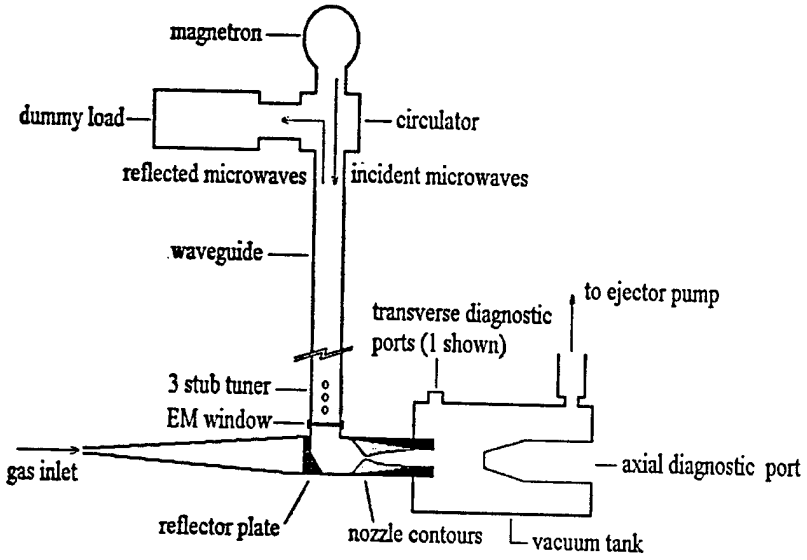

Fig.9. Schematic of the microwave-driven plasma wind tunnel facility.

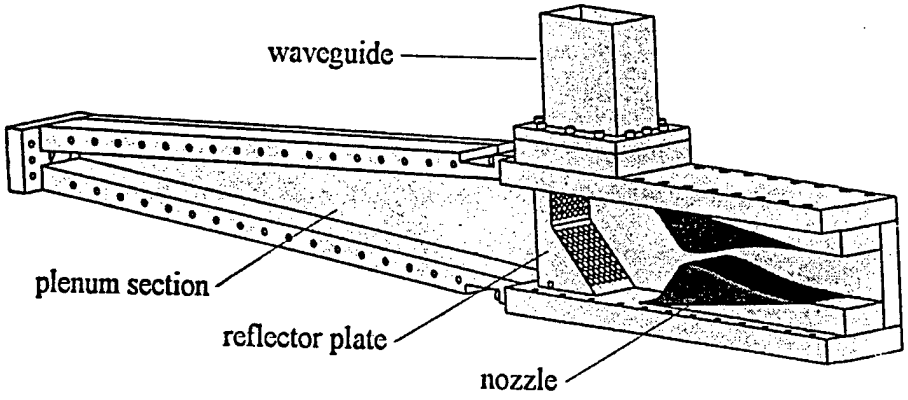

Fig.10. Plenum and nozzle cutaway view.

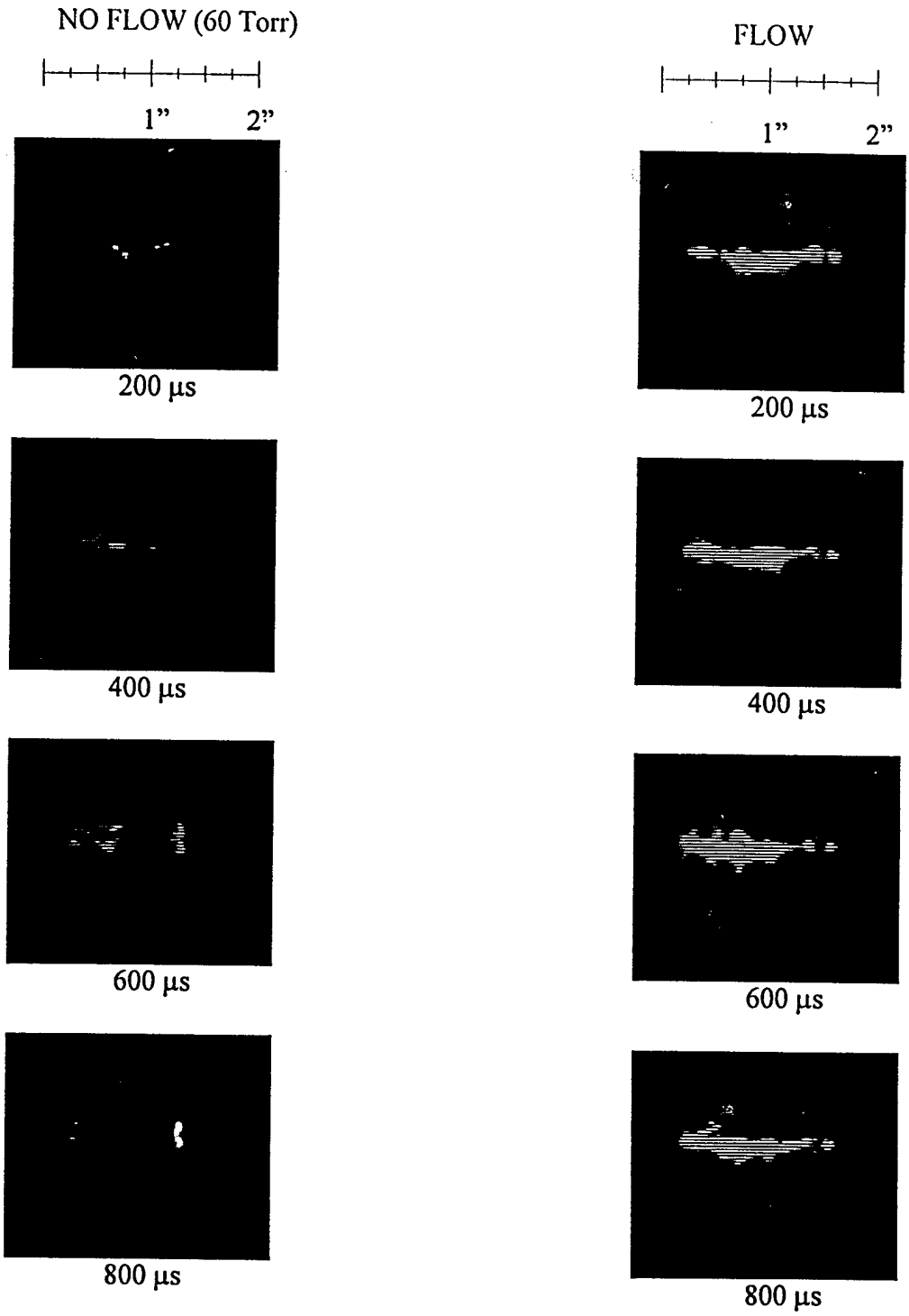

Fig.11. Comparison of plasma with and without the flow

APPENDIX III: Microwave Energy Addition

1. **V.P. Chiravalle**, R.B. Miles, and E.Y. Choueiri, *"Laser Propulsion Using a Molecular Absorber,"* Paper #AIAA-98-3932, 34th AIAA/ASME/SAE/ASEE Joint Propulsion Conference & Exhibit, Cleveland, OH, July 13-15, 1998.

2. **V.P. Chiravalle,** R.B. Miles, **and E.Y.** Choueiri, "Numerical Simulation of Microwave-Sustained Supersonic Plasmas **for Application** to Space Propulsion," Paper #AIAA-01-0962, 39th AIAA Aerospace Sciences Meeting & Exhibit, Reno, NV, Jan. 8-11, 2001.

APPENDIX III: Microwave Energy Addition

1. **V.P. Chiravalle**, R.B. Miles, and E.Y. Choueiri, *"Laser Propulsion Using a Molecular Absorber,"* Paper #AIAA-98-3932, 34th AIAA/ASME/SAE/ASEE Joint Propulsion Conference & Exhibit, Cleveland, OH, July 13-15, 1998.

2. **V.P. Chiravalle,** R.B. Miles, **and E.Y.** Choueiri, "Numerical Simulation of Microwave-Sustained Supersonic Plasmas **for Application** to Space Propulsion," Paper #AIAA-01-0962, 39th AIAA Aerospace Sciences Meeting & Exhibit, Reno, NV, Jan. 8-11, 2001.

AIAA-98-3932

Laser Propulsion Using a Molecular Absorber

Vincent P. Chiravalle, Richard B. Miles, and Edgar Y. Choueiri

Mechanical and Aerospace Engineering Department
Princeton University, Princeton NJ 08544
USA

34th AIAA/ASME/SAE/ASEE
Joint Propulsion Conference & Exhibit
July 13-15, 1998 / Cleveland, OH

Laser Propulsion using a Molecular Absorber

V.P. Chiravalle*, R.B. Miles†, and E.Y. Choueiri‡
MAE Dept.
Princeton University
Princeton, New Jersey 08544

AIAA-98-3932§

Abstract

Unlike the conventional approach of using a laser sustained plasma to heat a propellant, molecular absorption of laser energy makes it possible to avoid the frozen flow losses associated with the high temperature and complex chemistry of a plasma. The molecular absorption concept is developed by exploring several thermodynamic pathways using a 1-D fluid theory for energy addition in the supersonic regime and different pathways are shown in H-K coordinates. The absorption physics of a promising molecular absorber, SF_6, is described at arbitrary laser beam intensities using a two-temperature non-equilibrium model, which is then applied to calculate the nozzle length required to achieve a specific impulse of 250 sec through a 300 K isothermal expansion in the supersonic section. The results of this conversative example case for energy addition illustrate that over a length of less than 1 m laser power on the order of 20 kW can be absorbed in the supersonic region of a 10 g/sec H_2 flow without creating a plasma.

1 Introduction

As high-power laser technology continues to mature the possibility of using a laser to generate rocket thrust for propulsion applications grows more feasible. The laser propulsion concept was first introduced by Kantrowitz[1] , more than twenty five years ago, and was experimentally demonstrated by Krier et. al.[2] and by Myrabo[3] . As with any thermal propulsion system, the efficiency of conversion of laser beam energy into the kinetic energy of propellant gas is a critical figure of merit. In addressing laser thruster performance it is useful to consider both the absorption efficiency as well as the the propulsion efficiency. In the context of laser thrusters, the propulsion efficiency is a measure of how much absorbed energy appears as kinetic energy of the propellant at the nozzle exit.

The established approach for achieving energy conversion is to create a laser sustained plasma (LSP) in the flowing propellant. The plasma is localized near the focal point of a laser beam, and laser energy is absorbed through the electron inverse bremsstralung process. As the propellant gas flows through and around the stationary plasma high bulk temperatures are sustained which can be in excess of 10,000 K in gases such as argon. Stable LSPs have been created and observed in the laboratory[4, 5]. Absorption efficiencies as high as 86 % for LSPs in argon have been reported by Keefer et. al.[4]. Several attempts have been made to model the physical interactions occurring in laboratory LSPs using two dimensional numerical simulations[6, 7]. Although the coupling of laser energy to a plasma has been found to be quite high, the overall propulsion efficiency is not as good. There are several processes that degrade the efficiency. In general, plasma radiation is a significant contributor, and in the case of molecular propellants such as hydrogen, dissociative frozen flow losses are also important. The equilibrium fraction of dissociated hydrogen is known to vary exponentially with temperature, and the reduction of frozen flow losses in hydrogen thermal thrusters necessitates

*Graduate Student. Mechanical & Aerospace Engineering. AIAA

†Professor. Mechanical & Aerospace Engineering. Associate Fellow AIAA

‡Assistant Professor. Mechanical & Aerospace Engineering. Senior Member AIAA

§This work was supported by an AASERT award from the Air Force Office of Scientific Research (AFOSR).

finding a way to add significant amounts of energy without completely dissociating the propellant. The dissociation fraction of hydrogen for various temperatures and densities is shown in Fig. 1.

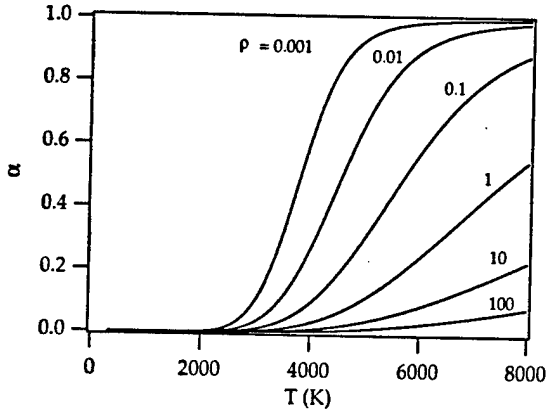

Figure 1: The calculated equilibrium dissociation fraction of H_2, as a function of temperature and density. The units of ρ are kg/m^3.

A different approach for energy addition, one that does not utilize a plasma, is the molecular absorption of radiation in the supersonic regime. Adding energy using a molecular absorber involves the excitation of an internal mode such as rotation or vibration of a seed molecule, the seed molecule subsequently transfers its energy to the propellant gas by relaxation collisions. The molecular absorption approach for laser propulsion was previously identified by Caledonia et. al.[8] in 1975. More recently, molecular absorption has been considered as an energy addition mechanism in the supersonic region for air in a proposed hypersonic wind tunnel and has been the focus of an ongoing research effort[9, 10].

The central issues with this approach involve the choice of the thermodynamic path over which energy is added and the choice of the seed molecule, with its associated set of physical parameters. Fig. 2 illustrates the conventional approach of energy addition in the plenum and the concept of energy addition in the supersonic region using a molecular absorber. The goal of this paper is to explore relatively simple pathways, such as a constant temperature expansion, to gain insight into the more complicated cases that may be of use to laser propulsion. The interaction between the seeded propellant mixture and the laser beam is described in general terms, using a familiar quasi-one dimensional model. It is understood that this approach is useful in a restricted sense, and is intended as a starting point for more realistic numerical simulations. This formalism is then applied using absorption data for SF_6 to calculate the length of the energy addition region in a laser thruster with molecular absorption.

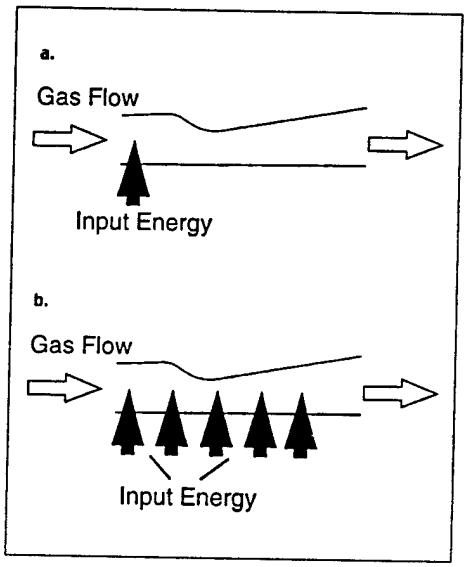

Figure 2: Laser rocket propulsion concepts : a: Energy addition using a laser sustained plasma in the plenum region. b: Energy addition in the supersonic region using a molecular absorber.

2 Fluid Model for Energy Addition

Within the constraints of one dimensional theory, the physics of an absorbing fluid in steady state is expressed by the fluid conservation equations,

$$\frac{1}{A}\frac{dA}{dx} + \frac{1}{\rho}\frac{d\rho}{dx} + \frac{1}{u}\frac{du}{dx} = 0 \quad (1)$$

$$\frac{dp}{dx} + \rho u\frac{du}{dx} = 0 \quad (2)$$

$$c_p\frac{dT}{dx} + u\frac{du}{dx} = c_p\frac{dT_0}{dx}. \quad (3)$$

It is assumed also that the gas is ideal and perfect i.e. with $p = \rho RT$ and constant c_p. T_0 is the total temperature of the fluid and

$$\dot{m}c_p\frac{dT_0}{dx} = -\frac{dP_w}{dx}. \quad (4)$$

The laser power, P_w, which is assumed to be uniform across the beam cross section is described by Beer's law written in conversation form,

$$\frac{dP_w}{dx} = -\kappa P_w. \tag{5}$$

The absorption coefficient, κ, is in general a function of the gas thermodynamic variables T and ρ and the laser intensity, I. There are more variables in this system than equations relating them. When the nozzle area, A, is specified everywhere and when the laser power incident to the energy addition region, P_{w0}, is known, the above equations uniquely determine the thermodynamic and mechanical state of a gas with a given set of initial conditions.

If a transformation is performed, expressing all quantities in terms of the optical length, $\tau = \int \kappa dx$, the conservation equations can be solved without reference to the properties of the absorbing species[8, 11]. The solution in physical space is recovered, for a chosen absorber, by reversing the transformation. There are limitations to the effectiveness of this approach since the radius of the nozzle is now a function of τ. Choosing $A(\tau)$ to give a specific shape in physical space is not intuitively obvious.

This difficulty can be removed, if instead of constraining the nozzle to have a given profile in space, an additional relation among the fluid variables is specified. The enlarged system of equations is solved with A as a variable. In this way the nozzle size and shape, consistent with a specified thermodynamic constraint, such as the isothermal condition, are found. The additional relation can be chosen as

$$\frac{dH}{dK} = \chi, \tag{6}$$

with kinetic energy, $K = \frac{u^2}{2}$, and enthalpy, $H = c_p T$. Going a step further, all the variables that describe the fluid, A, T_0, ρ, T, and u, can be written in terms of M^2, γ and χ,

$$\begin{aligned}
\frac{1}{A}\frac{dA}{d\tau} &= \frac{((\gamma-1)\chi+\gamma)M^2-1}{2-\chi(\gamma-1)M^2}\frac{dM^2}{d\tau},\\
\frac{1}{T_0}\frac{dT_0}{d\tau} &= \frac{(\gamma-1)(\chi+1)}{(1+\frac{\gamma-1}{2}M^2)(1-\chi(\gamma-1)M^2)}\frac{dM^2}{d\tau},\\
\frac{1}{\rho}\frac{d\rho}{d\tau} &= -\frac{(\gamma-1)\chi+\gamma}{2-\chi(\gamma-1)M^2}\frac{dM^2}{d\tau},\\
\frac{1}{T}\frac{dT}{d\tau} &= \frac{\chi(\gamma-1)}{2-\chi(\gamma-1)M^2}\frac{dM^2}{d\tau},\\
\frac{1}{u}\frac{du}{d\tau} &= \frac{1}{M^2(2-\chi(\gamma-1)M^2)}\frac{dM^2}{d\tau},
\end{aligned} \tag{7}$$

where for the moment χ is an unspecified function of M^2. The above equations trace curves in a five dimensional space parametized by M^2.

Another way to visualize the above relations is to look at their trajectories in H-K coordinates[12] . In the H-K plane each horizontal line, $\chi = 0$, corresponds to a constant temperature process and each vertical line, $\chi \to \infty$, corresponds to a constant pressure process. Three other basic cases are heat transfer with constant area, adiabatic, isentropic expansion and constant Mach number heating of the gas. The appropriate χ functions for these three cases are given below

$$\chi = (1-\gamma M^2)/M^2(\gamma-1), \tag{8}$$

$$\chi = -1, \tag{9}$$

$$\chi = 2/(\gamma-1)M^2, \tag{10}$$

where Eq. 8 refers to the constant area heat transfer case, Eq. 9 refers to the adiabatic, isentropic expansion case and Eq. 10 refers to the constant Mach number case. The example cases just discussed are illustrated in Fig. 3, and do not exhaust the set of

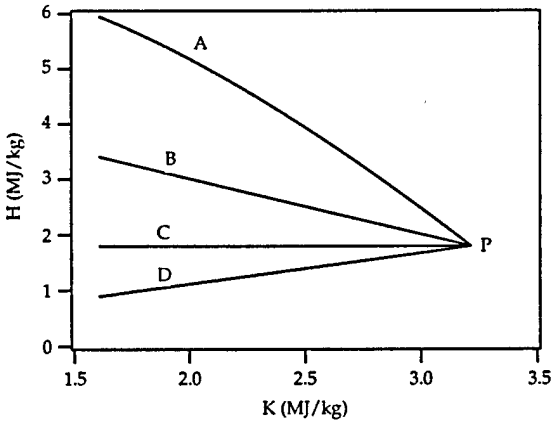

Figure 3: H-K coordinates of four trajectories in the supersonic regime that converge at point P. The conditions at P represent a fluid at T=300 K with M=3.0 and $\gamma = 1.39$. (A) cooling with constant area, (B) adiabatic, isentropic expansion, (C) isothermal expansion, and (D) heating at constant Mach number.

possible curves in H-K space. Any function $\chi(M^2)$ defines a path for the thermodynamic and mechanical parameters of the fluid to traverse. The task with regard to laser propulsion is to identify the χ function or set of functions which achieve a required

exhaust velocity, while having desirable characteristics in terms of efficiency of laser energy addition and nozzle size.

An attempt is made in the following sections to do this by solving the case of $\chi = 0$, isothermal flow, using a realistic model of a molecular absorber, SF_6. An isothermal energy pathway was selected for the examples in this work to ensure that the temperature would remain below the dissociation limit everywhere in the nozzle. The solution is obtained for the fluid variables in τ-space first, then the results are transformed back into physical space by computing the SF_6 absorption coefficient at each point in the nozzle. SF_6 was chosen because of its exceptionally high absorption coefficient at 10.6μm, the wavelength of commercial CO_2 lasers. As discussed later the required SF_6 absorption data exist in a narrow temperature range around 300 K, and for this reason 300 K was used in all the example cases computed here.

3 Study Case: Isothermal Expansion

Consider an isothermal expansion taking place in the supersonic region of a laser thruster. The laser enters at the nozzle exit and propagates in the direction of the throat, as seen in Fig. 4.

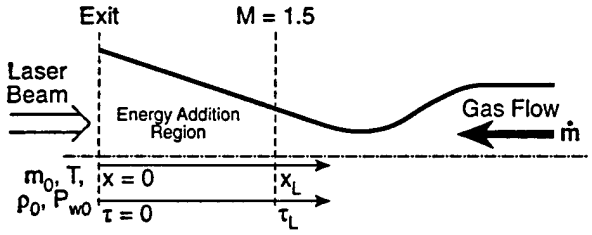

Figure 4: The orientation of the laser beam propagation relative to the fluid flow in the examples considered in this study. The non-dimensional optical length, τ, and the physical axial length are measured relative to the nozzle exit where the laser beam enters and the fluid conditions are specified.

The energy addition term of Eq. 3 is related to the power extracted from the laser beam. In τ-space Eq. 5, describing the evolution of the beam power, can be written as

$$\frac{dP_w}{d\tau} = -P_w. \tag{11}$$

The solution is an exponential function of τ. τ is measured relative to the nozzle exit, and the direction of increasing τ corresponds, in physical space, to marching upstream toward the throat, Fig. 4. With this expression for P_w and the isothermal condition, analytic solutions for M^2 and ρ can be obtained as a functions of τ and of the conditions at the nozzle exit. These are used to compute the flow properties at each section of the nozzle and are given below

$$M^2 = M_0^2 + \frac{2\Gamma}{\gamma}\left[1 - \exp -\tau\right], \tag{12}$$

$$\rho = \rho_0 \exp \Gamma \left[1 - \exp -\tau\right]. \tag{13}$$

The non-dimensional parameter Γ has the form $\Gamma = P_{w0}/\dot{m}RT$ and in physical terms it is proportional to the ratio of incident laser beam power to flow enthalpy.

4 SF_6 Absorption Physics

Gaseous SF_6 is a strong absorber of infrared radiation at the $C0_2$ laser wavelength of 10.6μm. A spherical top molecule, SF_6 has six fundamental vibrational modes, one of these, designated by the ν_3 quantum number, corresponds to an infrared active band. In addition to vibrational motion the SF_6 molecule also has rotational energy components, described collectively by the quantum number J. The excitation of SF_6 by radiation at 10.6μm can be understood in terms of a transition from a state where none of the vibrational modes are excited, the vibrational ground state, to a state of higher energy where the ν_3 mode is excited, $\nu_3 = 1$. Let N_1 be the number density of SF_6 in the vibrational ground state with a rotational quantum number, J_1. Let N_2 be the corresponding number density for a state with only the ν_3 vibrational mode excited, $\nu_3 = 1$, and with rotational quantum number J_2. The values of the rotational quantum numbers are found to be $J_1 = 67$ and $J_2 = 66$ using the theory presented by Herzberg[13] together with the appropriate molecular constants for the ground and excited states, determined by Bobin[14]. The absorption coefficient can be expressed as a function of N_1 and N_2 according to the equation below,

$$\kappa = \sigma(N_1 - \frac{g_1}{g_2}N_2). \tag{14}$$

σ is the absorption cross section for the transition described above and is a function of the gas properties, T and ρ. The ratio of degeneracies, g_1/g_2 for large

J is approximately 1/3. Based on the measurements by Anderson[15] in pure SF_6 at 100 torr and 300 K, the value of κ is 3500 m^{-1}. σ was determined by computing N_1 and N_2 at these conditions and solving Eq. 14 using the experimental value for κ. At 300 K available data for the absorption coefficient of SF_6-air mixtures[15] show that κ varies linearly with ρ over several orders of magnitude. This implies that the dependence of σ on ρ is negligible. Therefore in this paper it is assumed that σ for the transition at 10.6μm in a SF_6-H_2 mixture is a constant at 300 K. With σ known, the absorption coefficient can be extrapolated to high laser beam intensities using Eq. 14.

To understand the effect of laser intensity on κ, it is necessary to explore the physics contained in the N_1 and N_2 terms. At equilibrium conditions N_2 and N_1 are determined by the Boltzmann relation and depend entirely on the thermodynamic temperature. Situations may arise when the translational and vibrational modes of the fluid become uncoupled, for instance when a fluid is perturbed by a tightly focused laser or when a shock wave passes through the fluid. In such a case N_1 and N_2 are described in terms of two temperatures, a translational temperature, T, and a vibrational temperature, T_{vib}. Energy transfer from one mode of vibration to another occurs on a short time scale relative to energy transfer to a translational mode. The evolution of the fluid vibrational energy, e_{vib}, is described by a conservation equation which in steady-state is

$$\dot{m}\frac{de_{vib}}{dx} = \frac{\rho A(e^*_{vib} - e_{vib})}{\beta} + \kappa P_w. \qquad (15)$$

β, the characteristic time for vibrational relaxation, was measured for pure SF_6 by Burak et. al.[16] and was found to approximately 140 μsec torr. This value was adopted in this work, although one would expect the relaxation time to be shorter for an SF_6-H_2 mixture than for pure SF_6 because, as a consequence of the smaller molecular mass of H_2, the collision frequency between SF_6 and H_2 is greater than the corresponding collision frequency for pure SF_6. Eq. 15 can be transformed from physical space into τ-space in the same way as the other fluid conservation equations. When this is done a coefficient, $1/u\kappa$ appears, which is the characteristic flow residence time. The flow residence time is the time required for the fluid to travel a distance equal to the distance over which the laser beam intensity drops by a factor of $1/e$. de_{vib}/dx can be neglected in Eq. 15 when two criteria are met simultaneously, the flow residence time, σ, is much longer than the vibrational relaxation relaxation time, β, and the difference between the vibrational energy that the flow would have at equilibrium, e^*_{vib}, and the flow vibrational energy, e_{vib}, is the same order of magnitude as e_{vib}. e_{vib} is a function of T_{vib} and e^*_{vib} is a function of T. The conditions for neglecting de_{vib}/dx are summarized below,

$$\sigma \gg \beta,$$
$$e^*_{vib} - e_{vib} \sim e_{vib}. \qquad (16)$$

The functional forms of the terms, N_1, N_2, e_{vib} and e^*_{vib}, are given in Ref. [15].

A two-temperature approach was put forth by Anderson[15] to treat saturation absorption in SF_6 at high laser intensities. The model presented in that work is applied here to compute the SF_6 absorption coefficient and is strictly valid at room temperature, 300 K, where absorption data was collected. The present implementation of the model differs from the one used by Anderson in one way, only absorption from the ground state is considered here for the sake of simplicity. The original model considered absorption from both the ground state and an excited state. The present model is more conservative in the sense that at high laser beam intensities the absorption coefficient is less because absorption by excited states is not considered.

5 Results for a Supersonic Isothermal Expansion with SF_6 as an Absorber

To assess the potential of laser propulsion using a molecular absorber it is necessary to get a rough answer to some basic questions regarding how much energy can be deposited in the supersonic region of an expanding nozzle flow, whether the expansion can begin at a low enough temperature to avoid hydrogen dissociation and if the nozzle size in such a system is so large as to be impractical. As discussed in the previous sections, one possible way of introducing the laser into the supersonic energy addition region is to direct the beam from downstream through the nozzle exit. For nozzles where the supersonic expansion ratio is sufficiently gradual the one dimensional theory developed in this paper may not be a bad approximation.

The fluid conditions and laser beam power are specified at the nozzle exit. Using Eq. 12 and Eq. 13 the conditions at all other points upstream of the

exit in the energy addition region are uniquely determined. The nozzle exit conditions were chosen to be reasonable values for an expanded supersonic flow, such as $M_0 = 3.0$ and $\rho_0 = 0.001$ kg/m^3. T was set to 300 K for reasons discussed earlier and the mass flow rate was selected as 10 g/sec to keep the required nozzle exit diameter in the 5-10 cm range. The propellant mixture consisted of H_2 with an SF_6 concentration of 2 %. The conditions at the nozzle exit correspond to a specific impulse of 250 sec. The laser beam power incident to the nozzle exit was a parameter to be specified for each run. The computation marched forward toward the throat from the exit, and was concluded when the flow achieved $M = 1.5$. For a given run, the first step was to find the point in τ-space where $M = 1.5$, this was accomplished using Eq. 12. Then for all points in the energy addition region, Eq. 15 was solved numerically for T_{vib} assuming, $de_{vib}/dx \approx 0$, and the absorption coefficient was calculated using Eq. 14. Knowing κ at all points in the energy addition region, the nozzle radial profile and all the fluid conditions were determined as functions of axial length.

Twenty two runs were made with the nozzle exit conditions discussed above, varying the laser beam power for each run. For a given value of laser power, the non-dimensional optical length at the position where $M = 1.5$, denoted τ_L, was calculated and the corresponding position, x_L, was then determined. Fig. 5 shows how x_L varies with laser power. The laser beam power, Γ, is non-dimensionalized in terms of $\dot{m}RT$. The absorption coefficient, κ, at the point where $M = 1.5$, is used to non-dimensionalize x_L. The largest nozzle size of 0.72 m occurs when $\Gamma = 5.0$. This case is also the case where most of the laser beam power is absorbed in the supersonic region. The fraction of laser beam power absorbed in the supersonic region to the incident laser beam power is shown in Fig. 7. As the laser beam power is increased two trends occur, the required nozzle size in the supersonic energy addition region decreases and the fraction of absorbed power decreases, i.e. more of the laser power passes through the intended energy addition region into the throat region. Looking at Fig. 5 and Fig. 7, it is evident that there is a limit for Γ, which can be found by solving Eq. 12 for Γ as $\tau \to \infty$. For the specified Mach number at the nozzle exit, $M_0 = 3.0$, the limit is $\Gamma = 4.72$. The laser beam power corresponding to $\Gamma = 4.72$ is 24 kW ($\dot{m}$ = 10g/sec) and represents the minimum amount of input power, $\dot{m}c_p dT_0/dx$, required to satisfy the isothermal condition from $M = 1.5$ to $M = 3.0$. Laser beams of greater power propagate through the supersonic energy addition region without being completely attenuated, i.e. $\eta < 1$.

Among the cases computed the results for Γ of 5.63, 9.67 and 23.12 are presented. The ratio of flow residence time to vibrational relaxation time is plotted in Fig. 8, and it is seen that σ is at least an order of magnitude larger than β. The ratio of vibrational temperature to translational temperature is given in Fig. 6, and is everywhere greater than 1. It is evident, therefore, that the criteria for neglecting de_{vib}/dx are satisfied in the cases considered. As the laser beam power is increased, T_{vib} increases, raising N_2 and lowering N_1. The net effect is to decrease κ.

The computed nozzle profile for the case with $\Gamma = 5.63$ is shown in Fig. 9. At the nozzle exit the radius is 3.5 cm. The right most point on the graph corresponds to the $M = 1.5$ point, where the radius is 0.47 cm. The total length is 68 cm with an area expansion ratio of 56.

6 Conclusions

The concept of laser propulsion using a molecular absorber was studied by choosing a simple isothermal pathway for energy addition, and by implementing a model of SF_6 absorption. The results indicate that significant amounts of energy can be deposited in the supersonic region without paying too unreasonable a penalty in terms of nozzle length. Although one energy addition pathway was explored in depth in this paper, other traditional cases such as constant Mach number energy addition, and other less familiar χ functions should also be studied. To do so with SF_6, however requires additional absorption data to describe how σ varies in the high T regime, since data of this type are not available. For an isothermal expansion over a given density range the amount of energy added to the flow is directly proportional to the temperature. The specific impulse of the example cases studied here was 250 sec, operation at a higher temperature, although not high enough to cause dissociation, would produce a significantly higher specific impulse.

References

[1] A. Kantrowitz. Propulsion to orbit by ground-based lasers. *Astronautics and Aeronautics*, 10:74–76, 1972.

[2] H. Krier, J. Black, and R.J. Glumb. Laser propulsion 10 kw thruster test program results. *Journal of Propulsion and Power*, 11:1307–1316, 1995.

[3] L.N. Myrabo, D.G. Messitt, and F.B. Mead Jr. Ground and flight tests of a laser propelled vehicle. In *AIAA 36th Aerospace Sciences Meeting*, Reno, NV, January 1998. AIAA 98-1001.

[4] R. Welle, D. Keefer, and C. Peters. Laser-sustained plasmas in forced argon convective flow, part 1: Experimental studies. *AIAA Journal*, 25:1093–1099, 1987.

[5] A. Mertogul, D. Zerkle, and H. Krier. Investigation of CO_2 laser-sustained hydrogen plasmas. *Journal of Propulsion and Power*, 8:1123–1125, 1992.

[6] S. Jeng and D. Keefer. Theoretical investigation of laser sustained argon plasmas. *Journal of Applied Physics*, 60:2272–2279, 1986.

[7] A. Mertogul and H. Krier. Two-temperature modeling of laser sustained hydrogen plasmas. *Journal of Thermophysics and Heat Transfer*, 8:781–790, 1994.

[8] G.E. Caledonia, P.K.S. Wu, and A. N. Pirri. Radiant energy absorption studies for laser propulsion. Final Report NASA-CR-134809, NASA Lewis Research Center, 1975.

[9] R.B. Miles, G.L.Brown, W.R. Lempert, R. Yetter, G.J. Williams Jr., S.M.Bogdonoff, D. Natelson, and J.R. Guest. Radiatively driven hypersonic wind tunnel. *AIAA Journal*, 33:1463–1469, 1995.

[10] R.B. Miles and G.L. Brown. Energy addition mechanisms for radiatively-driven wind tunnel: Predictions & experiments. In *AIAA 29th Plasmadynamics and Lasers Conference*, Albuquerque, NM, June 1998. AIAA 98-2748.

[11] W.G. Vincenti and C.H. Kruger. *Introduction to Physical Gas Dynamics*. John Wiley & Sons, 1965.

[12] D.T. Pratt and W.H. Heiser. Isolator-combustor interaction in a dual-mode scramjet. In *AIAA 31st Aerospace Sciences Meeting*, Reno, NV, January 1993. AIAA 93-0358.

[13] G. Herzberg. *Molecular Spectra and Molecular Structure II. Infrared and Raman Spectra of Polyatomic Molecules*. D. Van Nostrand Co., 1945.

[14] B. Bobin, C.J. Borde, J. Borede, and C. Breant. Vibration-rotation molecular constants for the ground and ($\nu_3 = 1$) states of SF_6 from saturated absorption spectroscopy. *Journal of Molecular Spectroscopy*, 121:91–127, 1987.

[15] J.D. Anderson Jr. and J.L. Wagner. CO_2 laser radiation absorption in SF_6-air boundary layers. In *AIAA 11th Aerospace Sciences Meeting*, Washington, D.C., January 1973. AIAA 73-262.

[16] J.I. Steinfeld, I. Burak, D.G. Sutton, and A.V. Nowak. Infrared double resonance in sulfur hexafluoride. *Journal of Chemical Physics*, 52:5421–5434, 1969.

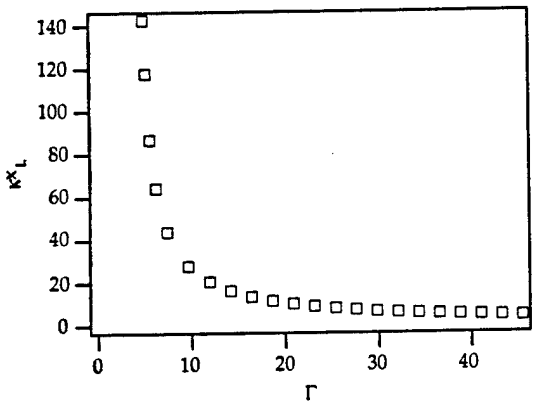

Figure 5: The calculated nozzle length for supersonic energy addition versus the laser beam power incident at the nozzle exit. 22 cases were considered. The left most point corresponds to having $\Gamma = 5.0$.

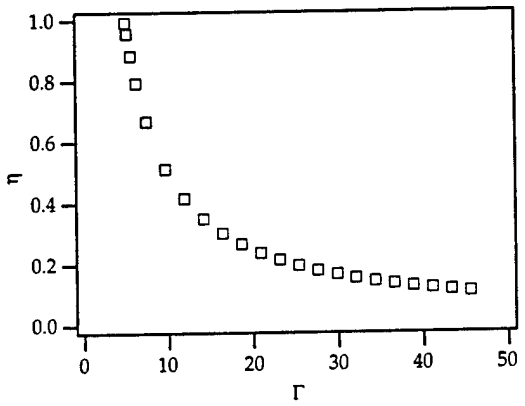

Figure 7: The fraction of laser beam power absorbed in the supersonic region, η, versus the laser beam power incident at the nozzle exit.

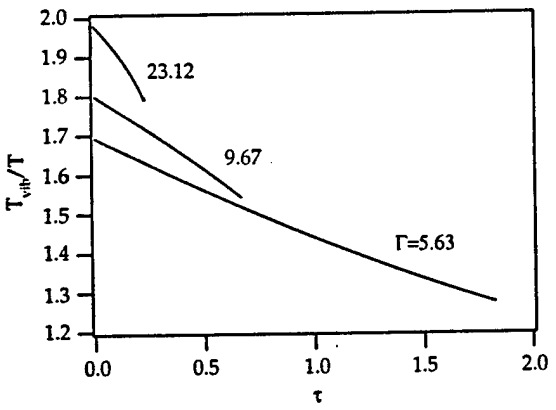

Figure 6: The ratio of SF_6 vibrational temperature to the fluid translation temperature, 300 K, as a function of the non-dimensional optical length, τ.

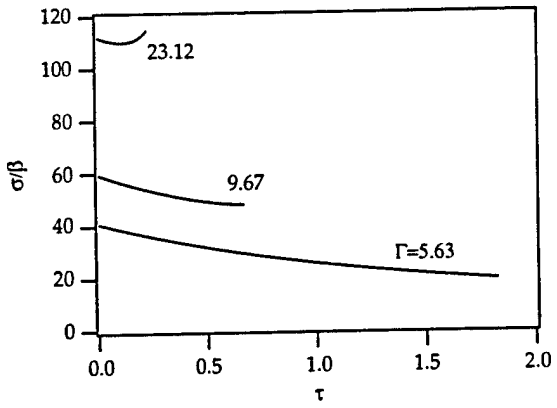

Figure 8: The ratio of the characteristic flow residence time to the vibrational relaxation time of SF_6 as a function of the non-dimensional optical length.

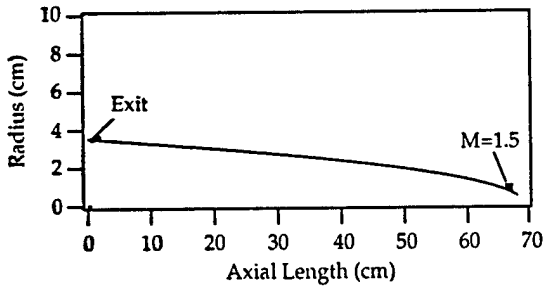

Figure 9: The computed nozzle profile, nozzle radius versus axial length, for supersonic energy addition with $\Gamma = 5.63$.

AIAA-01-0962

Numerical Simulation of Microwave-Sustained Supersonic Plasmas for Application to Space Propulsion

V. P. Chiravalle, R. B. Miles and E. Y. Choueiri

Mechanical and Aerospace Engineering Department
Princeton University, Princeton NJ 08544
USA

39th AIAA Aerospace Sciences Meeting & Exhibit
8-11 January 2001 / Reno, NV

Numerical Simulation of Microwave-Sustained Supersonic Plasmas for Application to Space Propulsion*

V.P. Chiravalle† R.B. Miles‡ and E.Y. Choueiri§
Princeton University, Princeton, New Jersey 08544

AIAA-2001-0962¶

Abstract

The concept of adding energy to an expanding supersonic flow using a microwave-sustained plasma is explored numerically by solving the complete system of both the Maxwell equations and the Navier Stokes equations for the case of an argon flow in a realistic thruster geometry. Results show that when an additional amount of power, equal to 45 % of the power deposited in the plenum, is added to the supersonic flow a toroidal plasma forms, but only a 3 % increase in specific impulse is achieved. It is concluded that future work relating to this concept should concentrate on finding ways to confine the plasma to the centerline.

*This research was funded by an AASERT grant from AFOSR with additional support from NSF.

†Graduate Student, Mechanical & Aerospace Engineering, AIAA

‡Professor, Mechanical & Aerospace Engineering, Associate Fellow AIAA

§Assistant Professor, Mechanical & Aerospace Engineering, Senior Member AIAA

¶Presented at the 39th AIAA Aerospace Sciences Meeting and Exhibit, Reno, NV, January 8-11, 2001.

1 Introduction

1.1 Motivation

The conventional approach for electrothermal space propulsion systems has been to heat a propellant gas to a high temperature in the plenum and then to expand the flow in a nozzle and produce thrust. Examples of such systems are resistojets, arcjets, and microwave electrothermal thrusters. For all these systems, the specific impulse is limited to the maximum average temperature that can be achieved by heating a low molecular weight propellant in the plenum. For a state of the art 2 kW hydrazine arcjet the specific impulse is roughly 600 sec[1]. Both arcjets and microwave electrothermal thrusters make use of a high temperature plasma to heat the flow. The plasma in an arcjet is sustained by electric current emitted from a cathode; in the case of a microwave electrothermal thruster, microwave energy is used to sustain the plasma. The fact that a microwave-sustained plasma can be created without electrodes and can be maintained away from the material surfaces of the thruster, may allow for large reductions in thruster erosion and significant improvements in overall lifetime, compared with arcjets. From a fundamental point of view the maximum average temperature that can be achieved for a given propellant in a microwave

electrothermal thruster is limited by the reflection of microwave power from the plasma, an effect that gets more pronounced as the temperature and electron density of the gas increases. One possible way to circumvent this limitation and to realize higher performance in terms of specific impulse and thrust is to add additional energy to the propellant in the supersonic region of the flow, creating a supersonic "afterburner". This can be accomplished by using additional microwave energy to create another plasma in the supersonic region of flow. To date numerical simulation of microwave-sustained plasmas has concentrated on the high pressure, subsonic regime[2]. The goal of the present work is to apply a computational model of similar sophistication as existing models in the supersonic regime and to show a case where a stable microwave-sustained argon plasma at 2.45 GHz can exist under these conditions as well.

1.2 Previous Work

Unlike resistojets and arcjets, which have been studied extensively for more than thirty years and have matured to the point of routine utilization in various spaceflight operations, microwave electrothermal thrusters have yet to be tested in space. The physics of microwave-sustained discharges at high pressures in subsonic flows has been a topic of research for many years and is well understood[3]. Different configurations have been explored for coupling microwave power to a gas, the most promising for thruster applications is the cylindrical resonant cavity design, employing either the TM_{011} or TM_{012} microwave mode structure. The first thruster of this kind was build in the early 1980's and it consisted of a cylindrical microwave resonant cavity at 2.45 GHz and a quartz tube, arranged concentrically[4]. He or N_2 gas flowed through the quartz tube, where the walls stabilized the microwave plasma on the centerline. The gas then exited through a quartz nozzle connected to the tube. It was shown that the ratio of power absorbed by the plasma to the incident power delivered to the cavity, the microwave coupling efficiency, could be made to exceed 95% with proper tuning of the cavity for discharges sustained at pressures from 40 to 1000 torr. Excessive heating and erosion of the quartz nozzle limited the input power to less than 2 kW for mass flow rates in the range of 100 mg/sec. Another prototype thruster utilizing a cylindrical resonant cavity at 2.45 Ghz with a free-floating plasma inside the cavity has operated successfully at power levels of up to 2.2 kW and pressures as high as 3 atm with He, N_2, NH_3 and H_2 as propellants[5]. In that design the plasma is stabilized by flow swirl created from tangential gas injection into the cavity. The gas exits the cavity through a graphite nozzle. Spectroscopic measurements were made of free-floating He plasmas in the cavity, stabilized by a bluff body, and the results indicate that the electron temperature of these discharges is roughly constant at 12,000 K over a range of incident powers from 0.5 to 1.0 kW and a range of pressures from 1.0 to 3.0 atm[6].

In addition to these experimental efforts, numerical work has been done to model the physical processes occurring in microwave-sustained discharges. The size, shape, location and peak temperature of the free-floating He discharges, stabilized by a bluff body, discussed above have been reasonably well predicted by a computational model consisting of a low Mach number formulation of the Navier Stokes and the Maxwell equations[2]. In a TM_{011} or TM_{012} resonant cavity the oscillating electric field has both a radial and an axial component, and the magnetic field has an azimuthal component. In that work the parabolized Navier Stokes equations were solved by a time-implicit finite difference technique, and the Maxwell equations relating the three electromagnetic field components were solved using a time-explicit finite difference technique. The time dependent solu-

tion for the electromagnetic field was then averaged over several wave periods to obtain energy addition terms for the fluid equations. Thermodynamic equilibrium was assumed, in the sense that both electrons and heavy species have the same temperature and that the electron concentration is determined from the Saha relation. Subsequently, the model was extended to include a converging flow geometry so that realistic thruster configurations could be simulated, and a parametric study of the effect of nozzle throat area, discharge pressure and absorbed power on the location of the plasma in a resonant cavity thruster was performed[7]. For simulations at a microwave frequency of 0.915 GHz, a helium mass flow rate of 1.9 g/sec (1 atm plenum pressure) and an incident power of 40 KW, a toroidal plasma was observed off the cavity centerline. As the cavity length was changed, detuning the cavity from resonance and reducing the power absorbed by the plasma, it was shown that the plasma would move back on the centerline.

1.3 Outline

The physical model and the numerical techniques used in the present study are described briefly in §2. The results from a computation of a microwave sustained supersonic argon plasma, are presented in §3. The validity of a critical model assumption, that electrons and heavy species have the same temperature, is discussed in §4.

2 Physical Model

The physical model used in this work shares many common features with the model of Ref. [2], there are some important differences, however. In both cases a fluid model is coupled to a electromagnetic model that solves the Maxwell equations. In the previous work high pressure, low Mach number flows were considered, where the solution of the parabolized Navier Stokes equations could be considered adequate. In this work the complete set of Navier Stokes equations are solved, using modern CFD techniques. In the work of Ref. [2] the Maxwell equations are solved using a time marching technique, in contrast to the finite element approach pursued in this work. In addition because the electromagnetic field relations are formulated in terms of the Helmholtz wave equation in this work, it is necessary only to solve for the two components of the electric field. One point of similarity is that both models assume thermodynamic equilibrium, and all transport properties and the plasma conductivity are calculated accordingly in both cases. This may be a point were both models fail, however, since at least for the problem considered here it is shown in §4, that in the region of intense energy addition the results are not consistent with equilibrium conditions.

2.1 Flowfield Configuration

Argon was chosen as the propellant gas of interest in this study purely to illustrate the supersonic energy addition concept; a practical electrothermal thruster would use a low molecular weight gas. The geometry of the problem considered here is illustrated in Fig. 1. Argon, at a flow rate of 200 mg/sec, enters a conical nozzle with a half angle of 15 deg, an inlet radius of 0.0625 in, and a length of 0.8 in. These dimensions represent a realistic nozzle geometry. Sonic conditions are assumed at the gas injection port where the temperature is 5000 K and the pressure is 0.2 atm. These conditions correspond to the addition of 670 W of power in the subsonic plenum section of this hypothetical thruster. The nozzle is concentric with a cylindrical waveguide with a radius of 3.0 in. In Fig. 1 a plasma is shown inside the nozzle region, labeled Section A. The Navier Stokes equations are

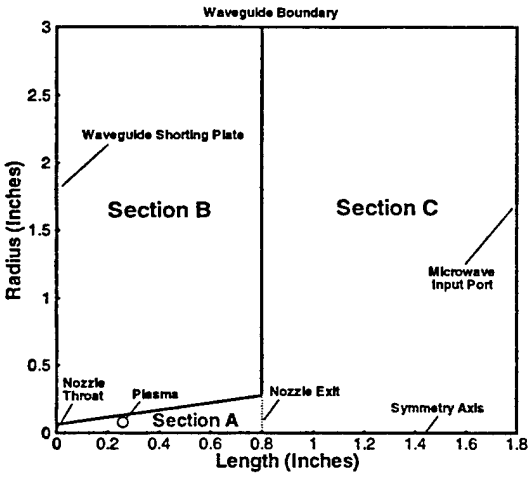

Figure 1: Diagram showing the geometry of the numerical simulation.

solved in section A. The microwave field is computed throughout the entire waveguide, sections A, B and C. It is assumed that the walls of the waveguide and the shorting plate, which lies along the y-axis in Fig. 1, are perfect conductors. The walls of the nozzle are labeled Section B in Fig. 1 and consist of alumina ceramic, which has a dielectric constant of 9.0. The nozzle walls fill the entire cross section of the waveguide. A real microwave thruster would have a radial antenna protruding into section B, which would act to couple microwave energy into the cavity. The three dimensional field pattern associated with a radial antenna is not considered in the present model, but rather a microwave transmission region, labeled Section C, is added to the computational domain so that microwave energy can propagate from the microwave input port into the regions of interest, sections A and B. There is no interaction between the exhaust gas and the microwave field in section C. It is assumed that gas which has moved through the nozzle exhausts into a perfect vacuum. The value of the complex electric field is specified at the microwave input port, using the theoretical expression for a cylindrical TM_{01} mode with the amplitude chosen so that a desired value of total power is absorbed by the plasma. The present case assumes that an additional 300 W of power is absorbed by the plasma in the supersonic section. Now the equations that describe the fluid variables and the microwave field components are discussed along with the numerical techniques used to solve them.

2.2 Navier Stokes Equations

The unsteady axisymmetric Navier Stokes equations, which describe the conservation laws of mass, momentum and energy for the gas in the nozzle, can be written in cylindrical coordinates in the follow differential vector form[8]

$$\frac{\partial r\mathbf{U}}{\partial t} + \frac{\partial r\mathbf{F}(\mathbf{U})}{\partial x} + \frac{\partial r\mathbf{G}(\mathbf{U})}{\partial r} = \mathbf{S}, \qquad (1)$$

where x and r are the axial and radial directions, respectively. $\mathbf{U} = (\rho, u, v, E)^{\mathrm{T}}$ is the vector of conservation variables, with gas density as ρ, axial velocity as u, radial velocity as v and total energy density (thermal plus kinetic) as E. The flux vectors, $\mathbf{F}(\mathbf{U}) = \mathbf{F}^{\mathbf{c}}(\mathbf{U}) + \mathbf{F}^{\mathbf{d}}(\mathbf{U})$ and $\mathbf{G}(\mathbf{U}) = \mathbf{G}^{\mathbf{c}}(\mathbf{U}) + \mathbf{G}^{\mathbf{d}}(\mathbf{U})$, are functions of the conservation variables and contain both convective and diffusive terms. The convective flux vectors are

$$\mathbf{F}^{\mathbf{c}}(\mathbf{U}) = \begin{bmatrix} \rho u \\ \rho u^2 + p \\ \rho uv \\ u(E+p) \end{bmatrix},$$

$$\mathbf{G}^{\mathbf{c}}(\mathbf{U}) = \begin{bmatrix} \rho v \\ \rho uv \\ \rho v^2 + p \\ v(E+p) \end{bmatrix},$$

while the diffusive flux vectors are

$$\mathbf{F^d(U)} = \begin{bmatrix} 0 \\ \tau_{xx} \\ \tau_{xr} \\ -q_x + u\tau_{xx} + v\tau_{xr} \end{bmatrix},$$

$$\mathbf{G^d(U)} = \begin{bmatrix} 0 \\ \tau_{xr} \\ \tau_{rr} \\ -q_r + u\tau_{xr} + v\tau_{rr} \end{bmatrix}.$$

In the previous relations p is the gas pressure. The viscous stresses are given by

$$\begin{aligned} \tau_{xx} &= \frac{4}{3}\mu\frac{\partial u}{\partial x} - \frac{2}{3}\mu\left(\frac{\partial v}{\partial r} + \frac{v}{r}\right), \\ \tau_{rr} &= \frac{4}{3}\mu\frac{\partial v}{\partial r} - \frac{2}{3}\mu\left(\frac{\partial u}{\partial x} + \frac{v}{r}\right), \\ \tau_{xr} &= \mu\left(\frac{\partial u}{\partial r} + \frac{\partial v}{\partial x}\right), \end{aligned}$$

with μ equal to the viscosity. The heat fluxes are

$$\begin{aligned} q_x &= -k\frac{\partial T}{\partial x}, \\ q_y &= -k\frac{\partial T}{\partial r}, \end{aligned}$$

with T equal to the gas temperature and k equal to the thermal conductivity. The right hand side of the equation, S, contains source terms that are due to cylindrical symmetry of the problem and the microwave energy addition term; its functional form is given below

$$\mathbf{S} = \begin{bmatrix} 0 \\ 0 \\ p + \frac{2}{3}\left(\tau_{xr} - \frac{2\mu v}{r}\right) \\ \langle \mathbf{i} \cdot \mathbf{E} \rangle \end{bmatrix}.$$

In the above expression i is the current density vector and E is the electric field vector. The microwave energy addition term $\langle \mathbf{i} \cdot \mathbf{E} \rangle$ is described in §2.3.

A conservative finite volume numerical discretization is used to integrate the governing equations(1) in time until a steady state is reached, an approach that has been thoroughly validated by several authors[8, 9, 10]. The conservative variables U are stored at the center of each cell on the grid and updated after each time step. The convective and diffusive fluxes are evaluated separately at the boundaries of each cell. A flux limited scalar dissipation technique has been employed to ensure that non-linear stability criteria are satisfied[9]. A simple Euler finite difference is used for marching forward in time, with the largest time step size determined as discussed in Ref. [9]. The Navier Stokes code performs bilinear interpolation from values stored in a table, to compute the equation of state and the transport properties in the equations above. These properties are stored as functions of gas density and internal energy (energy per unit mass). The interpolation table for argon, used for the calculations in this paper, was generated by a widely used and well validated chemical equilibrium code, described in Ref. [11].

2.3 Maxwell Equations

As mentioned previously, for a TM_{01} mode in a cylindrical waveguide there are three components of the electromagnetic field, E_r, E_z, and H_θ. The relationships among these components are expressed by the Maxwell equations. When considering a time periodic electromagnetic field of angular frequency ω it is convenient to describe any one of the components of the field, represented by Φ, in terms of a complex amplitude, in the following way

$$\Phi = \frac{1}{2}\left(\phi e^{-i\omega t} + \phi^* e^{i\omega t}\right). \qquad (2)$$

By writing each component in the form of Eqn. 2, substituting into the Maxwell equations and simplifying it can be shown that the complex amplitude of

each of the three components of the electromagentic field obeys the Helmholtz wave equation. For a problem involving microwave energy addition to a plasma, only the electric field components need to be determined, as will be discussed shortly. In cylindrical coordinates the Helmholtz equation for the complex amplitude of the axial electric field, E_z is

$$\frac{1}{r}\frac{\partial}{\partial r}r\frac{\partial E_z}{\partial r}+\frac{\partial^2 E_z}{\partial x^2}+\beta^2 E_z=0. \quad (3)$$

The corresponding equation for the complex amplitude of the radial component, E_r is

$$\frac{1}{r}\frac{\partial}{\partial r}r\frac{\partial E_r}{\partial r}+\frac{\partial^2 E_r}{\partial x^2}+\left(\beta^2-\frac{1}{r^2}\right)E_r=0. \quad (4)$$

In these equations the complex propagation constant β is such that $\beta^2 = \frac{\omega^2}{c^2}\left(1-i\frac{\sigma}{\epsilon_0\omega}\right)$, where c is the speed of light, ϵ_0 is the dielectric permitivity of free space and σ is the complex conductivity of the plasma.

The complex conductivity is responsible for the coupling between fluid and the microwave field. The complex conductivity is a function of the electron number density N_e and total electron collision frequency ν according to the following expression

$$\sigma=\frac{N_e e^2}{m_e(\nu+i\omega)}, \quad (5)$$

where e is the electron charge and m_e is the mass of an electron. Assuming equilibrium conditions the total collision frequency is a function of the gas temperature T, the electron number density N_e and the atomic number density N_A, as discussed in Ref. [12]

$$\nu=6.2\times10^3\sigma_{eh}\sqrt{T}N_A+3.0\times10^{-5}N_eT^{-3/2}. \quad (6)$$

The first term in the equation above represents the contribution from electron-atom collisions and the second term represents the contribution from electron-ion collisions. In this work the electron-atom collision cross section σ_{eh} was taken to be $10^{-20}\mathrm{m}^2$. Having determined σ using the above formula, the volume energy addition term is determined as given below

$$\langle \mathbf{i}\cdot\mathbf{E}\rangle=\frac{1}{4}(\sigma+\sigma^*)(E_rE_r^*+E_zE_z^*). \quad (7)$$

The finite element method is used to solve both Eqn. (4) and Eqn. (3) separately. This method breaks the two dimensional computational domain (x,r plane) into finite elements and assumes, at any point inside one of these finite elements, that an electric field component can be expressed as a weighted average of its respective value at the corners of that particular finite element. Quadrilateral finite elements are used in this work, and first order bilinear interpolation functions are used as the basis functions for the weighted averaging. In solving both for E_r and E_z a matrix is generated, implicitly relating the values of E_r and E_z respectively at every point on the grid. These matrices are inverted using a standard numerical algorithm for band-diagonal matrices.

2.4 Boundary Conditions

In this section the boundary conditions for the quantities in the calculation are reviewed, starting first with the microwave fields. The finite element method requires that at a boundary either the function itself or its derivative is specified. At the inlet port the values of E_r and E_z are specified, as discussed in the previous section. Along the waveguide boundary it is assumed that $E_z = 0$, since tangential electric fields cannot exist on the surface of a perfect conductor. The corresponding boundary condition for the radial electric field is $\partial rE_r/\partial r = 0$. Along the shorting plate boundary the following conditions hold true, $E_r = 0$ and $\partial E_z/\partial z = 0$. Finally at the waveguide centerline, the cylindrical symmetry of the problem implies that $E_r = 0$ and $\partial E_z/\partial r = 0$.

Now the boundary conditions for the fluid variables are discussed. Because of the cell-centered scheme used by the Navier Stokes solver it is necessary to specify the values of the convective fluxes, $\mathbf{F^c(U)}$ and $\mathbf{G^c(U)}$, at the physical boundaries of the nozzle domain. At the nozzle throat the values of the convective fluxes are specified, corresponding to sonic flow at 5000 K and 0.2 atm. At the nozzle exit the convective fluxes are calculated based on the values of the conservative variables $\mathbf{U}$, at the adjacent cell centers. Along the nozzle wall and centerline boundaries the convective fluxes are specified so that there is no mass, momentum or energy flux through these respective boundaries. In addition to the above specifications for the convective fluxes, the no slip conditions, $u = 0$ and $v = 0$, are applied at the nozzle wall boundary and the temperature of the nozzle wall is fixed at 500 K. This facilitates the computation of the diffusive fluxes, $\mathbf{F^d(U)}$ and $\mathbf{G^d(U)}$, at these locations. It is assumed that the diffusive fluxes are zero at the gas inlet and exit ports. At the nozzle centerline the diffusive fluxes are calculated by extrapolating the values of $\partial u/\partial x$ and $\partial T/\partial x$ from the interior domain, and enforcing cylindrical symmetry, by setting v and all partial derivatives with respect to r equal to zero.

3 Simulation Results

The numerical problem formulated in the previous section was solved using a desktop computer, and the results are now presented.

The time-averaged values of the axial electric field, $\frac{1}{2}(E_z E_z^*)$ are presented in Fig. 2 for the case when a plasma is present in the nozzle. There are two areas of maximum field intensity in Fig. 2, one that is entirely inside the alumina nozzle region, section B in Fig. 1, and one that spans both sections B and C. The plasma forms in the region between these two maxima. The maximum field strength is roughly 0.55 kV/cm. The corresponding time-averaged value of the radial field is shown in Fig. 3. In the case without a plasma, there is no change in the radial field. The axial field, however, shows a distinct difference as illustrated in Fig. 4. The maxima inside the nozzle has a straight boundary at about $x = 0.4$ in when the plasma is not present. When the plasma forms it deforms this boundary, pushing the electric field contours to the left, away from the interior of the plasma. This effect is exactly what would be expected if a metal conductor were placed inside the nozzle at this location. In choosing the geometry of the problem in this paper, it was the intention to model the electric fields in a resonant cavity thruster as closely as possible. This goal has been achieved because the radial field in Fig. 3 drops off to zero at the interface between the alumina nozzle and the microwave transmission section, $x = 0.8$ in, and if another shorting plate were placed in the waveguide at this location a resonant cavity would be created.

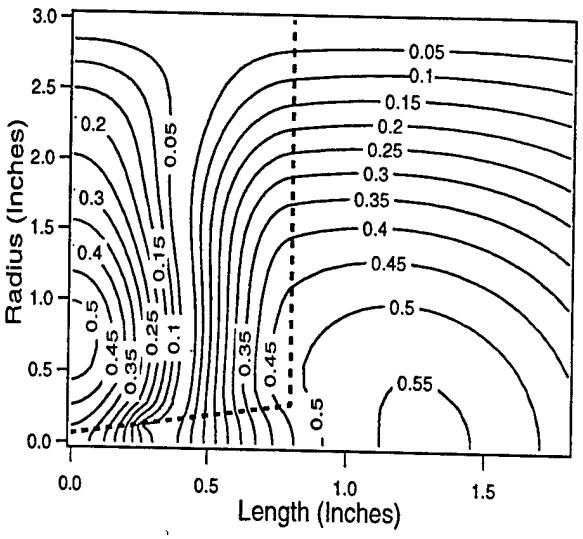

Figure 2: Time-averaged value of the axial electric field with a plasma inside the nozzle.

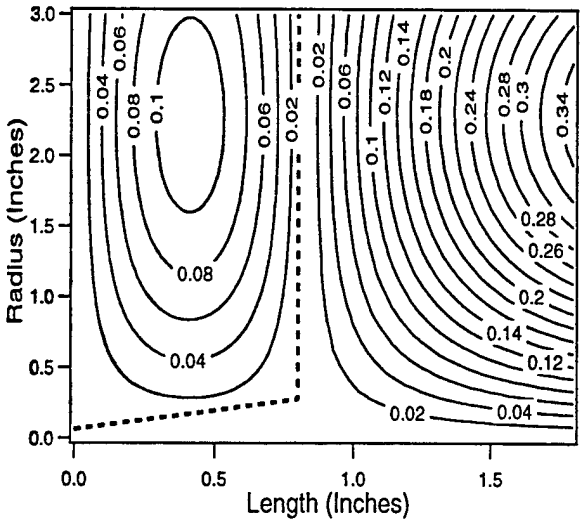

Figure 3: Time-averaged value of the radial electric field.

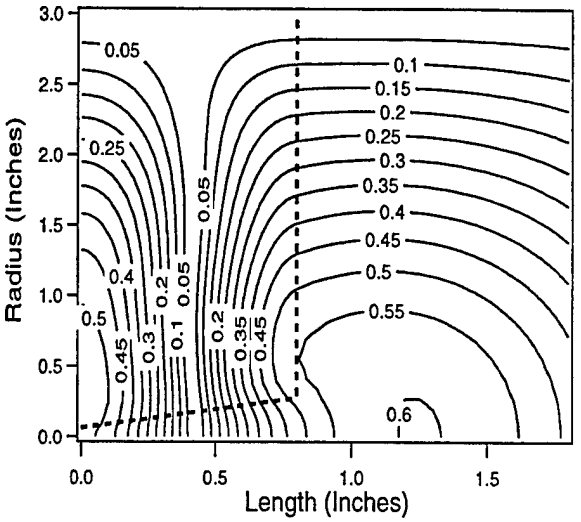

Figure 4: Time-averaged value of the axial electric field without a plasma inside the nozzle.

The physical properties of the plasma are now discussed. The plasma has a toroidal shape located relatively close to the nozzle wall as evidenced by the temperature contours presented in Fig. 5. In this regard the plasma seen here is similar to some of the plasmas computed in Ref. [7]. The maximum temperature is about 9100 K, at a location of $x = 0.27$ in and $y = 0.12$ in. This temperature is more than 4000 K hotter than the temperature at the gas inlet. The corresponding pressure at this location is about 26 torr. The pressure contours are shown in Fig. 6. A shock structure is established in the nozzle due to the energy addition, as evidenced by the pressure rise along the nozzle centerline at about $x = 0.4$ in. The pressure at the exit of the nozzle is roughly 1 torr and the Mach number close to the centerline at the exit is about 5, as shown in Fig. 7. The hottest point of the plasma, the 9100 K point, occurs where the Mach number is 0.52. The electron number density at this point is about 10^{15} cm^{-3}, as indicated in Fig. 8. This electron number density corresponds to an ionization fraction of about 4.1%. Moving 0.1 inches downstream of this point the electron number density drops by four orders of magnitude to roughly 10^{11} cm^{-3}. The volume heating rate at the maximum temperature point is 43 kW/cm^3. A maximum volume heating rate of 68 kW/cm^{-3} occurs at a point slightly upstream of the maximum temperature point. The Mach number at this point is 0.29. Most of the energy addition occurs in the subsonic viscous boundary layer.

Without a plasma the thrust of this hypothetical thruster is 0.451 N and with a 300 W plasma in the supersonic section, the thrust is 0.464 N. The corresponding values of specific impulse with and without energy addition are 227 sec and 233 sec respectively. The total power (300 W) added to the supersonic flow as a percentage of the 670 W input power in the plenum is 45%, which results in only a 3 % increase in thrust and specific impulse. 79 % of the power added to the plasma in the supersonic section, 237 W, is removed by conduction through the

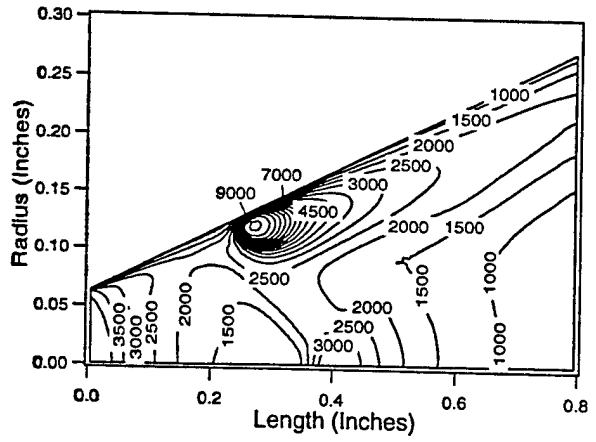

Figure 5: Temperature contours in K for the flow inside the nozzle.

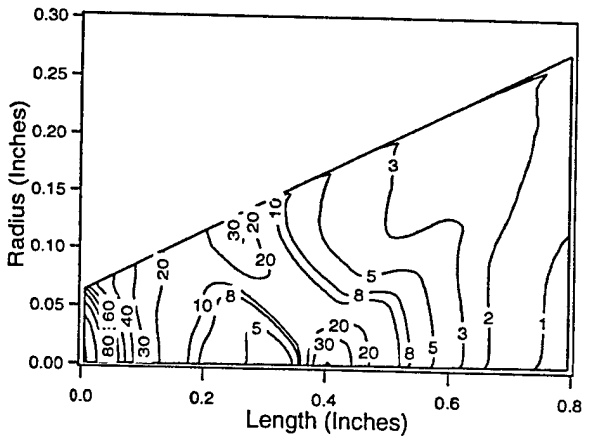

Figure 6: Pressure contours in torr for the flow inside the nozzle.

nozzle wall, assuming that the nozzle wall is maintained at 500 K. A real ceramic nozzle in this situation would have a two dimensional temperature profile and the maximum temperature would probably be higher than what was assumed in these calculations. A higher wall temperature would make the supersonic energy addition process more efficient. It is, of course, more desirable if the plasma were kept away from the nozzle wall altogether, confined in some way to the centerline of the flow.

4 Investigation of Model Assumptions

The validity of some of the assumptions in the model are now explored. For the Navier Stokes equations or for any fluid approximation to be valid, the characteristic length and time scales must be larger than the length and time scales associated with collisions on an atomic level. In this work the characteristic length L_c is defined in terms of the gas temperature T as $\frac{T}{\partial T/\partial x}$ and the characteristic time is defined as $t_c = L_c/u$. The mean free path of argon atoms can be estimated with the formula $\lambda_p = 1/N_A\sqrt{2}\pi d^2$, where d is the diameter of an argon atom. In this work d is taken to 4×10^{-10} m. The ratio L_c/λ_p throughout the entire flow field is never less than 10, and in most of the domain it is greater than 100. A typical value for the characteristic length in the region just before the gas exhaust port is about 0.8 in and in the plasma it is roughly 0.2 in. This indicates that fluid theory is accurate, at least in describing the heavy particle species. Using the values of total electron collision frequency it is possible to find $t_c\nu$. $t_c\nu$ is everywhere greater than 100, and in the region where the plasma is located it is closer to 10^6. From this it is obvious that a fluid description of the electrons is accurate as well.

One final question is whether both the electrons and the heavy particles do indeed have the same temperature, as assumed in this work. This can be accomplished by considering what the electron temperature would need to be in order for all the energy absorbed by the electrons from the microwave field, equal to $\langle \mathbf{i} \cdot \mathbf{E} \rangle$, to be transferred to the heavy particles through elastic collisions. The rate of energy

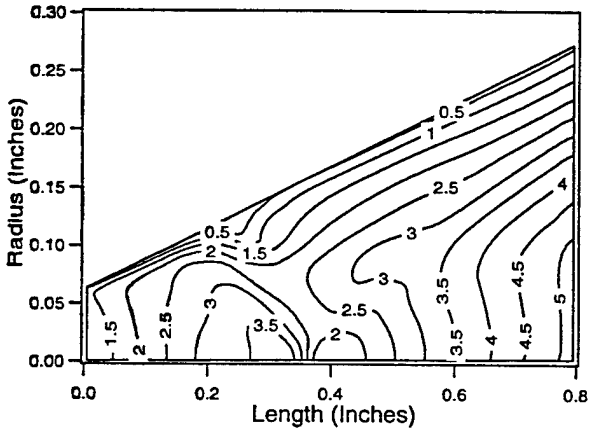

Figure 7: Mach number contours for the flow inside the nozzle.

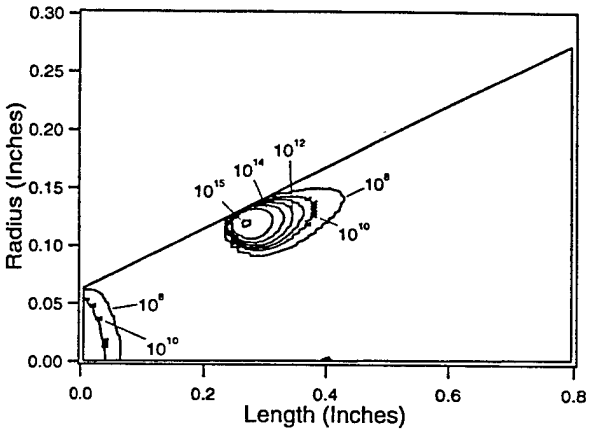

Figure 8: Electron number density contours in cm^{-3} for the flow inside the nozzle.

transfer is determined by the following formula

$$\xi = 3k_b N_e \nu \frac{m_e}{m_A} (T_e - T), \qquad (8)$$

where k_b is the Boltzman constant, m_A is the mass of an argon atom (or ion) and T_e is the electron temperature. Taking the values of heavy species temperature T, volume heating rate and gas density computed by the numerical model it is possible to solve Eqn. (8) for the electron temperature, if it is further assumed that the ionization level is determined by the gas density and the electron temperature (instead of the heavy species temperature) according the Saha equilibrium relation. When this is done for a point close to the maximum temperature point of the plasma, the electron temperature is found to be roughly 1.5eV (17,000 K), which is significantly higher than the heavy species temperature (9100 K). The corresponding electron number density is $4 \times 10^{16} cm^{-3}$, which is about an order of magnitude higher than the value predicted assuming that the electrons and heavy species have the same temperature. Therefore, at the density levels associated with this expanding flow in order for all the energy absorbed by the electrons to be transferred to the heavy particles it is necessary for a certain degree of non-equilibrium to exist.

5 Conclusions

A fully coupled calculation, solving both the Navier Stokes and Maxwell equations has been performed for a supersonic argon flow in a realistic thruster geometry, expanding upon research done on subsonic plasmas. Like certain situations involving subsonic microwave-sustained plasmas, the plasma in this calculation has a toroidal shape and is located relatively close to the nozzle wall in the viscous boundary layer. The maximum temperature in this plasma is about 9100 K and the electron number density is roughly $10^{15} cm^{-3}$. The presence of such a plasma distorts the axial electric field pattern in the thruster, forcing the electric field out of the region where the plasma is located. It has been shown that most of the energy added to this supersonic plasma is conducted through the nozzle walls, in this case where the wall temperature is 500 K. The specific impulse of this hypothet-

ical thruster increased, nevertheless, from 227 sec to 233 sec. Future work with this problem should concentrate on finding a way to confine the plasma to the nozzle centerline, if it is possible to do so. Finally a check was performed to verify the validity of the continuum fluid assumption and the approximation that the electron and heavy species temperatures are the same. There is conclusive evidence that the continuum fluid assumption is valid for both electrons and heavy particles, whereas the assumption of a single fluid temperature is inaccurate. Therefore it is recommended that a model including separate temperatures for both the heavy species and the electrons be applied to this problem.

References

[1] P. G. Lichon and J. M. Sankovic. Development and demonstartion of a 600-sec mission-average i_{sp} arcjet. *Journal of Propulsion and Power*, 12:1018–1025, 1996.

[2] S. Venkateswaran and C. L. Merkle. Numerical investigation of bluff-body stabilized microwave plasams. *Journal of Propulsion and Power*, 11:357–364, 1995.

[3] Y. P. Raizer. *Gas Discharge Physics*. Springer-Verlag, 1997.

[4] S. Whitehair and J. Asmussen. Microwave electrothermal thruster performance in helium gas. *Journal of Propulsion and Power*, 3:136–144, 1985.

[5] D. J. Sullivan and M. M. Micci. Development of a microwave resonant cavity electrothermal thruster prototype. In 23rd *International Electric Propulsion Conference*, Seattle, WA, September 1993. IEPC-93-036.

[6] P. Balaam and M. M. Micci. Investigation of stabilized resonant cavity microwave plasmas for propulsion. *Journal of Propulsion and Power*, 11:1021–1027, 1995.

[7] D.A. Schwer, S. Venkateswaran, and C. L. Merkle. Analysis of microwave-heated rocket engines for space propulsion. In *AIAA 29th Joint Propulsion Conference*, Monterey, CA, June 1993. AIAA 93-2105.

[8] R. Broglia, M. Manna, H. Deconinck, and G. Degrez. Development and validation of an axisymmetric navier-stokes solver for hypersonic flows. Technical Note 188, von Karman Institute for Fluid Dynamics, 1995.

[9] L. Martinelli. *Calculations of Viscous Flows with a Multigrid Method*. PhD thesis, Princeton University, 1987.

[10] G.L. Brown, A.P. Ratta, R.W. Anderson, L. Martinelli, W.R. Lempert, and R.B. Miles. Fluid mechanics in a radiatively driven hypseronic wind-tunnel - prediction and preliminary experiment. In 19rd *AIAA Advanced Measurement and Ground Testing Technology Conference*, New Orleans, LA, June 1996. AIAA-96-2199.

[11] S. Gordon and B. J. McBride. Computer program for calculation of complex chemical equilibrium compositions and applications: Part 1 analysis. Reference Publication NASA-RP-1311, NASA Lewis Research Center, 1994.

[12] R.G. Jahn. *Physics of Electric Propulsion*. McGraw-Hill, 1968.

APPENDIX IV: Radiatiely-Driven, Hypersonic Wind Tunnel

1. P. Barker, J. Grinstead, A. Morgan, **R. Anderson**, P. Howard, G. Brown, R. Miles, R. Lipinski, K. Reed, G. Pena, L. Schneider, *"Radiatively-Driven Wind Tunnel Experiment with a 30 kW Electron Beam,"* Paper #AIAA-99-0688, 37th AIAA Aerospace Sciences Meeting and Exhibit, Reno, NV. Jan. 11-14, 1999.

2. **R.W. Anderson**, G.L. Brown, and R.B. Miles, *"Performance Characterization of a Radiativley Driven Hypersonic Wind Tunnel,"* Paper #AIAA-99-0822 37th AIAA Aerospace Sciences Meeting & Exhibit, Reno, NV, Jan. 11-14, 1999.

3. P. Barker, J. Grinstead, P. Howard, **R. Anderson,** G. Brown, R. Miles, R. Lipinski, G. Pena, L. Schneider, R. Howard, ***"A 150 kW Electron Beam Heated, Radiatively-Driven Wind Tunnel Experiment,"*** Paper #AIAA-2000-0159, 38th Aerospace Sciences Meeting & Exhibit, Jan. 10-13, 2000, Reno, NV.

4. **K. Raman, R.W. Anderson,** G.L. Brown, R.B. Miles, and M. Costantino, *"An Ultra-High Pressure, Ultra-High Reynolds Number, Blow-Down Wind Tunnel: Design and Preliminary Experiments,"* Paper #AIAA-2000-0534, 38th AIAA Aerospace Sciences Meeting and Exhibit, Reno, NV, Jan. 10-13, 2000.

5. P. Barker, P. Howard, **R. Anderson**, R. Miles, G. Brown, R. Lipinski, G. Pena, J. Grinstead, and R. Howard, "Proof-of-Principle Energy Addition Experiments for the REDHWT/MARIAL II Hypersonic Wind Tunnel," Paper #AIAA-2000-2276, 21st AIAA Advanced Measurement Technology and Ground Testing, 31st AIAA Plasmadynamics and Lasers, 34th AIAA Thermophysics, Fluids 2000 Conferences, Denver, CO, June 19-22, 2000.

6. **R.W. Anderson**, G.L. Brown, and R.B. Miles, *"Performance Models and Predictions for the RDHWT/MARIAH II Hypersonic Wind Tunnel,"* Paper #AIAA-2000-2274, 21st AIAA Aerodynamic Measurement Technology and Ground Testing Conference, Denver, CO, June 19-22, 2000.

AIAA

AIAA-99-0688
Radiatively Driven Wind Tunnel Experiment with a 30 kW Electron Beam

P. Barker, J. Grinstead, A. Morgan, R. Anderson, P. Howard, G. Brown, R. Miles.
Princeton University, Princeton, NJ

R. Lipinski, K. Reed, G. Pena, L. Schneider.
Sandia National Laboratories, Albuquerque, NM

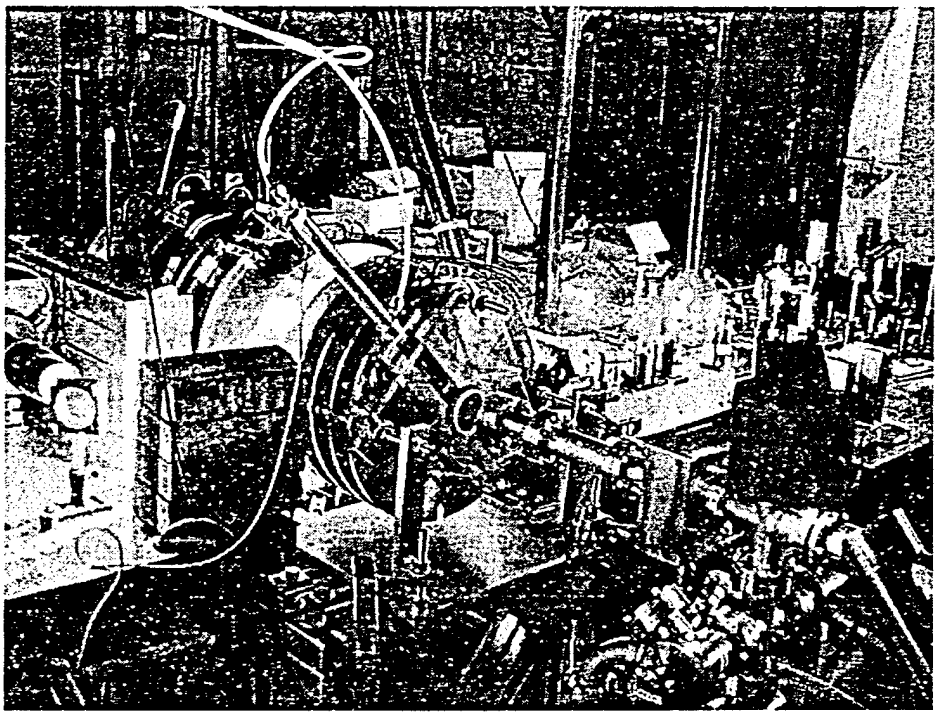

Scattered laser light illuminates the wind tunnel during electron beam heating. The laser was used to determine temperature in the flow

37th AIAA Aerospace Sciences Meeting and Exhibit
January 11-14, 1999 / Reno, NV

Radiatively Driven Wind Tunnel Experiment with a 30 kW Electron Beam

P. Barker, J. Grinstead, A. Morgan, P. Howard, B. Anderson, R. Miles, G. Brown
Department of Mechanical and Aerospace Engineering, Princeton University

R. Lipinski, K. Reed, G. Pena, L. Schneider
Sandia National Laboratories, Albuquerque

Controlled energy addition to a supersonic flow has been demonstrated using a 1 MeV electron beam (e-beam). Within the duration of the e-beam pulse (500-750 μs) the increase in total enthalpy, absorbed power, and change in Mach number with time were measured during the heating process. Time resolved shadowgraph images show a steady transition from the unheated flow to the e-beam heated flow, demonstrating that on the time scale of these experiments a stable flow, with a higher total enthalpy, was achieved with heat addition from an electron beam.

Introduction

High power directed energy sources such as electron beams and lasers are being investigated as a means of adding energy to supersonic air, increasing both flow entropy and total enthalpy in a controlled manner. A ground test facility based on this concept, including a final expansion to hypersonic conditions, has been termed the radiatively driven hypersonic wind tunnel (RDHWT)[1]. Such a facility has the potential to overcome the poor flow quality and short runtime of current hypersonic test facilities, because the flow temperature can be kept low enough to avoid thermal chemistry and containment problems created in the plenum of conventional facilities. To reach flight conditions above Mach 10, while maintaining a relatively low temperature throughout the wind tunnel, high plenum pressures in the 10 000 atmosphere range will be required. For a full scale Mach 12-15 hypersonic test facility, it is envisioned that multi-megawatt (50 MW) energies and pressures of greater than 10 000 atmospheres will be required

To date, work on the RDHWT has focused on the demonstration of stable radiatively heated flow that can be both modeled and experimentally verified. The first proof of principle experiment demonstrated laser energy addition to a supersonic flow using a 10 kW continuous wave CO_2 laser as the energy source[2]. In this experiment the laser beam was focused into a Mach 4.3 supersonic flow of N_2 seeded with trace quantities of SF_6 to absorb the laser radiation. Absorption and thermalization of the laser beam energy within the supersonic region of the flow produced a steady decrease in Mach number reaching a steady state value of Mach 3.9. This experiment demonstrated that steady, stable flow with and increase in total enthalpy could be achieved with this type of energy addition process.

Electron beams are an attractive source of energy because of their inherent efficiency (80%) when compared to laser sources. In addition the electron beam does not excite a well defined set of internal energy states, as in the laser case, but instead, energy transfer by collisions with air molecules results in excitation, ionization and dissociation. Thermalization of this energy is accomplished by further collisions with the molecules in the flow.

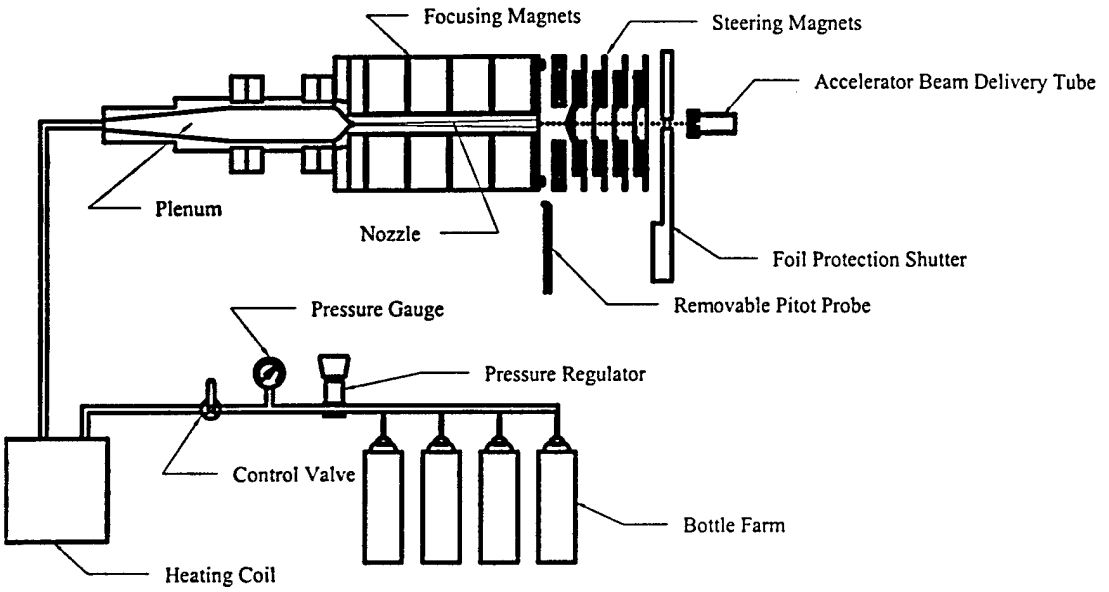

Figure 1. Diagram of the electron beam heated wind tunnel

In this paper we present the most recent results, utilizing a high power electron beam for energy addition.

The Wind Tunnel and E-beam Facility

A Mach 3.9 blow down wind tunnel was constructed for the electron beam, energy addition experiment. A schematic of this facility is shown in figure 1. The electron beam was introduced into the nozzle of the wind tunnel through the nozzle exit, and was focused into the diverging profile of the nozzle by a strong axial magnetic field that increased from exit to throat. Gas for the tunnel flow was supplied by twelve 2400 psi cylinders of breathing air, connected together by a gas manifold system which was regulated to provide a flow rate of 0.5 kg/s, and nominal plenum pressure of 1250 psi (85 atm). The nozzle flow was heated by passing it through a 17 foot long electrically heated stainless steel pipe placed between the gas manifold and the plenum. A nominal plenum temperature of 400 K was maintained for the e-beam experiment. Plenum conditions were maintained as close as possible to the above values for all tunnel runs so that results from different flow diagnostics could be compared. The nozzle was constructed of aluminum with a throat diameter of 6 mm and an exit diameter of 20 mm. The nozzle flow was exhausted into the ambient laboratory air at local atmospheric pressure (12.4 psi). The electron beam entered the nozzle through a series of beam steering magnets. A cone and apertures were placed at a distance of approximately 4 cm from the nozzle exit to stagnate the flow, thereby decreasing the pressure on the 5 mil beryllium foil used to couple the electron beam out of the accelerator. To reduce gas density in the path of the e-beam, gaps in the steering magnets allowed a radial outflow of gas ahead of the foil. Magnets were also placed along the length of the nozzle to focus the e-beam within the nozzle. Figure 2 is a photograph of the wind tunnel and e-beam facility used for this experiment and located at Sandia national laboratories in Albuquerque, NM.

Flow Diagnostics

Both probe and optical diagnostics were employed to quantify the temperature, pressure, density and velocity of the unheated and heated flow. Pressure transducers and thermocouples were used within the plenum, along the nozzle,

and at the nozzle exit in the absence of energy addition. During energy addition probes could not be used at the nozzle exit due to heating and electrical and x-ray interference by e-beam. To measure flow properties at the nozzle exit during energy addition optical techniques were employed since they were non-intrusive and did not block the e-beam, and more importantly they could be carried out remotely from the experiment be effectively shielded from x-rays.

Probe Measurements

Thermocouple and strain gauge pressure transducers were used to measure temperature and pressure in the plenum for each experimental run. In the absence of energy addition a static pressure probe was used for measurements at the nozzle exit. The slow temporal response (0.5 s) of this probe precluded its use during the short 750 μs e-beam heating duration.

Fast response (2 μs) piezo-electric pressure probes were placed along the length of the nozzle to record dynamic changes in pressure during energy addition, and also for pressure measurements in a Pitot probe. However, high energy Bremsstrahlung X-rays produced in the air and metallic surfaces of the accelerator interfered with operation of the piezo-electric pressure transducers. These x-ray induced signals were much larger than the pressure signals expected during energy addition. This interference was presumed to be due to the production of charges following ionization within the piezo-electric crystal. As a result of this, and despite the application of lead shielding at the nozzle exit, no pressure differential due to e-beam heating could be measured.

Fast measurements of total temperature could not be made during energy addition due to the slow response time of the total temperature probe assembly, and to the high levels of noise pickup by the fast differential amplifiers. In future, the use of thin film resistance gauges may prove more fruitful for lower noise temperature measurements.

Optical Measurements

Static Temperature

Laser induced thermal acoustics (LITA) was employed to measure the speed of sound and static temperature at the center of the flow[3]. A

Figure 2. Photograph of wind tunnel and accelerator

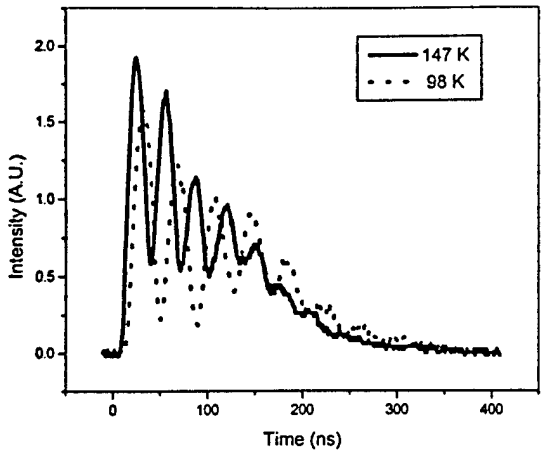

Figure 3. LITA signals used to determine temperature in the nozzle flow.

new variant of the LITA technique was developed for use in the e-beam heated flow [4]. Static temperature measurements were carried out for a variety of delays within the e-beam heating period. These measurements varied from 98 K in the unheated flow to a maximum of 147 K for heated flow. A 5% uncertainty was obtained from static measurements in the unheated flow. Figure 3 is a plot of LITA signals used to determine static temperature in each of these two cases. The frequency of oscillation of each waveform is proportional to the square root of the temperature. Calibration of frequency with temperature was carried out with a thermocouple in room air.

Velocity

A small (approximately 2 mm wide), laser induced plasma was created near the exit of the nozzle. The flow velocity was determined by measuring the displacement of the plasma over time. The initial creation of the plasma and the location of its center of mass 10 μs later were recorded on a single image with a single laser pulse. To obtain measurements at regular intervals over the energy addition period many runs at different times within the e-beam heating period were performed. The velocity measurements during the experiment had an uncertainty of 2 % or approximately 15 ms^{-1} for most runs. The velocity was determined to vary from 783 ms^{-1} to 752 ms^{-1} from the heated to unheated flow. Figure 4 is an image of the laser plasmas in the flow and their creation 10 μs earlier. The centers of the plasmas have moved 7.8 mm giving a velocity of 780 ms^{-1}. The speckles in the image are due to x-rays incident on the detector.

Density

Rayleigh scattering of an ArF laser beam was used to measure flow density across the nozzle

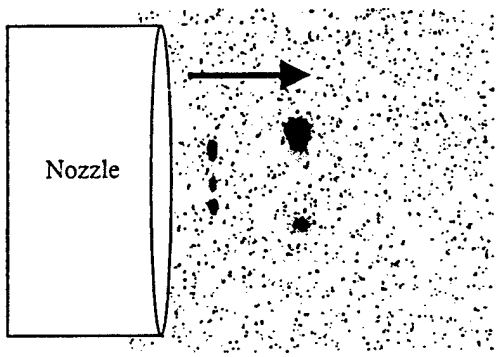

Figure 4. Plasma velocimetry image used to determine a velocity of 780 ms^{-1} in the unheated flow.

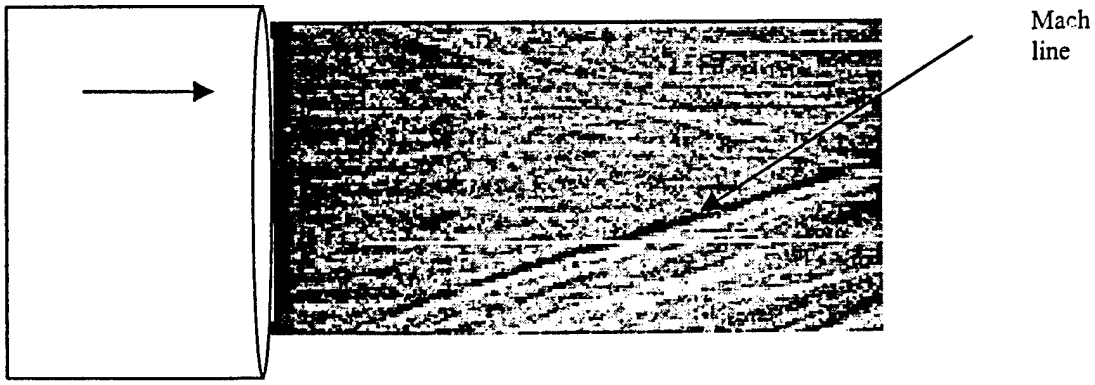

Figure 5. Shadowgraph of unheated flow at exit of nozzle

exit plane. Rayleigh scattered light is directly proportional to gas density and laser intensity. Because laser intensity varies from shot to shot, calibration of signal intensity to density for each shot was required. To calibrate Rayleigh the scattering images to absolute density, both the core flow at the nozzle exit and a small region of the surrounding ambient air were imaged. Ambient air density was calculated from temperature and pressure measurements during the tunnel run.

During energy addition, measurements of flow temperature were carried out at exactly the same time as the density measurements. As the LITA measurements use the same ArF laser, Rayleigh scattered light is also observed from this measurement. Subsequent analysis of the Rayleigh scattering images showed a significant spatial overlap between Rayleigh scattered light from the density measurements and the LITA measurements. We are presently investigating methods to subtract this deleterious interference from the images.

Shadowgraph

A series of 32 consecutive shadowgraph images of the flow were used for time resolved measurements of flow stability and Mach number over the entire energy addition period. The framing rate of these images varied from 10 to 100 kHz depending on the e-beam duration. The Mach lines produced by a small cone placed in the flow were used for these measurements. Figure 5 is a shadowgraph image of the unheated flow illustrating the position of the Mach lines used to determine Mach number. The white lines in the image are damaged pixels in the CCD chip.

Unheated flow

Prior to the energy addition experiments the nozzle flow was characterized using a combination of standard probes as well as optical measurements. Three methods were used to determine the Mach number of the unheated flow:

1) The ratio of the static pressure to plenum pressure via the isentropic flow relations, as measured by a static pressure probe at the nozzle exit and by a pressure probe in the plenum.
2) The ratio of the static temperature to plenum temperature via the adiabatic flow relations, as measured by LITA and a thermocouple in the plenum
3) The ratio of flow velocity and speed of sound, as measured by plasma velocimetry and LITA static temperature measurements. The speed of sound was calculated from the static temperature, assuming an ideal gas with a specific heat ratio of 1.4 for all temperatures.

Table 1 is a summary of Mach number measured by each of these methods and the uncertainty in each determined by the standard error from repeated measurements.

Table 1. Comparison of Mach number for the unheated flow for three different methods.

Method	Mach Number	Uncertainty
p/p_0	3.89	0.01
T/T	3.91	0.03
$U/C_s(T)$	3.87	0.02

CFD calculations give a Mach number of 3.75 which disagrees with the measured value of 3.90 in table 1. We believe this discrepancy is due to inward expansion of the constrained nozzle by the thermal expansion. An estimate of the nozzle temperature shows a change in the throat diameter sufficient to change the nozzle area ratio producing a Mach 3.9 flow. We are currently trying to quantify this effect.

Heated flow

The energy addition results can be divided into two parts corresponding to different magnet and accelerator configurations. In the low power configuration the e-beam was not tightly focused into the nozzle and most of the power was deposited into the nozzle wall. The high power data set represents a final set of measurements in which the e-beam power was increased and a stronger magnetic field focused the beam more tightly into the nozzle. During these runs

significantly more power was absorbed in the flow and less on the wall.

Low Power

Temporally resolved shadowgraph measurements of Mach number for the heated flow were made with the fast framing camera. Single shot measurements of velocity and static temperature at the nozzle exit were also used to determine Mach number for different times during the e-beam duration. These measurements were made at the center of the nozzle, and at a distance of approximately 3 mm from the nozzle exit plane. Figure 6 is a plot of Mach angle with time for both the shadowgraph and velocity temperature measurements for approximately 50 kW input into the nozzle. The Mach number decreased from Mach 3.9 to 3.2, and a steady state was reached within 400 to 500 μs. These results indicate that at least part of the e-beam energy is absorbed and collisionally relaxed on a timescale as fast as the transit time of the flow in the nozzle.

The total enthalpy of the unheated flow was calculated from measurements of plenum temperature. The total enthalpy at the nozzle exit during e-beam heating was calculated from static temperature and velocity measured at a single point at the centerline of the nozzle exit. An average change in total enthalpy of 7% was calculated from measurements made with the 50 kW runs. This corresponds to an average change in total enthalpy of 20 kJ/kg, or 10 kW of absorbed power measured on the centerline of the flow for a flow rate of 0.5 kg/s. Figure 7 is a plot of power absorbed when the flow had reached steady state at 400 and 500 μs after e-beam turn on. Each data point represents a single set of measurements for a single run of the wind tunnel and e-beam facility. The large uncertainties for each run are primarily due to uncertainties in the optical measurements of temperature (5%) and velocity (2%).

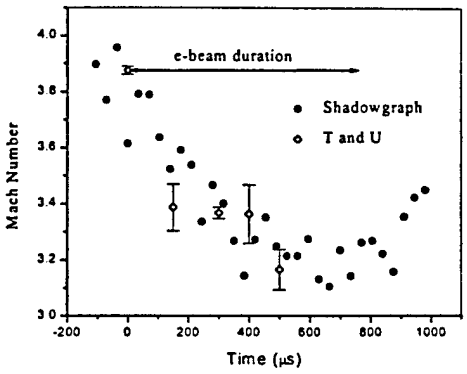

Figure 6. Comparison of Mach number calculated from shadowgraph Mach angle and average values calculated from velocity and temperature measured at nozzle exit.

The measurements of total power deposited in the flow were compared with numerical simulations performed with the CYLTRAN module of the Integrated Tiger Series (ITS) code [5]. For the low power case the code predicts approximately 5 kW is deposited into the flow and 46 kW into the nozzle. This is consistent with the uncertainty in our calculations for 10 kW of absorbed power. It should also be noted that due to the Gaussian like electron beam profile, measurements of absorbed power will be higher on the centerline than the average power absorbed in the flow.

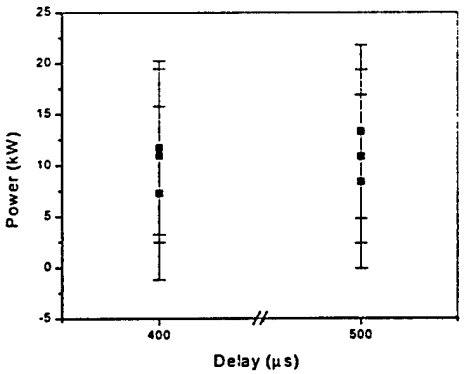

Figure 7. Absorbed power calculated from velocity temperature and mass flow rate at 400 and 500 μs after the e-beam is turned on. All measurements were made on the centerline of the flow.

High power

Due to limited experimental time only shadowgraph imaging was used for nozzle exit diagnostics in the high power experiments. Two shadowgraph images taken for this increased power level are shown in figure 8. In this final run the e-beam was focused deeper into the nozzle than on all previous runs. The flow was heated for 750 μs and each image is a 3.5 μs exposure. The Mach angle is observed to change across the flow, due to the finite size and the Gaussian like profile of the non-centered e-beam.

Figure 9 is a plot of Mach number calculated from each of the 32 shadowgraph images. For this power level the Mach number drops from 3.9 to an approximate minimum of 2.3. An upper limit estimate of change in total enthalpy and power absorbed can be determined from the Mach number measurements, under the assumption that the velocity does not change significantly during energy addition (For the low power case this was a good approximation since the velocity changes by approximately 2%). The decrease in Mach number to 2.3 corresponds to a temperature of 262 K for a velocity of 750 ms^{-1}. A change in total enthalpy of approximately 150 kJ/kg and 40 kW of absorbed power was calculated assuming that the e-beam power was localized and is heating approximately only half the flow.

CYLTRAN simulations of power deposition for this high power case predict 57 kW of power absorbed into the flow, and 96 kW into the wall. As in the low power case this compares well with that estimated from measurements. However, in this case the e-beam was not centered in the nozzle and the measured power should be lower than the peak power, as we have found.

Conclusions

The power absorbed by the flow was determined

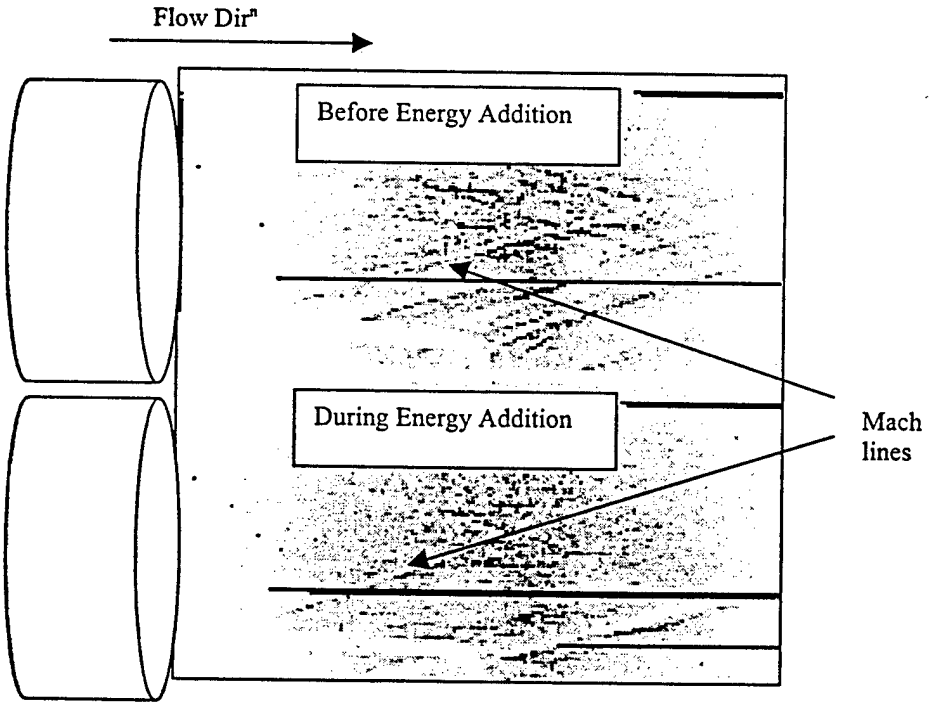

Figure 8. *Shadowgraph image of e-beam heated flow. The electron beam heated the flow for 750 μs; approximately 90 kW enters the nozzle.*

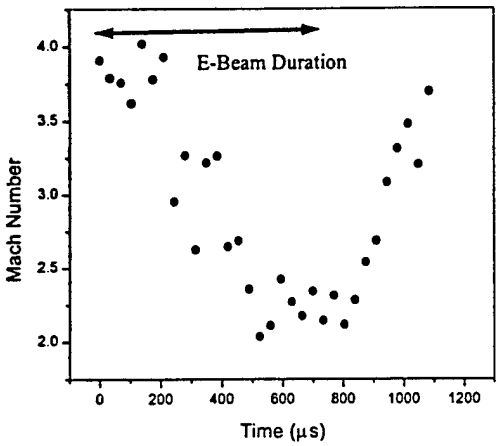

Figure 9. Change in Mach number calculated from 32 shadowgraph images for 90 kW

for the low power, energy addition experiments. However, as the change in total enthalpy was small compared to total enthalpy of the unheated flow, a large uncertainty in both the total enthalpy and power absorbed in the flow was obtained. The amount of power deposited into the walls of the nozzle could not be measured in this experiment, and thus a total power/energy partition within this experimental system could not be determined. If, in the future, all the energy can be coupled into the flow by strong focusing, optical measurements of absorbed power as used in this experiment could, in principle, be used to determine the degree to which thermalization has occurred. The fast thermalization time measured on the order of approximately 500 μs indicates that in a larger scale facility where higher pressures will be used thermalization should be more rapid.

Limited experimental time did not allow an extensive spectroscopic search for impurities in the flow. However, some spectrally resolved measurements of e-beam induced fluorescence in the air were recorded and this emission was confined to the 400 - 250 nm region. The strongest emission, at 390 nm, was identified as N_2^+. This data was primarily taken to investigate whether spectral interference would occur at the Rayleigh scattering wavelength of 193 nm. Electronically excited NO also emits in this spectral region and the absence of this emission indicates that no significant quantities of NO in this excited state exist in the flow.

The optical measurements were particularly successful because they could be carried out remotely from the e-beam, and thus could be effectively shielded against the x-rays. Shielding from x-rays will be important for implementation of any future diagnostics, whether optical or probe, in an e-beam heated tunnel.

As in the laser energy addition experiment, a steady transition from the unheated flow to a steady heated flow was observed. This was temporally resolved by the shadowgraph imaging and steady state was achieved after approximately 500 μs. The electron beam did not uniformly heat the flow, and this observed as a non-uniform Mach angle change across the flow. Future work will address e-beam shaping or use of multiple e-beams to produce a more uniform heating profile.

In summary, stable energy addition by e-beam heating has been successfully demonstrated and the changes in Mach number (0.7), total enthalpy (20 kJ/kg) and power (10 kW) absorbed were measured on the center line of the nozzle flow for 50 kW e-beam power. For the final runs an increased e-beam power (90 kW) and tighter focusing produced a large change in Mach number, from 3.9 down to a minimum of 2.3. With this change in Mach number an estimated power of 40 kW was absorbed in a localized region of the flow. In future, experiments that address flow quality, thermalization, and long term flow stability will give a more complete picture of e-beam heating of a supersonic flow.

Acknowledgements

The authors would like to acknowledge the Air Force Research Laboratory, MSE Technical Applications Inc. and Princeton University for support of this research. We would also like to thank the Air Force Research Laboratory for the loan of the ultra fast framing camera.

References

1. R. Miles, G. Brown, W. Lempert, R. Yetter, G.J. Williams, S.M. Bogdonoff, D. Natelson and J.R. Guest, AIAA Journal, **33**, 1463, (1995)

2. A. Morgan, P. Barker, R. Anderson, G. Brown, and R. Miles, AIAA-98-2498, 20th Advanced Measurement and Ground Testing Technology Conference, Albuquerque, NM, June (1998)

3. E.B. Cummings, Opt. Lett., **19**, 1361, (1994)

4. P. Barker, J. Grinstead and R. Miles, Submitted Opt. Lett., Dec. (1997)

5. J. A. Halbieb, R. P. Kensek and G. D.Valdez, IEEE Transactions on Nuclear Science, **39**, 1025, (1992)

AIAA 99-0822
Performance Characterization of a Radiatively Driven Hypersonic Wind Tunnel

R. W. Anderson, G. L. Brown, and R.B. Miles
Mechanical and Aerospace Engineering
Princeton University
Princeton, NJ

37th AIAA Aerospace Sciences Meeting and Exhibit
January 11-14, 1999 / Reno, NV

Performance Characterization of a Radiatively Driven Hypersonic Wind Tunnel

*R.W. Anderson**, *G.L. Brown*†, *R.B. Miles*†
Department of Mechanical and Aerospace Engineering
Princeton University
Princeton, New Jersey 08544 U.S.A.

Abstract

The radiatively driven wind tunnel concept is analyzed with the aim of identifying performance capabilities and limits. These fundamental limitations result firstly from the thermodynamics of the heat addition to a supersonic flow and secondly from trade-offs in upstream stagnation temperature and pressure and radiant energy addition. For a given stagnation temperature and pressure, the analysis firstly identifies an optimized thermodynamic path in the Mollier diagram to achieve the highest possible Mach number for given atmospheric conditions in the test section. These idealized paths enable performance envelopes to be obtained and the sensitivity to changes in stagnation conditions to be seen. These envelopes are shown on a Mach number, altitude plot and are compared with conventional facilities. Design trade offs are considered within the constraints identified. The inverse problem of designing an area distribution to achieve a thermodynamic path close to the ideal is discussed. In the particular case of electron beam radiation a design is achieved which is close to the ideal.

Introduction

The radiatively driven hypersonic wind tunnel was conceived in an effort to overcome some of the limitations of conventional, isentropic expansion, hypersonic testing facilities. In this concept energy is added to the supersonic flow downstream of a nozzle throat via radiative sources such as lasers, electron beams, or microwaves. This provides several critical advantages over many of the existing hypersonic testing facilities currently available, which include isentropic blowdown facilities, combustion and arc heated tunnels, and impulse tunnels. A detailed introduction of the concept can be found in [1] and progress in modelling and understanding the fluid mechanics and energy addition processes as well as the results of recent proof of principle experiments can be found in [2], [4], [5], [7]. In this study the radiatively driven hypersonic wind tunnel (RDHWT) concept is further analyzed in an effort to examine performance capabilites and limitations as a function of high pressure and energy addition technologies and to compare these with conventional facility limitations.

The Mollier diagram in Figure 1 illustrates the concept, and illuminates its primary advantage over isentropic blowdown facilities. To reach a set of test conditions in the atmosphere, for example point 5, an isentropic facility must begin with a very high stagnation enthalpy which corresponds to a stagnation temperature in excess of 4,000 K. By starting at point 1, however, at lower entropy and total enthalpy than the desired test conditions, heat can be added downstream of the throat to generate entropy and increase the stagnation enthalpy until the desired test entropy is reached at point 4. Then the flow can be expanded isentropically further until the desired conditions are reached at 5. By utilizing this alternative path, the maximum temperature of the flow can be dramatically lowered, extending the achievable Mach number range that is typically imposed by high temperature chemistry and throat survivability limitations. For example, to achieve characteristic flight conditions at Mach 10 requires a stagnation temperature of approximately 5,200 K. In the case of the RDHWT, a simple calculation based on an assumption that all the radiative heat is added at one "effective" temperature gives:

$$\frac{\dot{Q}}{\dot{m}} = h_{o,f} - h_{o,i} = T_{eff}(s_f - s_i) \qquad (1)$$

where $h_{o,i}$ and s_i are the plenum enthalpy and entropy, $h_{o,f}$ and s_f are the desired flight conditions, and T_{eff} is a characteristic static temperature at

* Graduate Student, Mechanical & Aerospace Engineering, AIAA

†Professor, Mechanical & Aerospace Engineering, Senior Member, AIAA

which heat is added. For the same nominal flight conditions which require a stagnation temperature of 5,200 K, an effective temperature for radiative heat addition is found to be approximately 1000 K [4].

Numerical Models

The fluid mechanical issues involved in the design of such a facility are numerous. Energy absorption, thermalization, flow stability and uniformity, wall heat transfer, and throat survivability are all important aspects of a detailed design. To examine these issues a detailed model employing the unsteady Navier Stokes equations has been developed. The flow solver is based on the Flo103 code developed by Jameson and Martinelli [9], but it has been extended very considerably in order to include the complexities of the RDHWT problem. At the stagnation pressures and temperatures required for operation of the RDHWT, real gas effects are very important, and a tabulated equation of state developed by NIST, is therefore used in conjunction with the solver. The equation set has been extended to include axisymmetric nozzle geometries, as well as a heat flux term which is coupled in with adjunct solvers for laser or electron beam radiation. In the laser case the adjunct solver is a raytracing procedure developed by R. More from LLNL, which is fully coupled in time with the flow solver[16]. In the electron beam case, a Monte Carlo simulation is used iteratively with the flow solver to arrive at a steady state solution[6]. Detailed discussion of the development and validation of the Navier Stokes solver can be found in [2].

To address more fundamental thermodynamic issues in a more efficient way a quasi one-dimensional flow solver has also been developed. The governing equations are employed in the following conservative form:

$$\frac{\partial \mathrm{w}}{\partial t} + \frac{\partial \mathrm{f}}{\partial x} = \mathrm{W} \qquad (2)$$

where the conserved variable, flux, and source vectors are:

$$\mathrm{w} = \begin{pmatrix} \rho \\ \rho u \\ \rho E \end{pmatrix} \mathrm{f} = \begin{pmatrix} \rho u \\ \rho u^2 + p \\ \rho u H \end{pmatrix} \mathrm{W} = \begin{pmatrix} 0 \\ 0 \\ \dot{q} \end{pmatrix} \qquad (3)$$

These equations are semidiscretized in space using a 2nd order accurate, cell center, finite volume method. The required artificial dissipation scheme utilized is a SLIP scheme using Van Leer's limiter[14]. The resulting set of ordinary differential equations:

$$\frac{d(wV)}{dt} = R(w) \qquad (4)$$

where V is the cell volume, and $R(w)$ is the residual, is integrated forward in time using a 4th order Runge-Kutta marching scheme. For steady state calculations local time stepping is used to accelerate convergence. The methodology parallels that of Flo103, simplified to one dimension and without the added complexity of viscous considerations.

Performance Envelopes

In order to compare the potential of the RDHWT concept with the capabilities of conventional facilities, some fundamental performance limits must be identified. Smith and Laster [3] have provided a summary of performance limitations for conventional facilities in terms of achievable Mach number at a given altitude, and their summary is reproduced in Figure 2. The limitiations with respect to the identified manned airbreathing flight corridor are evident. There are further important limitations of very short run times for impulse tunnels and contamination of the air due to dissociation and non-equilibrium chemistry.

An important constraint on the performance of the RDHWT is the high pressure front end driver, and one of the aims of the present study was to examine possible trade-offs between temperature and pressure of the front end driver. For this purpose we have chosen a range of stagnation pressures from 10,000 atm to 14,000 atm and stagnation temperatures from 800 to 1,400 K. These conditions are consistent with anticipated stagnation volumes required for run times in excess of one second.

With these nominal conditions as a constraint, there is a limitation on the achievable performance (test conditions) which is imposed by how much heat can be added to the flow and at what temperature. It is evident that for test conditions at the lowest altitudes (small $s_f - s_i$), to achieve a given Mach number the heat must be added at the highest possible temperature while at the same time not choking the flow. In this sense an upper bound on the capability (lowest altitude for a given M) is to add heat at a constant Mach number near Mach 1, and we have chosen Mach 2 to provide some margin with respect to thermal choking.

Lines of constant Mach number, while adding heat, are uniquely defined as can be seen by examining the differential 1-d gasdynamic energy equation, i.e.:

$$d(h + \frac{1}{2}u^2) = dq$$

which for constant Mach number becomes

$$dh + M^2 a da = T ds$$

and since the speed of sound a is a function of h and s, a trajectory dh/ds is uniquely defined at any state. If we continued to add heat at constant Mach number, eventually static temperatures in the flow would

be reached at which significant contamination would occur. For this study we choose a nominal bound on the static temperature to be 2,500 K. In seeking limitations on performance this identifies a second leg in the optimal thermodynamic path, which is then heat addition on an isotherm out to the final entropy corresponding to a specific altitude. The final leg of the path is an isentropic expansion to the desired thermodynamic state of the atmosphere. This process uniquely defines a final Mach number for a given set of stagnation conditions, since along this path the total heat added (found by integrating Tds) is the change in total enthalpy, i.e.:

$$\int dq = h_{o,f} - h_{o,i}$$

and

$$h_{o,f} = h + \frac{1}{2}M^2a^2$$

where h and a are the desired atmospheric conditions and M is therefore the maximum achievable M at these conditions. This process allows a performance envelope to be calculated for given stagnation conditions; it provides a margin against thermal choking and allows tradeoffs to be explored.

Another fluid mechanical consideration is that of the pressure gradient dp/dx. Adverse pressure gradients may lead to separation of boundary layers, and so in general are to be avoided. A comparison between the constant Mach number line and the isobar through point 2, as in Figure 3, illustrates that in the real gas regime near point 2, a constant Mach number line is approximately a constant pressure flow. As the ideal gas regime is reached, constant Mach number results in decreasing pressure and increasing favorable pressure gradients. A less conservative choice for the trajectory of this heat addition would be constant pressure, but this would lead in due course to thermal choking of the flow. Choosing constant Mach number has the benefit of avoiding both choking and adverse pressure gradients.

In order to identify tradeoffs associated with possible upstream stagnation conditions, and to investigate the Mach number which can be achieved based on these conditions, several of these paths were integrated using the high pressure equation of state database developed by NIST. Starting from 10,000 atm, for example, three families of trajectories were calculated from stagnation temperatures of 800, 1000, and 1400 K. The constant Mach number heating paths are shown on the Mollier diagram of Figure 4. If heat is then added at 2,500 K, a relationship between the highest Mach number which can be achieved at a given flight altitude condition can be calculated by considering the total heat added and the final isentropic expansion to the atmospheric state at various altitudes. The resulting performance limitation envelopes are summarized in Figure 5. Similar calculations were performed from 14,000 atm and are summarized in Figures 6 and 7.

An interesting tradeoff in the design of a front end, in terms of material limitations, exists in determining whether it is more advantageous to design for higher pressures or higher temperatures. Figures 5 and 7 examine this sensitivity in terms of varying the stagnation temperature. To see the sensitivity to pressure variations at a fixed stagnation temperature, the two performance envelopes for 10,000 atm and 14,000 atm at a stagnation temperature of 1,000 K are compared in Figure 8. In this range both parameters have comparable effects on performance.

Another tradeoff issue is the choice of the maximum static temperature. As this temperature is increased, formation of NO_x becomes a concern. However, this also allows us to achieve higher Mach number, especially at higher altitude flight conditions. Three calculations of performance envelopes were done for the stagnation conditions of 14,000 atm and 1,000 K for maximum static temperatures of 2500, 3000, and 3500 K. The resulting performance envelopes are shown in Figure 9. For dynamic pressures in the neighborhood of 2000 psf, there is little to no advantage, as most or all of the heat is added at constant Mach number, and the maximum static temperature does not play a significant role in the heating process. At higher altitudes, however, increased Mach numbers are achievable because an increasingly significant portion of $\int dq$ is calculated as $T_{max}\int ds$, so that there becomes a clear advantage in raising T_{max}.

Yet another constraint in optimizing Mach number might be to consider adding heat at Mach numbers lower than 2. This was not pursued since the Mach number becomes increasingly sensitive to area distribution as the sonic limit is approached, and some margin must be provided to avoid choking. The concern is compounded by the increased sensitivity of Mach number to area at high pressure, where the fluid is very much less compressible than an ideal gas at the same temperature.

One Dimensional Electron Beam Model

Now that some optimal thermodynamic paths have been identified, it remains to be determined how closely these paths can be followed using a candidate source for radiative heat addition. For this purpose we have investigated in this paper the electron beam as a radiative source. With this in mind a one dimensional model of electron beam absorption has been developed in conjunction with R.J. Lipinski at Sandia National Laboratories. This model was developed by applying a 2-D Monte Carlo electron beam simulation to the specific case of a uniform

electron beam confined by a strong axial magnetic field. Four initial beam voltages were considered at 1,2,5, and 10 MV. A set of power deposition curves as a function of axial distance were generated, and these curves were used to generate an equation for volumetric heating as a function of areal mass density penetrated by the beam. An empirical formula which provided a good fit to the four cases was obtained by Lipinski, and is as follows:

$$q = \rho j \left(2.2 + \frac{0.8}{E_0}\right) \exp\left(-\frac{(w - w_0)^2}{w_1^2}\right) + 1.5 \exp\left(-\frac{w^2}{w_1^2}\right) \quad (5)$$

where

$$w = \int \rho \, dx$$

$$w_0 = .2E_0^{1.22}$$

$$w_1 = .16E_0$$

and where E_0 is the initial electron voltage in MV. Using this formulation, local power deposition can be calculated by keeping track of w integrated along the beam path, along with the local current density and air density. Figure 10 illustrates these deposition profiles in a constant density medium.

This formulation has allowed us to employ the quasi one dimensional solver utilizing these formulas for the heat flux term to obtain solutions for the coupled system of a flow with electron beam energy addition.

Example Electron Beam Facility Design - The Inverse Problem

It remains to be determined whether these optimal thermodynamic paths can be achieved within the additional constraints of a realistic supersonic nozzle area distribution and the physics of the electron beam absorption. This is an inverse problem in that an area distribution is sought such that the energy deposition is as close to the ideal as possible to achieve maximum performance and the final state is air at the desired Mach number and altitudes. To investigate this question an example facility has been designed using the quasi one dimensional flow solver and electron beam model.

The stagnation conditions chosen for this example are 10,000 atm and 1,000 K. The test conditions we aimed for (based on interest in a particular application) are atmospheric conditions with a dynamic pressure of approximately 2000 psf and a Mach number of approximately 10. We note that the optimal trajectory in Figure 4 gives a maximum Mach number of approximately 10.5 with these stagnation conditions. A scale for the facility must also be chosen, which will be a tradeoff between power requirements and test section area. For this example we choose a nominal test section diameter of 0.5 m, which at 2000 psf and Mach 10 requires a beam power of approximately 40 MW. A summary of some of the key parameters for this design can be found in Figure 11.

Iteration of the design to achieve atmospheric flight conditions was achieved through a semi-automated procedure. An initial conical area distribution was chosen for simplicity, and the length of the nozzle was chosen such that a 1 MeV beam would deposit the majority of its energy near the throat at approximately Mach 2. This resulted in a final state which was not at atmospheric conditions. An optimization procedure was then utilized to tailor the area distribution further such that the final state was moved closer to atmospheric conditions.

The optimization procedure is as follows. The design variables are a set of control points, r_k, which are radii used to generate a nozzle profile by spline interpolation. The objective function is a metric for the deviation in temperature and pressure at the exit from the desired atmospheric conditions:

$$I(r_k) = \left(\frac{p - p_0}{p_0}\right)^2 + \left(\frac{T - T_0}{T_0}\right)^2$$

which is to be minimized. A vector of sensitivies, dI/dr_k is generated by finite differences, requiring one flow solution for each design variable. For these one dimensional solutions using an algebraic model for the radiation source, this is not unduly expensive. Finally a step is taken in the direction of steepest descent, $r_{k,n+1} = r_{k,n} + \alpha dI/dr_{k,n}$. In this way the final state can be driven into the atmosphere by adjusting the area distribution, which in turn adjusts the density profile and consequently the energy absorption profile.

The thermodynamic path resulting from this design procedure can be seen in Figure 12. The constraints of the energy absorption physics prevent us from achieving the optimal thermodynamic path, but it is surprisingly close. If the electron beam is brought in from the test section, there will always be some energy absorption in the region that, optimally, would be isentropic. In practice the electron beam can be delivered from further upstream to obtain a more highly optimized design. The final Mach number achieved with this example design is approximately 9.5, whereas the optimal Mach number is approximately 10.5.

These are early results and further optimization of the design may be be achieved by considering two or more electron beams, of varying energies also delivered well upstream of the test section. This would provide more control over the shape of the deposition profile, which, as is clear from the thermodynamic paths discussed, ultimately determines the

performance of the system.

Concluding Remarks

A way of identifying the ideal performance envelopes for the RDHWT concept in terms of upstream stagnation conditions has been found. This has enabled comparisons with conventional hypersonic facility limitations and preliminary design trade off studies to be made. Potentially realizable conditions have been considered and the resulting performance capabilities along with long run times and the anticipated low contamination of the air give the concept critical advantages. A specific tunnel design based on the absorption of 1 MeV electron beam radiation has been found by a steepest descent optimization technique and the resulting thermodynamic path is qualitatively close to the ideal one. More highly optimized designs in this and other higher performance cases could be expected if several beam energies are used and the beam is introduced well upstream of the test section. It is anticipated that simliar analyses will now be considered for other potential radiative energy sources.

References

[1] R. Miles, G.L. Brown, W.R. Lempert, R.A. Yetter, G.J. Williams and S.M. Bogdonoff, "Radiatively Driven Hypersonic Wind Tunnel", AIAA Journal, 33, No. 8, August, 1995.

[2] G.L Brown, A.P. Ratta, R.W. Anderson, L. Martinelli "Fluid Mechanics in a Radiatively Driven Wind Tunnel - Prediction and Preliminary Experiment", AIAA Paper 96-2199, June, 1996.

[3] V.K. Smith, M.L. Laster, "Hypersonic T&E Challenges for the 21st Century", International Test and Evaluations Association Annual Symposium, Albuquerque, NM, October, 1992.

[4] G.L. Brown, R.W. Anderson, A.E. Morgan, P.F. Barker, R.J. Lipinski, and R.B. Miles, "The Fluid Mechanics of a Radiatiatively Driven Wind Tunnel: Predictions and Experiment", AIAA Paper 98-2747, June 1998.

[5] R.B. Miles, G.L. Brown, "Energy Addition Mechanisms in a Radiatively Driven Wind Tunnel - Predictions and Experiments", AIAA Paper 98-2748, June, 1998.

[6] R.J. Lipinski and R.P. Kensek, "Conceptual Desing for an Electron-Beam Heated Hypersonic Wind Tunnel," Sandia Report SAND97-1595, Sandia National Laboratories, Albuquerque, NM, July 1997.

[7] P. Barker, J. Grinstead, A. Morgan, R. Anderson, P.Howard, G. Brown, R. Miles, R Lipinski, K. Reed, G. Pena, L. Schneider. "Radiatively Driven Wind Tunnel Experiment with a 30 kW Electron Beam", AIAA-99-0688, January, 1999.

[8] L. Martinelli, "Calculations of Viscous Flows with a Multigrid Method", Princeton University, MAE Dept., Ph.D. Thesis 1754T, June, 1987.

[9] L. Martinelli and A. Jameson, "Validation of a Multigrid Method for Reynolds Averaged Equations", Princeton University, Princeton, NJ, AIAA Paper 88-0414, January, 1988.

[10] L. Martinelli, A. Jameson and F. Grasso, "A Multigrid Method for the Navier-Stokes Equations", Princeton University, Princeton, NJ AIAA Paper 86-0208, January, 1986

[11] A. Jameson, "Numerical Solution of the Euler Equation for Compressible Inviscid Fluids", Department of Mechanical and Aerospace Engineering, Princeton University, Princeton, NJ, Report No. 1643.

[12] A. Jameson, W. Schmidt, and E. Turkel, "Numerical Simulation of the Euler Equation by Finite Volume Methods using Runge-Kutta Time-Stepping Schemes", AIAA Paper 81-1259, AIAA 5th Computational Fluid Dynamics Conference, 1981.

[13] A. Jameson, "Analysis and Design of Numerical Schemes for Gas Dynamics 2. Artificial Diffusion and Discrete Shock Structure", accepted for publication in International Journal of Computational Fluid Dynamics, August, 1994

[14] A. Jameson, "Analysis and Design of Numerical Schemes for Gas Dynamics 1. Artificial Diffusion, Upwind Biasing, Limiters and their Effect on Accuracy, Multigrid Convergence", International Journal of Computational Fluid Dynamics, 4, p. 171, 1995.

[15] R.J. Lipisnki, "Private Communication", Sandia National Laboratories, Albuquerque, NM, July, 1998.

[16] R. More, "Private Communication", Lawrence Livermore National Laboratory, Livermore, CA, 1995.

[17] S. Macheret, C. Meinrenken, G. Williams, W. Lempert, W. Gillespie, W. Lempert, R. Miles, "Radiative Energy Addition to High Pressure Supersonic Air", AIAA Paper 96-1984, July 1996.

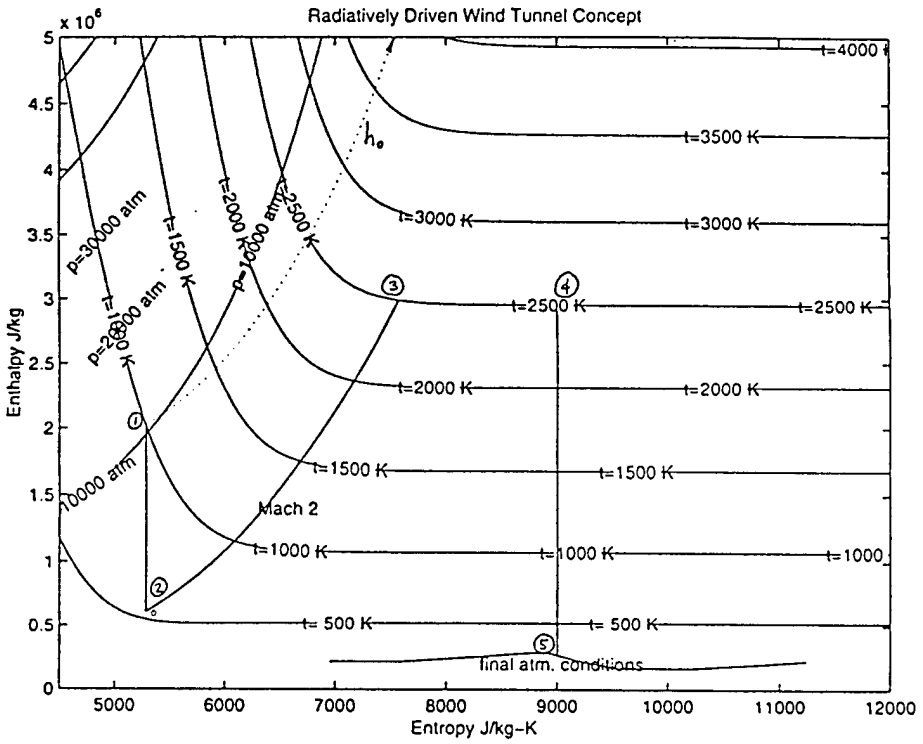

Figure 1.

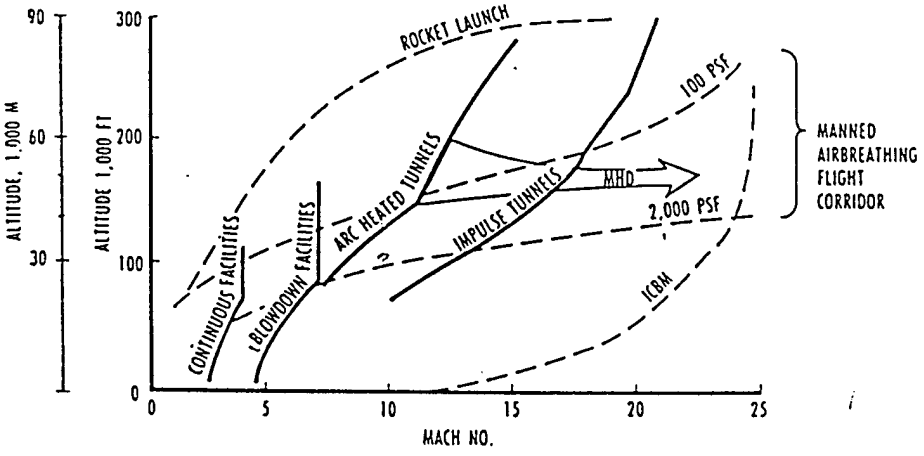

Figure 2. [3]

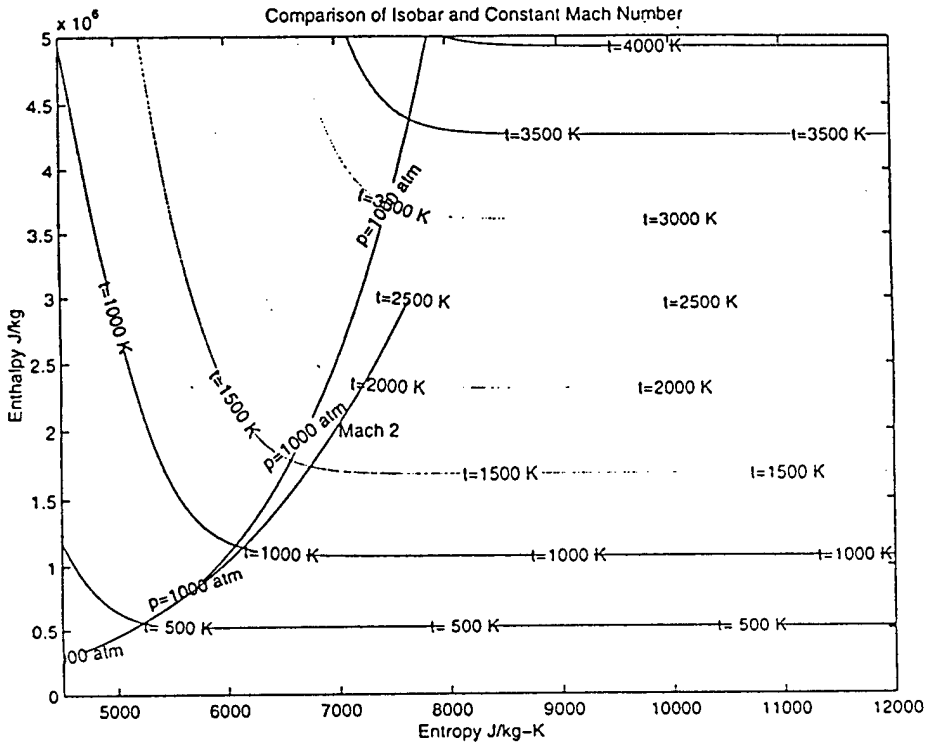

Figure 3.

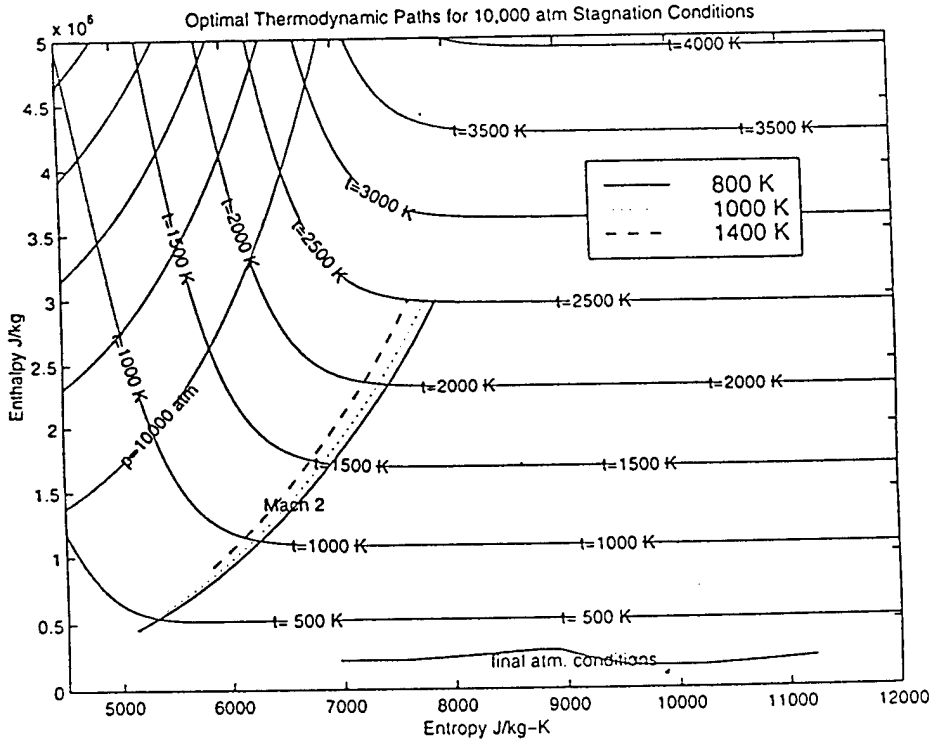

Figure 4.

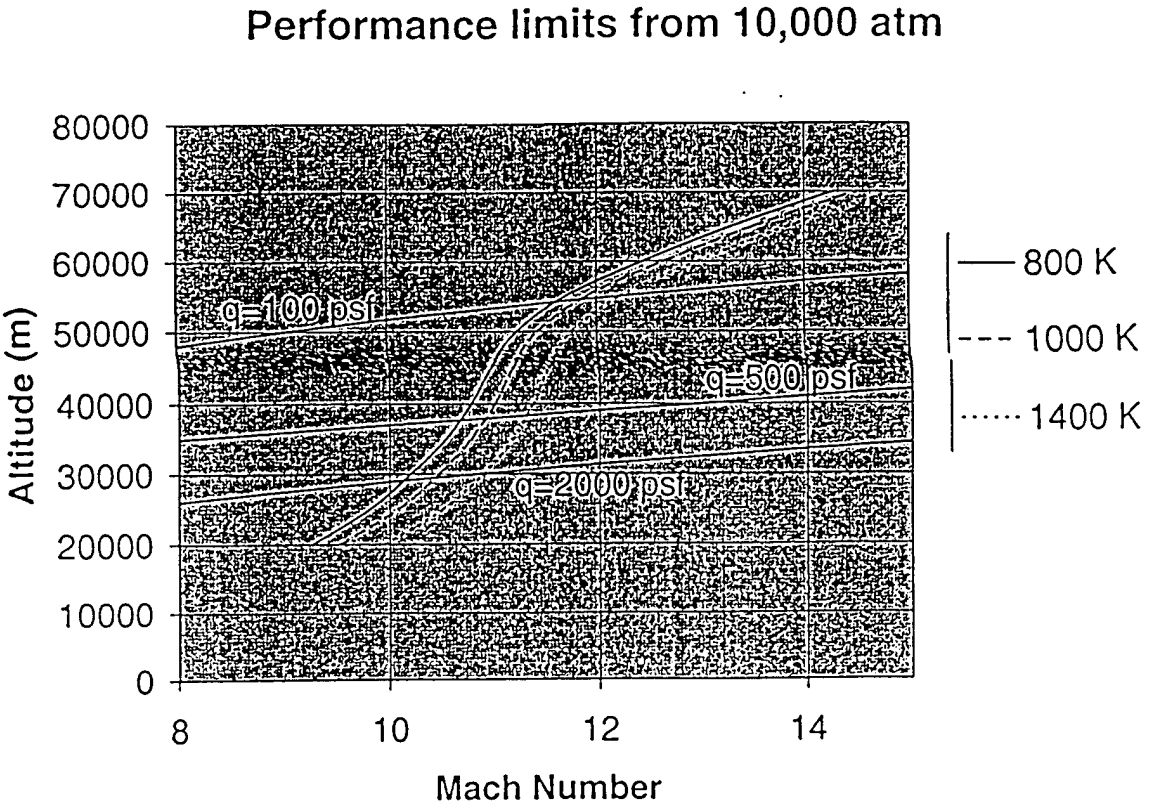

Figure 5.

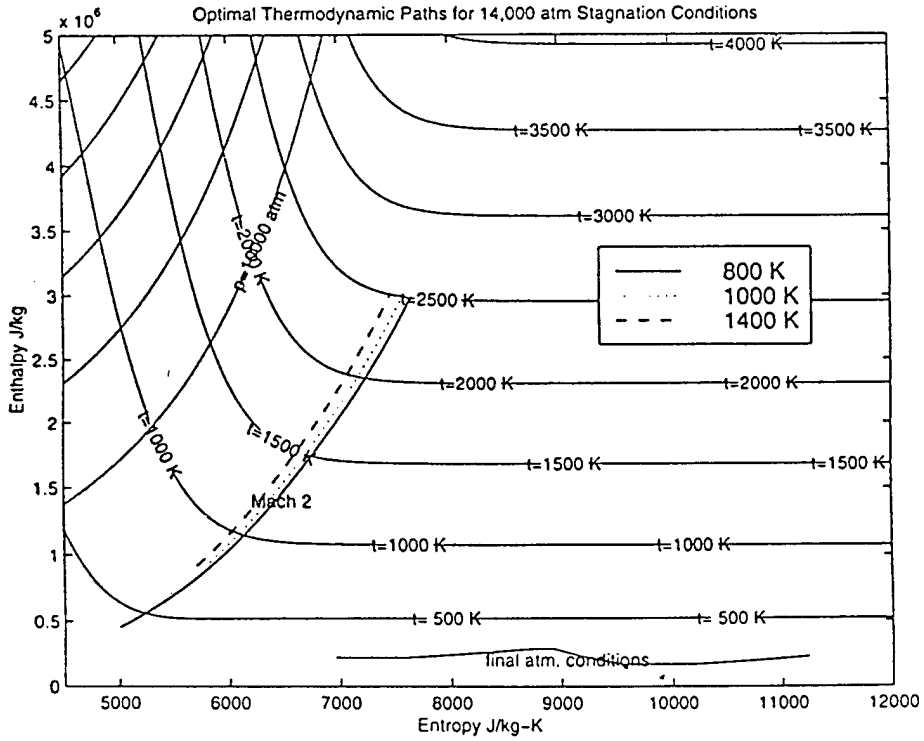

Figure 6.

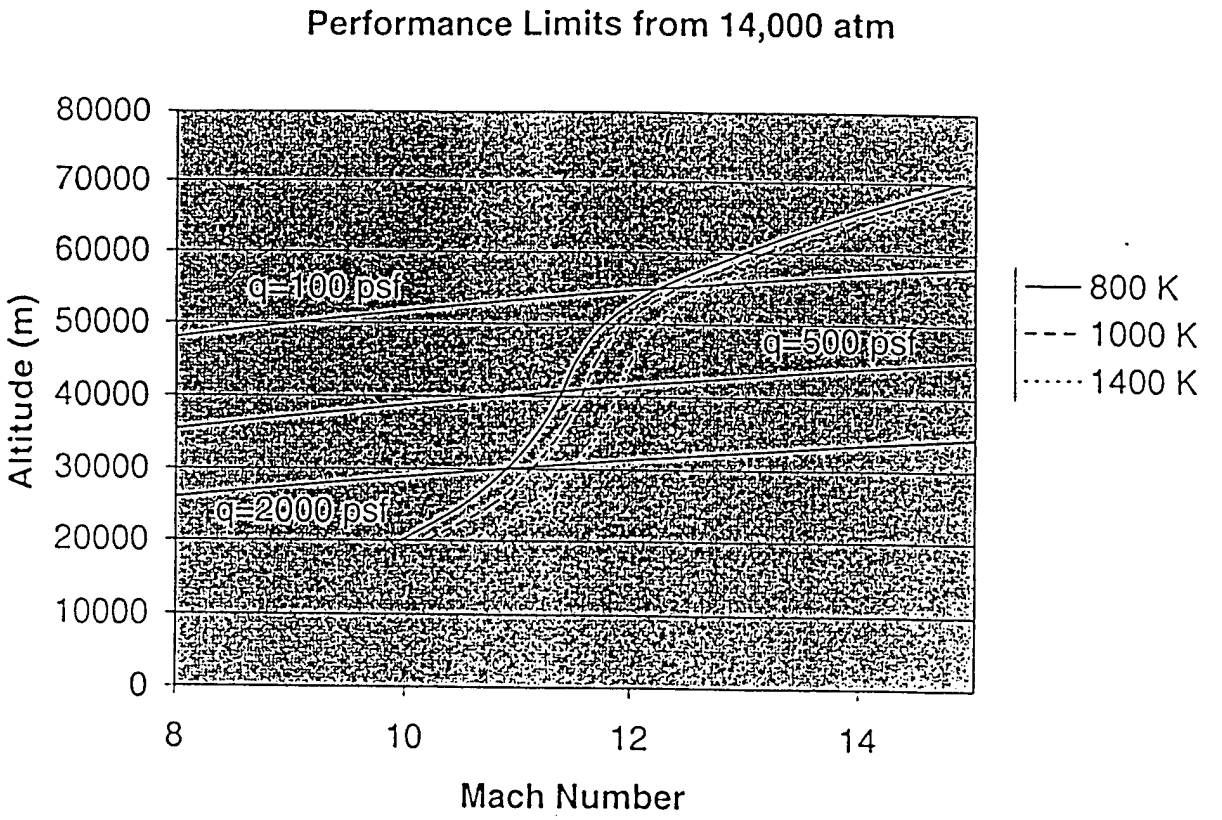

Figure 7.

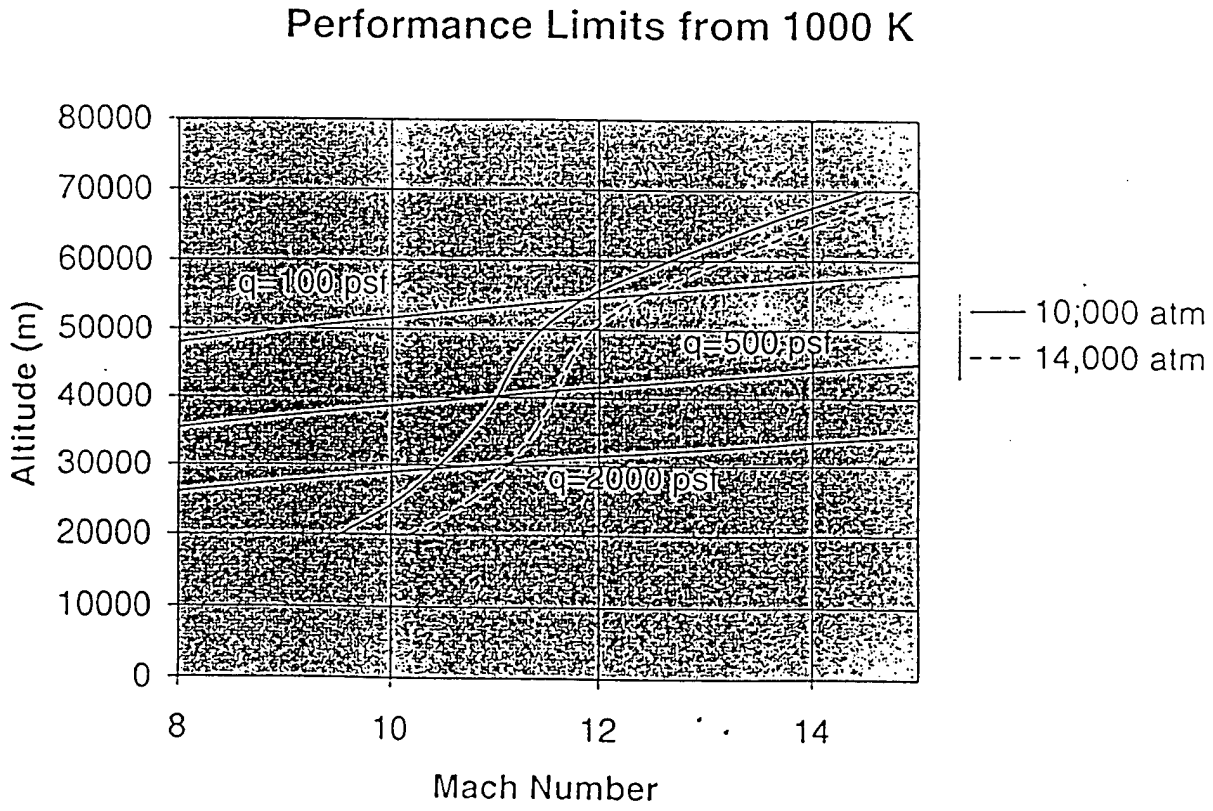

Figure 8.

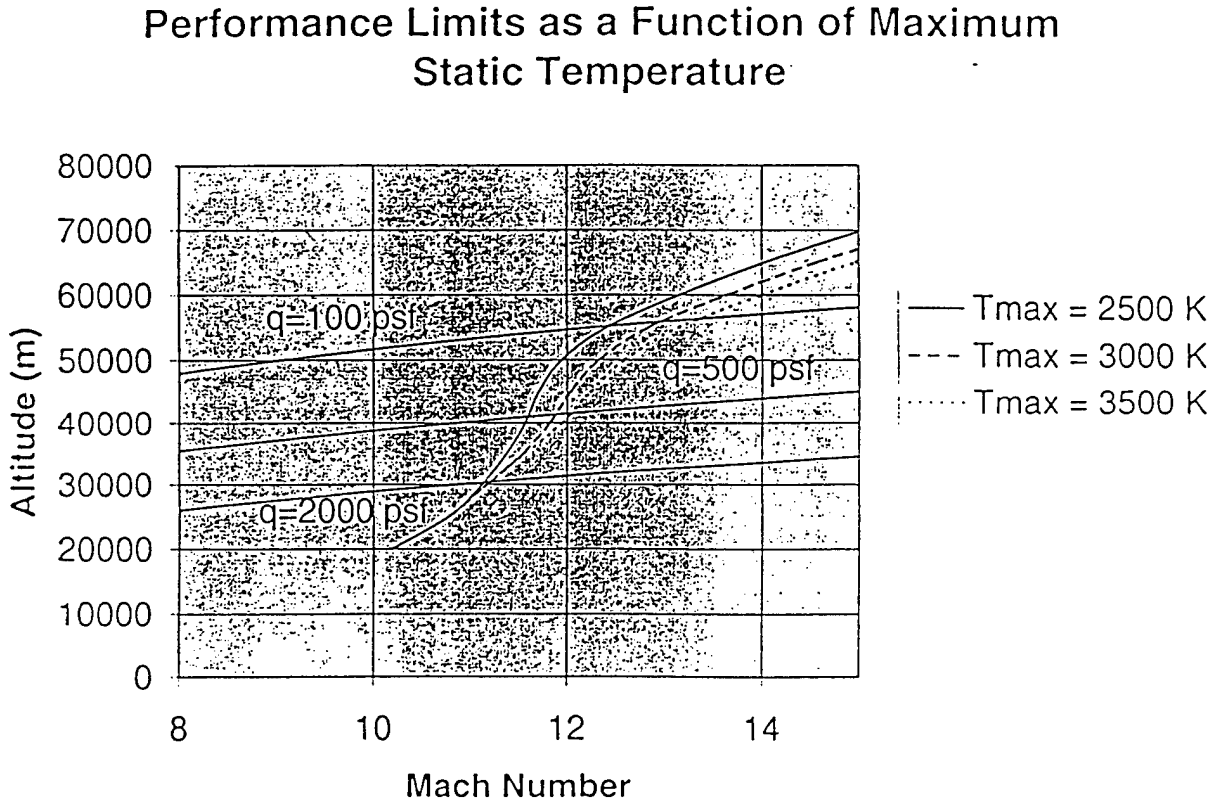

Figure 9.

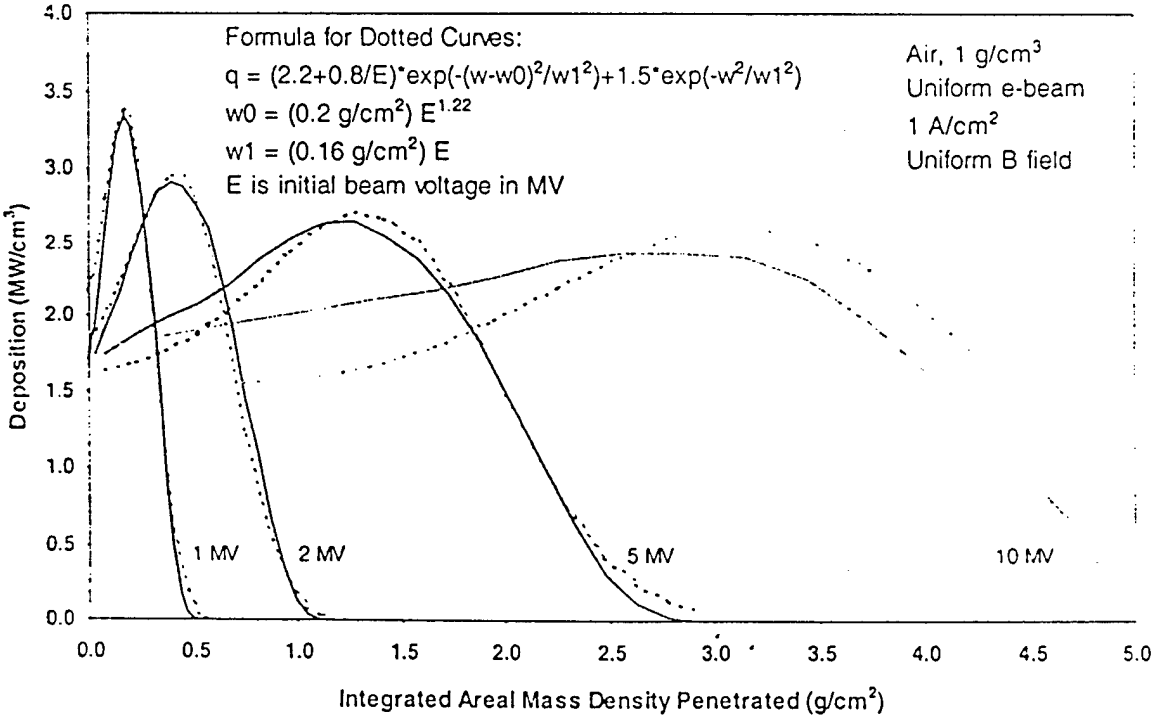

Figure 10.

10 katm, 1000 K Electron Beam Facility Design

Test Conditions:

flight conditions @ 28,900 m
p = .0166 atm
T = 239 K
M = 9.5
q = 2235 psf

Plenum conditions:

h_0 = 1.9 MJ/kg
p_0 = 10,000 atm
T_0 = 1000 K

Geometry:

d* = 2.25 mm
d_{test} = 52.2 cm
length = 1.2 m

Energy Addition:

1 MeV Electron beam
dQ/dt = 38 MW
(dQ/dt)/(dm/dt*u^2/2*A) = 2.53

Figure 11.

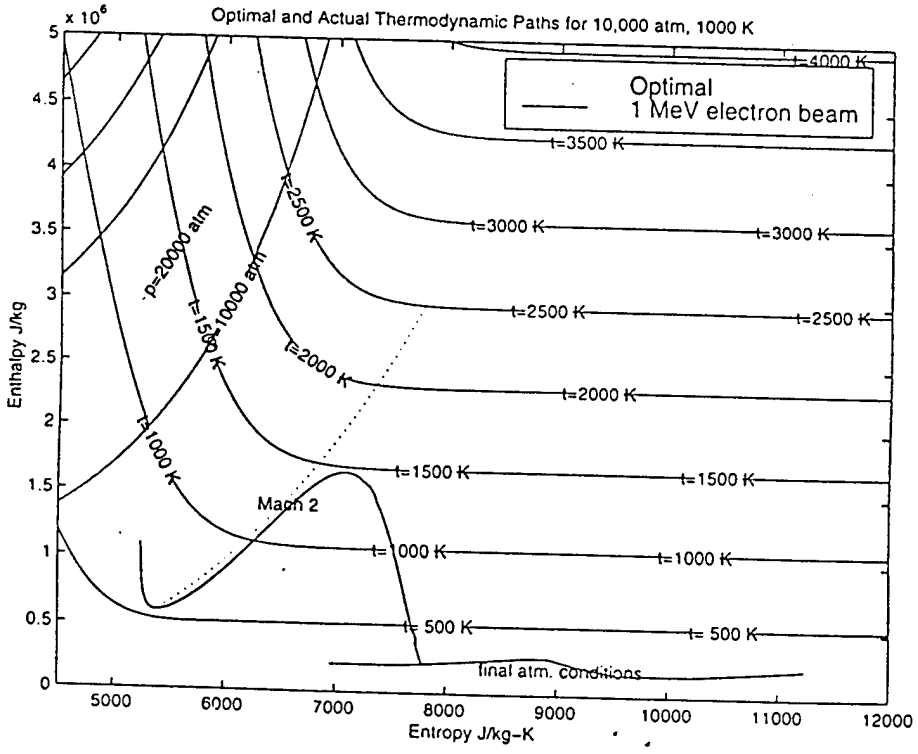

Figure 12.

AIAA-2000-0159
A 150 kW Electron Beam Heated Radiatively Driven Wind Tunnel Experiment

P. Barker, J. Grinstead, P. Howard, R. Anderson, G. Brown, R. Miles
Princeton University, Princeton, NJ

R. Lipinski, G. Pena, L. Schneider
Sandia National Laboratories, Albuquerque, NM

R. Howard
Sverdrup Technology

38th Aerospace Sciences Meeting & Exhibit
10-13 January 2000 / Reno, NV

A 150 kW Electron Beam Heated Radiatively Driven Wind Tunnel Experiment

P. Barker, J. Grinstead, P. Howard, R. Anderson, R. Miles, G. Brown
Department of Mechanical and Aerospace Engineering, Princeton University

R. Lipinski G. Pena, L. Schneider
Sandia National Laboratories, Albuquerque

R. Howard
Sverdrup Technology

Controlled energy addition to a supersonic flow using a 700 keV electron beam has been demonstrated at currents up to 300 mA and for durations up to 3.2 ms. Measurements of electron beam diameter and current were used to characterize beam transport through the steering magnets and nozzle. These measurements demonstrate that good magnetic control of electron beam transport has been attained, allowing propagation through the nozzle with less than 0.5 % of power input into the nozzle being deposited on the nozzle walls. The good agreement between these measurements and modeling allowed an estimation of power deposition in the flow during blow down conditions. Time resolved shadowgraph images and measurements of static pressure along the nozzle during this heating period show that stable, steady flow is achieved within 900 μs of beam turn on, and that steady flow is maintained for the remainder of the heating period. Preliminary results of flow temperature, density and chemistry are presented and further improvements to these measurements in continuing experiments are discussed.

Introduction

The radiatively driven hypersonic wind tunnel (RDHWT) is being developed to overcome short run times and flow quality limitations imposed by high plenum temperatures in current hypersonic test facilities [1]. A facility based on the RDHWT concept promises to overcome these limitations, primarily because the temperature of the flow can be maintained below a value where significant erosion of containment materials and thermal production of non-air species occurs. A facility with a test section of 0.5 meters in diameter capable of dynamic pressures of 2000 psf at Mach 13 would expect to have a run time from seconds to minutes. This type of wind tunnel, which has been called a missile scale facility, would require radiative power on the order of 10 to 100 MW, a plenum pressure of 20 000 atmospheres, and a temperature of approximately 1000 K.

The radiatively driven wind tunnel concept requires energy to be added in the supersonic region of a nozzle flow to increase the total enthalpy and entropy to that required for specific hypersonic flight conditions whilst minimizing

temperatures throughout the heating path. A range of thermodynamic heating paths can be achieved through judicious choice of experimental conditions such as nozzle contour, plenum pressure and temperature, and directed energy heating source. Determination of an ideal path for particular flow conditions has been discussed in previous papers and is currently being refined for the missile scale facility.

We have recently demonstrated that high power laser beams and electron beams are suitable energy sources for a RDHWT at a nominal power level of 10 kW, and increase both flow entropy and total enthalpy in a controlled manner[2,3]. To date, work has focused on the demonstration of a stable, radiatively heated supersonic flow that can be modeled and experimentally verified.

Electron beams are an attractive source of energy because of their inherent efficiency (80%) when compared to laser sources (< 20 %). In addition, the electron beam does not excite a well defined set of internal energy states, as the laser does, but instead transfers energy by collisions with air molecules, resulting in excitation, ionization and dissociation. Thermalization of this energy is accomplished by further collisions with the molecules in the flow. Solenoidal magnets must be used to couple the electron beam into the flow and to focus it into the nozzle. To focus the beam into a nozzle the magnetic field must be increased as the diameter of the nozzle decreases.

This paper presents the interim results of the latest electron beam experiment, which follows on from the first demonstration of electron beam heating of a supersonic flow in 1998 [3]. The latter experiments demonstrated, for the first time, controlled electron beam heating of a Mach 3.9 flow, as well as a steady transition to a stable heated flow. The change in Mach number (0.7), total enthalpy (20 kJ/kg) and total power (10 kW) absorbed by the flow were measured on the center line of the nozzle flow for a 50 kW e-beam power input. For the final runs in these experiments, increased e-beam power (90 kW) and tighter focusing produced a large change in Mach number, from 3.9 down to a minimum of 2.3. With this change in Mach number an estimated power of 40 kW was absorbed into a localized, central region of the flow.

Whilst these experiments demonstrated that e-beam heating at this power level was a viable option for the RDHWT, further experiments were required to provide data that could be more readily compared with the computational models of the e-beam heating process. This required:

1) tighter focus of the electron beam into nozzle to prevent energy loss to the walls and, in a larger scale facility, eventual catastrophic heating of the nozzle walls
2) measurements of pressure along the nozzle in the presence of x-rays
3) optical measurements of density, temperature and velocity at the nozzle exit.

Other objectives were to:

4) demonstrate e-beam heating at the 100 kW level as an important milestone towards the 10 – 100 MW power levels required for a missile scale facility.
5) measure flow uniformity whilst keeping the e-beam from the wall
6) measure concentrations of non-air species produced by e-beam ionization and dissociation.

The Wind Tunnel Facility

A Mach 3.9 blowdown wind tunnel was constructed for the electron beam, energy addition experiment. The electron beam was introduced into the nozzle of the wind tunnel through the nozzle exit, and was focused into the diverging profile of the nozzle by a strong axial magnetic field that increased from exit to throat. Compressed air for the tunnel flow was supplied by a 140000 scf tube trailer that was connected to the gas heater and plenum through 160 ft of stainless steel tubing. A regulator was used to initiate the flow and maintain the required pressure at the plenum. This pressure was typically either 1500 or 2000 psi. The nozzle flow was heated by passing it through a 17 foot long electrically heated stainless steel pipe placed between the regulator and the plenum. A nominal plenum temperature of 400 K was achieved for time periods of seconds for the e-beam experiment. Plenum conditions were maintained as close as possible to the above values for all tunnel runs so that results from different flow diagnostics could be compared.

The nozzle was constructed of aluminum with a throat diameter of 8 mm and an exit diameter of 27.5 mm, and the nozzle flow was exhausted into the ambient laboratory air at approximately the local atmospheric pressure (12.1 psia). The electron beam entered the nozzle through a series of beam steering magnets. A cone and apertures were placed at a distance of approximately 4 cm from the nozzle exit to stagnate the flow, thereby decreasing the pressure on the 5 mil beryllium foil used to couple the electron beam out of the accelerator. To reduce gas density in the path of the e-beam, gaps in the steering magnets allowed a radial outflow of gas ahead of the foil. Magnets were also placed along the length of the nozzle to focus the e-beam within the nozzle. The magnitude of axial magnetic field is plotted in figure 2. The field increases towards the nozzle throat in order to focus the electron beam into the nozzle.

The Electron Beam Accelerator

The Hawk accelerator at Sandia National Laboratories in Albuquerque, NM, was used to generate the electron beam that was injected into the nozzle airflow. The Hawk is a Van de Graff type accelerator capable of producing beams up to 1 MeV and 1 A for up to 1 ms. For this experiment we operated the accelerator at 700 keV, with currents up to 300 mA, and for durations not exceeding 3.2 ms.

The configuration of the magnets, nozzle, plate, and foil was shown in figure 1. The bent solenoidal array of magnets transports the electron beam from the accelerator into the nozzle. The bend is employed to minimize the stagnation pressure on the foil. A 1.27 cm thick cast steel plate separates the magnets from the accelerator in order to isolate the magnetic fields from the accelerator transport tube. The beam enters a magnetic cusp formed when the solenoidal fields are captured by the steel plate. The beam also must pass through a 0.25 mm thick beryllium foil in order to leave the vacuum of the accelerator and enter the air flow. The relative locations of the magnets, Be foil, and steel plate were adjusted to maximize capture of the beam onto the field lines without undue heating of the foil.

Electron Beam Transport and Power Deposition

The Integrated Tiger Series (ITS) code [4] was used to model the beam behavior and energy deposition in the nozzle flow and the gas between the nozzle and accelerator. This Monte Carlo code follows the trajectory and interactions of one beam electron at a time, including the generation of secondary electrons. The primary measurement of importance is the amount of power deposited into the air within the nozzle during blowdown, as a function of distance from the throat (z), and radial distance from the axis (r). This measurement is difficult because sensors in the flow during blowdown disturb the flow and would also be disturbed by the flow. Our approach was to measure beam conditions in stagnant air, compare the results to the ITS code predictions, and then use the ITS code to extrapolate to blowdown conditions. We also can estimate the power deposition without the use of the ITS code.

Initially, a measurement of beam dimension was compared to the ITS code. This was measured as a function of z by observing e-beam fluorescence on a 0.15 mm sheet of Mylar. Figure 3 shows the predicted and measured beam radii (Gaussian) and the nozzle radius. The agreement between the ITS code and the measured radii is reasonable. The average beam diameter between z=20 and z=50 cm is about 35% of the nozzle diameter.

The total beam current as a function of z was measured by collecting charge at each z location with a carbon disk grounded through a 50 ohm resistor. The voltage across the resistor was used to determine the beam current. This probe was calibrated against a commercial Pearson probe in separate measurements. Figure 4 shows the results of a series of current measurements in 12.1 psia non-flowing air. Also shown are the ITS predictions using the same input conditions as for the diameter predictions in figure 3.

The current decreases dramatically as the beam penetrates the nozzle. This reduction is not primarily due to absorption or scattering in the air but to reflection of the electrons by the converging magnetic field. A measurement of these reflected electrons was obtained by

observing the e-beam fluorescence on a Mylar sheet (0.15 mm) at z=50 cm, with and without a carbon beamstop at z=45 cm. The image was observed to be 56% brighter without the beamstop, indicating that 56% of the beam entering the nozzle is reflected out. This is consistent with the numbers shown in figure 4. To dramatically decrease the amount of reflected electrons requires the cathode of the accelerator to be placed in a solenoidal magnetic field that extends to the nozzle throat. This is required to prevent the beam acquiring angular momentum as it enters the field of the nozzle. Such a case was modeled (without any air) to see the effect for this geometry, and the result was 97% current transport (see square in figure 4).

To estimate the amount of power deposited in the nozzle air during a blowdown shot, the average energy of the electrons entering the nozzle (after losing energy to the air between the nozzle and the accelerator) must be determined. Then an estimate of the fraction of that energy deposited into the nozzle air must be made.

The air density at the nozzle exit is 0.0034 g/cm^3 without e-beam heating and flows at about 1 kg/s into ambient air of about 0.0010 g/cm^3 for about 7 seconds before the beam shot. The air is cold and dense while flowing but returns to about the plenum temperature (373 K) when it hits the magnets and apertures. Since the beam is bent, we estimate that about half the air along the beam path is flowing and cold, and half is nearly stagnant and at room temperature before the beam turns on (see figure 1). Beam heating is estimated to decrease the density of the blowing air to 0.0026 g/cm^3, and the still air to 0.00168 g/cm^3. Thus, the estimated energy of the electrons as they enter the nozzle is about 520 keV ($\pm$ 30 keV).

In 0.8 atm air about 56% of the beam current entering the nozzle got reflected out, and the estimated energy loss in those electrons under blowdown conditions is about 130 keV. If the same fractions hold true with blowdown air, we estimate that about 33% of the accelerator beam power enters the nozzle, and 14% is reflected, leaving 19% deposited in the blowdown air in the nozzle. For the base case with 200 mA in the accelerator, this is 25 kW deposited in the nozzle air.

We ran the ITS code using the air density profile expected for a 1500 psi, 373 K blowdown condition without beam heating and with an average air density of 0.00168 g/cm^3 between the nozzle and the accelerator. Figure 5 shows the predicted power deposition rate with 200 mA at the accelerator. The code predicts that there will be significant beam heating down to about 30 cm from the throat and that less than 1% of the beam energy will be lost to the nozzle walls. The predicted power deposited in the nozzle air is 24 kW; this includes the effects of magnetic reflection, scattering in air, and energy loss by the beam before the nozzle. This is close to the value estimated above. Under steady conditions, the beam will penetrate a bit more deeply into the nozzle because it will heat and thin the air in the nozzle.

Flow Diagnostics

Both probe and optical diagnostics were employed to quantify the temperature, pressure and density of the unheated and heated flow. Pressure transducers were used within the plenum, and placed along the nozzle. The pitot pressure was measured at the nozzle exit in the absence of energy addition. During energy addition, probes could not be used at the nozzle exit because they block the incoming electron beam. To measure flow properties at the nozzle exit during energy addition, optical techniques were employed since they are non-intrusive and can be carried out remotely from the experiment and be effectively shielded from x-rays.

Probe Measurements

Plenum pressure and pitot pressure at the nozzle exit were determined for each run using strain gauge transducers (Honeywell) with a temporal response of approximately 0.5 s. Plenum temperature was also measured in each experimental run with a type K thermocouple.

Fast response (15 kHz) fiber optic pressure probes (Optrand) were placed along the length of the nozzle to record changes in pressure during energy addition. These transducers were modified to reduce interference from high energy Bremsstrahlung X-rays produced in the air and by metallic surfaces of the accelerator. The

transducers were modified to prevent light from x-ray scintillation within the fiber optic reaching the detector at the end of the fiber. X-ray interference was tested by firing the electron beam at a carbon disk placed at the exit of the nozzle. No interference was detected.

Optical Measurements

Mach number and flow visualization

A series of 32 consecutive shadowgraph images of the flow were used for time resolved measurements of flow stability and Mach number over the entire energy addition period. The images were obtained on an ultrafast CCD framing camera with a maximum frame rate of 1 MHz. The framing rate was varied so that the entire e-beam heating period was recorded on 32 frames. The Mach number was determined from the Mach angle produced by a small cone placed in the flow. Figure 6 is a shadowgraph image of the unheated flow illustrating the position of the Mach lines used to determine Mach number. The white lines in the image are damaged pixels in the CCD chip.

Static temperature measurements

Laser induced thermal acoustics (LITA) was employed to measure the speed of sound and static temperature at the center of the flow. This new variant of the LITA technique was used successfully in the preceding e-beam experiments and has been described elsewhere to achieve a temperature uncertainty of 5% [5]. Figure 7 is a plot of LITA signals used to determine static temperature. The frequency of oscillation of each waveform is proportional to the square root of the temperature. Calibration of frequency with temperature was carried out with a thermocouple in room air.

Density

Rayleigh scattering of an ArF laser beam was used to measure flow density across the nozzle exit plane. Rayleigh scattered light is directly proportional to gas density and laser intensity. Because laser intensity varies from shot to shot, calibration of signal intensity to density for each shot was required. To calibrate Rayleigh scattering images to absolute density, both the core flow at the nozzle exit and a small region of the surrounding ambient air were imaged. Ambient air density was calculated from temperature and pressure measurements during the tunnel run. The beam from the ArF laser was focused down to a sheet using a cylindrical lens so that the beam was approximately 2mm wide. The beam was positioned to be approximately 1 cm away from the nozzle to minimize elastically scattered light from the nozzle. This interference prevented accurate density measurements in the previous energy addition experiments.

NO concentration measurements

Absorption measurements were made to determine the number density of NO created in the flow by e-beam excitation. Collimated light at wavelengths of 226 nm and 237 nm, corresponding to the (1,0) and (0,0) in the A-X band of NO in a resonance lamp, were passed through the flow. The light was then collected by a lens and directed into a spectrometer (Acton 0.5 m). Spectra were recorded on an intensified CCD camera.

Unheated Flow Measurements

Prior to the energy addition experiments, the nozzle flow was characterized using a combination of standard probes as well as optical measurements. The ratio of the Pitot pressure to plenum pressure was used to determine an exit Mach number via the isentropic flow relations. The exit Mach number was also determined from the ratio of the static temperature to plenum temperature via the adiabatic flow relations, as measured by LITA and a thermocouple in the plenum. Mach numbers of 3.85 and 4.0 were determined from these techniques respectively and they are in reasonable agreement with the value of 3.86 calculated for the nozzle contour. The consistency between these experimental methods served as a check on the transducers used in the experiment as well as for verification of the computational model used to predict the unheated flow. Figure 8a are plots of pressure and temperature in the plenum recorded during blowdown over a 20 second time period. Pressure traces taken with the fiber optic pressure transducers along the nozzle at 10 cm, 30 cm and 48.8 cm from the throat are also shown.

Figure 8b is a comparison between measured pressure profile at 5 points along the nozzle contour and that predicted by theory. This figure shows excellent agreement between predicted and measured pressure values.

E-beam Heated Flow

For e-beam heated operation the gas supply to the wind tunnel was turned on for approximately 10 seconds. Within the first 5 seconds of this blowdown period the plenum pressure and temperature reached the desired values for e-beam heating. The electron beam and magnets were fired when the temperature reached approximately 373 K (100 C). All data acquisition was triggered from a signal coincident with the energizing of the steering and focusing magnets, and these were fired exactly 400 ms before the electron beam. Further timing signals required for cameras, lasers and oscilloscopes were provided by two digital delay generators (Stanford Research Systems).

The electron beam was operated at 700 keV, with currents of up to 300 mA and for durations up to 3.2 ms. The beam transport system, which includes both the beam steering magnets and the focusing magnets, was operated in two configurations. These two configurations correspond to maximum current and half current in the magnets respectively. The first configuration corresponds to the tightest focusing achieved in this experiment and corresponds to a (1/e) Gaussian radius of 11 mm at the nozzle exit. The second configuration increased the beam radius to approximately twice that value and was used to determine the effect of a less concentrated heating profile on the flow. Unless specified otherwise all data presented in this paper were obtained with the maximum focused e-beam.

Static pressure measurement along the nozzle

Measurements of static pressure were recorded for the first time during energy addition in the presence of x-rays by using the fiber optic pressure transducers. Figure 9a are plots of pressure along the nozzle at the points 30 cm, 40 cm, and 47.5 cm from the throat. For reference, the temporal location of the e-beam is included. For this shot the e-beam duration was 1.8ms, with a current of 200 mA. This corresponds to an estimated power of 24 kW input into the nozzle flow when including the effects of magnetic reflection.

Figure 9b is a comparison between the measured pressure distribution along the nozzle and that calculated for a power of 45 kW absorbed into the nozzle. The CFD calculation does not include magnetic reflection and thus must be reduced by 56% to 24 kW. Calculations to include beam reflection are currently underway.

Even when these pressure increases cannot initially be compared to a model, they are a useful tool to indicate the penetration depth of the beam in the supersonic flow.

Figure 10 are plots of static pressure at the last three pressure taps along the nozzle, demonstrating e-beam heating for 3.2 ms at 30 cm, 40 cm and 48.8 cm from the nozzle throat. This was the longest duration heating experiment and indicates that steady, stable flow can be achieved over periods greater than 3 rise times. The 90 % rise time is determined to be 900 μs at plenum conditions of P_0 = 1460 psia and T_0 = 382 K. Approximately 12 kW is absorbed into the nozzle, assuming 56 % power loss due to magnetic reflection.

Static temperature

Static temperature measurements, which take approximately 0.5 μs, were carried out at the end of each e-beam heating period such that the measurements would reflect the steady state static temperature. Figure 11 is a plot of the LITA signal for the heated flow, for reference an unheated LITA trace is also shown for comparison. The frequency of the decaying oscillation that is used to determine temperature is not well defined in the heated case. This effect is believed to be due to the large variation in temperature in the measurement volume of crossed laser beams at the center of the flow. The measurement volume is approximately 5mm long perpendicular to the flow and 0.5 mm wide in the flow direction. The long dimension is a significant fraction of the 11 mm 1/e diameter of the e-beam at this location (50 cm from throat). The interaction region needs to be reduced to about 1 mm to minimize dispersion due to temperature gradients caused by the small e-beam. The power spectrum of the heated oscilloscope trace shows a range of frequencies corresponding to a range of frequencies. These

frequencies correspond to temperatures ranging from 120 to 250 K. These temperatures may not represent the full range of temperatures that exist within this 5mm region because higher temperatures also result in smaller signals. Further work is underway to increase the resolution in these experiments.

The LITA signal intensity is proportional to the square of the density and thus the LITA signal should be larger in the unheated flow than the heated flow because the density is decreased due to the higher temperatures. However, the LITA signal intensities were much stronger during e-beam heating than in the unheated flow. This effect is believed to be due to e-beam created species such as nitric oxide that absorb the 193 nm laser used in LITA. When these species are present more energy is deposited into the flow thereby increasing the density grating and hence the LITA signal. This process may also be in some part responsible for the dispersion observed in the LITA signal during heating, since significant absorption of laser power can change the temperature of the flow. To improve this measurement technique for the next part of this experimental series we have reduced the crossing angle of the pump beams and will investigate the frequency dependence and intensity dependence to minimize or eliminate dispersion.

Density

Preliminary results during e-beam heating indicate that the density calculated from Rayleigh scattering images is too high. This would is probably due to laser induced fluorescence of NO from the ArF laser at 193 nm. In the next round of experiments we will use the second harmonic of the Nd:YAG laser to produce Rayleigh scattering images. This light is at 532 nm in a wavelength region with few spectral interferences, but also with reduced scattering efficiency.

NO measurements

The gate voltage to the intensified CCD camera was used to determine the integrated exposure time of the NO absorption measurement. For most of these measurements an e-beam exposure duration of 2 ms was used. Exposure of the CCD camera was initiated 800 to 1000 μs after the e-beam was fired to acquire data during steady state flow (see Figure 9a). Because the spectra are recorded on a 2-D detector, spatial variations in absorption can be detected if the signals are strong and noise free. Background NO emission spectra were recorded and found to be comparable to the light from the lamp. To overcome this difficulty a spectrally brighter deuterium lamp was used to replace the NO lamp. The results from these spectral measurements are currently under analysis.

Summary and Conclusions

The preliminary results of the latest energy addition experiment have been presented. An understanding of and control over the e-beam have been achieved, allowing a demonstration of both beam bending to protect the accelerator foil from the flow and the ability to keep most of the beam energy from the wall. Both of these are important for all subsequent energy addition tests and of necessity in a full scale RDHWT facility. Magnetic reflection has been identified as a potential problem for efficient beam coupling and must be addressed in further energy addition experiments. Measurement of static pressure in the hard, high intensity x-ray environment has proven to be of prime importance in the characterization of e-beam heating and penetration during flow. These measurements have been used to compare with a computational model of the e-beam heating process and further flow calculations that include the magnetic reflection effect are underway. E-beam heating at a power level of 24 kW with a beam size of 11 cm at the nozzle exit has identified some problems with spatial resolution and spectral interference in some of the optical techniques. These techniques were used very successfully in the first energy addition experiments and these recent problems appear to be related to the non-uniform flow properties generated by heating over an 11 mm diameter at the nozzle exit and also an apparent increase in NO concentration. Ongoing optical measurements that will increase spatial resolution and decrease the deleterious effect of NO in the flow are being pursued in ongoing experiments in January of this year. We also plan to measure the velocity and temperature simultaneously to determine the change in enthalpy by e-beam heating.

Acknowledgments

The authors would like to acknowledge the Air Force Research Laboratory, MSE Technical Applications Inc. and Princeton University for support of this research.

References

1. R. Miles, G. Brown, W. Lempert, R. Yetter, G.J. Williams, S.M. Bogdonoff, D. Natelson and J.R. Guest, AIAA Journal, **33**, 1463, (1995)
2. A. Morgan, P. Barker, R. Anderson, G. Brown, and R. Miles, AIAA-98-2498, 20th Advanced Measurement and Ground Testing Technology Conference, Albuquerque, NM, June (1998)
3. P. Barker, J. Grinstead, A. Morgan, R. Anderson, G. Brown, R. Miles, R. Lipinski, K. Reed, G. Pena, L. Schneider, AIAA –99-0688, 37 th Aerospace Sciences Meeting,Reno NV, Jan 10, 1999.
4. J. A. Halbieb, R. P. Kensek and G. D.Valdez, IEEE Transactions on Nuclear Science, **39**, 1025, (1992)
5. P.F. Barker, J. H Grinstead, R.B. Miles, Optics Communications, September, (1999)

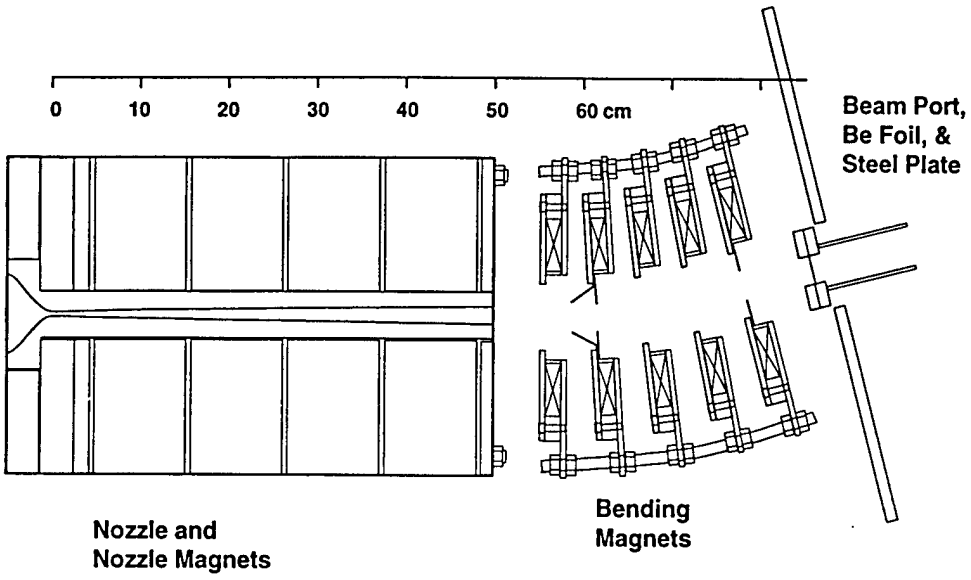

Figure 1. Configuration of the magnets, nozzle, plate, and Be foil. The electron beam propagates through the Be foil and is bent by the steering magnets into the nozzle. The solenoidal magnets around the nozzle focus the beam into the nozzle as it converges downstream.

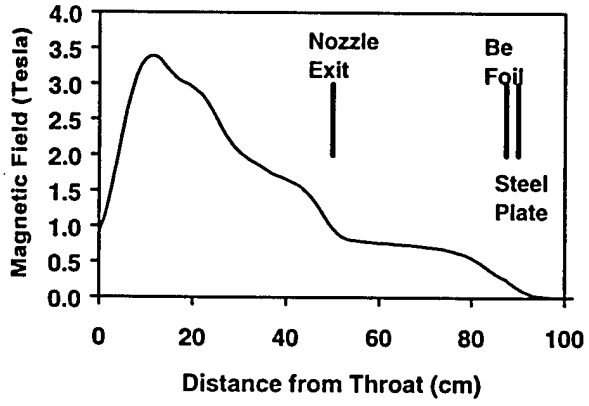

Figure 2. Magnetic field strength vs. distance from the nozzle throat showing the location of the Be foil at the end of the accelerator, the steel plate and the nozzle exit.

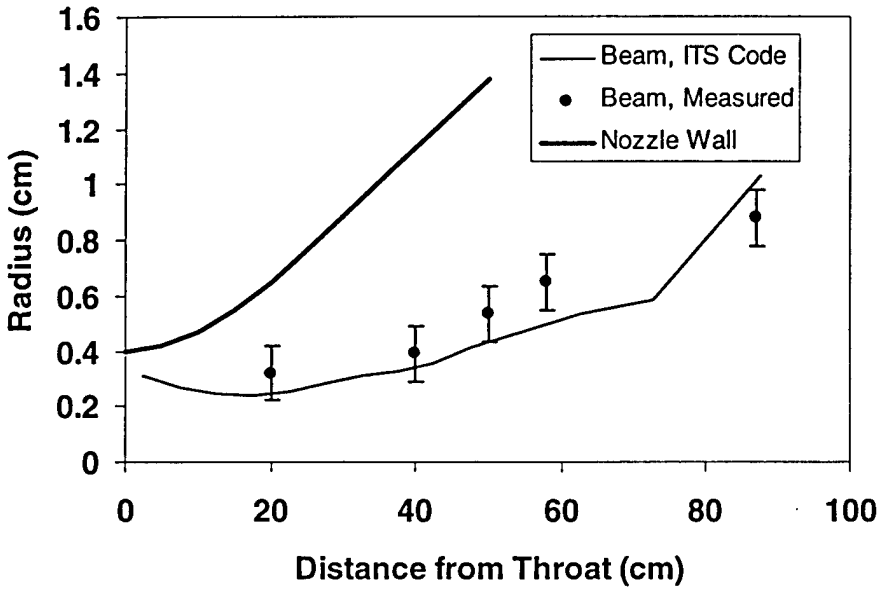

Figure 3. Beam and nozzle radius vs. distance from the throat in 0.8-atm air (nozzle removed).

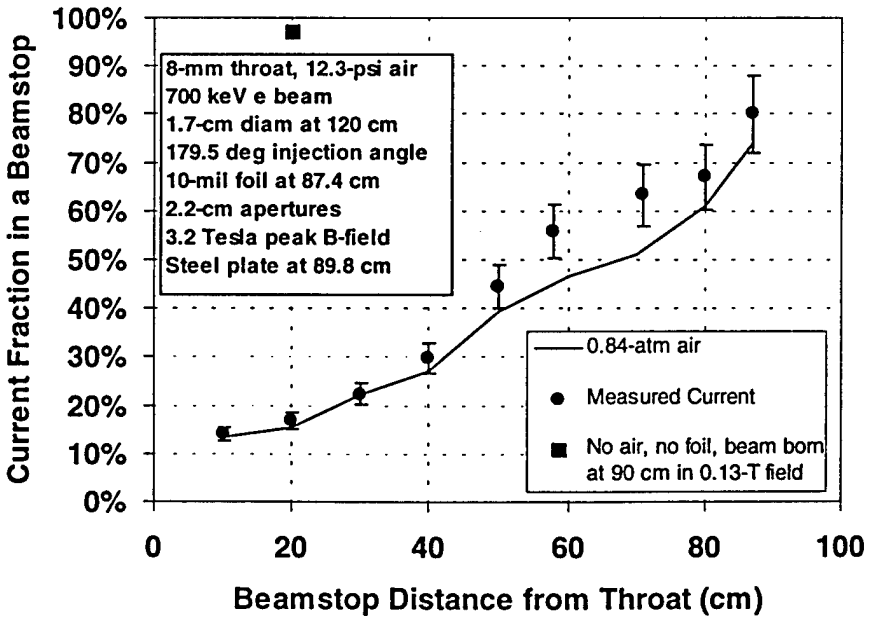

Figure 4. Beam current collected in a beamstop vs. distance from throat in 0.8-atm air.

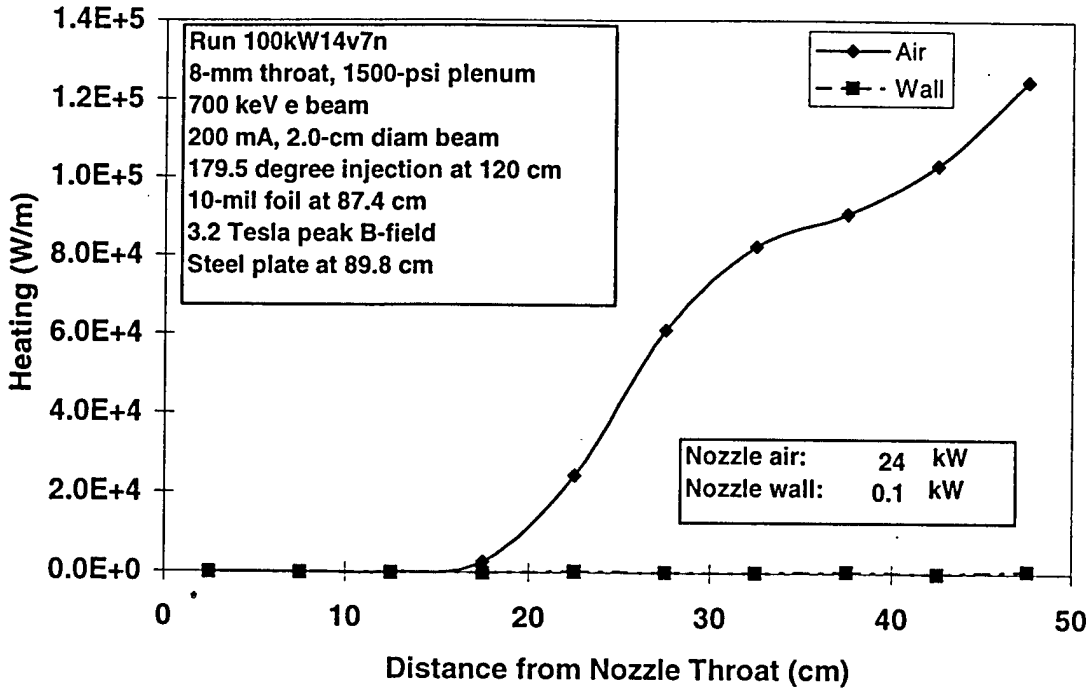

Figure 5. Beam power deposition predicted by ITS using unheated blowdown gas densities.

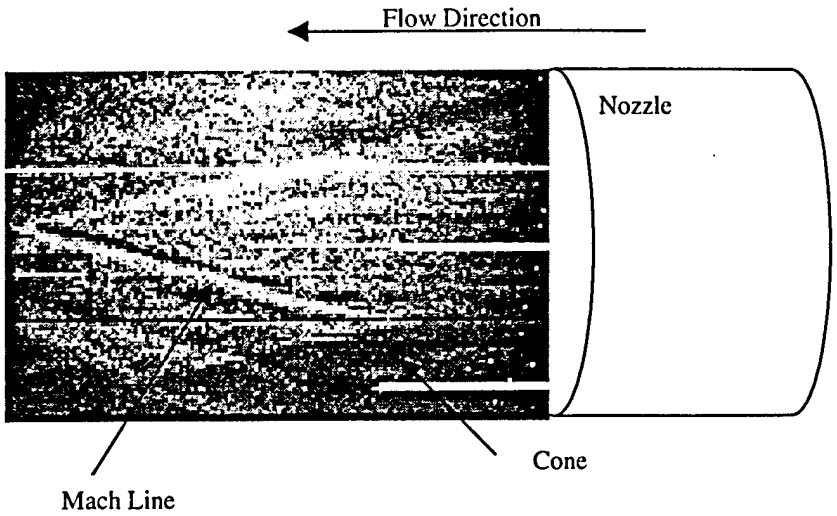

Figure 6. First shadowgraph image of thirty two consecutive images of the unheated flow used to produce shadowgraph movies. The position of the nozzle and the Mach lines produced by a cone placed in flow are shown.

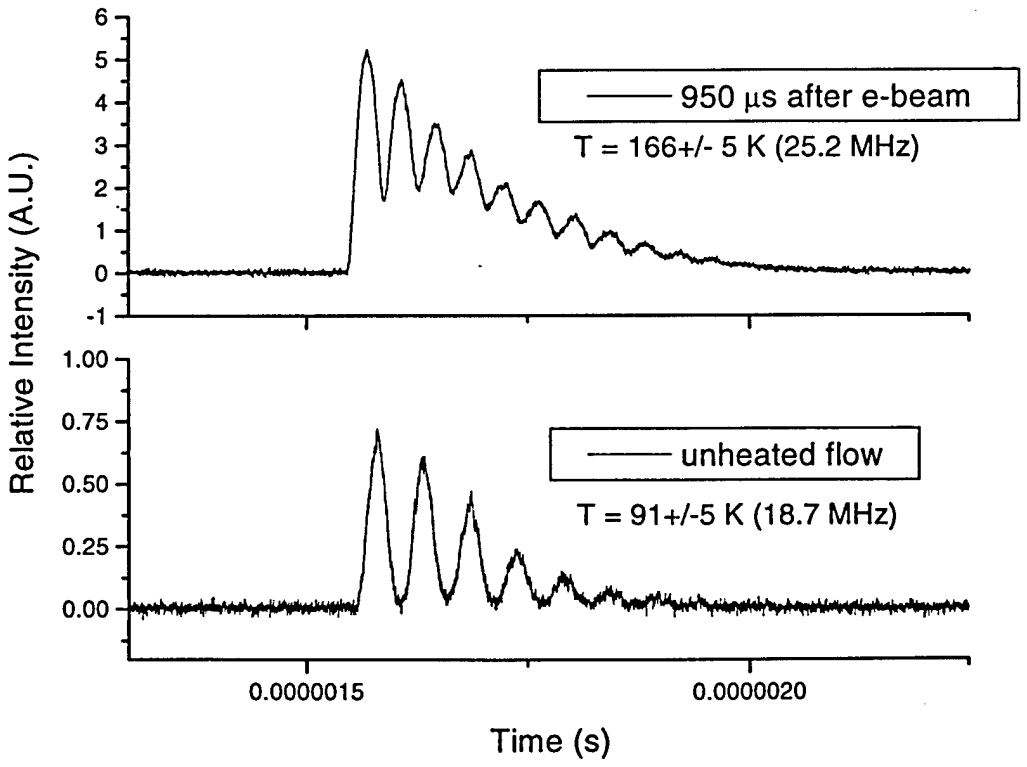

Figure 7. LITA signals used to determine static temperature in the supersonic flow. Traces for both unheated and heated flow are shown.

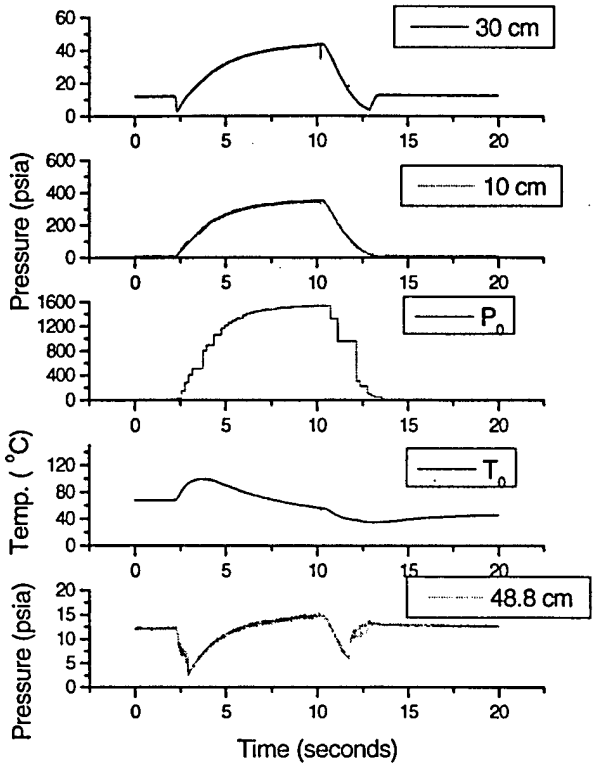

Figure 8a. Pressure and temperature in the plenum recorded during blowdown. Pressure traces taken with the fiber optic pressure transducers along the nozzle at 10 cm , 30 cm and 48.8 cm from the throat are also shown. During e-beam heating the electron beam was manually fired when the temperature reached approximately 373 K (100 C).

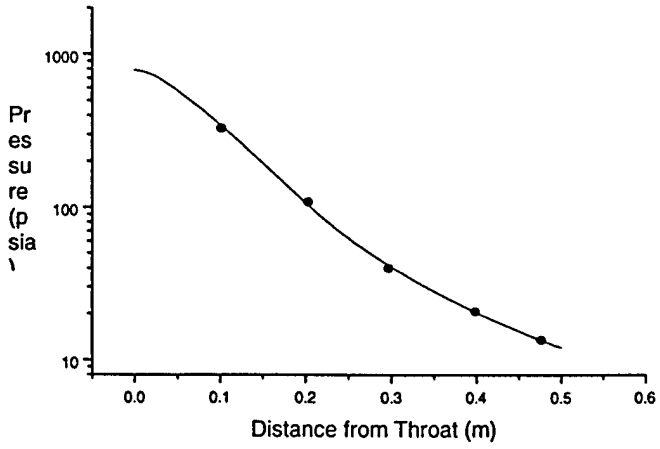

Figure 8b. A comparison of measured pressures along the nozzle and calculations. Plenum pressure of 1488 psi and temperature of 373 K.

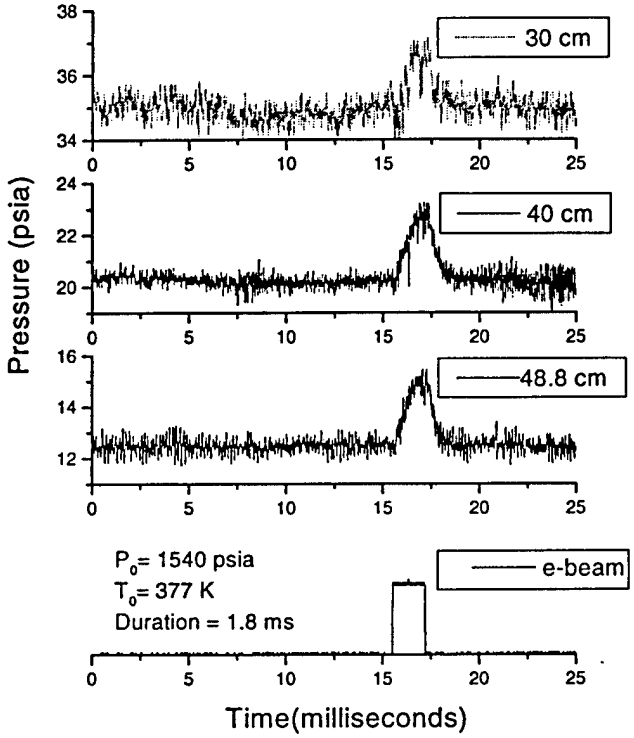

Figure 9a. Plots of pressure along the nozzle at the points 30 cm, 40 cm, and 48.8 cm from the throat. For reference the temporal location of the e-beam is included. For this shot the e-beam duration was 1.8ms with a current of 200 mA. This corresponds to a power of 24 kW input into the nozzle flow.

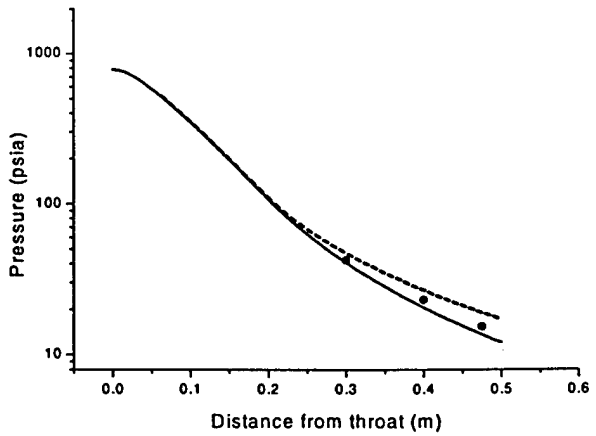

Figure 9b. A comparison between the measured pressure distribution along the nozzle and that calculated for a power of 45 kW absorbed into the nozzle. The calculation does not include magnetic reflection and thus must be reduced by 56 % to 25 kW. Calculations to include beam reflection are currently underway.

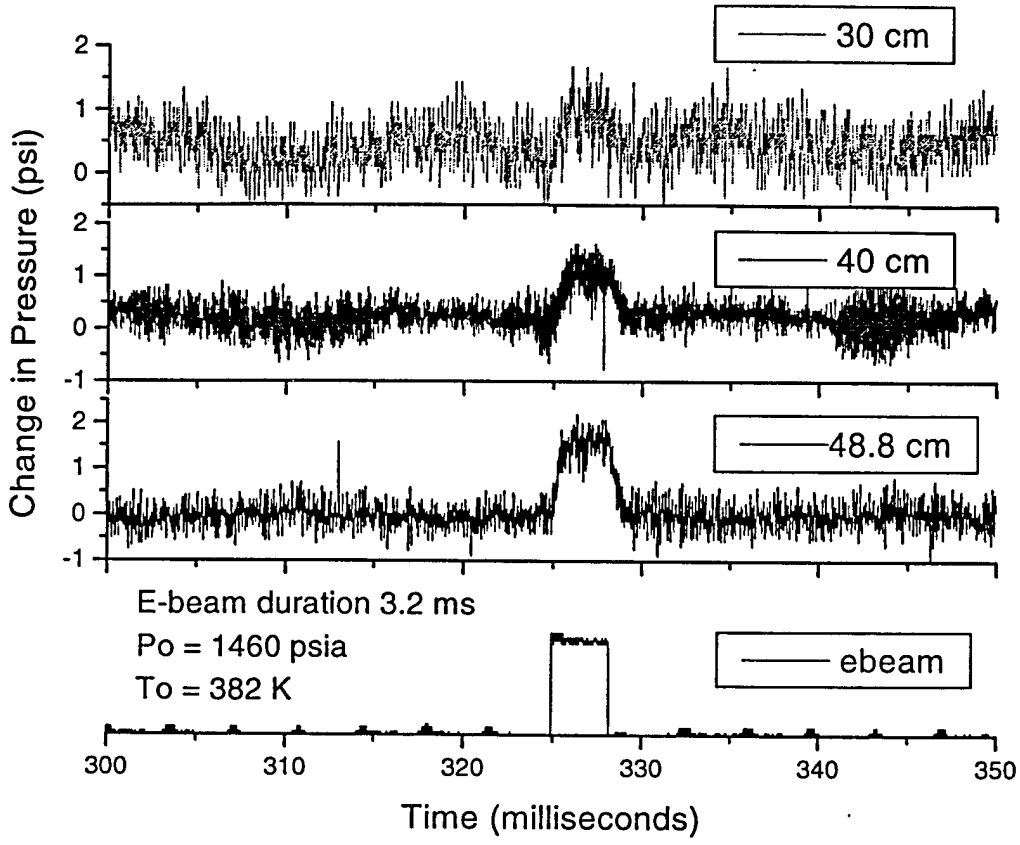

Figure 10. Plots of static pressure at the last three pressure taps along the nozzle demonstrating e-beam heating for 3.2 ms at 30 cm, 40 cm and 48.8 cm from the nozzle throat. This indicates that steady, stable flow can be achieved over times greater than 3 risetimes to steady state. The 90 % ristime is determined to be 900 μs at plenum conditions of P_0 = 1460 psia, and T_0 = 382 K. Approximately 12 kW is absorbed into the nozzle assuming 56 % power loss due to magnetic reflection.

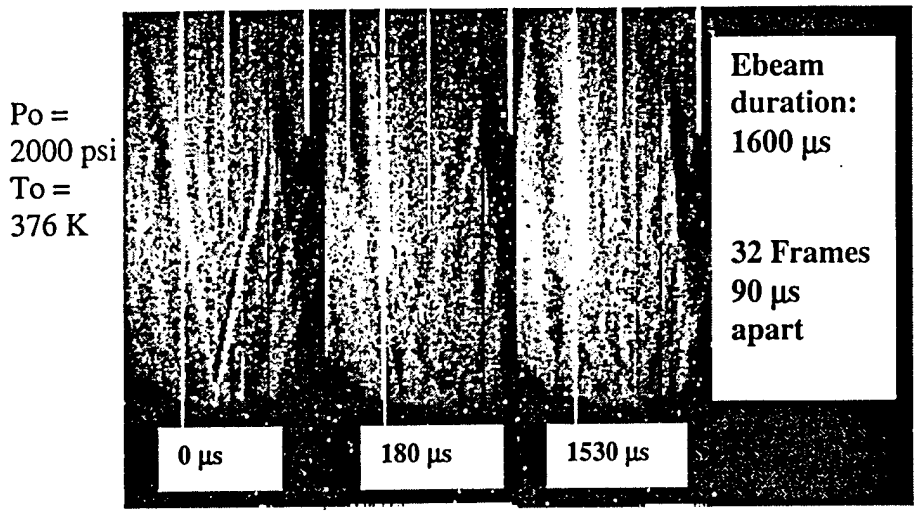

Figure 11. Three shadowgraph images of the e-beam heated flow show the evolution of the flow for different times during the heating duration. At 0 μs the Mach angle is well defined and corresponds to a Mach 4. Within 180 μs of the 1800 μs beam duration the Mach angle changes quickly decreasing by 8.5 degrees corresponding to a heated Mach number of approximately 2.5.

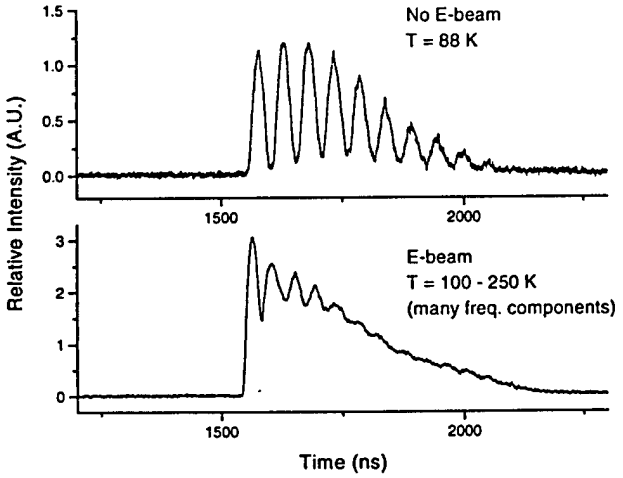

Figure 12. LITA traces of the unheated and heated flow with high magnetic field. The frequency of the unheated trace is not well defined indicating the possibility of dispersion due to signal averaging over a rapidly varying temperature profile or local temperature increase due to increased absorption by e-beam created NO.

AIAA 2000–0534

An Ultra-High Pressure, Ultra-High Reynolds Number Blowdown Wind Tunnel: Design and Preliminary Experiments

Kumar S. Raman
Princeton University

Robert W. Anderson
Princeton University

Garry L. Brown
Princeton University

Richard B. Miles
Princeton University

Marc Costantino
Lawrence Livermore National Laboratories

38th AIAA Aerospace Sciences Meeting and Exhibit
January 10–13, 2000/Reno, NV

AIAA 2000-0534

AN ULTRA-HIGH PRESSURE, ULTRA-HIGH REYNOLDS NUMBER BLOWDOWN WIND TUNNEL: DESIGN AND PRELIMINARY EXPERIMENTS

Kumar S. Raman, Robert W. Anderson*, Garry L. Brown+, and Richard B. Miles#
Department of Mechanical and Aerospace Engineering, Princeton University
Princeton, NJ 08544

Marc Costantino
Lawrence Livermore National Laboratory
Livermore, CA 94551

Abstract

A novel blowdown wind tunnel facility has been built and experiments are being performed to study transport properties of supersonic boundary layers at stagnation pressures up to 30000 psi (200 MPa) and unit Reynolds numbers up to 10^{10}/m. This study is motivated by the need for survivable throats and nozzles in hypersonic testing facilities and in particular, the radiatively driven hypersonic wind tunnel concept. The facility design is described, and preliminary results are presented and compared with predictions for stagnation pressures of 2200, 5000, and 10000 psi.

Introduction

Conventional wind tunnels based on the isentropic expansion of an ideal gas are limited in their abilities to duplicate hypersonic flight conditions due to the very high plenum temperatures required. The high plenum temperatures lead to severe throat erosion, limited run times, and dramatic alteration of the air chemical composition. In the radiatively driven hypersonic wind tunnel (RDHWT) concept of Brown and Miles [1], the plenum is kept at much lower temperatures (~ 900 K) and the air is maintained at moderate temperatures (< 2000 K) throughout the expansion process while heat is added radiatively to the flow downstream of the throat. The flow is then isentropically expanded to the desired thermodynamic condition. A detailed overview of the RDHWT principle is found in [1].

A key feature of the RDHWT is that the plenum is maintained at much higher pressures than would be required in an isentropic expansion facility running at the same Mach number. The primary benefit of ultra-high pressures is that due to real gas effects, in particular the increase of enthalpy with pressure at very high pressures, much less heat needs to be radiatively added to the flow compared to an ideal gas wind tunnel operating at the same plenum temperature. The advantage of high pressures is clearly seen on a Mollier diagram for air (figure 1).

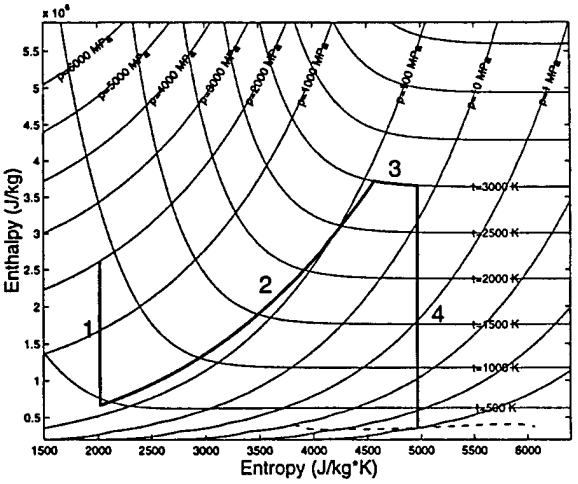

Figure 1. Mollier diagram for air showing the thermodynamic path of a full-scale RDHWT. Stages 1 and 4 are isentropic expansions. Stages 2 and 3 represent heat addition at constant Mach number and temperature respectively. [2]

A typical plenum pressure of a full scale RDHWT is 300000 psi (2000 MPa) while a typical plenum temperature is 900 K. The corresponding unit Reynolds number of the throat and nozzle flow is of order 10^{10}/m.

New issues arise with such extreme pressures and Reynolds numbers. One issue is the development of a

* Graduate Student, Department of Mechanical and Aerospace Engineering, Member AIAA.
+ Professor, Department of Mechanical and Aerospace Engineering, Senior Member AIAA.
# Professor, Department of Mechanical and Aerospace Engineering, Fellow AIAA.

predictive model that adequately accounts for turbulence and real gas effects. Tabulated equations of state for such extreme pressures are extrapolated from experiments conducted at much lower pressures. Simple turbulence models typically assume smooth walls and negligible pressure gradients, and have been validated only at much lower Reynolds numbers. An important issue is throat survivability and the development of strategies to cool the throat and nozzle walls. The wall shear stress, very large due to the high Reynolds number and dynamic pressure, may significantly erode a throat over many runs. A more subtle problem is that the wall temperature can recover to levels much higher than the plenum temperature due to a real gas effect. One can gain intuition for this problem by recalling that for an adiabatic wall and laminar boundary layer with constant properties and unity Prandtl number, the enthalpy along the wall is constant as we move downstream and is equal to the plenum enthalpy. Because the enthalpy of an ideal gas is a function of temperature alone, this implies that the wall recovery temperature is the plenum temperature. For a real gas, it is useful to consult the Mollier diagram and consider the example in figure 1. The first leg of the drawn path gives the thermodynamic state of the freestream fluid during the initial expansion from the plenum to supersonic speeds (Mach 2), the sonic point occurring near 900 MPa. Following a constant pressure line from the sonic point until it intersects the constant enthalpy line corresponding to the initial plenum enthalpy, one traces the local thermodynamic state through the boundary layer to the wall. It is readily seen that the throat recovers to a temperature greater than 1500 K though the plenum temperature was only 900 K. An analogous effect can be expected in the turbulent case but the practical implications are more serious due to the much higher heat transfer rates in this case.

A novel high pressure blowdown facility has been built to study nozzle boundary layer growth and heat transfer at Reynolds numbers of 10^{10}/m and at very high pressures where the recovery temperature is above the plenum temperature. Preliminary experiments have commenced to establish the dependence of the displacement thickness on Reynolds number at extremely high Reynolds numbers and to compare with predictions based on turbulence models validated at much lower Reynolds numbers. The facility design is described and preliminary results presented and compared with predictions.

Facility Overview

To achieve the unit Reynolds numbers of 10^{10}/m characteristic of a full scale RDHWT throat and nozzle flow, a high pressure blowdown facility with maximum operating pressure of 30000 psi at room temperature has been built. The Reynolds number is comparable to the full scale despite the lower pressures because of the dependence of viscosity on temperature and the relative incompressibility of air above 30000 psi.

Nozzle design and fabrication

The focal point of the facility is an axisymmetric supersonic nozzle developed by one of us (R.W.A.). It was designed using the flow solver based on the Flo103 code of Jameson and Martinelli [3] extended to axisymmetric nozzle geometries. Real gas effects become very important at pressures above 10000 psi so a key aspect of the model is a tabulated high pressure equation of state developed by NIST and used in conjunction with the solver. The Baldwin Lomax model is used to predict the turbulent boundary layer. This model assumes perfectly smooth walls and has been validated at lower Reynolds numbers than those seen in this experiment. The NIST equation of state is very reliable at the pressures encountered in the experiment so from the standpoint of the predictive model, the key sources of potential disagreement with experiment are high Reynolds number effects (including roughness) in the turbulence model. An extensive discussion of the CFD modeling is presented in Anderson et. al. [2].

The nozzle was designed by assuming choked flow at the throat and calculating an area distribution for the diverging section that would guarantee supersonic exit flow. The design issue was the balance between a sufficiently rapid expansion to maintain supersonic flow while allowing for an increased displacement thickness due to potential roughness effects; and a more gradual expansion to prevent possible condensation at the exit.

Surface roughness is a very important design aspect at these Reynolds numbers in terms of predicting the boundary layer growth and achieving a core supersonic exit flow. Law of the wall estimates based on throat conditions indicate that at the experiment Reynolds numbers, a surface finish of order 50 nm is needed to achieve a hydraulically smooth wall. The mechanical design of the nozzle by one of us (M.C.) was based on a special process developed to achieve a very fine surface finish. An aluminum mandrel was machined so that its outside diameter matched the prescribed contour. The mandrel was plated with nickel and the plated mandrel diameter was machined to match the inside diameter of a steel casing. The plated mandrel was pressed into the casing and the aluminum was

etched out leaving an axisymmetric contour. Figure 2 is a drawing of the nozzle.

Measurements of the wall surface roughness were taken using surface replication techniques. In this technique, a strip of triaphan film is placed in the nozzle exit and wetted with acetone. The film dissolves in the acetone and takes the shape of the surface. When the film dries, it is viewed under an atomic force microscope or scanning electron microscope and the peak to valley roughness is measured. In this manner, it was found that the nickel wall roughness was 200 nm. This measurement needs to be repeated as the roughness of the aluminum mandrel itself was found to be 750 nm using diamond stylus measurements. Though this is a very smooth surface, at our experiment Reynolds numbers, there may be a significant roughness effect. However, the surface finish is nearly an order of magnitude better than what is attainable using a numerically controlled milling machine.

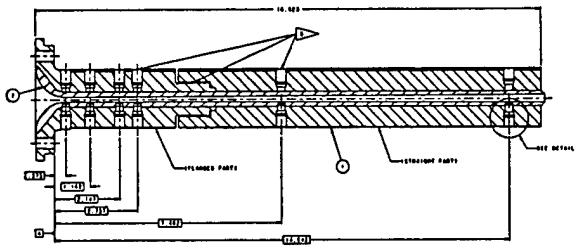

Figure 2. Supersonic nozzle built at LLNL.

The nozzle exit is 8.8 mm in diameter while the nozzle throat is 4 mm in diameter. The duct is approximately sixteen inches long from the throat. The latter 30 cm of duct is a very gradual expansion while the 10 cm immediately after the throat is a more rapid expansion.

A problem that arises due to this fabrication technique is that high pressure air is able to leak into the nickel-steel core gap through the pressure tap causing pressure sensors to communicate. This problem was solved by inserting thin copper bushings into each of the pressure ports having first wet the bushing and the inside hole surface with Loctite retaining compound. This technique has stopped the leak at 10000 psi, the highest pressure tested so far.

High pressure system

The nozzle mounts in a 3 liter pressure vessel comprised of three concentric steel cylinders press-fit together. The inner two cylinders are made of high strength steel and carry the gas pressure load. The outer cylinder is made of mild steel and is meant to absorb energy if either of the inner cylinders were to fail catastrophically.

The high pressure vessel and nozzle are contained in a 12'x15'x8' high barricade room in a pit in the lab floor. The barricade walls and ceiling are ¾" thick mild steel lined with ½" thick plywood for sound absorption. The barricade is designed to contain the high energy fragments if the vessel fails, contain the static overpressure in the case of a slow leak, and attenuate the impulse noise generated by the facility during a run. Noise tests demonstrate that if the operators wear ear protection, the barricade can attenuate the sound level to well within the safety standards for impulse noise. The high pressure is generated by a high pressure intensifier pump supplied by four 2400 psi air cylinders.

An optics and instrumentation room is located in the pit outside the barricade. A window in the steel wall provides optical access for laser diagnostics. Instrumentation lines run through the barricade to amplifiers in the instrumentation room. Figure 3 is a floor plan of the facility.

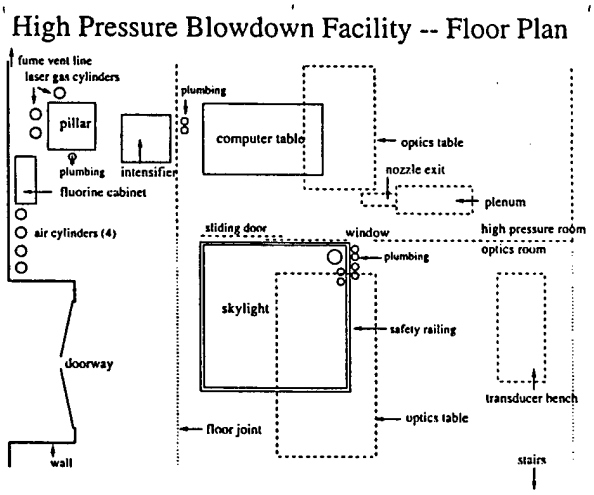

Figure 3. Floor plan.

Instrumentation and diagnostics

Six PCB piezoelectric high speed pressure sensors monitor the pressure along the nozzle wall during a blowdown. A Kistler piezoresistive high speed pressure transducer monitors the vessel pressure during pressurization and during a blowdown. A National Instruments data acquisition board monitors the

transducers and other signals during a run. A 100 mJ ArF laser and high speed camera are available for exit flow imaging.

Flow initiation and timing

During pressurization, the nozzle exit is blocked with a high pressure exit plug and the nozzle and plenum are brought to stagnation conditions. The exit plug is held by a pair of overlapping latch arms as shown in figure 4. The exit plug is a compound design consisting of male and female brass cylindrical pieces with a teflon washer in between to make the high pressure seal. A rubber stopper inserted before the plug provides a low pressure seal. As the pressure build up, the rubber pushes the brass which squeezes the teflon. At approximately 5000 psi, the rubber will have yielded and the teflon makes the seal. The flow is initiated when the latch is mechanically actuated and the plug is forced out by the flow. The data acquisition and laser systems are triggered off the pressure transducer nearest the exit.

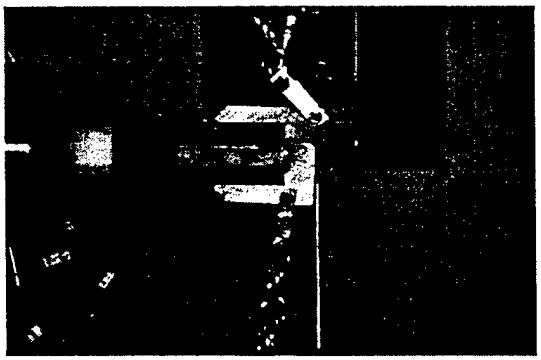

Figure 4. Nozzle exit during pressurization.

Results

We now present some preliminary results from blowdown experiments performed at stagnation pressures of 2200, 5000 and 10000 psi. In this discussion, P_0 refers to the stagnation pressure while P_1 through P_6 refer to the pressures at the pressure tap locations shown in figure 2 with P_1 referring to the pressure at the nozzle throat and P_6 the port nearest the nozzle exit. P_4 was not measured in these experiments. We would like to emphasize the highly preliminary nature of these results and acknowledge that more experiments must be performed before definitive conclusions can be reached.

P_0 = 2200 psi

Figure 5 is a pressure trace of the first twenty milliseconds of flow for 2200 psi plenum pressure.

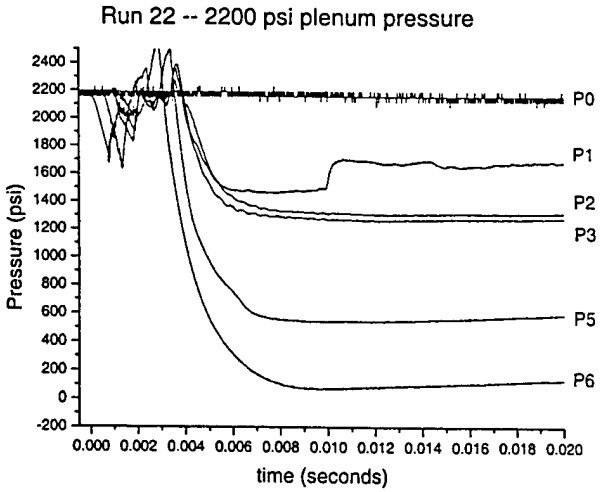

Figure 5. Pressure versus time for 2200 psi plenum pressure.

The unsteady pressure signal in the first few milliseconds of flow are interpreted as expansion and compression waves caused by the exit plug as it leaves the nozzle. The beginning of the steep expansion, occurring after approximately three milliseconds for P_6, corresponds to the time when the plug actually leaves the nozzle exit. This conclusion is supported by a Rayleigh scattering image of the flow taken four milliseconds after the flow starts (figure 6). Two parts of the plug can clearly be seen and the distance traveled by the plug is compatible with order of magnitude estimates of the plug's velocity as it leaves the nozzle.

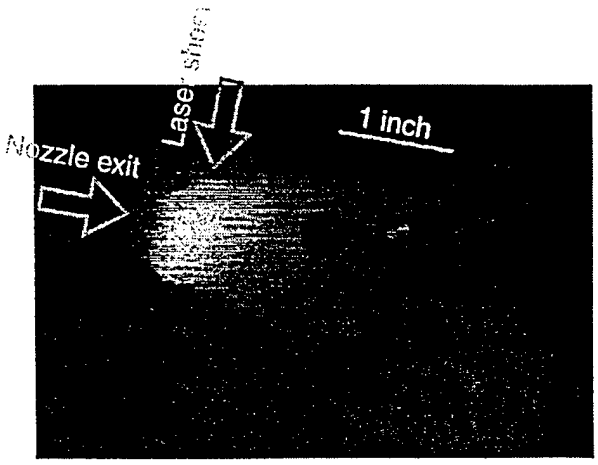

Figure 6. Rayleigh scattering image of the nozzle exit flow.

At this pressure, air behaves very much like an ideal gas and the sonic pressure is 1140 psi. Interpreting the period from 8 to 10 milliseconds as quasi-steady flow, figure 5 implies that the flow is subsonic at the physical throat and choked flow occurs between the third and fifth pressure ports. This suggests that the boundary layer growth rate is faster than the area expansion in the diverging section of the nozzle. The gradual pressure rise in the P_5 and P_6 traces may be attributed to the time it takes the boundary layer to develop in this unsteady flow. The sudden jump in the P_1 trace at 10 milliseconds could possibly be a compression wave propagating upstream associated with the sudden formation of an apparent throat in diverging section or it may be an unphysical artifact associated with the transducer. It is worth noting that P_5 and P_6 imply supersonic core flow at their respective locations. Once again, we emphasize the preliminary nature of these results.

P_0=5000 psi

Figure 7 is a pressure trace of the first twenty milliseconds of flow for 5000 psi plenum pressure.

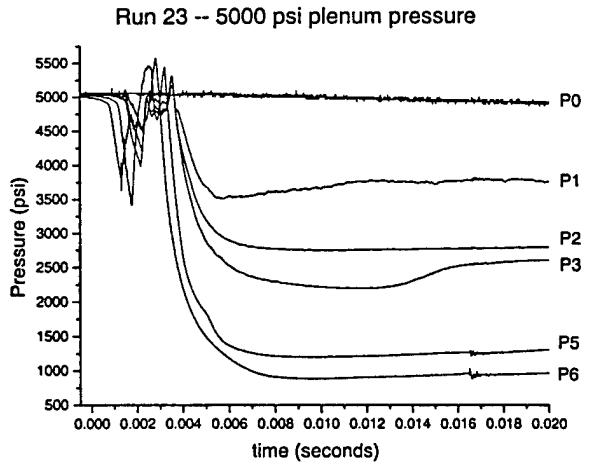

Figure 7. Pressure versus time for 5000 psi plenum pressure.

Once again, the startup transients associated with the flow release mechanism are observed in the first few milliseconds. Apparent quasi-steady behavior is observed after 7 milliseconds. The sonic pressure for this case is 2250 psi and the apparent throat is close to P_3 for much of the quasi-steady period. The rise in P_3 beginning at 14 milliseconds is likely due to a transition from weakly supersonic to subsonic flow caused by the boundary layer growth immediately downstream of this port. P_5 and P_6 clearly imply a supersonic exit flow.

P_0=10000 psi

Figure 8 is a pressure trace of the first ten milliseconds of flow for 10000 psi plenum pressure.

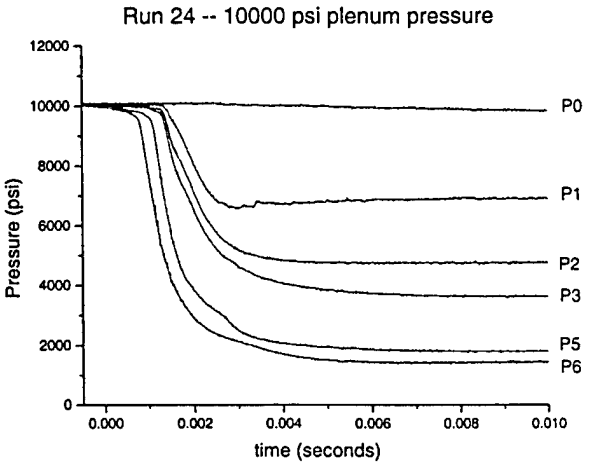

Figure 8. Pressure versus time for 10000 psi plenum pressure.

The higher pressure exerts a greater force on the exit plug resulting in the plug being forced out more quickly and efficiently. This explains the absence of a complicated starting transient. Quasi-steady flow is established within 5 milliseconds, quicker than in the low pressure runs. It is expected that the starting process will look similar for runs above 10000 psi.

The sonic pressure for this case is approximately 4500 psi implying that P_3, P_5, and P_6 read supersonic pressures. The observation that the sonic point is further upstream than in the 2200 or 5000 psi cases is consistent with the higher Reynolds number (and slower boundary layer growth rate) of the 10000 psi case. It is expected that for pressures above 10000 psi, the sonic point will move closer to the physical nozzle throat. This is not surprising because the nozzle was designed to be run at 30000 psi.

Comparison with predictions

Figures 9 through 11 compare the measured quasi-steady wall pressure distributions with predictions for the three cases considered. With the exception of P_6 in the 2200 psi case, the measured pressures are consistently higher than the predictions suggesting that the boundary layer is growing much faster than predicted by the design model. An estimate of the displacement thickness was obtained from the pressure measurements for the 10000 psi case and is compared with prediction in figure 12.

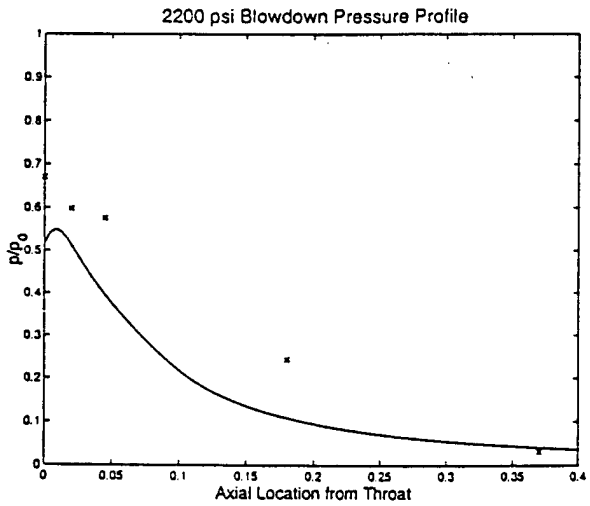

Figure 9. P/P_0 vs. distance from throat. 2200 psi

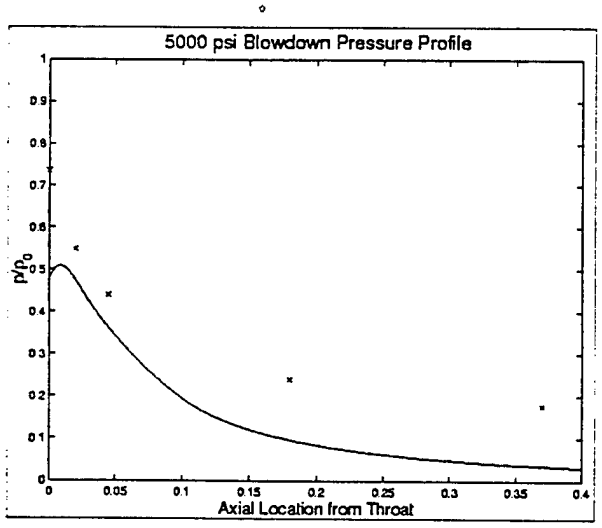

Figure 10. P/P_0 vs. distance from throat at 5000 psi.

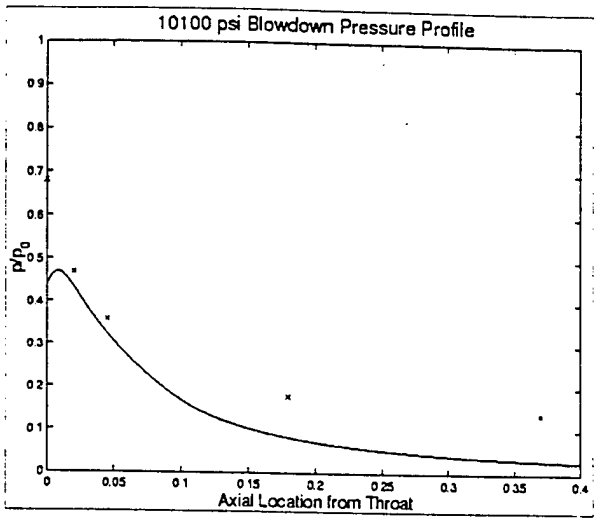

Figure 11. P/P_0 vs. distance from throat at 10000 psi.

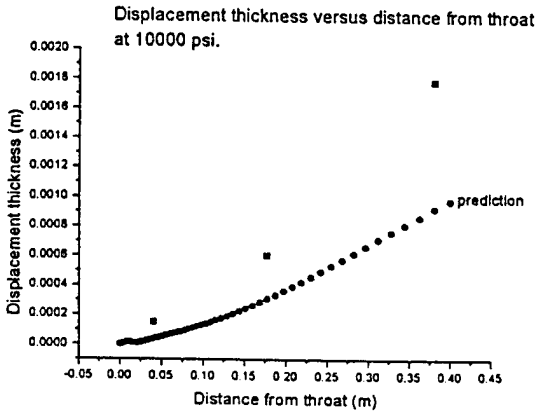

Figure 12. Growth rate of displacement thickness at 10000 psi plenum pressure: prediction and experiment.

There are a number of possible reasons for the large deviation of experiment from prediction. Preliminary measurements of the surface roughness indicate that the roughness may be an order of magnitude higher than that required for the hydraulically smooth wall assumed by the design model. The experiment Reynolds numbers were lower than the design value. The model assumes that the boundary layer begins at the physical throat but the measurements indicate that there may be some growth in the converging section. This effect would be less important at higher Reynolds numbers. Most importantly, these experiments are highly preliminary and more experiments must be performed before definitive conclusions can be reached.

Concluding Remarks

A high pressure, high Reynolds number blowdown wind tunnel has been built to run at stagnation pressures of 30000 psi and successfully tested at 10000 psi. The designed nozzle has achieved supersonic exit core flow at 2000, 5000, and 10000 psi with improving performance at higher pressures despite an apparently rough wall. The displacement thickness was found to grow much more rapidly than prediction and caused the sonic point to occur downstream of the physical nozzle throat. This effect is most serious at the lower pressures.

Immediate future work includes completing the current series of experiments and testing at higher pressures. The next series of experiments will involve the installation of surface thermocouples to measure heat transfer rates with the ultimate intent of proposing a sensible wall cooling strategy for the full scale RDHWT.

Acknowledgements

The design of the high pressure barricade facility is based on a technique developed at Lawrence Livermore National Laboratory by one of us (M.C.). We particularly wish to acknowledge the contribution of William L. Stokes in building the high pressure facility at Princeton and in developing various novel aspects of the installation. We would like to thank Daniel Mumm for his technical expertise regarding the surface roughness measurements. We would also like to acknowledge Xingguo Pan for obtaining the Rayleigh scattering image of the exit flow.

References

[1] R. B. Miles, G. L. Brown, W. R. Lempert, R. Yetter, G. J. Williams Jr., and S. M. Bogdonoff. "Radiatively Driven Hypersonic Wind Tunnel", AIAA Journal, V. 33, p. 1463 (1995)

[2] R. W. Anderson, G. L. Brown, and R. B. Miles. "Performance Characterization of a Radiatively Driven Hypersonic Wind Tunnel", AIAA Paper 99-0822 (1999)

[3] A. Jameson, L Martinelli. Flo103 Navier Stokes Solver, Princeton University, Department of Mechanical and Aerospace Engineering.

[4] "Flow Experiments for the Radiatively Driven Hypersonic Wind Tunnel Research Program", Operational Safety Procedure, OSP-J111, Princeton University, Department of Mechanical and Aerospace Engineering.

AIAA-2000-2276

Proof of Principle Energy Addition Experiments for the RDHWT/MARIAH II Hypersonic Wind Tunnel

P. Barker, P. Howard, B. Anderson, R. Miles, G. Brown
Department of Mechanical and Aerospace Engineering, Princeton University

R. Lipinski, G. Pena
Sandia National Laboratories

J. Grinstead
National Institute of Standards and Technology

R. Howard
Arnold Engineering Development Center/Sverdrup Technologies

21st AIAA Advanced Measurement Technology and Ground Testing
31st AIAA Plasmadynamics and Lasers
34th AIAA Thermophysics
Fluids 2000
Conferences
19-22 June 2000/Denver, CO

Proof of Principle Energy Addition Experiments for the RDHWT/MARIAH II Hypersonic Wind Tunnel

P. Barker, P. Howard, R. Anderson, R. Miles, G. Brown
Princeton University

R. Lipinski, G. Pena
Sandia National Laboratories

J. Grinstead
National Institute of Standards and Technology

R. Howard
Arnold Engineering Development Center/Sverdrup Technologies

Lasers and electron beams have been used to study radiative energy addition to supersonic flow as part of the radiatively driven hypersonic wind tunnel (RDHWT)/Mariah II program. Over the last three years this extensive test program has provided proof of principle demonstrations of supersonic energy addition as well as characterization of the resulting radiatively heated flow properties. This paper discusses the three major experiments that have been performed in support of this program, including the experimental design, and characterization of the flow and the radiative sources used. These proof of principle experiments consist of a laser and an electron beam energy addition at the 10 kW level and a more recent 100 kW electron beam experiment. Where possible, these results have been compared with both 1-D and 2-D CFD models

Introduction

Short run times and the creation of impurities severely limit the ability to duplicate useful hypersonic flight conditions in conventional ground test facilities. These limitations result primarily from the requirement for high plenum temperatures in the isentropic expansion process. For duplicating flight conditions above Mach 8, the plenum temperature must exceed 3000 K, and plenum pressures of 100's of atmospheres are required. Because of these extreme conditions only short run times in the millisecond range are feasible. These high temperature conditions also result in the production of nitric oxide and other radicals that reduce flow quality, and can affect combustion chemistry and aero-optics measurements in these facilities.

The radiatively driven hypersonic wind tunnel (RDHWT) concept aims to overcome these limitations by minimizing the temperature required in the plenum[1,2,3]. This is achieved by adding energy into the supersonic region of a conventional isentropic wind tunnel. Adding energy in this way, while expanding the flow, increases the total enthalpy and entropy to that desired for particular flight conditions, whilst maintaining the temperature below a value where containment and chemical purity are not compromised. In the radiatively heated tunnel, the local temperature and density of the flow are determined by the heating distribution and the nozzle profile. Because the entropy is increased in this process the plenum entropy must be lower than in a conventional wind tunnel. This implies that the plenum pressure must be much higher than in a conventional tunnel.

A medium scale facility with a test section diameter of 0.5 to 1.0 meters that is capable of dynamic pressures of 2000 psf operating at Mach 12 has been proposed [4]. This quasi-

continuous facility would have a run time from seconds to minutes and would require radiative power on the order of 10 to 100 MW. This facility requires a plenum pressure of 23 000 atmospheres, and a temperature of approximately 750 K [4].

This paper discusses the energy addition experiments that are a subset of the larger RDHWT/Mariah II program. This program also includes the development of the high pressure driver required for the large scale facility, fluid dynamic studies of the high pressure, high Reynolds number flow, and CFD modeling of all of these components. For extended performance, magneto hydrodynamic (MHD) acceleration of the flow after the radiative energy addition is also being studied.

Sources for Energy Addition

Directed energy sources such as lasers, electron beams and microwaves have been proposed as potential energy sources because they are capable of depositing high energy in the supersonic flow whilst avoiding stagnation of the flow.

Lasers transfer energy to the flow by absorption of photons via resonance with molecular absorbers contained in the flow. Thermalization of this energy occurs by collisions between the optically excited molecules and the surrounding air molecules. This energy transfer process must be rapid, so that many absorption-relaxation events occur on a time scale that is short compared to the residence time of the molecule in the nozzle. Absorption implies that a spectral overlap must exist between the absorbing molecules and a laser capable of MW power. The most promising overlap exists between the HF laser operating at 2.7 μm and a manifold of ro-vibrational transitions in the CO_2 molecule. Absorption can also be accomplished by seeding low concentrations of a strong molecular absorbing species such as SF_6 into the flow. The effect of these impurities on flow quality must be addressed. Precautions must be taken to insure that significant radiant energy is not deposited on the nozzle walls. Laser beams can be focused into the nozzle using both lenses and mirrors, and further guiding within the nozzle by large boundary layer density gradients has been predicted [5]. Laser induced chemistry is unlikely to affect flow quality since the energy of the photons is much less than that required for either dissociation or ionization. However, at high intensities multi-photon effects will increase this probability.

Electron beams are an attractive source of energy because of their inherent efficiency (80%) when compared to laser sources (< 20 %). In addition, an electron beam does not excite particular internal energy states, but instead transfers energy by collisions with air molecules, resulting in excitation, ionization and dissociation. Thermalization of this energy is accomplished by further collisions with the molecules in the flow. The probability of electron-molecule collisions depends on the energy of the electrons, which can be controlled by the acceleration voltage. The higher the voltage, the lower the cross section, and the deeper the penetration depth. Thus, the power deposition depth can be tailored by controlling both the voltage and current of the accelerator. The radial profile of the beam can be controlled by magnetic fields, or by use of a number of electron beams. In the presence of a magnetic field the electrons travel along the field lines. Solenoidal magnets are used to couple the electron beam into the flow and to focus it into the nozzle. To focus the beam into the nozzle, the magnetic field must be increased to compensate for the decrease in nozzle diameter towards the throat.

Although high power microwave sources have been well developed, and are already available at the MW level, they do not yet seem attractive as energy addition sources. Firstly, there is an absence of strong molecular absorption features that overlap the available sources. And, even though the metallic nozzle would form a good waveguide that would keep the high power from being deposited in the nozzle wall, the microwaves cannot propagate in a region of the nozzle smaller than the wavelength of the microwaves. Finally, microwave energy cannot be added from far downstream or through the high temperature boundary layers, because microwave driven electric breakdown would occur in the boundary layer, or in the low pressure region downstream of the desired energy addition region.

Energy Addition Experiments

Energy addition experiments at power levels much lower than the target 10 to 100 MW scale are required to study and verify the basic properties of coupling radiative energy into a supersonic flow. They are also important for validating CFD models. As well as proof of principle experiments that test the ability to add energy to the flow, more detailed measurements of flow quality and uniformity are required. To achieve these objectives accurate characterization of both the radiative source, and its transport properties must be undertaken. We describe three experiments that have been carried out over the last three years, and discuss in detail the results obtained, and the implications of these results for further work.

10 kW Laser Energy Addition

This first energy addition experiment used a 10 kW CO_2 laser to deposit energy into a supersonic nozzle flow containing nitrogen. This laser, which emits at a wavelength of 10.6 μm, was resonant with the $(\nu_3 + \nu_6)$ vibrational transition of SF_6 molecules seeded into the flow. Following excitation the SF_6 molecules undergo collisional relaxation transferring energy from vibrational modes to translational energy on a time scale of 136 nanoseconds at one atmosphere, at 300 K in nitrogen.

A diagram of the energy addition experiment is shown in figure 1. The setup consists of a high pressure front end, a 0.5 m long copper nozzle, an exhaust chamber, and a beam delivery tube. The LHMEL I 10 kW CO_2 laser at Wright Laboratories was used as source of stable, continuous energy for durations of 0.1 to 5.0 seconds. The spatial profile of the laser was constant over most of its diameter ensuring a uniform heating profile. The beam was focused into the nozzle with a 1.5 m focal length zinc selenide (ZnSe) lens. This lens was chosen to ensure that the beam filled the nozzle as uniformly as possible. From theoretical considerations, seed concentrations of 1000 ppm were expected to be sufficient to absorb the energy before it reached the nozzle throat. However, in the experiment the seed level was reduced to 250 ppm because of significant laser beam absorption by the flow after it had exited the nozzle. A beam delivery tube was used to bring the beam as close as possible (3") to the exit of the nozzle, thereby reducing absorption of the beam by the gas in the exhaust chamber. A ZnSe window was placed at the end this tube to transmit laser radiation whilst maintaining the 1.4 psia pressure in the exhaust chamber. The exhaust chamber had four windows for optical access to the nozzle exit. The 0.5 m long nozzle (throat to exit) was constructed of copper for high thermal conductivity, and was polished to a surface accuracy of 1 microinch (root mean square) to reduce absorption on the nozzle walls. The conical nozzle had a throat diameter of 6 mm and exit diameter of 34 mm. A plenum pressure of approximately 325 psia and temperature of 15 °C was used for most experiments. Gas for all runs was supplied to the nozzle by four 304 SCF gas cylinders.

Diagnostics and Results

The nozzle was instrumented with five pressure transducers placed at equal locations 5 cm apart along the nozzle. A thermocouple and pressure transducer were mounted at the nozzle exit to measure the stagnation temperature and Pitot pressure. Shadowgraph images were taken at the nozzle exit through the exhaust chamber view ports, and Rayliegh/Mie scattering images were obtained at the exit with a Nd:YAG laser and intensified CCD camera.

Plenum pressure and temperature, as well as static pressure along the nozzle were obtained for each experimental run. Figure 2 is a plot of static pressure along the wall with and without energy addition. Excellent agreement is found between experiment and prediction [5], except near the nozzle exit where condensation occurred due to the low plenum temperature. In the energy addition case the pressure is seen to rise in qualitative agreement with predictions. Shadowgraph images of the flow around the Pitot probe at the nozzle exit are shown in figure 3a and 3b. These images show the shock structure produce by the Pitot probe, with and without energy addition. These images are part of a long sequence of images recorded as the flow evolves to the steady heated flow. In all cases a steady transition to the stable heated flow

was observed. The Mach number was determined by the change in Mach angle of the shock around the pitot tube. Results showed that the Mach number was reduced from 4.3 to 3.9 during energy addition, primarily due to the higher static temperature. The unheated Mach number of 4.3 was determined from static pressure measurements at the exit and the meaurement of plenum pressure using the isentropic flow relations. Note that a reduction in Mach number is an increase in total enthalpy. A higher Mach number is obtained in the RDHWT by a further isentropic expansion to the desired flow conditions.

Rayleigh scattering measurements indicated that significant condensation of the nitrogen flow occurred at the exit. As the laser heated the flow it was brought above the 72 K condensation temperature.

Prior to the 10 kW energy addition experiment, SF_6 absorption coefficients determined from the HITRAN data base were used to model the energy absorption process. From experiment these values were found to be inaccurate for the higher temperatures used in our experiment because they only accounted for ground state absorption (ν_3). Combinational hot band absorption in the ($\nu_3+\nu_6$) band must be included to more correctly model this process.

Qualitative agreement between data and measurements of pressure along the nozzle was obtained, but closer agreement with the heated data was not expected because the temperature dependent absorption coefficients were not known. Better knowledge of the absorption coefficients used in this experiment is required for a more complete theoretical description of the experiment. The most important outcome from this experiment was achieving controlled stable energy addition to the flow at the 10 kW level.

10 kW Scale Electron Beam Experiments

As in the 10 kW laser energy addition experiments, the goal of the first electron beam energy addition experiments was to demonstrate that stable heated flow could be produced. It was also an opportunity to develop and evaluate diagnostics and the overall design of the experiment before undertaking more extensive studies. As well as these proof of principle measurements a more complete characterization of the heated flow properties was attempted, with the principle aim of measuring the total enthalpy change with energy addition and power deposited in the flow.

For this experiment the Hawk accelerator at Sandia National Laboratories was used to provide electron beam energies up to 900 keV, and beam currents of up to 400 mA delivered to the nozzle flow. The machine is capable of higher currents for smaller time periods. The power is limited by the heating of the thin beryllium foil used to couple the electron beam out of the accelerator. A series of solenoidal magnets were used to guide the beam from the accelerator exit foil to the nozzle exit. The field becomes progressively stronger in regions closer to the throat as the diameter of the conical nozzle decreases. Figure 4a shows the location of the magnets with respect to the nozzle and accelerator, while figure 4b gives the magnitude of the magnetic field in the axial direction due to the sum of the fields from each magnet.

A Mach 3.9 blow down wind tunnel was constructed for the electron beam energy addition experiment. A schematic of this facility is shown in figure 5. The electron beam was introduced into the nozzle of the wind tunnel from downstream, and was focused into the diverging profile of the nozzle by the strong axial field of the solenoidal magnets. Gas for the tunnel flow was supplied by twelve 2400 psi cylinders of breathing air, connected together by a gas manifold system which was regulated to provide a flow rate of 0.5 kg/s, and nominal plenum pressure of 1250 psi (85 atm). To prevent condensation the flow was heated by passing it through a 17 foot long electrically heated stainless steel pipe placed between the gas manifold and the plenum. A nominal plenum temperature of 400 K was maintained for the e-beam experiment. Plenum conditions were maintained as close as possible to the above values for all tunnel runs so that results from different flow diagnostics could be compared. The nozzle was constructed of aluminum with a throat diameter of 6 mm and an exit diameter of 20 mm. The nozzle flow was exhausted into the

ambient laboratory air at local atmospheric pressure (12.4 psi). The electron beam entered the nozzle through a series of beam steering magnets. A cone and apertures were placed at a distance of approximately 4 cm from the nozzle exit to stagnate the flow, thereby decreasing the pressure on the 0.005 " thick beryllium foil used to couple the electron beam out of the accelerator. To reduce gas density in the path of the e-beam, gaps in the steering magnets allowed a radial outflow of gas ahead of the foil. A mechanical shutter was used to prevent impingement of particles onto the foil during a run. This shutter was opened for approximately 100 ms before and after the accelerator was fired. Magnets were also placed along the length of the nozzle to focus the e-beam into the nozzle. Due to the interference of stray fields from the focusing and steering magnets not all of the focusing magnets could be used. Because of this, not all electrons were coupled into the flow, but instead were lost to the face and inside walls of the nozzle. Figure 6 is a photograph of the wind tunnel, e-beam facility, and diagnostic equipment used for this experiment located at Sandia National Laboratories in Albuquerque, NM.

Diagnostics and results

Measurements of static temperature, velocity, and time resolved Mach number were used to characterize the flow. Static temperature was determined by using the LITA technique [6,7] which measures the speed of sound within a region of the flow defined by the crossed laser beams. Figure 7 shows the raw data for a heated and unheated measurement using this technique. The frequency of the damped periodic waveform is proportional to the speed of sound and the temperature was calculated from the speed of sound, assuming an ideal gas. For these experiments only the temperature in the center of the flow was measured. Measurements of velocity were accomplished using laser induced breakdown of a localized region of the flow. This simple method involves measuring the displacement of the luminous laser created plasma over a short time period, typically 10 microseconds. The displacement during this time was used to calculate velocity.

Temporally resolved shadowgraph measurements of Mach number for the heated flow were made with a fast framing camera capable of storing a sequence of 32 frames. The time delay between frames was adjusted to capture the evolution of the heating process. The change in Mach angle was used to determine a change in Mach number. However, to calibrate these angles the unheated Mach number was determined from measurements of velocity and static temperature at the nozzle exit. These measurements were also used to determine the Mach number for limited number of times during the e-beam duration. These measurements were made at the center of the nozzle, at a distance of approximately 3 mm from the nozzle exit plane. Figure 8 is a plot of Mach angle versus time for both the shadowgraph and velocity temperature measurements, for approximately 50 kW of electron beam power passing into the exit plane of the nozzle. The Mach number decreased from Mach 3.9 to 3.2, and a steady state was reached within 400 to 500 μs. These results indicate that at least part of the e-beam energy is absorbed and collisionally relaxed on a timescale as fast as the transit time of the flow in the nozzle.

Piezo-electric pressure transducers were used to measure the pressure along the length of the nozzle. However, the signal produced by e-beam induced x-rays passing through the piezoelectric crystal was much greater than the expected rise in pressure due to e-beam heating.

The total enthalpy of the unheated flow was calculated from measurements of plenum temperature. The total enthalpy at the nozzle exit during e-beam heating was calculated from static temperature and velocity measured at a single point on the centerline of the nozzle exit. An average change in total enthalpy of 7% was calculated from measurements made with the 50 kW runs. This corresponds to an average change in total enthalpy of 20 kJ/kg, or 10 kW of absorbed power measured on the centerline of the flow for a flow rate of 0.5 kg/s. Figure 9 is a plot of power absorbed when the flow had reached steady state at 400 and 500 μs after the e-beam turn on. Each data point represents a single set of measurements for a single run of the wind tunnel and e-beam facility. The uncertainties for each run are primarily due to

uncertainties in the optical measurements of temperature (5%) and velocity (2%).

The measurements of total power deposited in the flow were compared with numerical simulations performed with the CYLTRAN module of the Integrated Tiger Series (ITS) code. For the low power case, the code predicts approximately 5 kW deposited into the flow and 46 kW into the nozzle wall. This is consistent with the uncertainty in our calculations from experiments that indicate 10 kW of absorbed power. It should also be noted that due to the Gaussian like electron beam profile, measurements of absorbed power will be higher on the centerline than the average power absorbed in the flow.

Due to limited experimental time only shadowgraph imaging was used for nozzle exit diagnostics in two higher power runs. For this power level, the Mach number determined from the Mach angle dropped from 3.9 to an approximate minimum of 2.3. An upper limit estimate of the change in total enthalpy and power absorbed can be determined from the Mach number measurements, assuming the velocity does not change significantly during energy addition. For the low power case this was a good approximation since the velocity changes by less than 2%. The decrease in Mach number to 2.3 corresponds to a temperature of 262 K for a velocity of 750 ms^{-1}. A change in total enthalpy of approximately 150 kJ/kg and 40 kW of absorbed power was calculated assuming that the e-beam power was localized and was only heating half the flow.

CYLTRAN simulations of power deposition for this high power case predict 57 kW of power absorbed into the flow, and 96 kW into the wall. As in the low power case, the prediction compares well with the results estimated from the measurements. However, in this case the e-beam was not centered in the nozzle and the measured power should be lower than the peak power, as we have found.

100 kW electron beam experiments

In the 10 kW electron beam experiments we have demonstrated that controlled stable energy addition can be produced, and measurements of temperature, velocity, and Mach number allowed some quantitative comparisons with models. However, interpretation of these measurements was limited by the inability to measure and control the electron beam power deposition leading to large uncertainties in the fraction of electron beam power deposited into the nozzle walls.

The 100 kW energy addition experiments were planned to address these issues, and equally importantly to increase the power level to 100 kW. The objectives of this experiment were to:

1) demonstrate e-beam heating at the 100 kW level as an important development towards the 10 – 100 MW power levels required for a missile scale facility.

2) measure flow uniformity whilst keeping the e-beam from the wall

3) measure concentrations of non-air species produced by e-beam ionization and dissociation.

To more fully characterize the flow, the following improvements to the 10 kW experiments were required:

1) focusing the electron beam more tightly into the nozzle to prevent energy loss to the walls.

2) measuring static pressure along the nozzle in the presence of x-rays.

3) measuring power input into the nozzle flow

4) determining change in enthalpy and power absorbed in the flow by measurements of density, temperature, velocity and Mach number at the nozzle exit.

The 100 kW experiment was similar to that described in the 10 kW experiments. The nozzle area ratio was the same as that used in the 10 kW e-beam experiment, but the diameter of the nozzle was increased to further reduce loss of e-beam power on the walls. In this process the nozzle throat was increased from 6 mm to 8 mm in size. This also increased the mass flow rate up to approximately 1 kg/s. For most runs plenum conditions of P_0 = 1500 psia and T_0 = 378 K were used. These conditions produce a pressure

matched flow when the flow is unheated. For some runs a higher plenum pressure of 1700 psi was used. The working gas used in all experiments was compressed air, which was supplied from a 140 000 SCF tube trailer. The higher capacity afforded by the trailer allowed experimentation for longer periods with constant plenum conditions.

Significant improvements to the beam transport were achieved over the 10 kW experiment. Instead of the direct line of sight transport of the beam from the accelerator to nozzle as employed in the first experiments, a bent solenoidal array of magnets was used. This bend minimized both the heat and pressure load on the foil by the stagnation of the nozzle gases, as well as significantly reducing the number and speed of particles impinging on the foil. This demonstration of beam transport is important for future experiments and will be required for a full scale facility. A 1.27 cm thick cast steel plate placed between the accelerator and the focusing and steering magnets was used to isolate the magnetic fields from the accelerator transport tube. This allowed more complete control of the electron beam within the accelerator. The relative locations of the magnets, Be foil, and steel plate were adjusted to maximize capture of the beam onto the field lines without undue heating of the foil. Figure 10a shows the bent solenoidal array for steering magnets with respect to the accelerator and nozzle. Figure 10b is a plot of the total magnetic field strength vs. axial distance from the accelerator to nozzle throat.

Beam Transport and Diagnostics

The CYLTRAN code was used to model the beam behavior, and the energy deposition in the nozzle flow and gas between the nozzle and accelerator. The primary prediction of importance is the amount of power deposited into the air within the nozzle during blowdown, as a function of distance from the throat (z), and radial distance from the axis (r).

In the absence of nozzle flow, the measurement of beam profile axial power is relatively simple and can be compared to the CYLTRAN code. The beam dimension was measured as a function of axial distance from the throat by observing e-beam fluorescence on a 0.15 mm sheet of Mylar. The agreement between the CYLTRAN code and the measured radii is reasonable and the average 1/e beam diameter between z=20 and z=50 cm was approximately 35% of the nozzle diameter.

The total beam current as a function of axial distance was measured by collecting charge at each z location with a carbon disk grounded through a 50 Ohm resistor. The voltage across the resistor was used to determine the beam current. This probe was calibrated against a commercial Pearson probe in separate measurements.

The current was found to decrease dramatically as the beam penetrates the nozzle. This is primarily due to reflection of the electrons by the converging magnetic field. A measurement of these reflected electrons was obtained by observing the e-beam fluorescence on the Mylar sheet at z=50 cm, with and without a carbon beamstop at z=45 cm. The image was observed to be 56% brighter without the beamstop, indicating that 56% of the beam entering the nozzle is reflected out. To dramatically decrease the amount of reflected electrons requires the cathode of the accelerator also to be placed in a solenoidal magnetic field that extends from the cathode to the nozzle throat. This is required to prevent the beam acquiring angular momentum as it enters the field of the nozzle.

A more direct method was used to measure the power in the electron beam at any specific location across the exit of the nozzle. The rise in temperature due to e-beam heating of the thermocouple was used to determine the power at radial locations across the nozzle exit. A Type-K thermocouple 1.5 mm in diameter was shielded on one side so that forward electrons could be distinguished from reflected electrons. The shield was made of copper with a 4.0 mm outer diameter and 0.76 mm wall thickness. This thickness was sufficient to stop 1 MeV electrons. The local beam power in the forward and backward direction is proportional to the temperature change, so the total beam power is proportional to a 2-D integral under the Gaussian curve. The ratio of this integral for the two curves is the ratio of the reflected beam power to the forward-going beam power. Specifically, the fraction of beam power reflected from within the

nozzle is 0.324 for the 717 keV beam, and 0.271 for the 884 keV beam with no flow.

Centerline temperature measurements during blowdown indicates that the reflected fraction is 0.28 for both voltages, which is in good agreement with the no flow measurements. So the no flow numbers were used to determine the fraction of power reflected out of the nozzle. The relative power deposition at the nozzle exit with and without blowdown was measured and the ratio (with/without) was 0.80 and 0.85for 717 kV and 884 kV, respectively. The total power deposited in the nozzle air during blowdown was calculated according to:

$$P_{NA} = \left(V_{acc} - V_{foil} - V_{st.air}\right) I_{acc} f_{I,n.ex} f_{P,fnf} (1 - f_{ref})$$

where V_{acc} is the beam voltage in the accelerator, V_{foil} is the voltage lost in the accelerator beryllium foil, $V_{st.air}$ is the voltage lost in stagnant air on the way to the nozzle exit, I_{acc} is the beam current in the accelerator, $f_{I,n.ex}$ is the fraction of total beam current making it to the nozzle exit in stagnant air, $f_{P.fnf}$ is the beam power fraction ration (flow/no-flow), and f_{refl} is the reflected power fraction at the nozzle exit.

Table 1 summarizes the various parameters and estimated uncertainties for the standard blowdown conditions used during the experiment. The uncertainties were estimated from reproducibility and goodness of fit. In general, the power deposited in the nozzle air has an uncertainty of about 15%.

Flow diagnostics and results

The electron beam heated flow experiments were performed at the conditions summarized in table 1. Modeling and prediction of the energy addition process has to date been performed for the 26 kW and 55 kW power levels.

The primary aim of the flow diagnostics is to determine the change in total enthalpy, and the power absorbed. The power absorbed in the flow can be determined by the difference between the total power of the flow with and without heating. This is calculated from the total enthalpy and mass flux in each case. Formally this is written as:

$$\dot{q} = \iint \left[\rho_h v_h (c_p T_h + \tfrac{1}{2} v_h^2) - \rho_u v_u (c_p T_u + \tfrac{1}{2} v_u^2) \right] dA \quad (1)$$

where ρ is the density, v the velocity, and T the temperature at each area element. The subscripts h and u refer to heated and unheated flow properties. C_p is the specific heat of air at constant pressure.

Two dimensional axisymmetric CFD calculations of the heated flow were used to make a number of simplifications which allow us to determine the change in total enthalpy and power more simply with little loss in accuracy. A discussion of these calculations is provided elsewhere[4]. The results of these calculations show that for the 26 kW and 55 kW cases most of the change in total enthalpy is due to the change in static enthalpy (C_pT) rather than in the kinetic energy per unit mass ($1/2\ v^2$) component of the total enthalpy. In fact calculations show that $1/2(v_h^2 - v_u^2)$ was less than 2 % of $Cp(T_h - T_u)$. The above holds even though most of the total enthalpy at the exit is contained in the kinetic energy per unit mass. A further simplification shows that the velocity changes are negligible for these two cases. With these simplifications the total power absorbed by the flow is given by:

$$\dot{q} = \int \frac{v C_p (p_h - p_u)}{R} dA$$

Since the pressure is essentially constant across the nozzle exit the power added to the flow is given simply by:

$$\dot{q} = \frac{c_p \Delta p v A}{R}$$

where Δp is the pressure difference between the heated flow and unheated flow, which is constant across the flow, A is the flow area at the exit. Using the same assumptions that were used in the power calculation, the total enthalpy distribution can be determined from a simultaneous measurement of pressure and the radial density distribution. The change in total

enthalpy at each radial location can then be calculated from:

$$\Delta h = \frac{c_p}{R}\left(\frac{p_h}{\rho_h} - \frac{p_u}{\rho_u}\right)$$

Although the pressure is constant across the flow, a radial measurement of density is required to determine the change in enthalpy across the flow.

From the above equations, the power absorbed by the flow and the total enthalpy distribution can be determined by measurements of velocity, density and pressure with and without e-beam heating. Measurement of static temperature could also be used in conjunction with pressure to determine density.

The radial change in total enthalpy was determined for each power level from the calculated radial temperature under the assumption that almost all the change in total enthalpy was due to the change in static enthalpy. Radial changes in the static enthalpy were determined by subtracting the static enthalpy of the unheated flow at each radial location from the unheated values at the same location. A Gaussian curve was fitted to the derived total enthalpy and is shown in figure 11. Only the central part of the total enthalpy profile was used in the fit because we could not measure the pressure distribution in the outer regions of the flow where, because the flow is not pressure matched there is a local radial gradient in pressure. The full widths at half maximum of the total enthalpy curves are approximately equal to the e-beam width, as measured by the thermocouple survey and mylar fluorescence.

Velocity was measured using the laser induced breakdown method as described in the 10 kW e-beam energy addition experiments. In the 100 kW tests the velocity was measured in two locations of the flow at each power level. A measurement on the centerline and another at a radial distance of 5 to 6mm mm showed that the velocity did not change significantly across the flow. For all power levels the velocity was found to be essentially constant across the flow and not significantly different from thew unheated case, within the accuracy of the measurement (5%). A small variation in radial velocity was predicted by the calculations and justifies the constant velocity approximation that was used to determine the absorbed power in the flow. An average velocity of 770 m/s was measured for the 25 kW, 55 kW, 73 kW and 90 kW power levels.

The amount of power absorbed in the flow was determined by the static pressure rise at the nozzle exit and the velocity. Figure 12 shows plots of the power input into the flow versus power absorbed by the flow, for the five power levels used in this experiment. The straight line in the graph corresponds to complete thermalization. The uncertainties in absorbed power are calculated from the uncertainties in the static pressure and the velocity measurements. The most significant contribution to this uncertainty is the uncertainty in pressure. Within the uncertainties of the measurement all power levels except the 73 kW case appear to thermalize.

In order to provide a complete understanding of the heated flow we chose to measure static temperature, pressure, velocity, and density at the nozzle exit, and static pressure along the nozzle profile. Mach number was determined from Pitot pressure measurements and static pressure at the last pressure tap. The flow was also imaged using fast shadowgraph imaging.

The static pressure along the nozzle was measured at five locations, including the nozzle exit, using fiber optic pressure transducers. These transducers (Optrand Corp.) allowed measurements of static pressure in the presence of x-rays produced by the e-beam. The response time of these transducers is approximately 100 μs. However, the small (0.5 mm) dimensions of the pressure taps and the time for the flow to reach steady state combined to give a response time of 800 μs for the 26 kW cases. In all other higher energy experiments the pressure did not come to steady state. For this data, steady state pressure values were determined from extrapolations from a non-linear least squares fit using the function:

$$y = y_0 + a(1 - e^{-(x-x_c)/\tau})$$

The use of this function was validated by a fit to the 26 kW data that comes to steady state during

its 2.0 ms heating duration. Multiple fits showed that the average value obtained was close to the actual value at steady state. An example of one of these fits is given in figure 13a. The time constant τ determined for each power level is different because the beam penetrates deeper into the flow for higher powers. Figure 13b is a fit to the 55 kW data where the pressure does not come to steady state. In such cases, the pressure must be extrapolated from the fit. An average pressure rise for each power level was calculated using data from multiple runs, each at the same nominal power conditions.

Figure 14 shows the static pressure distribution along the nozzle obtained at the 26 kW and 55 kW power levels compared with calculations. In each case, the pressure is lower than calculated, and the uncertainties for each point are the standard deviations calculated from approximately ten separate experiments at this power level. Only the last pressure tap measurement is shown at the 55 kW power level At this location the orifice diameter of this pressure tap was extended to increase its time response. Other data were recorded at input power levels of 75 kW, 90 kW, and 112 kW, and pressure rises of 5.0 psi, 6.9 psi, 8.4 psi were measured at the last pressure tap for each of these cases. The steady state pressure could not at the other pressure taps upstream because of their slower response time.

The 10 kW e-beam experiments used laser induced thermal acoustics (LITA) to measure the static temperature at the center of the flow. However, due to the rapid variation of the radial heating profile strong frequency dispersion in the LITA signal was observed. Because of the non-uniform temperature profile point measurements of static temperature using LITA were abandoned in favor of determining the temperature from simultaneous density and pressure measurements.

Density at the exit plane of the nozzle was measured using single laser pulse Rayleigh scattering. The density is directly proportional to the scattered light. The second harmonic output of a Nd:YAG laser at a wavelength of 532 nm was chosen rather than the ArF laser operating at 193 nm to avoid spectral interference with potential molecular absorption and fluorescence in the ultraviolet, particularly from NO and excited N_2. For most measurements the laser beam was formed into a line and directed across the nozzle exit, approximately 5 mm from the exit. Line excitation was used instead of sheet illumination to maximize the signal to noise ratio. Planar images using sheet illumination in the x-r plane were also taken to give a better idea of flow uniformity along the axial direction. Figure 15a and 15b are images of the unheated flow and the heated flow at 90 kW using sheet illumination. The uniform luminosity of the central core of the flow indicates a constant density as expected in the unheated case. The lower density, higher temperature boundary layer can be seen at the edge of the high intensity central core flow. The 90 kW image shows a large reduction in intensity at the center of the flow, indicating a large reduction in density in this region, and a concomitant increase in temperature. The density increases on either side of this centrally heated core, to values above the unheated case at the same location. The most striking feature revealed by these images was the large asymmetry in density either side of the core flow. Other runs at these conditions showed significant image-to-image variation in this region, indicating unsteady flow in the outer part of the flow close to the boundary layer.

Line Rayleigh scattering images were converted to radial density profiles for each power level. These images are similar to those shown in figure 15, except the width of the laser was decreased in the axial direction using a long focal length lens (1.0 m). To convert these images to density they must be normalized for variation in laser intensity and camera response. Normalizing images were recorded by capturing the Rayleigh scattered light from the uniform density room air at the nozzle exit. The non-zero background in each image due to dark charge and light scattered from surfaces is also recorded in each image. This was subtracted from the Rayleigh images of the flow and the normalizing images. To convert signal intensity to density, the temperature of the static air adjacent to the nozzle flow was measured, and using the local atmospheric pressure, the density was calculated from the ideal gas equation of state. This calibration region was recorded in each Rayleigh scattering imaged and served as a density calibration point for each image. To convert the density images to density profiles, the images

were summed in the axial (r) direction. Figure 16 are graphs of calibrated density measured across the exit of the flow. These were derived from the single shot Rayleigh line images using the procedure described above. For comparison the calculated density profile is shown for the 26 kW and 55 kW cases. Reasonable agreement between the measured density and the calculated values are found. However, the calculated density is lower in the center of the flow and higher near the boundary layer. This disagreement may be connected to the fact that the inviscid energy addition calculations do not include the boundary layer, even though as shown in figure 15a and 15b this region of the flow is clearly perturbed by the heating process. We determined during experimentation that the beam was not centered at the nozzle exit. This alignment, which was difficult to achieve, was found to vary with accelerator voltage. It was measured to be off axis by up to 2 mm from the centerline. Although the beam was not centered at the exit it may have been centered deeper within the nozzle. A non-centered beam implies that the centerline density measurements would be higher by ~10% than the true centerline value, assuming a Gaussian profile with a 1/e density diameter of ~10 mm. The difference between the experimental and predicted values is approximately 20% higher than the measured value. However, if misalignment were the only reason for the disparity between the measurements and calculations, the density in the outer regions of the flow would be approach the value for prediction and experiment. Because this is not the case we believe misalignment is not the only reason for the observed discrepancy. An uncertainty of 0.3 kg/m^3 in the density measurements was determined from the spread in density measured from multiple unheated flow measurements at the same nominal plenum conditions.

Static temperature at the nozzle exit was determined from the density measurements and the static pressure measurements at the pressure tap closest to the nozzle exit. The ideal gas equation of state was used to relate the pressure and density to the temperature. Figure 17 contains the radial temperature profile calculated for the 26 kW and 55 kW cases, as well as the corresponding values determined from numerical simulations. The estimated uncertainty derived from the uncertainties in the pressure and density is included with each plot. The temperatures derived from the measurements are lower than the calculated values and probably stem from the differences in density as discussed above.

Mach number was determined from Pitot pressure and static pressure measurements. Static exit pressure was measured at the tap closest to the nozzle exit. The Pitot probe was mounted on a x-y translation stage so that a radial survey could be taken at each power level. These measurements were performed for the 26 kW, 55 kW, 73 kW and 90 kW power levels. Figures 18a and 18b show the measured and calculated radial variation in Mach number across the nozzle exit flow for the 26 kW and 55 kW input into the nozzle. In order to estimate the uncertainty in these series of measurements the procedure was also carried out for the unheated flow. These values are shown in figure 18 and follow the trend indicated by the calculated values. The scatter in the measurements of constant Mach number across the unheated flow gives an uncertainty of 0.05. The calculations predict the width of the Mach number profile increases with power, as well as the drop in Mach number on the centerline. The most obvious difference between the data and calculations is the apparent radial offset of the data with respect to the calculated values. This is probably due to the non-centered alignment of the electron beam into the nozzle. When the data is translated by approximately 2 mm to account for beam misalignment a better overlap between the data and calculations is found. This offset was not readily observable in the density measurements because these were made in a plane perpendicular to the Pitot measurements. Part of the electron beam entering the nozzle was blocked by the Pitot probe as it is was translated across the flow. The maximum power blocked was estimated to be approximately 10% of the total power input into the nozzle assuming a Gaussian 1/e e-beam diameter of 10 mm blocked by a 2mm wide probe.

As in the 10 kW measurements, time resolved shadowgraphs of the unheated flow were recorded for the 26 kW, 55 kW, 73 kW and 90 kW cases. Figures 19a and 19b show two images which are part of a 32 frame time-sequence, each is integrated over 10 μs, and the time between each frame is 50 μs. Figure 19a is the first image of this sequence that was

recorded 100 μs prior to the e-beam turn-on. Figure 19b is the 23rd frame of the sequence and was recorded 1 ms after e-beam turn on. The heated flow appears to have reached steady state in the 1 ms e-beam heating duration. The Mach number was calculated from the change in Mach angle at the center of the flow. The heated Mach number of 2.1 is in good agreement with the value of 2.0 at this power level determined from the Pitot pressure survey measurements. The Mach angle is curved across the flow in contrast to the straight line observed in the unheated case. This is due the non-uniform heating profile and agrees with the measurements of Mach number obtained using the Pitot probe and static pressure. For all power levels a steady increase to steady state was observed. The shadowgraph measurements, which are sensitive to the second spatial derivative in density, did not have the sensitivity to observe the unsteadiness in the outer parts of the flow found in the Rayleigh scattered measurements.

For e-beam energy addition, ionization and dissociation create non-air species. Nitric oxide and ozone are two radicals that are produced by the passage of an e-beam through air. Both absorption and laser induced fluorescence techniques were used to measure the concentration of NO. Both NO absorption spectroscopy and laser induced fluorescence are well developed techniques for NO detection. Whilst NO fluorescence is a sensitive technique, absorption was used to provide a more quantitative estimate of NO concentration. For the NO absorption measurements a high pressure xenon arc lamp was used as an intense source of continuum radiation in the 200 to 250 nm spectral region that overlaps the A-X electronic transition in NO. To maximize the sensitivity of this technique a three pass absorption length through the flow was employed, and corresponds to approximately 3 cm. In this optically thin regime, the concentration of NO is proportional to the reduction in intensity of the lamp light as it is passed three times through the flow during the energy addition period. No reduction in intensity was observed at any of the power levels used in the experiment. Although the exact NO concentration could not be determined from these measurements, an upper bound can be inferred from the sensitivity of the measurement of intensity. Using the temperature and density measurements an upper bound of 200 ppm or 0.02 % of NO was determined. An ArF laser emitting at 193 nm was used to excite the X-B, X-D electronic bands of NO. A 193 nm mirror was used as a reflective filter to discriminate against Rayleigh scattered light. A faint signal was detected in the center of the flow where heating was maximal. Because 200 ppm is easily seen using fluorescence experiments it is probable that the concentration of NO is much less than the upper bound of 200 ppm. Even this level is a trace concentration and would not be expected to significantly affect flow chemistry or aero-optical experiments.

Conclusions

The results of three energy addition experiments have been presented and in each case stable, controlled energy addition has been demonstrated. The experience gained in each experiment has allowed us to build a suite of computational and diagnostic techniques that can been used together to characterize the radiatively heated flow. The new techniques that have been developed at these modest power levels will be used in the large scale experiments. The last two experiments described in this paper have focused on the study and development of electron beam energy addition. We have determined that the power coupled into the flow was thermalized up to a maximum value of approximately 100 kW used in this experiment. Through the measurements and analysis of electron beam transport we have developed the tools to determine how much energy was deposited into the flow, including the deleterious effects of magnetic reflection that reduced the amount of power absorbed. The absence of measurable NO concentration in the flow suggests that good flow quality can be maintained with e-beam heating.
At the highest power levels (75 kW, 95 kW and 112 kW) used, the flow in the unheated annulus around the heated central core appeared to be unsteady even though the central region was measured to be stable. This effect is created by the non-uniform heating profile which forces mass to move into this annulus and away from the central heated core of the flow. A more detailed study of the effects of non-uniform

radial heating must be addressed in future experiments.

Acknowledgements

This work was sponsored by the U.S. Air Force Arnold Engineering Development Center (AEDC) and conducted through the Department of Energy (DOE)-National Energy Technology Laboratory at the Western Environmental Technology Office under DOE Contract Number DE-AC22-96EW96405.

References

1. Radiatively Driven Hypersonic Wind Tunnel, R. Miles, G. Brown, W. Lempert, R. Yetter, G. Williams, S. Bogdonoff, AIAA Journal, **33**, 1463, (1995)

2. The fluid mechanics of a radiatively driven wind-tunnel: Predictions and experiment, G.L. Brown, R.W. Anderson, A.E. Morgan, P.F. Barker, R.J. Lipinski and R.B. Miles, AIAA 29th Plasmadynamics and lasers conference, AIAA-98-2747, July 15-18, (1998)

3. Energy addition mechanisms for radiatively-driven wind tunnel: Predictions & experiments, Richard Miles and Garry Brown, AIAA 29th Plasmadynamics and lasers conference, AIAA-98-2747, July 15-18, (1998)

4. Performance models and predictions for the RDHWT/MARIAH II hypersonic wind tunnel, R. Anderson, G. Brown, 21st AIAA Aerodynamic Measurement Technology and Ground Testing Conference, June 19-22, (2000)

5. Numerical simulation and design of a radiatively driven hypersonic wind tunnel, R. Anderson, PhD Dissertation, Department of Mechanical and Aerospace Engineering, Princeton University, (2000)

6. E.B. Cummings, Optics Letters, **19**, 1361, (1994)

7. Single-pulse temperature measurement in supersonic air flow with predissociated laser-induced thermal gratings, P.F. Barker, J.H. Grinstead, R.B. Miles, Optics Communications, **168**, 177, (1999)

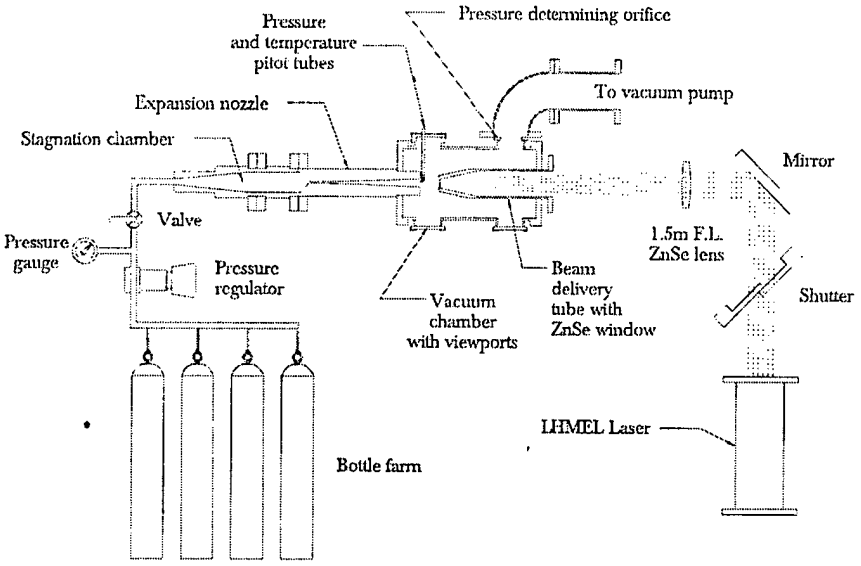

Figure 1. Diagram of the experimenal setup for the 10 kW laser experiments.

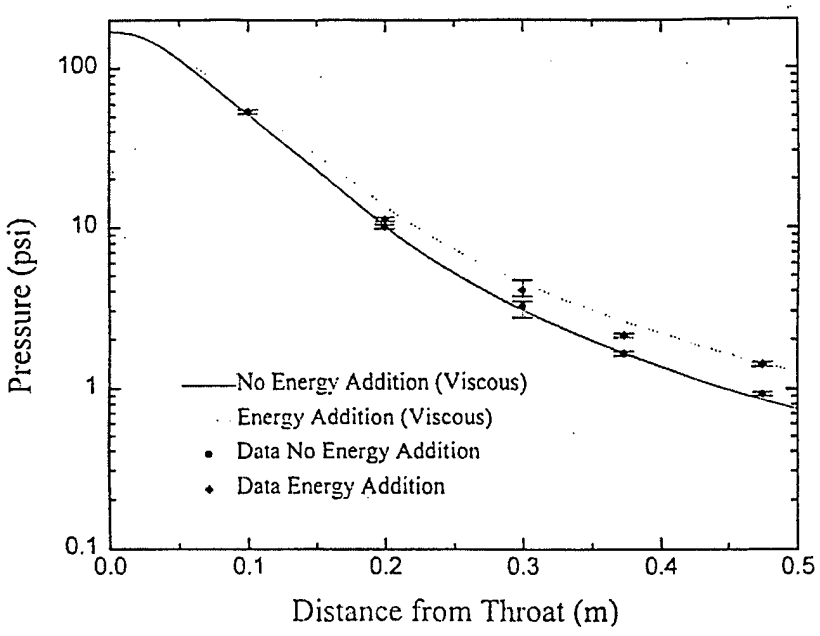

Figure 2. A comparison between measured and calculated static pressure along the nozzle with and without energy addition.

Figure 3a. Shadowgraph of flow around pitot pressure and total temperature probe at the nozzle exit with no energy addition. Flow is from right to left.

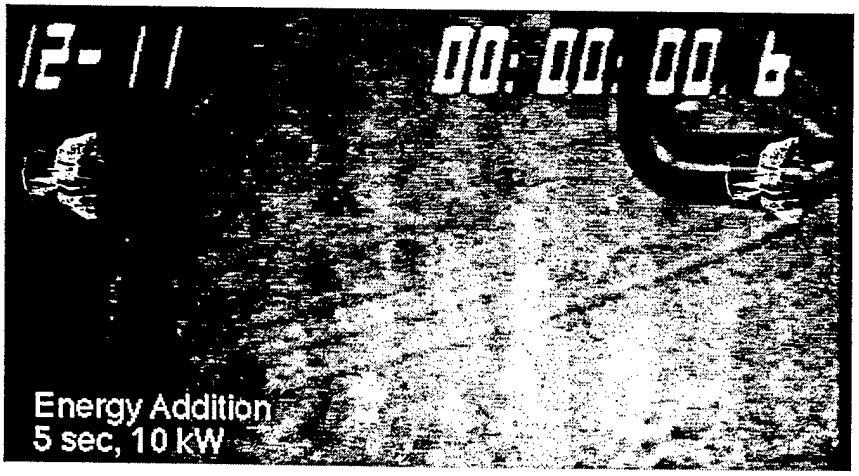

Figure 3b. Shadowgraph of flow around pitot pressure and total temperature probe at the nozzle exit with energy addition. Flow is again from right to left. A comparison between the Mach angle of Figures 7.4a and 7.4b shows a decrease in Mach number from 4.3 to 3.9.

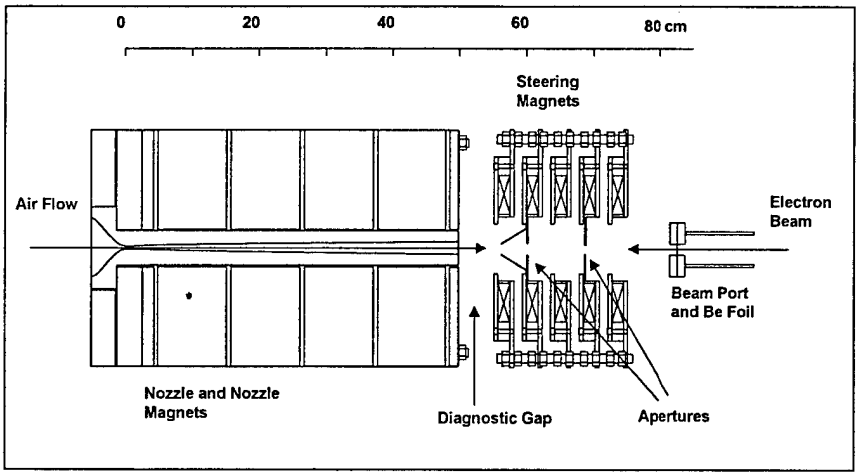

Figure 4a. Configuration of the magnets with respect to the nozzle and beam port of the accelerator.

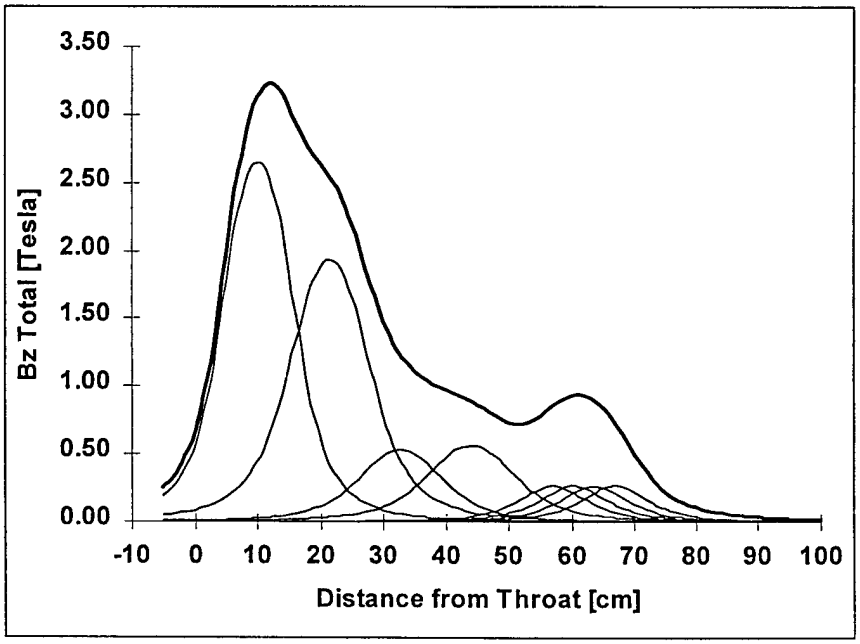

Figure 4b. The magnetic fields calculated for each magnet as well as total field (solid line)due to each magnet.

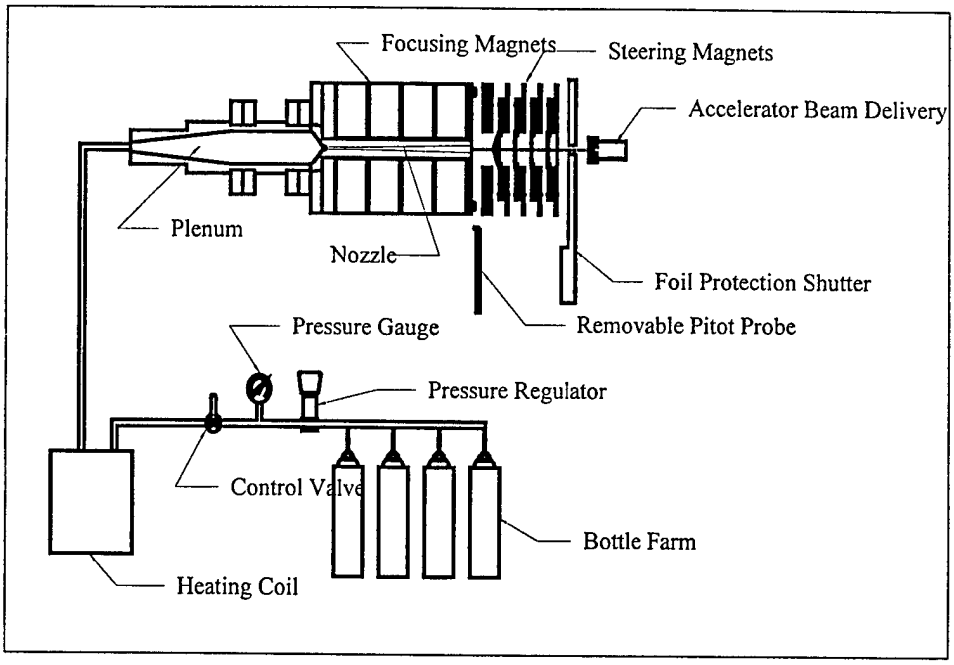

Figure 5. A diagram of the 10 kw scale electron beam energy addition experiment.

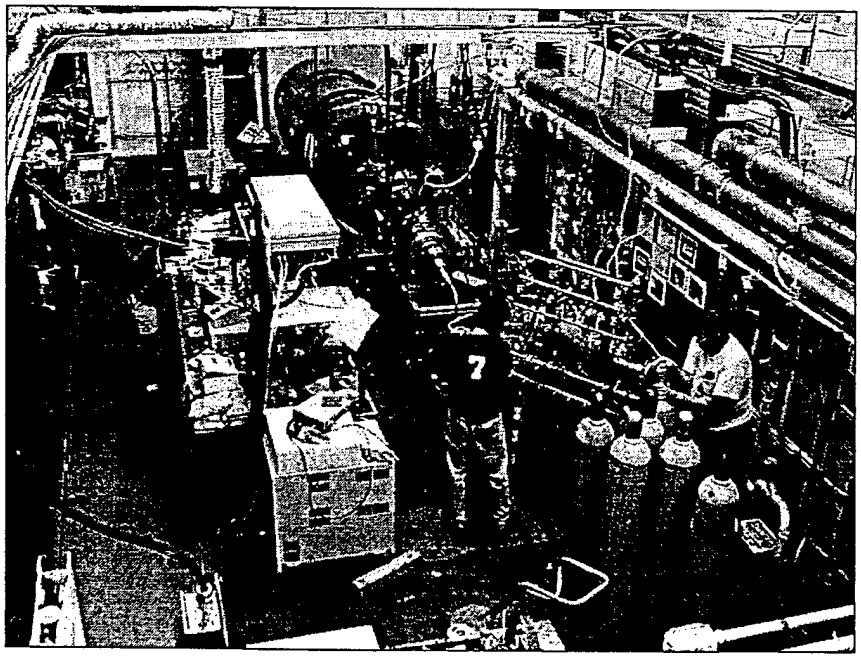

Figure 6. A photograph of the 10 kW scale electron beam experiment including the 1 MeV Hawk accelerator (blue cylinder in background), the nozzle and magnets, and the gas manifold system in the foreground. The laser systems used for diagnostics are at the left of the photograph.

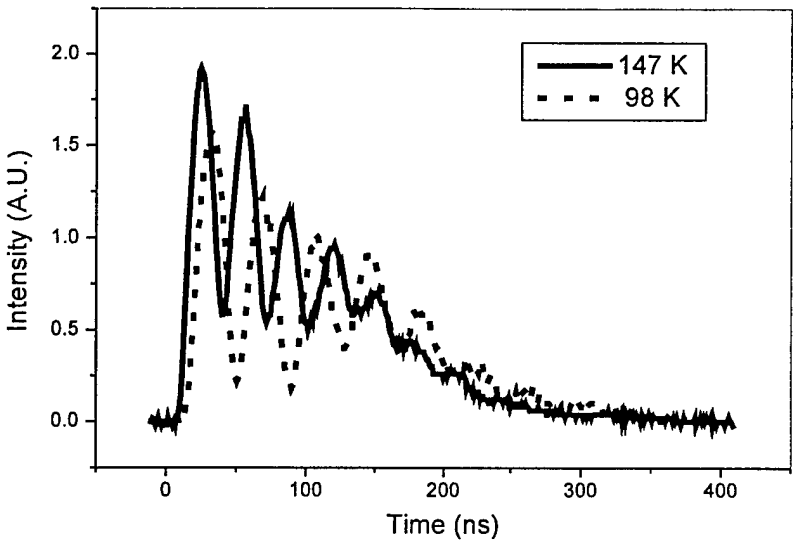

Figure 7. LITA signals used to determine static temperature in the nozzle flow.

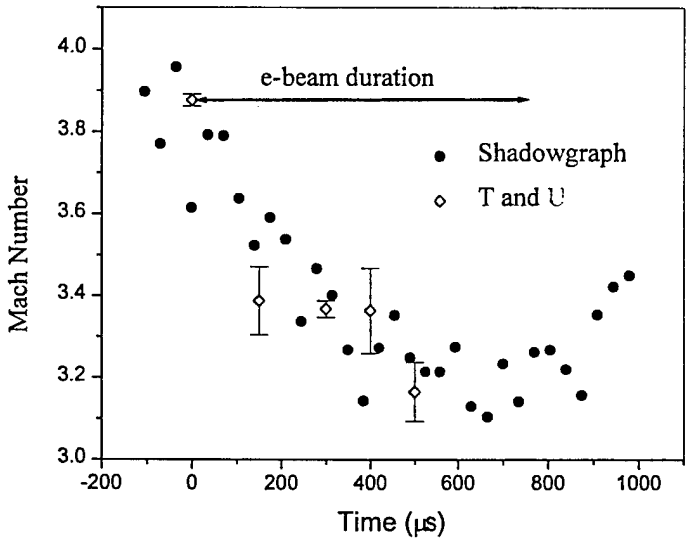

Figure 8. Comparison of Mach number calculated from shadowgraph Mach angle and average values calculated from velocity and temperature measured at nozzle exit.

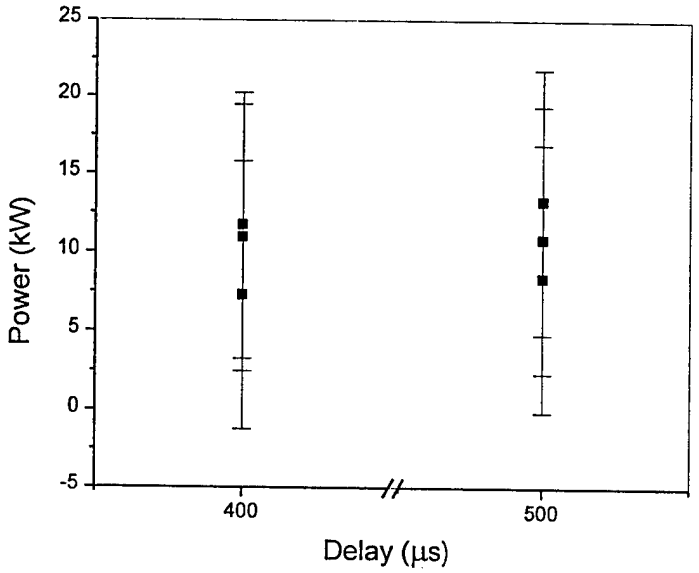

Figure 9 Power absorbed when the flow had reached steady state at 400 and 500 μs after e-beam turn on. Each data point represents a single set of measurements for a single run of the wind tunnel and e-beam facility.

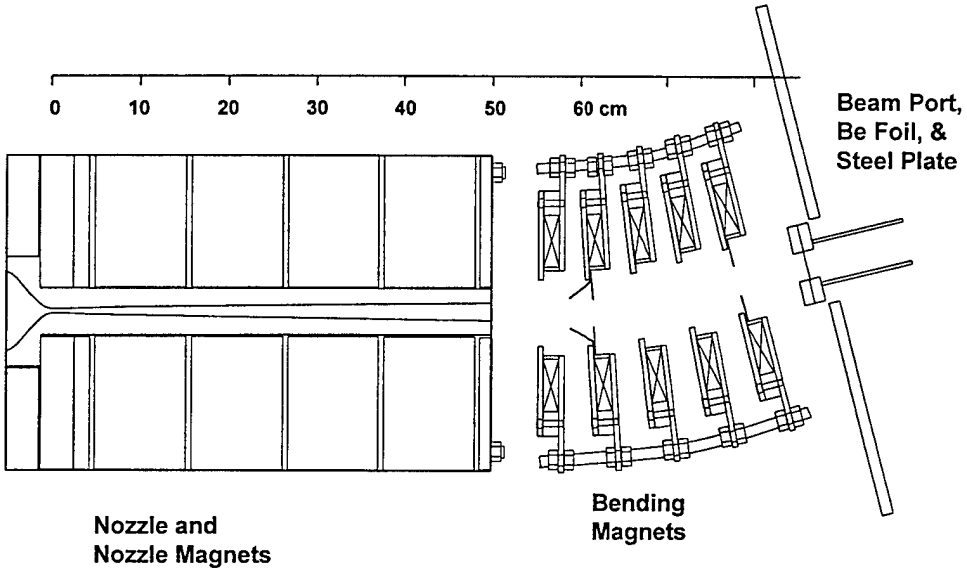

Figure 10a. Configuration of the magnets, nozzle, plate, and Be foil. The electron beam propagates through the Be foil and is bent by the steering magnets into the nozzle. The solenoidal magnets around the nozzle focus the beam into the nozzle as it converges downstream.

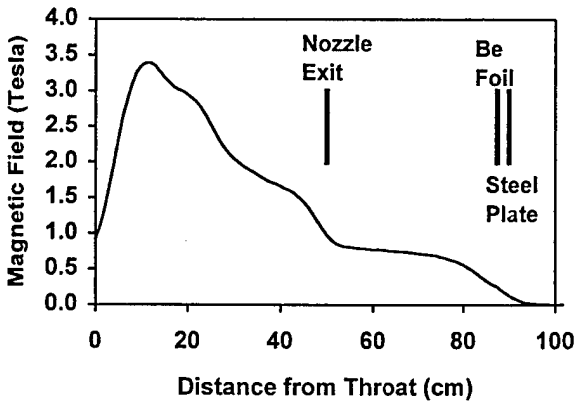

Figure 10b. Magnetic field strength vs. distance from the nozzle throat showing the location of the Be foil at the end of the accelerator, the steel plate and the nozzle exit.

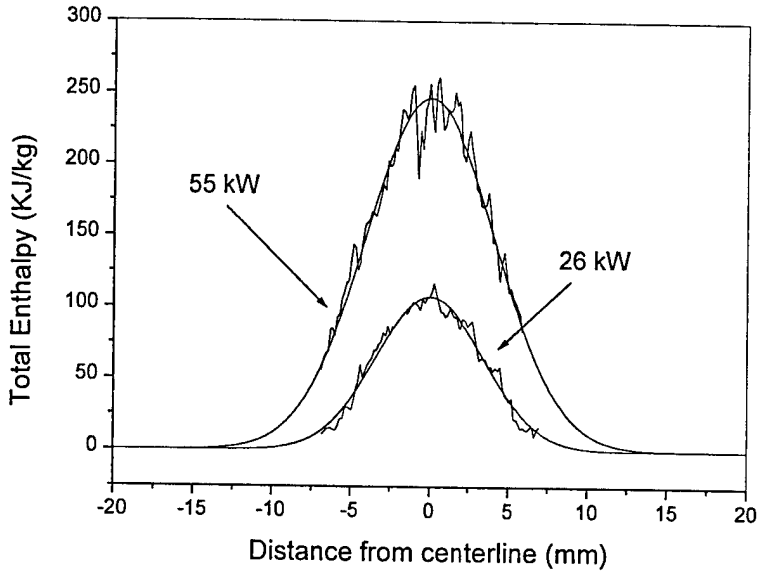

Figure 11. Radial change in total enthalpy for the 26 kW and 55 kW power input into the nozzle. A Gaussian is fit to the data.

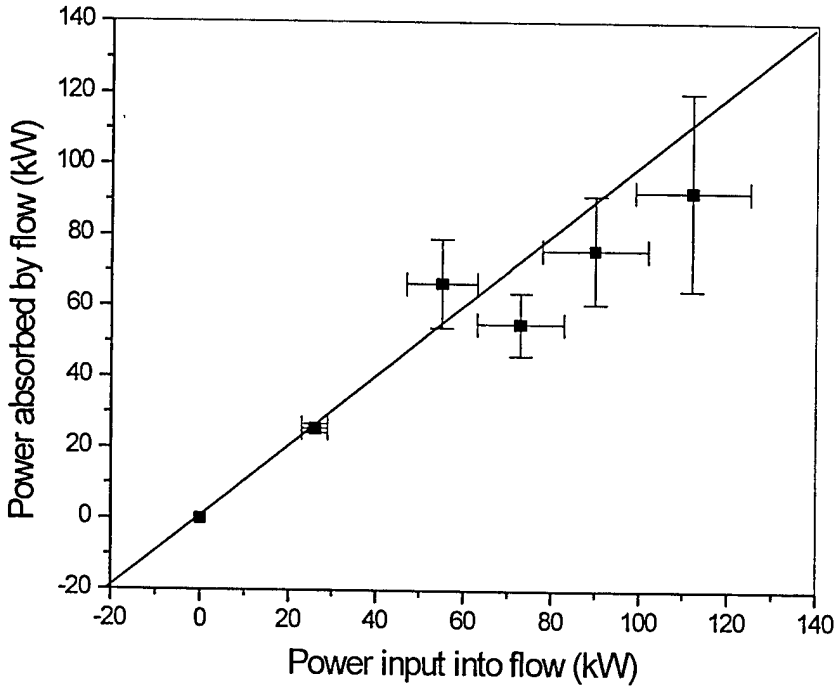

Figure 12. Power absorbed in the flow calculated from flow properties versus power input into the nozzle determined from beam power measurements.

Table 1. Summary of the electron beam parameters and power introduced into the nozzle used during the 100 kW electron beam experiment.

Total beam voltage (kV)	668	677	827	831	833	832
Foil Pearson current (mA)	200	400	300	370	460	400
Beam duration (ms)	2.4	1.2	1.5	1.2	0.8	1.0
Plenum pressure (psia)	1500	1500	1500	1750	1750	1750
Air exit temp, unheated (K)	90	90	90	90	90	90
Ave beam diam in bending magnets (cm)	1.3	1.3	1.3	1.3	1.3	1.3
Ratio of power into nozzle, flow/noflow	0.80	0.80	0.85	0.85	0.85	0.85
Ratio of power at nozzle, reflected/forward	0.32	0.32	0.27	0.27	0.27	0.27
Total beam power (kW)	134	271	248	308	383	333
Power entering nozzle, no flow (kW)	48	101	117	145	181	178
Power entering nozzle, blowdown (kW)	39	80	100	124	154	151
Beam power leaving nozzle (kW)	12	26	27	33	42	41
Beam power deposited in nozzle air (kW)	**26**	**55**	**73**	**90**	**112**	**110**
1-sig uncertainty in deposited power	**14%**	**14%**	**13%**	**13%**	**13%**	**12%**

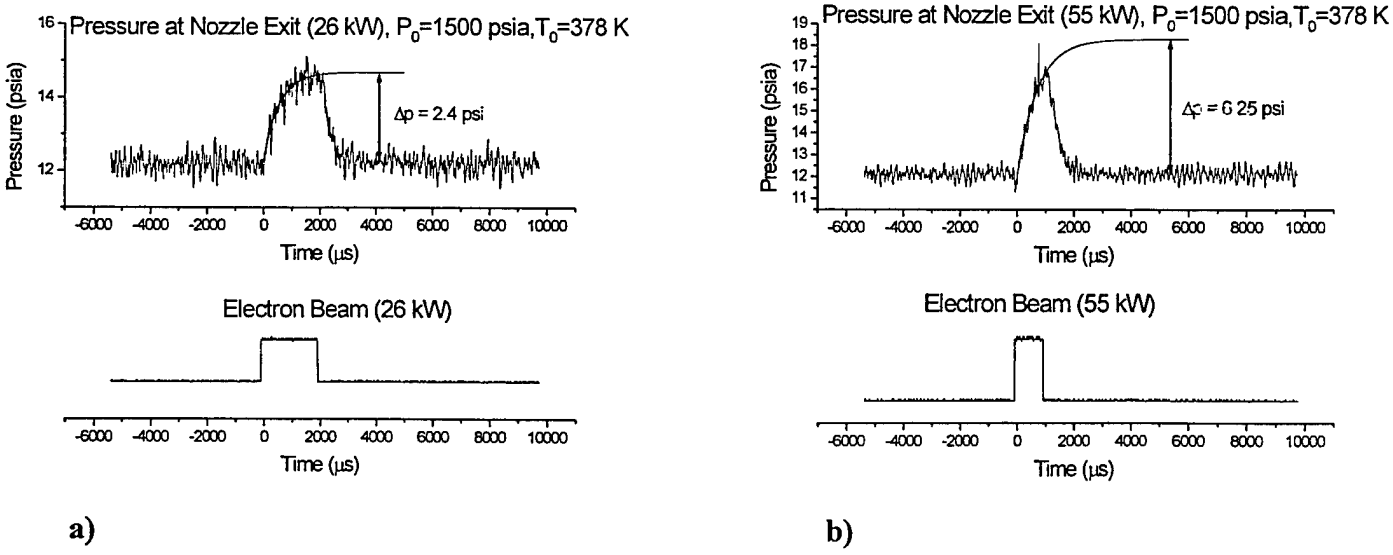

Figure 13. Pressure traces during e-beam energy addition on the last pressure tap nearest the nozzle exit for the a) 26 kW nad 55 kW power levels. The extrapolated pressure determined from each fit is also indicated.

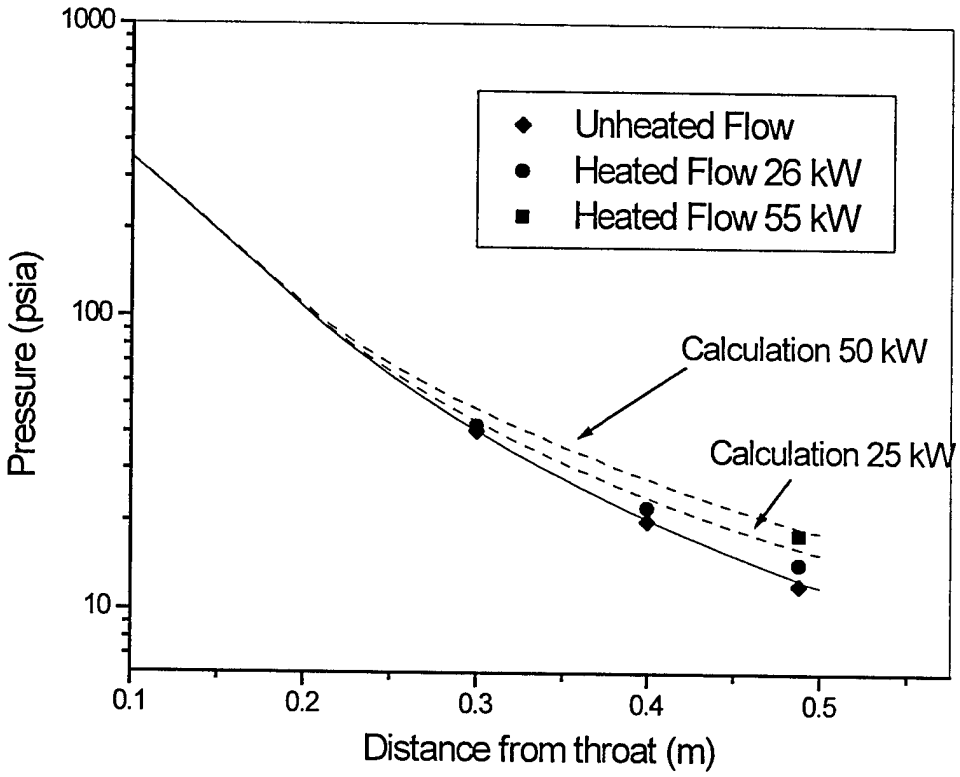

Figure 14. A comparison of measured static pressure for the 26 kW and 55 kW with the calculated values along the nozzle.

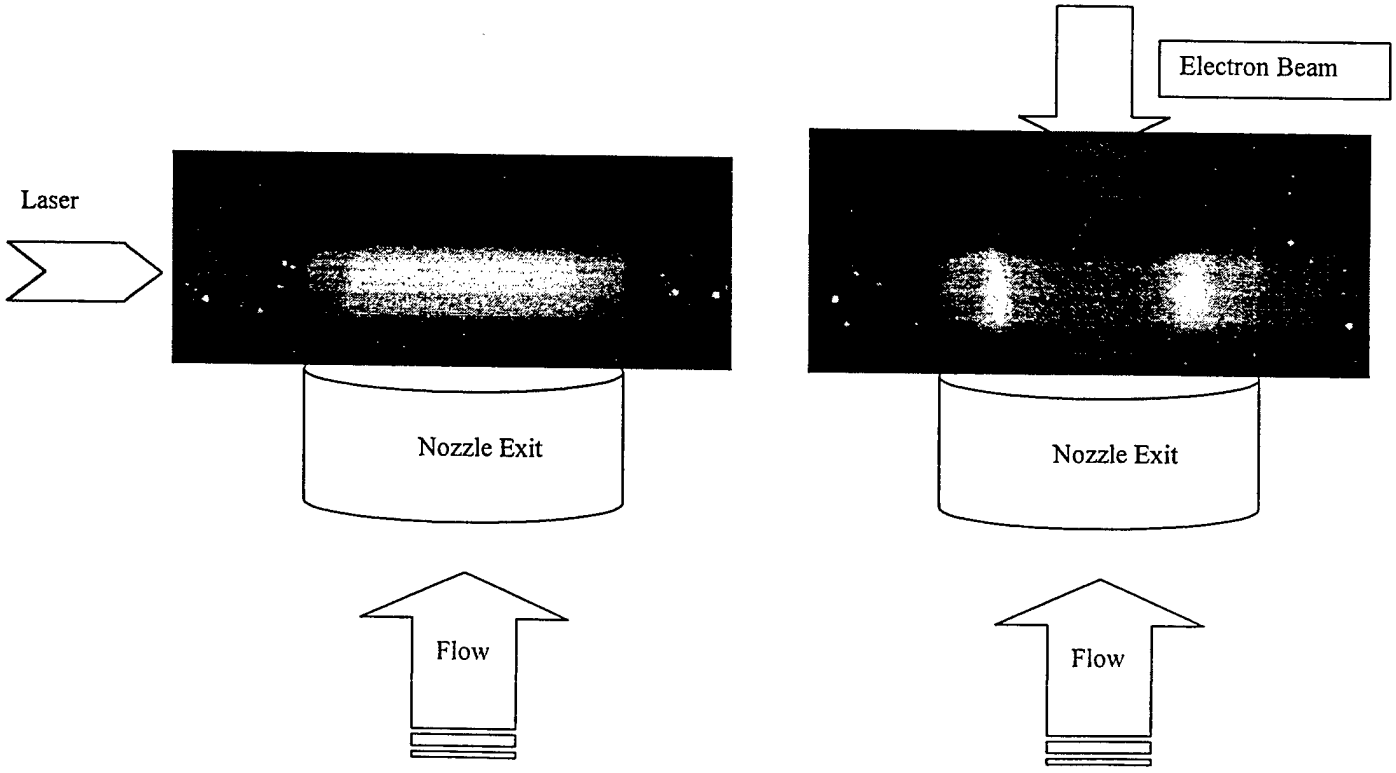

Figure 15. Rayleigh scattering images of the flow, a) unheated b) heated with 90 kW. P_0 = 1770 psia, T_0=378 K

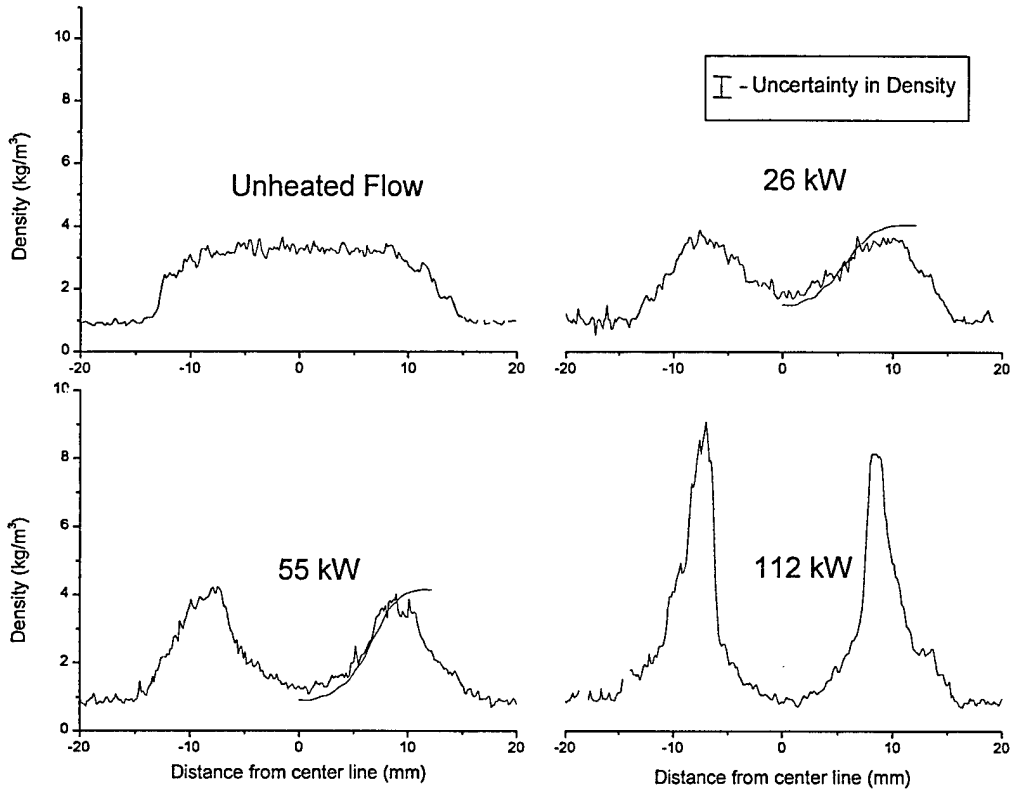

Figure 16. Density profiles at the nozzle exit derived from line Rayleigh scattering images for different powers input into the nozzle.

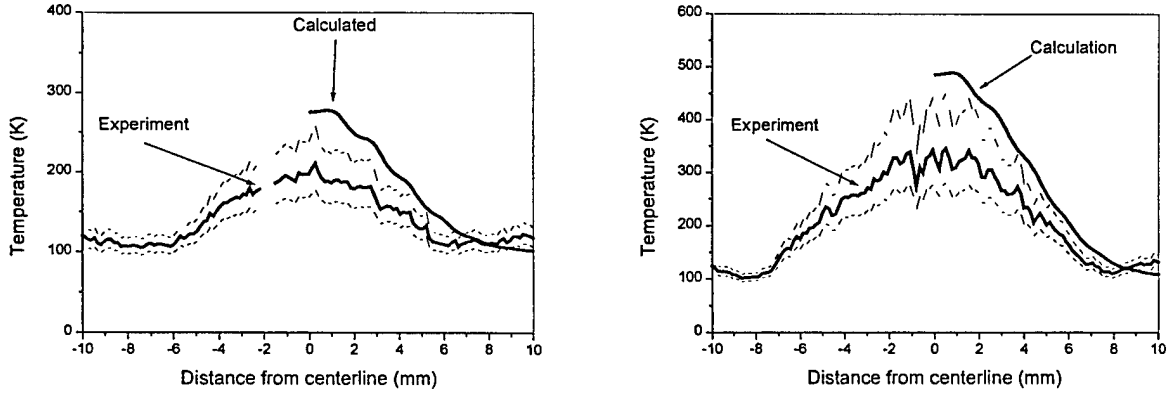

Figure 17. Nozzle exit temperatures determine from the static pressure and density for 26 kW and 55 kW. For comparison the calculated temperature profiles for these power levels are included.

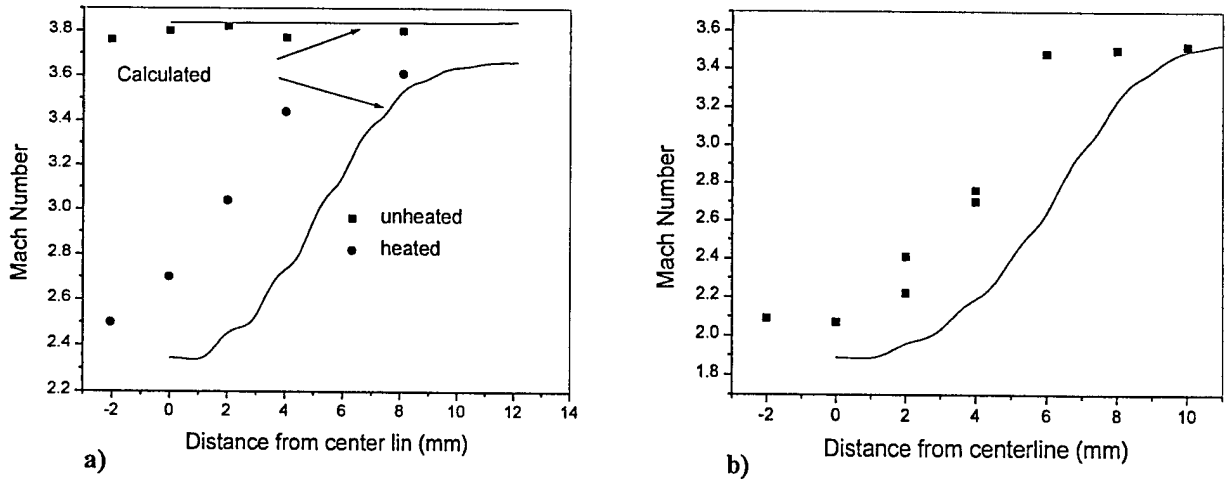

Figure 18. Mach number profile across measured across the exit plane for the 26 kW and 55 kW power levels. The Mach number was determined from the Pitot pressure and static pressure.

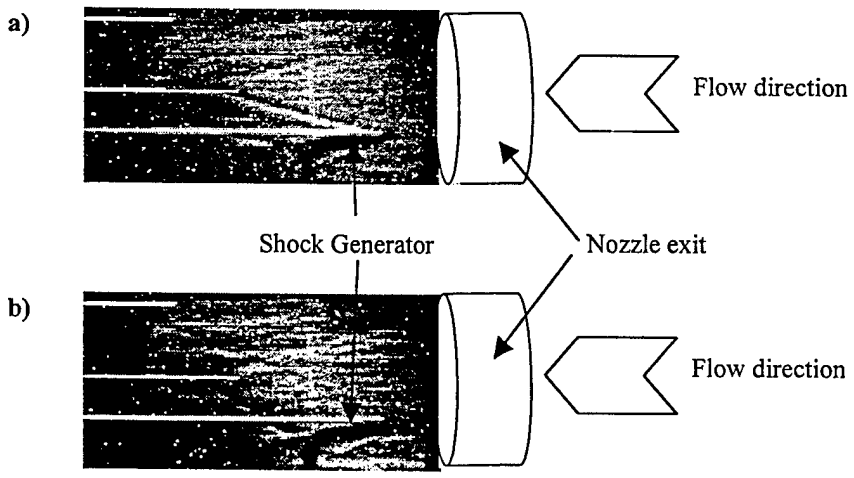

Figure 19. Shadowgraph images of the a) unheated an b) heated flow. Approximately 90 kW of e-beam power was input into the nozzle for the heated case.

AIAA 2000–2274

Performance Models and Predictions for the RDHWT/MARIAH II Hypersonic Wind Tunnel

R. W. Anderson, G. L. Brown, and R.B. Miles
Princeton University, Princeton, NJ 08540

21st AIAA Aerodynamic Measurement Technology and Ground Testing Conference
June 19–22, 2000/Denver, CO

Performance Models and Predictions for the RDHWT/MARIAH II Hypersonic Wind Tunnel

R. W. Anderson,* G. L. Brown, † and R.B. Miles ‡
Princeton University, Princeton, NJ 08540

The radiatively driven hypersonic wind tunnel is a new concept for extending hypersonic ground testing capabilities to higher Mach numbers while maintaining true flight conditions. A suite of numerical models which range in complexity from pure thermodynamics to the solution of fully coupled, time-dependent, Reynolds-Averaged Navier-Stokes equations with radiative models has been developed in support of the development of the RDHWT concept. This suite of models has facilitated insights central to the current development status of the concept. The current state of the modeling effort is discussed and the main results and insights obtained from these models is summarized.

Nomenclature

$\mathcal{I}$	Design objective function
α	Design objective weighting factor
α_0	Laser absorption coefficient
β_M	Design objective weighting factor
β_T	Design objective weighting factor
δ_L	Laser beam width
c_0	Nominal speed of sound
M_q	Mach number of heat addition
$\dot{Q}$	Radiative heating rate
q	Radiative heating per unit mass
p_d	Dynamic pressure
d^*	Nozzle throat diameter
d_t	Test section diameter
A_t	Test section area
T_q	Maximum temperature of heat addition
$h_{0,i}$	Plenum stagnation enthalpy
$h_{0,f}$	Test section stagnation enthalpy
L	Total nozzle length
L_M	Nozzle length over which heat is added at constant Mach number

Introduction

THE RDHWT concept is based upon the idea that if the total stagnation enthalpy required in the test section of a wind tunnel is generated not only in the plenum, but also by the addition of heat from a radiative source to the supersonic portion of the flow, the maximum static temperature of the flow can be substantially lowered, and the operational envelope can be considerably extended. An introduction to the concept may be found in [1], and the detailed studies of the concept which provide the basis for this paper may be found in [2]. High energy (≈ 1 MeV) electron beam radiation, laser radiation (specifically the high powered HF laser absorbed by CO_2 in air), and microwaves, have been considered as radiative sources. Effort has been focused particularly on the first two, since microwave absorption requires some additional energy source to achieve the necessary conductivity, and there is a difficulty in introducing high power microwaves through the boundary layer without breakdown.

Recently the concept has been investigated using a hierarchy of models ranging from pure thermodynamics to the full compressible Reynolds Averaged Navier Stokes equations with algebraic turbulent closure, fully coupled with models for laser beam energy addition, and indirectly coupled with a Monte Carlo simulation for electron beam energy addition.

The resulting analyses facilitated by these models have been central to the development of the concept. The thermodynamic models allow detailed envelopes of idealized operation to be defined, as well as illuminating functional relationships between key parameters such as required powers, stagnation conditions, throat sizes, and test conditions. The idealized thermodynamic models also provide goals for the synthesis of designs in one dimension. Such synthesis provides insight into the realizability of the thermodynamic models while constrained by fluid mechanical considerations and the absorption physics of a candidate source. In particular this line of analysis has been extensively carried out in the case of electron beam radiation.

Many issues arise which require two-dimensional or axisymmetric models, including boundary layer con-

*Graduate Student, Mechanical & Aerospace Engineering, Princeton University.
†Professor, Mechanical & Aerospace Engineering, Princeton University. Senior Member AIAA.
‡Professor, Mechanical & Aerospace Engineering, Princeton University. Senior Member AIAA.

AMERICAN INSTITUTE OF AERONAUTICS AND ASTRONAUTICS PAPER 2000-2274

siderations and the stability of coupled flow-radiation systems. A two-dimensional and axisymmetric flow solver which computes both steady and unsteady, inviscid, viscous, and turbulent flows, which incorporates equations of state at high pressure as well as models for radiative heat addition, has also been developed and utilized extensively. Results in this case include insights into the stability of laser based energy addition, the behavior of laser beam propogation in the presence of boundary layers, at the conditions typical of the RDHWT, and predictions for both laser and electron beam experiments in the range of 10 - 60 kW [3]. In the course of this development, an integral model for the turbulent boundary layer which incorporates the law-of-the-wall was developed, implemented, validated, and utilized. This integral model makes explicit calculation of unsteady flows at high Reynolds numbers possible [2]. It is also being used for predictions of heat transfer and recovery temperature in studies of throat survivability.

Thermodynamic Models

The idealized thermodynamic model for RDHWT operation may be illustrated on a Mollier diagram, as shown in Fig. 1b. The process consists of four legs: 1) isentropic expansion from stagnation conditions to $M_q > 1$, 2) heat addition at constant Mach number M_q, 3) heat addition at constant temperature, T_q, and 4) isentropic expansion to test conditions. These choices provide the highest test section Mach number corresponding to given static (atmospheric) conditions in the test section, while preventing both thermal choking and adverse pressure gradients [2].

With this idealized thermodynamic path it is now possible to calculate in a rather straightforward manner the achievable Mach number at a final test state given a set of initial (plenum) conditions. We can simply integrate $T\,ds$ along the chosen path until the desired final entropy is reached, to arrive at a heat added per unit mass q. The final Mach number can then be calculated from $h_{o,f} = h_{o,i} + q$ and $h_0 = h + \frac{1}{2}u^2 = h + \frac{1}{2}M^2a^2$, where $h_{o,i}$ and $h_{o,f}$ are the plenum (initial) and test section (final) stagnation enthalpies, respectively, where h and a are known from the final atmospheric static conditions. Several other important quantities are uniquely defined by this same calculation. The required heat addition per unit area of the test section may be computed from

$$\frac{\dot{Q}}{A} = \frac{\dot{m}q}{A} = \rho a M q$$

where the quantities on the right hand side are known. The throat diameter normalized with respect to test section diameter

$$\dot{m} = \rho^* a^* A^* = \rho a M A$$

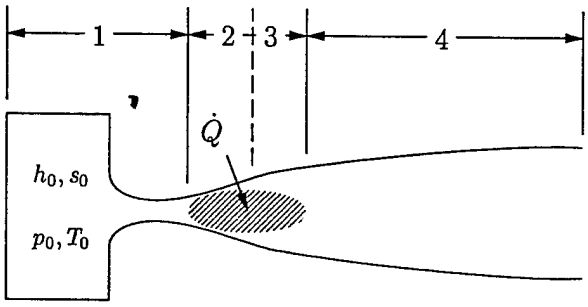

a) Concept Schematic

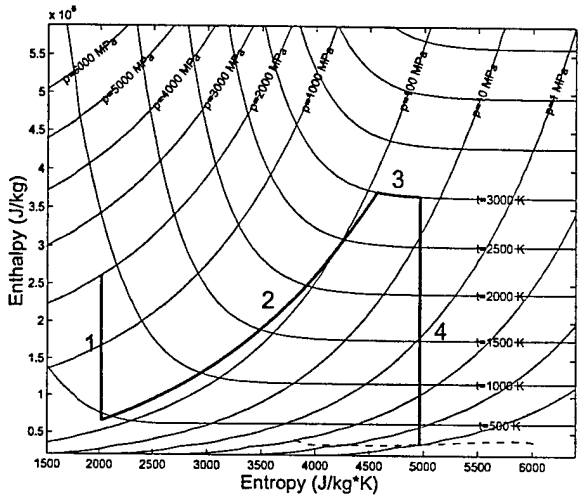

b) Concept Thermodynamics

Fig. 1 RDHWT Concept

$$\frac{d^*}{d_t} = \sqrt{\frac{\rho a M}{\rho^* a^*}}$$

is easily determined as well. Both of these parameters provide important guidance with respect to possible design choices. The required heating power places limits on the size of the test section area, and the throat size provides nominal focusing requirements for radiative sources of energy. The computation of thermodynamic states at high pressure is accomplished using the National Institute of Standards and Technolog (NIST) database for air, "N14" [4].

Two summary figures which incorporate the results of this thermodynamic analysis are shown in Figures 2 and 3. They summarize the relevant information on $p_0 - T_0$ and $M - alt.$ diagrams respectively. In particular, lines of constant Mach number on the $p_0 - T_0$ diagram show the initial possible states which achieve a given performance goal, and provide critical information for the design of a high pressure delivery system, including radiative heating requirements, and throat size restrictions. The $M - alt.$ diagram emphasizes tradeoffs with respect to achievable dynamic pressures in the test section for a given Mach number and set of stagnation conditions.

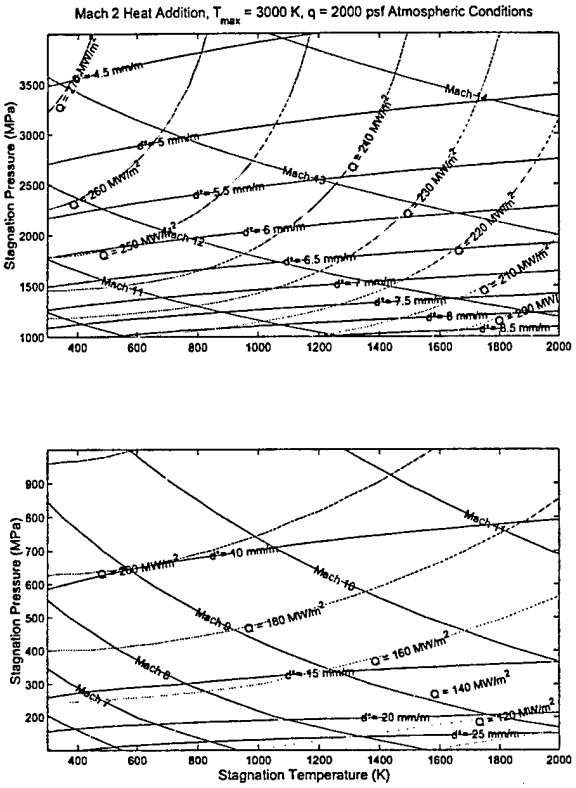

Fig. 2 Idealized Performance: Mach 2 Heating, T_q=3000 K, p_d =2000 psf. Isolines of Required Power per Unit Area Test Section, $\dot{Q}/A_t$, Achievable Mach Number, and Required Throat Diameter per Unit Diameter Test Section, d^*/d_t.

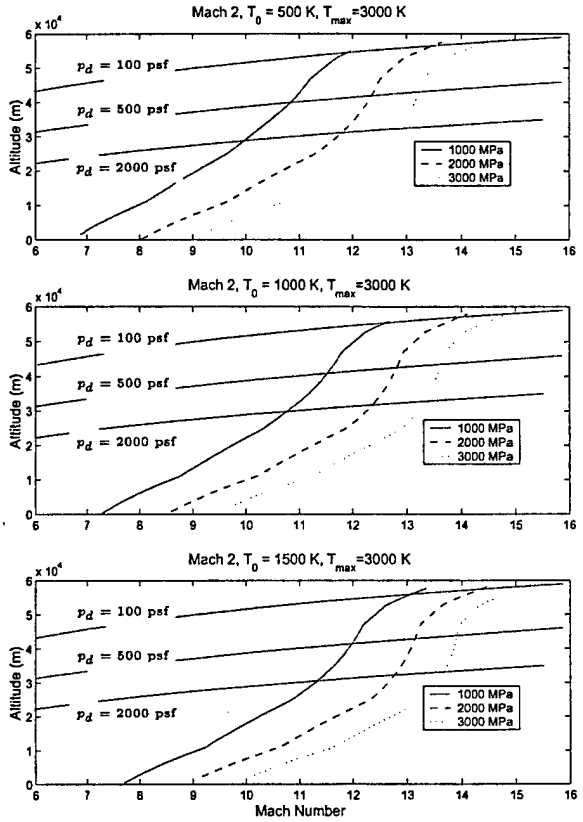

Fig. 3 Idealized Performance: M_q = 2, T_q=3000 K. Envelopes of achievable Mach number at atmospheric altitudes for p_0 = 1000, 2000, 3000 MPa and T_0 = 500, 1000, 1500 K.

One Dimensional Coupled Models and Nozzle Shape Design

The thermodynamic model assumes that heat may be added in a completely arbitrary way, i.e., in any amount at any thermodynamic state. This is in general not possible, since the heating processes are constrained by the radiation absorption physics. In addition, the nozzle shape has a large influence on the flow thermodynamics, and it is constrained by fluid mechanical considerations, e.g., its shape in the supersonic regime must at the very least be monotonic in area. At the next level of complexity, a model which couples one-dimensional gasdynamics with absorption physics of candidate sources was developed to investigate the existence of solutions which approximate the idealized thermodynamic theory. This model solves the quasi-one-dimensional Euler equations in conservative form using a finite volume discretization in space [2], a 4-stage Runge-Kutta discretization in time [2], and scalar flux limited dissipation utilizing the Jameson SLIP model [5] [6] with a Van Leer flux limiter.

Two models of radiative heat addition are employed within this flow solver. The first was developed for use with laser applications and is a simple Beer's Law formulation, which relies on the knowledge of an absorption coefficient which depends on local fluid properties. The second is a one-dimensional model for electron beam energy deposition developed by R.J. Lipinski [7].

These components form the basis for a design method which generates nozzle shapes that minimize a metric for the deviation from the ideal thermodynamics, and hence achieve minimal deviation from the optimal test section Mach number. This metric, or objective function, is chosen to be

$$\mathcal{I} = \frac{1}{L_M M_q}\int_0^{L_M} \Delta M \, dx + \alpha \frac{1}{L T_q}\int_0^{L} \Delta' T \, dx + \gamma P_0/\dot{Q}, \tag{1}$$

where

$$\Delta M = \begin{cases} M - M_q & : \quad M > M_q \\ \beta_M (M_q - M) & : \quad M < M_q, \end{cases}$$

and

$$\Delta' T = \begin{cases} \beta_T (T - T_q) & : \quad T > T_q \\ T_q - T & : \quad T < T_q; x > L_M \\ 0 & : \quad T < T_q; x < L_M. \end{cases}$$

The first term integrates the deviation from constant Mach number, with a weighting factor β_M to preferentially penalize low Mach numbers (to avoid choking).

The second term integrates excess temperature over the entire length of the nozzle with a weighting factor β_T, as well as integrating low temperatures over the constant temperature length of the nozzle. The final term simply assures that the incident radiative power is absorbed by the flowfield. The relative weighting of the three terms is achieved by choosing the factors α and γ. In practice a discrete representation of Eq. 1 is employed [2]. The variables which are to be varied in a search for the minima of Eq. 1 are the radii of a set of "control points" $\mathcal{R}_k$ which are interpolated to form a nozzle shape, which is then discretized to form the flow and radiation solving mesh. The interpolation from control points to nozzle shape utilizes the cubic interpolant construction of Fritsch and Carlson [8] to retain the important property of monotonicity.

The optimization method employed [2] is the downhill simplex search method of Nelder and Mead [9], which guarantees a local minimum of the system. It is not the most efficient method available, but robustness was favored in this choice over efficiency, since evaluation of the objective function is not particularly expensive numerically, and this method has the distinct advantage of requiring only values of $\mathcal{I}$, as opposed to values and gradients of $\mathcal{I}$.

Both the flow solver and the design method have been extensively validated against test cases [2] which exhibit known behavior. It turns out that the design space generated by this objective function with electron beam energy addition exhibits multiple minima over a reasonable design domain. Consequently, care must be taken in initializing the simplex search. A simple heuristic based on sequentially searching spaces of higher dimension has been found to work well in practice [2]. Solutions which minimize the objective function with few degrees of freedom are used as initial conditions for searches with increasing degrees of freedom.

These methods have been employed in the initial phases of design of a facility capable of Mach 12 operation utilizing a 1 MeV electron beam energy source. The thermodyanamic theory of the first section was employed to choose a set of stagnation conditions capable, in theory, of achieving Mach 12 test conditions with a dynamic pressure of p_d=2000 psf ($\approx$ .1 MPa), and with no restrictions on static temperature reached during heating. The chosen conditions were 2000 MPa and 1000 K.

As can be seen from Figs. 4 and 5, reasonable designs can be synthesized within the constraining engineering parameters. The "efficiency" of this particular design with no static temperature limitation is quite high, with a final test section Mach number of 12.3, as compared to the idealized thermodynamic model value of 12.4.

If the static temperature during heating is limited to 2500 K, the resulting design is shown in Figs. 6 and 7.

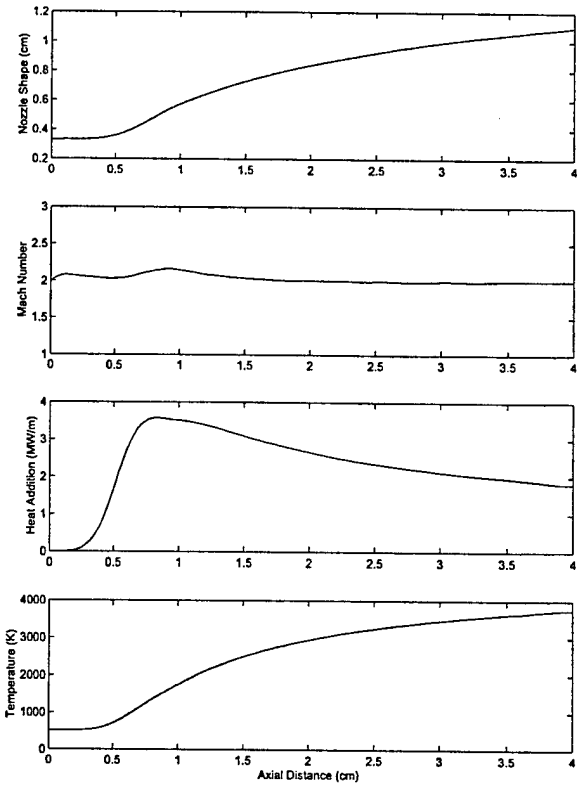

Fig. 4 Mach 12 Design axial properties using N=8 control points. 1 MeV electron beam. p_0 = 2000 MPa, T_0 = 1000 K.

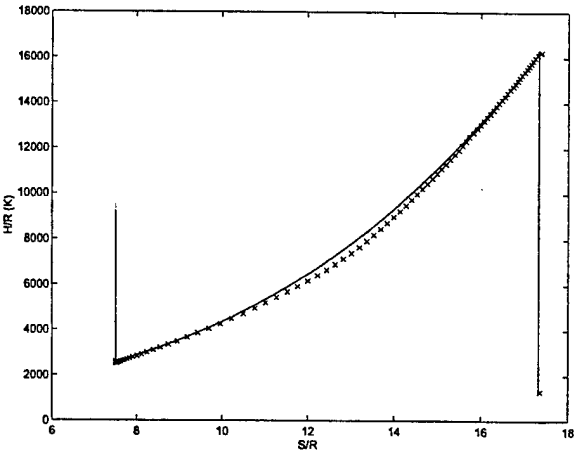

Fig. 5 1 MeV Design Refined to 8 design points: Mollier Diagram. 'x' - Modeled Path. '-' Idealized Path. Modeled M_f = 12.3, Ideal M_f = 12.4.

This case is much more difficult for the optimizer, as the criteria for heat addition changes discontinuously from constant M to constant T. Some "overshoot" of the desired Mollier diagram path is evident in Fig. 7, which results in heat addition at $T > T_q$, which in turn results in insufficient entropy generation to reach precisely the desired test conditions. Nevertheless, the design and solution form a quite reasonable starting

point for a more detailed design process.

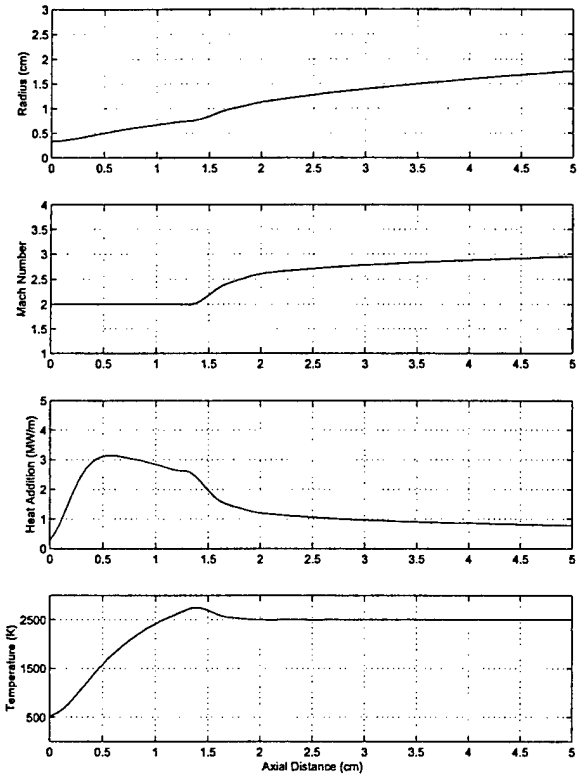

Fig. 6 1 MeV Design with $T_q = 2500$ K refined to 32 design points.

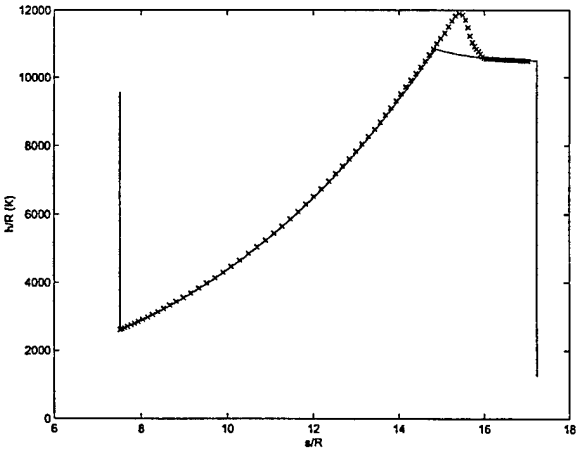

Fig. 7 1 MeV Design with $T_q = 2500$ K. refined to 32 design points: Mollier Diagram. 'x' - Modeled Path. '-' Idealized Path.

In particular, multidimensional effects of electron beam heating are critical considerations and require a fully coupled electron beam modeling capability to explore fully and efficiently. The current two-dimensional electron beam modeling capability is discussed in a following section.

Two Dimensional Coupled Models

The next level of complexity to be investigated is to examine effects that can be attributed to the system being multi-dimensional. Both two-dimensional heating and the effects of viscous boundary layers have important consequences for the design of a RDHWT. Stability of the flowfield with a coupled radiative source of heat in multidimensions is a primary concern, especially in the case of laser radiation.Another critical issue is the potential for the radiative source to impinge upon the walls of the nozzle, resulting in a destructive heat flux. These considerations motivated the development of a two-dimensional Reynolds Averaged Navier Stokes solver which incorporates equations of state at high pressure, to be used in conjunction with models for laser and electron beam radiation in two dimensions. The models are constructed such that the two dimensions may have either a planar or an axisymmetric form, to be chosen appropriately as required.

The full governing equations to be discretized are the Navier-Stokes equations in two dimensions,

$$\frac{\partial \mathbf{w}}{\partial t} + \frac{\partial \mathbf{f}}{\partial x} + \frac{\partial \mathbf{g}}{\partial y} + j\mathbf{h} = \frac{\partial \mathbf{R}}{\partial x} + \frac{\partial \mathbf{S}}{\partial y} + j\mathbf{T} + \mathbf{W}$$

where

$$\mathbf{w} = \begin{pmatrix} \rho \\ \rho u \\ \rho v \\ \rho E \end{pmatrix} \quad \mathbf{f} = \begin{pmatrix} \rho u \\ \rho u^2 + p \\ \rho uv \\ \rho uH \end{pmatrix}$$

$$\mathbf{g} = \begin{pmatrix} \rho v \\ \rho uv \\ \rho v^2 + p \\ \rho vH \end{pmatrix} \quad \mathbf{h} = \frac{1}{y}\begin{pmatrix} \rho v \\ \rho uv \\ \rho v^2 \\ \rho vH \end{pmatrix}$$

$$\mathbf{R} = \begin{pmatrix} 0 \\ \tau_{xx} \\ \tau_{xy} \\ \tau_{xx}u + \tau_{xy}v - q_x \end{pmatrix} \quad \mathbf{S} = \begin{pmatrix} 0 \\ \tau_{yx} \\ \tau_{yy} \\ \tau_{yy}v + \tau_{yx}u - q_y \end{pmatrix}$$

$$\mathbf{T} = \frac{1}{y}\begin{pmatrix} -\rho u \\ \tau_{xy} \\ \tau_{yy} - \tau_{\theta\theta} \\ u\tau_{xy} + v\tau_{yy} - q_y \end{pmatrix} \quad \mathbf{W} = \begin{pmatrix} 0 \\ 0 \\ 0 \\ \dot{q} \end{pmatrix}$$

and where the total energy is $E = e + \frac{1}{2}(u^2 + v^2)$ with e denoting internal energy; the total enthalpy is $H = E + p/\rho$; p is the pressure with $p = p(\rho, e)$ and $\dot{q}$ is the volumetric heating source term. The components of the viscous stress tensor τ are given by

$$\tau_{xx} = \mu\left[\frac{4}{3}\frac{\partial u}{\partial x} - \frac{2}{3}\frac{\partial v}{\partial y} - j\frac{2}{3}\frac{v}{y}\right]$$

$$\tau_{yy} = \mu\left[\frac{4}{3}\frac{\partial v}{\partial y} - \frac{2}{3}\frac{\partial u}{\partial x} - j\frac{2}{3}\frac{v}{y}\right]$$

$$\tau_{\theta\theta} = \mu\left[-\frac{2}{3}\left(\frac{\partial u}{\partial x} + \frac{\partial v}{\partial y}\right) + \frac{4}{3}\frac{v}{y}\right]$$

$$\tau_{xy} = \mu \left(\frac{\partial u}{\partial y} + \frac{\partial v}{\partial x} \right)$$

The factor j allows the equations to take the form appropriate for axisymmetric geometries when $j = 1$ and for planar geometries when $j = 0$.

These governing equations are solved [2] using a cell-centered finite volume discretization in space, both Runge-Kutta and Jameson multi-stage discretizations in time, and scalar flux limited dissipation using the Jameson SLIP model with a Van Leer limiter [5] [6]. The 4th order Runge-Kutta integration method is used when time accurate solutions are sought, and a 5-stage Jameson scheme with coefficients optimized for convergence are used to obtain steady-state solutions. For steady-state calculations, a number of convergence acceleration techniques are applied, including local time stepping and FAS multigrid [2].

Electron Beam Modeling

The electron beam model in two-dimensions incorporates the flow solving capability just described with a heating field which is provided by the Monte-Carlo electron beam solving code CYLTRAN. This code is described in [10] and is being used by Dr. R.J. Lipinski of Sandia National Laboratories in conjunction with the authors. The code follows the trajectory, through the nozzle, of a large number of electrons (typically 10^5) in a confining magnetic field, which is imposed by currents about the axis of the tunnel, with magnetic field lines approximately parallel to the walls of the nozzle. Collisions are modeled via cross-sections for the gas molecules, and the energy lost to the gas through collisions is found. This energy provides a heating source term in the Navier-Stokes or Euler equations of fluid flow. The two solutions are iterated to a steady state by transferring density fields from the flow solution to the electron beam solver, and heat deposition fields from the electron beam solver to the flow solver. Typically, 4 or 5 solutions of each system are required to obtain a reasonably converged steady-state coupled solution.

This methodology has been used to design and predict the results of several proof-of-principle experiments involving electron beam energy addition to supersonic flows. The results of the latest electron beam experiments involving 26 kW and 55 kW of electron beam power may be found in [3].

Laser Energy Addition

The laser is modeled via a raytracing algorithm. The raytracing algorithm is fully coupled with the flow solver so that the entire system may be simulated for unsteady interaction calculations. The laser raytracing algorithm employed is due to More [11]. The physical basis for the method is the theory of geometrical optics, in which gradients of the index of refraction result in a beam steering effect via Snell's law

$$\frac{\partial \mathbf{k}}{\partial s} = \frac{\omega}{c} \nabla n \tag{2}$$

and the geometrical optics equation

$$\frac{\partial \mathbf{r}}{\partial s} = \frac{c}{\omega n} \mathbf{k}. \tag{3}$$

where $\mathbf{r}$ is a position vector, $\mathbf{k}$ is the propagation vector of the beam, ω is the frequency of the laser light, and c is the speed of light. As the ray propagates through the medium, it transfers heat to the flowfield via Beer's Law

$$\frac{\partial I}{\partial s} = -\alpha I$$

where I is the beam power, and α is a coefficient of absorption relevant to the particular laser as well as the medium through which it is propagating. The index of refraction for air is computed as

$$n = \sqrt{1 + \alpha_n \rho} \tag{4}$$

where $\alpha_n = 1.25 \times 10^{-3}$ m^3/kg, and n is the index of refraction. These basic equations are the foundation of the method. Details of the implementation and validation of the raytracing method are contained in [2].

With a realistic nozzle shape, there are the complexities of the streamwise gradients generated by the expansion, in addition to the refraction of the rays near the wall. Intuitively, the path of the rays in the resulting flow field is highly unsteady and each ray is refracted by the wall boundary layer and "randomly" traverses the whole flow between the boundary layers , thereby heating the flow more or less uniformly in the mean. This is a very significant result, in that it provides the one-dimensional analysis and design with a firm basis for extrapolation to the multidimensional system in the case of laser radiation. The case with which to demonstrate this point is the flow through an axisymmetric, conical, supersonic nozzle, which is a simple model of the heating section of an RDHWT. The stagnation pressure is 3000 atm, which generates sufficient density for a strong coupling between the flow field and ray path. The exit Mach number for unheated flow is approximately 5.7. At $t = 0$, the laser beam is "turned on" and directed into the exit of the nozzle. In the one-dimensional case, the laser fills the nozzle (by definition). In the two-dimensional case, the laser is of width $\alpha_0 \delta_L = .088$, and power $\dot{Q}/\frac{1}{2}\rho^* c^{*3} A^* = 1$, where starred quantities refer to throat conditions. α_0 is a nominal absorption coefficient, and δ_L is nominal beam width. The resulting Mach number histories in the two cases are shown in Figure 8. Though the transients differ, the final quasi-steady behavior is very nearly the same. The one-dimensional solution is steady, whereas the two-dimensional solution exhibits the highly unsteady ray

paths found when the refractive index is sufficiently large and dependent on the density. The details of this calculation and the rapid variation of the ray paths were described in [12].

In order to further understand the nature of the unsteadiness and the characteristics of the flow that is generated, we can examine time histories of flowfield properties in the unsteady regime as a function of the system parameters. We consider the simplest case of a uniform supersonic flow and a single laser beam propagating upstream and initially parallel to the flow direction. Depending on the physical parameters, we find an essential instability leading to a periodic unsteadiness.

A typical time history of Mach number in the unsteady regime is shown in Figure 9. At $t = 0$, the laser beam is "turned on," and the heat addition depresses the local Mach number at the measurement point. After several characteristic times $tc_0\alpha_0$, a periodic fluctuation is evident, with a well defined frequency of oscillation. This fluctuation is the result of unsteady heat addition upstream of the measurement point. This unsteady heat addition corresponds to the path of the laser sweeping back and forth in a periodic manner. A sequence of 12 images, ordered from left to right, and top to bottom, which display the beam path unsteadiness is shown in Figure 10. Plotted also behind the beam path are contours of density. The interaction of the density field and the beam path is not obvious from these images. Figure 11 provides some additional insight. With the same sequence of images, but zoomed into the region of most significant heat addition, the derivative of the index of refraction in the y direction is computed, and regions of positive and negative dn/dy are displayed as white and grey regions, respectively. The sequence of events which control the oscillation can now be more easily identified. When the beam path is in regions of $dn/dy < 0$, it will bend in the negative y direction, and vice versa. In the first frame, the beam is entirely in a region of $dn/dy < 0$. In the time between the first and second frames, there are two major effects that determine the evolution of the system. The first is heat addition along the beam path, and the second is convection of the flowfield. The effect of heat addition is to locally depress the density, which promotes regions of $+dn/dy$ for $y > y_b$, and $-dn/dy$ for $y < y_b$, where y_b is the y location of the beam. As the flowfield is convected downstream, and heat is added, the beam enters a region of $dn/dy > 0$ and starts to be refracted in the $+y$ direction. This process continues until the beam is swept to the other side, where local heat addition and convection again reverse the sign of dn/dy. Two complete oscillations are depicted in the sequence. One perspective of the fundamental cause of the unsteady interaction is the "lag" of the interface separating regions of positive and negative dn/dy behind the position of the laser beam.

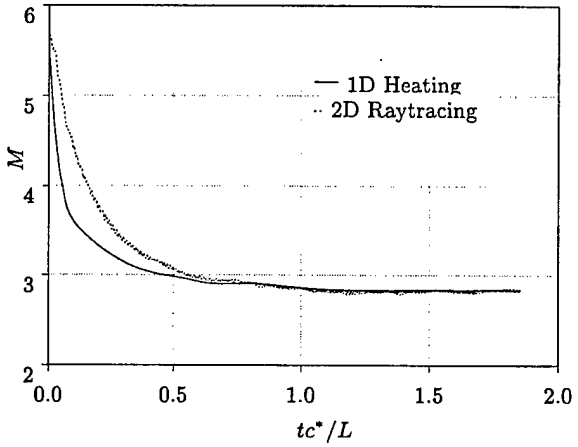

Fig. 8 Inviscid, Supersonic Nozzle Flow - Recovery of One-Dimensional Behavior.

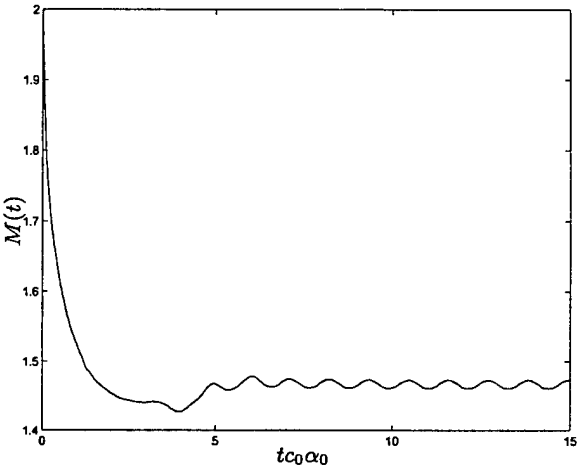

Fig. 9 Representative Periodic Mach Number Time History. $\dot{Q}/\frac{1}{2}\rho_0 u_0^3 \delta_L = 1$, $M = 2$.

When this interface "overtakes" the beam, it is redirected in the opposite direction. This is the source of a new "instability" to our knowledge, and we are still exploring the dimensionless variables which best characterize the resulting frequency and dynamics.

A major feature of these results is that heat addition to an RDHWT by laser beam results in a strong beam steering instability which directs the laser beams into the walls. The preceding calculations assume specular reflection from the wall, with no heat loss. Of course actual wall impingement with beam intensities on the order of MW/cm^2 would be destructive. However, the presence of a hot, low density boundary layer near the wall which would exist under RDHWT conditions provides a gradient in refractive index which refracts the beam away from the walls as it progresses upstream through the nozzle. To repeat the unsteady analy-

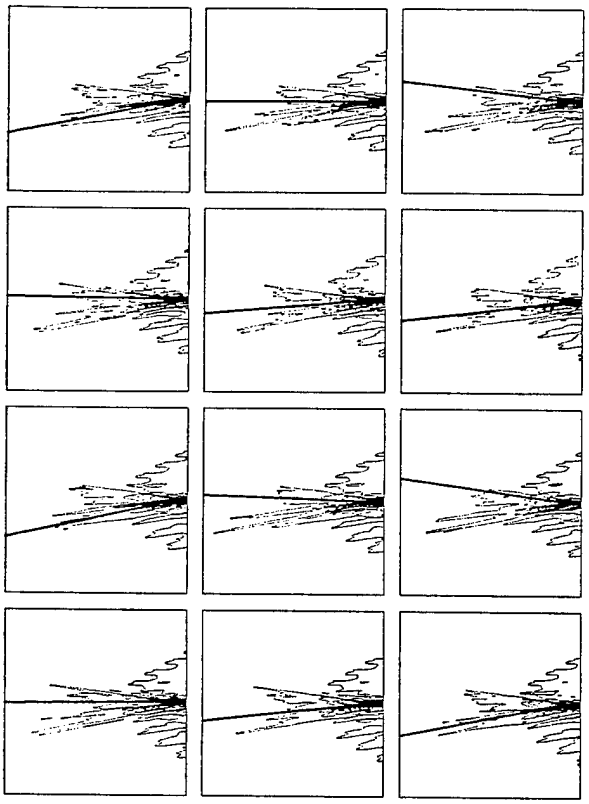

Fig. 10 Unbounded Domain Unsteady Regime - Density Field Through Two Periods of Oscillation. $\dot{Q}/\frac{1}{2}\rho_0 u_0^3 \delta_L = 1$, $n_0 = 1.12$, $M = 2$, $\alpha_0 \delta_L = .073$.

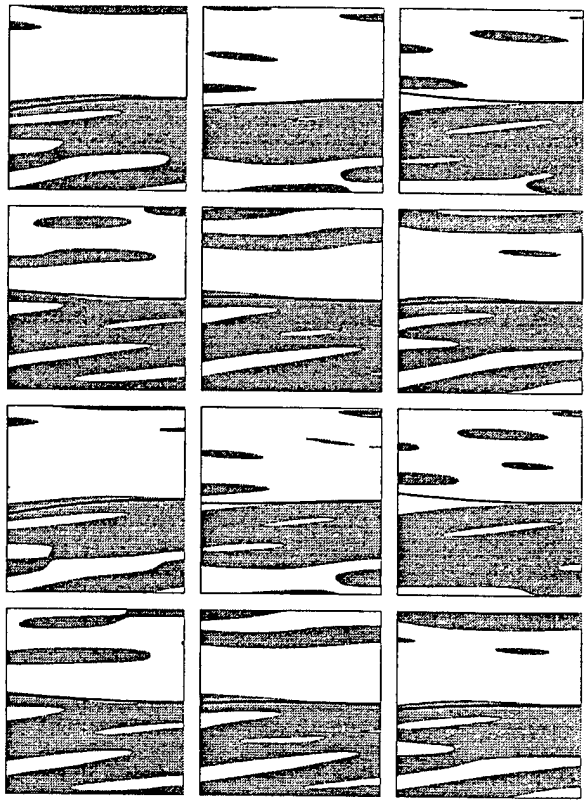

Fig. 11 Unbounded Domain Unsteady Regime - Sign of dn/dy. White regions - $dn/dy > 0$. Grey regions - $dn/dy < 0$. $\dot{Q}/\frac{1}{2}\rho_0 u_0^3 \delta_L = 1$, $n_0 = 1.12$, $M = 2$, $\alpha_0 \delta_L = .073$.

sis of the previous section with a viscous, turbulent boundary layer using the methodology developed thus far is not feasible due to its extreme computation cost for these very high Reynolds numbers. This is due to the restrictions on the time step near the wall which must be imposed globally to achieve time accuracy. A wall function method has been developed to overcome this problem, but a first step is to examine the solution at the first instant in time when the laser beams are "turned on." A steady-state solution of RANS for these conditions, though expensive, is entirely feasible due to the use of the convergence acceleration methods, in particular the multigrid technique. The unheated solution for the same nozzle analyzed in the previous section is solved using the RANS equations and the Baldwin-Lomax turbulence model. The resulting density field is used in an uncoupled, one pass raytracing calculation. The resulting beam path is shown in Figure 12. As hypothesized, the gradients of refractive index in the boundary layer result in total internal reflection. This is shown on an expanded vertical scale to illustrate the steering effect.

While this is an encouraging result for the use of lasers as a source of heat for the RDHWT, the dynamics of the resulting coupled system cannot be determined from this result. Heat addition in the boundary

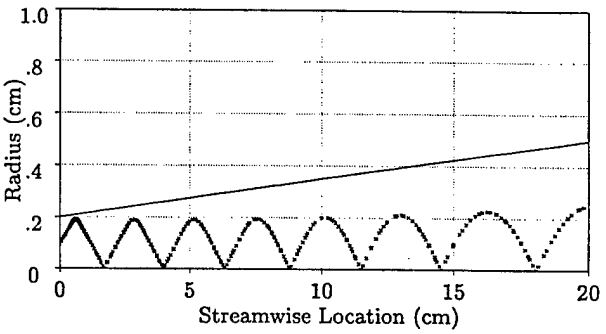

Fig. 12 Total Internal Reflection of Laser Beam in Unheated, Turbulent, Supersonic Boundary Layer. $p_0 = 3000$ **atm. Vertical Scale Expanded** $\times 10$.

layers will generate pressure perturbations which may have adverse effects such as boundary layer thickening or even separation, and would certainly affect the wall recovery temperature. In order to make unsteady calculations feasible, it is necessary to find an alternative way of computing the physics of the turbulent boundary layer to an approximation which is still accurate enough for our purposes, but much less expensive numerically.

Wall Function Technique for the Near Wall Flow

Fully resolved turbulent boundary layer calculations using a RANS model require a mesh spacing near the wall that will capture the laminar sublayer. As the Reynolds number is increased, this layer becomes exceedingly thin, necessitating a very fine mesh spacing normal to the wall to resolve the gradients, which results in cells of a very large aspect ratio. When an explicit time integration scheme is employed on such a mesh, the time step required for numerical stability in the normal direction becomes exceedingly small compared to the time step in the other coordinate directions, limiting the rate of convergence to steady-state, or the time scale over which unsteady behavior may be examined. By taking advantage of the "law of the wall" for flow in the near wall layer, and extending it to compressible flows of real gases, an analytical model has been developed and substituted for this region. This has reduced the cost of high Reynolds number wall flow calculations (typically 10^{10}/m) by up to three orders of magnitude.

The fundamental idea to overcome this limitation is to substitute an analytical form for the boundary layer near the wall. For incompressible flows the "law of the wall" is commonly expressed as the "log law"

$$u^+ = \frac{1}{\kappa} \ln y^+ + B$$

where $u^+ = u/u_\tau$, $y^+ = y u_\tau / \nu$, and $u_\tau = \sqrt{\tau_w/\rho}$, κ is the Kármán constant and B is another constant. For incompressible flow the idea is to use this analytical form near the wall and to find u_τ by matching this near wall flow to the rest of the flow at some location y^+ which imposes a new set of boundary conditions for the numerical boundary. In order to employ this idea for flows of RDHWT interest, the "law of the wall" must first be extended to the case of compressible flows of a real gas with and without heat transfer and for arbitrary equations of state.

The Boussinesq hypothesis that the turbulent stress is

$$\tau_t = -\rho \overline{u'v'} = \rho \nu_t \left(\frac{\partial \overline{u}}{\partial y} \right) \tag{5}$$

requires an expression for the eddy viscosity ν_t. The Prandtl mixing length hypothesis assumes that ν_t is the product of a mixing length, l, and a velocity scale. If this velocity scale is, as Kármán proposed, $l \frac{\partial \overline{u}}{\partial y}$, we have

$$\tau_t = -\rho \overline{u'v'} = \rho l^2 \left(\frac{\partial \overline{u}}{\partial y} \right)^2 . \tag{6}$$

Furthermore, if the mixing length scale is taken proportional to the distance from the wall, i.e., $l = \kappa y$, where is κ is known as the Kármán constant, equation (5) is then

$$\tau_t = \rho (\kappa y)^2 \left(\frac{\partial \overline{u}}{\partial y} \right)^2 . \tag{7}$$

Finally, it is assumed that $\tau_t = \tau_w$, which implies a small dp/dx. Equation (7) may be transformed to "wall coordinates" $u^+ = \overline{u}/u_\tau$ and $y^+ = y u_\tau / \nu_w$ and rearranged to give:

$$\frac{\partial u^+}{\partial y^+} = \left(\frac{\rho_w}{\rho} \right)^{1/2} \frac{1}{\kappa y^+} . \tag{8}$$

The density profile may be related to the velocity through the Crocco-Busemann relation

$$\frac{h}{h_w} = \left(\frac{H_e}{h_w} - 1 \right) \frac{u}{u_e} - \frac{u^2}{2 h_w} + 1$$

which in wall coordinates is

$$\frac{h}{h_w} = \left(\frac{H_e}{h_w} - 1 \right) \frac{u^+}{u_e^+} - \frac{u_\tau^2}{2 h_w} (u^+)^2 + 1.$$

With the additional assumptions of constant c_p and Z in the near wall layer, we have the following expression for the density in the near wall layer

$$\frac{\rho_w}{\rho} = \frac{h}{h_w} = \left(\frac{H_e}{h_w} - 1 \right) \frac{u^+}{u_e^+} - \frac{u_\tau^2}{2 h_w} (u^+)^2 + 1. \tag{9}$$

By defining heat transfer and compressibility parameters

$$\alpha = \left(\frac{H_e}{h_w} - 1 \right) \frac{1}{u_e^+}, \qquad \beta = -\frac{u_\tau^2}{2 h_w},$$

and substituting into (8), we arrive at the differential form of our complete compressible law of the wall

$$\frac{\partial u^+}{\partial y^+} = \frac{1}{\kappa y^+} \left(1 + \alpha u^+ + \beta u^{+2} \right)^{1/2} . \tag{10}$$

This equation is indeed separable and an exact solution is

$$u^+ = \frac{1}{2\beta} \left\{ \alpha + \sqrt{\alpha^2 + 4\beta} \sin \left[A + \frac{\sqrt{\beta}}{\kappa} \ln \left(\frac{y^+}{y_0^+} \right) \right] \right\},$$

where

$$A = \arcsin \left(\frac{2\beta u_0^+ - \alpha}{\sqrt{\alpha^2 + 4\beta}} \right) .$$

This equation may be solved for u_τ by matching to the Baldwin-Lomax calculation for the outer layer at every streamwise station.

Recovery Temperatures and Heat Transfer

Some essential results from the computation of high Reynolds number compressible boundary layers are the wall recovery temperature and heat transfer rates. In particular, such calculations allow the examination of real gas effects on these quantities. Real gas effects have a large impact on wall recovery temperatures, as can be seen in Fig. 13. Plotted in this figure are the wall temperatures for a adiabatic flat plate flow of air with a freestream density of 700 kg/m^3. The wall recovery temperature is well in excess of the freestream

stagnation temperature. For an ideal gas, the recovery temperature is much closer to the freestream stagnation temperature. This result also illustrates the accuracy of the wall function method, with deviations in T_w/T_∞ being less than 10% from the fully resolved case.

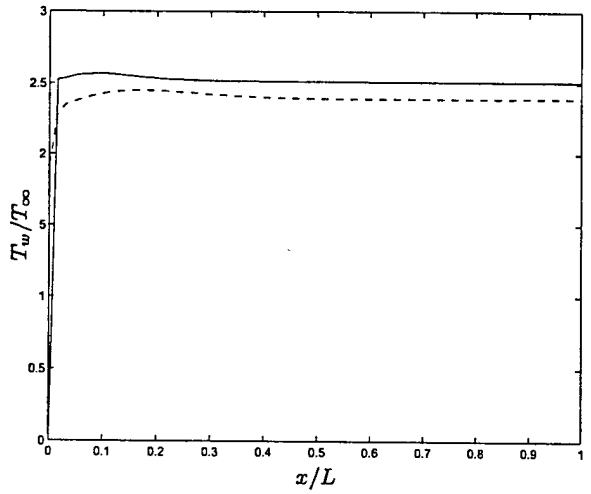

Fig. 13 Wall Recovery Temperature at High Density. $\rho_\infty = 700$ kg/m^3. $Re_L = 1.2 \times 10^{10}$. $M = 1.1$. '–' **- Wall function profile. '...' - Fully Resolved Profile. Fully Resolved Mesh - 64 × 128. Wall Function Mesh - 64 × 96.**

When the temperature of the wall is prescribed, there is heat transfer to or from the wall. Figure 14 is an example calculation of wall heat transfer rates in flows of a real gas at very high Reynolds number, where $T_w = T_\infty$. Again, the accuracy of the wall function method gives results which deviate less than 10% from the fully resolved calculation.

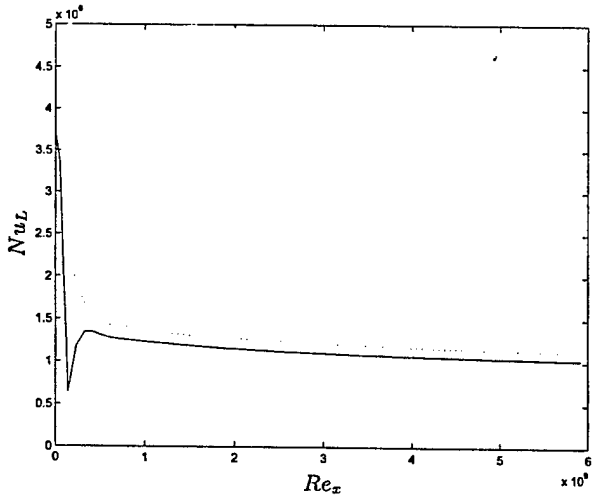

Fig. 14 Nusselt Number for Real Gas Flow. $M = 1.1$. $Re_L = 5.9 \times 10^9$. $T_w = T\infty$. '–' **- Fully resolved result. '...' - Wall Function Result. Fully Resolved Mesh - 64 × 128. Wall Function Mesh - 64 × 96.**

Concluding Remarks

With the current focus shifting towards electron beam energy addition as a candidate source of energy for the RDHWT, the integration of electron beam and flow solving capability must now move forward. Coupled unsteady solutions will provide insight into the stability issues directly related to the transverse variations in local heat deposition. While the electron beam has the advantage of allowing heating profiles which are kept away from the walls of the nozzle, this raises critical questions about the stability of such a flowfield as it is strongly expanded out to hypersonic Mach numbers. Such investigations are the current focus of the predictive and modeling research effort.

The capabilities described herein have not only been applied to conceptual investigations as reported here, but also to experimental development and predictions [3] [13] [14] [15] [16]. The utility of such predictive capability has been repeatedly proven in the context of the experimental efforts, as well as in the conceptual investigations of large scale facilities. To be understood and predicted, the complexities of the flow and its coupling with radiative sources, at the extreme conditions of the RDWHT, require such models.

Acknowledgement

This work was sponsored by the U.S. Air Force Arnold Engineering Development Center (AEDC) and conducted through the Department of Energy (DOE)-National Energy Technology Laboratory at the Western Environmental Technology Office under DOE Contract Number DE-AC22-96EW96405.

References

[1]Miles, R., Brown, G. L., Lempert, W. R., Yetter, R., Williams, G. J., Bogdonoff, S., Natelson, D., and Guest, J. R., "Radiatively Driven Hypersonic Wind Tunnel," *AIAA Journal*, 1995.

[2]Anderson, R. W., *Numerical Analysis and Design of a Radiatively Driven Hypersonic Wind Tunnel*, Ph.D. thesis, Princeton University, 2000.

[3]Barker, P., Howard, P., Anderson, R., Miles, R., Brown, G., Lipinski, R., Pena, G., and Grinstead, J., "Proof of Principle Energy Addition Experiments for the RDHWT/MARIAH II Hypersonic Wind Tunnel," Tech. Rep. AIAA-00-0688, AIAA Paper, 2000.

[4]Lemmon, E., Jacobsen, R., Penoncello, S., and Friend, D., "Thermodynamic Properties of Air and Mixtures of Nitrogen, Argon, and Oxygen from 60 to 2000 K at Pressures to 2000 MPa," *J. Phys. Chem. Ref. Data*, 1999.

[5]Jameson, A., "Analysis and Design of Numerical Schemes for Gas Dynamics 1, Artificial Diffusion, Upwind Biasing, Limiters and their Effect on Multigrid Convergence," *Int. J. of Comp. Fluid Dyn.*, Vol. 4, 1995, pp. 171–218.

[6]Jameson, A., "Analysis and Design of Numerical Schemes for Gas Dynamics 2, Artificial Diffusion and Discrete Shock Structure," *Int. J. of Comp. Fluid Dyn.*, Vol. 5, 1995, pp. 1–38.

[7]Lipinski, R., "One Dimensional Electron Beam Model," Private Communication.

[8]Fritsch, F. and Carlson, R., "Monotone Piecewise Cubic Interpolation," *SIAM J. Numer. Anal.*, Vol. 17, No. 2, April 1980.

[9]Nelder, J. and Mead, R., *Computer Journal*, Vol. 7, 1965, pp. 308–313.

[10]Habeib, J., Kensek, R., Mehlhorn, T., G.D.Baldez, Seltzer, S., and Berger, M., *ITS Version 3.0: The Integrated TIGER Series of Coupled Electron/Photon Monte Carlo Transport Codes*, Sandia National Labortories, Albuquerque, NM, 1984.

[11]More, R. and Kosaka, K., "Wave-Front Curvature in Geometrical Optics," *Physical Review E*, Vol. 57, 1998.

[12]Brown, G., Ratta, A., Anderson, R., Martinelli, L., Lempert, R., and Miles, R., "Fluid Mechanics in a Radiatively Driven Hypersonic Wind-Tunnel - Predictions and Preliminary Experiment," AIAA Paper 96-2199, Princeton University, June 1997.

[13]Barker, P., Grinstead, J., Morgan, A., Anderson, R., Howard, P., Brown, G., and Miles, R., "Radiatively Driven Wind Tunnel Experiment with a 30kW Electron Beam," AIAA Paper 99-0688, Princeton University, January 1999.

[14]Barker, P., Morgan, A., and Grinstead, J., "Electron Beam Energy Addition Experiment," Tech. rep., Princeton University, 1998.

[15]Morgan, A., Barker, P., Anderson, R., Brown, G., and Miles, R., "Preliminary Experiments in the Development of a Radiatively Driven Hypersonic Wind Tunnel," Tech. rep., AIAA Advanced Measurement and Ground Testing Technology Conference, June 1998.

[16]Raman, K., Anderson, R., Brown, G., Miles, R., and Costantino, M., "An Ultra-High Pressure, Ultra-High Reynolds Number Blowdown Wind Tunnel: Design and Preliminary Experiments," Tech. rep., 38th AIAA Aerospace Sciences Meeting and Exhibit, January 2000.